A PRECISE MEASUREMENT OF THE CP-VIOLATION PARAMETER $Re(\varepsilon'/\varepsilon)$ AND OTHER KAON DECAY PARAMETERS

BY

LAWRENCE K. GIBBONS

AUGUST, 1993

Enrico Fermi Institute

The University of Chicago

Dissertation

A PRECISE MEASUREMENT OF THE CP-VIOLATION PARAMETER $\mathrm{Re}(\varepsilon'/\varepsilon)$ AND OTHER KAON DECAY PARAMETERS

BY

LAWRENCE K. GIBBONS

AUGUST, 1993

THE UNIVERSITY OF CHICAGO

A PRECISE MEASUREMENT OF THE CP-VIOLATION PARAMETER $Re(\varepsilon'/\varepsilon)$ AND OTHER KAON DECAY PARAMETERS

A DISSERTATION SUBMITTED TO
THE FACULTY OF THE DIVISION OF THE PHYSICAL SCIENCES
IN CANDIDACY FOR THE DEGREE OF
DOCTOR OF PHILOSOPHY

DEPARTMENT OF PHYSICS

BY
LAWRENCE K. GIBBONS

CHICAGO, ILLINOIS
AUGUST, 1993

ACKNOWLEDGMENTS

My first thanks go to Bruce Winstein, my advisor. I have gained invaluable insight into both physics and analysis in my work with him. He has also become a good friend over my years in Chicago, and I have greatly enjoyed our time together.

The work presented here is the culmination of the efforts of many people over the last decade. A very solid foundation for this analysis was established by a key group: Y.B. Hsiung, J.R. Patterson, B. Winstein, H. Yamamoto and T. Yamanaka. My special thanks go to Bob Hsiung, with whom I have shared many projects that were made pleasurable by his company and ability, and who has stuck with this analysis to the end. S. Somalwar, B. Tschirhart, B. Winstein, and T. Yamanaka have all made substantial contributions to the final stages of the analysis as well.

Our task could have been much harder were it not for the high quality of the data obtained during our run. My thanks to G. Blair, G.J. Bock, J.C. Brisson, R. Coleman, P. Debu, G.D. Gollin, M. Karlsson, J.K. Okamitsu, V. Papadimitriou, B. Peyaud, K. Stanfield, R. Stefanski, E. Swallow, R. Turlay, B. Vallage, Y.W. Wah, R. Winston, and M. Woods, as well as to those already mentioned, for their efforts in building and maintaining the experiment. Many of these people have also made important contributions to the analysis, as have later additions to the group: A. Barker, R.A. Briere, J. Enagonio, G. Makoff, E. Ramberg, B. Schwingenheuer, S. Somalwar, and B. Tschirhart.

I have greatly appreciated the help of Roy Briere and Bernhard Schwingenheuer over the last few years. We have had many helpful discussions, and during the final stages of writing this document they have generously and patiently acted as my "hands in Chicago" when I was out of town and provided housing when I was in town.

I am grateful to the Province of Alberta and the University of Chicago for fellowships provided over my first several years as a graduate student.

Finally, I would like to thank my parents, Anne and Earl Gibbons, for their unwavering support and their confidence, and Ritchie Patterson, whose friendship has greatly enriched my last few years.

TABLE OF CONTENTS

LIST OF TABLES

LIST OF ILLUSTRATIONS

ABSTRACT

This thesis describes the measurement of several kaon parameters by the E731 experiment at the Fermi National Accelerator Laboratory (Fermilab). The most important measurement was that of the direct CP-violation parameter $Re(\varepsilon'/\varepsilon)$. We have found $Re(\varepsilon'/\varepsilon) = (7.4 \pm 5.2(\text{stat}) \pm 2.9(\text{syst})) \times 10^{-4}$, which is not significantly different from zero. Precise determinations of the K_S lifetime and $K_L - K_S$ mass difference have been made, yielding $\tau_S = (0.8929 \pm 0.0016) \times 10^{-10} s$ and $\Delta m = (0.5286 \pm 0.0028) \times 10^{10} \hbar s$. Finally, new measurements of $\phi_{+-} \equiv \arg(\eta_{+-})$ and of the phase difference $\Delta\phi \equiv \phi_{00} - \phi_{+-}$, have been made. The results, $\phi_{+-} = 42.2° \pm 1.4°$ and $\Delta\phi = -1.6° \pm 1.2°$, help to limit CPT-violating effects in the kaon system. Our new results for Δm and ϕ_{+-} resolve a longstanding discrepancy between the measured value for ϕ_{+-} and the natural phase $\tan^{-1}(2\Delta m/[\Gamma_S - \Gamma_L])$.

CHAPTER 1

INTRODUCTION

The search for symmetries and invariance principles within physical systems has often contributed dramatically to our understanding of those systems. Indeed, some of the greatest insights have stemmed from experiments that have discovered an invariance principle or symmetry when none was expected, such that of Michelson and Morley [1], or have discovered a violation where a symmetry was expected.

In the study of elementary particles and their interactions, the consequences of the search for symmetry have not been inconsequential. Of particular interest in this field are the three discrete symmetries of space inversion or parity (P), charge conjugation (C), and time reversal (T). It has been known for some time [2, 3, 4, 5] that a local field theory which is invariant under proper Lorentz transformations is then invariant under the operation of the product CPT. This CPT symmetry immediately leads to some very basic predictions, such as the equality of the masses, the lifetimes, and the magnitudes of the electric charge for a particle and its antiparticle [6].

One elegant means of preserving the CPT symmetry of particle interactions would be to have interactions that were invariant under each of the three individual operators C, P and T. This belief held firmly until Lee and Yang [7] proposed that parity violation in weak interactions could explain the $\tau - \theta$ puzzle, where two particles seemed to be identical (and were, in fact, the K^+), but were thought to be different because they decayed into two different final states of opposite parity: a 3π state with odd parity and a 2π state with even parity. With the strong evidence for parity conservation in the strong and electromagnetic

interactions that existed at the time, even Lee and Yang seemed hesitant to believe their own hypothesis that the $\tau - \theta$ puzzle was, in fact, an indication of parity violation, stating

> This argument, however, is not to be taken seriously because of the paucity of our present knowledge...

They did suggest, however, that parity nonconservation could be established by the observation of an angular asymmetry in the $\beta-$decay of oriented nuclei, or in an asymmetry in the distribution of angles between the muon and the electron in the sequence of decays $\pi \to \mu + \nu$ and $\mu \to e + \nu + \nu$. This proof was soon after furnished by the celebrated ^{60}Co experiment of Wu *et al.* [8], and shortly thereafter in the pion decay sequence by Garwin *et al.* [9] and Friedman and Telegdi [10]. The confirmation of parity violation led rapidly to the recognition of the $V - A$ nature of the weak interaction, proposed independently by several groups [11, 12, 13, 14].

At the time of the discovery of parity violation, it was recognized that charge conjugation symmetry was simultaneously violated with parity in these experiments. It was soon afterward realized that some of the symmetry of the weak interactions could be restored by considering the operator product CP [15]. The prototypical example of CP symmetry is the neutrino. By operating with the product CP, the physically observed states with a left-handed neutrino and a right-handed antineutrino can be transformed from one to the other. Operating with P or C alone, however, transforms the neutrinos into one of the charge conjugate states, which have not been observed. Kaons again shattered this world-view when in 1964 Christenson, Cronin, Fitch and Turley [16] discovered evidence of CP violation in decays of the long-lived component of the neutral kaon.

It has been almost 30 years since that initial discovery of CP violation, yet we know little more about the true origin of CP violation now than we did at that time. The origin of C and P violation is less a mystery — they arise from the left-handed nature of the interactions of the W boson. While the phenomenon of CP violation can be naturally accommodated within our current understanding of particle interactions (the "Standard Model"), its introduction is via the presence of a somewhat *ad hoc* CP-violating phase, and we still lack the knowledge of the origins of this phase. It is also possible that CP violation

arises from interactions entirely outside of the Standard Model — we currently do not have enough information to exclude this possibility.

This thesis will focus on a new determination of the CP violation parameter $Re(\varepsilon'/\varepsilon)$ in the decay of the K_L meson into two pions. As a byproduct, our experiment is sensitive to many of the fundamental parameters of the neutral kaon system, which will also allow us to probe the validity of the more fundamental CPT symmetry. These parameters include the K_S lifetime (τ_S) and the difference in mass between the K_L and K_S ($\Delta m \equiv m_L - m_S$). We will also measure the phase difference $\Delta\phi \equiv \phi_{+-} - \phi_{00}$ and the phase ϕ_{+-}. The parameters $Re(\varepsilon'/\varepsilon)$, ϕ_{+-}, and $\Delta\phi$ will be defined in the following section.

1.1 Kaon Phenomenology and CP Violation

There exist in the literature many fine reviews of kaon phenomenology, and of CP violation and CPT violation within the $K^0 - \bar{K}^0$ system [17, 18, 19, 20, 21, 22, 23]. This section will cover the basic phenomenology of the neutral kaon system, primarily as the backdrop for our determination of $Re(\varepsilon'/\varepsilon)$. For the sake of clarity, we will assume that CPT is valid during most of this discussion. The implications of CPT symmetry will then be outlined in the following section. Finally, possible sources of CP violation will be examined in the third section, with the emphasis placed on CP violation within the minimal Standard Model.

The K^0 and $\bar{K}^0$ mesons are strangeness eigenstates produced via the strong interaction, and are charge conjugates of each other. It was recognized very early on [24] that the decay of the K^0 into a final state like $\pi^+ + \pi^-$ has several consequences. The most obvious is the observation that the weak interaction responsible for the K^0 decay does not preserve strangeness. What is even more interesting, however, is that the final state of charge conjugate decay is identical to the final state of the original process, which implies that the weak interaction responsible for the K^0 decay mixes the K^0 and $\bar{K}^0$. The mixing can occur through virtual $\Delta S = 2$ transitions like $K^0 \leftrightarrow \pi^+ + \pi^- \leftrightarrow \bar{K}^0$. We would like to examine this system to identify the weak eigenstates, since it is the decay process that defines the particles with definite masses and lifetimes.

In the Wigner-Weisskopf formalism first applied to the $K^0 - \bar{K}^0$ system by Lee, Oehme and Yang [25] and later extended or reformulated by (among others) Wu and Yang [26], Sachs [27], and Bell and Steinberger [28], we begin with an effective second order hamiltonian $\mathbf{H}_{eff}$ operating on a two state system with time-dependent amplitudes a and $\bar{a}$ for the K^0 and $\bar{K}^0$ states, respectively. By necessity, $\mathbf{H}_{eff}$ contains terms second order in the weak hamiltonian in order to incorporate the $\Delta S = 2$ processes that mix the K^0 and $\bar{K}^0$. The Schrödinger equation is then

$$i\frac{d}{dt}\begin{pmatrix} a \\ \bar{a} \end{pmatrix} = \mathbf{H}_{eff}\begin{pmatrix} a \\ \bar{a} \end{pmatrix}. \tag{1.1}$$

$\mathbf{H}_{eff}$ is a 2×2 matrix connecting the K^0 and $\bar{K}^0$ states, which can be divided into two individually hermitian matrices $\mathbf{M}$ and $\mathbf{\Gamma}$, with

$$\mathbf{H}_{eff} = \mathbf{M} - i\mathbf{\Gamma}/2. \tag{1.2}$$

$\mathbf{\Gamma}$ is the absorptive term responsible for the decay of the kaon to the physically accessible states, and hence is dubbed the decay matrix. $\mathbf{M}$ is often called the mass matrix, and its off-diagonal elements would mix the K^0 and the $\bar{K}^0$ states even in the absence of decay (ie., if $\mathbf{\Gamma} = 0$). We wish to find the eigenstates $|K_{L,S}\rangle$ of the effective hamiltonian with definite masses $m_{L,S}$ and lifetimes $\tau_{L,S} = 1/\Gamma_{L,S}$, that is, with a time dependence

$$|K_{L,S}(t)\rangle = e^{-im_{L,S}t}e^{-\Gamma_{L,S}t/2}\,|K_{L,S}(0)\rangle\,. \tag{1.3}$$

Equation 1.1 then becomes the matrix equation

$$\mathbf{H}_{eff}\,|K_{L,S}\rangle = (m_{L,S} - i\Gamma_{L,S}/2)\,|K_{L,S}\rangle \tag{1.4}$$

Were the weak interaction invariant under the operation CP, constructing the weak eigenstates would be trivial since we simply would need to identify the CP eigenstates. The K^0 and the $\bar{K}^0$ are CP conjugate states, but there is an ambiguity in the phase relationship between these two states. Because the strong and electromagnetic interactions are invariant under the operation CP, they do not connect the K^0 and the $\bar{K}^0$ and hence do not define a phase relationship between them. The weak interactions, which violate C

(and CP) do define such a relationship, but only up to a factor of $\exp(-\imath\phi S)$, where S is the strangeness of the kaon under consideration. Thus we have

$$\begin{aligned} CP\left|K^0\right\rangle &= e^{-\imath\phi S}\left|\bar{K}^0\right\rangle = e^{-\imath\phi}\left|\bar{K}^0\right\rangle \\ CP\left|\bar{K}^0\right\rangle &= e^{-\imath\phi S}\left|K^0\right\rangle = e^{+\imath\phi}\left|K^0\right\rangle . \end{aligned} \tag{1.5}$$

The phase ϕ is physically unobservable, so we can choose a convenient convention. Here we will choose

$$CP\left|K^0\right\rangle = \left|\bar{K}^0\right\rangle , \tag{1.6}$$

though one often finds $\phi = \pi$ used in the literature as well. With this phase convention, we can define the two states with definite CP to be

$$\begin{aligned} |K_1\rangle &\sim |K^0\rangle + |\bar{K}^0\rangle \qquad && (CP = +1) \\ |K_2\rangle &\sim |K^0\rangle - |\bar{K}^0\rangle && (CP = -1), \end{aligned} \tag{1.7}$$

which would be the desired weak eigenstates were CP conservation not violated.

The kaon system is quite unique in the sense that there are a limited number of CP eigenstates which are dominant decay modes — the 2π and 3π modes. If the weak interaction conserved CP, then the decay of the CP-odd K_2 state into the CP-even 2π final state would be forbidden. This results in the lifetime of the K_2 being much longer than that of the K_1. A long-lived state was predicted by Gell-Mann and Pais [24], and observed soon after by Lande *et al.* [29] in 1956.

The discovery of Christenson *et al.* [16] in 1964 of the decay of this long lived state into the 2π final state at about the 0.2% level shattered the hope that the weak interaction was at least invariant under CP. Even stronger evidence for the CP-violating nature of this decay[1] arose when the interference of the CP-violating and CP-conserving 2π decay amplitudes was demonstrated in 1965 by Fitch *et al.* [30].

One method of accommodating the observed CP-violation of this decay within the phenomenology is to suppose that each weak eigenstate is close to one CP eigenstate, but contains a small admixture of the opposite eigenstate. In the notation of Sachs [21], the long-lived and short-lived states become

[1] It might have been a different neutral particle with a mass similar to the neutral kaon responsible for the 1964 observation.

$$
\begin{aligned}
|K_S\rangle &= \frac{1}{\sqrt{1+|\epsilon-\bar{\epsilon}|^2}}\left(|K_1\rangle + (\epsilon-\bar{\epsilon})\,|K_2\rangle\right) \\
|K_L\rangle &= \frac{1}{\sqrt{1+|\epsilon+\bar{\epsilon}|^2}}\left(|K_2\rangle + (\epsilon+\bar{\epsilon})\,|K_1\rangle\right).
\end{aligned}
\tag{1.8}
$$

In the K^0 and $\bar{K}^0$ basis, the eigenstates are

$$
\begin{aligned}
|K_S\rangle &= \frac{1}{\sqrt{2(1+|\epsilon-\bar{\epsilon}|^2)}}\left((1+\epsilon-\bar{\epsilon})\,|K^0\rangle + (1-\epsilon+\bar{\epsilon})\,|\bar{K}^0\rangle\right) \\
|K_L\rangle &= \frac{1}{\sqrt{2(1+|\epsilon+\bar{\epsilon}|^2)}}\left((1+\epsilon-\bar{\epsilon})\,|K^0\rangle - (1-\epsilon-\bar{\epsilon})\,|\bar{K}^0\rangle\right).
\end{aligned}
\tag{1.9}
$$

In this form, it is manifest that CP violation can result as an asymmetric mixing of particle and antiparticle, in this case the K^0 and the $\bar{K}^0$.

Substituting the latter form into Equation 1.4, we can then identify

$$
\epsilon = \frac{\langle \bar{K}^0 | \mathbf{H}_{eff} | K^0 \rangle - \langle K^0 | \mathbf{H}_{eff} | \bar{K}^0 \rangle}{2\Delta m + i(\Gamma_S - \Gamma_L)} \qquad (\overline{CP}) \tag{1.10}
$$

and

$$
\bar{\epsilon} = -\frac{\langle \bar{K}^0 | \mathbf{H}_{eff} | \bar{K}^0 \rangle - \langle K^0 | \mathbf{H}_{eff} | K^0 \rangle}{2\Delta m + i(\Gamma_S - \Gamma_L)} \qquad (\overline{CPT}) \tag{1.11}
$$

to first order in ϵ and $\bar{\epsilon}$. In these expressions, Δm is the mass difference between the long and short lived weak eigenstates,

$$
\Delta m \equiv m_L - m_S. \tag{1.12}
$$

Note that while $|K^0\rangle$ and $|\bar{K}^0\rangle$ are orthogonal, the weak eigenstates $|K_S\rangle$ and $|K_L\rangle$ will not be orthogonal if CP or CPT is violated. From Equation 1.8 we have

$$
\langle K_L |\, K_S \rangle \approx 2(Re\epsilon - iIm\bar{\epsilon}). \tag{1.13}
$$

If we now impose the requirement that the effective hamiltonian is CPT invariant, we have the properties that the diagonal elements of the hamiltonian are equal,

$$
\left\langle \bar{K}^0 \right| \mathbf{H}_{eff} \left| \bar{K}^0 \right\rangle = \left\langle K^0 \right| \mathbf{H}_{eff} \left| K^0 \right\rangle, \tag{1.14}
$$

and that the off diagonal elements in the mass and decay matrices are complex conjugates,

$$
\left\langle K^0 \right| \mathbf{M} \left| \bar{K}^0 \right\rangle = \left\langle \bar{K}^0 \right| \mathbf{M} \left| K^0 \right\rangle^*, \tag{1.15}
$$

and

$$\left\langle K^0 \right| \Gamma \left| \bar{K}^0 \right\rangle = \left\langle \bar{K}^0 \right| \Gamma \left| K^0 \right\rangle^* . \tag{1.16}$$

Equation 1.14 forces $\bar{\varepsilon} = 0$. From the assumption that $\mathbf{M}$ and $\mathbf{\Gamma}$ are hermitian, Equation 1.10, can be rewritten in the simpler form

$$\varepsilon = \frac{ImM_{12} - \frac{1}{2}\imath Im\Gamma_{12}}{\imath\Delta m - \frac{1}{2}(\Gamma_S - \Gamma_L)}, \tag{1.17}$$

where $M_{12} = \langle K^0 | \mathbf{M} | \bar{K}^0 \rangle$ and $\Gamma_{12} = \langle K^0 | \mathbf{\Gamma} | \bar{K}^0 \rangle$.

By choosing ε small, we have in fact implicitly chosen a phase convention between the $|S| = 1$ and $|S| = 0$ sectors. A more careful consideration of the problem shows that the only condition necessary for $\varepsilon \neq 0$ (that is, to have CP violation) is to have M_{12} and Γ_{12} not relatively real. The experimental observation that CP violation is small simply implies that the angle between M_{12} and Γ_{12} is small (about 6 mrad given the measured level of CP violation [31]). A different phase convention could be chosen such that M_{12} and Γ_{12} would each have a large overall phase, in which case the CP-violating parameter ε would be large. It is possible to choose a basis state where M_{12} and Γ_{12} would both be real were there no CP violation. Then the size of ε is a reflection of the size of CP violation, and the assumption that ε is a small parameter in the preceding discussion is valid. We will discuss this phase convention further in the explicit context of the $\pi\pi$ decays, but will assume this convention until then without further reference.

From the preceding expressions, it is clear that the both the mass matrix and the decay matrix can contribute to the asymmetric mixing of the K^0 and the $\bar{K}^0$. Now the off diagonal elements of Γ_{12} are given by

$$\left\langle K^0 \right| \Gamma \left| \bar{K}^0 \right\rangle = \sum_f A_f^* \bar{A}_f, \tag{1.18}$$

where the sum runs over all the final states f physically accessible to the kaon. The decay amplitudes A_f and $\bar{A}_f$ are the weak amplitudes for the decay of the K^0 and $\bar{K}^0$ respectively, into the final state f. The total decay amplitude for the K^0 ($\bar{K}^0$) is $A_f \exp(\imath\delta_f)$ ($\bar{A}_f \exp(\imath\delta_f)$), where δ_f is the phase shift induced by final state interactions. From equations 1.17 and 1.18, we see that ε receives a contribution from the decay matrix only if there exists a state such that A_f and $\bar{A}_f$ are not relatively real. If we consider some final state f

that is an eigenstate of CP, it is interesting to consider the ratio of amplitudes for the long and short eigenstates to decay into this final state,

$$r_f = \frac{\langle f | \mathbf{H}_{eff} | K_L \rangle}{\langle f | \mathbf{H}_{eff} | K_S \rangle}. \tag{1.19}$$

Using Equation 1.9 to express this in terms of a_f and $\bar{a}_f$, we have

$$r_f = \frac{(a_f - \bar{a}_f) + \varepsilon(a_f + \bar{a}_f)}{\varepsilon(a_f - \bar{a}_f) + (a_f + \bar{a}_f)}. \tag{1.20}$$

If a_f and $\bar{a}_f$ are not relatively real, then Equation 1.20 implies that any CP violation which comes from the decay matrix will not only affect the asymmetric $K^0 - \bar{K}^0$ mixing through its contribution to ε, but will also directly contribute a term to the ratio of the (loosely speaking) CP-violating and CP-conserving amplitudes.

In the case of the CP-violating $\pi^+\pi^-$ decay of the K_L, if we define

$$\chi_{\pi^+\pi^-} = \frac{a_{\pi^+\pi^-} - \bar{a}_{\pi^+\pi^-}}{a_{\pi^+\pi^-} + \bar{a}_{\pi^+\pi^-}}, \tag{1.21}$$

then

$$r_{\pi^+\pi^-} = \frac{\varepsilon + \chi_{\pi^+\pi^-}}{1 + \varepsilon\chi_{\pi^+\pi^-}} \approx \varepsilon + \chi_{\pi^+\pi^-}, \tag{1.22}$$

the latter using the fact that CP violation in this decay is known to be small. The contribution to CP violation from a term outside the mixing is manifest in this form. Note that χ_f for different final states f are in general not equal.

We can now see that we have two possible origins for a CP violating effect. In one case, the K^0 and the $\bar{K}^0$ mix asymmetrically, resulting in a small admixture of a CP-violating eigenstate in a primarily CP-conserving state. In the second case, the K^0 and the $\bar{K}^0$ *decay* asymmetrically, leading to a CP violating amplitude directly in the decay, as well as contributing to the asymmetric $K^0 - \bar{K}^0$ mixing through virtual processes. The latter effect has been appropriately dubbed "direct" CP violation. Almost 30 years of effort have gone into establishing whether the observed CP violation arises from mixing in the mass matrix alone, or whether direct CP violation also occurs. One of the most important tasks of the proposed B meson factory is also to search for direct CP violation in the $B^0 - \bar{B}^0$ system, where CP violation in mixing is expected to be much smaller, but direct effects much larger.

Before examining direct CP violation in the $\pi\pi$ system more closely, let us examine the consequences of having mixing arise only in the mass matrix.

1.1.1 CP Violation from Mixing

To examine the experimental evidence we have on CP violation, we must first define the experimentally accessible quantities. For decay modes where the final state has a definite CP, it is interesting to consider the ratio of CP violating to CP conserving amplitudes for the decay modes. For the $\pi\pi$ decay modes, this is simply the quantity r defined above. In a more traditional notation, we have for the charged decay mode

$$\eta_{+-} \equiv \frac{\langle \pi^+\pi^- | \mathbf{H}_{eff} | K_L \rangle}{\langle \pi^+\pi^- | \mathbf{H}_{eff} | K_S \rangle} = r_{\pi^+\pi^-}, \tag{1.23}$$

and for the neutral mode

$$\eta_{00} \equiv \frac{\langle \pi^0\pi^0 | \mathbf{H}_{eff} | K_L \rangle}{\langle \pi^0\pi^0 | \mathbf{H}_{eff} | K_S \rangle} = r_{\pi^0\pi^0}. \tag{1.24}$$

If only the asymmetric $K^0 - \bar{K}^0$ mixing in the mass matrix contributes to the CP violating amplitudes, then $\chi = 0$ in Equation 1.22 for both decay modes, and we are left with

$$\eta_{+-} = \eta_{00} = \varepsilon. \tag{1.25}$$

Experimentally, both the phases and the magnitudes of η_{+-} and η_{00} are accessible for verification. From equation 1.17, the phase of ε is given by

$$\phi_\varepsilon = \tan^{-1}\left(\frac{2\Delta m}{\Gamma_S - \Gamma_L}\right) - \tan^{-1}\left(\frac{Im\Gamma_{12}}{2ImM_{12}}\right). \tag{1.26}$$

Since we are assuming only the mass matrix contributes to CP violation, $Im\Gamma_{12} = 0$ and we are left with the "natural" phase for ε,

$$\phi_\varepsilon = \tan^{-1}\left(\frac{2\Delta m}{\Gamma_S - \Gamma_L}\right). \tag{1.27}$$

This natural phase is often referred to as the "superweak" phase, for reasons that will become clear later in this chapter. Obviously, Equation 1.25 implies both that we should observe

$$|\eta_{+-}| = |\eta_{00}| \tag{1.28}$$

and

$$\phi_{+-} = \phi_{00} = \tan^{-1}\left(\frac{2\Delta m}{\Gamma_S - \Gamma_L}\right), \tag{1.29}$$

where ϕ_{+-} and ϕ_{00} are the phases of η_{+-} and η_{00}, respectively.

Average values for $|\eta_{+-}|$ and $|\eta_{00}|$ have been calculated by the Particle Data Group [32] based on the current knowledge of the K_L and K_S lifetimes, the branching ratio measurements for the $K_L \to \pi\pi$ decay modes, and the direct measurements of $|\eta_{+-}|$, $|\eta_{00}|$, and $|\eta_{+-}/\eta_{00}|$. Their best fit results are

$$\begin{aligned} |\eta_{+-}| &= (2.268 \pm 0.023) \times 10^{-3} \\ |\eta_{00}| &= (2.253 \pm 0.024) \times 10^{-3}, \end{aligned} \tag{1.30}$$

which are consistent with the prediction of Equation 1.28, that is, with the hypothesis that the observed CP violation in K_L decays is due to mixing alone.

In addition to the magnitudes of η_{+-} and η_{00}, we can examine their phases. As we will see later, a comparison of the phases will turn out to be much more a test of the assumption[2] of CPT than a test of the source of CP violation being solely due to mixing. To make the comparisons in Equation 1.29, we need measurements of the mass difference (Δm), of the K_S and K_L lifetimes[3] (τ_S and τ_L), and of the phases themselves. Measurements of Δm have been made by comparing the interference between the K_S and K_L amplitudes, both in the semileptonic decay modes [33] and in the $\pi^+\pi^-$ mode [34, 35]. The former method was actually suggested [36] even before the discovery of the K_L. The current world average is $\Delta m = (0.5351 \pm 0.0024) \times 10^{10}\ \hbar s^{-1}$ [32]. The value of τ_S is known on average at the 1/4% level, with $\tau_S = (0.8922 \pm 0.0020) \times 10^{-10}\ s$. Combined with the current knowledge of the K_L lifetime, these values imply that the phase of ε is

$$\phi_\varepsilon = 43.73^\circ \pm 0.14^\circ. \tag{1.31}$$

As a part of this thesis work, we have recently published [37] new determinations of the values of Δm and τ_S. These new results have not been included in the averages listed above, and will be presented in detail later.

The phase ϕ_{+-} of η_{+-} has also been measured previously by studying the the interference in $\pi^+\pi^-$ decays [38, 39, 40]. The current world average [32] is $\phi_{+-} = 46.6^\circ \pm 1.2^\circ$.

[2] Actually, CPT coupled with the assumption of unitarity.

[3] Though since $\Gamma_S \approx 580\Gamma_L$, τ_L does not significantly affect the natural (superweak) phase.

This value is over 2 standard deviations away from the superweak phase. There are two recent measurements of the phase difference $\Delta\phi \equiv \phi_{00} - \phi_{+-}$, one based on a subset of the data used in this experiment [41], and another from the NA31 experiment [40] at CERN, which has been performing a set of experiments on the neutral K system that parallels our own. The values obtained for $\Delta\phi$ were

$$\begin{aligned} &-0.3^\circ \pm 2.4^\circ \pm 1.2^\circ && \text{(This experiment, partial data set)} \\ &+0.2^\circ \pm 2.6^\circ \pm 1.2^\circ && \text{(NA31).} \end{aligned} \tag{1.32}$$

In both cases, the first errors are statistical and the second are systematic. Together, these measurements imply $\Delta\phi = -0.1^\circ \pm 1.9^\circ$. A new result for $\Delta\phi$ that supersedes our previous measurement listed above has recently been published [37], along with a new determination of ϕ_{+-}. These new measurements will also be part of the package of results on neutral kaon physics presented in this thesis.

The other quantity of interest in terms of experimental accessibility is the charge asymmetry δ in the semileptonic decays $K_L \to \pi^\pm e^\mp \nu_e$ and $K_L \to \pi^\pm \mu^\mp \nu_\mu$. The charge asymmetry in terms of the decay rates Γ to the final states with a positive or negative lepton is given by

$$\delta = \frac{\Gamma(K_L \to \pi^- \ell^+ \nu_\ell) - \Gamma(K_L \to \pi^+ \ell^- \bar{\nu}_\ell)}{\Gamma(K_L \to \pi^- \ell^+ \nu_\ell) + \Gamma(K_L \to \pi^+ \ell^- \bar{\nu}_\ell)}. \tag{1.33}$$

To first order in CP violating quantities, a straightforward calculation using the $K^0 - \bar{K}^0$ representation of the K_L given in Equation 1.9 (with $\tilde{\varepsilon} = 0$) yields

$$\delta = 2\frac{1 - |x|^2}{|1 - x|^2} Re\varepsilon. \tag{1.34}$$

The parameter x is a measure of the violation of the $\Delta S = \Delta Q$ rule, which states that in semileptonic hadronic decays, the change in the total electric charge[4] of the hadrons is the same as the total change in strangeness. In terms of the kaon decay, if the $\Delta S = \Delta Q$ is exact, then only the K^0 can decay to a final state with a positive lepton ℓ^+, and only the $\bar{K}^0$ can decay to a final state with a negative lepton ℓ^-. More precisely,

$$x = \frac{\langle \pi^- \ell^+ \nu_\ell | \, \mathbf{H}_{eff} \, | \bar{K}^0 \rangle}{\langle \pi^- \ell^+ \nu_\ell | \, \mathbf{H}_{eff} \, | K^0 \rangle} = \left(\frac{\langle \pi^+ \ell^- \bar{\nu}_\ell | \, \mathbf{H}_{eff} \, | K^0 \rangle}{\langle \pi^+ \ell^- \bar{\nu}_\ell | \, \mathbf{H}_{eff} \, | \bar{K}^0 \rangle} \right)^*, \tag{1.35}$$

[4] Measured in units of the magnitude of the electron charge.

where the latter equality follows from the assumption of CPT. The current upper limits on $|x|$ are still relatively high at the several percent level. In the standard model, the $\Delta S = \Delta Q$ rule is exact at the tree level, and while higher order processes allow a violation of the $\Delta S = \Delta Q$ rule, these processes are expected to be highly suppressed [42].

For the purposes of comparing ε to η_{+-} and η_{00} we will here assume that the $\Delta S = \Delta Q$ rule is exact. Equation 1.34 then relates the charge asymmetry directly to the mixing parameter, $\delta \approx 2Re\varepsilon$. It is interesting to note that in this case, the semileptonic decays do not contribute at all to mixing (since the K^0 and $\bar{K}^0$ semileptonic channels are distinct), yet vestiges of the mixing still appear in the decay. Combining all of the information on δ from the electron and muon decay channels, the current world average for the charge asymmetry is $\delta = 0.00327 \pm 0.00012$ [32]. If we combine this value with the value for ϕ_ε obtained above from the superweak phase, we can estimate

$$|\varepsilon| = (2.26 \pm 0.08) \times 10^{-3}, \tag{1.36}$$

which is in good agreement with the values of η_{+-} and η_{00} given above.

One can also consider CP violation in the 3π decay modes of the K_S, though experimentally this is a much more difficult mode to study. Again defining η to be the ratio of the CP-violating to CP-conserving decay amplitude in a decay mode,

$$\eta_{+-0} \equiv \frac{\langle \pi^+\pi^-\pi^0 | \mathbf{H}_{eff} | K_S \rangle}{\langle \pi^+\pi^-\pi^0 | \mathbf{H}_{eff} | K_L \rangle} = 1/r_{\pi^+\pi^-\pi^0}, \tag{1.37}$$

and

$$\eta_{000} \equiv \frac{\langle \pi^0\pi^0\pi^0 | \mathbf{H}_{eff} | K_S \rangle}{\langle \pi^0\pi^0\pi^0 | \mathbf{H}_{eff} | K_L \rangle} = 1/r_{\pi^0\pi^0\pi^0}, \tag{1.38}$$

the current experimental information places upper limits on $|\eta_{+-0}|$ and $|\eta_{000}|$ at the 10% level [32]. The situation is also more complicated in the $\pi^+\pi^-\pi^0$ case because there are CP even final states available in this decay, though K_S decays to these states are expected to suppressed by the angular momentum barrier.

From this first glance at what we know about experimentally about CP violation, it is clear that if direct CP violation occurs, its effect is small. Hence to attempt to observe direct CP violation, a dedicated experiment with carefully controlled systematic uncertainties is desirable. The primary goal of this experiment was to limit (or if possible observe!) the

contribution of direct CP violation in $\pi\pi$ decays of the neutral kaon. This goal will be the primary focus for the remainder of the thesis.

1.1.2 Direct CP Violation in $\pi\pi$ Decays

In the previous discussion, we saw that we could ascertain the overall effect of CP violation by comparing the ratio η of the amplitudes of the CP-violating and CP-conserving processes. However, this does not help us break down the contributions from direct CP violation in the decay matrix and from mixing in the mass matrix. For a particular final state f, we have only (*c.f.* Equation 1.22) $\eta = \varepsilon + \chi_f$, where ε is the mixing contribution and χ_f is the contribution from direct CP violation to that final state. One way of isolating the mixing and decay contributions is to compare the level of CP violation in two different CP-violating final states. The two CP-violating decays $K_L \to \pi^+\pi^-$ and $K_L \to \pi^0\pi^0$ allow such a comparison. Another way is to search for CP-violating decays, such as the rare $K_L \to \pi^0\nu\bar{\nu}$ decay, where the CP-conserving decay amplitudes are highly suppressed. An observation of such a decay mode would then essentially be a signal of direct CP violation. In this experiment, we use the first approach[5]

To determine what the observable effect of having direct CP violation in the $K_L \to \pi\pi$ decays should be, we need to consider the fact that there will be final state interactions between the two pions in the decay process. Since these final state interactions are strong, we have no recourse but to formulate the discussion in terms of the strong eigenstates, that is, the isospin eigenstates. In the case of two pions, Bose symmetry implies that only the $I = 0$ and $I = 2$ final states are allowed. We would like to determine an expression for the values of $\chi_{\pi^+\pi^-}$ and $\chi_{\pi^0\pi^0}$ (*c.f.* Equation 1.21), for which we will need the amplitudes for a K^0 and a $\bar{K}^0$ to decay to $\pi\pi$ final states with $I = 0$ and $I = 2$. First let us define

$$\langle I | \mathbf{H}_{eff} \left| K^0 \right\rangle = a_I \equiv A_I e^{i\delta_I}, \tag{1.39}$$

where I denotes the isospin ($I = 0, 2$) of the $\pi\pi$ final state. The overall amplitude (a_I in Equation 1.21) has been separated into an amplitude A_I corresponding to the weak decay

[5]Since this approach involved the use of an intense K_L beam, we were also able to obtain limits on some rare decay modes of the K_L relating to CP violation [43, 44, 45, 46, 47].

process itself, and a phase shift δ_I from the final state interactions. From our assumption of CPT symmetry, we also have (see, for example, reference [21])

$$\langle I | \mathbf{H}_{eff} \left| \tilde{K}^0 \right\rangle = \bar{a}_I \equiv A_I^* e^{i\delta_I}. \tag{1.40}$$

We will now explicitly adopt the Wu–Yang phase convention [26] hinted at previously and take A_0 to be real. This fixes the relative phase between the $|S| = 1$ and the $S = 0$ sectors, which are not connected by the strong and electromagnetic interactions. As noted in reference [23], when the level of direct CP violation is calculated for a particular model, one chooses a phase convention which simplifies the calculation in that model. This convention will generally not be the Wu–Yang convention, and one will find contributions to direct CP violation from ImA_0. The physical observables are, however, independent of the choice of phase.

Breaking down the $\pi^+\pi^-$ and $2\pi^0$ eigenstates into their $I = 0$ and $I = 2$ components, we have

$$\begin{aligned} |\pi^+\pi^-\rangle &= \sqrt{\tfrac{2}{3}}|0\rangle + \sqrt{\tfrac{1}{3}}|2\rangle \\ |\pi^0\pi^0\rangle &= -\sqrt{\tfrac{1}{3}}|0\rangle + \sqrt{\tfrac{2}{3}}|2\rangle \end{aligned} \tag{1.41}$$

When we substitute these expressions and Equations 1.39 and 1.40 into Equation 1.21, we obtain in the $\pi^+\pi^-$ case

$$\begin{aligned} \chi_{\pi^+\pi^-} &= \frac{iImA_2 e^{i(\delta_2-\delta_0)}}{\sqrt{2}A_0 + ReA_2 e^{i(\delta_2-\delta_0)}} \\ &= \frac{\varepsilon'}{1+\omega/\sqrt{2}}. \end{aligned} \tag{1.42}$$

In the last expression we have introduced the parameters

$$\varepsilon' \equiv \frac{i}{\sqrt{2}} e^{i(\delta_2-\delta_0)} \frac{ImA_2}{A_0}, \tag{1.43}$$

and

$$\omega \equiv \frac{ReA_2}{A_0} e^{i(\delta_2-\delta_0)}. \tag{1.44}$$

The latter is a parameter measuring the ratio of the CP-conserving $\Delta I = 3/2$ amplitude to the CP-conserving$\Delta I = 1/2$ amplitude in $K_S \to \pi\pi$ decays. Experimentally, we know that the $\Delta I = 3/2$ transitions are suppressed, with

$$|\omega| \sim \frac{1}{22}. \tag{1.45}$$

Since ω is small, from Equation 1.43, we can see that ε' sets the scale for direct CP violation, and from the preceding section, we also know that ε'must be small as well. Substituting this into Equation 1.22, and keeping only terms to first order in ε' and ω, the form for η_{+-} becomes

$$\eta_{+-} \approx \varepsilon + \varepsilon'. \tag{1.46}$$

A similar calculation for the neutral mode gives

$$\chi_{\pi^0\pi^0} = \frac{-2\varepsilon'}{1 - \sqrt{2}\omega}, \tag{1.47}$$

and again to first order in $\varepsilon'$and ω the form for η_{00} becomes

$$\eta_{00} \approx \varepsilon - 2\varepsilon'. \tag{1.48}$$

If there is direct CP violation in the $\pi\pi$ decay of the neutral kaon, then we have just shown that the ratio of CP-violating to CP-conserving amplitudes will be different for the $\pi^+\pi^-$ and $2\pi^0$ final states[6]. The geometrical relation between the different CP-violating amplitudes is illustrated in the Wu-Yang diagram in Figure 1.

The phase of ε' follows from its definition:

$$\phi_{\varepsilon'} = \delta_2 - \delta_0 + \frac{\pi}{2}. \tag{1.49}$$

The $I = 0$ and $I = 2$ final state phase shifts have been measured in other experiments, and in a recent compilation, Ochs [48] obtains $\delta_2 - \delta_0 = -43° \pm 6°$. This implies that the phase of ε' is $\phi_{\varepsilon'} = 47° \pm 6°$. Comparing this phase to the phase of ε obtained above, we see the ε' and ε are almost parallel, a convenient but accidental coincidence. To a good approximation then, we have CP violation parametrized by $Re(\varepsilon'/\varepsilon)$, and CPT violation parametrized by $Im\varepsilon'/\varepsilon$. The latter would result if, for example, the $K^0 - \bar{K}^0$ mixing asymmetry were different for the K_L and K_S ($\bar{\varepsilon} \neq 0$ in Equation 1.9.

In an experiment, what we have direct access to are the decay rates for the different $K \to \pi\pi$ decays. Expressed in terms of the decay rates, a signal for direct CP violation in $K \to \pi\pi$ decays is deviation of the double ratio of rates,

$$\frac{\Gamma(K_L \to \pi^+\pi^-)/\Gamma(K_S \to \pi^+\pi^-)}{\Gamma(K_L \to \pi^0\pi^0)/\Gamma(K_S \to \pi^0\pi^0)} = \frac{|\eta_{+-}|^2}{|\eta_{00}|^2} \approx 1 + 6Re(\varepsilon'/\varepsilon), \tag{1.50}$$

[6] Whether the splitting is large enough to be measured is a separate issue.

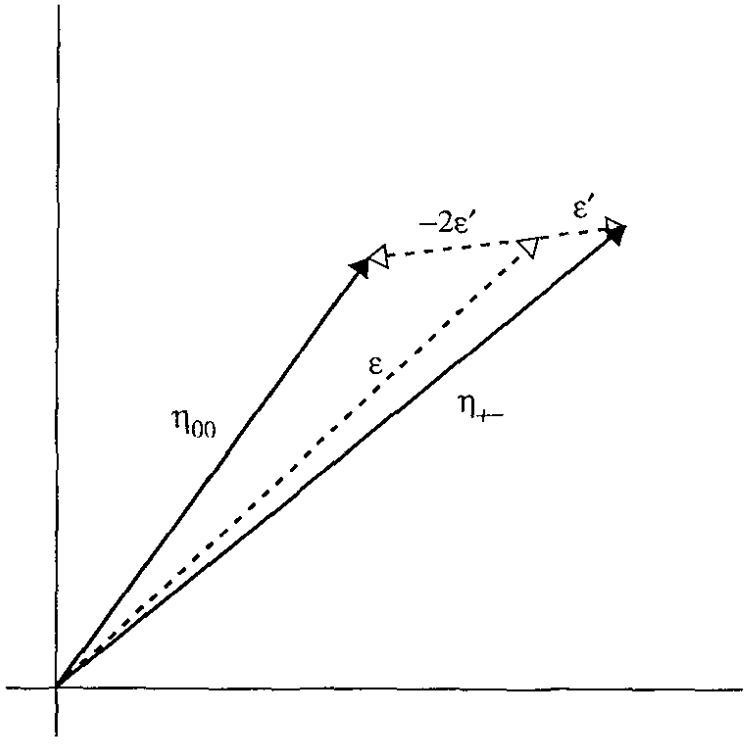

Figure 1. The Wu-Yang phase diagram for $K \rightarrow \pi\pi$ decays. The phase and magnitude of ε' relative to ε have been greatly exaggerated for the sake of clarity.

away from unity. Since $Re(\varepsilon'/\varepsilon)$ is expected to be small, this deviation is approximately $6Re(\varepsilon'/\varepsilon)$. There has been quite an industry to measure $Re(\varepsilon'/\varepsilon)$ over the past 30 years, and the more recently published results are presented in Table 1. In 1988, the NA31 group published evidence [49] for direct CP violation at the 3 standard deviation level. An initial result [50] from our group based upon 20% of the data presented here was, however, consistent with no direct CP violation. There is approximately a two standard deviation discrepancy between the NA31 publication and our initial result. The analysis presented here also reanalyzes the data used in reference [50], so this result will supersede the previous one. The $Re(\varepsilon'/\varepsilon)$ analysis will be the focus of this thesis, and the results of this analysis have been recently published [51].

Table 1. Recently published measurements of $Re(\varepsilon'/\varepsilon)$. The first errors listed are statistical, the second systematic.

Collaboration	Year	$Re(\varepsilon'/\varepsilon)$ (10^{-4})
Yale–BNL [52]	1985	17 ± 82
Chicago–Saclay [53]	1985	$-46 \pm 53 \pm 24$
Chicago–Elmhurst–FNAL-Princeton–Saclay (FNAL E731) [54]	1988	$32 \pm 28 \pm 12$
CERN–Dortmund–Edinburgh–Mainz–Orsay–Pisa–Siegen (CERN NA31) [49]	1988	$33 \pm 7 \pm 8$
FNAL E731 [50]	1990	$-4 \pm 14 \pm 6$

1.2 Tests of CPT Invariance

In the phenomenological analysis of CP violation in the $\pi\pi$ decays of neutral kaons given above, many of the results we obtained rested on the assumption that the weak hamiltonian underlying $\mathbf{H}_{eff}$ was invariant under CPT. Also implicit was the assumption of unitarity (the condition that probability is conserved), which entered in the assumption that the mixing matrix $\mathbf{M}$ and the decay matrix $\mathbf{\Gamma}$ are both hermitian. As the primary concern of this thesis is the measurement of $Re(\varepsilon'/\varepsilon)$, we will only briefly discuss some of the tests of CPT symmetry open to the kaon system and accessible by our experiment.

As we remarked above, CPT invariance is a very general property, arising in any local field theory which incorporates proper Lorentz transformations. However, there have been several issues recently raised which question the validity of assuming CPT. For example, Kobayashi and Sanda [55] question the applicability of the CPT theorem to QCD because the proof of the CPT theorem used the properties of asymptotically free states, while the quarks and gluons are confined and do not appear in such states. Furthermore, one might question the validity of the assumption that the world is described by a local field theory. We may well be seeing the low-energy effective interactions of some more fundamental process. If, for example, a string theory turns out to be a valid description of nature, then the nonlocal nature of such a theory could lead to CPT-violating phenomena. Indeed, there

have even been recent speculations that such phenomena could lead to observable effects in the $K^0 - \bar{K}^0$ system [56].

We have hinted above that the phases ϕ_{+-} and ϕ_{00} could be used as a possible test of CPT violation. Equation 1.29 can be divided into two different tests, and different assumptions will enter each test. In the first test, we wish to compare the phases ϕ_{+-} and ϕ_{00} directly, that is, to measure the phase difference $\Delta\phi$. Using Equations 1.46 and 1.48, we find that the effect of ε' on the phase difference is given approximately by

$$\Delta\phi \approx 3Re(\varepsilon'/\varepsilon)\tan(\phi_\varepsilon - \phi_{\varepsilon'}). \tag{1.51}$$

Using the uncertainties given above in the previous measurements of $Re(\varepsilon'/\varepsilon)$ and in the $\pi\pi$ final state phase shifts, we can limit the contribution from direct CP violation to the phase difference to be under 0.2°. The experimental values for the phase above are consistent with CPT, but further improvement is needed.

The other phase comparison we can make is the agreement between ϕ_{+-} and the superweak phase $\tan^{-1}(2\Delta m/[\Gamma_S - \Gamma_L])$. To make this comparison, however, we have to neglect the contribution of Γ_{12} in Equation 1.17 to the phase. If we assume that the $\Delta S = \Delta Q$ law is not significantly violated, and that CP violation in the 3π decays is not anomalously large, then the $\pi\pi$ contribution is expected to dominate by a factor of $\Gamma_S/\Gamma_L \approx 580$. The $\pi\pi$ contribution to $Im\Gamma_{12}/\Gamma_S$ is [21] of order $|\omega||\varepsilon'/\varepsilon|$, so the contribution of Γ_{12} to the phase of ε is expected to be extremely small. The phase ϕ_ε (and therefore the phase ϕ_{+-}) should thus be very close to the superweak phase. The current experimental data summarized above is clearly not in the best of agreement with this assertion.

The latter test is, unfortunately, a somewhat model dependent one since the assumption that the semileptonic and 3π contributions to Γ_{12} are small could be questioned. If we are questioning the validity of CPT, it is not clear that it is fair to make model-dependent assumptions about these rates. Since the $\Delta S = -\Delta Q$ amplitude is only limited at the 2% level, and CP violation in 3π decays is only limited at the 10% level, a completely model independent estimate of ϕ_ε is actually much poorer. Recent estimates [55] have placed the value of ϕ_ε within the 39.5° to 47.4° range at the 90% confidence level. It is still interesting to probe the experimental discrepancy between ϕ_{+-} and the superweak phase.

If the discrepancy is not an artifact of the measurements, then it *is* an indication of some new physics, even if not CPT violation.

Let us now turn back to CP violation and briefly investigate our current understanding of possible sources of CP violation.

1.3 Theories of CP Violation

1.3.1 Introduction

It was shown very early on that CP violation could arise through the presence of a dispersive contribution to the mass matrix [57]. Such an interaction would have the form [21]

$$M_d \sim \int \frac{dE}{E - m_K} \sum_c \bar{A}_c(E)^* A_c(E), \tag{1.52}$$

where A_c ($\bar{A}_c$) is the amplitude for the virtual decay of the K^0 ($\bar{K}^0$) to any channel c that is coupled to the kaon by the weak (or other) interaction. Contributions to such a term arise naturally in the current Standard Model of particle interactions. If these dispersive terms are present, however, then contributions to direct CP violation are also expected in this model.

In 1964, Wolfenstein [58] postulated that CP violation could occur through a new $\Delta S = 2$ interaction. To accommodate the small size of observed CP violating effects, and to not be observable in other decays, this interaction would have to be on the order of 10^7 times weaker than the standard interaction (i.e., a 10^6 TeV mass scale). Hence this interaction was dubbed the "superweak" interaction. Superweak interactions would contribute solely to the dispersive term in the mass matrix, since the $\Delta S = 2$ interaction could not mediate a $\Delta S = 1$ decay, and we would observe no direct CP violation. In the $K \to \pi\pi$ decay, we would have $\varepsilon'/\varepsilon = 0$. Such an interaction has not been definitively excluded.

For the remainder of this discussion, we will focus on origin of CP violation within the Standard Model itself.

1.3.2 CP Violation in the Standard Model

1.3.2.1 The CKM Matrix

Within the framework of the standard electroweak interactions, CP violation can arise naturally in the interactions of the quarks with the charged gauge bosons $W^{\pm}$. There have been many reviews over the last few years [59, 60, 23, 61] which cover the origin and calculation of CP-violating phenomena quite fully, and we will only touch on the general features here. The weak interactions are not diagonal in the basis of quark flavor, which is preserved in the strong interaction. They are rather of the form

$$g\left[\bar{u}_j V_{ji} \gamma_\mu (1-\gamma_5) d_i W^\mu + \text{h.c.}\right], \tag{1.53}$$

where the repeated indices are summed over. The coupling between the up-type quarks $\mathbf{u} = (u, c, t)$ and the down-type quarks $\mathbf{d} = (d, s, b)$ is given by the 3×3 unitary matrix

$$\mathbf{V} = \begin{pmatrix} v_{ud} & v_{us} & v_{ub} \\ v_{cd} & v_{cs} & v_{cb} \\ v_{td} & v_{ts} & v_{tb} \end{pmatrix}. \tag{1.54}$$

While $\mathbf{V}$ has in principle 18 real parameters, the true number of free parameters is smaller. The unitarity constraint, $V_{ji}^* V_{jk} = \delta_{ik}$, provides 9 conditions, reducing the number of free real parameters to 9. In addition, another $(2 \times 3 - 1 = 5)$ parameters can be removed by redefining the relative phases of the $\mathbf{u}$ and $\mathbf{d}$ quarks. The number of free real parameters reduces to four, and a typical convention [32] is to choose the quark phases such that the parameters can be represented by 3 angles θ_{ij} in the first quadrant and one complex phase δ. $\mathbf{V}$ then becomes

$$\mathbf{V} = \begin{pmatrix} c_{12}c_{13} & s_{12}c_{13} & s_{13}e^{i\delta} \\ -s_{12}c_{23} - c_{12}s_{23}s_{13}e^{i\delta} & c_{12}c_{23} - s_{12}s_{23}s_{13}e^{i\delta} & s_{23}c_{13} \\ s_{12}s_{23} - c_{12}c_{23}s_{13}e^{i\delta} & -c_{12}s_{23} - s_{12}c_{23}s_{13}e^{i\delta} & c_{23}c_{13} \end{pmatrix}. \tag{1.55}$$

where, $c_{ij} = \cos\theta_{ij}$ and $s_{ij} = \sin\theta_{ij}$. The complex phase δ can be moved by redefinition of the quark field phases, but cannot in general be removed. As noted by Jarlskog [62], all CP-violating phenomena are proportional, independent of phase convention, to the quantity

$$J = Im[V_{us}V_{cb}V_{ub}^{*}V_{vs}^{*}] = Im[V_{\alpha a}V_{\beta b}V_{\alpha b}^{*}V_{\beta a}^{*}]. \tag{1.56}$$

In the rightmost quantity, the repeated indices are *not* summed over; the Greek indices simply indicate an up-type quark, and the Latin indices a down-type quark.

V, the Cabibbo–Kobayashi–Maskawa (CKM) matrix was first introduced by Kobayashi and Maskawa [64], and generalizes the mixing concept originally introduced by Cabibbo [63]. Kobayashi and Maskawa noted that the complex phase(s) arising for 3 (or more) generations of quarks lead to interactions that are not invariant under CP.

The coupling strength between two quarks becomes weaker as the distance between the two generations (corresponding to the i and j indices above) to which the two quarks belong increases. This hierarchy of coupling strengths leads to a convenient parametrization of the CKM matrix originally introduced by Wolfenstein [65] in powers of the sine of the Cabibbo angle, $\lambda = \sin\theta_{12}$. To order λ^3, the CKM matrix becomes

$$\mathbf{V} = \begin{pmatrix} 1-\frac{\lambda^2}{2} & \lambda & A\lambda^3(\rho - \imath\eta) \\ -\lambda & 1-\frac{\lambda^2}{2} & A\lambda^2 \\ A\lambda^3(1-\rho-\imath\eta) & -A\lambda^2 & 1 \end{pmatrix}. \tag{1.57}$$

Here A is a quantity of order unity, and within this representation, the parameter J becomes simply

$$J \approx A^2\lambda^6\eta, \tag{1.58}$$

which makes the relation between CP violation and the imaginary component of the CKM matrix manifest.

A common pictorial illustration of the parameters relevant to CP violation is the "unitarity triangle" one obtains by applying the unitarity condition to the first and third columns of the CKM matrix:

$$V_{ud}V_{ub}^{*} + V_{cd}V_{cb}^{*} + V_{td}V_{tb}^{*} = 0 \tag{1.59}$$

To first order in λ, we can take $V_{ud} \approx 1$, and the unitarity condition becomes

$$V_{ub}^{*} + V_{td} = A\lambda^3. \tag{1.60}$$

The triangle one obtains from this relationship, which is a triangle in the ρ–η plane, is pictured in Figure 2. The area of the triangle is proportional to the measure of CP violation, J.

In order to evaluate the level of direct CP violation in $K \to \pi\pi$ decays expected in the CKM framework, we need to evaluate some of the parameters of the CKM matrix. A very complete discussion of information on individual elements of the CKM matrix can be found in [59]. Here we will only note that the value of A can be obtained from the rate of semileptonic B→D decays. A typical value obtained [66] from the analysis of the observed rates is $A = 0.9 \pm 0.1$.

To examine the allowed ranges of the parameters ρ and η, we turn to several different phenomena. In particular, the observed level of CP violation in the $K^0 - \bar{K}^0$ system, mixing of other neutral mesons, and decays involving $b \to u$ transitions are most helpful.

Within the CKM paradigm, CP violation arising from asymmetric $K^0 - \bar{K}^0$ mixing (and hence the value of ε) is dominated by the contribution of the box diagram shown in Figure 3. While the expression for ε in Equation 1.17 has both dispersive and absorptive contributions, we know experimentally that the dispersive term dominates, which implies ε is given largely by ImM_{12}. For $m_t > M_W$, evaluation of the box diagram yields

$$M_{12} = \frac{G_F^2}{12\pi^2} F_K^2 B_K m_K M_W^2 \left[\lambda_c^2 \eta_1 S(x_c) + \lambda_t^2 \eta_2 S(x_t) + 2\lambda_c \lambda_t \eta_3 S(x_c, x_t)\right], \qquad (1.61)$$

where F_K is the kaon decay constant (161 MeV) and B_K is the ratio of the true matrix element to that obtained using vacuum insertion (lattice calculations [67] give $B_K = 0.8 \pm 0.2$).

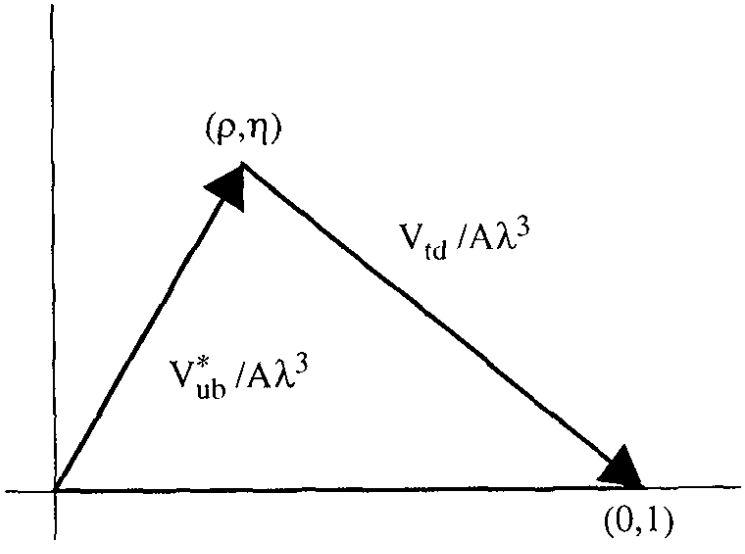

Figure 2. The unitarity triangle.

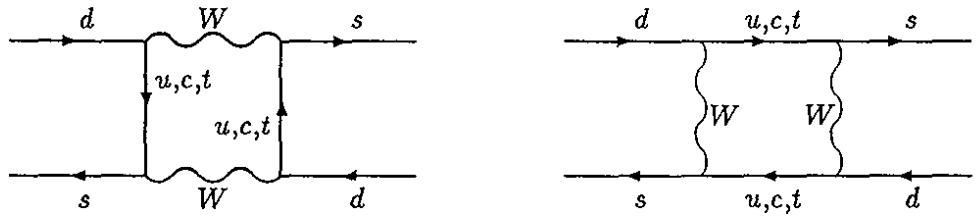

Figure 3. The box diagrams which are expected to provide the dominant contribution to CP violation in $K^0 - \bar{K}^0$ mixing.

The terms in the brackets correspond to the contribution from the different internal fermion lines, with $\lambda_i = V_{id}^* V_{is}$ giving the coupling strengths, $x_i = m_i^2/M_W^2$, and the Inami-Lim functions [68] $S(x_i), S(x_i, x_j)$ giving the correction to box diagram calculations originally made with arbitrary internal quark masses. The η_i are the short distance QCD corrections [61, 69] to the operators, with η_1, η_2, η_3 approximately 0.85, 0.62 and 0.36, respectively. Evaluating the expression for M_{12} with $m_t > M_W$ gives [66]

$$|\varepsilon| \approx (2.7 \pm 0.7) \times 10^{-3} \left[1 + \frac{4}{3} A^2 (1 - \rho) x_t^{0.8}\right] \tag{1.62}$$

With this form we can see that the relationship between $|\varepsilon|$, ρ and η combined with our experimental knowledge of ε define a hyperbolic constraint in the ρ–η plane shown in Figure 4[7] for a *fixed* top quark mass of $m_t = 140$ GeV/c^2.

In evaluating the K_L–K_S mass difference, there are significant contributions from long range processes from virtual transitions through intermediate states like π^0, $\pi\pi$, η, etc. in addition to the short range contributions from the box diagram. While we can use the observed value of ε to limit the CKM parameters A, ρ and η, it is difficult to use the mass difference for this purpose because of these long range contributions.

Particle–antiparticle mixing is not the sole domain of the kaon system. Box diagrams similar to that for the kaon system should mediate mixing in the $D^0 - \bar{D}^0$, $B_d^0 - \bar{B}_d^0$ and $B_s^0 - \bar{B}_s^0$ systems, for example. Mixing has already been observed in the B system, and can also help constrain the CKM parameters. The mixing parameter $x_d = \Delta M/\Gamma_B$, where ΔM is the mass difference between the B_d^0 and $\bar{B}_d^0$ mass eigenstates and Γ_B is the B-meson decay width, is expected to be dominated by box diagrams similar to those in Figure 3, with b-quarks replacing the s-quarks and with a t-quark on the internal fermion legs. The

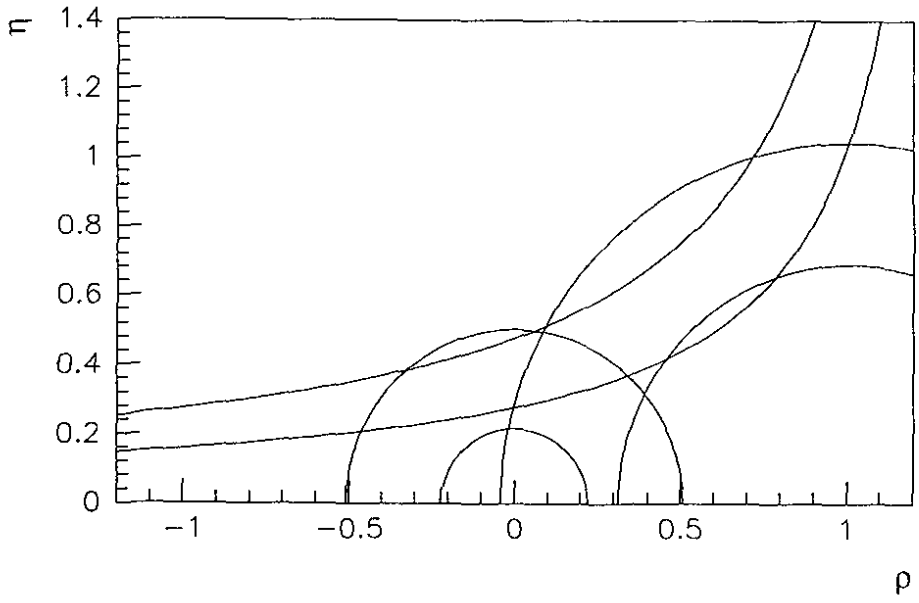

Figure 4. The one standard deviation constraints on ρ and η which result from the measurements of $|\varepsilon|$, x_d and $|V_{ub}|/|V_{cb}|$. *Plot courtesy J.R. Patterson.*

evaluation of this gives, to a good approximation [23],

$$x_d = \frac{1}{6}A^2\left[(1-\rho)^2+\eta^2\right]x_t^{0.8}\left[\frac{\sqrt{B_B\eta_B}f_B}{120\text{MeV}}\right]^2. \tag{1.63}$$

B_B and f_B are analogous to the similar parameters in the K system, and η_B is again the short range QCD correction. To illustrate the constraint provided by this relationship, we will use the value [66]

$$\sqrt{B_B\eta_B}f_B = 200 \pm 35 \text{ MeV}. \tag{1.64}$$

The latest experimental information from CLEO II [70] and ARGUS [71] implies[8] a world average of $x_d = 0.658 \pm 0.088$. Combining the expression above for x_d with this information, we obtain the annulus offset to the right in Figure 4.

Finally, the rate of semileptonic $b \to u$ decays gives a measure of the matrix element V_{ub}. To date the measurement technique uses only the upper end of the lepton spectrum to differentiate the $b \to u\ell\nu$ decays from the much more copious $b \to c\ell\nu$ decays. There is still considerable theoretical uncertainty in extracting $|V_{ub}|$ from the endpoint spectrum alone,

[8]This value was extracted using the value $(F_+B_+^2/(F_+B_+^2 + F_0B_0^2) = 0.5$, where B_+ (B_0) is the B^+ (B^0) semileptonic branching fraction, and F_+ (F_0) is the production fraction.

and the most recent analysis from CLEO II [72] implies

$$\frac{|V_{ub}|}{|V_{cb}|} = 0.08 \pm 0.03, \tag{1.65}$$

where the error is dominated by the theoretical uncertainty, which has been estimated by combining the spread of values obtained from different models and the uncertainty within the models themselves. Our current knowledge of $|V_{ub}|/|V_{cb}|$ translates into the annulus centered at zero in Figure 4. If the theoretical uncertainties in extrapolating the endpoint lepton spectrum to the full spectrum were sharpened, or the measurements themselves could be improved to use a larger fraction of the lepton spectrum, the bounds on the allowed region of η from this measurement could be considerably sharpened, perhaps as much as a factor of 3.

From the constraints shown in Figure 4, a value for the CP-violating phase δ in the first quadrant is preferred, though there is still a small region of overlap with the second quadrant. The only information which places a lower bound on η comes from the constraint placed by ϵ. If mixing does arise entirely within the standard model, then our current information places η roughly in the range from 0.2 to 0.5. As we mentioned above, however, mixing could arise entirely from a superweak interaction, and we cannot yet place a lower bound on η with complete certainty until a *direct* CP-violating effect has been established.

With this background in hand, let us now turn to consider the level of direct CP violation in $K \to \pi\pi$ decays we should expect in this model.

1.3.2.2 Direct CP violation in $K \to \pi\pi$ decays

If the CP-violating phase δ of the CKM matrix is truly the source of the mixing CP violation we have observed in both the $\pi\pi$ and semileptonic neutral kaon decays, we would then in general expect to observe direct CP-violating effects as well. In a phase convention more convenient for calculating $Re(\epsilon'/\epsilon)$ within the standard model, the definition for ϵ' becomes

$$\epsilon' = \frac{i}{\sqrt{2}} e^{(\delta_2 - \delta_0)} \left[\frac{Im A_2}{Re A_0} - \omega \frac{Im A_0}{Re A_0} \right]. \tag{1.66}$$

The dominant contribution to ϵ' then comes from the contribution to $Im A_0$ of the $\Delta I = 1/2$ operator corresponding to the strong penguin diagram pictured in Figure 5. This graph

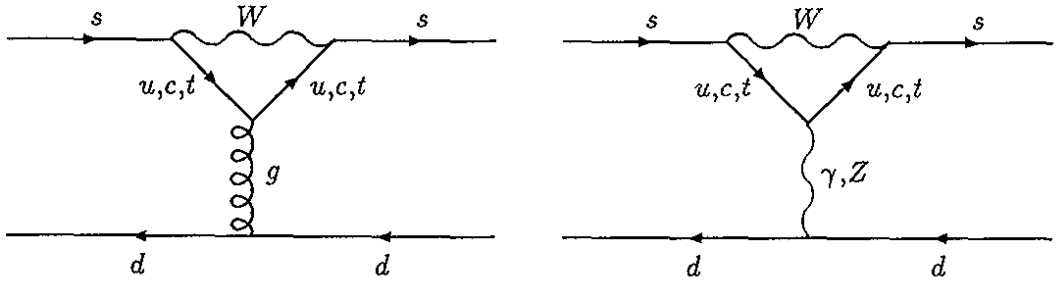

Figure 5. The strong (left) and electroweak (right) penguins.

leads to an effective operator

$$Q_6 = \sum_q \bar{s}(1+\gamma_5)q\bar{q}(1-\gamma_5)d, \tag{1.67}$$

and it is the relatively large value expected for this matrix element which make the penguin contribution important.

For moderate values of the $m_t \sim M_W$ or greater, however, the situation becomes more complex because the electroweak penguin diagram also shown in Figure 5 begins to become important. This diagram corresponds to a $\Delta I = 3/2$ operator, and hence contributes to ε' though it contribution to ImA_2. While this diagram is suppressed by order α relative to the strong penguin, this suppression is partially cancelled by the fact that it is not suppressed by ω. Furthermore, while the strong penguin has a relatively weak dependence on the top quark mass, for $m_t > M_W$ the electroweak penguin grows almost quadratically in m_t/M_W [73]. This leads to a partial cancellation of the strong penguin contribution for moderate (about 140 GeV/c^2) values of m_t, and to almost complete cancellation for large (over 200 GeV/c^2) values of m_t.

There has been much effort placed on the evaluation of $Re(\varepsilon'/\varepsilon)$ over the last few years, with results ranging from as small as 10^{-4} up to several 10^{-3}. Perhaps the only hard conclusion one can draw from these calculations is that, from an experimentalist's point of view, $Re(\varepsilon'/\varepsilon)$ is *small*! The theoretical situation has greatly improved very recently with two new calculations of $Re(\varepsilon'/\varepsilon)$ at next-to-leading order. We will, however, defer further discussion of these results until Chapter 11.

1.3.2.3 CP violation in the neutral B system

There has been much interest of late in the topic of the potential for observing CP-violating phenomena in the B system, which is unique in that a large phase in the V_{ub} and V_{td} elements should here lead to large CP-violating effects. The CP-violating phenomena in this system, however, take on a very different flavor than in the K system. One important difference stems from the fact that there are many final states open to both the B_S and B_L. As a result, the B_S and B_L lifetimes are expected to be almost identical, and these two states can not be isolated by simply allowing the B_S component to decay away, as we can in the kaon system. The small lifetime difference also renders the charge asymmetry in semileptonic B decays small (*c.f.* Equations 1.17 and 1.34), and taken together, it will be very difficult to detect CP violation from mixing via the charge asymmetry.

Thus to study CP violation in the B system, the best way to approach the issue will be to look for asymmetries in the decay rates of the B^0 and $\bar{B}^0$ to final states which are CP eigenstates, such as ΨK_S. Of course, as is the case in the kaon system, measuring only a single asymmetry cannot distinguish between mixing (either within the Standard Model or from a superweak effect) and direct CP violation. A second mode, such as the $\pi^+\pi^-$ decay mode, will be necessary to make this distinction. In the literature, discussions of these studies are generally couched in terms of extracting the different inner angles of the unitarity triangle by measuring the decay rates to several final states.

Unfortunately, the modes in the B system which are expected to exhibit sizable CP-violating effects also have small branching ratios. It will be some time before the large number of B decays (of order 10^8) needed to unambiguously disentangle the various possible sources of CP violation in this system are accumulated. If the m_t is not exceedingly large, the kaon system is still the most promising system in which to discover new CP-violating phenomena over the next decade.

1.4 Overview of this Thesis

We have discussed many of the basic issues relevant to the measurements we can perform in this experiment. The rest of the thesis will describe the measurement technique. In the next chapter, the issues affecting a measurement of $Re(\varepsilon'/\varepsilon)$ and how these issues affected the design of our experiment, will be discussed. Following this, we will examine the detector itself and give a brief description of the data collection run. Chapters 4 through 6 will present the analysis of the data, covering the calibration techniques, and the different reconstruction and background subtraction techniques in the $\pi^+\pi^-$ and $2\pi^0$ decay modes.

After the description of the data samples, we will change course and examine the methods used to determine the values of $Re(\varepsilon'/\varepsilon)$ and the other kaon parameters. As we will soon see, our experimental method requires understanding the acceptance of the detector at a precise level. Chapter 7 will detail the Monte Carlo simulation of our experiment that we used to determine the acceptance. The fitting techniques used in extracting the physical parameters are covered in great detail in Chapter 8. Many of the issues presented are quite technical, and though they will enter into our final systematic determination at a small level, they will be very important as considerations for future experiments using this technique. The results of the fits for $Re(\varepsilon'/\varepsilon)$ and the other parameters of the kaon system will be presented separately in Chapter 9, along with a discussion about of the assumptions that were made regarding CPT and CP violation within each fit. A reader who sidesteps Chapter 8 should still understand the essential issues of this particular chapter.

The final part of the analysis involved the determination of the systematic uncertainty on each of the particular measurements. In Chapter 10, we will focus on the systematic checks and the final systematic uncertainty for our measurement of $Re(\varepsilon'/\varepsilon)$, with contributions to the uncertainty in the other parameters noted where important. With our measured parameters and systematic uncertainties all in hand, we will conclude in Chapter 11 by relating our findings back to the issues presented in this chapter.

CHAPTER 2

THE EXPERIMENTAL TECHNIQUE

The measurement of $Re(\varepsilon'/\varepsilon)$ at a level more precise than 0.001 is truly an experimental challenge. It entails measuring the double ratio of rates (Equation 1.50) to a precision better than 0.5%. Such precision not only requires collecting a large number of $K \to \pi\pi$ decays in all of the four modes, but also requires strict controls of the biases one faces in extracting the double ratio of rates. This chapter will outline many of issues one faces in measuring this double ratio, and then discuss how the techniques employed by the E731 experiment eliminate or greatly reduce sensitivity to these issues. Finally, we will outline how these techniques further enable us to extract other properties of K decays from the same data set. This chapter will involve itself only with the general ideas involved in our measurement technique. The detector itself is described in more detail in the following chapter.

2.1 The Measurement

The first problem to be dealt with in this measurement is obtaining adequate statistics in both the K_S and K_L $\pi\pi$ decay modes. Consider the instantaneous decay rate for K^0s produced in a target:

$$\frac{d\Gamma(2\pi)}{d\tau} \propto |e^{-\tau/2\tau_S + i\Delta m} + \eta e^{-\tau/2\tau_L}|^2, \tag{2.1}$$

where τ_S and τ_L are the K_S and K_L lifetimes, Δm is the $K_L - K_S$ mass difference, and τ is the kaon proper time. Since $|\eta|$ is of order 0.23% only, a 2π event sample from a detector close to a kaon production target would be completely dominated by decays of the K_S. While

accurate measurements of η_{+-} and η_{00} could be made in principle by detecting decays from a region where the K_S and interference terms in (2.1) are of comparable order ($\tau \approx 12\tau_S$), this is in practice difficult because the relative numbers of K^0s and $\bar{K}^0$s produced must be accurately known. Thus for a practical measurement, separate sources for K_L and K_S decays seem to be required, one source located far from the decay volume to give a primarily K_L sample, and one source close to the decay volume for the K_S sample.

Once two separate sources for the K_S and K_L samples are used, care must be taken that biases in the relative collection efficiencies of the two samples do not arise. The response of any detector will change over time, but the ratio of K_S and K_L samples in either the $\pi^+\pi^-$ (charged) or $2\pi^0$ (neutral) decay mode has to be robust against such changes. Furthermore, the design of the experiment should guard against differences in the relative loss of K_S and K_L because of spurious ("accidental") activity in the detector. Accidental activity results not only from random noise in the detector and readout electronics, but also from particles other than the decay products passing through the detector. These particles result from interactions between the primary beam and the beam dump, and from other decays close in time to the kaon decay of interest. Hence the number of kaon decays collected will depend on the intensity of the primary beam not only because of the number of kaons produced, but also because of the variation in the loss of kaons due to other intensity-related effects. The experiment must be designed to control biases not only from changes in rates of K_S and K_L production, but also from changes in accidental loss.

No detector will be able to cover all of the solid angle open to the kaon decay products, even with the large forward boosts available in fixed target experiments. In general, the acceptance of the detector will be a function of the location of a kaon decay and of the laboratory energy of the kaon. The lifetime difference between the K_L and K_S leads to different distributions of decays along the decay volume, and hence to different overall corrections to the number of observed events to obtain the true K_L/K_S ratio. The design of the experiment must allow one to keep strict control of any biases in these corrections.

Other K_L decay modes also present difficulties in obtaining a clean, large sample of $K_L \to 2\pi$ decays. Detection of $\pi^+\pi^-$ decays, with two charged particles in the final state, must compete with $\pi^+\pi^-\pi^0$ and semileptonic ($\pi^\pm\ell^\mp\nu$) decays with branching ratios from 60

to 200 times larger than that of the $\pi^+\pi^-$. Similarly, the $2\pi^0$ mode has to compete with the more prodigious $3\pi^0$ mode. The π^0 decays almost immediately into two photons, yielding a four photon $2\pi^0$ final state that can sometimes be mimicked by the $\pi^+\pi^-\pi^0$ decay. The $\pi\pi$ decays must be filtered from this morass of other K_L decays without a bias at the trigger level. For example, in the test run for this experiment [54] we discovered that it would be very difficult to reject the $\pi^\pm e^\mp \nu_e$ (Ke3) decays at the trigger level without causing a larger loss of $\pi^+\pi^-$ decays in the vacuum beam relative to the loss in the regenerator beam. Rather than introduce a bias that could be very difficult to control, we chose to accept the Ke3 decays when collecting the data, and eliminate them later in an unbiased fashion in the off-line analysis.

Finally, to extract $Re(\varepsilon'/\varepsilon)$, one will compare the proper time distributions of the charged mode decays to those of the neutral mode. Since this requires boosting the reconstructed kaons back to their rest frames, the relative energy scale between the charged and neutral must be strictly controlled to prevent biases in this comparison.

The following sections will describe the major principles used by the E731 experiment to control these effects. A brief description of the individual elements of the detector will be given in the following chapter, and more detailed discussions of the detector can be found in earlier documents [74, 75, 76].

2.2 Double Beams and the Regenerator

In the E731 experiment, two nearly parallel beams were produced by collimating the products of a proton beam impinging on a beryllium target. The detector was located far (over 100 m) downstream of this production target, which gave us ample room to magnetically sweep charged particles out of the secondary beam and gave neutral hyperons sufficient time to decay away. What was most important for our measurement technique, however, was that the detector was far enough from the target to allow essentially all of the K_S component of the K^0s and $\bar{K}^0$s produced in the target to decay away. This left two neutral beams of K_Ls (with some neutrons) entering our decay region.

At the upstream end of the decay volume for the experiment, one of the K_L beams passed

through two interaction lengths of boron carbide (B_4C), yielding a sample of coherently regenerated K_Ss. Downstream of the regenerator, the $\pi\pi$ decay rate was then described by

$$\frac{d\Gamma_R}{dz} \propto aF(p)\left\{|\rho(p)|^2 e^{-z/\gamma\beta c\tau_S} + |\eta|^2 e^{-z/\gamma\beta c\tau_L} + |\rho||\eta| cos(\Delta m z/\gamma\beta c + \phi_\rho - \phi_\eta)\right\}, \quad (2.2)$$

where p is the kaon laboratory momentum, z is the distance from the downstream end of the regenerator, ρ is the coherent regeneration amplitude, γ and β are the usual Lorentz boost factors, c is the speed of light, and a is the total absorption of the kaon beam. For our regenerator, $|\rho/\eta|$ was typically in the range 10-20, so the K_S decay term dominated the $\pi\pi$ decay rate in the regenerator beam. In the other (vacuum) beam, the rate was given by

$$\frac{d\Gamma_V}{dz} \propto F(p)|\eta|^2 e^{-z/\gamma\beta c\tau_L} \quad (2.3)$$

In both 2.2 and 2.3, $F(p)$ is the flux of K_Ls at momentum p in the beam. To accommodate possible asymmetries between the two beams, the regenerator alternated between the two K_L beams after small fixed intervals (every minute), effectively making $F(p)$ identical in the two beams. This also rendered biases from asymmetries in the detector negligible.

Decays from both beams to a common decay mode, either $\pi^+\pi^-$ or $2\pi^0$, were detected simultaneously[1]. It is particularly important that biases in the collection and reconstruction efficiencies were kept to a minimum by keeping all triggering, reconstruction and analysis cuts strictly independent of the beam in which a decay occurred.

Many of the advantages of simultaneously collecting the K_L and K_S decays to a common mode are clear. Changes in the detector response as a function of time will then affect the K_L and K_S decays identically, and hence will cancel completely in the ratio of K_L/K_S (the "single" ratio). Similarly, losses due to accidental activity in the detector will cancel to first order. Because both beams have the same source as their origin, intensity fluctuations in the primary proton beam will also cancel in each of the single ratios.

Why, though, use a regenerator to produce the K_S decays? Why not use a second target far downstream of the first? It is certainly an advantage to have the production target far upstream of the detector. This reduces the rate from other extraneous particles produced

[1]In the last approximately 20% of the data, all four of the $K \to \pi\pi$ modes were collected simultaneously. While collecting the $2\pi^0$ and $\pi^+\pi^-$ decays simultaneously is not crucial for the success of our technique, it does allow several more systematic cross checks.

in the target and beam pile and allows the charged particles to be swept out of the beam, both of which reduce the accidental rate in the detector. In coherent regeneration, there is essentially no momentum transfer between the kaon and the target. This yields a sample of K_S decays with an angular distribution relative the beam direction identical to that in the K_L sample from the vacuum beam. As we shall see, the transverse momentum of a decay will provide a powerful tool for rejecting backgrounds, and having identical angular distributions prevents any bias from entering into the background rejection. The momentum distributions of the K_S and K_L samples obtained using a regenerator are also very similar, which means that effects due to the finite resolution of the detector will be very similar in the K_S and K_L samples.

The use of the regenerator is particularly nice because the single ratios become physically meaningful. As we can see by comparing Equations 2.2 and 2.3, the incident kaon flux cancels in the K_S/K_L ratio and we are left with a measure of $|\rho/\eta|$. Since the same regenerator was used throughout the run, the regenerator provides us with a very powerful physical check (namely, we should always measure the same regeneration amplitude) to apply to different subsets of the $\pi\pi$ decays collected.

Now the regeneration amplitude ρ is related (see Appendix I) to the difference in the forward scattering amplitudes $f(0) - \bar{f}(0)$ of the K^0 and $\bar{K}^0$ by

$$\rho \approx \imath\pi \frac{f(0) - \bar{f}(0)}{k} N g(L, p), \tag{2.4}$$

where $k = p/\hbar$ is the kaon wavenumber, N is the density of scatterers, and g is a complex geometric parameter which is a function of the length L of the regenerator and of the kaon momentum. Regge theory predicts [77] that the difference in the forward amplitudes is dominated by a the exchange of a single Regge trajectory, that of the ω meson. This leads to the particularly simple form for the momentum dependence of the difference:

$$\frac{f(0) - \bar{f}(0)}{k} = A p^{\alpha} e^{-\imath\frac{\pi}{2}(2+\alpha)}. \tag{2.5}$$

Analyticity leads to the constraint between the power α and the phase of $f(0) - \bar{f}(0)$, $\phi_{f-\bar{f}} = -\pi(2+\alpha)/2$. In the high momentum range available in a kaon beam produced at Fermilab, deviations from this power-law dependence are expected to be very small.

The power-law momentum dependence and the analyticity prediction have been verified in previous experiments [78, 79, 80] to work very well at E731 kaon energies.

The expected power-law behavior adds one more physical constraint for controlling biases in the measurement of $Re(\varepsilon'/\varepsilon)$. From the charged and neutral single ratios we obtain a measure of ρ/η_{+-} and ρ/η_{00}. Since our measurement really entails measuring a difference between η_{+-} and η_{00}, we cannot directly compare the magnitude of the regeneration amplitude extracted from the single ratios in each of the two modes. The momentum dependence, however, should be identical in the two modes, and hence we should extract consistent slopes in each mode. Since orthogonal elements of the detector are used to detect the two different modes and since the backgrounds in the two different modes are quite different, a physical parameter which can be independently extracted in the two modes and then compared gives a powerful systematic check. It is particularly useful in limiting biases due to possible nonlinear differences in the energy scales of the two modes.

There are some disadvantages associated with this technique. The most important is an additional background due to scattering in the regenerator. In addition to coherent regeneration, where the kaon interacts coherently with all the nucleons in the regenerator, there is diffractive regeneration, where there is a finite momentum transfer between the kaon and a particular nucleon. There are also inelastic processes where the nucleus which scatters the kaon breaks up or the nucleus or nucleon enters an excited state. Regeneration and kaon scattering are discussed in more detail in Appendix A.

The other, more minor, disadvantage associated with this technique is due to the difference in the K_S and K_L lifetimes. As mentioned above, this leads to different average acceptances for the K_S and K_L samples. We use a Monte Carlo simulation of the detector to determine the corrections needed in the two modes. It is important to remember that the acceptance function $\epsilon(p,z)$ is *identical* for the vacuum and regenerator beams. By using bins (in p and z) with sizes large relative to the inherent resolution of the detector, we reduce our sensitivity to smearing in the event reconstruction, which is generally the hardest aspect of a detector to simulate accurately.

We will now move on to discuss the general characteristics of the detector required by this experiment.

2.3 Detector Requirements

We will focus on three main aspects of designing a detector for an experiment using the double beam: (a) acceptance corrections, (b) detection of the $K \rightarrow 2\pi^0$ decays and background elimination in this mode, and (c) detection of the $K \rightarrow \pi^+\pi^-$ and elimination of the background. In both modes we wish to reconstruct the kaon laboratory momentum and the decay position so that we may compare the observed distributions to Equations 2.2 and 2.3 above.

2.3.1 Acceptance Corrections

One of the most important aspects of designing the detector was to keep the acceptance calculation mentioned in the previous section as simple as possible. To aid in this, all of the geometrical limitations of the detector were defined by active veto elements. This largely reduced the problem of determining the acceptance to measuring the edges of several planar counters located at well known distances from the target.

To aid in studying the detector performance and acceptance, we collected high statistics samples in the $3\pi^0$, $\pi^+\pi^-\pi^0$, and Ke3 decay modes.

2.3.2 $K \rightarrow 2\pi^0$ Decays

For $2\pi^0$ decays, the energies and positions of the four photons in the final state had be measured, which required an electromagnetic calorimeter. In order to accurately determine the kaon momentum, the calorimeter needed to have high resolution. As we will describe later, by using the positions of the photons in the calorimeter in addition to their energies, we can determine the distance of the kaon decay from the calorimeter. Thus to obtain an accurate determination of the decay position, the calorimeter must also had to be segmented to allow an accurate measurement of the photon positions.

To obtain a large enough sample of decays in a reasonable time, the intensity of the kaon beam had to be quite high. This meant that the calorimeter had to be sufficiently radiation hard to not be damaged by the high rate of particles passing through it, and to have a rapid

response. To keep biases at a minimum, it also helped to have a high resolution device. An array of lead glass crystals, where the Çerenkov light produced in the electromagnetic shower is measured, best satisfied these demands at the time of the experiment.

The most problematic background from the viewpoint of triggering came from $K_L \to 3\pi^0$ decays. Many of these decays could be eliminated from the $2\pi^0$ sample simply by counting the number of isolated islands of energy (clusters) in the calorimeter and requiring the count to be four. Because of the possibility of photons escaping the detector or landing very close to each other ("fusing") in the calorimeter, this background could still mimic the four photon final state. This problem was reduced by introducing many planes of veto counters to detect any photon from decays in our decay volume escaping the detector. A finely segmented calorimeter also helped to reduce the number of fused photons.

The four photon final state could also be mimicked by the $\pi^+\pi^-\pi^0$ decay when the two charged pions caused hadronic showers in the calorimeter. These could be effectively eliminated with a hodoscope bank following the calorimeter.

2.3.3 $K \to \pi^+\pi^-$ Decays

The $\pi^+\pi^-$ decay required measuring two charged particles in the final state. For triggering purposes, we used two planes of hodoscopes. The trajectories of the particles were measured using two pairs of drift chambers. A dipole analyzing magnet between the two pairs allowed the momentum of each particle, and hence of the kaon, to be measured. The decay position of the kaon could be determined by extrapolating the trajectories measured in the upstream chambers to a common point.

The major backgrounds to the $\pi^+\pi^-$ decays, the $\pi^+\pi^-\pi^0$ and $\pi^\pm\ell^\mp\nu$ decays, all have a neutral particle in addition to the two charged particles in the final state. Since the two charged particles can pick up a large transverse momentum which will be balanced by the neutral, the two charged particles in these decays will in general have a much more asymmetric topology than those from $\pi^+\pi^-$ decays. A simple means of favoring the $\pi^+\pi^-$ decays at the trigger level was therefore obtained by requiring a symmetric up-down, right-left topology for hits in the hodoscope trigger planes.

By placing enough material at the end of the detector to filter all but muons, the $\pi^{\pm}\mu^{\mp}\nu_{\mu}$ decays could be vetoed at the trigger level. As mentioned earlier, the Ke3 background could not be rejected without biasing the relative K_L and K_S acceptance, and were rejected off-line later using the ratio of energy measured in the lead glass to momentum measured in the charged spectrometer.

Finally, the charged and neutral energy scales had to be tied to each other. This was accomplished by calibrating the lead glass with tracks from electron-positron samples measured in the charged spectrometer. The samples came both from special electron calibration runs and from the Ke3 sample collected with the $\pi^+\pi^-$ decays.

2.4 Sensitivity to Other Kaon Parameters

The preceding sections have outlined the major considerations affecting the design of the experiment for measuring $Re(\varepsilon'/\varepsilon)$. Great care has been taken to obtain careful, high statistics measurements of the distribution of decays in momentum and position downstream of the regenerator. If we examine Equation 2.2 more carefully, we see that we in principle have sensitivity to many other parameters of kaon decay. Using the vacuum beam as a normalization, we can obtain the flux of kaons on the regenerator. Then from the shape of the distribution immediately downstream of the detector, we have good sensitivity to the K_S lifetime. Farther downstream the interference term becomes more significant, allowing us to probe both the $K_L - K_S$ mass difference, Δm, and the overall phase $\phi_\rho - \phi_\eta$.

Using a regenerator to measure the phase rather than a target again has advantages and tradeoffs. The biggest advantage is that the initial state of the kaon is very well known since we are starting with an essentially pure K_L beam. In contrast, with a target, we need to know the relative numbers of K^0s and $\bar{K}^0$s produced. The biggest drawback to using a regenerator is that the phase that is really measured is the difference of the phase of η and the regeneration phase. For a $\Delta\phi$ measurement, this is not a serious issue as the regeneration phase cancels when comparing the charged and neutral mode phases. To measure individual phases ϕ_{+-} and ϕ_{00}, however, we must use the analyticity constraint

on the power law and phase of $f - \bar{f}$ (Equation 2.5) to isolate the phase of interest from the measured phase $\phi_\rho - \phi_\eta$.

2.5 Summary

This chapter has presented the some of the major issues facing a precise measurement of $Re(\varepsilon'/\varepsilon)$ and described generally both how these issues affect the technique and detector used to make this measurement and how this method gives us sensitivity to other parameters of kaon decay. The following chapters will describe the detector, analysis and fitting techniques used in more detail.

CHAPTER 3

THE APPARATUS AND RUN

In the previous chapter, the basic techniques used to measure $Re(\varepsilon'/\varepsilon)$ in this experiment were outlined. Here we give a description of the kaon beam production, the detector, and special features of the run. Excellent descriptions and illustrations of the various detector elements for E731 have already been given references[74, 75] if more detail is needed.

3.1 The Kaon Beams

The E731 experiment was located in the Meson Center beam line at Fermilab. The two kaon beams used in the experiment were formed from the secondary particles produced by the interaction of an 800 GeV primary proton beam with a beryllium target. The proton beam was delivered in a 20 second "spill" once every minute, with 3×10^{11} to 2×10^{12} protons delivered in each spill. Within a spill, the protons arrived in 2 ns "buckets" every 18 ns, with the number of protons in each bucket varying by about a factor of 2 from bucket to bucket. This radiofrequency (RF) structure provided the basic timing used in our trigger, and can be clearly seen in the TDC plots for our trigger elements[1] (Figure 6).

The target consisted of a square beryllium rod measuring 36 cm long and 3.2 mm on a side. The proton beam profile was roughly Gaussian with a width of 0.4 mm. The beam

[1] A trigger element TDC measured the time between an initial pulse supplied by the trigger and a stop pulse from activity in the trigger element. The origin of the scale is arbitrary, and the first signal to reach the TDC is not necessarily the signal which formed the trigger.

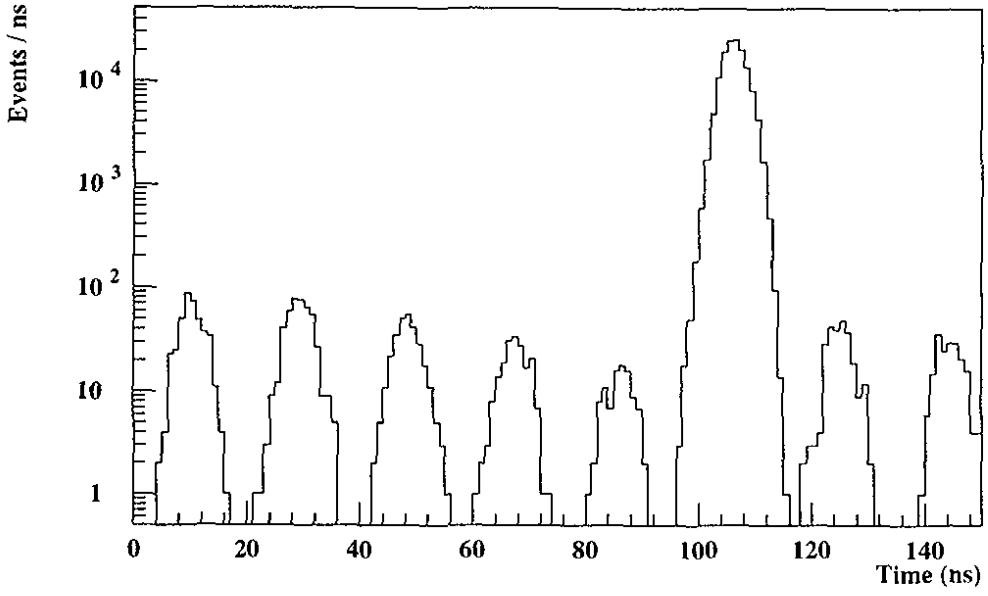

Figure 6. The distribution of arrival times relative to the trigger for the $2\pi^0$ trigger signal $E_t > 28$ GeV (see neutral triggering) in events that have satisfied the $\pi^+\pi^-$ trigger. The 18 ns structure of the accelerator can be clearly seen in the bunching of activity. The large peak corresponds to the "bucket" in which the decay causing the $\pi^+\pi^-$ trigger occurred.

position on the target was monitored throughout each spill with a wire chamber, with the center of the beam spot generally contained within ± 0.25 mm of the target center.

Secondary neutral beams were produced using the collimation scheme pictured in Figure 7a. The first stage of collimation used a two-hole copper collimator 5.8 m in length to form the two almost parallel beams. The collimator began 9 m downstream of the target and contained two tapered channels oriented nominally 5 mrad from the proton beam in the horizontal direction. At the upstream end of the collimator the channels presented 6.65×6.65 mm square faces centered 5.8 mm above and below the target location. Each beam channel subtended a solid angle of 3 nanosteradians. The beam edges were then further defined by several sets of steel collimators ranging in length from 1.2 m to 1.8 m. The two collimators defining the edges between the beams were located 25 m and 49 m downstream of the target. The outer edges of the beams were defined by two sets of horizontal and vertical collimators 52 m and 83 m from the target.

To help reduce unwanted backgrounds and detector activity, it was useful to reduce the

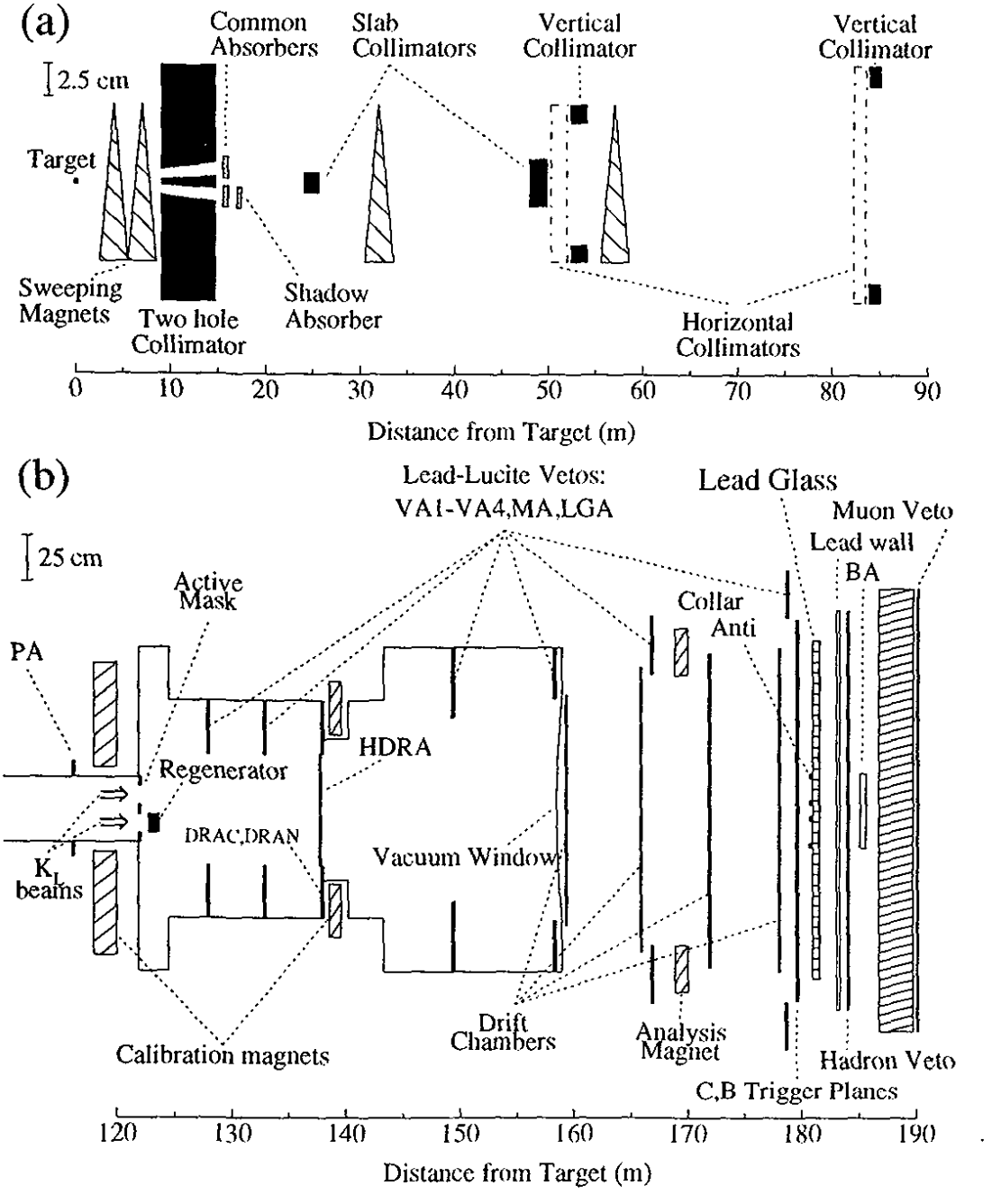

Figure 7. Illustration of the experimental apparatus used in this experiment. Part (a) is a sideview of the layout of the collimation and sweeping system used to produce the two beams. Part (b) shows the apparatus used to detect the decay products.

neutron to kaon ratio in the secondary beams. The neutron production spectrum is peaked more strongly in the forward direction than the kaon spectrum, so the 5 mrad "targetting angle" between the proton beam and the kaon beams served to decrease this ratio without greatly sacrificing beam intensity. The ratio was further reduced with an absorber in each beam made of 50.8 cm of beryllium and 7.6 cm of lead positioned just downstream of the copper collimator. This "common" absorber also served to eliminate photons from the beam. The resulting ratio was about one neutron per kaon entering our detector region. The regenerator beam required further reduction of the neutron flux to keep interactions in the regenerator at a manageable level, so a second 45.7 cm beryllium absorber always shadowed the regenerator. Charged particles were swept out of the beam with several sweeper magnets.

To further reduce beam interaction rates and prevent undue loss or scattering of decay products, the entire beam path and decay volume from 17 m to 160 m was held at a vacuum under 0.015 torr. The downstream end of the vacuum was sealed by a 1.22 m diameter window. The window, made from 0.127 mm of mylar and 0.584 mm of Kevlar 29, was as thin as possible to keep multiple scattering at a minimum.

The decay region considered in this experiment began 110 m downstream of the target. This left ample time for hyperons in the beam and the K_S component of the kaons to decay away. In the beam which finally reached our decay volume, there were roughly equal numbers of K_L and neutrons, and the number of Λ particles were about 0.05% of the number of K_L in the energy range (20 GeV/c to 160 GeV/c) of interest. At our mean energy of about 70 GeV/c, the K_S component of the original K^0 (or $\bar{K}^0$) produced at the target has decayed to be under 10^{-6} of the K_L component at the beginning of our decay volume.

For a spill of 3×10^{11} protons, roughly 25 million K_L entered the decay volume in the vacuum beam. Only a small fraction of these, about 2%, decayed in the largest fiducial volume we consider.

3.2 The Detector

The apparatus used in this experiment is illustrated in Figure 7b. Most of the detector elements had a role to play in the detection of and reconstruction of both $\pi^+\pi^-$ and $2\pi^0$ decays, though some were designed primarily for one or the other mode. The components which play a role common to both the $\pi^+\pi^-$ and $2\pi^0$ decay modes will be described first.

The detector divides up naturally into two subsystems, one to detect the four photon $2\pi^0$ final state and one to detect the two charged particle $\pi^+\pi^-$ final state. Each subsystem also has elements for background rejection peculiar to the final state of interest. A list of the detector elements and their locations is given in Table 2. There are several components of the detector with a common function in the charged and neutral modes which we will first discuss.

The coordinate system to be used throughout this thesis defines the z axis along the beam direction. The x and y axes are then defined by the horizontal and vertical directions transverse to the beam, respectively.

3.2.1 Common Elements

3.2.1.1 The Regenerator

The regenerator, pictured in Figure 8, consisted of four blocks of boron carbide (B_4C), each 19.0 × 8.9 × 8.9 cm in size. These blocks totalled two interaction lengths, for which coherent regeneration is a maximum (see Appendix I). The blocks were spaced on average 3.5 cm apart. Within each gap there were veto counters made with 6 8.90 × 1.74 × 0.63 cm overlapping fingers of scintillator. These counters served to reduce backgrounds from inelastic interactions within the regenerator and also to veto kaon decays within the regenerator. A 1.25 cm lead piece at the very end of the regenerator converted photons from $2\pi^0$ decays within the regenerator, defining a sharp boundary for the upstream location of the the $2\pi^0$ decays in the regenerator beam. Another set of veto counters located 1.75 cm downstream of the lead detected the conversion products. Since these counters were also in veto at our trigger level, $\pi^+\pi^-$ decays upstream of the counters were also vetoed. This resulted in the

Table 2. The detector elements and their positions.

Detector Element	m from target	Detector Element	m from target
Pinching Anti	116.118	Drift Chamber 1	159.292
Sweeper Anti	119.59	Drift Chamber 2	165.867
Sweeper Magnet	119.59	Magnet Anti (MA)	166.836
Active Mask	121.893	Analyzing Magnet	168.865
Regenerator	123.550	Drift Chamber 3	171.857
Vacuum Anti 1 (VA1)	127.855	Drift Chamber 4	178.004
Vacuum Anti 2 (VA2)	132.819	Lead Glass Anti (LGA)	178.710
V hodoscope	137.792	C Hodoscope	179.502
Lead sheet	137.804	B Hodoscope	179.520
T hodoscope	137.815	Collar Anti (CA)	180.700
DRAC veto counter	137.826	Lead Glass Array	181.809
DRAN veto counter	137.866	Lead Wall	182.7
Separator Magnet	139.008	μ1 Hadron Veto	183.996
Vacuum Anti 3 (VA3)	149.309	Back Anti (BA)	185.047
Vacuum Anti 4 (VA4)	158.291	3.2m Steel Muon Filter	186.7
Vacuum Window	158.965	μ2 Muon Veto	189.914

downstream scintillator face defining the upstream edge of the decay region for the $\pi^+\pi^-$ mode, while the downstream face of the lead defined the upstream edge of the decay region for the $2\pi^0$ mode. To precisely determine the true double ratio, we must therefore know the size of the gap between the lead piece and the downstream veto counters at the 1 mm level. We will further discuss issues related to this gap in Chapters 8 through 10.

3.2.1.2 The Upstream Mask

The behavior of the acceptance in the farthest upstream region of the vacuum beam was defined by a precision veto counter (the "active mask" or AM) located 121.9 m from

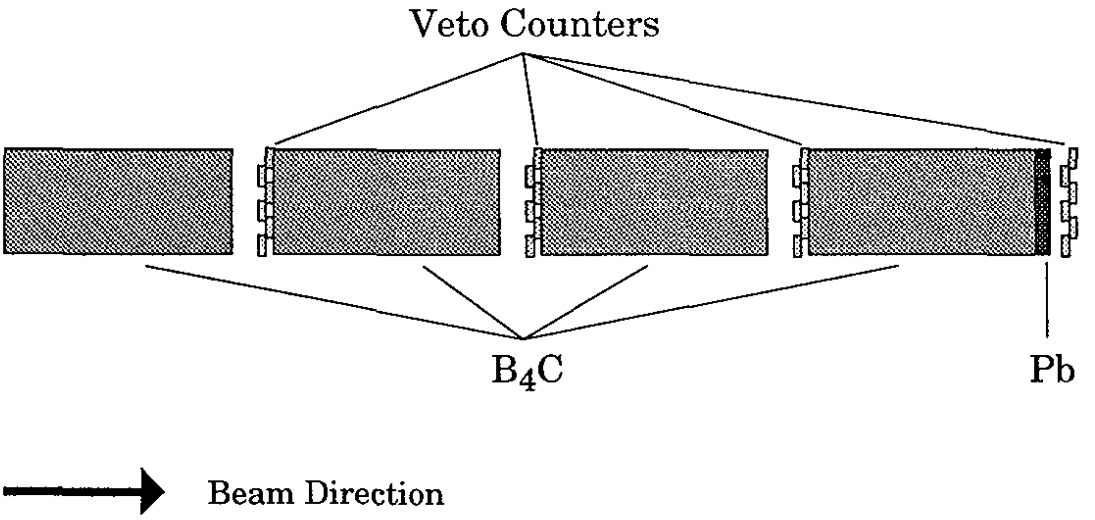

Figure 8. The makeup of the regenerator.

the target. The mask consisted of two layers of 2.54 cm thick lead with scintillator behind each layer. Holes were milled in the lead to allow the beam and decay products to pass and the scintillator was aligned flush to the edges. The holes were sized and positioned such that (a) no products from decays in the regenerator beam which occurred upstream of the regenerator could sneak past the regenerator (and regenerator anticounters) and (b) products from decays upstream of the mask in the vacuum beam were limited by the mask or another active counter farther downstream, and not by "dead" material (such as the box enclosing the regenerator). The effective edges of the mask were determined with electrons from Ke3 decays.

3.2.1.3 The HDRA

The HDRA (for Hodoscope and Decay Region Anticounter) was a trigger and veto system used in both the charged and neutral modes. Its makeup is shown in detail in Figure 9, while the physical properties of its components are listed in Table 3. Originally, the hodoscopes were intended to tag the beam in which a $K \rightarrow \pi^0\pi^0$ decay occurred by converting one of the four photons and measuring the e^+e^- trajectories in the charged

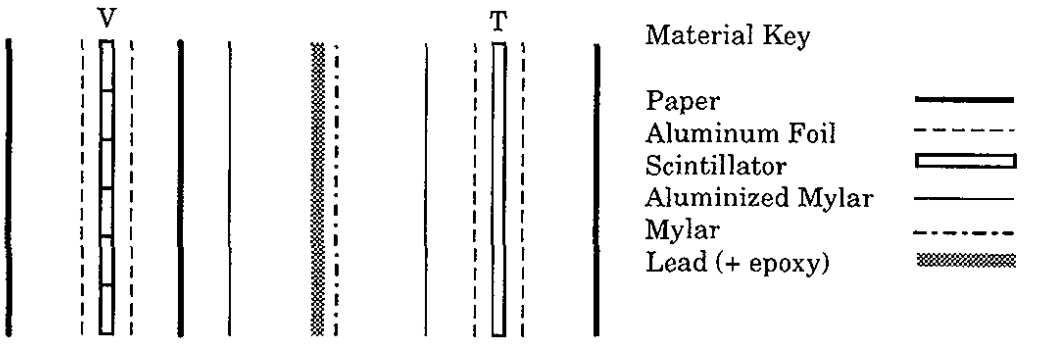

Figure 9. An exploded view of the material contained within the HDRA. The 0.5 mm lead sheet, bonded to a mylar sheet for support, was not always in place.

spectrometer. A 0.5mm lead sheet converted exactly one photon 25% of the time, and this process could be differentiated from decays with charged products by looking for a signal in the trigger (T) counters just downstream of the lead in conjunction with the absence of any signal in the veto (V) counters immediately upstream of the lead. Both the T and V hodoscopes consisted of 6 1 mm thick staves of NE110 scintillator. A more detailed description of this technique can be found elsewhere [81].

The $\pi^+\pi^-$ events simply used the T and V counters as trigger hodoscopes. These events could not be collected with the sheet in place because of the unacceptably large multiple scattering in the lead. As a result, the $2\pi^0$ and $\pi^+\pi^-$ events were initially collected separately.

During the run we found that the $2\pi^0$ events in which no photons converted would yield a more accurate result than the conversion events. This allowed us both to remove the lead sheet and to extend our fiducial region into the decay volume downstream of the HDRA for $2\pi^0$ mode. Using the downstream events does, however, require careful measurement of the materials listed in Table 3 to obtain the levels of kaon regeneration and photon conversion at this plane.

Table 3. A list of the materials in the HDRA and their physical properties. The thicknesses are averaged over the beam region, while the radiation lengths are averaged over the illuminated region. The lead sheet was not always present (see text). $(f - \bar{f})/k$ is given at 70 GeV/c.

Material	Thickness (mm)	Density (gm/cm^3)	Atomic Weight	$\frac{f-\bar{f}}{k}$ (mb)	$\frac{f+\bar{f}}{k}$ (mb)	Radiation Length (percent)
Scintillator	2.17	1.03	13.0	1.15	33.10	0.497
Mylar	0.11	1.39	96.1	8.29	239.57	0.044
Aluminum	0.05	2.70	27.0	2.07	59.21	0.058
Paper	0.38	0.63	94.1	10.89	229.51	0.066
Lead	0.515	11.35	207.2	9.71	326.28	8.9

3.2.2 Neutral Detection

As mentioned in the previous chapter, the neutral portion of the detector was designed with two primary purposes in mind. The first, of course, was the detection of the 4 photon final state resulting from the $K \to \pi^0\pi^0$, $\pi^0 \to \gamma\gamma$ decay chain. The second was to reduce background from the 6 photon $K_L \to 3\pi^0$ decays. This decay mode could mimic the $2\pi^0$ decay mode because (a) photons would sometimes escape detection, and (b) 2 photons would sometimes land near to each other ("fuse") in the electromagnetic calorimeter, resulting in their showers appearing to the trigger as a single shower. Some combination of these two processes would make the $3\pi^0$ decay appear to have a 4 photon final state. This section will discuss the electromagnetic (EM) calorimeter and the photon veto system. The discussion of the neutral trigger will occur in Section 3.3.

3.2.2.1 The Lead Glass Calorimeter

The heart of the $2\pi^0$ detection was the electromagnetic calorimeter located 181 m downstream of the target. An excellent, detailed discussion of this calorimeter has already been given in reference [74], thus only an overview of the array configuration and reconstruction will be given here.

The picture of a typical $2\pi^0$ event in Figure 10 serves to illustrate the configuration of this element of the detector. The calorimeter consisted of 804 blocks of Schott F-2 lead glass arranged in a circular array with two holes near the center through which the kaon beams passed. Each block measured 5.82×5.82 cm^2 in the x and y directions, and 60.17 cm along the z direction. Since the radiation length of this material is $X_0 = 3.21$ cm, the calorimeter was 18.74 radiation lengths deep. The radius of the array was about 0.93 m.

Phototubes were pressure mounted to the back of each block to collect the Çerenkov light produced by EM showers from photons and electrons striking the array. The phototubes were 10 stage Amperex 2202 tubes with bialkali photocathodes and applied base voltages near -1200V. The gains obtained were of order 1.2×10^5, but would change by about 1% for a 1V high-voltage change. The voltages were monitored at the 1 volt level, but from the stability of the measured gains we know that the voltages were actually stable to within a fraction of a volt throughout the run. In addition, a xenon flash lamp system was pulsed every two seconds to monitor the combined response of each block and its phototube throughout the run. The entire array was housed in a light-tight room to reduce noise from external light sources.

Signals from the phototubes passed through 83.8 m of RG58 cable to allow time for the formation of the trigger before digitization. The signals were then integrated over a 150 ns gate and digitized in 9 LeCroy 2280 analogue to digital converter modules (ADCs). Though the Pb glass response measured with the Çerenkov light was very fast, the long gate was necessary because of the pulse broadening in the delay cables and also because of the scintillation component of the light produced in the shower which has a much longer time scale than the Çerenkov light. These ADC modules had a 12 bit accuracy, but operated with a dual range to effectively extend the dynamic range to 15 bits. The low to high range crossover point corresponded to roughly 16 GeV, and the high to low range gain difference was measured for each channel at the 0.1% level. The information in the array was sparsely read out, a given block being recorded only if its energy was above a certain threshold. For all data collection when neutral triggers were collected, the readout threshold was 5 counts (about 25 MeV). When only charged triggers were collected, a higher readout threshold of 20 counts was used.

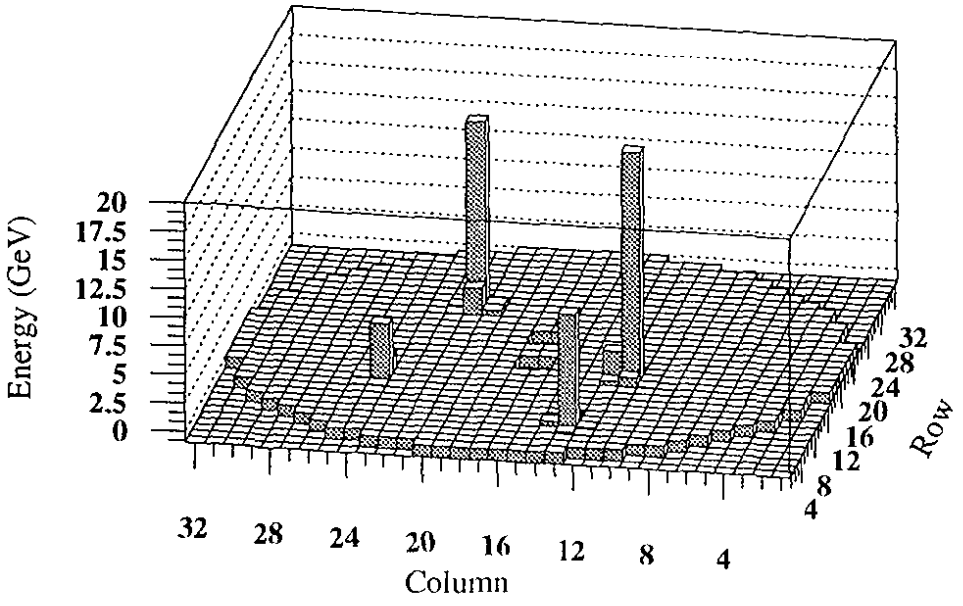

Figure 10. The lead glass calorimeter with a typical $2\pi^0$ event. The two holes to pass the kaon beam can be seen in the center of the array.

While the fast response of the lead glass made it useful in the high rate environment of a fixed target experiment, a major drawback is the inherent nonlinearity of its response. The nonlinearity results because of the reabsorption of the Çerenkov light as it travels through the block. An electromagnetic shower will tend to produce its peak number of particles farther into a material the higher the energy of the showering particle. This results in the peak Çerenkov light production occurring farther into the block for higher energy showers, and hence less total attenuation as the light travels to the phototube. This attenuation was the most severe and varied most rapidly for the shorter wavelength Çerenkov light, so Wratten 2A filters were placed before the phototubes to block light with wavelengths under 430 nm. While causing about a 50% light loss, the filters passed light in a regime where the absorption was a minimum and where the wavelength-dependence of the absorption is negligible. These effects both improved the resolution beyond the loss of photostatistics and

simplified the calibration of the glass. With the filter in place, typical absorptions were of the order 3.5% – 4%, corresponding to nonlinearities roughly behaving like $E_{\text{true}} \propto E_{\text{measured}}^{0.97}$.

During the run, the absorption of the Çerenkov light by a block tended to increase because of radiation damage, particularly for blocks near the center of the array. The transmission decreased by 5% per week in the most seriously affected blocks. To avoid serious degradations in resolution, much of the damage was cured with the ultraviolet light supplied by two 400 W Hg vapor lamps. Curings required at least a four day shutdown and were done about once a month.

For each block, the absorption and gain were determined several times during the run (see Chapter 4) from electron samples obtained from special calibration runs and from Ke3 decays. As Figure 10 shows, the EM shower from an incoming electron develops across several blocks. To reconstruct the total energy in a shower, the energies from a 3×3 array of blocks (a "cluster") centered on the block of maximum energy were summed together. This sum was then corrected as described in reference [74] for threshold effects, pedestal shifts, leakage into blocks outside of the 3×3 array, and the nonlinearity described above. These corrections were extensively studied using both EGS simulations and the above electron samples.

The photon response in the lead glass is somewhat different from the electron response because the photons do not begin to emit Çerenkov radiation until after their initial conversion into an e^+e^- pair, while an electron begins emitting upon entry into the glass. A photon responds as the sum of the electron and positron showers in a block foreshortened by the photon conversion depth t_0. The conversion depth varies according to $e^{-t_0/\frac{7}{9}X_0}$, but the conversion depth was not known on an event by event basis. A correction to the response averaged over all conversion depths was made, but the variation in depths added an additional contribution to the photon resolution.

The average energy resolution for electrons was well described by

$$1.5\% + 5\%/\sqrt{E}, \tag{3.1}$$

where the energy E is measured in GeV, though it varied from block to block because of variations in the light attenuation of the blocks and quantum efficiencies of the phototubes. The overall photon resolution was about 1% worse.

The position of a photon or electron in the array can be extracted from the pattern of energy sharing in the 3×3 cluster. By summing the energies in each column of the cluster and comparing the ratio of the edge column sums to the center column sum, the x position can be obtained independently of the y position of the particle striking the block. Similarly, the y position can be obtained independent of the x point of impact using the sums of rows. Corrections to the positions were then made using the measured variations of the individual block sizes from the average block size given above. This method resulted in an average position resolution of 2.8 mm. The resolution did vary across a block, changing from 1.5 mm for a particle landing near a block edge, to 4.0 mm for a particle striking the center.

The signals from the lead glass were used for triggering purposes as well as being integrated and digitized later on. For this purpose, the signals from the array were viewed by two devices in addition to the ADCs.

The first device was used to provide a very rapid measure of the total energy (E_t) in the array at any time. For this purpose, the lead glass array was subdivided into 3×3 groups of blocks, and the signals from the blocks in each 3×3 group were sent to an "adder". The adder siphoned one eighth of the signal from each block before passing the signal into the delay cables, then formed an analogue sum of the siphoned signals. The sums of the 92 adders were themselves routed on two paths. On one path, each sum was integrated with a 30 ns gate and digitized. This gate was much shorter than the gate for the individual blocks, and was useful to help identify clusters that arrived either earlier or later than the trigger of interest, that is, arrived "out of time". On the other path, the adder outputs were summed together to yield the estimate of the total energy in the glass.

The second device was a hardware cluster finder (HCF), which counted the number of clusters[2] in the lead glass calorimeter. The ability to count clusters at the trigger level led to a factor of ten reduction in the trigger rate. The signals from each block were viewed by the HCF via a capacitive coupling, and each of the signals was digitized by a 30 MHz 6 bit flash ADC. A block registered a hit if its energy content was above about 1 GeV. Figure 11 shows the energy content of all blocks with signals above the sparse readout threshold and all blocks above the HCF threshold for a subset of $2\pi^0$ events. The 1 GeV threshold was

[2]In this context, a cluster refers to a contiguous island of blocks all above the HCF threshold.

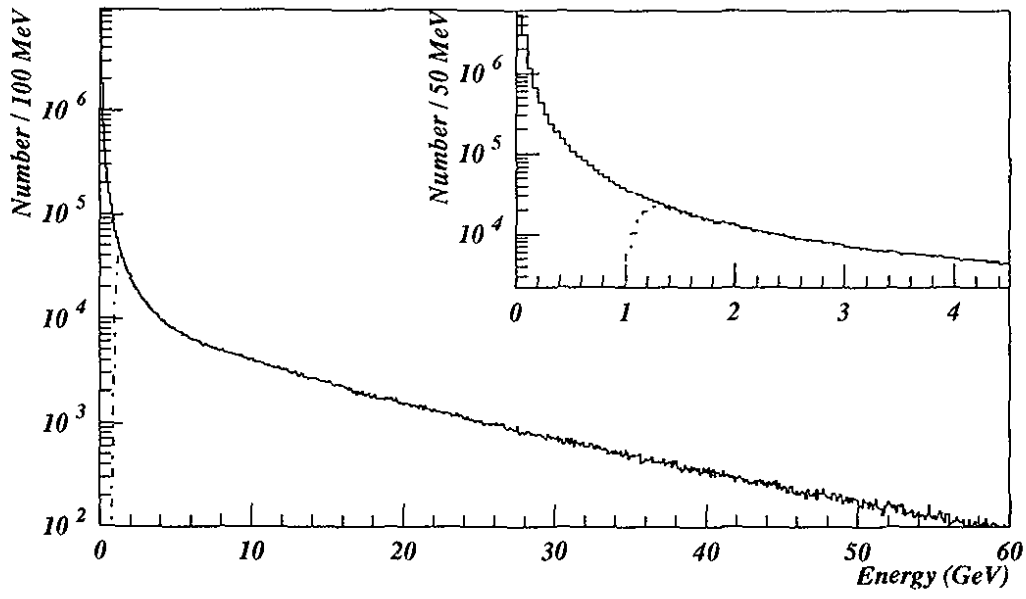

Figure 11. The distribution of energies in individual blocks for $2\pi^0$ events. The solid histogram shows the distribution of all blocks above the 5 count ADC readout threshold. The dot-dash histogram shows the same energy distribution for all blocks above the hardware cluster finder (HCF) threshold. The inset is a blow up of the HCF threshold region.

low enough to allow a high efficiency for detecting decays of lower energy kaons while high enough to prevent the loss of events where two photons landed quite close together in the array or where there was accidental activity (for example, the tail of activity from a shower which occurred in a previous bucket) in the array. Details of the HCF construction and cluster-finding algorithm have been published elsewhere [75, 82].

3.2.2.2 The Neutral Veto Systems

A photon veto counter (the "collar anti" or CA) covered the inner halves of the sixteen blocks around the two beam holes. The counter consisted of 8 radiation lengths of material (4.45 cm of copper followed by 2.8 cm of lead) to convert incoming photons followed by scintillation counters to detect the electrons and positrons from the resulting EM shower and veto the event. If the veto counter were not there, a substantial fraction of the EM shower of photon (or electron) which would have landed in the region covered by the CA

would have been lost in the beam holes. The reconstruction of the energy and position of these photons would have been very difficult, and the determination of the acceptance would require a very detailed understanding of the energy loss of photons as a function of energy, distance of impact from the beam hole edge, and angle of impact. The CA, on the other hand, provides a clean edge which can be accurately determined with electrons from Ke3 decays, and limits photons to regions in those blocks where the energy and position measurements were largely insensitive to the detailed loss down the holes.

The remaining photon veto counters served to reject background from $3\pi^0$ decays and to a lesser degree from other charged decays. The counters in most of these veto banks consisted of a scintillator plane to detect charged particles followed by two lead lucite sandwiches to convert and detect photons. Each sandwich had 5 layers each of lead and lucite and totalled 3 radiation lengths. All counters faced the beam direction. Four sets of these counters (the "vacuum antis", VA1 - VA4) were arranged in rings inside the pipes enclosing the decay volume, two on either side of the HDRA. Another set in a square ring surrounded the aperture of the charged analysis magnet and was dubbed the Magnet Anti (MA). A final ring just upstream of the lead glass (the "Lead Glass Anti" or LGA) detected particles that would have just missed the lead glass array.

At the far upstream end were two sets of counters to detect photons from $3\pi^0$'s that decayed in the beam pipe preceding the large decay volume proper. The most upstream was the "pinching anti", which consisted of a layer of lead followed by a layer of scintillator collaring the beam pipe. This counter also faced the beam. A rather more unconventional counter system was the "sweeper anti", where sheets of scintillator actually lined the outside surface of the beam pipe from 117.8 m to 121.4 m. Photons which converted in the beam pipe would have escaped detection by the VAs, but could now be vetoed by these scintillator panels.

A scintillator plane ("DRAC") followed by several radiation lengths of lead and a second scintillator ("DRAN") plane filled the area at the HDRA between the rectangular T and V hodoscope planes and the cylindrical vacuum pipes. Any decay products missing the hodoscopes struck these anticounters and vetoed the event.

Photons from $3\pi^0$ decays could escape detection not only by passing outside of the

detector, but also by remaining in a beam and leaving through a beam hole. To detect these photons, an anticounter, the "BA", made from 48 layers of 0.33 cm lead sandwiched with lucite was placed behind the lead glass covering both beams. The entire anticounter was 28.1 radiation lengths deep, hence electromagnetic showers were generally confined to the first two thirds. Hadronic showers, such as those initiated by neutrons in the beam, characteristically deposited their energy deep into the detector. By comparing the energy deposit in the last third relative to the first two thirds of this device, events with photons which passed down one of the beam holes in the calorimeter could be vetoed without unintentionally vetoing a large number of good events because of the interactions of hadrons in the neutral beam with the device.

Finally, a hodoscope plane ($\mu 1$) just downstream of the lead glass rejected $\pi^+\pi^-\pi^0$ decays that mimicked the four photon $2\pi^0$ decays when the pions showered in the lead glass. A 21 radiation length lead wall behind the glass and lead collar around the beam region prevented any particles from an electromagnetic shower in the glass from registering in $\mu 1$. Particles from hadronic showers, however, could pass through the wall and be detected in the hodoscope.

3.2.3 Charged Detection

3.2.3.1 Introduction

In the detection of the $\pi^+\pi^-$ decays, triggering and measurement used independent separate elements of the detector. This is unlike the case of $2\pi^0$ decays, where the major elements of triggering and measurement used the lead glass array. The momenta and trajectories of charged decay products were measured in a drift chamber spectrometer, but the signals from the drift chambers arrived over too broad a time span to be used in the formation of a fast clean trigger unbiased by products from decays in other buckets. Triggering instead relied upon several hodoscope planes. The following sections will discuss the spectrometer and track reconstruction, then the trigger elements and the trigger itself.

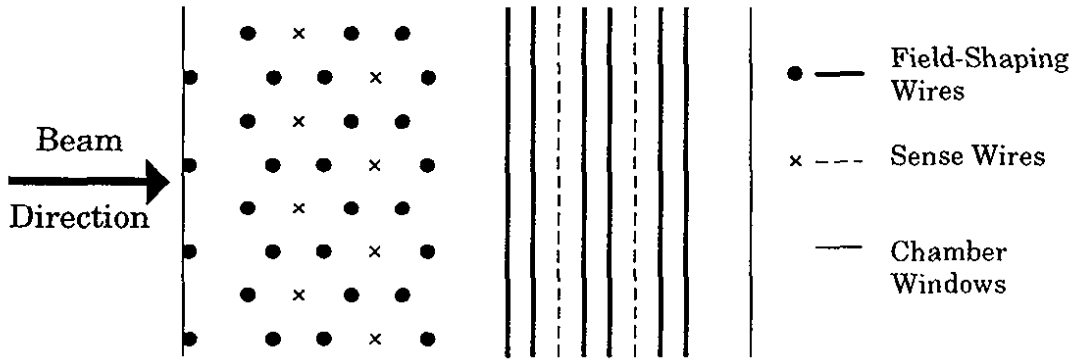

Figure 12. Layout of the field shaping and sense wires used in all drift chambers. This is the view looking down on the chambers, with the vertical wires which measure x positions in the front (left) and the horizontal wires which measure y positions in the rear of the chamber.

3.2.3.2 The Drift Chamber Spectrometer

The charged spectrometer consisted of two pairs of drift chambers that measured the charged particle trajectory upstream and downstream of a momentum analyzing magnet. Helium bags were placed between all of the drift chambers to reduce the effects of multiple scattering on the measurement of particle trajectories and momenta.

As shown in Figure 12, the cells of the drift chamber consisted of a sense wire located at the center of a hexagon defined by six field shaping wires. The wires in a sense plane were separated by 12.7 mm, and both the x- and y- views of each chamber had two sense planes offset by half that distance. This yielded a maximum drift distance of 6.35 mm perpendicular to a wire and an unambiguous determination of the side of the wire by which a particle passed. The chamber farthest upstream was the smallest, measuring 1.26×1.26 m and containing 101 sense wires in each plane. Each successive chamber increased in size, the largest being 1.77×1.77 m with 140 sense wires per plane.

The field shaping wires were made of 100 micron gold-plated copper-beryllium and the sense wires were 25 micron gold-plated tungsten. In constructing these chambers, the tolerance on wire placement was about 25 microns. More details on the construction of the chambers can be found in reference [81].

The chambers used a gas mixture of 50% Argon and 50% Ethane. With the applied voltage of $-2650V$, the drift velocities in these chambers were of the order of $50\mu m/ns$.

To reduce aging effects on the chambers, two measures were taken. First of all, the applied high voltage was ramped down to 80% of its nominal value during the 40 seconds between each spill. During this time, the dark currents were typically 0.1–0.2 μamps per chamber. In addition, a small amount of alcohol (about 1%) was added to the argon-ethane as a quenching agent to help prevent breakdown and slow the chamber aging process. Ethanol was initially used, but was replaced later in the run with isopropyl alcohol.

The pulses from the drift chambers were amplified and discriminated in front end cards mounted on the chambers themselves. The discriminated signals were then sensed by LeCroy 4291B time to digital converters (TDCs) with a resolution of 1 ns. The TDCs were operated in *common stop* mode, where an incoming pulse would trigger a TDC channel and a later stop pulse from the first level trigger would stop all triggered channels from counting further. The resulting inverted time distribution is shown in Figure 13. The sharp edge near 240 nsec corresponds to tracks which pass very near to a sense wire. A TDC channel would be dead for 250 ns after registering a hit, and was inhibited from registering later hits for a much longer time if a first level trigger was satisfied. This prevented particles from decays in later buckets "erasing" the desired hit information and causing inefficiencies or degrading the resolution. As described in reference [76], the time distribution can be inverted to obtain a conversion from TDC time to a distance from the sense wire. The time to distance conversion assumed that the first drift electrons to arrive at the sense wire were those in the plane of the sense wire.

Between the second and third drift chambers, the charged particles were given a transverse momentum kick by a dipole magnet with a vertical field of about 4 kG. The magnet gap measured 1.46 m. The transverse momentum kick transferred, $\Delta p_t = (q/c)\int B\,dz$, was typically 200 MeV. $\int B\,dz$ was measured on a 2 inch square grid, and the kick interpolated between grid points. The field map is shown in Figure 14. There was in addition a very small horizontal field component in this magnet. Its effect on the momentum measurement was negligible, though it did introduce a very small bend in a particle's vertical trajectory.

The dipole field was already negligible at the two chambers closest to the magnet,

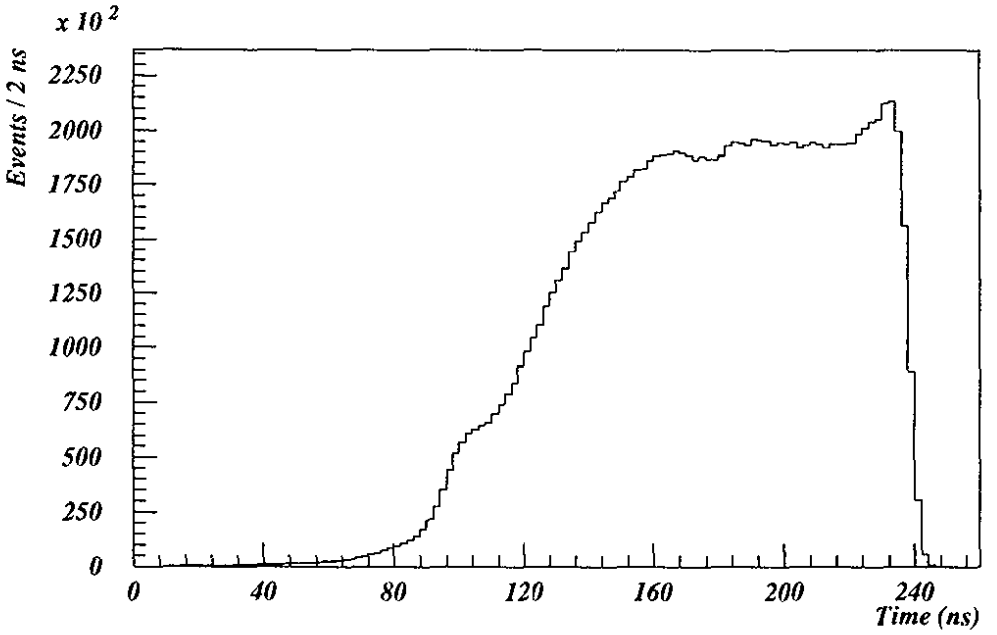

Figure 13. The distribution of chamber drift times for in-time two track events.

so particles followed straight line trajectories between the upstream two chambers and between the downstream two chambers (neglecting multiple scattering effects). This greatly simplified the track finding algorithm and momentum calculation.

3.2.3.3 Charged Particle Tracking

Before turning to a description of the trigger, we will briefly outline the tracking algorithm used to reconstruct the charged particle trajectories. The algorithm used was fairly straightforward.

Tracks in the x and y views were found independently, though the same general method was used to find the segments in both views. The main difference between the two views was that horizontal segments had to be found in the upstream and downstream chambers independently because of the large p_t kick given in that view by the magnet, while vertical trajectories could be found in all four chambers simultaneously. Two wires which registered hits, each from a plane in a different chamber, were chosen first. If a line connecting these two wires projected too far from the decay volume for upstream x and for y segments, or

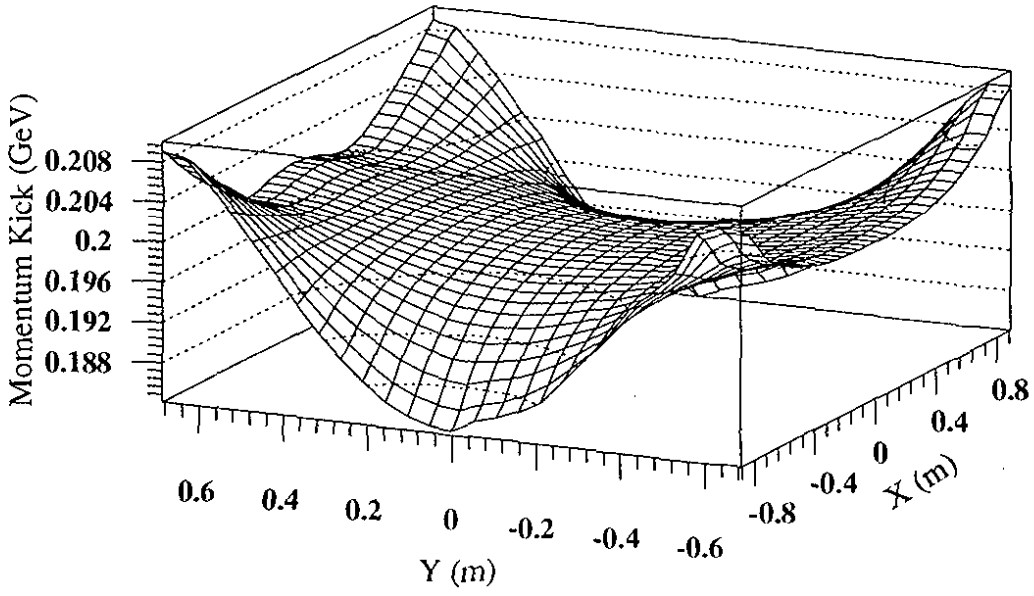

Figure 14. Transverse momentum kick of the analysis magnet as a function of the x and y position of a charged particle at the "bend plane" of the magnet.

too far from the lead glass for downstream x segments, this segment was rejected. The line was projected into the other relevant sense wire planes, and a hit wire within 1.5 cm of the projection was assigned to the track. An x track segment candidate, either upstream or downstream, had to have at least 3 of the 4 possible planes hit. A y track was accepted if it had hits on 5 of the 8 possible planes. No track segments were allowed to share hits, and the two wires chosen within a chamber had to be within the same drift cell. After the track segment candidates were identified, the drift distance information from the TDCs was used to refine the location of the particle's passage. A least squares fit to these measured points yielded direction tangents and intercepts for each of the candidate segments.

To a very good approximation, the bending of the particle could be viewed as occurring at a single "bend plane" at the center of the magnet, which simplified the task of matching the upstream and downstream x track segments. The upstream and downstream segments were projected to the bend plane, and segments were paired if their projections were separated by less than 1.5 cm.

The x and y segments were matched by pairing the tracks to be consistent with the

cluster positions measured in the lead glass. After matching, the hit positions are refined once more to correct for small (of order mrad) chamber rotations and differences in signal propagation time along the sense wires (about a 6 ns difference from one end of a sense wire to the other in the largest chamber). In addition, the upstream and downstream y track segments were refit separately. Because the analysis magnet did impart a very small p_t kick in the y view, better accuracy was obtained for projecting the measured particle trajectories when the separate segment fits were used.

One complication to this scheme arose from a small inefficiency with the chambers. While the individual plane efficiencies were generally close to or better than 99%, there was still a 5% chance that at least one plane of an x segment would miss a hit, and a 10% chance that one or more of the planes on a y segment would miss a hit. To ensure finding a track, several different pairings of planes were used as sources for the initial two hits.

An inefficiency in one plane also made the determination of the direction of the drift in the complementary plane more difficult. In the x view, two candidate track segments, passing on either side of the unpaired wire, were generated. The candidate matching best with a downstream segment was kept. In the y view, the track fit to the other chambers was used to predict the direction of the drift for the unpaired hit.

It was useful to examine the sum of the two measured drift distances in one view of a chamber. This sum should equal the 6.35 mm separation in x (or y) of the two wires, though a small correction was needed because of the 1.1 cm z separation of the two planes when the particle was not travelling parallel to the z axis. The deviation of the measured sum from this cell size is shown in the solid histogram in Figure 15 for events with two in-time (see below) tracks. The resolution of each plane can be deduced from the width of the central peak. We have achieved resolutions in the 95–105 (105–115) micron range for the smaller (larger) chambers.

The low side tail agrees very well with the expected delta ray production. Because a TDC channel was dead immediately after registering a hit, only delta rays that produced ionization that arrived *earlier* than the ionization from the primary particle was seen. The drift electrons from those delta rays registered in the TDC rather than the ionization from the primary particle, which made the drift distance, and hence the sum of distances, ap-

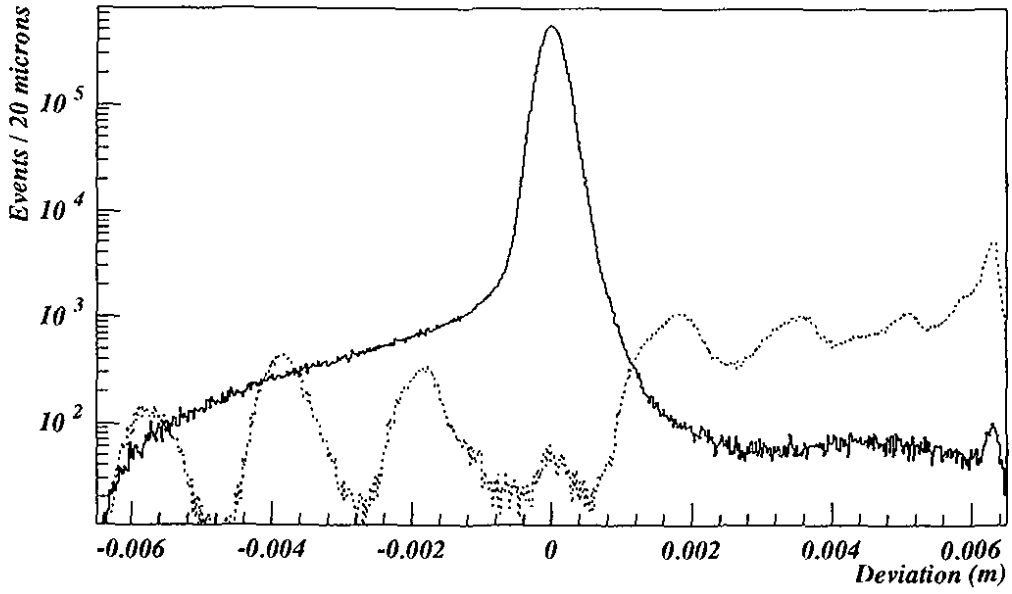

Figure 15. The deviation of the sum of drift distances from the nominal cell size of 6.35 mm. The solid histogram is the distribution for in-time two track events. The dot-dash histogram is the distribution for tracks that have been identified as out-of-time (see text) in events with two other in-time tracks.

pear too small. There was roughly a 0.5% chance per plane per track for a delta ray to cause a mismeasurement of the drift distance of 500 microns (5 standard deviations on the resolution) or more. The high side tail comes almost exclusively from tracks passing very close to the sense wire. The ionization pattern can fluctuate to occur near to the upstream or downstream end of a cell rather than close to the z location of the sense wire. This will result in a long drift time being registered, and since we assume the drift electrons arrive from the x (or y) direction, the track position will be placed too far from the wire.

The sum of drift distances had several uses in trackfinding. First of all, because of delta rays and electronic noise, sometimes neighbouring wires in a sense plane will both register hits that could be candidates for a track. Generally, the wire that yields the best sum of distance when paired with the hit in the other plane will be the proper choice. In the y trackfinding, the sum of distance can be used to properly assign hits to two tracks that are almost horizontal and hence have tracks that pass close to the same sense wires.

Since the maximum drift time spans many buckets, often decays in nearby buckets will

leave tracks in the drift chamber that can be fully reconstructed. Since we are looking for $\pi^+\pi^-$ decays, we want events with two tracks, and these extra out of time tracks would cause event loss. The sum of distances provides a means for identifying and throwing away out of time tracks. From the drift speed of 50 microns/ns and the bucket separation of 18 ns, we expect that all the drift distances will be mismeasured by 0.9 mm, or the sum of distance mismeasured by 1.8 mm. An x or y segment will be flagged out-of-time when 2 or more of the chambers have a sum of distance that deviates from 6.35 mm by more than 1 mm (7 times the resolution on the sum of distance!). The distribution of the sum of distances for out-of-time tracks identified in events with two other in-time tracks is shown as the dot-dashed histogram in Figure 15. The expected 1.8 mm shift between the peaks can be clearly seen. The pile-up and dilution of the peak structure on the high side (late buckets) is an artifact of the time-to-distance conversion which will assign a maximum drift distance of 6.35 mm to any given hit. The small central peak in the out-of-time distribution results from the small chance to have *very* early false TDC times from δ rays in two separate chambers which each cause a 1 mm mismeasurement of the sum of distance in both of the chambers. The delta rays cause this algorithm to flag in in-time segments as out-of-time with a probability of 0.07%, resulting in a 0.28% event loss. By ridding events of the out-of-time tracks, however, there is an 8% recovery of 2 track events, far outweighing the small loss.

Once the particle trajectories have been measured, the momentum of the particle can be deduced by comparing the measured upstream (up) and downstream (dn) direction tangents $\theta_{x,y}$ of its measured track. Since $\theta_{x,y} = p_{x,y}/p_z$, we obtain

$$\left| \frac{\theta_x^{up}}{\sqrt{1+(\theta_x^{up})^2+(\theta_y^{up})^2}} - \frac{\theta_x^{dn}}{\sqrt{1+(\theta_x^{dn})^2+(\theta_y^{dn})^2}} \right| = \frac{|\Delta p_t|}{|p|}.$$

The average momentum resolution we obtained was under 1%, with a momentum dependence given by

$$\frac{\sigma_p}{p} = 0.45\% \oplus 0.012p\%, \tag{3.2}$$

where the momentum p is measured in GeV. The constant term results from multiple scattering of the particle between the first and last drift chambers. The term linear in

momentum results from the finite resolution of measuring the space points in each chamber, and hence in measuring the direction tangents.

3.2.3.4 The Trigger Hodoscopes and Veto Banks

The long drift times in the chamber system made the chambers unsuitable for use as an element of the first level trigger. The drift times span many buckets, so the chambers cannot distinguish between particles passing through in different buckets, and the coincidence gates would have to be too long for the rapid formation of a first level trigger needed in a high rate experiment. Several planes of scintillator trigger hodoscopes were therefore installed to provide the fast signals needed.

The downstream end of the charged decay volume was defined by the T and V hodoscopes, which we have described earlier.

Two more scintillator planes, the B and C hodoscopes, were located 1.5 m downstream of the last drift chamber. These banks were made from 1 cm thick staves of scintillator. They were segmented as shown in Figure 16 in order to define a simple topological trigger requirement based on the expected symmetry of the $\pi^+\pi^-$ decays. The paddles in these counter banks did not overlap so that a single particle could not falsely appear as two particles.

There was also a bank of scintillator counters (the $\mu 2$ bank) located behind the 3.2 m length of steel. This bank was used to identify muons, both for triggering purposes in special chamber alignment runs (see Section 4.1.2) and for vetoing Kμ3 decays while collecting the $\pi^+\pi^-$ sample.

3.3 The Event Triggers

The triggers used in the experiment were very simple – relying largely on simple pattern recognition based on the hit patterns in the trigger hodoscopes or in the calorimeter to identify $\pi\pi$ decays. The triggers were kept completely independent of the regenerator position and of the beam from which the particle decayed. This philosophy resulted in

triggers with minimal biases and no preference over decays from the vacuum beam relative to those from the regenerator beam (or vice versa).

The triggers were formed in two stages. The first level triggers were based only on information which could be obtained very quickly, such as the hit patterns in the trigger hodoscopes, the veto counter signals, and the total energy in the lead glass. These triggers were formed within about 450 ns of the actual decay, and a successful trigger at this stage initiated the TDC counting and gated the sample and hold circuits in the ADC modules. The timing for all of the first level triggers was defined by a 53 MHz RF signal provided by Fermilab and synchronized with the proton bucket structure.

The second level of trigger used information which took longer to obtain, either because the detector element had a slow response (*eg.* the drift chambers), or because the pattern recognition took some time. If an event failed at this stage in the trigger, that event would be aborted before the lengthy processes of ADC digitization and event building began.

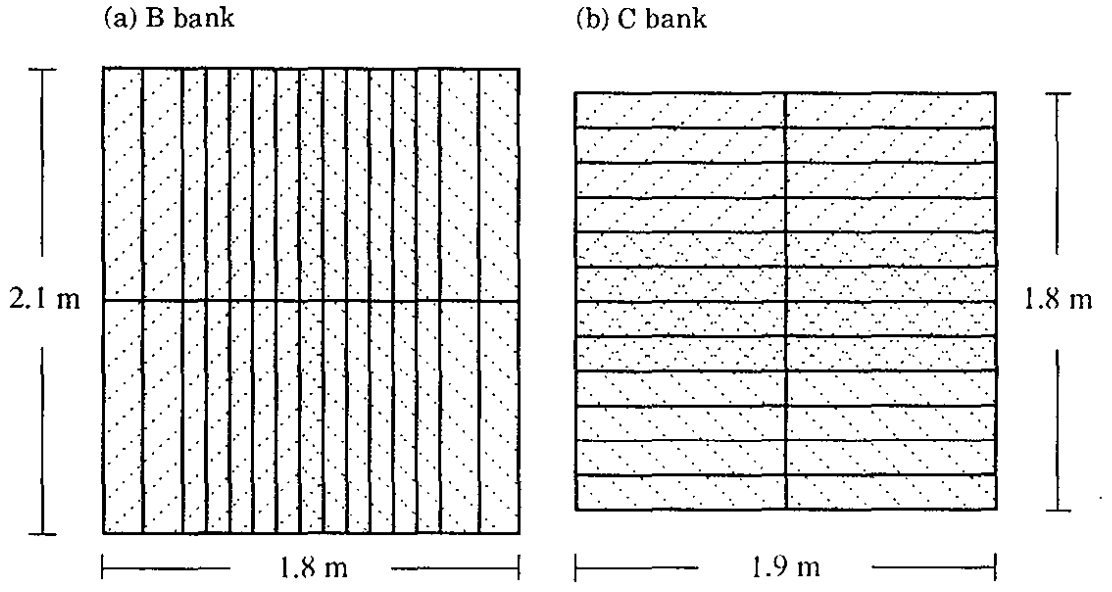

Figure 16. The B and C hodoscope banks used for charged triggering. The hatching illustrates the definition of the left and right "halves" in the B bank (and top and bottom "halves" in the C bank) used by the charged mode trigger. Staves with both directions of hatching are overlap regions which can belong to either half.

3.3.1 Neutral Triggering

The neutral trigger was designed to accept 4 photon $2\pi^0$ decays as well as some 6 photon $3\pi^0$ decays, while simultaneously minimizing false triggers from $3\pi^0$ decays with missing and/or fused photons and accidental activity. Since we were interested in $2\pi^0$ decays with energies above 40 GeV, the heart of the first level neutral trigger simply required the total energy in the calorimeter to satisfy $E_t > 28$ GeV. Since much of the accidental activity resulted from activity in the calorimeter which occurred in different buckets, or from muons from the target, both of which show little apparent energy in the calorimeter, the accidental triggers were greatly reduced by this requirement.

The remainder of the first level neutral trigger required no activity in the various veto counters previously described. The event was vetoed if any signal was observed in the AM, PA, SA, VA2-VA4, DRAN, MA or LGA. VA1 was not used because of the activity in that counter induced by interactions in the regenerator. The BA rejected events if more than 5 GeV was observed in the first two thirds of that counter and under 10 GeV in the last third. These vetos helped to reduce the number of triggers from $3\pi^0$ decays with missing particles.

A minimum signal of 25 minimum ionizing particles was required for the CA to reject the event, well above the level for the CA to be fired accidentally by stray particles from photon showers in the calorimeter.

Hadronic events (such as $K_L \to \pi^+\pi^-\pi^0$ decays) were rejected when an energy deposit equivalent to 5 or more minimum ionizing particles was observed in $\mu 1$. Finally, any activity in the regenerator anticounters (RAs) would veto an event.

At the second level of trigger, a factor of ten reduction in the trigger rate was obtained by counting the number of isolated clusters of energy in the lead glass with the HCF. The HCF needed about 20 μsec to count, which was too slow to form part of the first level trigger, and entered at this level as a veto (if necessary) before the much longer (750 μsec) digitization process of the ADC channels started. Events with four clusters were accepted as candidate $2\pi^0$ events. We accepted 0.05% of all first level triggers independent of the HCF information in order to monitor the operation of the HCF.

During the $2\pi^0$ running, events with 6 HCF clusters were accepted in addition to the 4 cluster events to obtain a sample of $3\pi^0$ decays for studying the detector and systematic effects. For most of the run, these events were prescaled by a factor of 8, though for the last 20% of running, all 6 cluster triggers were accepted.

3.3.2 Charged Triggering

The first element used for the $\pi^+\pi^-$ trigger was supplied by the T and V hodoscopes in the HDRA. We required that a pulse height greater than the equivalent of 1.5 minimum-ionizing particles be seen in sum of signals from *either* the T hodoscope counters *or* the V hodoscope counters.

The B and C hodoscope banks were used to define a topological trigger which took advantage of the symmetry of the two-body $\pi^+\pi^-$ decays. In the B bank, at least two distinct paddles had to be hit by a minimum ionizing particle, with one particle in the left half of the bank and the other in the right half. As Figure 16 shows, a central counter could satisfy either the left or right trigger requirement. Because the beam holes straddled the vertical center of the detector, the requirements on the C hodoscope bank were not as severe. The trigger required at least one minimum ionizing particle to fire this bank. There was also a requirement that hits be seen in top and bottom "halves", but now there was a substantial overlap (2 staves on either side of center) in the definition of "top" and "bottom".

Kμ3 decays were rejected online by vetoing events when a minimum ionizing particle was detected in the $\mu 2$ scintillator bank. Vetos from signals in the lead lucite counters of the VA4 and LGA banks helped reduce the trigger rate from $\pi^+\pi^-\pi^0$ decays with at least one photon directed outside of the lead glass. Studies from the beginning of the run and our experience with the previous test run [81] indicated that it would be very difficult to reject the Ke3 decays at the trigger level without potentially introducing a bias into the sample of $\pi^+\pi^-$ decays collected. We therefore made no attempt to reject these events online, deferring their rejection until an unbiased offline analysis was made.

As in the neutral trigger, the regenerator anti counters vetoed inelastic kaon scatters. Activity in the mask or pinching anti also vetoed an event.

The trigger rate was reduced 30% by a second level trigger that required the second drift chamber to have hits registering in both its left and right halves. There was no overlap region in this case.

3.3.3 Other triggers

In addition to the triggers discussed above, there were a number of special purpose triggers collected simultaneously with the $\pi\pi$ triggers. The most important of these were:

- "Accidental" triggers, which were used to study the effects of random activity in the detector, and to determine the sources of such activity. The trigger source was a scintillator telescope aimed at the target pile, but out of the line of sight of the detector. The trigger rate was therefore proportional to the instantaneous beam intensity, but did not depend on the presence of activity in the detector. This trigger will be discussed further in Chapter 10.

- The "pedestal" trigger, which randomly triggered the readout of the full lead glass array without any readout threshold applied.

- The "flasher" trigger, which flashed the xenon lamp used to monitor the photo-tube gains throughout the run.

- The Kμ3 trigger, which was identical to the $\pi^+\pi^-$ trigger except that the $\mu 2$ bank was required to fire, rather than being in veto. This allowed us to collect and study $K_L \rightarrow \pi^\pm\mu^\mp\nu_\mu$ decays.

These and other more minor triggers constituted 7% of the recorded triggers. The pedestal triggers were collected between spills as well as during the spill.

3.4 The Run

The data collected for this analysis were obtained at Fermilab over the period August, 1987 through February 1988. The total data sample occupied approximately 5000 9-track data tapes. The details of the run and of the first data analysis pass have already been described in detail in references [74] and [75]. Rather than repeat those discussions, only a few details relevant to the remainder of the thesis will be covered here.

The data collection was initially divided into periods where either $2\pi^0$ or $\pi^+\pi^-$ decays were collected. Because we initially collected neutral data with the lead sheet present at the HDRA, $\pi^+\pi^-$ events could not be collected simultaneously with $2\pi^0$ events in these early runs. We alternated collection between charged and neutral running to ensure that we obtained an adequate sample of each mode. The proton beam intensity, the number of raw triggers recorded on tape, and the lead sheet status are summarized for each of these sets in Table 4.

Table 4. The characteristics of the $\pi^+\pi^-$ and $2\pi^0$ data subsets.

Subset	Proton Beam Intensity (10^{12} per spill)	Pb Sheet Installed	$2\pi^0$ Triggers to Tape (10^6)	$\pi^+\pi^-$ Triggers to Tape (10^6)
C1	0.3	No	–	16
N1	2.0	Yes	44	–
C2	0.3	No	–	70
N2	2.0	Yes	36	–
C3	0.3	No	–	82
N3	2.0	Yes	22	–
N4	2.0	No	8	–
C4	0.3	No	–	75
NC	0.8	No	61	61

At the end of the neutral subset N4, one of the drift chambers had to be brought off-line temporarily. Since the neutral conversion trigger which required the Pb sheet (and the

charged trigger) was of no use without all chambers operating, it was decided to study $2\pi^0$ collection with only the nonconversion trigger described above. The success of this test lead us to abandon the Pb sheet and conversion trigger in favor of collecting $2\pi^0$ and $\pi^+\pi^-$ events simultaneously in the subset NC. This was the first time in any experiment that all four of the $K \to \pi\pi$ decay modes were collected simultaneously.

Our earlier published result [50] was based on 80% of the data in the NC sample, which will often be referred to as the NCa subset later in the thesis. The results of analyses of each individual subset will presented in Chapter 10 as part of the systematic discussion.

Various special data samples were collected in short runs interspersed throughout the entire run. The two samples of most importance were used for calibrating the lead glass and aligning the chamber system. These will be discussed further in Chapter 4.

The analysis of this data essentially occurred in two stages. A first pass was made through all of the "raw" data tapes using preliminary calibrations of the detector elements and very loose analysis cuts. The cuts were designed loose enough that minor changes to the final calibrations would not change the final event sample. Candidate event types were identified and split into much smaller subsets of data summary tapes (DSTs). The data samples obtained included very large samples Ke3, $3\pi^0$ $\pi^+\pi^-\pi^0$ decays of the kaon, along with many samples useful for searching for very rare kaon decays. It is the final analysis and background subtraction of the $\pi\pi$ samples from this first pass analysis that is the focus of this thesis. Along the way, though, we will meet many of the other data samples we collected, particularly the Ke3 and $3\pi^0$ samples.

The first step will be to review the calibration and alignment procedures used by this experiment. We will then move on discuss the analysis of the $\pi\pi$ samples themselves.

CHAPTER 4

CALIBRATION AND PERFORMANCE

To successfully analyze this experiment without ultimately being limited by systematic uncertainties, we had to understand the detector very well. Perhaps the greatest efforts in analyzing this data set went into the calibration of the lead glass calorimeter and of the chamber system. The most difficult challenge was to understand the energy scale in the measurement of the $2\pi^0$ decays relative to that of the $\pi^+\pi^-$ decays to the order of 0.1%. This placed stringent requirements on the lead glass calibration.

The overall acceptance of the detector also had to be measured well over the course of the experiment, which meant that the positions of the defining apertures had to be tracked accurately over time. The most precise way of monitoring the effective edges of each counter was to measure the position and shift of each aperture edge with the large sample of electrons from Ke3 decays. Since one of the apertures was almost 50 m upstream of the first chamber, the best possible resolution was required of the drift chamber system for accurate pointing. Furthermore, the alignment of the drift chambers relative to each other and to fixed reference points in the detector had to be precisely tracked.

The calibration of the lead glass calorimeter using electron samples obtained in special calibration running has already been described in detail in reference [74]. The gist of the procedure will be reviewed, and the application of the technique to the sample of Ke3 electrons for the final set of calibrations will be discussed here.

This chapter will also discuss the alignment of the drift chamber system. The conversion

of drift time to drift distance has been described in reference [76], and will only be reviewed briefly here. The alignment procedure will focus on the methods used in the charged mode sample, since the chambers played a minimal role in the $2\pi^0$ analysis outside of calibration.

4.1 Drift Chamber Calibration and Alignment

4.1.1 Review of Time to Distance Conversion

The most fundamental calibration of the drift chamber system was the determination of the drift time to drift distance relationship. The quality of the calibration affected the resolution in every analysis, including the accuracy of the alignment procedure, so the first step in the chamber calibration and alignment was to determine this relationship.

The time to distance calibration was a straightforward procedure. It was based on the assumption that the illumination across a cell is uniform, which is a good assumption when averaged over all the cells in a single plane. Since the cell size is fixed at 6.35 mm, the time distribution (Figure 13) can be inverted and a signal arriving n nanoseconds after the earliest time corresponds to a distance d_n given by

$$d_n = 0.00635 \left(\sum_{i=1}^{n} t_i / \sum_{i=1}^{N} t_i \right), \tag{4.1}$$

where t_i is the total number of events arriving in the bin corresponding to i nanoseconds after the earliest time, and N is the total number of bins. This was done separately for each of the 16 sense planes.

The algorithm implemented was more detailed than this, since it corrects for effects like nonuniformities in the response across a drift cell. A detailed description of the full algorithm is in reference [76].

The detailed shape of the time to distance conversion will change as a function of time for several reasons, including changes over time in the precise ratio of argon and ethane in the gas mixture. The gas mixture was flowed continuously through the drift chamber system, and a new gas bottle was added to the gas supply about once every day. A time to distance calibration was done on average once every several days of running to prevent drifts in the calibration from seriously degrading the resolution. A plot of the resolution as

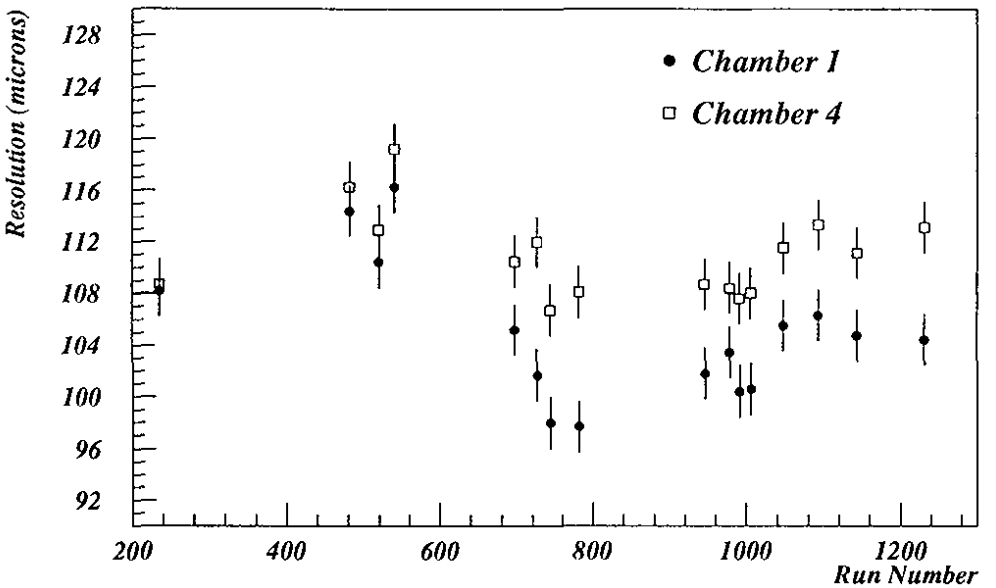

Figure 17. The average resolution in the smallest (circles) and largest (squares) drift chamber as a function run number.

a function of time for the smallest (1) and largest (4) chambers in the x view is shown in Figure 17. When operating conditions were optimal, several of the chambers achieved close to or better than a 100 micron resolution in each plane.

4.1.2 Chamber Alignment

The alignment of the drift chamber system was performed in two basic steps. The first was an internal alignment, where the positions of the chambers were determined relative to each other. After this first adjustment, the positions of the chambers were measured relative to the rest of the detector using the lead glass calorimeter and the production target as fixed reference points. The goal was to locate the chambers relative to themselves and to an external reference frame as a function of time with an accuracy approaching 10 microns.

The internal alignment itself involved two procedures: one to fix positions of the inner chambers in a coordinate system defined by the two outer chambers, and one to remove any residual rotation (about the z axis) between the outer chambers. The former procedure

Table 5. Rotation of the y view sense wires away from the perpendicular to the x view wires. For a positive rotation, the y wires are too high on the $+x$ side of the chamber.

Chamber	1	2	3	4
Rotation (μrad)	0	47	198	-150

could be accomplished by studying tracks that pass straight through the chamber system when the analysis magnet is off. To remove the true rotation between the outer chambers, however, we need events with at least two charged tracks originating from a common vertex. The measurement of the apparent "motion" of the production target and the calorimeter then yielded the motion of the outer chambers in a fixed coordinate system.

The most important alignment constants were the transverse offsets for each chamber and the rotation of the chamber about the z axis. The complete set of constants were generally updated once every day of running in the $\pi^+\pi^-$ data set, while the transverse offsets were adjusted two to three times a day.

We initially surveyed the chambers into position such that the maximum rotation about the x or y axis was of order 1 mrad or less. The only sizable affect from a rotation about these axes is to introduce an apparent offset between the two sense planes in a view[1]. All other effects, such as an apparent decrease in the cell size or transverse profile of the chamber, vary as the cosine of this angle and are negligible at the level of precision we needed.

Before the alignment procedure could begin in earnest, we had to know the relative angles between the x and y planes. The deviations from a 90° angle, listed in Table 5, were obtained from a survey of the chamber wires made during chamber construction. These values could be verified for consistency with the data, but were difficult to extract absolutely for reasons that will be outlined below. The accuracy on the survey measurements varied from 30 μrad in the smallest chamber to 20 μrad in the largest. If the x wires were vertical, a positive rotation θ of the y wires away from the horizontal corresponds to y wires which are too high on the $+x$ side of the chamber.

The diagram in Figure 18 helps make the sign convention above clear. Suppose the solid

[1]There is a 1.1 cm separation between the sense planes of the two views.

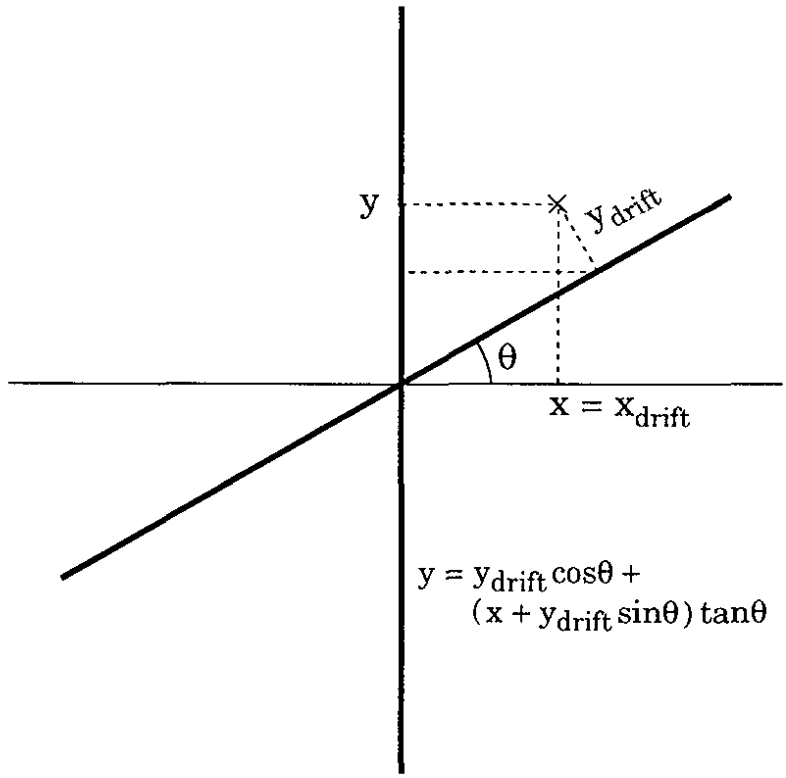

Figure 18. The effect on the measured coordinate of a particle if the x and y chamber sense wires are not perpendicular.

vertical line represents an x-view sense wire at $x = 0$, and the other solid line represents a y-view wire rotated away from its optimal horizontal position by an angle θ. For a particle passing through the point $\times$, the measured positions in the chamber system will be (x_{drift}, y_{drift}). Then the true y position y_t is given by

$$y_t = y_m \cos\theta + (x_m + y_m \sin\theta)\tan\theta \tag{4.2}$$

$$\approx y_{drift} + x_{drift}\theta, \tag{4.3}$$

where the latter is true to the accuracy we needed for the sizes of the angles given above. The angles given in the table have the same sign as the definition of θ.

For the rest of this discussion, we will assume these corrections have been made, and hence that the x and y measurements from a given chamber are in an orthogonal coordinate system.

4.1.2.1 Internal Alignment 1: The Muon Samples

The first step in alignment was to orient the second and third drift chambers in a system defined by the two outer chambers. The procedure used special samples of muons collected when the analysis magnet was turned off. This yielded a sample of tracks with a straight trajectory in both the x and y views through all four chambers.

The trigger used to obtain this muon sample simply required a coincidence between the B hodoscope and the $\mu 2$ hodoscope. Since muons originated in the beam dump as well as the target, no requirement on the T or V hodoscopes were made. The sample of muons thus obtained had a broad illumination over each chamber. Roughly 50,000 $B \cdot \mu$ triggers provided an adequate sample for chamber alignment, and such a sample could be accumulated very quickly, generally in a few spills.

Offline cuts removed out-of-time tracks and accidental coincidences. In addition, only high quality tracks were accepted: all 8 planes in each view had to be hit, and every sum-of-distance (*which uses only drift times and hence is independent of the plane offsets*) had to be within 450 microns of the nominal cell size. The latter minimized biases in the measured offsets due to δ-rays.

Once a suitable track was identified, a line segment in each view was defined by fitting to the x and y track positions measured in the first and fourth chamber. The difference between the track projection and the measured position for each x (y) plane in the inner two chambers was then recorded as a function of the y (x) position of the track in that plane. A plot of this residual in one of the y planes in chamber 3 versus the x track projection is given in Figure 19a. A linear fit to the residual versus position, as in Figure 19b, yields the offset and rotation for each plane.

In general each $B \cdot \mu$ samples had a statistical precision of 1 to 2 microns for the average plane offset and 3 microradians for the rotation. In systematic studies, however, the reproducibility of these measurements seemed to be closer to 5 microns for the offsets and 10 microradians for the rotations.

While this method can accurately align the inner two chambers in a coordinate system defined by the outer chambers, there remain degeneracies in the system because of possible

misalignment between the outer two chambers. If there is a rotation ϕ around the z axis between the outer chambers, then the coordinate system they define will leave a "screw rotation" within the alignment, where the ith chamber will be rotated out of true alignment by an angle $\phi_i = \phi(z_i - z_4)/(z_1 - z_4)$, where z_i is the location of the ith chamber. This rotation cannot be removed using only the single track $B \cdot \mu$ events. The same degeneracy which prevents this measurement also prevents the absolute measurement of the angle between the x and y planes mentioned above. The next section will discuss removing these angular degeneracies.

One last useful piece of information can be gleaned from the $B \cdot \mu$ sample. For each pair of planes in one view of a chamber, the effective separation (relative to the nominal separation of 6.35 mm) can be obtained from the distribution of the difference of the offsets measured in each plane. The measured separation will have contributions both from a true separation and from a chamber rotation about the x (or y) axis, as mentioned earlier. The x view distributions from the $B \cdot \mu$ alignments are shown in Figure 20. The different histograms for chamber 1 correspond to time periods between work on that chamber, where

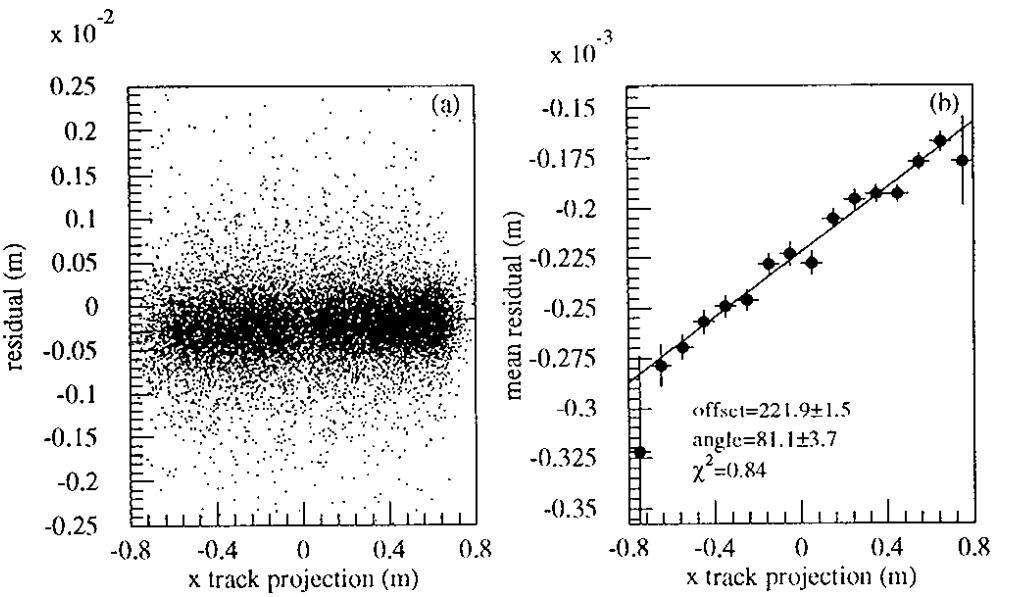

Figure 19. The residual between the measured and predicted position of a muon track in the downstream y plane of chamber 2. (a) The residual versus the x track projection. (b) The variation of the mean y residual with the x position, and the best fit line.

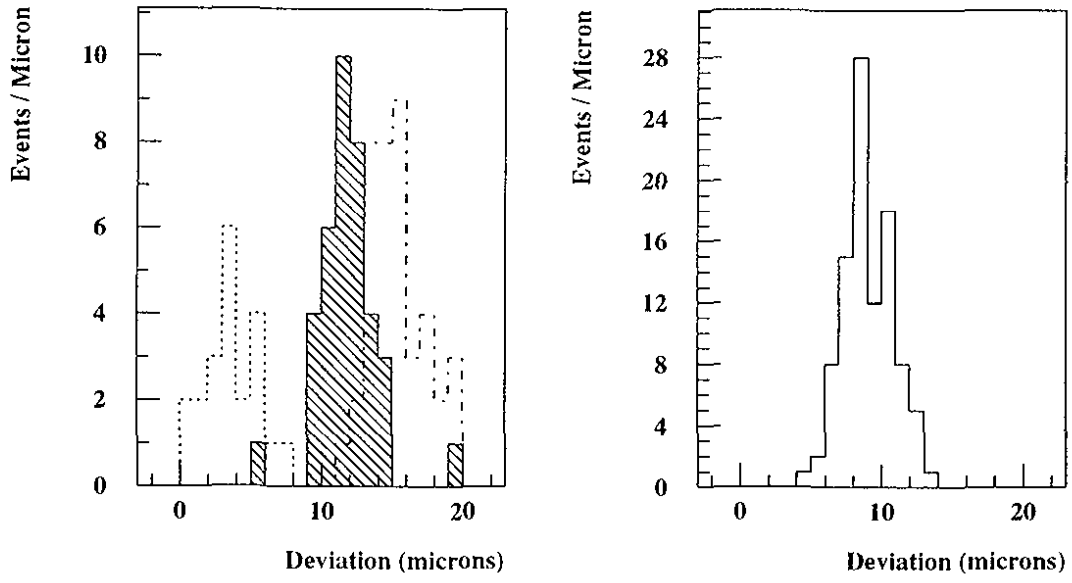

Figure 20. The deviation of the effective separation between two x planes within a chamber. (a) Chamber 1 - the three different histograms correspond to groups of $B \cdot \mu$ alignments between major chamber work. (b) Chamber 4 - little work was done on this chamber during the run.

changes in the y chamber rotation shift the effective offset. To refine the alignment, the two offsets for one view of a chamber were averaged, keeping the separation between the two planes at the average separation in a time period between work on that chamber.

The difference in the rotations between a plane pair can also be measured this way. There are no contributions to the measured difference aside from a true physical rotation of one plane relative to the other. The measured differences were within 8 μrad for all plane pairs, well within our desired tolerance.

4.1.2.2 Internal Alignment 2: Removing Screw Rotations

The next step in aligning the chambers was to remove any screw rotation in the system induced by a difference in rotation around the z axis between the first and last chambers. Decays with two charged particles in the final state provide a convenient sample for this measurement because the trajectories of the two particles lie in a plane. If, however, there

is a rotation ϕ between the chambers measuring these trajectories, then this will twist the two *measured* tracks out of a common plane.

The trajectories of the tracks coming from the vertex were measured in the two chambers upstream of the magnet. Let us consider the effect due to a rotation between these chambers. Let $\vec{t}_a = (\theta_{x_a}, \theta_{y_a}, 1)$ and $\vec{t}_b = (\theta_{x_b}, \theta_{y_b}, 1)$ be the direction tangents for the two charged particles a and b, respectively. Also let $\vec{x}_{a_i} = (x_{a_i}, y_{a_i}, z_i)$ and $\vec{x}_{b_i} = (x_{b_i}, y_{b_i}, z_i)$ be the positions of the two particles in chamber i $(i = 1, 2)$, and let $\vec{r}_i = \vec{x}_{b_i} - \vec{x}_{a_i}$ be the separation vector of the two particles in the plane of chamber i. For the true trajectories, the triple product

$$d_s = \vec{t}_a \times \vec{t}_b \cdot \vec{r}_1 = 0$$

because $\vec{r}_1$ lies in the plane defined by $\vec{t}_a$ and $\vec{t}_b$.

Now suppose that chamber 2 is rotated by an angle ϕ relative to chamber 1 and that this rotation is not corrected. The measured direction tangents become

$$\begin{aligned}
\begin{pmatrix} \theta^m_{x_\alpha} \\ \theta^m_{y_\alpha} \end{pmatrix} &= \begin{pmatrix} (x'_{\alpha_2} - x_{\alpha_1})/z_{21} \\ (y'_{\alpha_2} - y_{\alpha_1})/z_{21} \end{pmatrix} \\
&= \begin{pmatrix} \theta_{x_\alpha} \\ \theta_{y_\alpha} \end{pmatrix} + \begin{pmatrix} 2\sin^2(\phi/2) & \sin\phi \\ -\sin\phi & 2\sin^2\frac{\phi}{2} \end{pmatrix} \begin{pmatrix} x_{\alpha_2}/z_{21} \\ y_{\alpha_2}/z_{21} \end{pmatrix} \qquad (4.4) \\
&\equiv \begin{pmatrix} \theta_{x_\alpha} \\ \theta_{y_\alpha} \end{pmatrix} + \begin{pmatrix} \delta\theta_{x_\alpha} \\ \delta\theta_{y_\alpha} \end{pmatrix}
\end{aligned}$$

for each of the tracks $\alpha = [a, b]$. Here $z_{21} \equiv z_2 - z_1$ is the separation between the two drift chambers. The track tangent vectors will be distorted by $\vec{t}^m_\alpha = \vec{t}_\alpha + \Delta\vec{t}_\alpha$, with $\Delta\vec{t}_\alpha = (\delta\theta_{x\alpha}, \delta\theta_{y\alpha}, 0)$. This will in turn change the triple product d_s to

$$\begin{aligned}
d^m_s &= \vec{t}^m_a \times \vec{t}^m_b \cdot \vec{r}_1 \\
&= (\vec{t}_a \times \Delta\vec{t}_b + \Delta\vec{t}_a \times \vec{t}_b) \cdot \vec{r}_1 \qquad (4.5) \\
&= (\delta\theta_{ya} - \delta\theta_{yb}) r_{1_x} + (\delta\theta_{xb} - \delta\theta_{xa}) r_{1_y} \\
&= \frac{\vec{r}_2 \cdot \vec{r}_1}{z_{21}} \sin\phi + 2\frac{(\vec{r}_2 \times \vec{r}_1)_z}{z_{21}} \sin^2\frac{\phi}{2}
\end{aligned}$$

where we have used the fact that the true triple product vanishes and that

$$\Delta\vec{t}_a \times \Delta\vec{t}_b \perp \vec{r}_1.$$

The chambers were surveyed into position to limit the size of ϕ to a few hundred μrad, so in our sample $d_s^m \approx |\vec{r}_1||\vec{r}_2|\phi/z_{21}$ to a very good approximation. We measured the variation of d_s^m with $|\vec{r}_1||\vec{r}_2|$ in the charged mode using samples of Ke3 decays obtained near the time of each $B \cdot \mu$ alignment. Figure 21 shows a plot of this dependence for one of the alignments. z_{21} is known to better than 0.02%, so ϕ can be extracted from the slope ϕ/z_{12} of this dependence with accuracies in the range of 5 to 10 μrad. Figure 22 is a plot of ϕ as a function of time throughout the $\pi^+\pi^-$ running. The variation is quite smooth, with occasional breaks or isolated points due to work on the chambers.

A much smaller $\pi^+\pi^-\pi^0$ sample obtained during $2\pi^0$ running was used to measure ϕ for the remaining alignments. These measurements are also shown in Figure 22. The

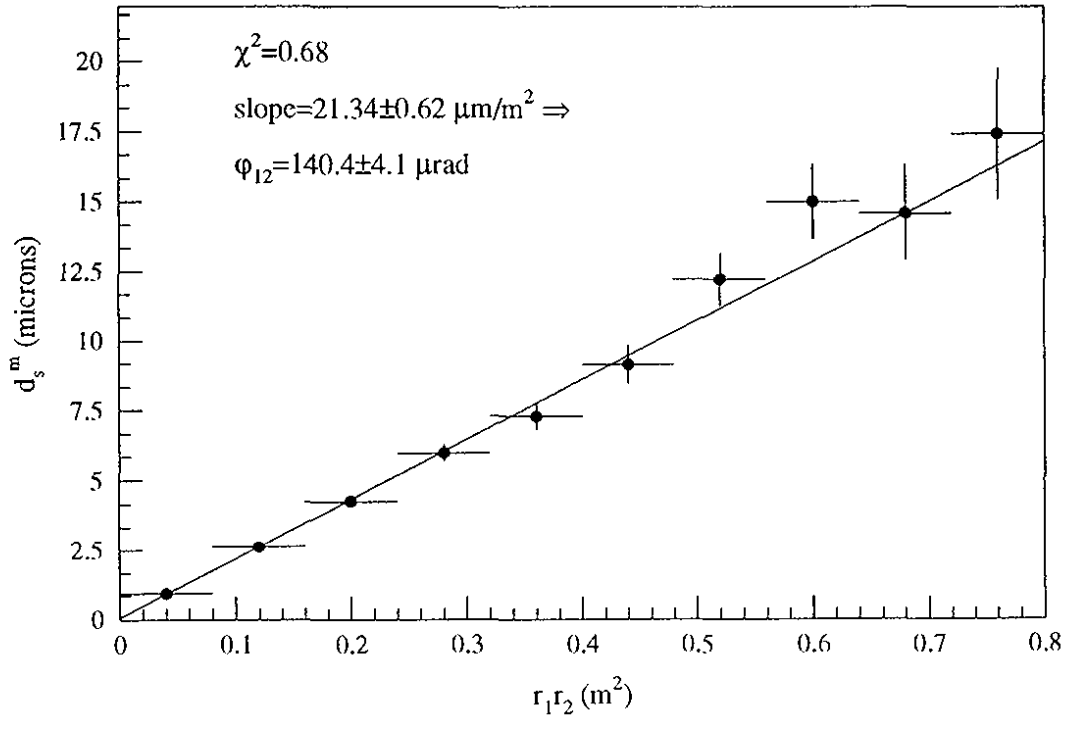

Figure 21. The variation of the mean of d_s^m with $|\vec{r}_1||\vec{r}_2|$ for one subset of Ke3 decays. The slope of the fit line is the ratio of the rotation angle and the separation between the first and second chambers .

chambers are not used extensively in the neutral mode, so the poorer accuracy of the $\pi^+\pi^-\pi^0$ measurements does not pose a problem.

Once the absolute rotation ϕ between chambers 1 and 2 was known, the rotation between chambers 1 and 4 was inferred by comparing ϕ to the rotation of chamber 2 obtained with the $B \cdot \mu$ alignment, and the screw rotation was then removed from the chamber system. In principle, the measurement of the angle between the x and y views of a chamber could have be refined by studying the variation in ϕ as the decay plane varied from horizontal through vertical, but the values from the survey were sufficiently accurate for our purposes.

4.1.2.3 External Alignment

The final stage in the chamber alignment was to align the chamber coordinate system to a coordinate system using the lead glass calorimeter and the production target as fixed points. Both the glass and the target provided fixed points in x and y, giving us a line

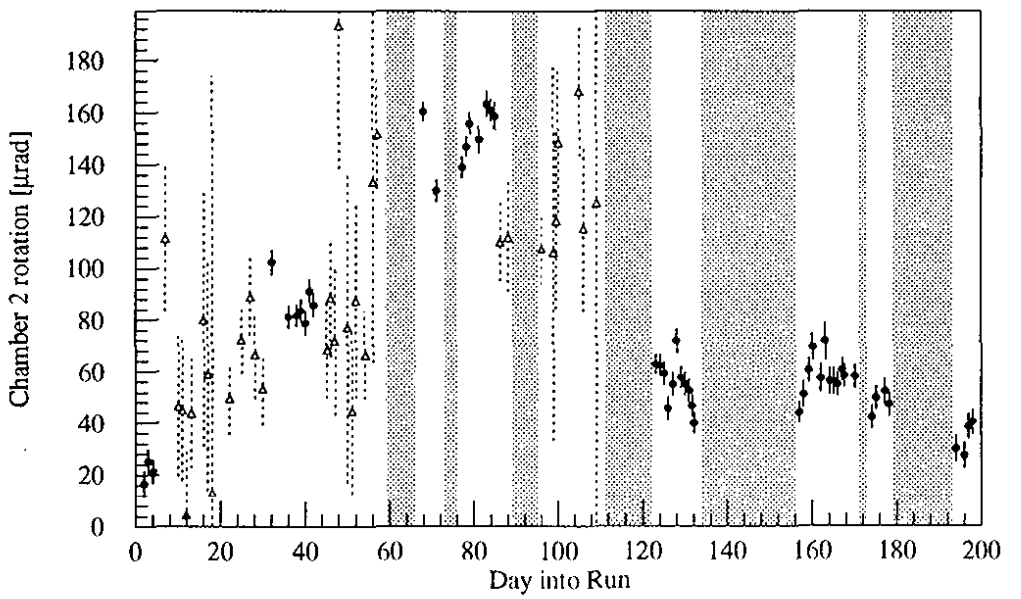

Figure 22. The rotation of chamber 2 about the z axis relative to chamber 1. The solid circles are measurements obtained with Ke3 decays accumulated in charged mode running. The open diamonds are measurements made with $\pi^+\pi^-\pi^0$ decays collected during neutral running. The gaps correspond to periods when no $\pi\pi$ data was collected due to accelerator shutdowns, etc.

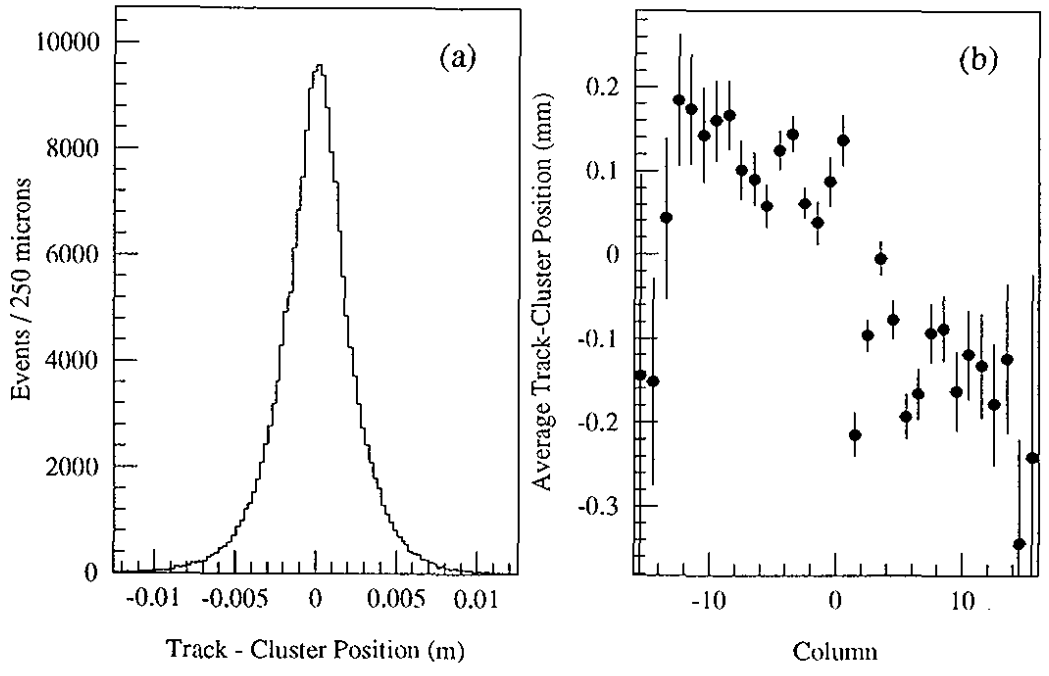

Figure 23. Distributions of the difference of measured track and cluster positions before alignment. (a) The overall track position - cluster position in the y view. (b) The average track position - cluster position in the y view versus row.

of sight for aligning the chamber centers. The lead glass also provided a measure of the chamber rotation angle about the line of sight.

The electrons from the Ke3 decays gave us information about the position of the chamber system relative to the lead glass via the comparison of the track projections at the glass with measured cluster position in the calorimeter. The average difference of the track and cluster positions integrated over the entire calorimeter gave a very good measurement of the average offset between the chamber system and the calorimeter. The overall difference between the track and cluster positions is shown in the y view for one alignment in Figure 23. The resolution on the cluster position measurement was 2.5 mm, and there were ample statistics to obtain the mean positions to better than 10 microns.

To obtain the rotation of the chamber system relative to the lead glass, the x (y) difference was studied as a function of the row (column) of the central block. There is a bias in the reconstructed cluster position as a function of the angle of the incoming particle of

order 70 μm/mrad, and by averaging the x (y) track-cluster difference over a row (column), this bias averages out. As Figure 23 shows, there were nonstatistical fluctuations in the measured difference from row to row and column to column of the order of 50 microns. These result from small uncertainties in the true positions of the blocks. The average trend in the x and y views both imply a rotation of about 300 microns, with an estimated systematic uncertainty of 50 μrad.

The data used in Figure 23 corresponds to 1 $B \cdot \mu$ alignment. For the other alignments, the track-cluster difference as a function of row or column were studied *relative* to that already shown. This gave a much smoother variation and hence we were able to determine the variation in the rotation from alignment to alignment quite accurately.

The apparent glass motion as a function of time is shown in Figure 24. In the neutral mode, we did not have enough statistics to measure the rotation, so the rotation measured in the closest charged mode sample was used. Tracking was not critical in the neutral analyses, so this did not pose any serious problem.

With one fixed point and the rotation measured at the glass, all that remained was to measure the target position. A large sample of $\Lambda \rightarrow p\pi$ decays in our vacuum beam provided a very accurate measure of the position. At our energy, the Λ's could be very cleanly identified by requiring $p_p/p_\pi > 3$, and $E_\Lambda > 130$ GeV. Track quality cuts similar to those in the $B \cdot \mu$ sample and cuts to eliminate background from K decay were also made.

The average target position measured with the Λ's for one alignment is shown in Figure 25. The single event resolution on the transverse target position was about 3 mm, and there were generally 50,000 to 100,000 Λ events available for each alignment. The apparent horizontal and vertical motions of the target from alignment to alignment are shown in Figure 26. In general the structure in the plots is real, and corresponds to a slow small shift of the chambers. An apparent motion of the target is highly amplified relative to the actual motion of the chambers because of the long lever arm from the first chamber to the target relative to the separation between the two chambers. A 1 mm shift in the target position corresponds to only a 120 micron motion of the upstream chamber. During neutral running, the target positions were measured with $K_L \rightarrow \pi^+\pi^-\pi^0$ decays in the vacuum beam, and have also been plotted in Figure 26. We actually have sufficient statistics in the Λ sample to

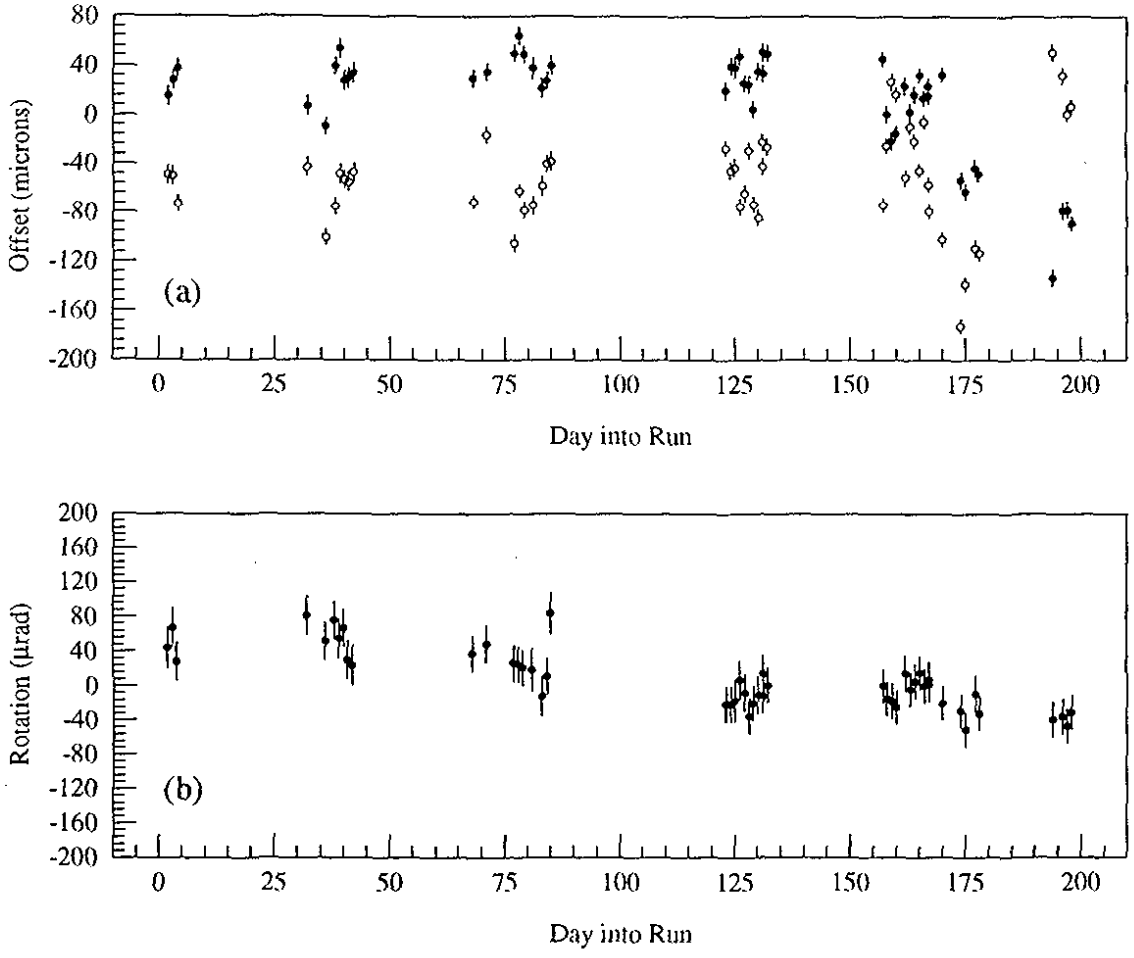

Figure 24. Apparent lead glass motion due to motion of the drift chamber system. (a) Transverse motion — the solid circles show the x motion, and the open circles the y motion. (b) Rotation about the z axis.

track the motion of the chamber system on a much finer time scale than the time between $B \cdot \mu$ runs.

We corrected the chamber system alignment based on the apparent target motion once every run, which generally corresponded to once every eight hours of data-taking. The first three points of Figure 26 have been expanded in Figure 27 to show the detailed apparent target motion, and how smooth the variations were in general. These adjustments made a small but noticeable improvement in the measurement of the transverse momentum of coherent kaons in $K \to \pi^+\pi^-$ decays.

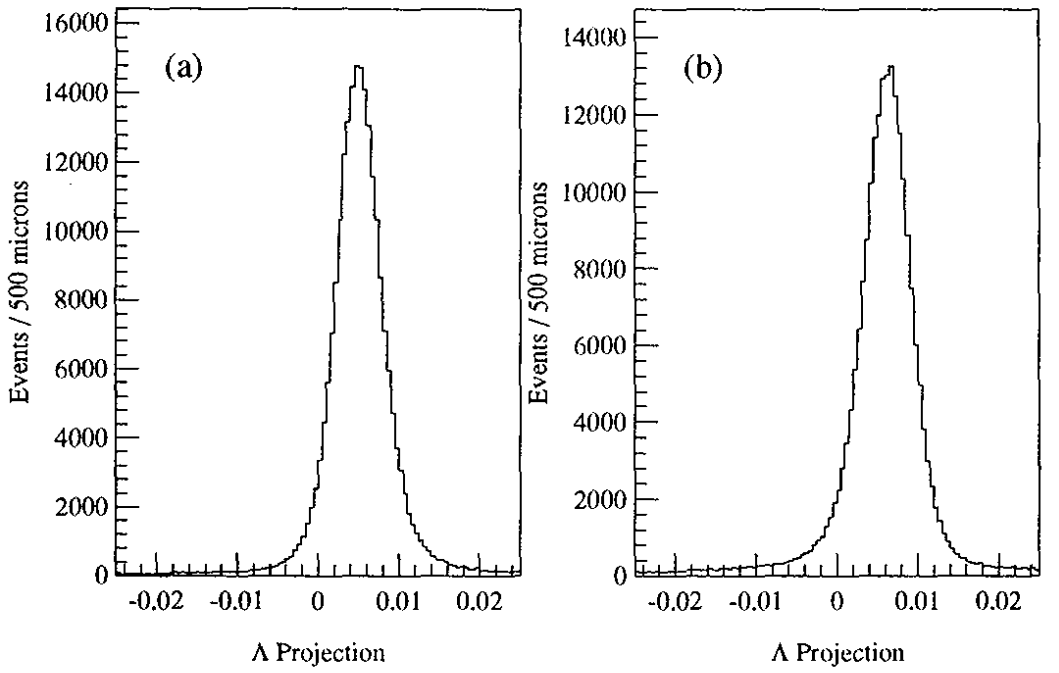

Figure 25. The projected location of reconstructed Λ decays from the $p\pi$ decay mode back to the plane of the target. (a) x projection. (b) y projection. There are also some $\bar{p}pi^+$ decays included.

This completes the discussion of chamber alignment. Because of the numerous large data samples that we were able to collect using a simple, unbiased, two track trigger, we have been able to successfully track the chamber motion as a function of time at the 20 micron level, where most of the uncertainty comes from the motion of the chambers between the alignments. This was very beneficial in later stages of the analysis, as it made the determination of the positions of the limiting apertures much simpler than it might otherwise have been.

4.1.3 Chamber Efficiencies

In general the chamber efficiencies were very good, with many of the planes having efficiencies of 99% or greater throughout the run. Some of the spot checks of the average efficiency for several of the planes during charged mode running are plotted in Figure 28.

The one problematic plane was the inner y plane of chamber 1. As seen in the figure,

the efficiency of the chamber degraded as the run progressed. This plane became increasingly sensitive to late arriving drift particles as the rate of outgassing within the chamber decreased. The late particles probably originated in the dead region between the x and the y high voltage planes. As the outgassing subsided, particularly in the smallest first chamber, there were fewer molecules that could trap these slowly drifting particles. If one shifted the chamber TDC distribution to view the tail of the distribution for this plane for this plane and also for an efficient plane, the observed distributions turned out to be markedly different (Figure 29). There were almost no late times in the efficient plane, while

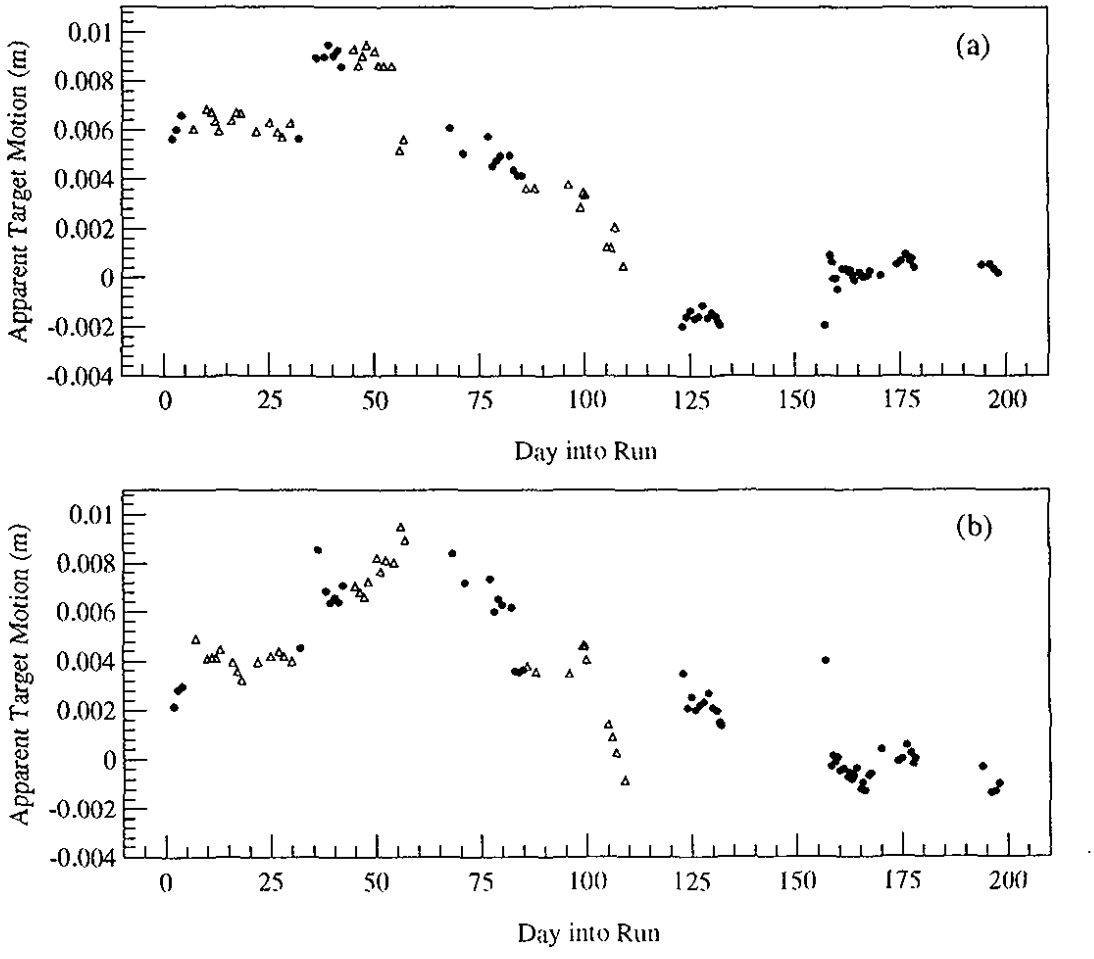

Figure 26. The apparent motion of the target position due to the motion of the drift chamber system as a function of time into the run. The motion has been tracked with $\Lambda \rightarrow p\pi$ decays (solid circles) and $K_L \rightarrow \pi^+\pi^-\pi^0$ decays (triangles). (a) Horizontal (x) motion. (b) Vertical (y) motion.

in the inefficient plane there is a broad distribution of late arrival times. These late arrivals reset the TDC, making the wire look inefficient in normal operation. The area under this late arrival peak relative to the area under the signal region is very close to the observed chamber inefficiency.

This problem was alleviated somewhat by bringing inhibit signals to the TDCs as fast as possible. The change in the inhibit timing resulted in the abrupt increase in efficiency in this plane. Because of the distant location of the TDCs from the trigger electronics, it was not possible to inhibit all of the late arrivals, and we were therefore left with a residual inefficiency in this plane. The tendencies are also visible in the inner planes of chamber 2, such as the X plane plotted in Figure 28, but have disappeared in the two chambers farthest downstream. The problems were alleviated as one goes downstream both because accidental activity in those chambers was lower, and because the extra time of flight of the charged

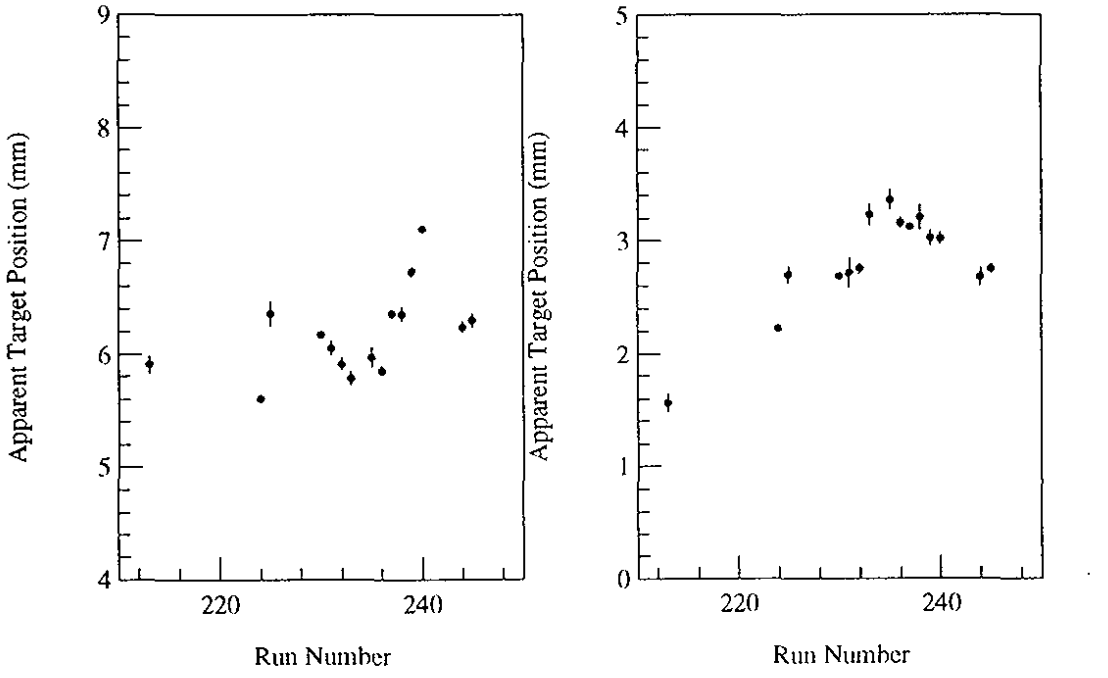

Figure 27. The apparent motion of the target position due to the motion of the drift chamber system as a function of time into the run over the first several alignment periods. The motion has been tracked with $\Lambda \rightarrow p\pi$ decays. *Left:* Horizontal (x) motion. Right: Vertical (y) motion.

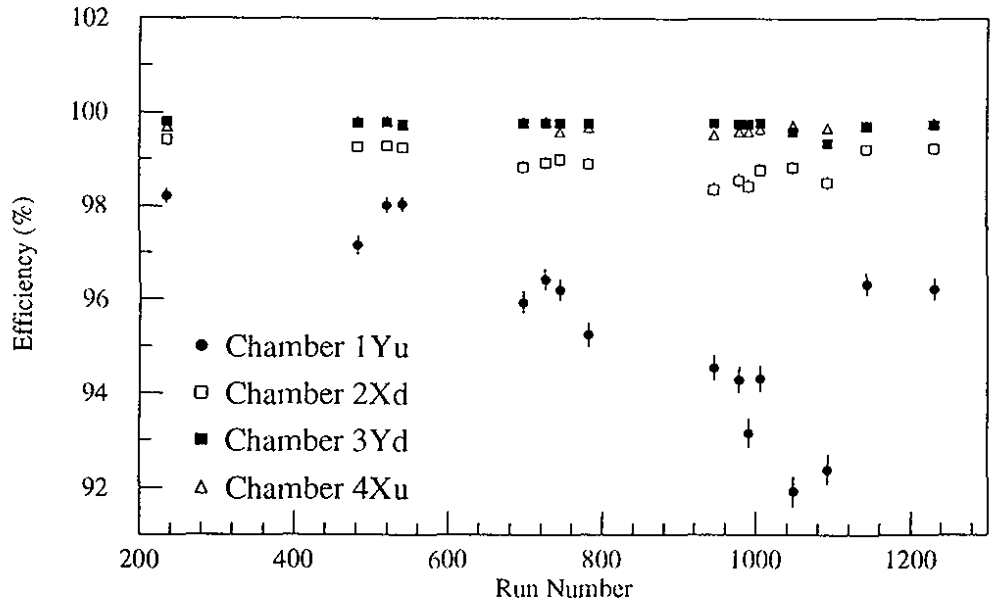

Figure 28. Chamber efficiencies during several of the $\pi^+\pi^-$ runs. One of the four planes from each chamber has been plotted. These efficiencies were measured using pions.

particle (roughly 20 ns between each chamber) gave us sufficient time to inhibit the late arrivals.

The other planes in chamber 1 were not seriously affected by these late hits. The inner x plane had efficiencies similar to the x plane shown for chamber 2, while the outer x and y planes had efficiencies in excess of 99.5%. The effect of this inefficiency on $Re(\varepsilon'/\varepsilon)$ turns out to be negligible. On one hand, the tracking efficiency was not seriously affected since the only seriously degraded plane was a y plane in which the tracks do not bend. Since the y track finding requires only 5 out of the 8 planes to register a hit, and all of the other planes are very efficient, the change in the probability that we lose a track is small (on the order 10^{-4}). On the other hand, since we collect the decays from the vacuum and regenerator beams simultaneously and since the problem occurs uniformly across the chamber, the inefficiency affects the K_S and K_L samples identically. This leads to the cancellation of any induced inefficiency in the single ratio for the $\pi^+\pi^-$ decay mode.

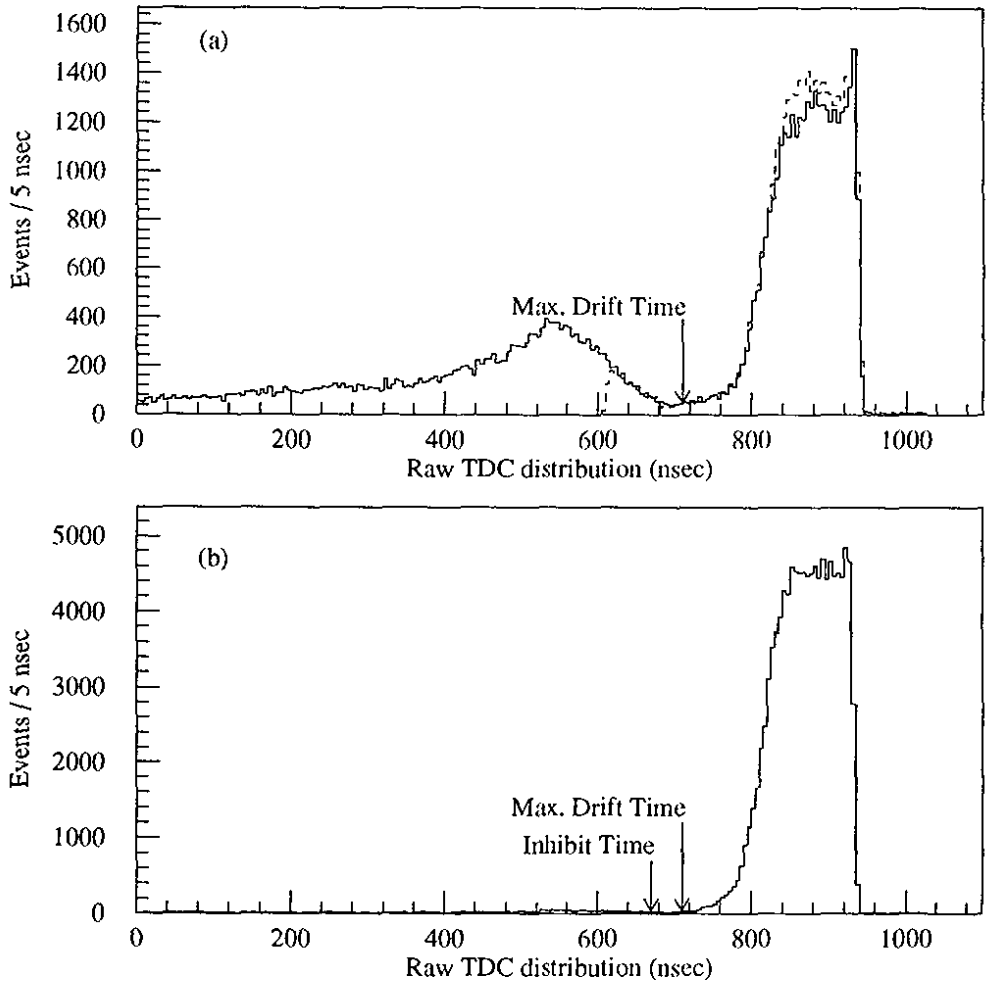

Figure 29. Raw chamber TDC times measured using a delayed common stop. The solid arrows indicate the position of the latest TDC times collected with normal running conditions. (a) Inner Y plane of chamber 1. The solid histogram was collected using no inhibit. The dashed histogram was collected with the standard inhibit time relative to the common stop for that chamber. (b) Outer Y plane of chamber 4. The small arrow indicates the standard inhibit timing for this plane, and the large arrow the maximum drift time used for tracking. Note the shift of this inhibit time relative to the inhibit timing in (a).

4.1.4 Momentum Scale

The last component of the chamber calibration and alignment was the tuning of the momentum scale. While a survey of the magnetic field was able to map the shape and obtain the scale at the 0.2% level, the overall scale of the field would change slightly when the magnet polarity was reversed. During the last two charged data sets (C4 and NC), the

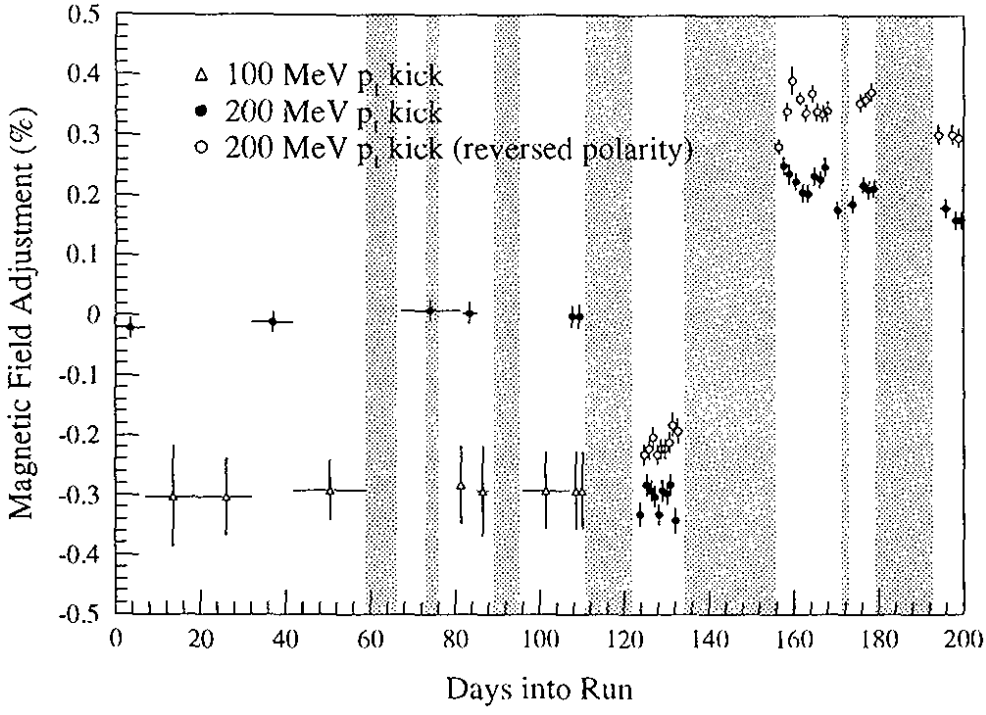

Figure 30. The magnetic field correction factors. The corrections are grouped into three magnet configurations: "normal" polarity with a 200 MeV p_t kick (*solid circles*), normal polarity with a 100 MeV p_t kick (hollow triangles), and reversed polarity with a 200 MeV p_t kick.

polarity was reversed about twice per day to allow a possible measurement of the charge asymmetry in Ke3 decays.

The $\pi^+\pi^-$ mass is given, to a very good approximation, by

$$m_K^2 - 2m_\pi^2 = p_1 p_2 \left(\theta^2 + \frac{2m_\pi^2}{p_1 p_2} \frac{p_1^2 + p_2^2}{p_1 p_2} \right). \tag{4.6}$$

If the scale of the magnetic field shifts by a small amount β, then each of the momenta will be shifted by that amount. When β is small enough, the dominant effect on the mass is to have $\Delta m_{\pi^+\pi^-}/m_K \approx \text{const} \times \beta$. Hence by monitoring the reconstructed $_{,}$mass, we were able to improve the average accuracy of the momentum measurements, and map the shifts in the magnetic field strength as a function of time. The resulting scale shifts are shown as a function of time in Figure 30. A clear shift of 0.1% can be seen between the field strengths for the two polarities. A small correction to the assumed ratio between high field strengths

and low field strengths was also necessary. The step near 150 occurred after work was done on the power supplies for the magnet.

4.2 Lead Glass Calibration

After the chambers were aligned and the momentum scale calibrated, the lead glass was calibrated by comparing the momentum of an electron measured in the charged spectrometer to the energy of its shower in the calorimeter. The goal of the calibration was to understand the mean response of the calorimeter at the 0.1% level. The calibration ultimately yielded a measurement of the nonlinearity and the gain for each of the 804 blocks

There were two samples of electrons used for this calibration. The first sample was obtained from special runs where e^+e^- pairs were created by converting photons in the beam with a copper foil. Calibration magnets upstream of the chamber system (see Figure 7b) separated the e^+e^- pairs vertically and horizontally so that each particle could be separately tracked in the chamber system. By adjusting the magnet settings, the electrons could be swept to illuminate the entire glass.

The calibration program using these special calibration electrons was very successful, and allowed us to understand the overall calorimeter response within $\pm 0.2\%$ over a 50 GeV range (Figure 31). The largest drawback was a lack of statistics, particularly in the few outermost rings of blocks in the array. The outer blocks also suffered because of an insufficient lever arm in momentum, which was needed to obtain an accurate measure of the nonlinearity of each block.

To probe the calorimeter response further, we had to turn to an electron sample with much higher statistics. With the calibration electron gains, it was very simple to isolate a second sample of electrons: those from Ke3 decays. Almost 40% of the sample of charged triggers were identifiable Ke3's, leading to a total sample of 120×10^6 electrons potentially available for calibration. For the same calibration shown in Figure 31, the electron response versus energy reveals structure (Figure 32) only hinted at by the calibration electron sample. Note that for this analysis, we will only be using $2\pi^0$ decays with a maximum photon energy of under 60 GeV, where the e^+e^- calibration is quite good.

Aside from different cuts to clean up the electron samples, the procedure to extract the two calibration constants for each block was essentially identical in both the calibration and Ke3 electron samples. The calibration procedure and the calibration electron sample have already been described in detail in reference [74]. A brief review of the model of the lead glass response and its impact on the calibration procedure will be presented here, but this section will focus on the identification of the Ke3 sample and on differences in the details of the calibration.

4.2.1 Review of the Lead Glass Response and the Calibration Procedure

As we mentioned in the previous chapter, the absorption of the Çerenkov radiation as it propagates through the lead glass leads to an intrinsic nonlinear response of the calorimeter. This essentially breaks the shower reconstruction algorithm into two pieces: to determine the number of photons present at the back of a block given the observed number n_i of ADC counts in that block, and to determine the energy of the original showering particle given the measured number of photons present in the 3×3 cluster of blocks for that shower. The first step requires the measurement of an effective "gain" for each block. This one number

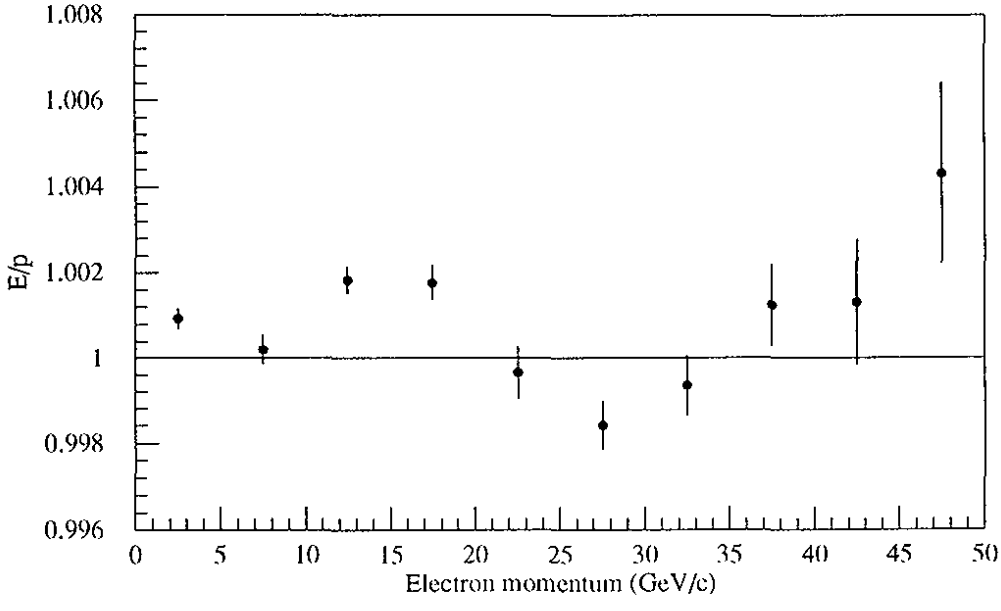

Figure 31. Mean value of the ratio of cluster energy to track momentum (E/p) versus momentum for electrons and positrons in one of the e^+e^- calibration sets.

will be the result of many effects, including the quantum efficiency of the photocathode, the fraction of area of the block covered by the tube, the actual phototube gain, and the conversion constant for that ADC channel. The second step relies on knowledge of the block's absorption α and of the variation $C(E,\alpha)$ in the Çerenkov light present at the back of the block for an incoming particle of energy E. We will first outline the procedure used to predict the response function $C(E,\alpha)$, and then describe the e^+e^- calibration procedure.

Çerenkov light is produced at an angle $\cos\theta_C = 1/\beta n$, where n is the index of refraction, so the light reaching the back of the block will have travelled farther than the distance from its production point to the back of the block. In the lead glass, with $n = 1.6$, the production angle is 51°, so most of the light produced will have to be reflected at least once by the side of the block before reaching the back. Because neighbouring blocks are not in optical contact, any light not reflected will be lost. For particles with $\beta \approx 1$, θ_C is equal to the critical angle for total internal reflection, so the light from shower particles travelling parallel to the longitudinal axis of the block will be completely contained within the block. For shower

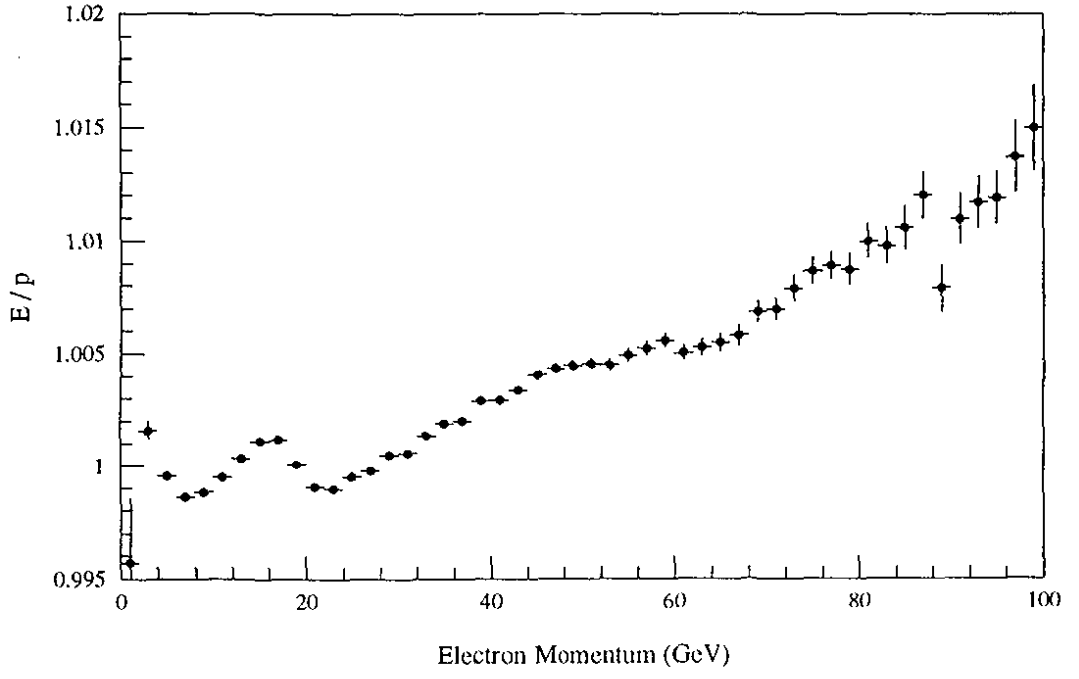

Figure 32. Mean value of the ratio of cluster energy to track momentum (E/p) versus momentum for electrons and positrons from Ke3 decays using the gains from the e^+e^- calibration set of Figure 31.

particles produced off-axis, a small amount of light will be lost, but we neglect this in our model.

Assuming a uniform absorption α' within a block, the number of Çerenkov photons present at the back of the block for an electron of incident energy E is

$$N(E,\alpha) = \tilde{g}E \int_0^L \tilde{f}(E,\ell) e^{-\alpha'(L-\ell)/\cos\theta_C} d\ell, \tag{4.7}$$

where L is the length of the block, and $\tilde{g}$ is the number of photons produced per GeV. The function $\tilde{f}(E,\ell)$ is the fractional amount of light produced at a depth ℓ radiation lengths into the block, normalized such that $\int_0^\infty f(E,\ell)d\ell = 1$. Its shape as a function of ℓ is similar to that of a gamma distribution [83]. A block's absorption is always scaled by the same factor $1/\cos\theta_C$, so throughout the analysis we use an effective absorption $\alpha = \alpha'/\cos\theta_C$.

A large number of electron showers were generated using the EGS [84] simulation program to study the longitudinal shower distributions $\tilde{f}(E,\ell)$ and to provide a correction table to map observed signals to true energies. A detailed description of the characteristics of these showers are presented in reference [74]. The 18 energies at which showers were generated ranged from 0.25 GeV to 90.51 GeV and were evenly spaced in $\ln E$. We found the position ℓ_{max} of the maximum of the longitudinal shower distribution varied with the energy of the incoming particle according to [74]

$$\ell_{max} = 1.022ln(E) + 3.15 \tag{4.8}$$

with E measured in GeV and ℓ_{max} in units of the 3.21 cm radiation length of the glass.

To obtain the response function $C(E,\alpha)$, $N(E,\alpha)$ was normalized to the total number of photons $\tilde{g}E$ produced in a shower and averaged over the ensemble of EGS showers generated at the energy E. The response function was then defined as

$$C(E,\alpha) = \left\langle \frac{N(E,\alpha)}{\tilde{g}E} \right\rangle / c_1(\alpha), \tag{4.9}$$

where $<>$ denotes the average over the ensemble of showers at energy E. The function $c_1(\alpha) \equiv \exp(-(L-5.157)\alpha)$ is very close to the response of a lead glass block with absorption α to a 1 GeV electron. This response is also folded into our definition of the "gain", that is, the gain becomes the correction needed to map the ADC counts directly to the true energy for a 1 GeV shower. $C(E,\alpha)$ then corrects for the different response at other energies. For

this experiment, with most absorptions in the range of 3% to 4%, the corrections were in the 8% - 10% range for typical shower energies.

The response function $C(E,\alpha)$ was fit reasonably well by a power-law behavior $E = (\sum n_i/g_i)^\beta$, with the power β given by

$$\beta = 1.0053 - 0.9106\alpha. \tag{4.10}$$

The deviations of the power-law from the proper correction $C(E,\alpha)$ were under 1% [74]. While the deviations were too large to allow to simply use a straight power law behavior for the cluster energy reconstruction, the near power-law behavior was still convenient. The final nonlinearity correction depended on the energy E of the original particle, but E was what we were trying to extract! Fortunately, C tends to vary as $\ln E$, so the approximate power-law prediction sufficed to provide an energy *prediction* E_p that we used to obtain the proper correction $C(E_p,\alpha)$. As we shall see, the calibration procedures also made use of this approximate behavior.

4.2.1.1 From electrons to photons

At this point, we need to remind ourselves that the ultimate goal of the calibration procedure is to be able to reconstruct the energies of photons from $2\pi^0$ decays. Unfortunately, electrons begin to emit Çerenkov radiation as soon as they enter the calorimeter, while photon showers do not emit any radiation until after the initial conversion to an e^+e^- pair. If the photon converts at a depth ℓ_0 radiation lengths into the block, then the photon will behave effectively as the sum of an electron shower with energy $E_e = \kappa E$ and a positron shower with energy $E_p = (1-\kappa)E$, but in a "foreshortened" block of length $L - \ell_0$.

We do not know the conversion depth ℓ_0 on an event by event basis, so we must make a correction based on the average difference in response between a photon and electron of energy E. We can generalize the definition of $N(E,\alpha)$ given in Equation 4.7 to depend on the conversion depth, that is,

$$N(E,\alpha,\ell_0) = \tilde{g}E\int_0^{L-\ell_0} \tilde{f}(E,\ell)e^{-\alpha'(L-\ell)/\cos\theta_C}\,d\ell. \tag{4.11}$$

After defining $C(E,\alpha,\ell_0)$ analogously to $C(E,\alpha)$, the average electron photon correction $R(E,\alpha)$ can then be calculated as

$$R(E,\alpha) = \int_0^L d\ell_0 \int_0^1 d\kappa P(\ell_0,\kappa)[\kappa C(\kappa E,\alpha,\ell_0) + (1-\kappa)C((1-\kappa)E,\alpha,\ell_0)], \qquad (4.12)$$

The probability function $P(\ell_0,\kappa)$ is given by the Bethe-Heitler spectrum,

$$P(\ell_0,\kappa) = (1+\frac{1}{42\zeta})^{-1} e^{-7/9\,\ell_0}(\kappa^2 + (1-\kappa)^2 + (\frac{2}{3} - \frac{1}{9\zeta})\kappa(1-\kappa)), \qquad (4.13)$$

where ζ is the zeta-function. For an absorption of 4%, the electron-photon difference R has values from 2% to 3% over the energy range of the photons we consider. Understanding this difference between the electron and photon response is very important for the success of the experiment, where we need to understand the average photon response at the 0.1% level. We will evaluate our understanding of the response to photons in later chapters.

4.2.1.2 The e^+e^- electron calibration

The method used to obtain the first set of calibration constants (g_i,α_i) for each block with the e^+e^- calibration samples utilized the near power-law behavior of the lead glass response. The procedure was an iterative one, where one first corrected the "measured energy" $E_m = \sum_{3\times3} n_i/g_i$ (and corrected for thresholds, etc. as described in reference [74]) to a quantity E'_m that should behave like a true power-law, $E_{true} = E'^{\beta}_m$.

The momentum p of the electron was measured in the charged spectrometer, and from Equations 4.7 and 4.9 we see that we should have $E_m/p = C(p,\alpha_i)$, where α_i is the current best guess for the absorption of the central block of the cluster. Using α_i and Equation 4.10 to give the best power-law approximation, a correction factor given by

$$d = \left(\frac{C(p,\alpha_i)}{p^{1/\beta-1}}\right)^{-1/\beta} \qquad (4.14)$$

was applied to E_m to give $E'_m = dE_m$.

A linear least squares fit to $\ln E'_m$ versus $\ln p$ was then done on an event by event basis, one fit for each block. Each event was weighted with the expected smearing both from the momentum measurement and the cluster energy measurement (see Equations 3.2 and

3.1). The momentum p was used to calculate both the momentum and energy resolution contributions to keep the fit stable from iteration to iteration. The slope of the fit gave a corrected power-law β' from which a new absorption for the central block, α_i' was inferred using Equation 4.10. The intercept of the plot was taken as the correction to the gain of the central block.

4.2.2 Ke3 Electron Calibration

Had there been sufficient statistics in the e^+e^- calibration samples, the procedure outlined above would have sufficed to calibrate the glass. Unfortunately, there were not enough electrons in the samples to determine the absorptions of blocks on the outer edge of the array independently. Instead we had to rely on a functional form based on the distance of the block from the center of the array to estimate these absorptions. Furthermore, there were insufficient statistics to probe the structure near 16 GeV.

For the final adjustment of the glass calibration we turned to the Ke3 sample in the vacuum beam. The Ke3 sample was initially identified by requiring that the ratio of cluster energy to track momentum satisfied $E/p > 0.85$. This left a sample of 120 million events in 5 different data subsets. However, hadronic showers by pions or protons satisfied this requirement several percent of the time, leading to a contamination of several percent in this sample. The following sections will describe the isolation of the electron sample, the study of the structure at 16 GeV, and the final calibration.

4.2.2.1 Ke3 isolation

The largest backgrounds in the Ke3 sample came from $\Lambda \rightarrow p\pi$ and $K_L \rightarrow \pi^+\pi^-\pi^0$ decays. The Λ decays were quite easy to eliminate. For the laboratory energies in which we are interested, the proton to pion momentum ratio satisfied $p_p/p_\pi > 3$. In order to survive long enough to decay within our decay volume, the Λ's also had to be very energetic. In Figure 33, one can see a clear Λ peak in the reconstructed $p\pi$ mass for $E_\Lambda > 130$ GeV, but not in the 100 to 130 GeV range. The momentum ratio cut has already been applied to obtain the samples shown. We are more concerned with rejecting background than

preserving signal for this sample, so we reject any event with $E_\Lambda > 100$ and with a $p\pi$ mass within 15 MeV of the nominal Λ mass. This mass cut minimizes contamination of the Ke3 sample by nongaussian tails on the $p\pi$ mass distribution.

There were several cuts applied to remove the $\pi^+\pi^-\pi^0$ decays from the sample. The most powerful was to look at the kinematics of the two tracks, assuming the two tracks were associated with charged pions. We could then examine the kinematics of these two tracks assuming that the π^0 was missing, as described in Appendix B. A plot of k_{+-0} (see Equation B.9) versus $\pi\pi$ mass is shown in Figure 34. The majority of the Ke3 decays have an unphysical negative value for k_{+-0}. However, for $m_{\pi\pi} < m_{K^0} - m_{\pi^0}$, the physically allowed region for $\pi^+\pi^-\pi^0$ decays, there is a small secondary peak from the background $\pi^+\pi^-\pi^0$ events in the Ke3 sample. The region with the lighter shading corresponds to the two dimensional cut $m_{\pi\pi} < 373$ MeV and $k_{+-0} > -0.04$ GeV^2 applied to eliminate the $\pi^+\pi^-\pi^0$ background.

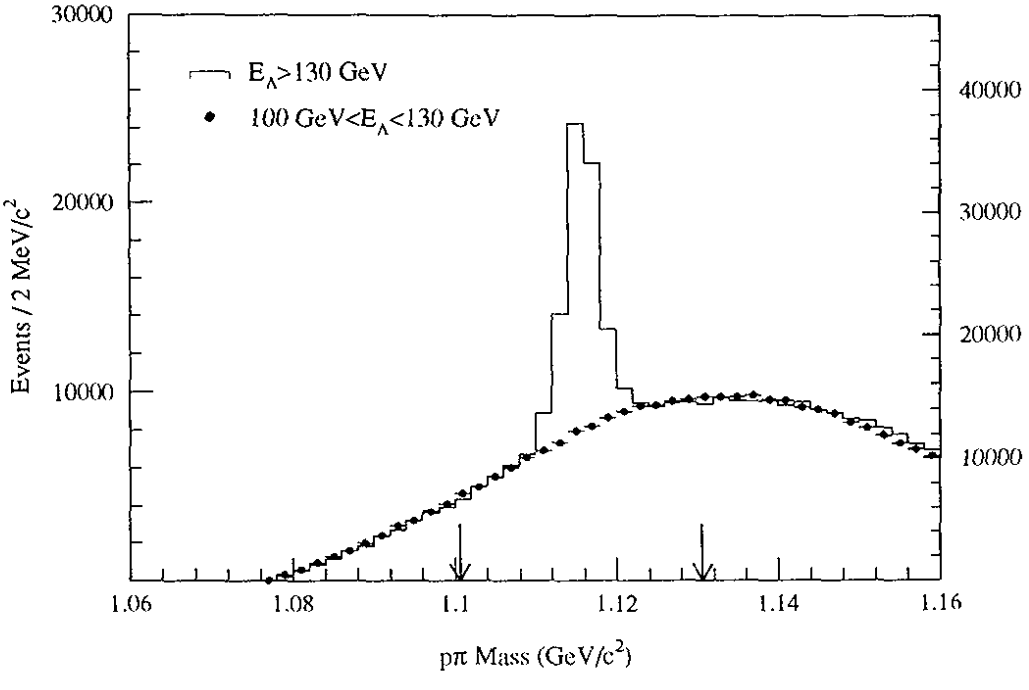

Figure 33. Reconstructed $p\pi$ mass for a sample of Ke3 candidates with only a loose E/p cut for Ke3 identification and the momentum ratio cut applied. The histogram shows the mass for events satisfying $E_\Lambda > 130$ GeV, (left scale) and the circles the mass for 110 GeV$< E_\Lambda <$ 130 GeV (right scale). The arrows indicate the applied mass cut.

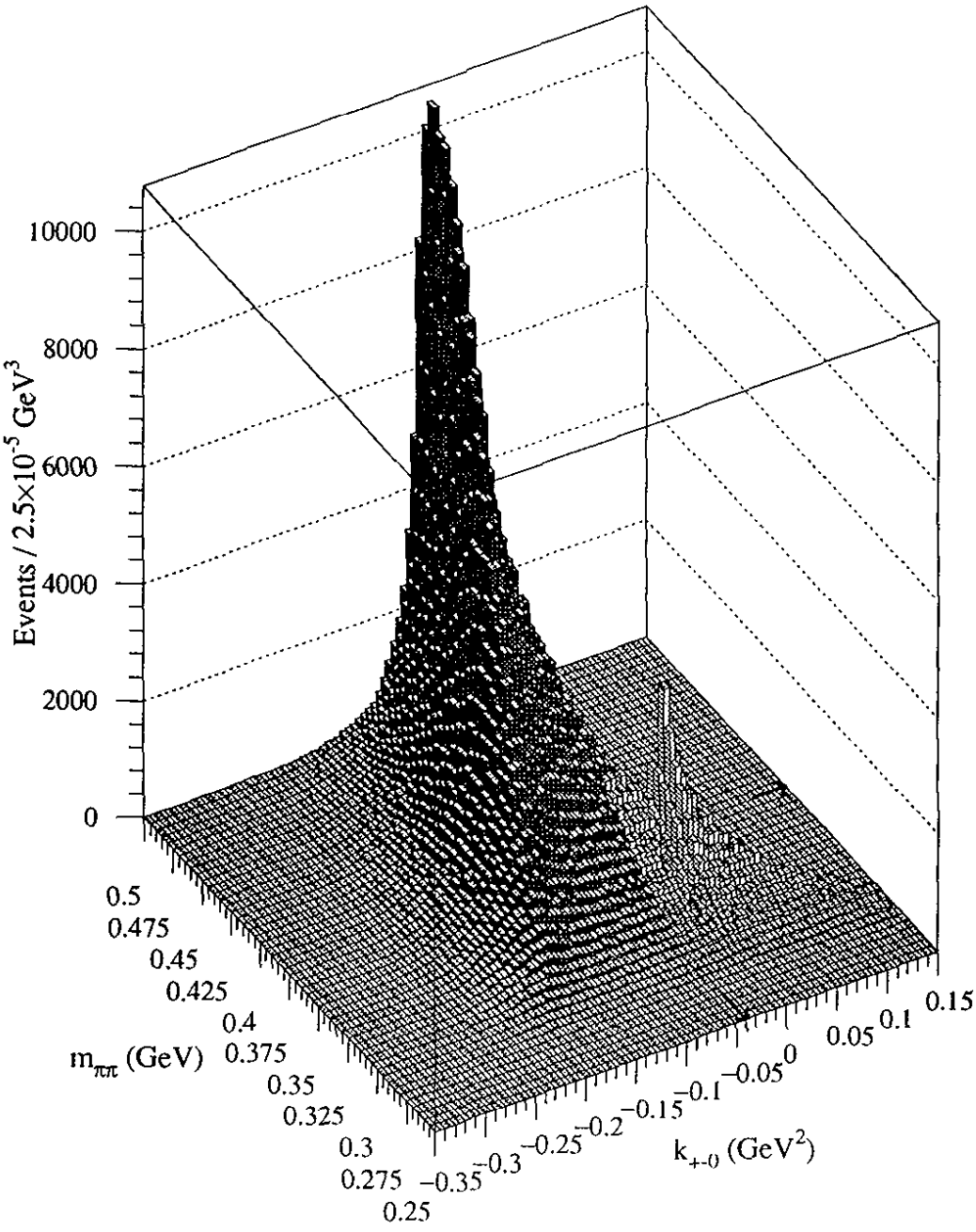

Figure 34. $m_{\pi\pi}$ versus k_{+-0} in the Ke3 sample. The small peak at the lower right is due to $\pi^+\pi^-\pi^0$ background. Events in the lightly shaded region demarcated by the two arrows are removed from the final Ke3 sample.

Another set of cuts were applied to the electron cluster shape. These included cuts on the broadness of the shower, originally designed to eliminate clusters with contributions from two merged photon showers, and deviations of the relative track and cluster positions that were significantly outside of resolution effects. The cuts were applied to reduce the contamination of events with bremsstrahlung, but were also very effective at eliminating showering pions. By studying Ke3 decays where one track is cleanly identified as an electron, we can study the effect of these cuts on the other pion when it has showered and has a large E/p. Only about 10% to 15% of these showering pions survived the shape cuts.

No cuts were specifically applied to reduce backgrounds from $\pi^+\pi^-$ or Kμ3 decays. A Kμ3 decay has to be doubly misidentified to make it into the final sample: the pion has to shower and be identified as an electron, and the muon has to *not* fire the μ2 veto to be identified as the pion. The pions were required to have a momentum higher than 4 GeV, and the probability of this double misidentification is of order 10^{-4}. For the $\pi^+\pi^-$ sample there is a several percent chance for one of the two pions to shower and be identified as an electron. When combined with the difference in branching ratios, the background is again expected to be only of order 10^{-4} in the Ke3 sample. After the electron shape cuts, both these modes will have residual contributions at the several 10^{-5} level, which we did not worry about.

The sample was also required to satisfy the Ke3 kinematics, with $m_{\pi e} < m_{K^0}$ and $p^{*2}_{\nu_{\|}|} > -0.005$ (GeV/c)^2 (see Equation B.6). Some resolution smearing is allowed in the latter quantity, which is plotted in Figure 35 before and after all of the background and misreconstruction rejection cuts (except the cut on $p^{*2}_{\nu_{\|}}$).

Finally, to avoid biases in the momentum and energy measurements, cuts were applied to ensure that the electron track was cleanly reconstructed, and additional cuts were applied on the track projections to keep the electron and pion well separated.

The final distribution of E/p before and after all cuts for the Ke3 sample from set NC is shown in Figure 36. The studies of the lead glass that follow relied most heavily on this set of electrons. From the reduction in the size of the tail on the high side of the distribution, we can see that the background from hadronic background has been greatly reduced. The remaining tail on the low side of the E/p distribution is mostly due to electrons that travel

some distance down a small gap at the corner of the blocks[2] before showering, and it could easily be reduced by cutting tracks which project near the corners.

4.2.2.2 The 16 GeV structure

As 16 GeV is near the low range to high range crossover point for the ADC modules, there was always the suspicion that a relative high range to low range gain mismatch was responsible for the behavior in E/p versus p in this region. The relative high to low range gain for each ADC channel was measured with a bench test and with the flasher, but it was difficult to get measurements more accurate than several tenths of a percent.

The illustration in Figure 37 helps to clarify the effect. In the ideal case, with the correct high to low range ratio, proper absorptions, etc., the distribution of E/p versus p would be flat. If the absorption was known properly, but there was a gain mismatch between high

[2]Caused by a 2 mm bevel along each long edge of each block

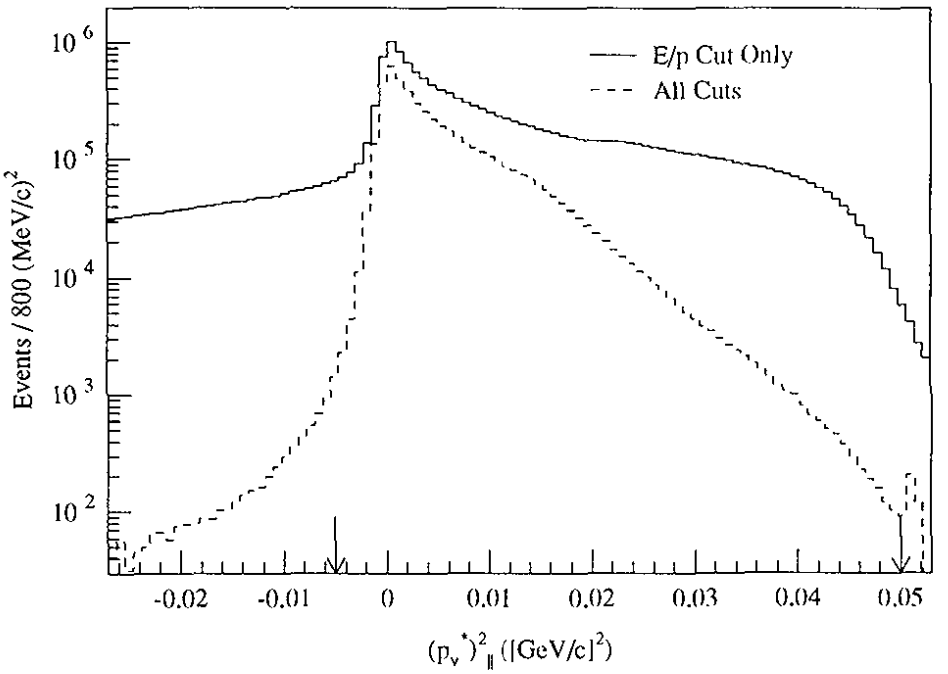

Figure 35. The Ke3 kinematic variable $p^{*2}_{\nu_\parallel}$ for Ke3 candidate calibration events after a loose E/p cut only (solid histogram), and after all but the kinematic cut (dashed histogram). The arrows indicate the analysis cut locations.

and low ranges, a step would be introduced in E/p versus p, as in part (a) of the figure. When one tried to find the best nonlinearity, it would try to compensate for the step, fitting a curve similar to the line in (a). When we use this new nonlinearity, a measurement of E/p versus p would give the residual between the measured E/p and the fit curve in (a), yielding the tilted distributions in (b).

This is essentially the structure we see in Figure 32, except that the data is blurred out because of differences in the crossover region and step mismatch from block to block. Using the clean electron sample identified above, we have studied the variance of E/p versus ADC counts for all blocks with electrons extending into the ADC high range. An example is shown in Figure 38a, with a linear fit to E/p in both the high range and the low range. It is straightforward to show that the necessary fractional correction to the high range gain is simply the difference in E/p measured in the high range and low range at the crossover point. We obtained this correction by extrapolating the high and low range fit in a block to that block's crossover point. After several iterations of this process, the process converged.

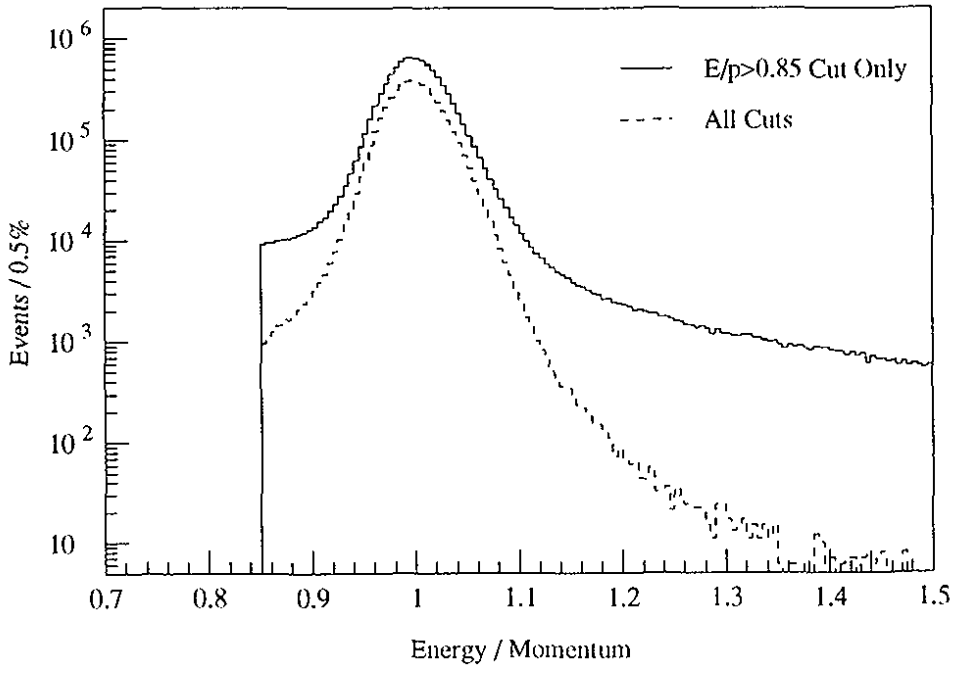

Figure 36. The E/p distribution for electrons in Ke3 decays with only the initial $E/p > 0.85$ selection criterion and (solid histogram) and with all other cuts (dashed histogram).

The distribution of corrections is shown in Figure 38b. The corrections were reproducible within 0.1%, both in this sample and an earlier sample of Ke3 decays.

4.2.2.3 Ke3 Calibration

After the above improved measurement of the relative high range to low range gain measurements, and improved measurements of the rate-dependence of pedestal shifts within the ADC modules, each sample of Ke3 electrons was used to recalibrate. Since the calibration constants from the e^+e^- calibrations were already quite good, we did not try to make an absolute measurement of the block absorptions as described above. Instead, we assumed any residual between the electron momentum p and the energy prediction $E = E_m/C(p,\alpha)$ would be very close to a residual power-law $p = E^{\Delta\beta}$. The new absorptions were then given

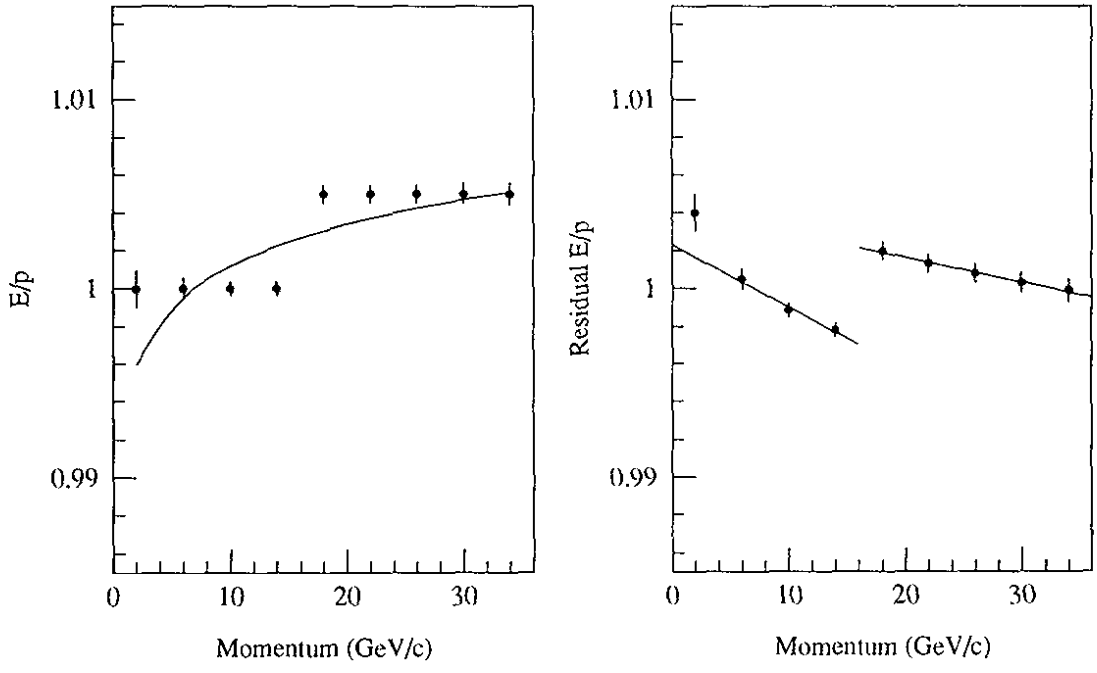

Figure 37. The distortion introduced into E/p by a 0.5% gain mismatch between the high and low ADC ranges. *Left:* E/p versus p with a gain mismatch, and the best fit nonlinearity nonlinearity which tries to compensate. The errors are representative of those available for an individual block. *Right:* The difference between the distorted E/p and the best fit nonlinearity. The linear fits in the high and low range regions yield a $0.51\% \pm 0.07\%$ measurement of the mismatch.

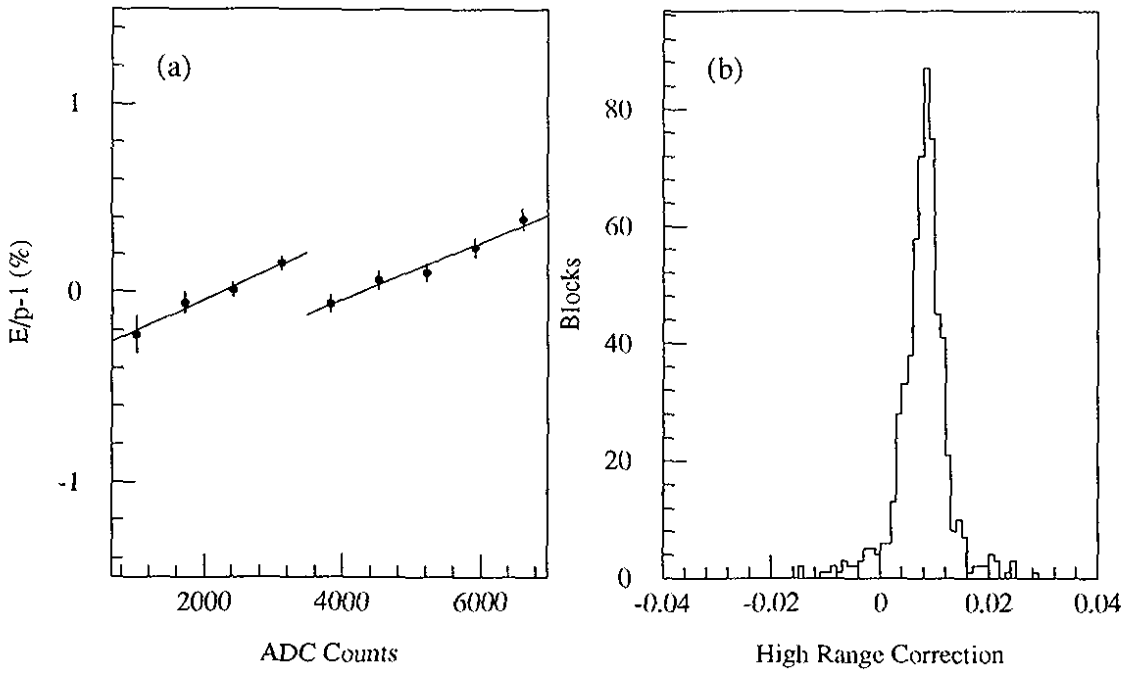

Figure 38. (a) E/p versus ADC counts for an individual block. The effect of the high range gain mismatch relative to the low range gain, coupled with the nonlinearity fit, clearly stands out. The gain mismatched by 0.6% of itself. (b) The fractional high range gain corrections for each corrected block.

by

$$\alpha_{new} = \frac{1.0053}{0.9106} - \Delta\beta\left(\frac{1.0053}{0.9106} - \alpha_{old}\right). \tag{4.15}$$

One possible bias still existed from electron bremsstrahlung upstream of the analysis magnet and radiative Ke3 decays. In both of these cases, when the electron momentum is above 40 GeV, the analysis magnet did not bend the electron enough away from the photon trajectory, resulting in a merging of the photon and electron clusters in the calorimeter. Thus the cluster energy would appear higher than the measured track momentum. While the electron cluster shape cuts should largely eliminate these events, we decided to limit the maximum electron momentum for the NC set calibration to 30 GeV. The minimum momentum accepted was 2 GeV.

After calibration, the resulting distribution of the mean of $E/p - 1$ vs p in the NC set over a 100 GeV range is shown in Figure 39. The average electron response appears to

be understood within 0.1% well beyond the 30 GeV maximum electron energy used in the calibration.

In charged mode sets earlier than the NC set, the readout threshold on the lead glass was 20 counts rather than 5. This made reliable calibration with the lowest energy electrons more difficult. From studies on the NC set with a 20 count threshold simulated in software, the calibration results could be reproduced quite reliably in the inner portions of the array by changing the allowed electron momentum range to be 10 GeV to 60 GeV. In addition, the higher threshold degrades the energy resolution, so an extra resolution term was added to compensate for this when weighting the events. For the outer three rings, where radiation damage was expected to be minimal, the absorptions obtained in the NC set were simply scaled as a group. The measured scale factors were almost flat in time, increasing only slightly as the run progressed.

For neutral mode sets earlier than the NC set, we tried to make the best use of all the calibrations available to obtain the most reliable photon reconstruction. For the middle 10×

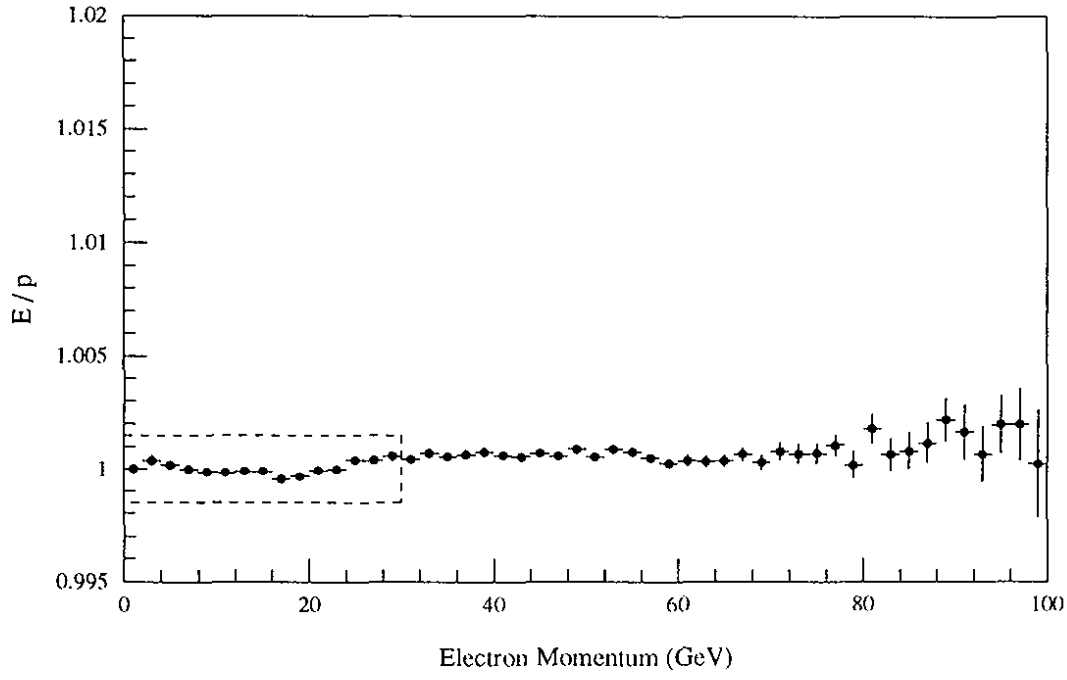

Figure 39. Mean value of the ratio of cluster energy to track momentum (E/p) versus momentum for electrons and positrons from Ke3 decays using the Ke3 calibration gains. The dashed box shows the momentum range used for the calibration.

10 subsection of the array, the e^+e^- samples had sufficient statistics to provide calibration constants. Because the beam intensity was highest during the $2\pi^0$ data taking, this inner portion of the array tended to suffer most from radiation damage in these sets. The e^+e^- calibrations were taken during each set, so they provide the best measure of the absorptions at those times. For the rest of the array, the Ke3 constants were extrapolated to the neutral sets using the flasher data. The constants from the two sets agreed very well on the boundary of the 10×10 subsection.

4.3 Conclusion

This concludes the discussion of the calibration of the components of the detector needed to reconstruct the $\pi\pi$ decays. In later chapters dealing with determining acceptance and modeling the response of the glass, the benefits of having preformed such detailed calibrations will become clear. For now, we will turn to the discussions of reconstruction and background subtraction in the $\pi^+\pi^-$ and $2\pi^0$ decays.

CHAPTER 5

$\pi^+\pi^-$ ANALYSIS

The analysis of the $\pi^+\pi^-$ decay mode was the more straightforward of the two decay modes. Our drift chambers gave us very good resolution, and allowed us to reduce the backgrounds to a minimal level by employing only a few, simple kinematic and topological cuts. Furthermore, the chamber response was very stable throughout the run, aside from the change in one plane's efficiency, and each chamber's motion could be tracked very precisely relative to the production target and the lead glass calorimeter. As a result, the charged analysis has not changed substantially from that used for the result[50] based on 20% of the data.

The following sections will describe the analysis and background subtraction for the $\pi^+\pi^-$ decays. For the analysis of both the $\pi^+\pi^-$ decay mode and the $2\pi^0$ decay mode (following chapter), the reconstruction and analysis cuts are all blind both to the beam in which the decayed occurred, and to the position of the regenerator (top beam or bottom beam). This ensured that the regenerator beam and vacuum beam were treated identically and avoided a major class of biases in the analysis. Only after all analysis was complete were the events divided into the regenerator beam and vacuum beam subsets for background subtractions, for comparisons to the Monte Carlo simulation, and for fitting. No cuts were applied on decays from one beam that were not applied on decays from the other.

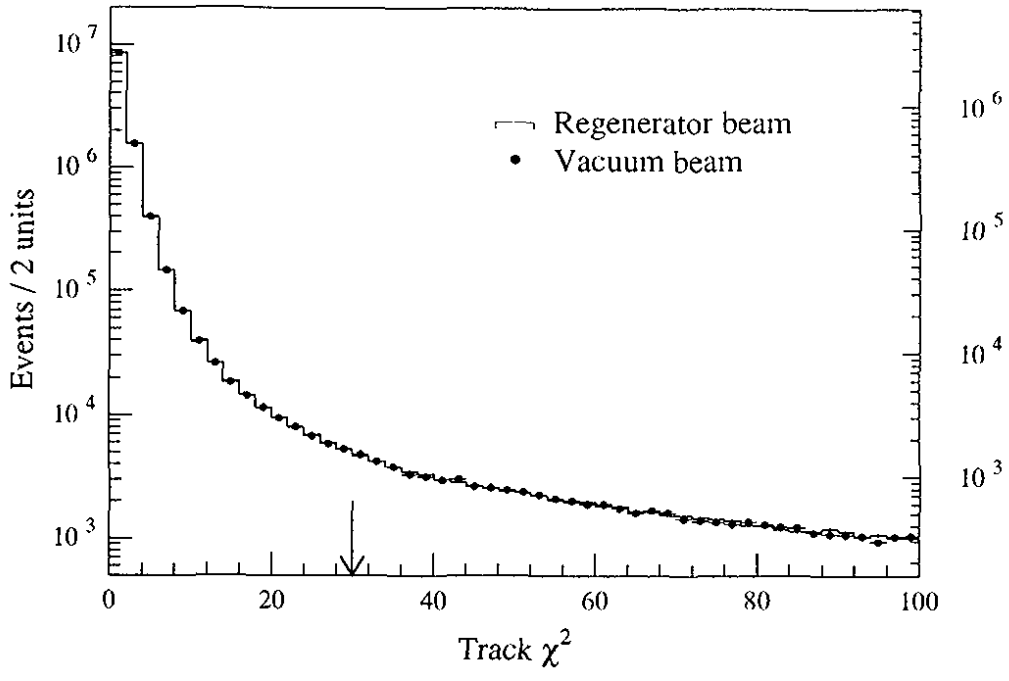

Figure 40. Track segment χ^2 (per degree of freedom) for the pion tracks from $\pi^+\pi^-$ decays. The histogram depicts the regenerator beam distribution (left scale), and the dots depict the vacuum beam distribution (right scale). The arrow indicated the position of the cut. All but the track quality cuts have been applied.

5.1 Reconstruction

5.1.1 Tracking-Related Cuts

The basic requirement for a $\pi^+\pi^-$ candidate was the reconstruction of two in-time tracks[1]. To minimize the misreconstruction background, we applied several cuts related to the quality of the tracks. The most basic cut was applied to the segment[2] χ^2 calculated for a linear fit to the locations of the individual hits measured in the drift chambers. The distribution of the reduced segment χ^2 (ie., χ^2/n_d, where n_d is the number of degrees of freedom) is shown in Figure 40 after all other cuts for decays from both the vacuum and regenerator beams. We make a cut on the reduced χ^2 at 30.

The long tail visible in the χ^2 distribution is populated almost solely by tracks where

[1] See Section 3.2.3 for the definition of in-time.

[2] Recall that a track "segment" is charged particle's trajectory measured in either the upstream pair or downstream pair of drift chambers.

one of the hits has a drift time that is too small to be consistent with the other hits on that track. This is the behavior expected from δ-rays, since the dead time of the TDC prevents a hit from being misregistered if the drift electrons induced by the pion reach the sense wire earlier than those induced by a δ-ray. We have modelled the δ-ray production in our drift cells to obtain the fraction of hits expected to contribute a large χ^2 as a function of the track position within the drift cell. This observed distribution in data agrees in absolute level and shape with the distribution expected from δ-ray production for our drift chamber gas and cell geometry.

For the pion momenta in this experiment, the δ-ray production probability is to very good approximation independent of momentum, and it is also independent of the x and y positions in the chamber. As a result, the production probability is identical in the vacuum and regenerator beams, and the event loss from the χ^2 cut cancels in the charge mode single ratio. This property is manifest in the vacuum and regenerator beam segment χ^2 distributions in Figure 40.

Another track quality cut is based on the fact that the projections of the measured upstream and downstream track segments to the effective bend plane of the analysis magnet are expected to meet. We therefore cut on the distance d_o between the two track segment projections at that plane. The resolution on d_o is

$$\sigma_{d_o}[\text{microns}] = 140 \oplus \frac{3020}{\text{p}_\pi[\text{GeV/c}]}, \tag{5.1}$$

where p_π is the momentum of the pion. The first term is due to the chamber resolution and the second to multiple scattering effects. The distribution of d_o is shown in Figure 41. We make a very loose cut, corresponding to 6.8 standard deviations on average, though there are non-gaussian tails from hard multiple scattering. The actual cut used, devised before the final alignment and time to distance calibration, was $d_o/s_o < 4$, where the old resolution function s_o is given by

$$s_o[\text{microns}] = 220 + \frac{2700}{\text{p}_\pi[\text{GeV/c}]}. \tag{5.2}$$

Once two quality tracks are in hand, we require that they are consistent with originating from a common vertex. We accomplish this by calculating the distance of closest approach d_c of the two tracks. The observed distribution for d_c is shown in Figure 42a for $\pi^+\pi^-$ decays

from both the regenerator and vacuum beams. The small mismatch visible between the two beams arises because the resolution on d_c scales almost linearly with the distance Δz from the decay location to the first chamber, and to eliminate the difference in this distribution introduced by the difference in the z distributions, we cut on the scaled quantity $d_c/\Delta z$ shown in Figure 42b. The small tail was due mostly to multiple scattering of the tracks. The applied cut was a function of the momentum of both tracks, $d_c/\Delta z < 4\sigma_{d_c}$, with

$$\sigma_{d_c} = 2.45 \times 10^{-5} + 8.5 \times 10^{-3} \left(\frac{1}{p_{\pi_1}^2} + \frac{1}{p_{\pi_2}^2} \right), \tag{5.3}$$

with the two track momenta, p_{π_1} and p_{π_2}, measured in GeV/c.

The spatial location of the decay vertex is initially defined as the midpoint of the shortest line segment joining the two tracks. We can improve the measurement of the vertex on average by using the fact that the higher momentum pion in a decay will suffer less from multiple scattering than the lower momentum pion. Using our initial vertex and two upstream track trajectories as starting values, the vertex and trajectories were refit with the

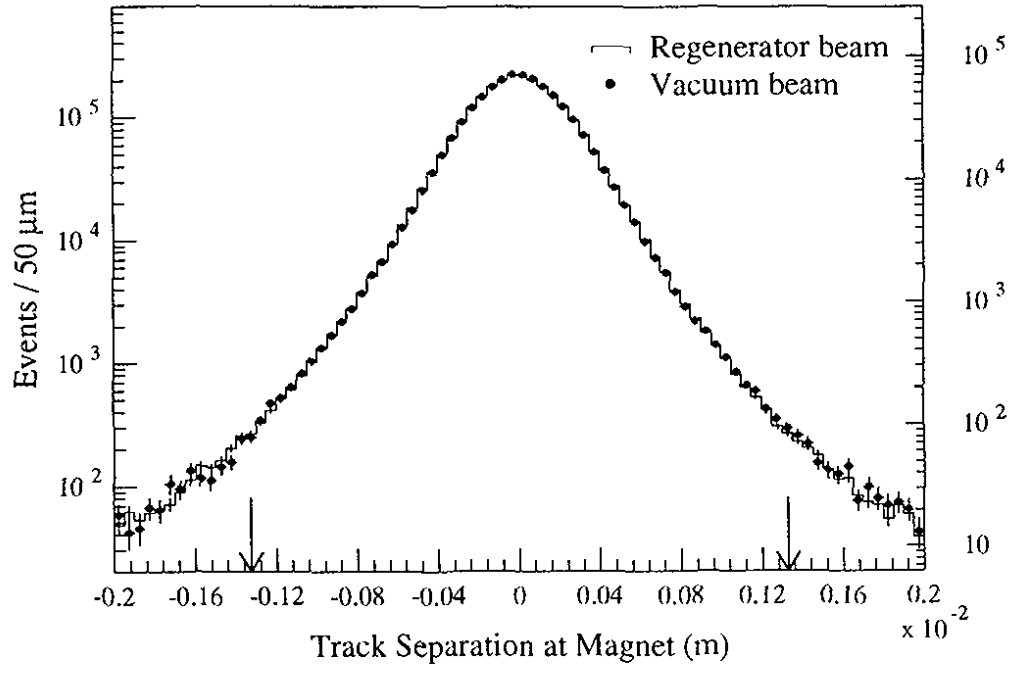

Figure 41. Separation d_o of upstream and downstream track segment projections at the magnet bend plane for the $\pi^+\pi^-$ samples after all other cuts. The histogram depicts the regenerator beam distribution (left scale), and the circles depict the vacuum beam distribution (right scale). The arrows show the average cut applied.

two pion trajectories weighted according to their multiple scattering probabilities and measurement smearing. This led to a 10% improvement in the transverse position resolution on the vertex, for an average resolution (in the x or y view) of 1.0 mm. The z resolution varied

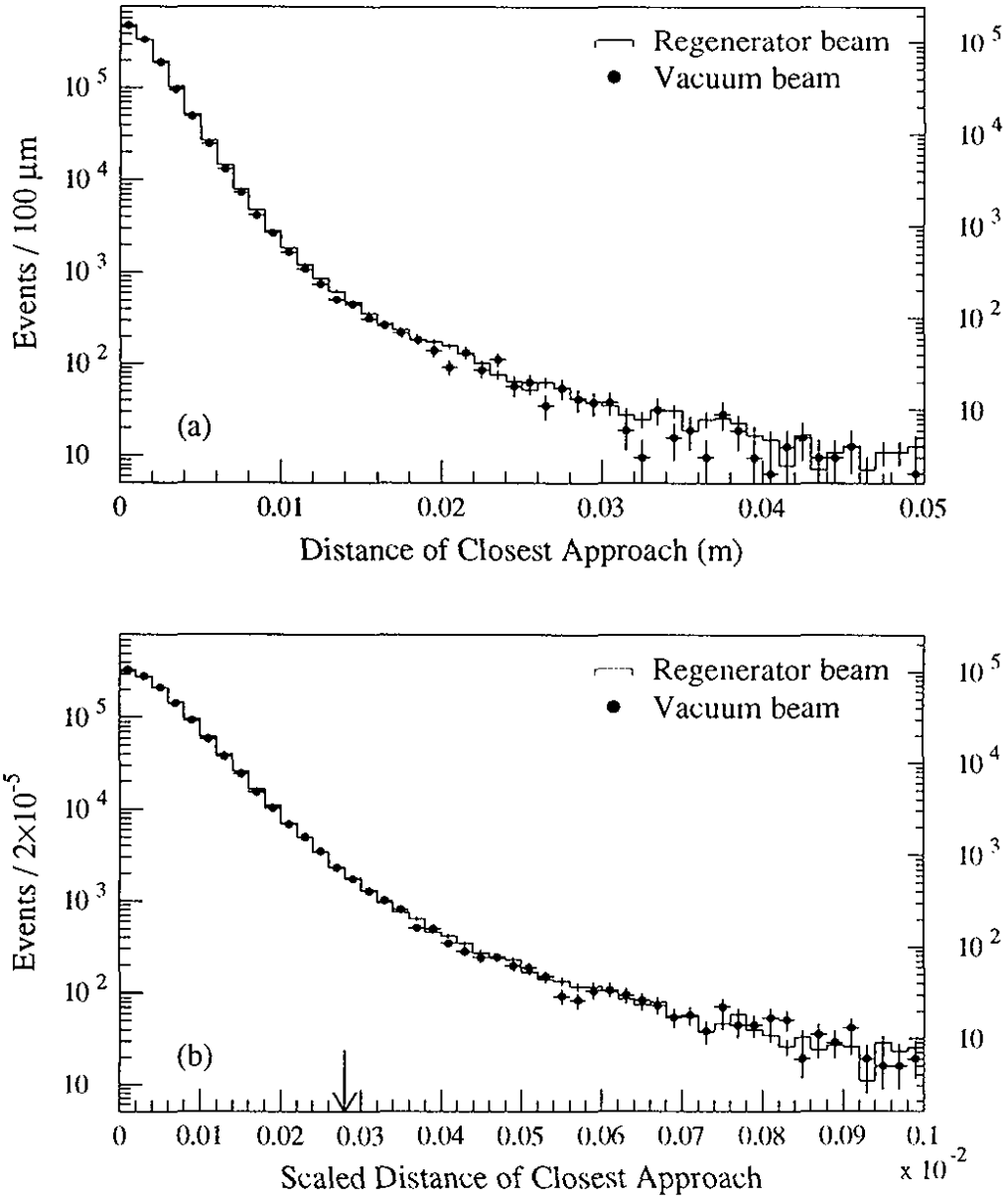

Figure 42. Distance of closest approach d_c for the two tracks measured in $\pi^+\pi^-$ decays after all other cuts. The histogram depicts the regenerator beam distribution (left scale), and the dots depict the vacuum beam distribution (right scale). (a) Raw d_c. (b) d_c scaled by the distance from the decay location to Chamber 1. The arrow marks the location of the average cut.

from 10 cm at the downstream end of the $\pi^+\pi^-$ decay volume to 25 cm at the upstream end (z=110 m).

The final cut that involved track reconstruction eliminated a configuration of the 2 tracks where the matching of the x track segments to y track segments, and of the track to the appropriate cluster in the calorimeter (see Section 3.2.3), could be ambiguous. This occurred when the separation of the two tracks in x was small. Because of the left–right symmetry requirement of the trigger, the two tracks could only be closely spaced in the x view when the pions were near the center of the array. The matching ambiguity was eliminated by requiring the x separation of the projection of the two tracks to the lead glass to be larger than 2 cm when at least one of the pions landed in one of the two central columns of blocks in the calorimeter.

This ambiguity was particularly important in the x view because the x segment carries the momentum information. Since the ratio E/p of the calorimeter cluster energy to the track momentum was needed to eliminate the Ke3 background (see next Section), it was imperative to have the proper matching between the x track segments and the lead glass clusters. A similar ambiguity did exist in the matching of the y segments to clusters when a pion landed within the central two rows of lead glass blocks. A mismatch in this view, however, has little effect on the reconstruction because neither the E/p calculation nor other kinematics calculations are strongly affected. Hence we eliminated only the events with an ambiguity in x.

5.1.2 Kinematics and Background Reduction

With two good quality tracks and their measured momenta $p_{\pi+}$ and $p_{\pi-}$, we next turn to the identification of $K \to \pi^+\pi^-$ decays and background reduction. Since the Kμ3 decays were largely removed at the trigger level, the most copious source of two track triggers were Ke3 decays. Triggers from Ke3 decays outnumbered those from $\pi^+\pi^-$ decays by two orders of magnitude! There were also significant contributions to the event sample from $K \to \pi^+\pi^-\pi^0$ and $\Lambda \to p\pi^-$ decays. These backgrounds were most serious in the vacuum beam, since they were greatly reduced in the regenerator beam because of the attenuation

in the regenerator and its shadow absorber. The most serious background in the regenerator beam was from kaon scattering in the regenerator.

The Ke3 decays could be efficiently rejected with little loss of $\pi^+\pi^-$ decays using the E/p variable mentioned above and in Section 4.2.2. The shape of the E/p distribution is shown in Figure 43a for pions from a sample of $\pi^+\pi^-\pi^0$ decays, and also for electrons from Ke3 decays. The E/p for pions from $\pi^+\pi^-$ decays after all other cuts are applied is shown in Figure 43b. The distributions shown are after the first analysis which loosely categorized the different decays and eliminated obvious backgrounds. The $\pi^+\pi^-\pi^0$ decays could be isolated from Ke3 decays using the kinematics of the observed tracks and photons, so no E/p cut was necessary to isolate this sample from Ke3 decays. This made the $\pi^+\pi^-\pi^0$ sample useful for studying the $\pi^+\pi^-$ loss due to the E/p cut.

The peak at low values of E/p corresponds to pions which do not shower in the calorimeter. The energy deposited by these pions varies relatively slowly as a function of momentum, and the difference between the vacuum and regenerator beams in this "minimum-ionizing" peak is due mainly to the difference in the momentum spectra of decays from the vacuum and regenerator beams. Since the minimum-ionizing peak is far from our E/p cut, this difference does not affect the fraction of events lost with the E/p cut. Furthermore, we compare the vacuum and regenerator beam distributions in small momentum bins, where the difference in the overall momentum spectrum shape is not important.

For the final $\pi^+\pi^-$ analysis, we require that both pions have $E/p < 0.80$. In the previous chapter, we saw that the electron E/p resolution was about 3%, so only the most pathological electrons will survive this cut of almost 7 standard deviations. On the other hand, from the E/p distribution in $\pi^+\pi^-\pi^0$ decays, we find that the probably for a pion to have $E/p > 0.8$ is 3.3%. Since there are two pions in the $\pi^+\pi^-$ decay, the total loss of $K \rightarrow \pi^+\pi^-$ decays is 6.5%, but the Ke3 background rejection is very close to 100%. One possible way for a bias to enter into the vacuum to regenerator beam ratio in a momentum bin would be to have the regenerator beam pions shower in blocks with a systematically different gain mismeasurement. From the Ke3 calibrations the gains of the majority of the blocks are determined at a level of 0.2% of themselves or better. Even in the outmost blocks with the fewest statistics, the gains are still known to better than 1% of themselves. For

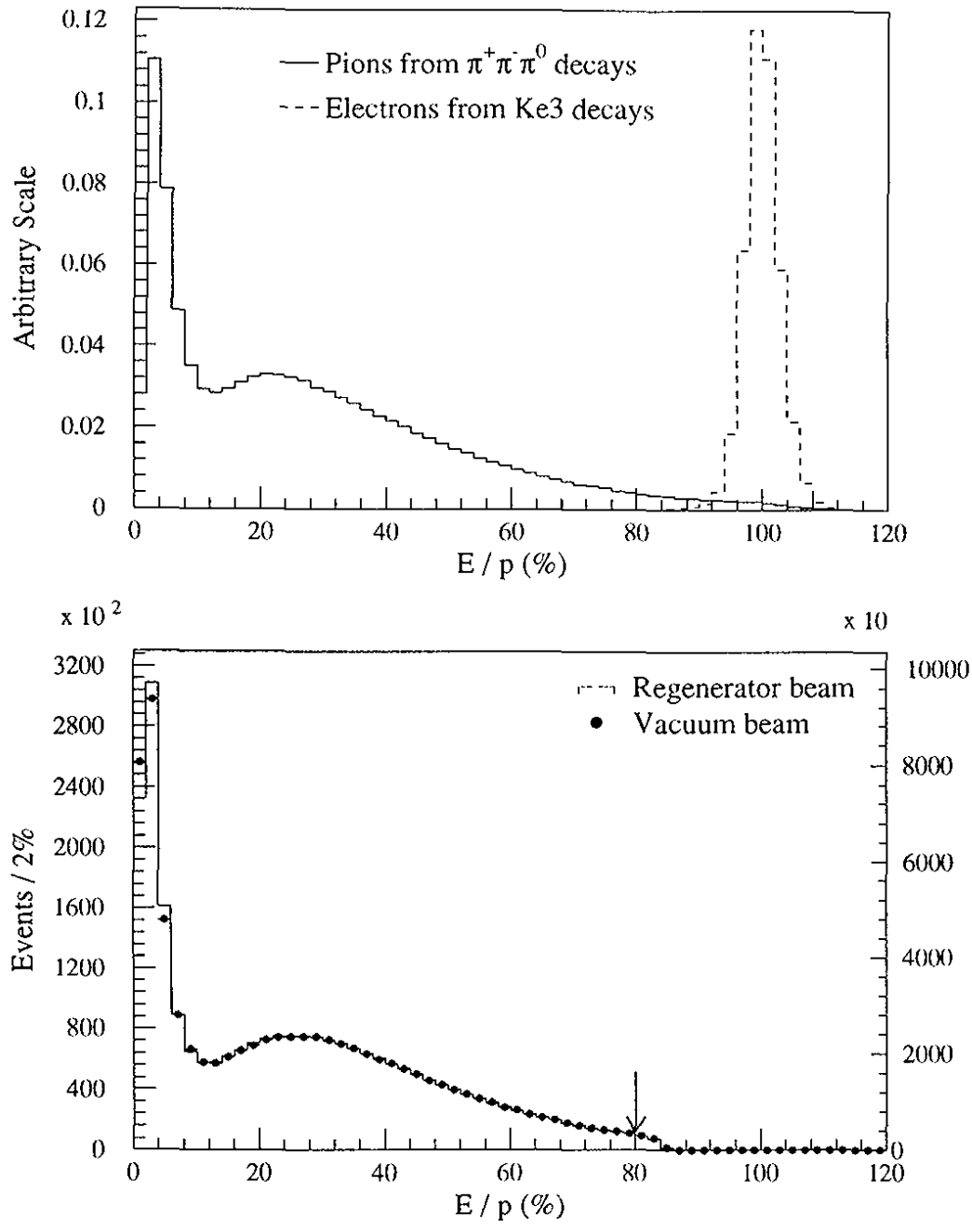

Figure 43. Shape of the E/p distribution for pions and electrons. (a) The solid histogram shows the spectrum for pions for a subset $\pi^+\pi^-\pi^0$ decays, and the dashed histogram shows the spectrum for electrons for a subset of Ke3 decays. The normalization of the two samples is arbitrary. (b) The E/p distribution for pions from $\pi^+\pi^-$ decays after all other cuts. The histogram shows the distribution for decays in the regenerator beam (left scale), and the dots show the distribution for decays in the vacuum beam (right scale). The cutoff at 0.85 is a result of the initial loose cut in the initial data reduction analysis pass. The final cut at 0.80 is indicated by the arrow.

arguments sake, let us suppose that the showering pions in decays from the regenerator beam consistently saw blocks that had fluctuated 0.3% high in the calibrations. From the level of E/p near our cut, this would result in under a 0.01% bias in the vacuum to regenerator beam ratio (or under 0.16×10^{-4} on $Re(\varepsilon'/\varepsilon)$).

To ensure that the background fraction from Ke3 decays was as small as possible, it was necessary to restrict the $\pi^+\pi^-$ sample to decays where the detected charged particles had landed within a region of the lead glass where the cluster energy could be reconstructed reliably. This led to two cuts on the track projections at the calorimeter. First of all, it is difficult to reconstruct the total energy in the electromagnetic showers of particles which strike the outer half of the outermost ring of blocks. A large fraction of the shower particles leak out of the outside edge of these blocks, and the fraction loss varies strongly with position. We therefore eliminated events if the tracks projected beyond the inner half of the outer blocks.

Electrons which struck the collar anti (CA) surrounding the inner half of the lead glass blocks around the beam holes would shower in the CA and deposit little energy in the lead glass. Since these electrons were not removed by the E/p cut, all tracks are required to project at least 1 mm outside of the CA. The resolution for projecting the x or y track segments to the calorimeter is of order 220 microns. Events with a track which projected into the beam hole, missing both the CA and the calorimeter, were also removed.

To keep the background fraction from the semileptonic Kμ3 decays at a minimum, it was necessary to restrict the $\pi^+\pi^-$ candidates to a regime where the muon veto was efficient. Since low energy muons could range out in the 3.2 m steel filter, we required that both of the particles tracked in the spectrometer have momenta greater than 7 GeV/c. This cut also reduced the fraction of events where a $\pi^+\pi^-$ decay was vetoed because of decay in flight with the resulting muon striking the $\mu 2$ veto bank. We also required that both tracks projected into the $\mu 2$ veto bank.

After the semileptonic backgrounds had been reduced, the largest remaining backgrounds had hadronic final states. These backgrounds are largely rejected by reconstructing the mass of the parent particle. Since we have no particle identification for separating hadronic species, we have to assume the masses of the daughter particles for the decay mode

under consideration. The relevant cases for this analysis are the two pion mass,

$$m_{\pi^+\pi^-} = \sqrt{\left(\sqrt{m_\pi^2 + |\vec{p}_1|^2} + \sqrt{m_\pi^2 + |\vec{p}_2|^2}\right)^2 - |\vec{p}_1 + \vec{p}_2|^2}, \tag{5.4}$$

and the $p\pi$ mass,

$$m_{p\pi} = \sqrt{\left(\sqrt{m_p^2 + |\vec{p}_p|^2} + \sqrt{m_\pi^2 + |\vec{p}_\pi|^2}\right)^2 - |\vec{p}_p + \vec{p}_\pi|^2}. \tag{5.5}$$

For the two pion mass, $\vec{p}_1$ and $\vec{p}_2$ are the momenta of the two pions measured upstream of the analysis magnet, and m_π^2 is the charged pion mass. To reconstruct the $p\pi$ mass, the track with the greater momentum ($\vec{p}_p$) is associated with the proton (or antiproton). This mass was used to reject Λ (or $\bar{\Lambda}$) decays.

At the trigger level, the $\Lambda \to p\pi$ decays formed a significant background to the $\pi^+\pi^-$ sample. As we mentioned earlier in the discussion about isolating the Ke3 sample (see Section 4.2.2), only the most energetic Λ's survive long enough to decay within the decay volume from which we accept $K \to \pi^+\pi^-$ decays ($z > 110$ m). Because the Λ's in this region were very energetic, the proton was very forward, and the track projection cut at the CA eliminated most of the Λ decays.

To remove the remaining Λ decays, we again use the property that the proton and pion at the energies under consideration must satisfy $p_p/p_\pi > 3$. When this momentum relationship for the two measured tracks is satisfied, we form the $p\pi$ mass given above. After all other cuts, 19 percent of the remaining $\pi^+\pi^-$ candidates satisfy this momentum relationship. For this subsample, $m_{p\pi}$ is plotted in Figure 44 both for decays with $E_\Lambda > 100$ GeV and for $E_\Lambda < 100$ GeV. There is clearly no Λ signal below 100 GeV, and in fact, our analysis indicates that the signal does not appear until the Λ energy is above 130 GeV. To be conservative, we eliminate any $\pi^+\pi^-$ candidate if it satisfies $E_\Lambda > 100$ GeV and has a mass $m_{p\pi}$ in the range from 1.10 GeV/c^2 to 1.13 GeV/c^2. The resolution of $m_{p\pi}$ measured in the Λ sample was 2.1 MeV/c^2. This mass cut was left quite broad to keep background from nongaussian tails at a negligible level.

When the momentum ratio is under 3, the $p\pi$ mass *always* reconstructs above the 1.166 GeV/c^2 cutoff in the mass plot of Figure 44.

The Λ decays do not enter as a noticeable background in the regenerator beam. A large fraction of the Λ decays in the vacuum beam come from the z region upstream of the

regenerator, but similar decays in the regenerator beam are vetoed. In addition, the neutral beam is highly attenuated by the regenerator and its shadow absorber, so the number of downstream decays is reduced by over an order of magnitude. Regardless of the small size in the regenerator, the Λ rejection cuts were made blind to the beam in which the decay occurred so that the vacuum and regenerator $\pi^+\pi^-$ samples were affected identically.

Our resolution on the $\pi^+\pi^-$ mass was 3.5 MeV/c^2, and we isolated the $\pi^+\pi^-$ sample using an analysis cut on this mass of 484 MeV/c^2 to 512 MeV/c^2. Because the $\pi^+\pi^-$ mass in $\pi^+\pi^-\pi^0$ decays is kinematically restrained to satisfy $m_{\pi\pi} < m_K - m_\pi$, the mass cut completely eliminated this potential background without any need to detect the two photons from the π^0 decay. In fact, no cuts are made in the $\pi^+\pi^-$ analysis on extra clusters in the calorimeter not associated with the tracks because the hadronic pion showers often produce spurious clusters.

The reconstructed $\pi^+\pi^-$ mass for decays from the regenerator and vacuum beam are

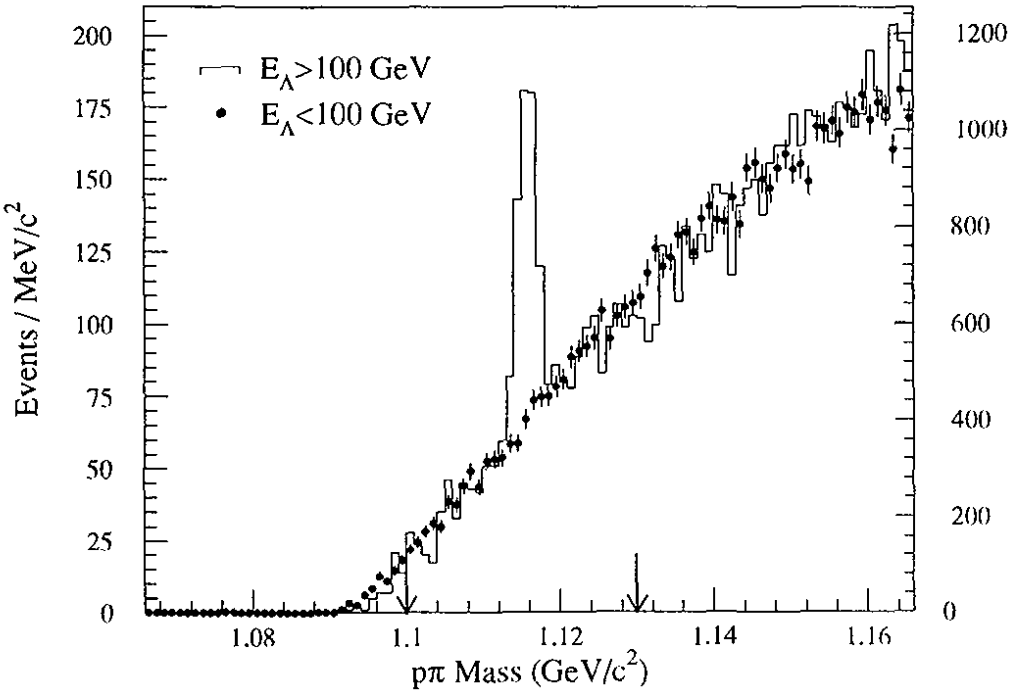

Figure 44. Reconstructed $p\pi$ mass for all $\pi^+\pi^-$ decay candidates in the vacuum beam which are consistent with $p_p/p_\pi > 3$. All $\pi^+\pi^-$ analysis cuts except the Λ rejection cuts have been applied. The Λ peak is visible for $E_\Lambda > 100$ GeV (solid histogram, left scale), but not for $E_\Lambda < 100$ GeV (solid circles, right scale). The arrows indicate the mass cut used on events with $E_\Lambda > 100$ GeV.

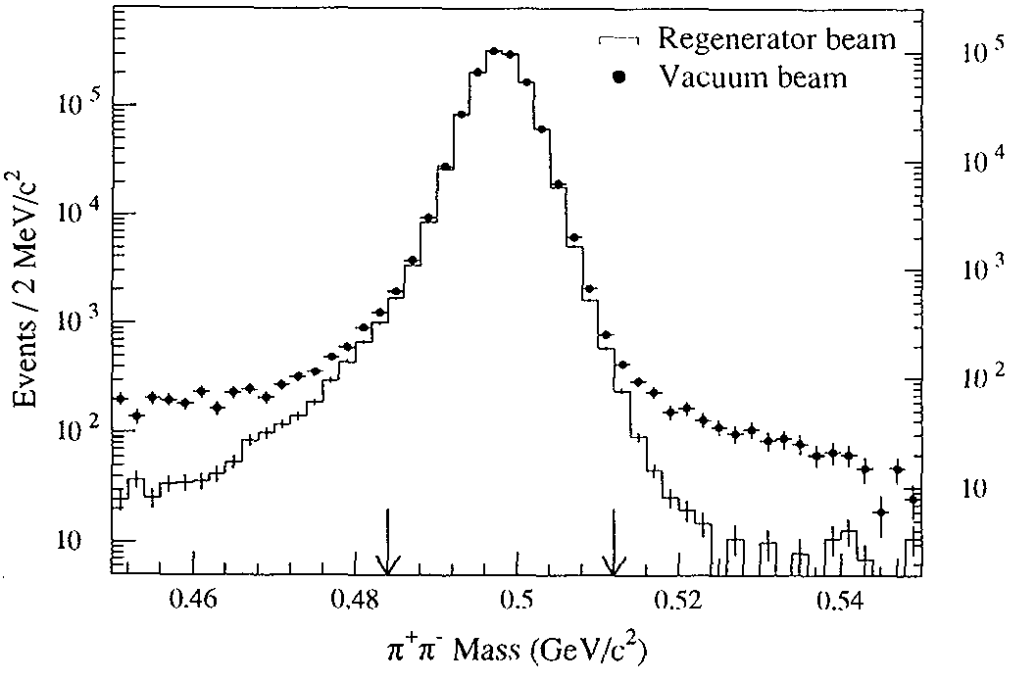

Figure 45. The reconstructed two pion mass for $\pi^+\pi^-$ candidates after all other cuts. The regenerator beam distribution is given by the histogram (left scale), and the vacuum beam distribution by the circles (right scale). The arrows indicate the position of the cuts used in the analysis. The radiative tail from $K \rightarrow \pi^+\pi^-\gamma$ decays is clearly visible in both beams.

shown in Figure 45. The broadening of the lower half of $\pi^+\pi^-$ mass distribution due to the radiative decay $K \rightarrow \pi\pi\gamma$ is clearly visible in the figure. This radiative tail is common to both the K_S and K_L decays[3]. The background visible in the wings of the vacuum beam distribution is from residual semileptonic decays. This background is just visible (at a much lower level) in the regenerator beam distribution at high mass, where it is not hidden by the radiative tail.

The mass distribution serves well to demonstrate the stability of the charged mode, both in terms of reconstruction and background levels. In Figure 46, the two pion mass distributions for the entire data set are overlaid on top of the distribution from the NC set used for our initial result presented in [50] and [74]. The line shape of the mass distribution in both the vacuum beam and regenerator beam is quite similar for the subset and for the

[3]The K_L radiative decay has a contribution from decays where the photon is emitted directly from the interaction vertex as well as from bremsstrahlung from one of the pions[85]. The photon from the direct emission process is quite stiff, and would shift the $\pi^+\pi^-$ mass outside of our signal region.

entire data set. This agreement exists in spite of the fact that the NC set was collected with a proton intensity three times that of the other subsets.

The final kinematic cut applied to this sample was a cut on the transverse momentum of the measured particles relative to the initial kaon trajectory. This cut helps to reduce both the residual semileptonic background in the vacuum beam and the diffractive and inelastic $\pi^+\pi^-$ backgrounds (see Appendix A) in the regenerator beam. For each $\pi^+\pi^-$ candidate, the square of the transverse momentum, p_t^2, was calculated by assuming that the kaon had scattered in the regenerator. The cartoon in Figure 47 helps to illustrate the calculation. The sum of the momenta measured for the two pion candidates gives the total kaon momentum $\vec{p}_K$ and hence the final kaon trajectory. We can project the kaon back along this trajectory from the decay vertex to the z location of the downstream face of the regenerator. To a very good approximation, the initial kaon trajectory will be along the line connecting this projection to the production target. The scattering angle θ between the initial and final kaon trajectories is then used to calculate the transverse square momentum:

$$p_t^2 = p_K^2 \sin^2\theta. \tag{5.6}$$

This p_t^2 calculation works very well, even when the kaon has scattered inside the regenerator, because the distance from the regenerator to the target is so large relative to the size of the regenerator. This ratio keeps the error introduced into the deduced initial kaon trajectory small. If z_r is the distance from the target to the downstream face of the regenerator, and the scatter occurred a distance Δz upstream of this face, then to first order in $\Delta z/z_r$ the relation between the true scattering angle θ_s and the measured angle θ_m is given by

$$\sin\theta_m = \sin\theta_s \left(1 - \frac{\Delta z}{z_r}\right). \tag{5.7}$$

To first order, this expression is independent of the initial small angle between the kaon trajectory and the z axis. Since the regenerator is under 90 cm long, and is located 123.5 m from the target, the error introduced is always under 3/4%.

The remaining background in the vacuum beam comes from a residual of semileptonic kaon decays. Because we do not detect the neutrino in these decays, the momentum sum of the two measured tracks was not in general along the initial kaon direction. Thus a p_t^2 cut

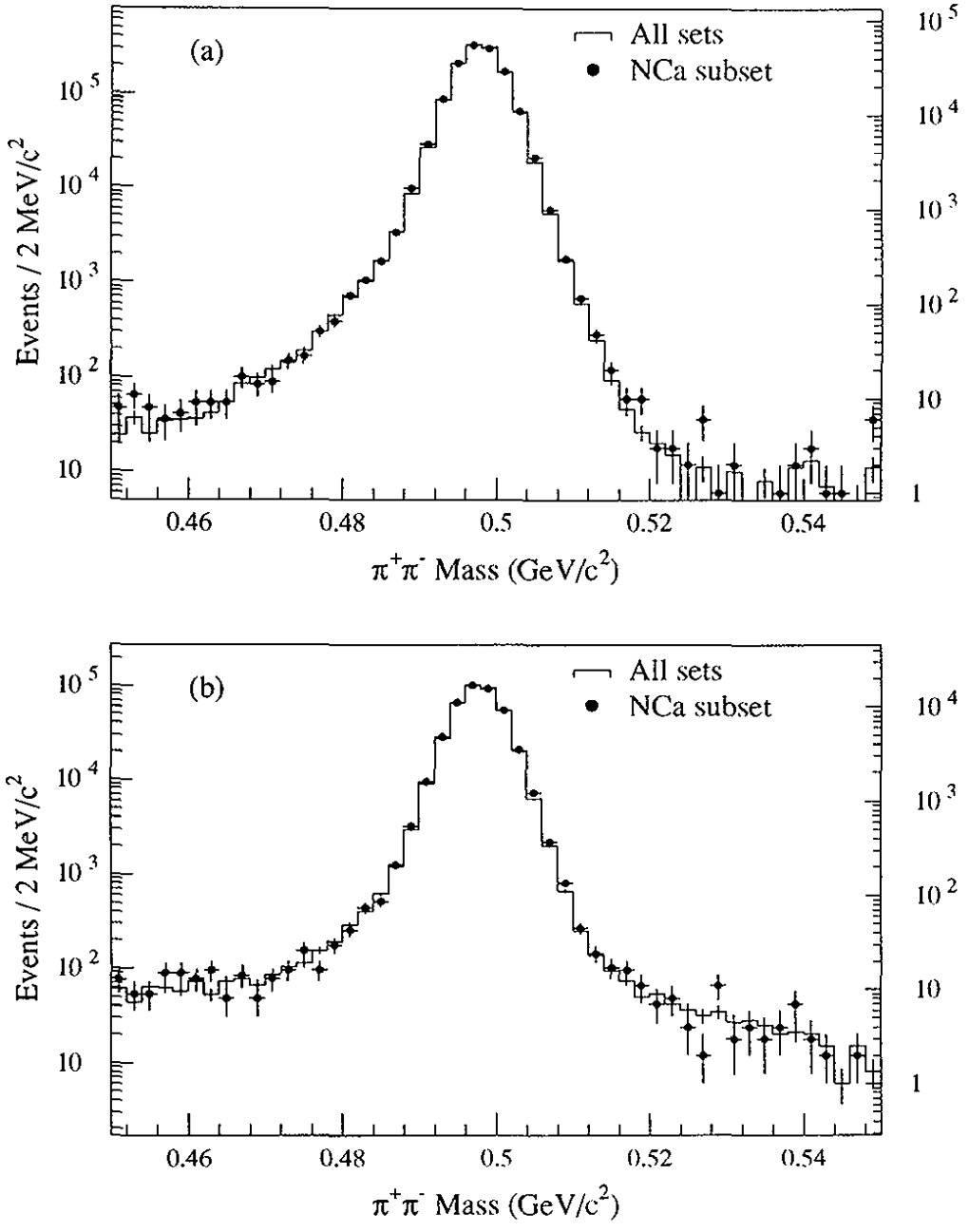

Figure 46. The reconstructed two pion mass for $\pi^+\pi^-$ candidates after all other cuts for the entire $\pi^+\pi^-$ data set and for the NC subset only. The histogram shows the distribution for the entire data set (left scale), and the dots show the distribution for the NCa subset (right scale). (a) Regenerator beam. (b) Vacuum beam.

was helpful in reducing the remaining semileptonic background. While the most natural calculation of p_t^2 in this case would involve comparing the total measured momentum to the kaon's trajectory, in this case the line connecting the target and the decay vertex, we wish to keep the analysis of the vacuum and regenerator beams identical. We therefore used the same calculation of p_t^2 for the vacuum and regenerator beams. This avoids introducing biases in the fraction of decays of coherent kaons lost because of the smearing of the measured p_t^2.

The p_t^2 distributions for the two beams are plotted in Figure 48. The bulge in the distributions just outside of our p_t^2 cut of 250 $(\mathrm{MeV}/c)^2$ is again due to the radiative decay $K \to \pi\pi\gamma$. The semileptonic decays give the steeply falling p_t^2 tail in the vacuum beam. The very small, flatter component visible at larger p_t^2 in the vacuum distribution is consistent with interactions of the beam with residual particles in the vacuum. In the regenerator beam, the decays with large p_t^2 are from kaons which regenerated inelasticly. Near the coherent peak, the contribution from diffractively regenerated kaons, with a steeper p_t^2 spectrum than the inelasticly regenerated kaons, results in the upturn in the spectrum.

5.1.3 Other Cuts and Summary

The final class of cuts applied in the $\pi^+\pi^-$ analysis were designed primarily to reduce potential biases from the acceptance correction. One important cut involved reverifying the trigger requirement for the event. Accidental activity in the detector could sometimes cause

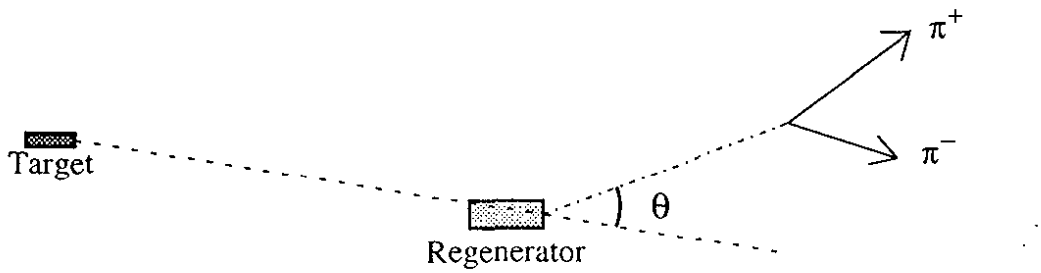

Figure 47. Schematic representation of the method used to calculate the kaon scattering angle in the regenerator. The momenta of the two pions measured in the drift chambers (solid lines) are combined to measure the kaon trajectory. The kaon is then projected from the decay vertex to the downstream face of the regenerator (dot-dash line). The original kaon trajectory is defined by the line connecting the projected kaon position at the regenerator to the target. The scattering angle θ is the angle between the two trajectories.

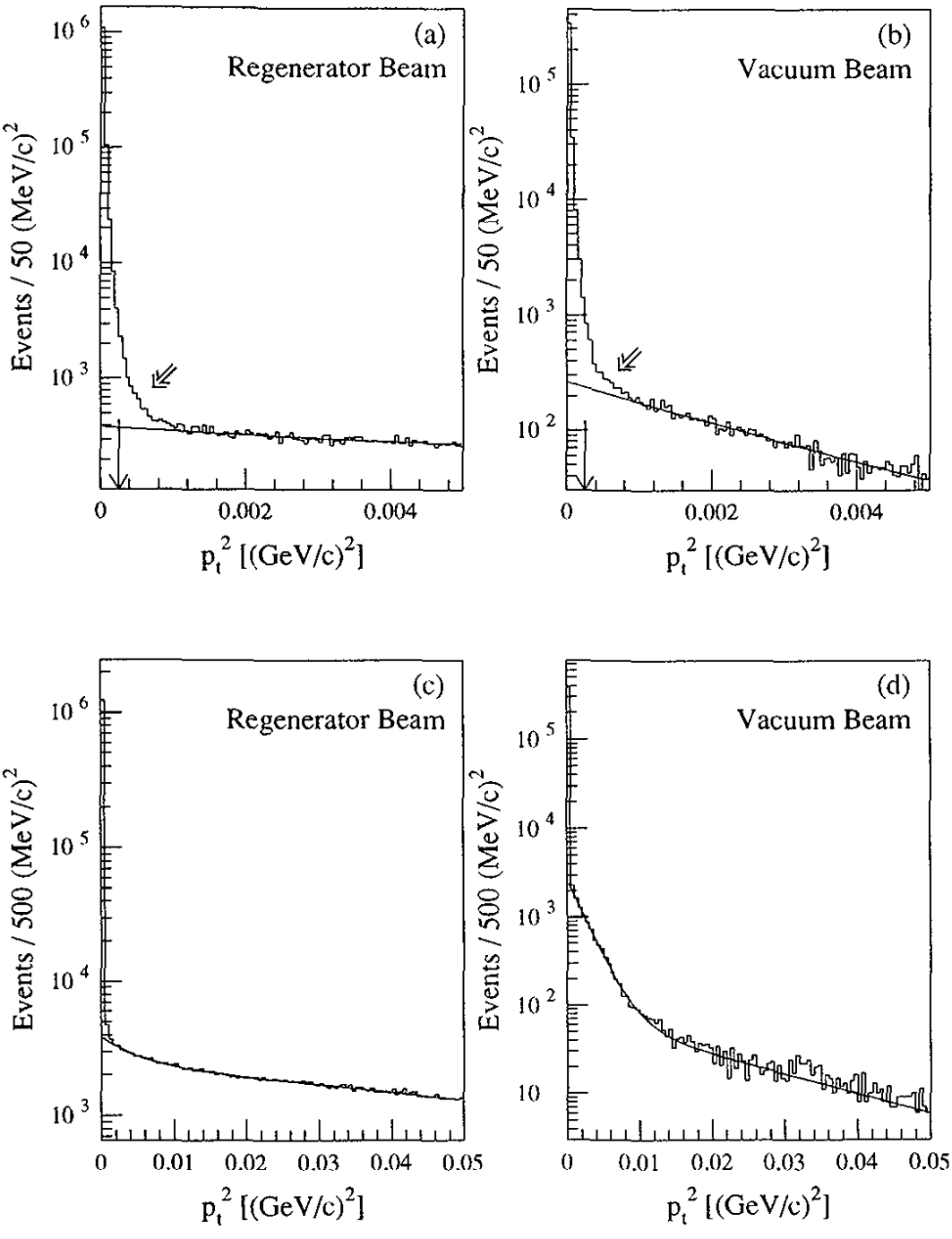

Figure 48. p_t^2 distribution for $\pi^+\pi^-$ candidates after all other cuts are applied for two different ranges of p_t^2. Parts (a) and (b) show the distribution out to 5000 $(\mathrm{MeV}/c)^2$ for the regenerator and vacuum beams, respectively. At this scale, the structure of the coherent peak, the location of the analysis cut (vertical arrow) and the radiative tail from $\pi^+\pi^-\gamma$ decays are all visible. Parts (c) and (d) show the distribution out to 50,000 $(\mathrm{MeV}/c)^2$ for the regenerator and vacuum beams, respectively, where the contributions from different background sources (see text) are more apparent. In all four parts, solid line is the best fit to the overall background shape.

an event to satisfy the trigger even though the decay products themselves would not. For example, both particles in an event could have passed through the top half of the B and C hodoscopes, clearly not satisfying the symmetric up–down, right–left trigger requirement. If however, a counter in the lower half of the hodoscopes registered a hit because of noise in the electronics or because a muon from the target pile happened to pass simultaneously through the bank, the event would be accepted.

Since the accidental activity is common in the vacuum and regenerator beams, we expected the gain of events from this process to be identical in these two beams. However, to make comparisons between the data and our Monte Carlo samples more meaningful, we reverified the triggers using the reconstructed tracks. We required the decay vertex to be upstream of the HDRA, the hits on the track in the second drift chamber to satisfy the east–west trigger requirement in that chamber, and the B and C hodoscope counters through which the tracks project to satisfy the trigger logic for those counter banks.

In addition to the trigger reverification, we also cut out decays where the tracks projected to within one to four millimeters of the limiting apertures. This reduced the sensitivity of the charged sample to the exact location of these apertures. Also, for decays which occurred in the vacuum beam upstream of the active mask, the decay products were not allowed to "cross beams", that is, both tracks had to pass through the mask aperture for the beam in which it decayed. While particles from decays in the regenerator beam that passed through that beams mask aperture always struck the regenerator and were lost, the larger angle products which cross from the vacuum beam could sometimes sneak past the regenerator. This cut eliminated the need to understand this effect in detail.

For coherent Monte Carlo decays which reconstruct in our final sample, the fractional event loss due to each cut is shown in Table 6. The momentum range in the table relevant to the $Re(\varepsilon'/\varepsilon)$ measurement is the 40 GeV/c to 160 GeV/c range. The momentum range from 20 GeV/c to 160 GeV/c is used for the remaining measurements. The distribution of kaon energy after all other cuts have been made is shown in Figure 49 for both the regenerator and vacuum beams. The similarity in the spectra for the two beams is apparent. The distribution of the distance of the $K \rightarrow \pi^+\pi^-$ decays ("z distribution") from the production target after all other cuts is shown in Figure 50. The location of the downstream end of the

regenerator is vividly apparent at the sharp turn on in decays at 123.5 m in the regenerator beam. The fall-off in the rate of accepted decays upstream of 120 m in the vacuum beam is governed by the upstream active mask, which clearly defines the acceptance in the upstream region.

5.2 Background Subtraction

After applying the background reduction cuts discussed above, the residual backgrounds were very small in the $\pi^+\pi^-$ decay mode, typically on the order of 0.1% to 0.3%. They could not, however, be neglected in the measurement of $Re(\varepsilon'/\varepsilon)$. For both the vacuum and regenerator beam samples, the background size is estimated by fitting the shape of the p_t^2 spectrum in the range 1500 $(\mathrm{MeV}/c)^2$ to 20000 $(\mathrm{MeV}/c)^2$, and extrapolating this fit underneath the coherent peak (0 to 250 $(\mathrm{MeV}/c)^2$).

The exponential behavior of the small beam interaction background in the vacuum beam p_t^2 spectrum is clear in Figure 48d, where all the momentum bins have been combined. However, the low statistics of this background made a two exponential fit to the background in individual momentum bins difficult. In this beam, therefore, the p_t^2 spectrum for decays within each 10 GeV/c momentum bin was fit using the form

$$\frac{dN_v(p_t^2)}{dp_t^2} = \alpha e^{-\beta p_t^2} + c, \tag{5.8}$$

where α, β and c are parameters of the fit. The exponential slopes (β) obtained in the fits are compatible with the hypothesis that the background in this beam is dominated by Ke3 decays. The constant term c accommodated the average beam interaction background.

The background level found when the fits are extrapolated under the coherent peak in each p bin, and the number of coherent $K \to \pi^+\pi^-$ decays remaining after background subtraction, are listed in Table 7. The overall background level was $0.341\% \pm 0.010\%$, where the latter error is statistical only.

Combining all of the momentum bins, we can fit the vacuum beam p_t^2 spectrum to the sum of two independent exponentials out to a p_t^2 of 50000 $(\mathrm{MeV}/c)^2$. This result of this fit is plotted as the curve in both Figure 48b and d. The individual semileptonic slopes measured

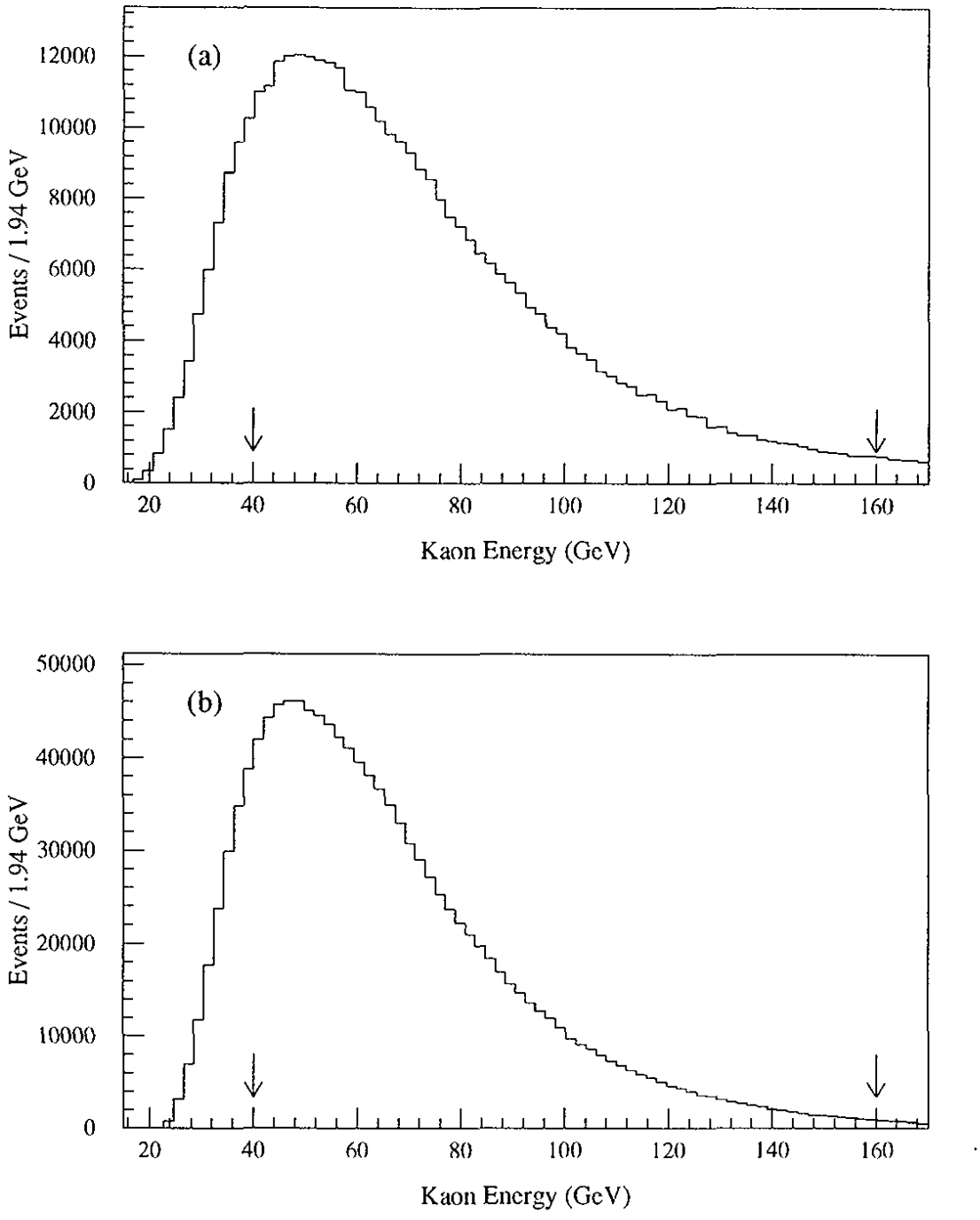

Figure 49. Distribution of the Kaon energy for the final $\pi^+\pi^-$ sample. The arrows mark the location of the cuts used in the $Re(\varepsilon'/\varepsilon)$ analysis. (a) Vacuum beam. (b) Regenerator beam.

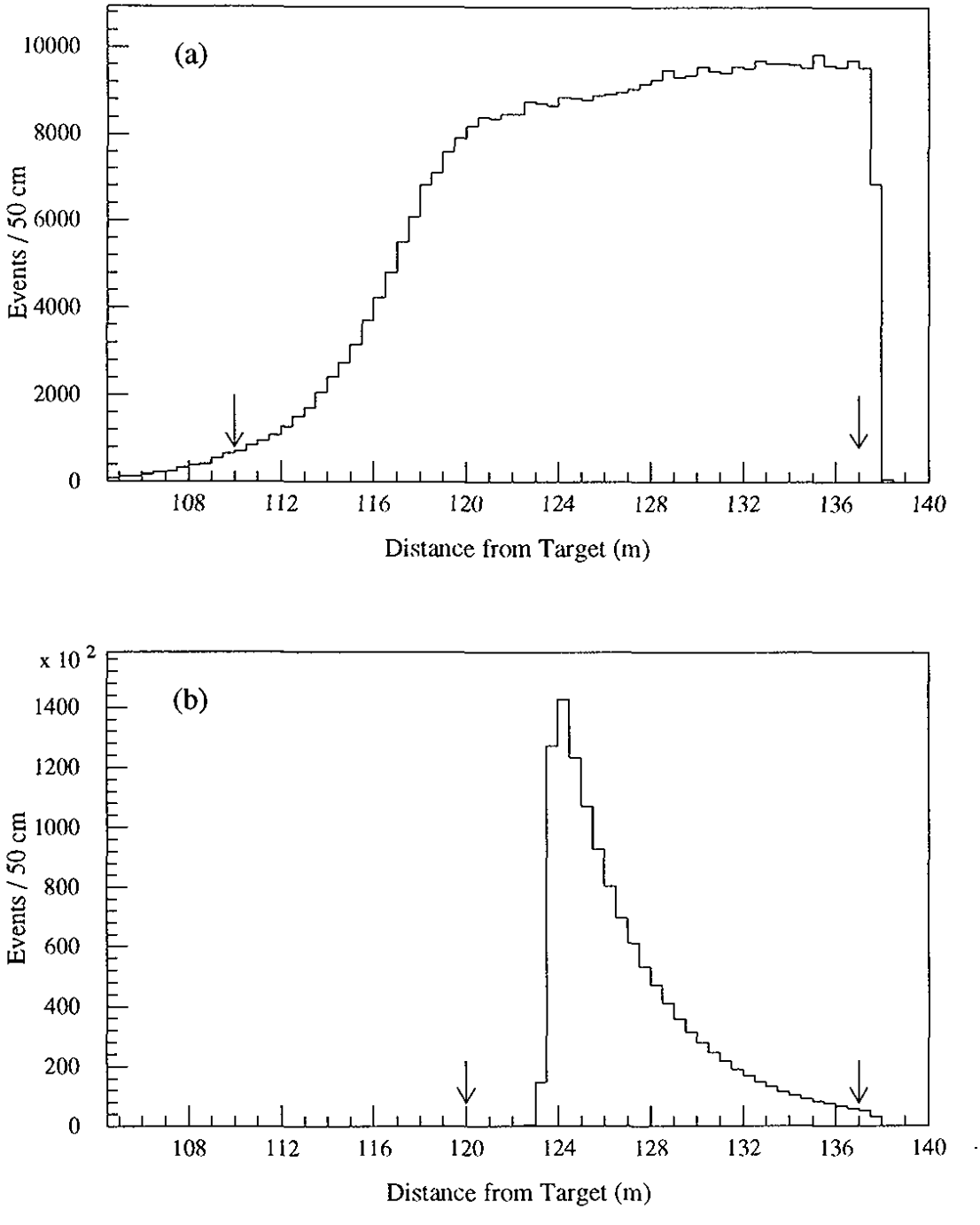

Figure 50. Distribution of the distance of the decays from the production target for the final $\pi^+\pi^-$ sample. The arrows mark the location of the cuts used in the $Re(\varepsilon'/\varepsilon)$ analysis. (a) Vacuum beam. (b) Regenerator beam.

Table 6. The fraction of coherent $\pi^+\pi^-$ decays lost as each analysis cut is applied sequentially, and when a cut is applied as the final cut. For the first sequential cut, the loss is relative to the number of $\pi^+\pi^-$ events which reconstruct within the fiducial energy and z region used in the fits. Each cut thereafter is normalized to the number of kaons left after the preceding cut. Here "K_L" and "K_S" have been used as shorthand for the vacuum and regenerator beams, respectively. The two momentum ranges are given in GeV/c.

Analysis cut	Sequential loss (%)				Loss as Final Cut (%)			
	40–160		20–160		40–160		20–160	
	K_L	K_S	K_L	K_S	K_L	K_S	K_L	K_S
Pions within calorimeter	3.77	4.68	7.12	7.93	1.09	1.35	2.14	2.49
Vacuum Window Aperture	0.04	0.05	0.15	0.22	0.02	0.03	0.11	0.16
Analysis Magnet Aperture	0.55	0.74	1.16	1.62	0.30	0.40	0.73	1.16
HDRA Aperture	0.03	0.01	0.05	0.02	0.02	0.00	0.04	0.01
Tracks Remain in Helium Volume	0.02	0.09	0.30	0.44	0.02	0.07	0.29	0.47
Λ cuts	2.71	1.98	2.38	1.75	0.56	0.34	0.48	0.30
$p_\pi > 7$ GeV/c	3.16	3.38	4.10	3.87	0.79	0.91	1.41	1.13
Track χ^2 [a]	0.04	0.05	0.04	0.05	0.02	0.02	0.02	0.02
Distance of Closest Approach	0.95	0.94	0.90	0.91	0.86	0.89	0.79	0.83
Track Separation at Magnet	0.04	0.05	0.06	0.06	0.03	0.04	0.05	0.04
$\pi \to \mu\nu$ decay veto	1.86	2.09	2.29	2.41	2.23	2.47	2.69	2.80
Mask Aperture	1.00	0.01	0.92	0.01	1.06	0.00	0.95	0.00
No pions in CA or beam hole	21.99	21.05	19.68	18.84	19.38	18.54	17.23	16.50
Chamber 2 Trigger Reverify	0.01	0.00	0.01	0.00	0.01	0.00	0.01	0.00
BC Hodoscope Trigger Reverify	1.89	1.95	1.92	1.92	1.74	1.80	1.77	1.77
$\pi^+\pi^-$ Mass	1.36	1.39	1.47	1.54	0.39	0.40	0.40	0.42
p_t^2	0.55	0.48	0.49	0.43	0.55	0.48	0.49	0.43

[a] Without $\delta - rays$. See text for loss estimates from $\pi^+\pi^-\pi^0$ studies.

within each momentum bin were consistent with the overall slope of 424 ± 15 (GeV/c)$^{-2}$. The slope obtained for the beam interaction background component for this fit was 51 ± 10 (GeV/c)$^{-2}$.

Table 7. The number of coherent $\pi^+\pi^-$ decays after background subtraction, and the total background fraction subtracted in each 10 GeV/c bin. The background levels are given in percent, and the errors on the background levels are the statistical errors only.

Momentum Range	Vacuum Beam		Regenerator Beam	
(GeV/c)	Data	Background (%)	Data	Background (%)
20-30	11712	0.31 ± 0.05	19059	0.158 ± 0.029
30-40	42092	0.34 ± 0.03	144363	0.165 ± 0.011
40-50	59701	0.37 ± 0.02	230593	0.160 ± 0.008
50-60	59983	0.40 ± 0.03	222405	0.157 ± 0.008
60-70	52227	0.37 ± 0.03	185010	0.153 ± 0.009
70-80	42380	0.34 ± 0.03	136064	0.150 ± 0.010
80-90	32525	0.32 ± 0.03	97159	0.145 ± 0.012
90-100	24702	0.28 ± 0.03	66862	0.144 ± 0.015
100-110	17689	0.27 ± 0.04	44144	0.143 ± 0.018
110-120	13241	0.26 ± 0.04	30246	0.143 ± 0.022
120-130	9704	0.26 ± 0.05	20461	0.142 ± 0.026
130-140	7056	0.25 ± 0.06	13414	0.142 ± 0.033
140-150	5486	0.25 ± 0.07	8656	0.141 ± 0.040
150-160	4286	0.24 ± 0.08	5654	0.141 ± 0.050
20-160	382783	0.340 ± 0.009	1224088	0.154 ± 0.004
40-160	328980	0.341 ± 0.010	1060667	0.152 ± 0.004

The systematic error in the background level is dominated by the uncertainty in the slope of the semileptonic background. The systematic contribution has been evaluated in part by varying the slope within the limits allowed by the fits to the p_t^2 spectra in the 1500 (MeV/c)^2 to 20000 (MeV/c)^2 range, and also be varying the range over which the fits were performed. In addition, the background fits were modified to fit for an exponential beam interaction component with fixed slopes of up to 60 (GeV/c)$^{-2}$. This modification introduced only small differences into the total number of events subtracted. The total systematic uncertainty in this background came to 0.010%, giving a total error in the $\pi^+\pi^-$

vacuum beam background fraction of 0.014%. In Monte Carlo studies of the behavior of the p_t^2 spectrum of the semileptonic background, we found the shape to begin to roll away from a perfect exponential for $p_t^2 < 2500$ (MeV/c)^2. While this rolloff would mean we are overpredicting the background level, the mismeasurement is at most 0.003% overall, well within the systematic uncertainty.

The form for the fits to the p_t^2 spectra in the regenerator beam is somewhat more complicated. After correcting for acceptance, we have found that the p_t^2 distribution in the charged mode is well described by the form

$$\frac{dN}{dp_t^2} \propto e^{-5.156p_t^2} + 0.546e^{-222.78p_t^2}, \tag{5.9}$$

where p_t^2 is measured in (GeV/c)^2. The latter, steeper, term corresponds to the diffractive regeneration background. The shallower term corresponds to the inelastic contribution, and is consistent with the inelastic slope measured in previous experiments [86]. The functional form we use to fit the momentum bin p_t^2 spectra fixes the inelastic and diffractive slopes to the values given in Equation 5.9, but allows the relative size of the two contributions to vary. The acceptance is expected to introduce an additional exponential falloff between the true and measured p_t^2 spectra, so the final functional form used in the fits was

$$\frac{dN_r(p_t^2)}{dp_t^2} = \alpha e^{-ap_t^2}\left(e^{-5.156p_t^2} + re^{-222.78p_t^2}\right), \tag{5.10}$$

where α, a and r are all parameters of the fits. The same p_t^2 range of 1500 (MeV/c)^2 to 20000 (MeV/c)^2 used in the vacuum beam fits was used here. The values for the diffractive to inelastic ratio r obtained in the 10 GeV/c momentum bin fits were statistically consistent with the value of 0.546 in the acceptance corrected spectrum in Equation 5.9.

The background levels obtained by extrapolating each momentum bin fit into the coherent region are listed in Table 7 along with the number of regenerator beam events remaining after background subtraction. The total background in the regenerator beam came to $0.152\% \pm 0.004\%$ for the momentum range used in the $Re(\varepsilon'/\varepsilon)$ analysis. The error here is statistical only.

The systematic error in the regenerator beam background level was conservatively estimated at 0.012%. If the various exponential slopes — the acceptance, diffractive and inelastic — are allowed to vary within the limits proscribed by the fits to the p_t^2 spectra in

the range $p_t^2 > 1500$ (MeV/c)^2, the change in the background level is much smaller than this systematic estimate. Fits where the diffractive to inelastic ratio r were fixed at 0.546 also resulted in a change much smaller than this systematic. Finally, the spectrum in each 10 GeV/c momentum bin was fit to the sum of two independent exponentials. In some of the momentum bins, the statistics at high p_t^2 were poor and as a result it was difficult to fit for the two exponential slopes as reliably as we wished. In spite of this, the backgrounds predicted using these fits differed very little in most of the momentum bins from those listed in Table 7. In the end, we inflated the systematic uncertainty to a level comparable to that in the vacuum beam. Combining the statistical and systematic uncertainties, we have a background level of $0.152 \pm 0.013\%$.

In principle, there are contributions to the regenerator beam background from semileptonic decays as well. The contribution from this source is extremely small, however, as an estimate of the rate based on the observed vacuum beam background fraction shows. Relative to the vacuum beam, the ratio of semileptonic decays to $\pi\pi$ decays is reduced in the regenerator beam by a factor of the order of $|\rho/\eta|^2$, with ρ the regeneration amplitude. For our momenta, this quantity is at least 100. We would therefore expect the semileptonic background fraction to be less than or of the order of 3×10^{-5}. In terms of a bias to $Re(\varepsilon'/\varepsilon)$ this corresponds to only 0.05×10^{-4}. The systematic uncertainty assigned to this background level more than adequately covers this bias in addition to the uncertainty in the noncoherent background level. We can also estimate the semileptonic background level from the number of events in the high side tail of the K_S mass distribution, where the $\pi^+\pi^-\gamma$ tail does not contribute. Extrapolating the tail above 0.53 GeV/c^2 of the mass plot in Figure 45 to the signal region, it appears that the background is of order $2 - 3 \times 10^{-5}$. This level agrees with our estimate based on the vacuum beam level.

After subtracting the backgrounds as a function of p_t^2 in both the vacuum and regenerator beams, we have overlaid the spectra from the two beams, and this overlay is shown in Figure 51. In spite of the very different background sources and p_t^2 spectra for those sources, the p_t^2 spectra in the two beams are very similar — down to the shape of the radiative tail from $\pi^+\pi^-\gamma$ decays. The agreement between the two spectra over four orders of magnitude helps to give us confidence in the background systematic uncertainties assigned above.

Implicit in the above discussion of the background subtraction is the assumption that the background fraction is constant as a function of z in each momentum bin. This should be a very good assumption in the regenerator beam, since both the background and the coherent signal are dominated by K_S decays over the length of this decay region. In the vacuum beam, there are differences in, for example, the variation of the $\pi^+\pi^-$ and Ke3 acceptance as a function of p and z, which could lead to small variations in the background as a function of z. Fortunately, for all of the measurements we make, our fitting technique requires only that we know the average number of events in the vacuum beam in each momentum bin. We will still, however, examine the z shape in this beam.

Because of the low background levels, it is difficult to examine this approximation in individual 10 GeV/c momentum bins. We can, at least, combine the momentum bins and then look in smaller z bins, and the resulting z dependence of the backgrounds is shown in Figure 52. For the regenerator beam, all of the momentum bins have been integrated

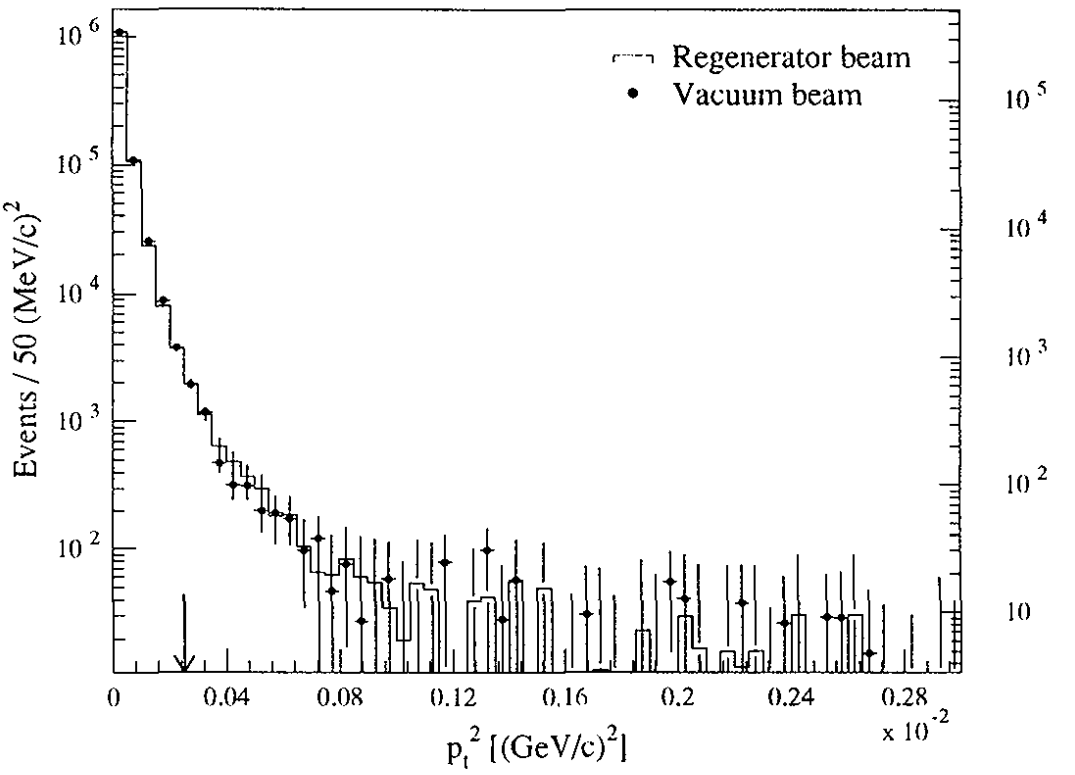

Figure 51. Overlay of the vacuum beam and regenerator beam p_t^2 spectra after background subtraction. The arrow indicates the position of the cut used in this analysis.

together, and we see no noticeable change in the background level across the fiducial z region.

For the vacuum beam, we cannot simply lump all of the momenta together to examine the background z dependence. At low momentum, the backgrounds are somewhat higher than at high momentum. On the other hand, very few low momentum $\pi^+\pi^-$ decays are accepted upstream of the active mask. Integrating all of the momentum bins together would thus introduce an artificial step in the background fraction z dependence at the mask. To sidestep this issue, we have examined the background fraction versus z in 40 GeV/c momentum bins, but have doubled the z bin size relative the regenerator beam study. The background fractions obtained in each 40 GeV/c bin are also plotted in Figure 52. Above 80 GeV/c, the shape is flat within our level of sensitivity. In the 40 GeV/c to 80 GeV/c range, the background does seem to climb as a function of z. If we substitute the background

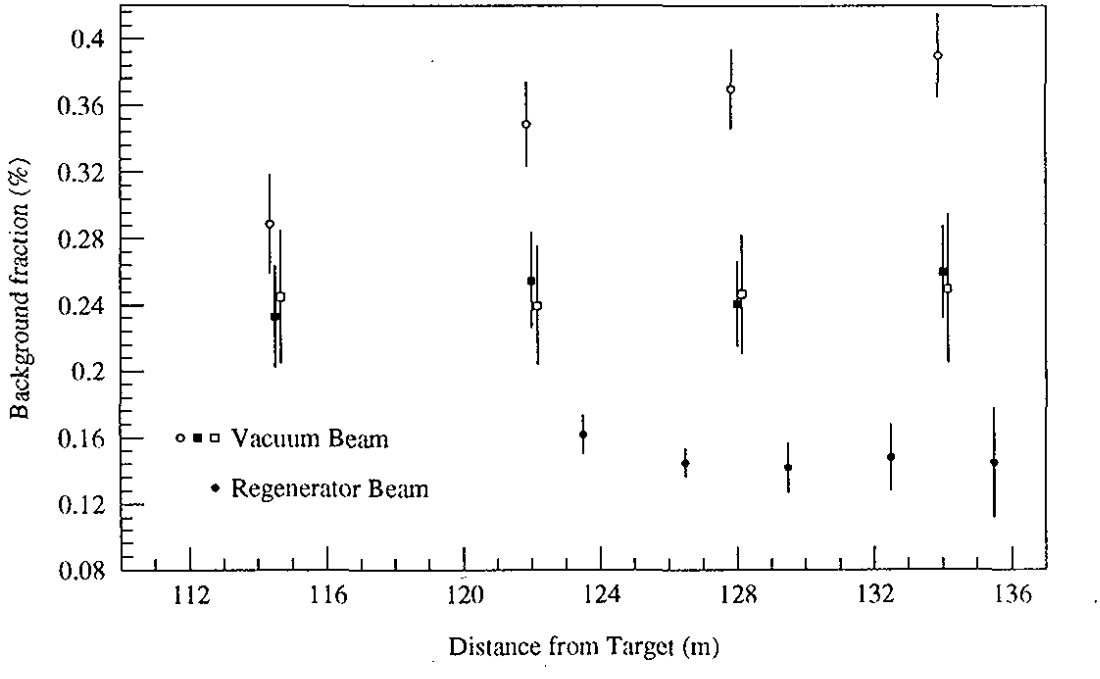

Figure 52. The measured $\pi^+\pi^-$ background fractions as a function of z. The solid dots are the regenerator beam background levels. The hollow points are the vacuum beam levels, where the circles have been measured in the momentum range 40 – 80 GeV/c, the squares in the range 80 – 120 GeV/c, and the triangles in the range 120 – 160 GeV/c. Not all of the vacuum beam points could be measured because of insufficient statistics.

levels obtained as a function of z for this momentum range, the change in the background level is much less that the systematic uncertainty assigned to the background subtraction.

5.3 Conclusion

For the $Re(\varepsilon'/\varepsilon)$ measurement, we have collected a sample of $328980 \pm 574 \pm 46$ $\pi^+\pi^-$ decays from our vacuum beam (after background subtraction), and $1060667 \pm 1030 \pm 138$ decays in the regenerator beam. The first errors are the statistical errors on the signal level, and the second errors are the uncertainties from the background contribution. The backgrounds in both beams were small, and relatively simple to understand at the level of precision we require. The overall background level in the vacuum beam was 0.34%, and we estimate an uncertainty in this value of 4% of itself. The regenerator beam background was smaller at 0.152%, and we estimate its uncertainty to be 8.5% of itself.

This completes the discussion of the analysis and background subtraction for the $\pi^+\pi^-$ decay samples. The simulation of these decays used to determine the acceptance will be deferred. We will present the analysis of the $2\pi^0$ decays, and then turn to a general discussion of the Monte Carlo simulation.

CHAPTER 6

$2\pi^0$ ANALYSIS

The technique to reconstruct the $2\pi^0$ decays from the four photons is described in [74]. The biggest change from that reference is in the background subtraction is that we now accept events from a larger z region, which has several new sources of background, and requires a mor e sophisticated background subtraction technique.

This chapter will review the reconstruction procedure and then describe the background subtraction in some detail.

6.1 Neutral Mass and Z Reconstruction

We began the reconstruction process with the energies and positions of the four photons from the $2\pi^0$ decay measured in the calorimeter. To reconstruct the position of the kaon decay and the four photon mass, the photons were paired using the π^0 mass as a constraint. The cartoon in Figure 53 illustrates the procedure. If we have paired photons a and b, then the z position z_{ab} of the π^0 decay is related to the π^0 mass by

$$\begin{aligned} m_{\pi^0}^2 &= 2E_aE_b(1-\cos\theta_{ab}) \\ &\approx E_aE_b\frac{r_{ab}^2}{(z_{glass}-z_{ab})^2}, \end{aligned} \tag{6.1}$$

where E_a and E_b are the energies of the two photons, θ_{ab} is the angle between the two photon trajectories, and r_{ab} is the separation of the photons in the calorimeter. We formed a second vertex position z_{cd} from the other pair of photons. Using the resolution contributions from

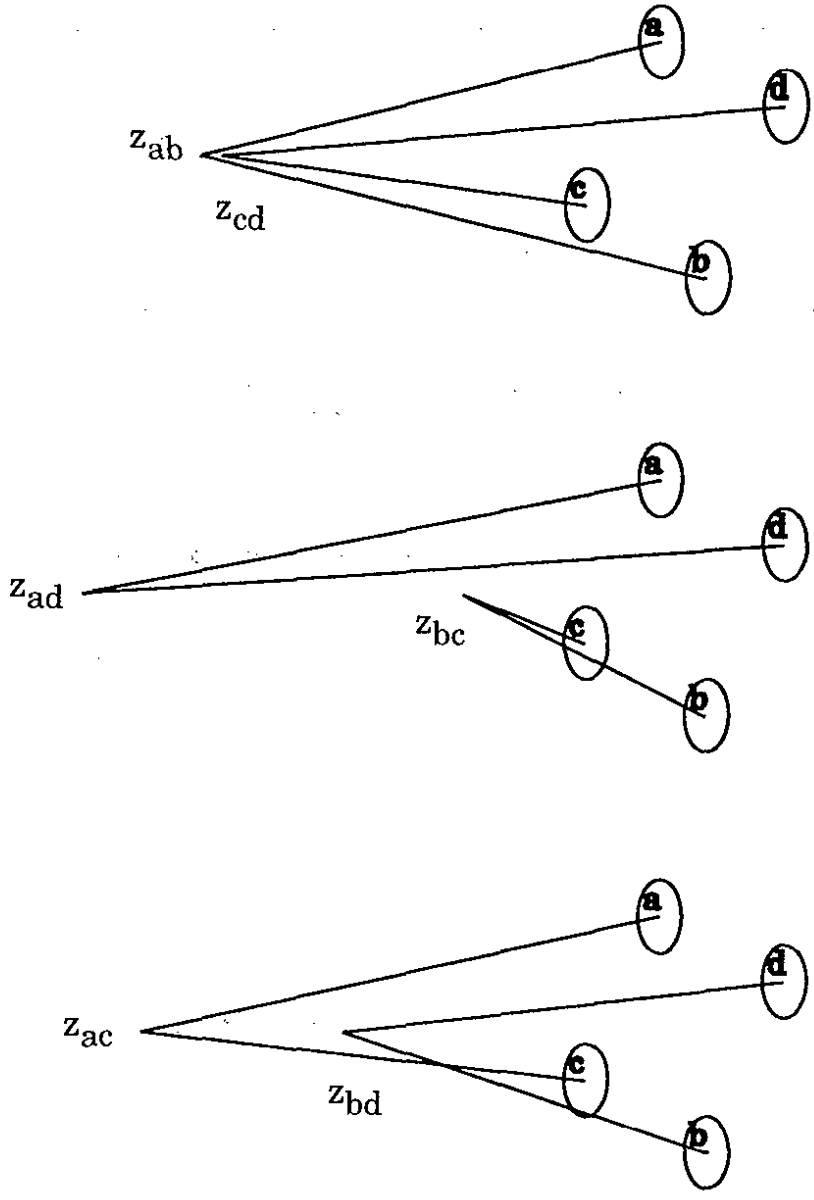

Figure 53. The z locations obtained for both π^0 decays in each of the three possible pairings of the four photons from a $K \to \pi^0\pi^0$ decay. The top pairing will give the best χ^2 for $z_{ab} = z_{cd}$.

each photon's energy and position, we could then form a χ^2 for the hypothesis that $z_{ab} = z_{cd}$,

$$\chi^2 = \frac{(z_{ab} - z_{cd})^2}{\sigma^2_{z_{ab}} + \sigma^2_{z_{cd}}}. \tag{6.2}$$

We chose the pairing with the best χ^2. The resulting χ^2 distribution for the best pairing in each event is shown for both the regenerator and vacuum beams in Figure 54 after all other cuts. For the final sample, the best χ^2 was required to be under 4.

The z of the kaon decay was taken as the weighted average of the two z positions, z_{ab} and z_{cd}, of the best pairing. With the z location of the kaon decay in hand, the $2\pi^0$ mass was then reconstructed from the four photons' energies and positions using

$$m^2_{\pi^0\pi^0} = 2\sum_{i>j} E_{\gamma_i} E_{\gamma_j}(1 - \cos\theta_{ij}). \tag{6.3}$$

$$\tag{6.4}$$

The cosine of the angle between the two photon trajectories, $\cos\theta_{ij}$, has been calculated

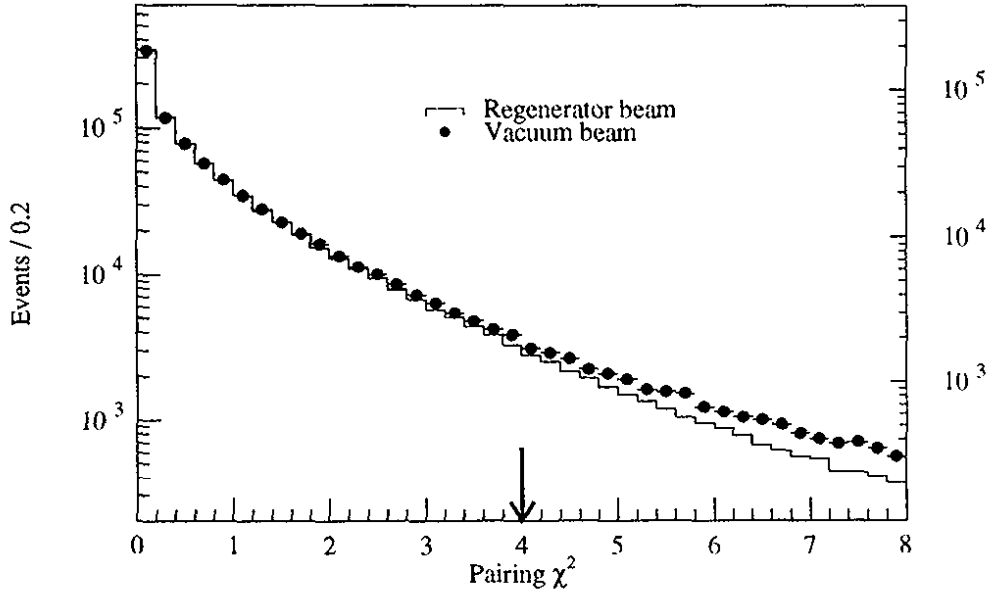

Figure 54. The $2\pi^0$ pairing χ^2 distribution for the regenerator and vacuum beams after all other cuts. The regenerator beam distribution is shown by the histogram (left axis) and the vacuum beam distribution is shown by the dots (right axis). The shapes of the two distributions differ at higher values of χ^2 because of the larger $3\pi^0$ and beam interaction backgrounds in the vacuum beam. The arrow marks the location of the analysis cut.

Table 8. Reconstructed $2\pi^0$ mass shift of the data relative to the Monte Carlo simulation in the five neutral subsets. Two of the subsets have been subdivided into time periods for which separate calibrations have been used. A negative shift implies the $2\pi^0$ mass in the data was lower than that in the Monte Carlo.

$2\pi^0$ subset	N1a	N1b	N2	N3	N4	NCa	NCb
$2\pi^0$ mass shift (MeV) (no pipe block clusters)	−0.76	−0.83	−0.71	−0.74	−0.63	−0.43	−0.44
$2\pi^0$ mass shift (MeV) (≥ 1 pipe block cluster)	−1.07	−1.40	−0.90	−0.94	−0.82	−0.65	−0.60

assuming that the kaon decayed on the z axis. This assumption has negligible effect on the mass.

The $2\pi^0$ mass distribution after all other cuts is shown in Figure 55 for the regenerator beam; the same distribution for the Monte Carlo simulation is also shown. Note that if there are residual nonlinearities in the calibration, this reconstruction technique leads to a shift in the reconstructed mass. We have observed such shifts in our data, and they are listed in Table 8 for each of the $2\pi^0$ subsets. Separate shifts are listed for events with and without photon clusters centered on one of the 24 pipe blocks. For the purpose of comparing the line shape predicted by our Monte Carlo simulation and observed in the data, we have shifted the reconstructed $2\pi^0$ mass of every event in the data. The mass shift applied varied from subset to subset to cancel the average shift observed in that set (shown in the table). Events with and without clusters in the "pipe blocks" received separate shifts. Aside from the average shifts, the Monte Carlo simulation tracks the observed mass spectrum very well. The shifts were not applied as part of the standard analysis, though we will use them later (Chapter 10) to help estimate the systematic effect of the residual nonlinearity.

The mass resolution with this reconstruction technique was close to 5.5 MeV, and we made a very loose $2\pi^0$ mass cut (474 to 522 MeV) in order to remain insensitive to the residual nonlinearities.

Because of fluctuations in the electromagnetic showers, we occasionally chose the wrong pairing. To keep the misreconstruction background to a minimum, we eliminated events if

the second best pairing had both a χ^2 within 8 of that of the best pairing, and a mass in the range from 470 to 526 MeV. The mispairing can be seen in the scatter plot of second best mass versus the χ^2 difference for the regenerator beam (Figure 56). About 1% of otherwise good kaons fail the mispairing cut.

6.2 Neutral Ring Number

Unlike the situation in the $\pi^+\pi^-$ mode, the transverse location of a kaon decay could not be measured in the $2\pi^0$ mode with the information available. This means that we could not measure the p_t^2 of the kaon to reduce the noncoherent kaon background. Instead we considered the center of energy (x_{CE}, y_{CE}) of the photons in the lead glass, given by

$$x_{CE} = \frac{\sum_{i=1}^{4} E_i x_i}{\sum_{i=1}^{4} E_i} \tag{6.5}$$

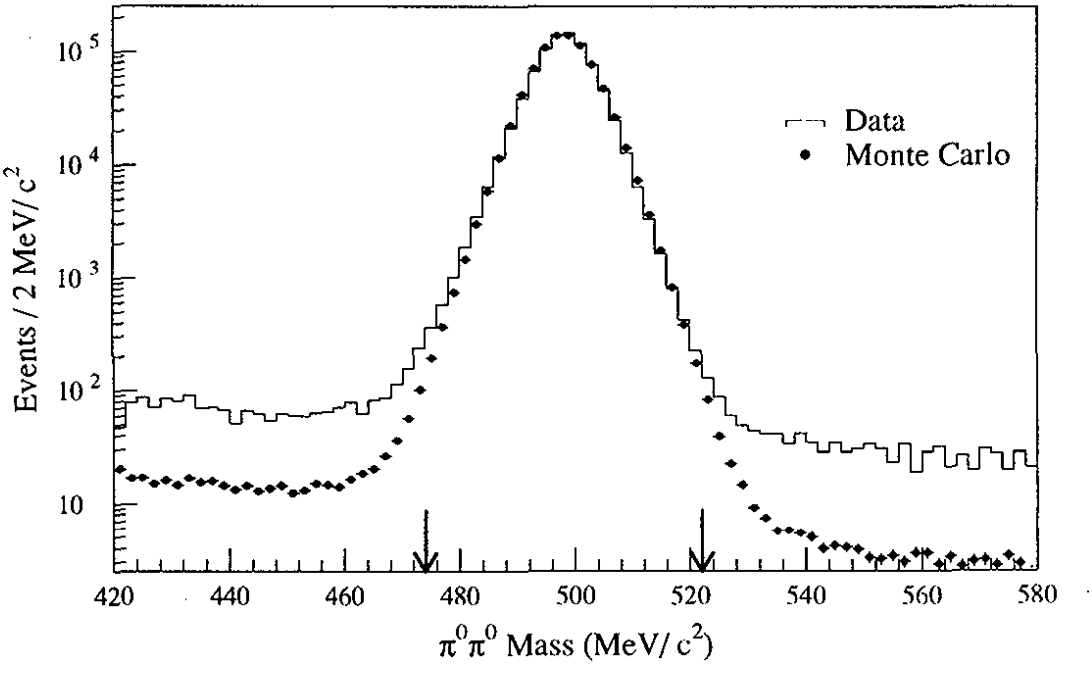

Figure 55. The reconstructed $2\pi^0$ mass after all other cuts for regenerator beam events. The predicted signal shape from the coherent Monte Carlo simulation is overlaid. The data have been shifted set by set according to the values in Table 8. The background has not been subtracted.

$$y_{CE} = \frac{\sum_{i=1}^{4} E_i y_i}{\sum_{i=1}^{4} E_i}, \tag{6.6}$$

where x_i and y_i are the x and y positions of the ith photon in the lead glass calorimeter.

The center of energy of the photons corresponds to the location where the kaon would have passed through the calorimeter had it not decayed. Hence for kaons which did not scatter, the center of energy should reconstruct within the beam. The two beams are clearly defined in the plot of the reconstructed center of energy in Figure 57. For this particular plot, the y position has been mapped to $-y$ if the regenerator was in the top beam. This effectively maps all coherent vacuum beam decays to the "upper" beam and all coherent regenerator beam decays to the "lower" beam in the plot.

While the two beams are clearly well separated, when one examines this plot on a log

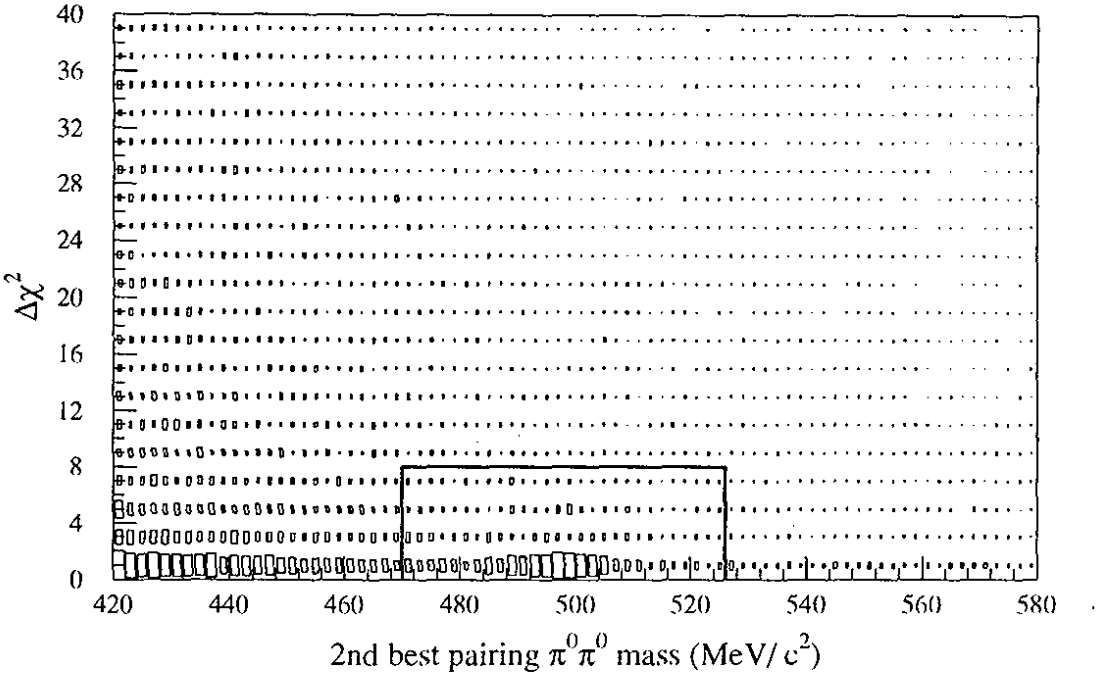

Figure 56. χ^2 difference between the best and next best pairing versus the next best $2\pi^0$ mass after all other cuts have been applied. The largest box corresponds to 105 events. The complete sample of regenerator beam $2\pi^0$ decays were used to make this distribution, though most of the events reconstructed outside of the limited region shown.

scale (Figure 58), one can see that there are a small number of kaons that reconstructed outside of the beam. The distribution of these events falls off as one moves away from the regenerator beam. These events correspond to kaons which scattered hard enough in the regenerator (or in the HDRA) to have their projected trajectory at the lead glass land outside of the beam. Some of the kaons scattered hard enough in the regenerator to actually reconstruct under the vacuum beam.

We divided the center of energy plot into square "rings" of area 1 cm^2, centered on each beam. Each event was then assigned the number of the ring into which the center of energy reconstructed. The distribution of ring number for each beam is shown in Figure 59. To

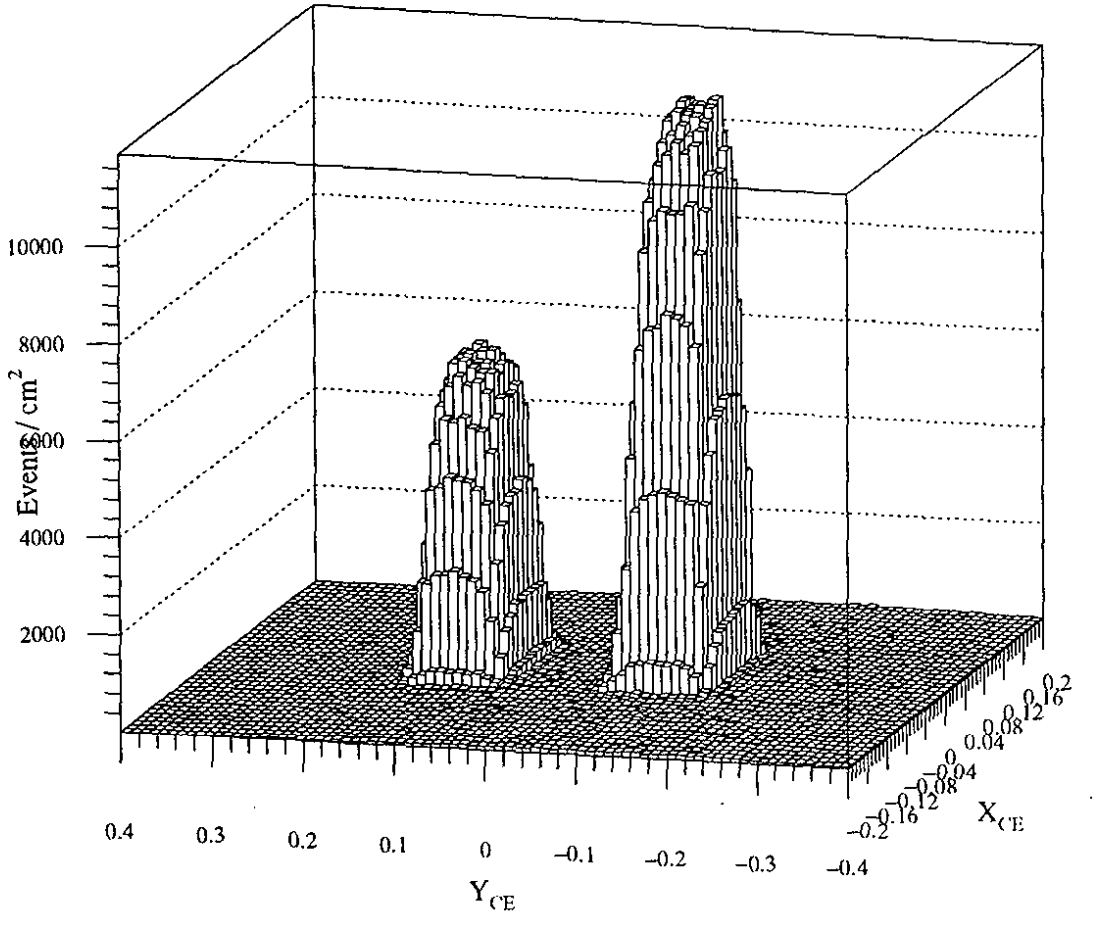

Figure 57. Distribution of the center of energy of $2\pi^0$ events passing all but the ring number cut. The y position has been negated when the regenerator was in the top beam. Regenerator beam decays are hence at right $(-y)$ and vacuum beam decays are at left $(+y)$

keep the signal to background ratio manageable, we accepted only events with ring number less than 112 (indicated by the arrow in the plot).

6.3 Other Cuts

In addition to the reconstruction cuts described above, several other cuts were applied to reduce the background level in the signal region defined by mass and ring number. One set of cuts reduced the $3\pi^0$ and neutron interaction background, while a second set reduced the inelastic background. Finally, several fiducial cuts simplified the acceptance determination.

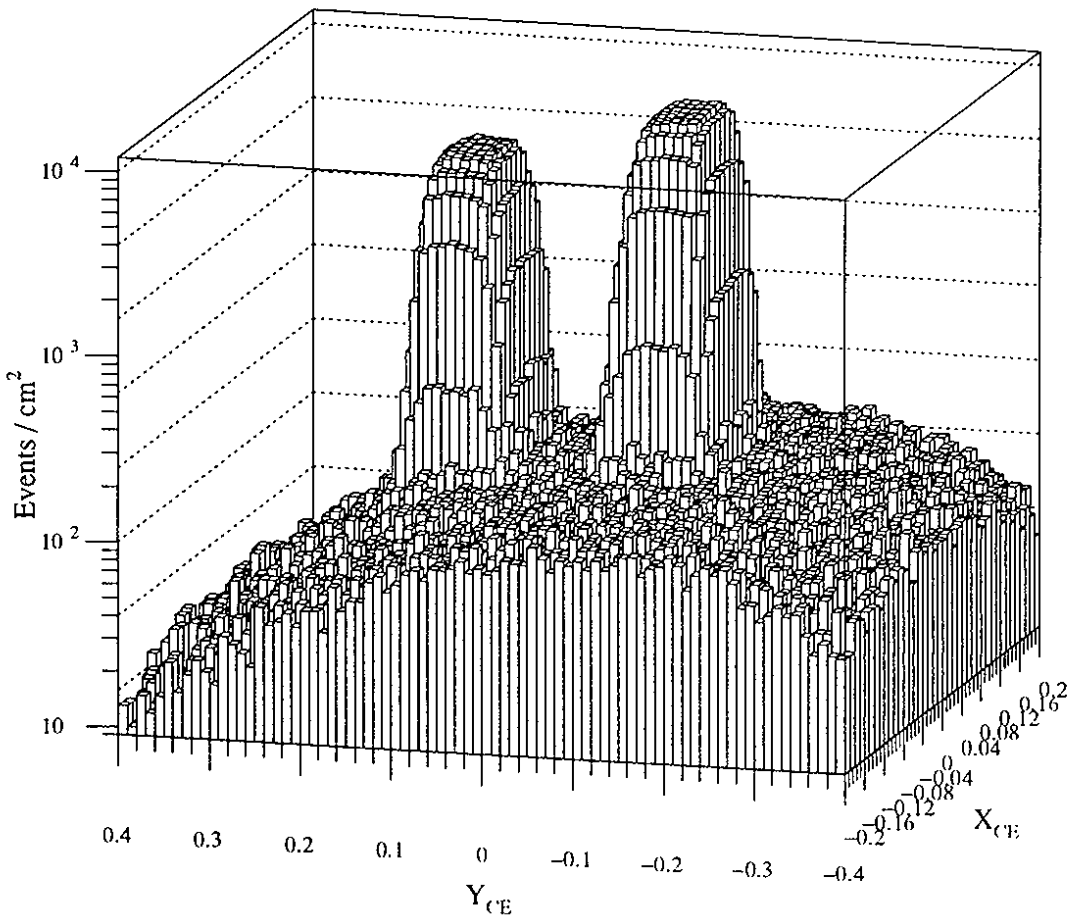

Figure 58. Distribution of center of energy on log scale, clearly showing a small, broad contribution centered on the regenerator beam from kaons which scatter at the regenerator.

Several types of cuts helped to reduce the background from $3\pi^0$ decays. The first cut simply tightened the restrictions on signals in the lead-lucite photon veto counters, reducing the chance for a photon to escape the detector. The cuts (in equivalents of minimum ionizing particles) for both the low intensity and high intensity data samples are listed in Table 9. The first bank (VA1) was quite close to the regenerator, and because of accidental activity from beam interactions with the regenerator we could not use this bank in the high intensity sample. The cuts were chosen to optimize the signal to background ratio. The MA bank around the analysis magnet was shadowed by other vetoes, and as a result our high intensity and low intensity cuts on the counter bank were not that different.

Because of the finite granularity of the calorimeter, photons which landed too close together were not resolvable into two separate clusters. These fused clusters sometimes lead to the misidentification of a $3\pi^0$ decay as a four cluster event when other photons were also unobserved or fused. Many of these fused photons were eliminated by comparing the observed cluster shape with the shape expected for an electromagnetic cluster. We used,

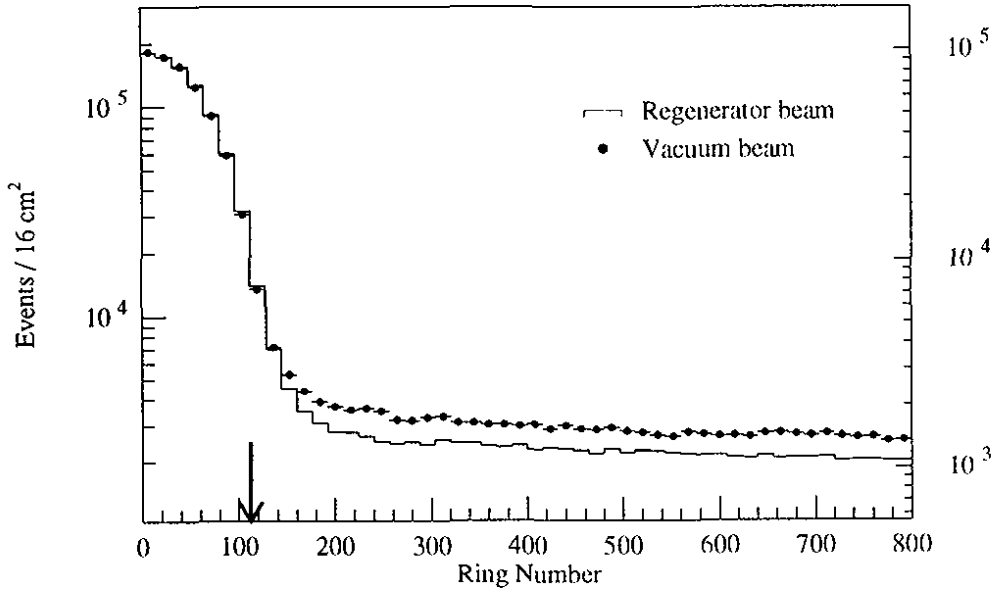

Figure 59. Ring number distribution for $2\pi^0$ decays in the regenerator (*histogram*, *left* scale) and vacuum (circles, right scale) beams after all other cuts. No backgrounds have been subtracted.

Table 9. Photon veto cuts in minimum ionizing equivalents applied in the $2\pi^0$ sample.

Veto Bank	Low Intensity cut	High Intensity Cut
VA1	2.6	none
VA2	1.3	6.0
DRAC	0.5	1.2
DRAN	0.6	1.5
VA3	1.0	1.8
VA4	1.5	3.0
MA	2.0	1.8
LGA	2.5	5.0

for example, the ratio of energy in the 3×3 cluster to that in a 5×5 cluster, and the ratios of energies in the outer rows (or columns) to the cluster energy.

Very soft photons from $3\pi^0$ decays could also be lost if the resulting cluster was below the hardware cluster-finding threshold of about 1 GeV. A direct search for soft clusters in the lead glass was infeasible because of remnant "clusters" from showers in other buckets within the long ADC gate. Recall that the adders, however, had a very short gate, and hence were not affected as severely by accidental clusters. By comparing the energy observed in the adders with that in the four clusters, events with extra soft clusters above roughly 600 MeV in energy could be eliminated effectively.

The effects on the mass distribution of the photon veto and lead glass and adder cuts can be seen in the vacuum beam $2\pi^0$ mass distribution shown in Figure 60.

To reduce the inelastic kaon scattering background (and the beam interaction background), we use the fact that extra charged particles are often produced in these interactions. By cutting on the number of hits in the drift chamber system and the presence of activity in the B and C hodoscopes, we eliminated many of the inelastic events not vetoed in the trigger. In rare cases when a photon from a $2\pi^0$ decay converted at the HDRA so that a single conversion electron [1] cluster carried most of the photon energy, the event had

[1] Electrons will often be used as a generic term for electrons and positrons throughout this thesis.

an acceptable pairing χ^2 and mass. These conversions were also suppressed by the cut on the number of drift chamber and hodoscope hits.

As we mentioned in Chapter 3, the collar anticounter cleanly defined the inner edge of the acceptance for $2\pi^0$ decays. This counter was in veto at the trigger level, but the veto itself was quite loose. In software, we tightened the cut to 5 minimum ionizing equivalents. In addition to defining the spatial extent of the calorimeter for allowable photons, we also wanted to define their energy threshhold clearly. For our final sample, we therefore required the minimum photon energy to be above 1.5 GeV. This cut made us much less sensitive to the simulation of the threshhold behavior of the hardware cluster finder. We also required the photon energy to be under 60 GeV. The latter cut will be discussed in some detail in Chapters 7 and 10.

The effects of the selection criteria (applied sequentially) on coherent $K \rightarrow \pi^0\pi^0$ decays

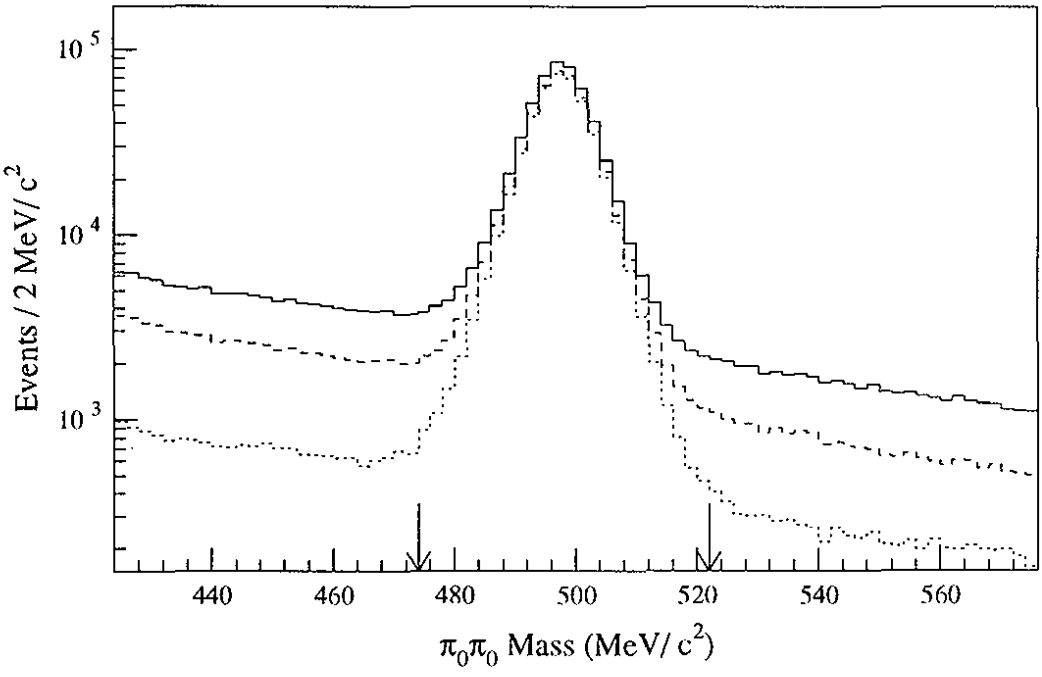

Figure 60. Effect of the photon veto and fusion cuts on the vacuum beam $2\pi^0$ mass distribution. The solid histogram has all cuts but the photon veto, fusion and soft cluster cuts, the dashed histogram has the photon veto cuts added, and the dashed histogram has all cuts added. The arrows show the location of the mass cuts.

Table 10. The fraction of coherent $2\pi^0$ decays in the regenerator beam lost after each analysis cut is applied as determined from the Monte Carlo simulation. In the "Sequential Loss" columns, the loss of the first cut is normalized to all $2\pi^0$ events which reconstructed within the fiducial energy and z region used for the $Re(\varepsilon'/\varepsilon)$ fits. Each cut thereafter is normalized to the number of kaons left after the preceding cut. The precision in this table is approximately 0.03% (only a small portion of the MC was used). Given the same p and z the efficiencies are similar in the vacuum and regenerator beams.

Analysis cut	Sequential loss (%)		Loss as Final Cut (%)	
	Lead Sheet	No Sheet	Lead Sheet	No Sheet
Chamber and hodoscope hits	21.37	1.12	15.49	0.06
Ring number	3.28	2.26	2.74	1.81
Photon veto	0.00	0.00	0.00	0.00
Minimum cluster energy	1.35	1.43	0.89	1.00
Maximum cluster energy	8.81	8.67	7.77	7.82
Cluster fusion cuts	0.90	0.80	0.90	0.79
Best pairing χ^2	3.09	2.50	2.76	2.21
Mispairing cuts	1.74	1.61	0.99	0.93
$2\pi^0$ mass	0.26	0.21	0.26	0.21

within our final fiducial volume are listed in Table 10. The loss of coherent events due to the cut on the drift chamber and B and C hodoscope activity shows a step, particularly in the lead sheet subset, because of photon conversions in the lead sheet. In the lead sheet sample, the calibration and analysis magnets were adjusted to cause the electrons from a photon conversion at the HDRA to converge at the calorimeter. The electrons would sometimes land sufficiently close to form a single cluster, hence the full energy of the original photon would be measured as a single cluster in the calorimeter and the decay would reconstruct as a reasonable four photon event. The e^+e^- pair register in the chambers and hodoscopes, of course, and these events were rejected. In the remaining sample, the conversions were less probable, and the magnets were not configured to reconverge the conversion pair. In these sets the only contribution came from events with a very asymmetric conversion.

The final energy distributions for the vacuum and regenerator beams are shown in Figure 61. The distributions in the two beams are again quite similar, though the vacuum

beam spectrum is somewhat enhanced at the low end because of the high acceptance for decays of the lower energy kaons downstream of the HDRA.

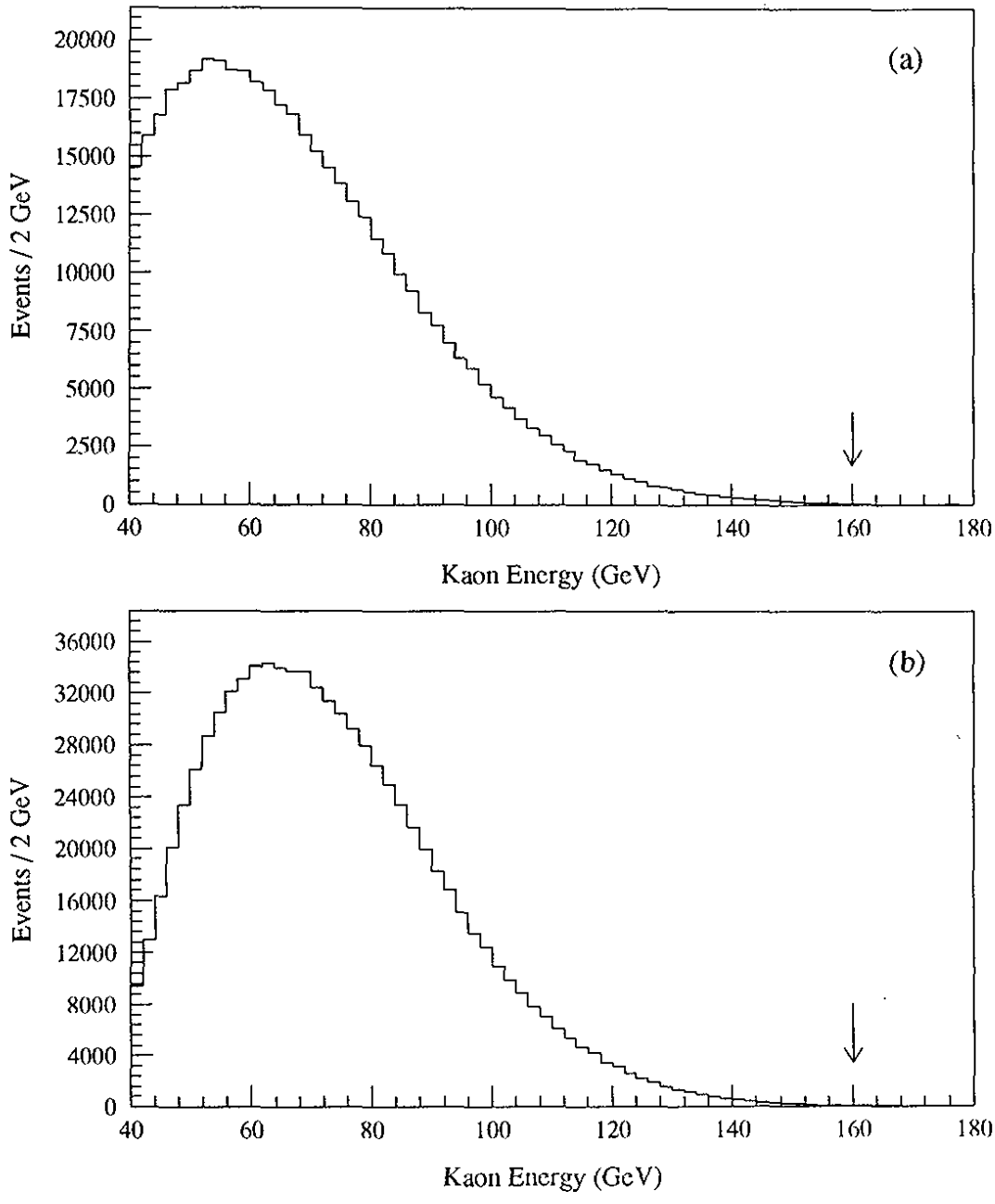

Figure 61. The kaon energy distribution for the entire $2\pi^0$ data set after all other cuts. (a) Vacuum beam. (b) Regenerator beam. The arrow marks the maximum energy used in this analysis.

Table 11. The parameters for the photon energy scale corrections, and the average correction applied, in the each $2\pi^0$ subset.

Subset	Slope ($E_K < 80$ GeV) [% per GeV]	Slope ($E_K > 80$ GeV) [% per GeV]	80 GeV correction [%]	Average Correction [%]
N1a	-1.7×10^{-3}	$+0.4 \times 10^{-3}$	-0.094	-0.06
N1b	-4.2×10^{-3}	-2.9×10^{-3}	-0.041	0.02
N2	-4.2×10^{-3}	-6.5×10^{-3}	+0.065	0.11
N3	-4.3×10^{-3}	-2.8×10^{-3}	+0.080	0.14
N4	-4.5×10^{-3}	-7.0×10^{-3}	+0.176	0.22
NCa	-5.0×10^{-3}	-3.3×10^{-3}	+0.324	0.39
NCb	-3.2×10^{-3}	$+0.9 \times 10^{-3}$	+0.313	0.37

6.4 Neutral Energy Scale

The final step in neutral reconstruction was the adjustment of the energy scale of the photons. As we saw in Chapter 4, the electron energy scale is understood very well over a 100 GeV energy range. Because of the difference in response of the calorimeter to electrons and photons, we need to check our ability to accurately reconstruct a photon's energy.

To quantify the nonlinearity, we took advantage of the coupling of the z and energy scales and examined the reconstructed position of the regenerator edge as a function of the kaon energy. We transformed the shift into a photon energy correction, which we parametrized as a bilinear function of kaon energy with a knee at 80 GeV. Table 11 lists the slopes above and below 80 GeV, the correction at 80 GeV, and the mean correction for each the $2\pi^0$ subsets.

A comparison of the z edge in the upstream region of the regenerator beam in the data and in the Monte Carlo simulation is shown after the correction in Figure 62a. On average the edges match quite well. As shown in Figure 62b, introducing a shift in the energy scale of only 0.05% in the data degrades the agreement between data and Monte Carlo noticeably. The χ^2 blows up by a factor of 3, and the shift of the regenerator edge between data

and Monte Carlo is clearly visible by eye. We estimate that the residual uncertainty in the *average* energy scale is under 0.03%. As we will discuss later, the residual uncertainty in the nonlinearity will dominate the systematic error from photon reconstruction uncertainties.

The coupling of the energy scale and z position has some subtle effects when the lead sheet is in place. Because of photon conversions in the lead sheet, there is approximately a 25% conversion correction to events upstream of the HDRA in the lead sheet data. Because residual uncertainties in the energy scale and nonlinearity can cause the reconstructed z position of decays on one side of the HDRA to shift systematically past the HDRA, we will either over or under correct some fraction of these events by the conversion probability. To minimize our sensitivity to this effect, we eliminated decays in the z region from 137 to 139 m from our final sample for the lead sheet data.

This ends the discussion of the reconstruction of the $2\pi^0$ decays. We will now describe the method used to determine the residual background level after applying the selection criteria described above.

6.5 Background Subtraction

There were four major classes of backgrounds that had to be subtracted from the coherent $2\pi^0$ data. The largest source of background resulted from $2\pi^0$ decays of scattered kaons. There were two sites producing this noncoherent background, the regenerator and the HDRA. Backgrounds from these two sites were treated independently. The $3\pi^0$ decays which reconstructed with only four clusters in the calorimeter constituted another class for both beams and were particularly important in the region downstream of the HDRA. Finally, inelastic interactions of neutrons in the two beams with material in the detector, particularly in the HDRA, would sometimes produce two π^0s that reconstructed under the kaon mass peak.

The background subtraction technique used the reconstructed $2\pi^0$ mass and ring number variables. The distribution of these variables for the vacuum beam sample is shown in Figure 63. The plot has been divided up into six regions, one corresponding to the signal region (region 2), and the other 5 corresponding to regions populated only by background. These

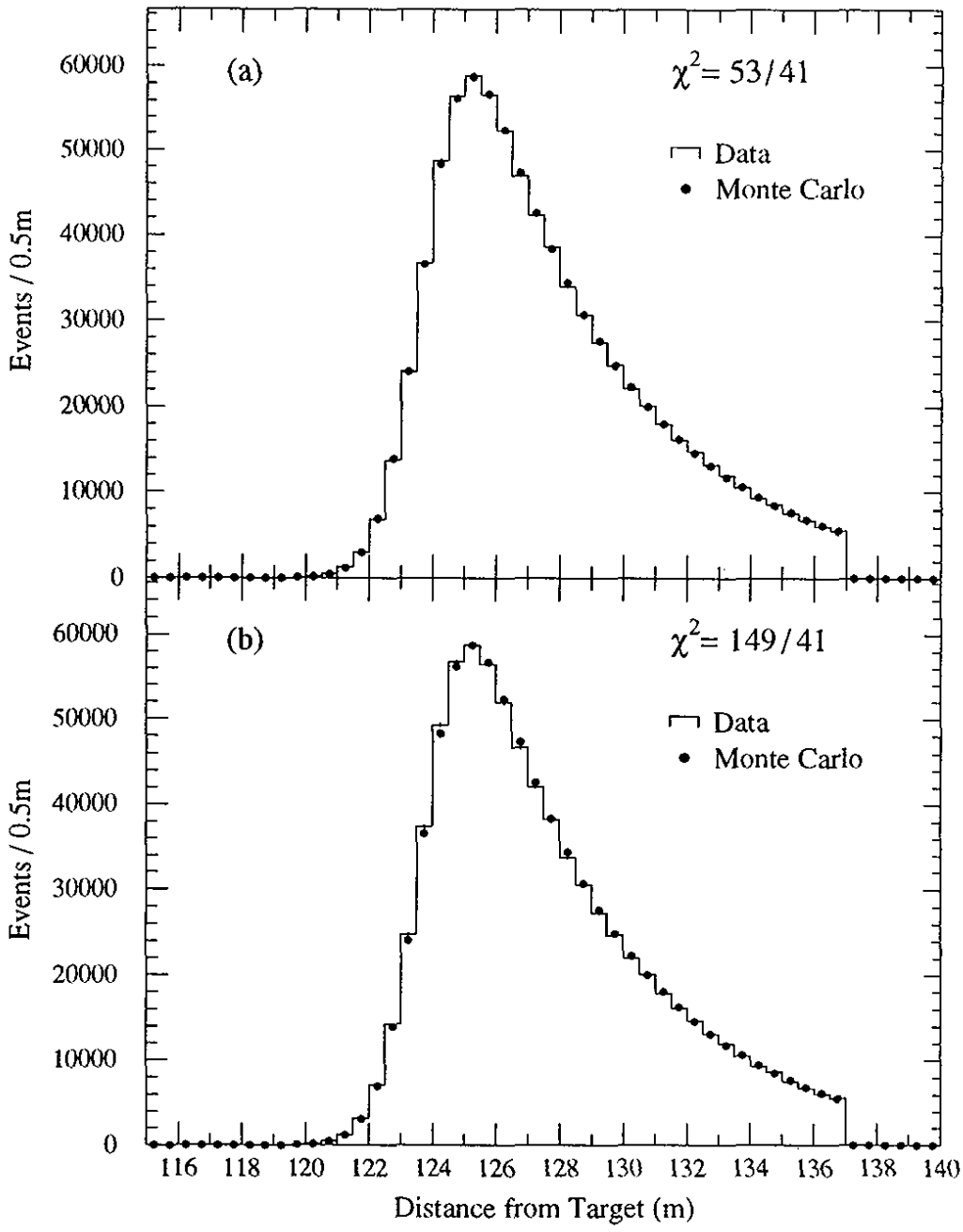

Figure 62. Data and Monte Carlo comparison of the upstream z after energy scale adjustments based on the position of the regenerator z edge. (a) The data has the standard adjustments. (b) The data has an additional 0.05% energy scale adjustment.

regions were used for normalizing Monte Carlo simulations of the different backgrounds. In essence, the $3\pi^0$ and beam interaction backgrounds were subtracted from the coherent *and* noncoherent kaons by extrapolating the mass sidebands under the mass peak. The noncoherent backgrounds were then extrapolated from large ring number to the coherent peak region. A more detailed explanation of the techniques used follows. The background subtractions were made in individual 1m by 10 GeV bins after the normalizations of the Monte Carlo simulated background samples were determined globally for the entire p and z fiducial regions.

A breakdown of the z distributions of the different backgrounds is shown in Figure 64, along with the data before and after subtraction, for the $K_L \to \pi^0\pi^0$ decays when no lead sheet was in place. This plot will be useful to refer to in the discussion of the background subtraction technique. The size of the background contribution from each of the background sources is summarized in Table 12.

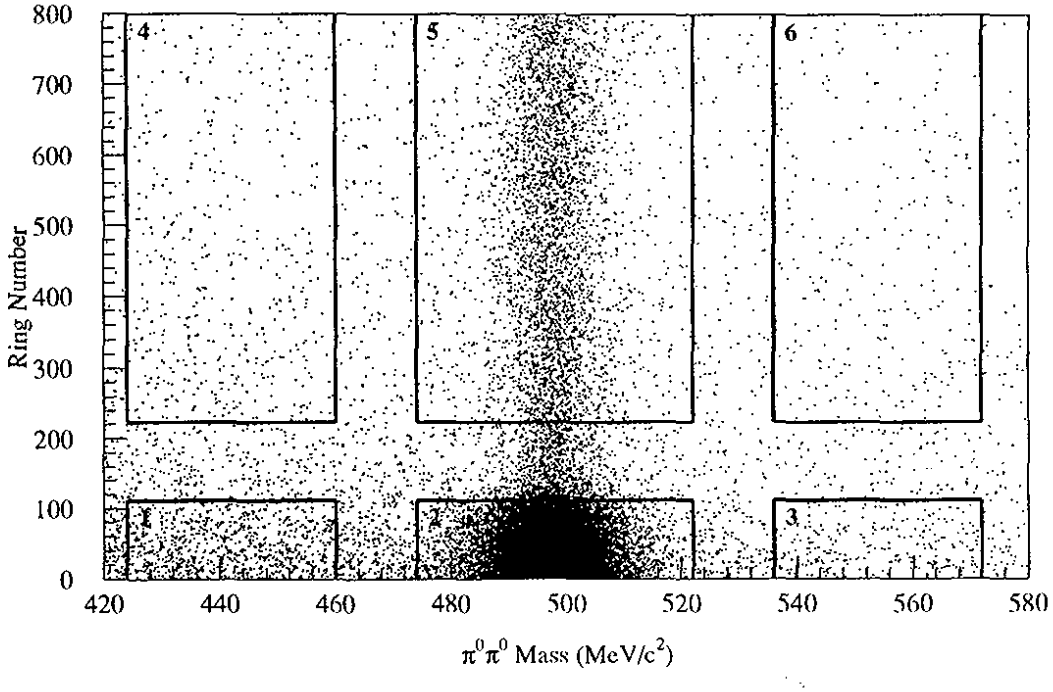

Figure 63. The six regions in the $2\pi^0$ mass versus ring number distribution used for background subtraction.

6.5.1 $3\pi^0$ and Beam Interaction Backgrounds

The $3\pi^0$ subtraction relied upon a Monte Carlo simulation of the background shape of the reconstructed mass distribution to make the interpolation from the background level in the mass sidebands to the level under the real $2\pi^0$ mass peak. The simulation of the shape was in theory not difficult: photon veto resolutions and gains could be adequately determined using $K_L \to \pi^+\pi^-\pi^0$ decays (see [76]), and their positions and sizes were well known. The actual calculation was, however, computationally very intensive since we wished to obtain a background sample close to 5 times the size of the observed background in the data. This entailed simulating 6×10^9 $K_L \to 3\pi^0$ decays and required over 3 months of dedicated use of 25 25-MIPS computers!

Once the $3\pi^0$ background Monte Carlo sample was finally in hand, it was normalized to the data using regions 1 and 3 outlined in Figure 63. Several pitfalls had to be avoided

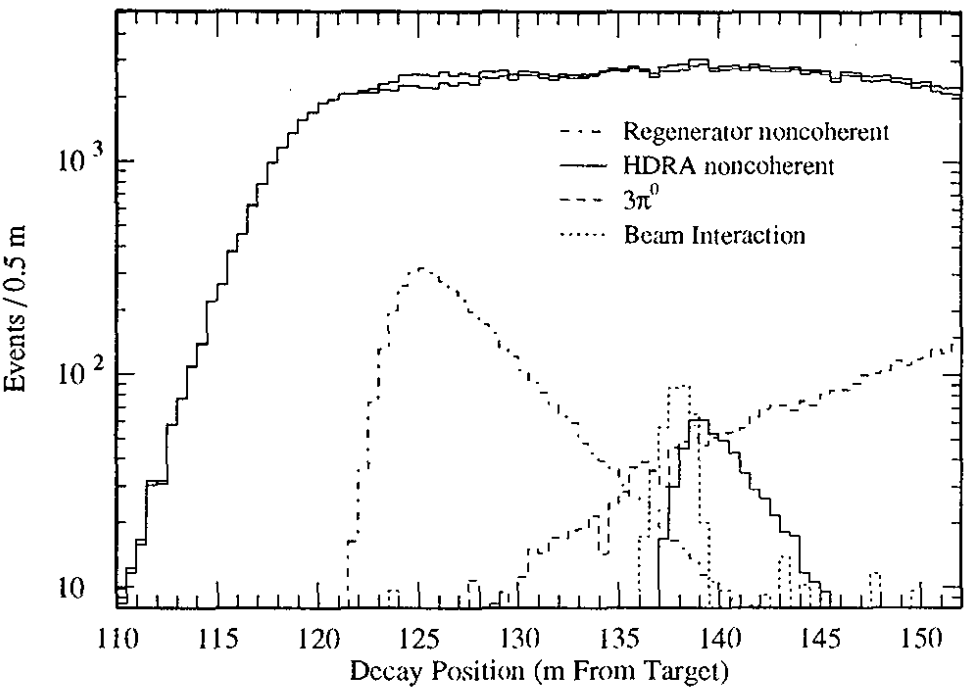

Figure 64. The z distribution of the different backgrounds to the vacuum beam $2\pi^0$ sample for the data subset with no lead sheet. The band at top shows the $2\pi^0$ z distribution before and after background subtraction. All cuts have been applied.

Table 12. The $2\pi^0$ background sources and sizes.

Source	Vacuum Beam Fraction (%)	Regenerator Beam Fraction (%)
$3\pi^0$ background	1.78 ± 0.03	0.049 ± 0.003
Beam Interaction	0.21 ± 0.02	0.027 ± 0.004
Regenerator Noncoherent Scattering	2.26 ± 0.04	2.53 ± 0.04
HDRA Diffractive Scattering	0.78 ± 0.02	0.027 ± 0.002
HDRA Inelastic Scattering	0.13 ± 0.02	0.027 ± 0.011

in this normalization. First of all, beam interactions with material in the beam produced a flat background in mass. Fortunately the material in the beam is localized at the two locations, the HDRA and the regenerator. This peak from the HDRA is in the vacuum beam is clearly visible in Figure 64, where the beam interaction background is shown as the dotted histogram. To avoid miscalculating the $3\pi^0$ normalization factor, only events reconstructing in the z regions 110m-122m, 125m-134m, and 142m-152m were used.

A similar normalization problem arose because of signal $2\pi^0$ events which were misreconstructed because, for example, of residual mispairings. These misreconstructions occurred both in data and signal Monte Carlo, and because of the way we define our acceptance, we do not want to subtract these events. The level of these misreconstructions can be seen clearly in the Monte Carlo mass distribution for the regenerator beam shown in Figure 55, where the misreconstructions constitute a substantial fraction of the events in the sidebands (this not the case in the vacuum beam). To avoid biasing the $3\pi^0$ normalization, the signal Monte Carlo was used to predict the ratio r of coherent events in the mass sidebands to coherent events in the mass peak. If d_s and d_p are the number of data in the signal region and in the mass sidebands, respectively, and b_s and b_p are the similar quantities for the $3\pi^0$ background, it is simple to show that the desired $3\pi^0$ normalization factor $a_{3\pi}$ is

$$a_{3\pi} = \frac{d_s - r d_p}{b_s - r b_p}. \tag{6.7}$$

If we had neglected this effect, the $3\pi^0$ background in the vacuum beam would have been overestimated by about 3% of itself. In the regenerator beam, however, the $3\pi^0$ background

is much smaller, and had we neglected the $2\pi^0$ misreconstructions, we would have overestimated the background by almost 70% of itself. In terms of the sensitivity of $Re(\varepsilon'/\varepsilon)$, neglecting this effect would have biased the result by 0.38×10^{-4}.

After subtracting the $3\pi^0$ background, the beam interaction backgrounds were estimated by linearly interpolating the residual background in the mass sidebands into the signal region in each pz bin. In regions of the detector with no material, this prediction would be consistent with zero if the $3\pi^0$ background were properly simulated, and this was indeed the case, as can be seen in the plot of the calculated beam interaction background shown in Figure 65. The width and position of the large peak are commensurate with our knowledge of the z resolution and HDRA location. The relative areas are proportional to the expected hadronic content of the two beams. A small background from beam interactions with the regenerator can also be seen in the regenerator beam plot in this Figure. The only evidence of a problem in the subtraction is in the regenerator beam upstream of the regenerator. This is simply due to a small resolution mismatch between the data and the signal Monte Carlo simulation, and is negligible at the 10^{-5} level in $Re(\varepsilon'/\varepsilon)$.

The mass distributions for candidate $2\pi^0$ events and the predicted background shapes

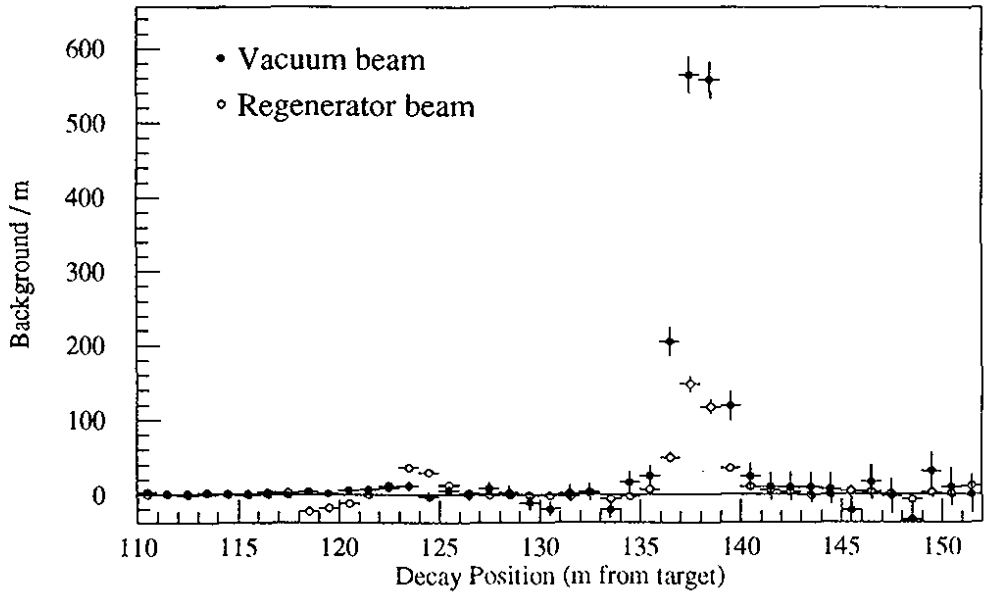

Figure 65. The z distribution of the calculated beam interaction background.

are shown in Figure 66. For the vacuum beam, the distributions for the entire z region and for the normalization z region only are plotted. The agreement is excellent in both cases, the former checking the combination of $3\pi^0$ and beam interaction shapes and the latter isolating the $3\pi^0$ shape. The agreement is also very good for the regenerator beam. In all three data distributions, the expected level of coherent misreconstruction in the mass sidebands has been subtracted.

The $3\pi^0$ and beam interaction backgrounds have been studied in individual 1 m z bins in the vacuum and regenerator beams for both the lead sheet and no lead sheet data samples. The mass backgrounds in 9 of these bins for the vacuum beam is shown in Figure 67. The lead sheet and no lead sheet data have been combined. Excellent agreement between the predicted and observed background shape was found in every z bin. These backgrounds have also been studied in 10 GeV momentum bins, and we found good agreement between predicted and observed background shapes as a function of momentum as well.

The statistical error on the $3\pi^0$ background subtraction amounted to 0.023% (0.003%) in the vacuum (regenerator) beam. The statistical error includes the errors from the number of events subtracted [2], the finite statistics of the $3\pi^0$ background Monte Carlo sample, and the normalization. The statistical errors on the beam interaction subtraction were 0.02% and 0.004% in the vacuum and regenerator beams, respectively.

Several checks were done to estimate the systematic contribution from the mass background subtraction. We have varied the $3\pi^0$ normalization method, using, for example, different normalizations for events with photons which hit the downstream photon vetoes rather than a single overall normalization constant. We have also studied the fluctuations in the result for different $2\pi^0$ mass cuts. All studies were consistent with a limit on the systematic error for the $3\pi^0$ plus beam interaction background of 0.015%. In Table 12 above, all of this error has been combined with the vacuum $3\pi^0$ statistical error.

[2] As discussed in chapter 8, the statistical errors used in the fits are those on the signal after background subtraction.

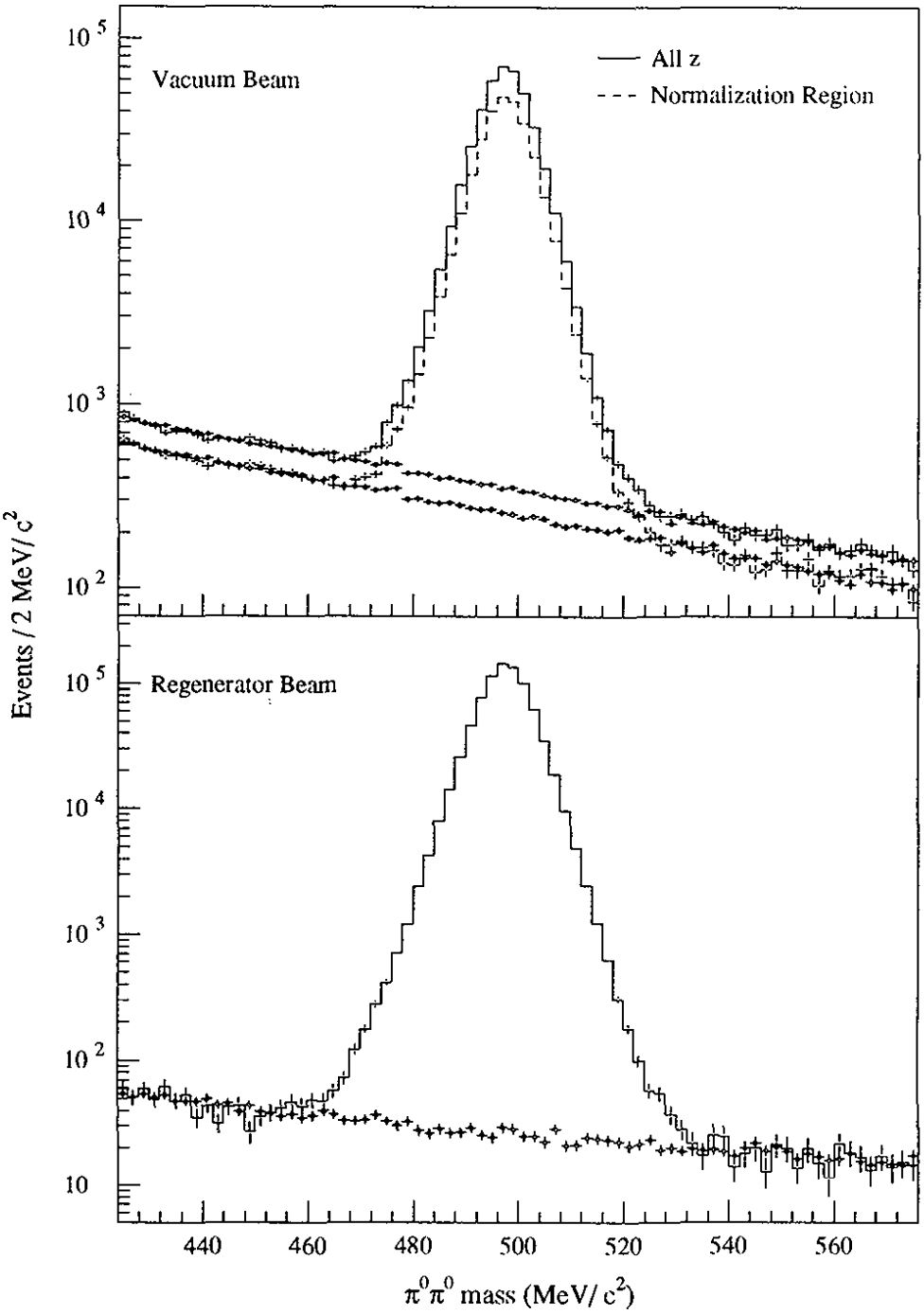

Figure 66. The $2\pi^0$ mass distribution and the background prediction. *Top*: The vacuum beam distributions for the fiducial z region (solid histogram) and the $3\pi^0$ background normalization z region (dashed histogram). *Bottom*: The regenerator beam distribution for the fiducial z region.

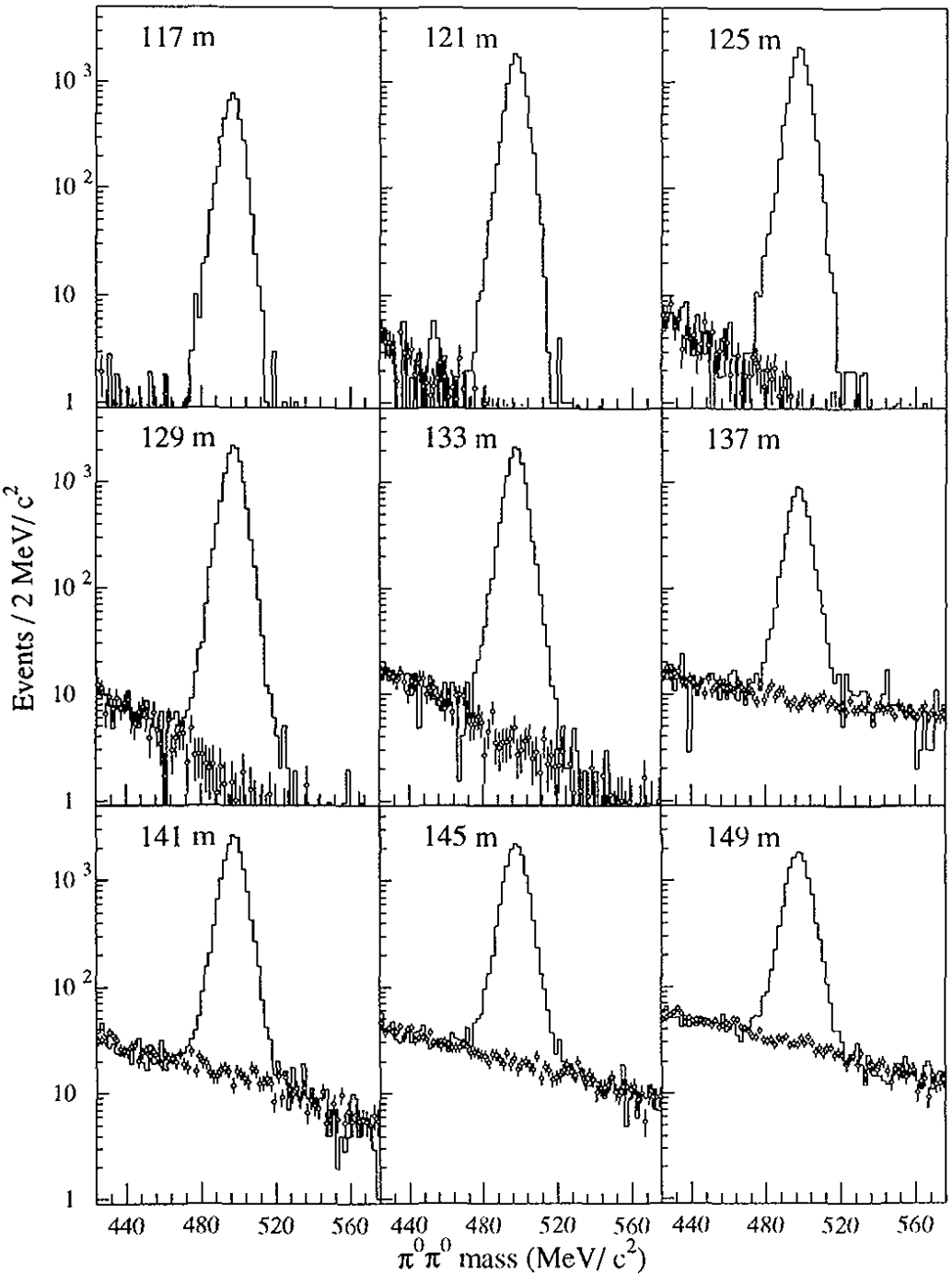

Figure 67. Observed $2\pi^0$ mass distribution and the $3\pi^0$ and beam interaction backgrounds in 9 individual 1 meter z bins. The $3\pi^0$ Monte Carlo normalization is common to all bins. Each plot is labelled with the upstream edge of the z bin. In the 137 m bin, we only used the data from the $2\pi^0$ subset with no lead sheet.

6.5.2 Noncoherent Backgrounds

As in the charged mode, decays of kaons which have scattered in material in the detector are background and need to be subtracted. Since we are accepting $2\pi^0$ decays from downstream of the HDRA, there are now two sources of scattered kaons, the regenerator and the HDRA. As Figure 64 shows, the backgrounds from these two sources are generally well separated in z, and we use this to our advantage. We use the ring number variable to subtract the noncoherent backgrounds, and the shape of the backgrounds in the ring number distribution for each source of noncoherent kaons was simulated with our Monte Carlo. The generation and normalization procedures for the two different scattering locations will be described below.

Before the noncoherent $2\pi^0$ backgrounds could be normalized, backgrounds from the $3\pi^0$ decays and beam interactions first had to be subtracted from the noncoherent $2\pi^0$ sample in region 5 shown in Figure 63. The same subtraction method used for the background in the coherent region was applied here. As in the coherent region, the predicted mass shape agreed with the observed background.

6.5.2.1 Regenerator Noncoherent Background

The fundamental problem with simulating the noncoherent backgrounds was determining the p_t^2 spectrum for the scattered kaons. For the regenerator, the p_t^2 spectrum could be measured with the $\pi^+\pi^-$ sample. As discussed in [74], the spectrum was corrected for acceptance as a function of p_t^2 and parametrized as the sum of two exponentials, a steep exponential for the diffractive contribution and a shallower exponential for the inelastic contribution. The resulting spectrum was

$$\frac{dN}{dp_t^2} \sim 3431e^{-5.2p_t^2} + 1875e^{-222.8p_t^2}, \tag{6.8}$$

where p_t^2 is measured in $(\mathrm{GeV}/c)^2$. This parametrization was fed into the Monte Carlo simulation to generate a sample of $2\pi^0$ decays from scattered kaons and reproduce the ring number distribution.

The charged sample used to determine the p_t^2 spectrum was the NC set, where charged and neutral data sets were collected simultaneously. This was also the highest intensity charged subset.

The Monte Carlo background simulation was normalized to the noncoherent tail in the ring number plot (region 5 in Figure 63). This was done using only events upstream of 134 m to avoid any contamination from the HDRA noncoherent background. The same z region around the regenerator excluded in the $3\pi^0$ normalization was also excluded here, to avoid double subtracting the beam interaction background.

6.5.2.2 HDRA Noncoherent Background

Since the HDRA formed part of the charged trigger, there was not a sample of $\pi^+\pi^-$ events to give us the kaon p_t^2 spectrum for the HDRA. Fortunately, the forward amplitudes have been measured at the precision we need [79, 78, 87]. The exceptions were oxygen and nitrogen, whose forward amplitudes could be reliably obtained from that of carbon using the measured atomic number dependence $A^{-0.758}$ [80] of the kaon regeneration amplitude. Optical model calculations also reproduce the measured p_t^2 spectra reliably [86]. All these amplitudes were fed into the Monte Carlo and scattered kaons were generated in both the vacuum and regenerator beams with the correct amplitude and phase relative the coherent kaons.

To normalize the diffractive sample, we subtracted the noncoherent background from the regenerator, the $3\pi^0$ background and the beam interaction background from the data in the range from 110m to 134m. The HDRA backgrounds do not affect this region, so we were left with the number of coherent data events in this z range. By comparing this number to the number of coherent Monte Carlo events in this region, we automatically obtained the correct normalization factor for the HDRA diffractive background Monte Carlo.

After the diffractive backgrounds were subtracted, there was a residual background from inelastic interactions of kaons in the HDRA that were not eliminated by the cuts on activity in the drift chambers and the B and C hodoscopes. To simulate the shape of this background, we use a previous measurement [86] of p_t^2 spectrum of inelasticly scattered

kaons. The spectrum was found to have approximately a $e^{-6p_t^2}$ dependence, independent of kaon momentum. We have generated a Monte Carlo sample with kaons scattered according to this spectrum at the location of the HDRA. The final result was insensitive to the exact value for the slope used. The generated sample was then normalized to the residual background in region 5 of Figure 63 after all of the previously discussed backgrounds were subtracted. This was done in the z range from 142 m to 150 m, though the final result was insensitive to the z range used.

To double check the inelastic shape, a sample of inelastic events were isolated by making a tighter cut on activity in the T hodoscope. The predicted inelastic background as a function of ring number and z agreed very well with the observed distribution in this isolated sample.

6.5.2.3 Noncoherent Summary and Errors

The overall agreement between data and Monte Carlo in the ring number distribution is illustrated in Figure 68. The predicted ring number distribution agrees very well with the data, both in the upstream region ($z < 134$m) where only the regenerator noncoherent background contributes, and overall, where both the HDRA and regenerator backgrounds contribute. The same is true for the regenerator beam distributions, though here the contribution from kaons scattering in the HDRA is very small. The data shown have had the $3\pi^0$ and beam interaction backgrounds subtracted in each ring number bin. The overall agreement is excellent.

The predicted ring number shapes have also been studied in 1 m bins for both the vacuum and regenerator beams in the lead sheet and no lead sheet samples. Figure 69 shows the data and Monte Carlo distributions for the same nine bins in Figure 67. The predicted and observed ring number shapes and levels agreed well in all of the z bins. For example, in linear fits to the data–Monte Carlo ratio, the number of bins with slopes as large as 2 standard deviations were consistent with the statistical fluctuations one would expect for the number of plots (42 bins $\times$ 2 beams $\times$ 2 sets = 168 distributions!). The data in the 1 meter z bin plots shown has again had the $3\pi^0$ and beam interaction backgrounds subtracted to allow

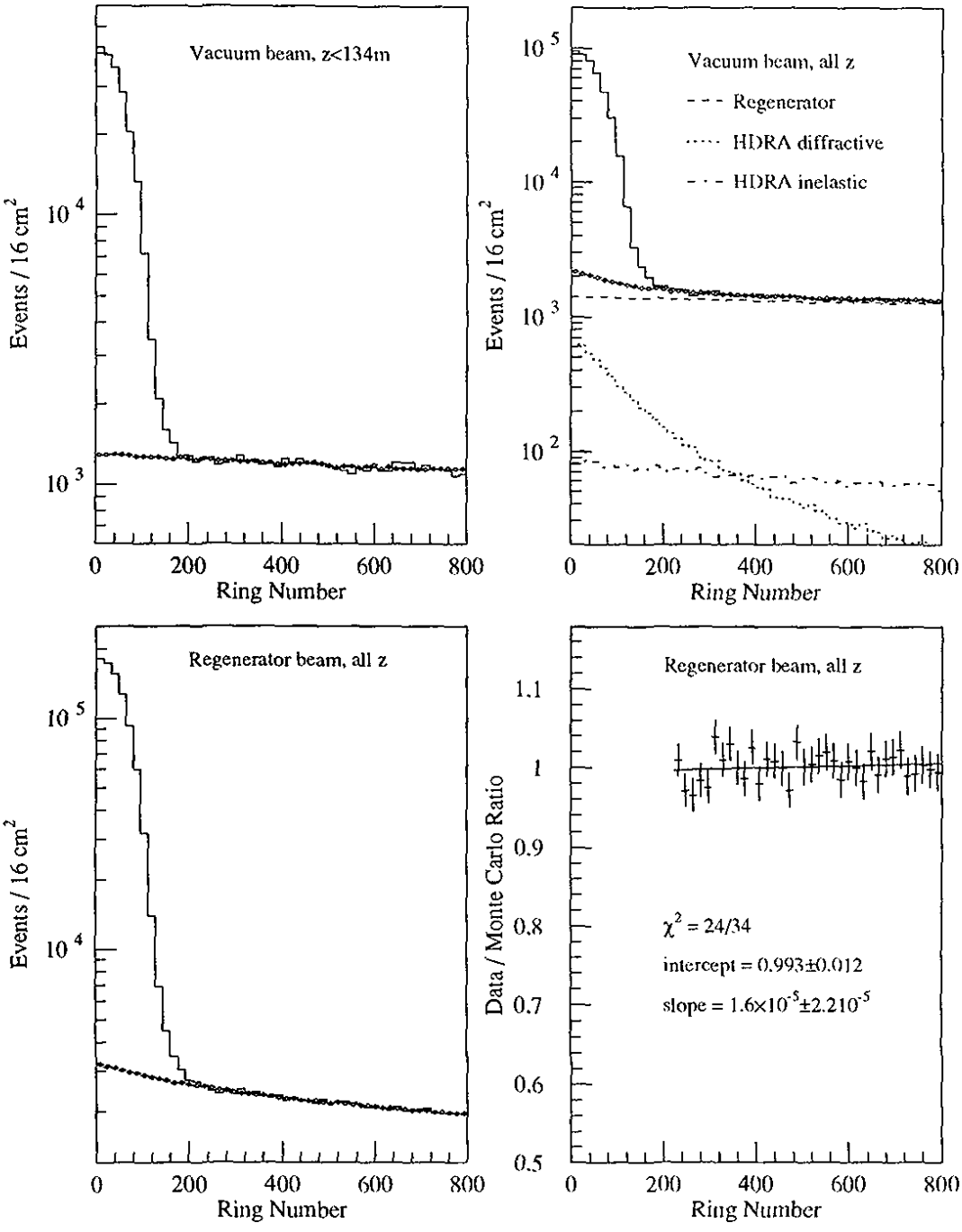

Figure 68. Observed ring number distributions in the $2\pi^0$ samples and the predicted backgrounds. In the first 3 plots, the solid histogram is data with the $3\pi^0$ and beam interaction backgrounds subtracted, and the open circles are the total predicted *noncoherent* background The last plot is the regenerator beam data–Monte Carlo ratio in the normalization range of the ring number variable. The slope of the vacuum beam ratio is also consistent with zero.

a direct comparison between the noncoherent backgrounds. Note in particular the z bin for 121 to 122 meters. The only significant background here is the regenerator noncoherent background. The regenerator itself is located 2 meters downstream of the end of this bin, so the background is entirely from noncoherent decays which have "smeared" upstream in the reconstruction! There is excellent agreement between the predicted and observed background levels in the ring number normalization region, another indication of the level to which we understand the detector. We have also studied these backgrounds in 10 GeV momentum bins, with similar results.

The statistical error on the number of noncoherent background events from scattering in the regenerator is 0.023% (0.018%) in the vacuum (regenerator) beam. As mentioned before, the statistical errors include contributions from the number of background events subtracted from the data, the statistical error on the Monte Carlo sample, and the normalization error. The systematic uncertainty was limited by studying the shape of the ring number distribution for the two beams and extrapolating the uncertainty to ring 0. The studies were statistically limited, and from the individual z bins and the overall shape, we have limited the uncertainty on the noncoherent background level from scattering in the regenerator to 1.2% of itself. The background in the vacuum and regenerator beam from the regenerator are correlated — if the regenerator beam background fraction were smaller, the vacuum beam fraction would also be smaller. Furthermore, this background almost cancels in the vacuum to regenerator beam ratio. However, we have chosen to ignore this correlation when assigning a systematic error, and have assigned the full 1.2% error to each of the beams.

The technique used to subtract the diffractive background from the HDRA relies upon knowledge of the regeneration amplitude and p_t^2 distribution for the materials in the HDRA. The uncertainty in the contributions from lead and carbon dominate, and they contribute at the level of 1.3%. In the experiments that measured the regeneration amplitudes we have used to simulate the diffractive background from the HDRA, there is a contribution to the uncertainty in the amplitudes from the value of η_{+-} assumed by those experiments. Where necessary, we have corrected the amplitudes using the current world average value for η_{+-} and the uncertainty in the value of η_{+-} has been included in the background

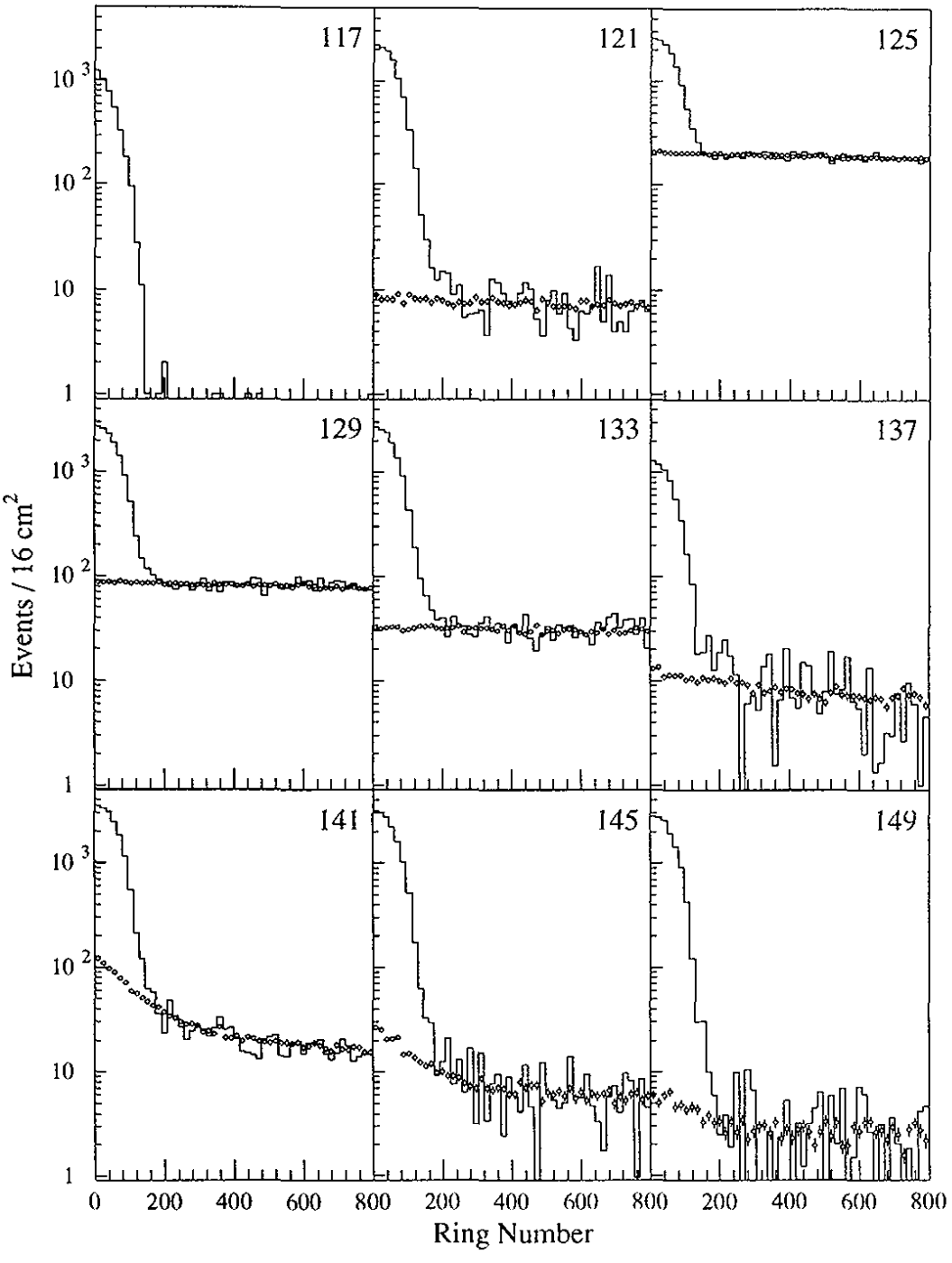

Figure 69. Observed vacuum beam $2\pi^0$ ring number distribution and predicted background shape in 9 individual 1 meter z bins. Each plot is labelled with the upstream edge of the z bin. In the 137 m bin, we only used the data from the $2\pi^0$ subset with no lead sheet.

uncertainty given above. The statistical uncertainties were 0.014% (0.002%) in the vacuum (regenerator) beam.

The inelastic HDRA contribution was the most difficult to limit systematically because of the low level of the background. The vacuum beam ring number shape agreed well, both within the total sample and the isolated inelastic sample mentioned previously. As mentioned earlier, the inelastic contribution could also be compared to the Monte Carlo inelastic sample by subtracting all of the other background components from the data. From studies of the shape of the tail of the ring number distribution for the inelastic samples, both overall and in 1 m bins, we have limited the uncertainty to 18% of itself.

In the regenerator beam studies of the isolated inelastic samples, we did observe a discrepancy in the overall ring number distribution at the level of 2 standard deviations. Since this background is so small, it was difficult to make meaningful studies in smaller z bins. The exact shape of the inelastic contributions is tricky to mimic, as there are comparable contributions expected from kaons which have scattered in the vacuum beam and crossed into the regenerator beam, and from kaons which have scattered within the regenerator beam itself. We have thus assigned a fairly conservative systematic uncertainty of 40% (of itself) to this background source. The statistical uncertainties on the background from inelastic scatters in the HDRA in the vacuum and regenerator beams were 0.006% and 0.002%, respectively.

6.6 Conclusion

This completes the discussion of the $2\pi^0$ reconstruction and background subtraction. The total number of events in each of the 10 GeV momentum bins, along with the total background fraction in each bin, is summarized in Table 13.

The final ingredient needed before we can extract the desired physics from the data samples is the acceptance for both the $\pi^+\pi^-$ and $2\pi^0$ decay modes. We will now turn to a more detailed discussion of the Monte Carlo simulation and the acceptance determination.

Table 13. The number of coherent $2\pi^0$ decays after background subtraction and the total background fraction in each 10 GeV bin for the lead sheet and no lead sheet data samples. The background levels are given in percent.

Momentum	Lead				No Lead			
Range	Vacuum		Regenerator		Vacuum		Regenerator	
(GeV/c)	Data	Bkg(%)	Data	Bkg(%)	Data	Bkg(%)	Data	Bkg(%)
40-50	45812	4.8	45667	1.6	30096	3.5	34700	1.4
50-60	51102	5.0	83563	1.7	34659	3.8	62948	1.6
60-70	46171	5.5	93830	2.2	31852	4.3	70311	2.0
70-80	36369	6.2	83444	2.7	25862	5.0	61841	2.6
80-90	26301	6.3	63474	3.2	18617	5.5	47401	3.1
90-100	16965	6.6	41124	3.9	12106	5.9	30694	3.7
100-110	9869	6.8	24102	4.5	7043	6.1	17605	4.4
110-120	5267	6.6	12821	5.2	3855	6.0	9360	5.2
120-130	2682	5.9	6188	5.8	1898	6.1	4383	6.0
130-140	1348	4.7	2626	6.4	941	4.8	1766	7.1
140-150	618	3.2	955	7.2	424	2.9	675	7.4
150-160	277	1.6	308	7.8	195	0.6	215	7.8
Total	242779	5.6	458101	2.7	167547	4.5	341897	2.6

CHAPTER 7

THE MONTE CARLO SIMULATION

7.1 Introduction

Because of the difference in the lifetimes of the K_S and the K_L and therefore different z distributions in the vacuum and regenerator beams, we must understand the acceptance of our detector as a function of z. There are really two categories of acceptance issues: roughly an "outer" acceptance, which is defined by the limiting apertures of the experiment, and an "inner" acceptance, which is determined by thresholds and the granularity of the calorimeter and drift chambers. The determination of the acceptance as a function of p and z is the most important role of our Monte Carlo simulation, and we will devote this chapter to the description of our modelling of both the outer and inner acceptances.

With the $\pi\pi$ acceptances in hand, we need to limit the potential systematic biases in these acceptances. We do not try to limit the acceptance using the $\pi\pi$ modes, but turn instead to the Ke3 and $3\pi^0$ modes. These two decay modes offer much better sensitivity to any potential biases in the acceptance, both because with the higher statistics it is harder to hide a small systematic bias, and because a higher fraction of the decays themselves probe the outer and inner acceptances.

The acceptance calculation was not the only role for the Monte Carlo simulation, however. In the $\pi\pi$ analyses, the simulation was also used for determining the background levels in some of the samples, and for studying systematic effects in all of the backgrounds. The use of the simulation also extended beyond the $\pi\pi$ analyses presented here, as the

simulation formed the underpinning of many rare decay and form factor analyses that were possible with our data set, but which are beyond the scope of this document. Finally, the accurate simulation of the high statistics Ke3 and 3π decay modes were necessary for the systematic study of the acceptance.

The disparate simulations required by these many different tasks led to the development of a very fundamental simulation package in which the kaon beam simulation, decay product propagation, and detector response were common to all of the simulations. The only differences in the various simulations were the kaon decay modes and their intrinsic dynamics. Furthermore, to prevent biases from entering into the $\pi\pi$ acceptance determinations, the tuning of the simulation based on the $\pi\pi$ data was kept to a minimum. Only the kaon production spectrum was tuned based on the observed $\pi\pi$ distributions, but since we will bin the data in small momentum bins, there is no bias introduced by this tuning.

For other inputs to the simulation package, we took as much as possible from first principles — survey measurements, EGS [84] electromagnetic shower simulations, previous experimental measurements, etc. — and used the high statistics decay modes only where necessary for a final tuning. Of course, counter and drift chamber wire efficiencies had to be determined from the data, but these were obtained using either muons or Ke3 decays. Most of this information affected the detector response and hence the "inner" acceptances. For the "outer" acceptances, the locations of the limiting apertures were tracked with the electrons from Ke3 decays after the final chamber alignment (see Section 4.1.2).

This chapter will describe the three major components of the Monte Carlo simulation, the kaon beam simulation, the kaon decays and propagation of the daughter particles, and the detector response. In addition to this, a representative comparison of the simulation to the $\pi\pi$ data will be presented for each of topics. Finally, after all the various elements of the simulation have been discussed, the z distributions of the different decay modes be examined. First presented are the high statistics modes, from which the limit on the systematic bias is obtained. Then for completeness, the $\pi^+\pi^-$ and $2\pi^0$ z distributions are presented. *Absolutely no* tuning was done to the z distributions in the Monte Carlo simulation. These distributions are the result of the careful attention to detail that has been

paid to the simulation of the kaon beam, the detector response and the decay kinematics over the past five years.

For many of the figures, reconstructed distributions in the $\pi^+\pi^-$ and $2\pi^0$ data are presented with the Monte Carlo simulation overlaid. In these cases, the full Monte Carlo statistics used for the final acceptance correction is shown, but the Monte Carlo is scaled to the size of the data samples. To set the scale for the rest of the chapter, the $\pi^+\pi^-$ simulation sample size was 25 times the $\pi^+\pi^-$ data sample size, the $2\pi^0$ simulation size with the lead sheet was 22 times the data size, and the $2\pi^0$ simulation size without the lead sheet was 26 times the data size.

7.2 The Kaon Beam

As we have mentioned, we are not strongly sensitive to the details of the kaon beam for the measurement of $Re(\varepsilon'/\varepsilon)$ and the other parameters. Our sensitivity to many of the details of the beam simulation that are covered in this section will be evaluated in Chapter 10. We have still, however, devoted much attention to the details of the simulation of the kaon beam. Having the correct beam shape and kaon momentum spectrum helps in our studies of the detector acceptance in several ways. With the correct momentum spectrum, we can compare our collected data to the simulated decays integrated over a broad momentum region, increasing our overall sensitivity for the detection of subtle biases. Furthermore, the details of the acceptance variation near the edges of some of the upstream limiting apertures depend weakly on the beam shape, so having the correct beam shape both limits biases in the acceptance calculation and simplifies the study of these edges.

Finally, while our detector is located quite far from the production target, the effects of $K^0 - \bar{K}^0$ interference were clearly visible in our data sample, even in the vacuum beam. The effects of decays of the residual K_S component of the original K^0 or $\bar{K}^0$ produced in the target were particularly visible at high momentum in the vacuum beam. Even had we neglected to incorporate these decays, the acceptance calculation would not have been significantly biased, since the acceptance for a kaon decay with a given momentum and z location, is unrelated to the details of the kaon propagation. Only the relative weighting

of the accepted distribution of decays between different regions of p and z is affected. We could simply have reweighted the acceptances obtained from a Monte Carlo without the interference and still obtained the precision needed for this experiment. However, it was extremely useful for us to be able to directly compare the simulated and measured decay distributions, which required the incorporation of the interference effects.

We therefore decided to use the full quantum mechanical description of the $K^0 - \bar{K}^0$ system for production and propagation of the kaon beam. This description also had the added advantage of making the Monte Carlo easily generalizable from the $\pi\pi$ decays to other kaon decays. To properly incorporate the full $K^0 - \bar{K}^0$ description into the simulation of the kaon beam, there are several necessary inputs. We need the production spectra of K^0 and $\bar{K}^0$ for interactions of the primary proton beam with the beryllium target. We need the transport function for the propagation of the kaons through the vacuum and various absorbers in the beam. Finally, we need the relative positions and orientations of the collimators which determine the final shapes of the two beams. The following subsections will describe our simulation of each of these inputs.

7.2.1 Production Spectrum

The Monte Carlo simulation begins with the generation of the production spectrum of the neutral kaons. There are several ingredients we use to construct this spectrum. First of all, we wished to reproduce the energy spectrum and angular divergence of the K^0 and $\bar{K}^0$ produced in the beryllium target. This spectrum, however, has not been measured directly, so to form the foundation for our production spectrum, we instead used the Malensek [88] parametrization of the K^+ and K^- production spectrum for protons incident on a beryllium target.

For production of a particle with momentum p into a solid angle $d\Omega$ centered at a polar angle θ and an azimuthal angle ϕ, Malensek presents a general form for the spectrum of

$$\frac{d^2N}{dp\,d\Omega} = \frac{B}{400} x \frac{(1-x)^A(1+5e^{-Dx})}{(1+p_t^2/M^2)^4}. \tag{7.1}$$

In this expression, x is the ratio of the produced particle's momentum p to the beam energy E_B, $x = p/E_B$, and p_t is the transverse momentum of the produced particle relative

the incident beam direction, $p_t = p \sin\theta$. B, A, D and M^2 were then determined using experimental data for particles produced with a 400 GeV/c proton beam. Both p and p_t are measured in GeV/c. For charged kaons, the best parametrizations had these constants:

	B	A	D	M^2
K^+	14.15	2.924	19.89	1.164
K^-	12.33	6.107	17.78	1.098

To build on this spectrum, we need to know how the dilution factor d_K, defined by

$$d_K \equiv \frac{K^0 - \bar{K}^0}{K^0 + \bar{K}^0}, \tag{7.2}$$

is related to the relative numbers of K^+ and K^- produced. A naive association based only on the strange quark content of the neutral and charged kaons would imply directly associating $K^0 \leftrightarrow K^+$ and $\bar{K}^0 \leftrightarrow K^-$. That is, the dilution factor would be

$$d_K = \frac{K^+ - K^-}{K^+ + K^-}. \tag{7.3}$$

However, the dilution factor extracted by the CERN NA31 experiment as part of their dedicated $\Delta\phi$ measurement [40] indicated that a better description of the dilution factor is given by

$$d_K = \frac{K^+ - K^-}{K^+ + 3K^-}. \tag{7.4}$$

A simple argument [89] for this form for the dilution factor can be made based on the valence quark content of the beam particles, in this case, protons. Because the parton-parton scattering process is strongly forward-peaked, and our nominal targetting angle of 4.8 mrad is dominated by the forward center of mass region, only the valence quarks of the proton contribute significantly to the kaon production of interest to us. For the valence quarks of the target nucleon to contribute to a kaon in our beam, they would essentially have to backscatter.

Now let σ_{ud} be the cross section for producing a $u\bar{u}$ or a $d\bar{d}$ pair, and σ_s be that for producing an $s\bar{s}$ pair, out of the sea. If we look at the K^+ production cross section, it will then be proportional to $2\sigma_s + \sigma_{ud}\sigma_s$, since the kaon could be produced using either of the valence u quarks of the proton, or with a u quark from the sea. From similar valence quark counting we have the following cross sections:

K^+: $2\sigma_s + \sigma_{ud}\sigma_s$	K^0: $\sigma_s + \sigma_{ud}\sigma_s$
K^-: $\sigma_{ud}\sigma_s$	$\bar{K}^0$: $\sigma_{ud}\sigma_s$

From this table,we see that a better assignment of relative production cross sections is $K^0 \leftrightarrow (K^+ + K^-)/2$ and $\bar{K}^0 \leftrightarrow K^-$. This assignment is equivalent to the dilution factor in Equation 7.4.

Because there were of order 10% errors in the experimental data used to derive this spectrum, and because the change from the 400 GeV incident proton energy of the measurements to our own beam energy of 800 GeV is quite large, we did not expect the extrapolation of the Malensek spectrum to our own beam to be perfect. We therefore tuned the spectrum using 80% of the vacuum beam $\pi^+\pi^-$ decays in the NC subset (about 20% of the total sample of $\pi^+\pi^-$ decays. The multiplicative correction factor $\xi(p)$ which we measured was

$$\xi(p) = 1 + 0.603315x - 0.0428304x^2 - 0.101624x^3 + 0.0180224x^4, \tag{7.5}$$

where $x = p[\text{GeV}/c]/100$. This correction factor is plotted in Figure 70. This correction affects only the overall rate as a function of momentum, neither the dilution factor nor the p_t spectrum at a given momentum were affected. This correction changes by a factor of 20% over the range from 40 GeV/c to 150 GeV/c, while the spectrum entering our decay volume drops by a factor of 4.5 over the same range.

The final energy spectrum tuning for all of the sets was done by adjusting the targetting angle. The nominal targetting angles were 4.8 mrad in x and 0 mrad in y. Since the target is centered between the two beams, we would expect that the two beams would see the same average kaon production angle, and hence have the same average energy. If the y-targetting angle were not zero, however, we would expect a small shift in the average energy with a dependence of roughly

$$E_t - E_b \approx 0.5\theta_y[\text{mrad}], \tag{7.6}$$

where E_t (E_B) is the mean energy in the top (bottom) beam in GeV, and θ_y is the y targetting angle. When $\theta_y > 0$, the proton beam is falling relative the kaon beam in the direction towards the detector. A deviation of the x targetting angle away from the nominal angle simply shifts the average kaon energy. The acceptance was known well enough at the time of this procedure that biases in the average energy in each beam induced by possible

acceptance mismatches were negligible on the scale of the splitting we observed between the two beams. The x and y targetting angles that we input to the simulation for each data subset based on the observed kaon energies in the top and bottom beams for each data subset are plotted in Figure 71. The x targetting angle measured is very stable, independent of the beam intensity.

The y targetting angle was correlated with the intensity of the proton beam because the latter was adjusted by a vertical tuning of the beam far upstream of the target. The tuning for the high intensity sets appears to have been quite similar, as the y targetting angles for the high intensity sets were quite similar. To reduce the intensity, however, a much different beam tune appears to have been used in the early as opposed to the late data sets. The final data set, with an intensity between the low and high intensity, has a y targetting angle which falls between the angles of the low and high intensity sets.

One amusing check of the reliability of these targetting angles is based on a scan of the proton beam over the target which occurred during just before we collected the C3 data

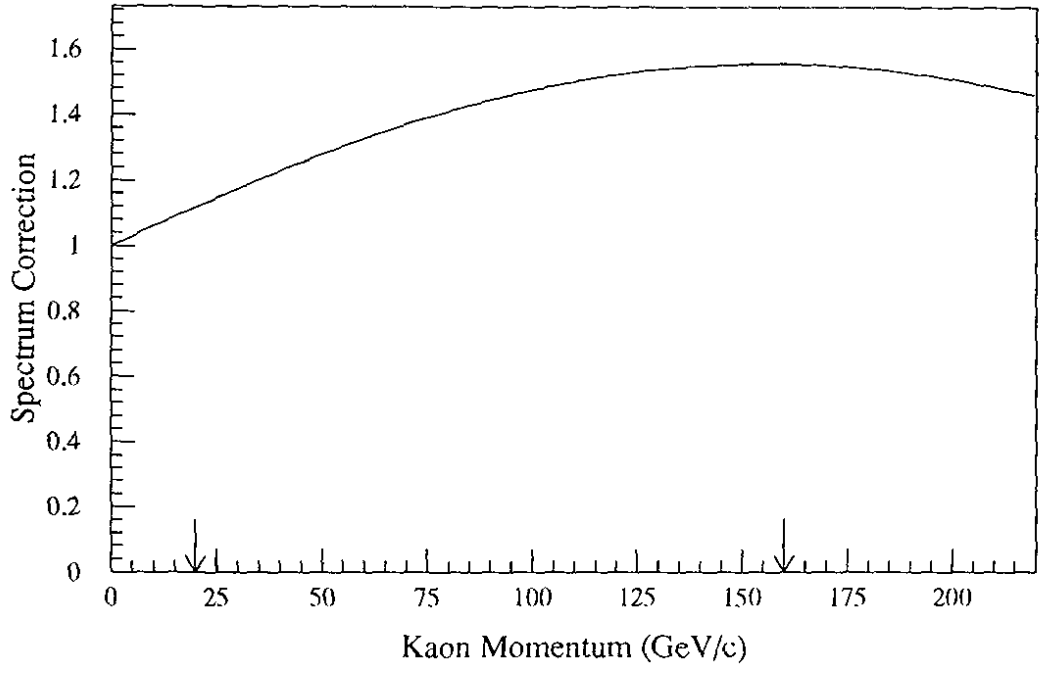

Figure 70. Momentum-dependent correction factor needed to bring the Malensek energy spectrum into agreement with the vacuum beam spectrum observed in our $\pi^+\pi^-$ NC subset. The arrows denote the maximum kaon momentum range used in these analyses.

subset. We expected the maximum event yield when the proton beam was centered on the target. During the scan however, we found that maximum rate occurred when the proton beam was about 600 microns "higher" than the supposed center of the target. This was rather surprising, since the target was surveyed into position and should have been much more precisely aligned than this implied. However, the wire chamber used to measure the beam position was located 1 m upstream of the target, and at that time we were assuming a targetting angle of zero in the vertical (y) direction. If we make the more reasonable assumption that the target was in the correct place, and that the proton beam simply passed at a different height through the wire chamber than through the target, the implied targetting angle is 0.6 mrad (with the same sign definition as above). This agrees very well with the 0.55 mrad angle deduced from the difference in top and bottom beam energies.

The final energy spectra produced in the Monte Carlo are compared to the observed $\pi^+\pi^-$ and $2\pi^0$ spectra in Figures 72 and 73. The spectra agree quite well in both sets,

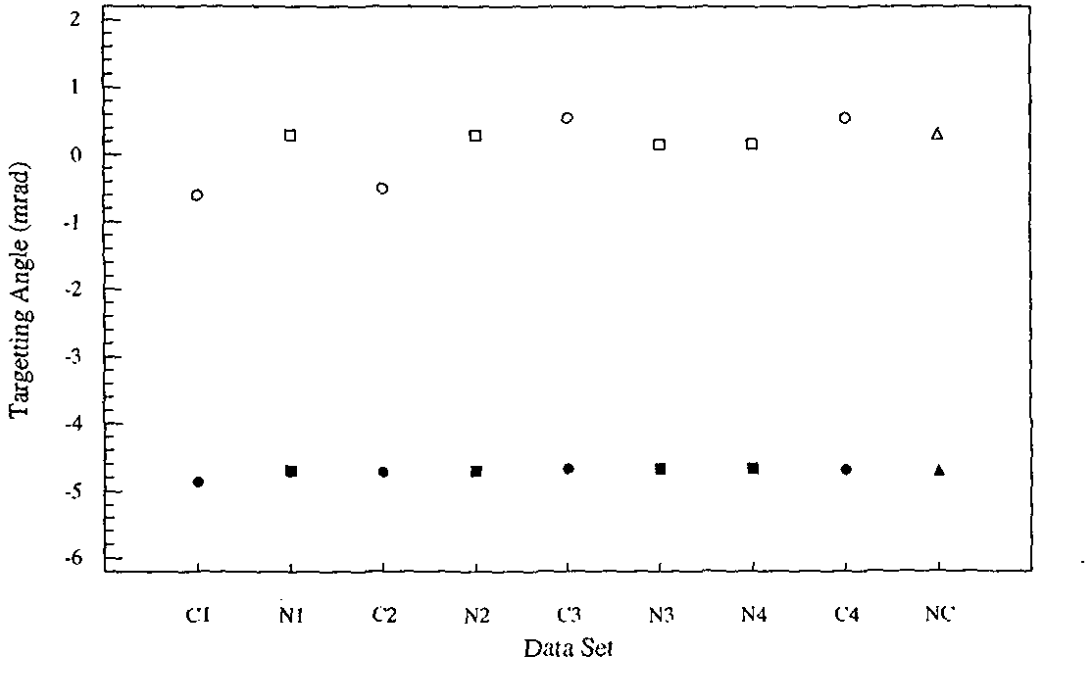

Figure 71. Inferred x and y targetting angles for the nine data collection periods. The x (y) targetting angles are plotted as solid (hollow) points. For both the x and the y angles, the highest intensity points are the squares, the medium intensity are the triangles, and the lowest intensity are the circles.

though there is perhaps a bowing of a few percent between the central region and the extreme ends of the energy range used in this experiment for the charged mode.

7.2.2 Kaon Transport

Once a K^0 or $\bar{K}^0$ is produced within the production target, it must be propagated to its point of decay. While the K^0 and $\bar{K}^0$ are the natural eigenstates to consider for the kaon production, which occurs via the strong interaction, it is much simpler to describe the evolution of the produced kaon via its weak decay eigenstates, the K_S and K_L. For a K^0 or $\bar{K}^0$ produced at the target, the initial K_S and K_L amplitudes are

$$\begin{pmatrix} a_S \\ a_L \end{pmatrix} = \kappa_+ \begin{pmatrix} 1 \\ 1 \end{pmatrix}, \quad \text{and} \quad \begin{pmatrix} a_S \\ a_L \end{pmatrix} = \kappa_- \begin{pmatrix} 1 \\ -1 \end{pmatrix},$$

respectively, with the normalization $\kappa_\pm = (1 \pm \varepsilon)/\sqrt{2(1+|\varepsilon|^2)}$.

Given initial K_S and K_L amplitudes, propagation of the kaons through the vacuum is trivial — the K_S and K_L component amplitudes are simply propagated without any interference:

$$\begin{pmatrix} a_S \\ a_L \end{pmatrix} \rightarrow e^{-im_L} \begin{pmatrix} a_S e^{\tau(i\Delta m - \Gamma_S/2)} \\ a_L e^{-\tau\Gamma_L/2} \end{pmatrix}, \tag{7.7}$$

where a_S and a_L are the initial K_S and K_L amplitudes, and the proper time τ is related to the propagation distance Δz and the momentum p by

$$\Delta z = \frac{p[\mathrm{GeV}/c]}{m_K[\mathrm{GeV}/c^2]} c\tau. \tag{7.8}$$

There is, however, material in the beam. The kaon must pass through the remainder of the target, the beryllium and lead of the common absorber. If the kaon is in the regenerator beam, it must also pass through the shadow absorber and then through the regenerator. In addition to the attenuation of the kaon beam through these materials, the scattering and regeneration in these materials affect the makeup of the beam which finally reaches the decay volume in terms of the relative K_S and K_L content, the final energy spectrum, and the angular spread of the beam.

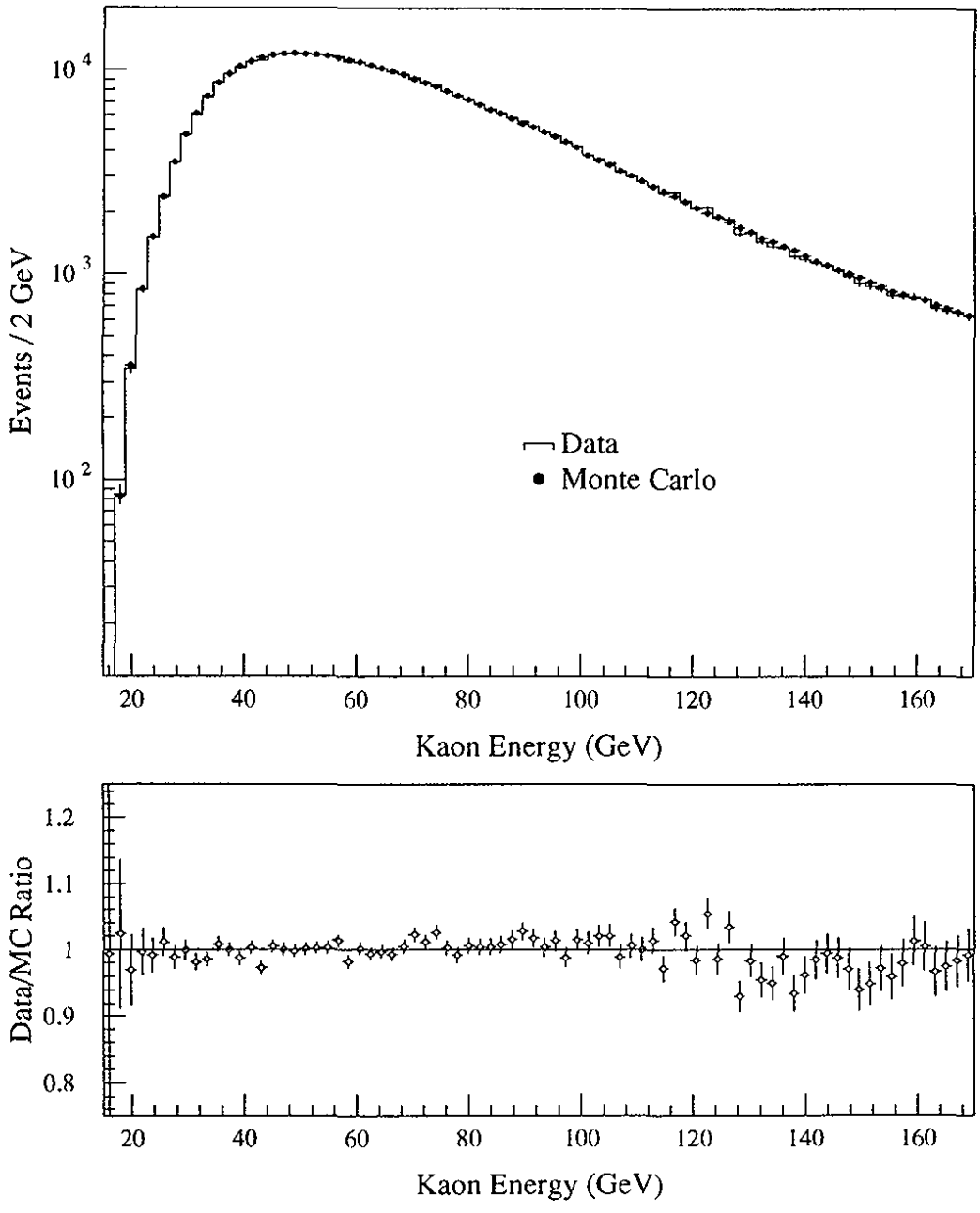

Figure 72. The kaon energy spectrum for the $\pi^+\pi^-$ decay sample in data and Monte Carlo simulation. *Top:* The data spectrum is plotted as a histogram and the simulation as dots. *Bottom*: The ratio of data events to Monte Carlo simulation.

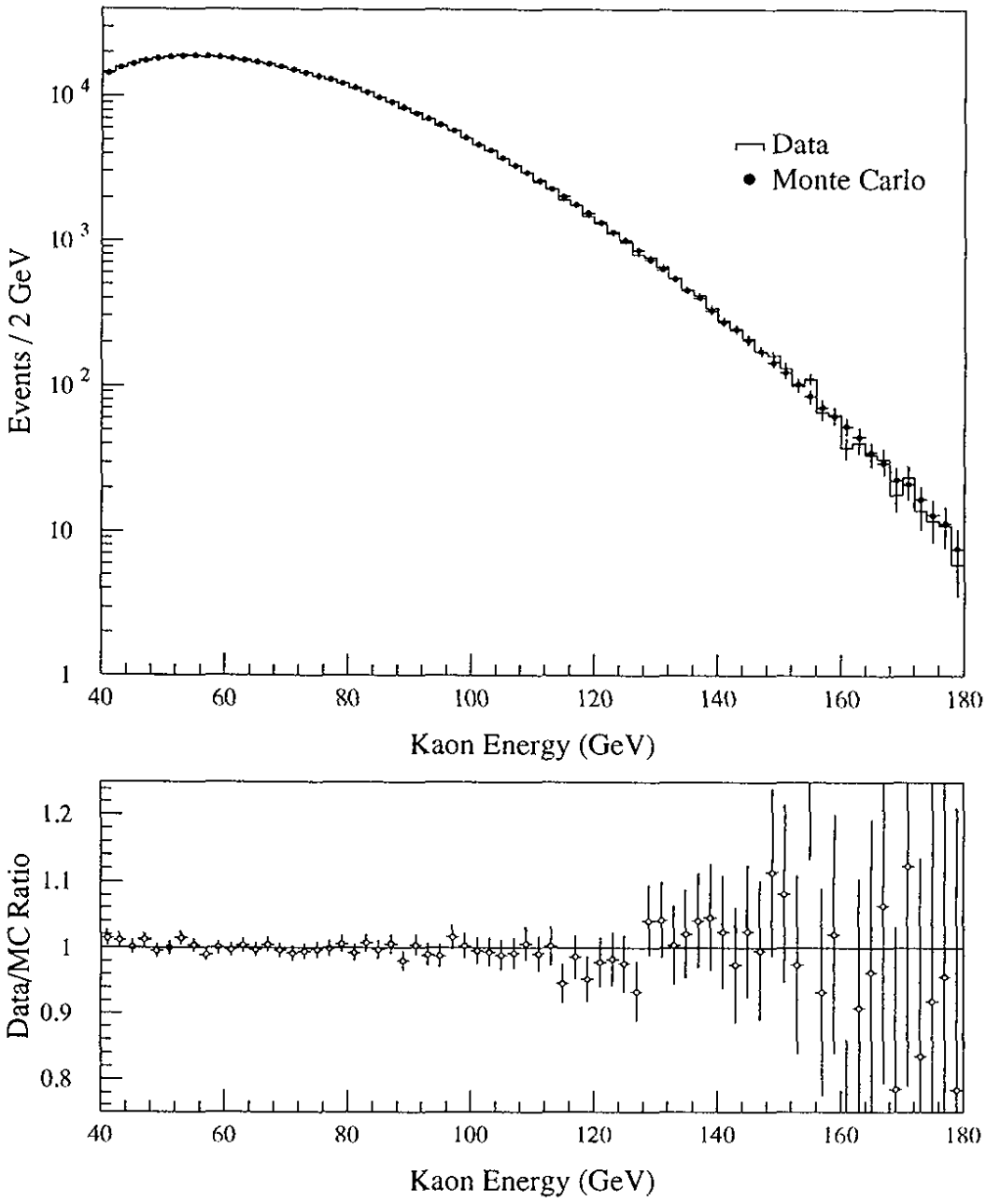

Figure 73. The kaon energy spectrum for the $2\pi^0$ decay sample in data and Monte Carlo simulation. *Top:* The data spectrum is plotted as a histogram and the simulation as dots The predicted background contributions have been added to the coherent $2\pi^0$ Monte Carlo simulation. *Bottom*: The ratio of data events to the Monte Carlo simulation.

Table 14. *Probability and exponential slope for single elastic scattering of kaons in each of the absorber elements in the kaon beam.*

Absorber Component	Single Scattering Probability (%)	Exponential Slope ([GeV/c^2]^2)
Beryllium, Common Absorber	8.6	65
Lead, Common Absorber	17.8	420
Beryllium, Movable Absorber	7.8	65

The coherent, forward regeneration of the kaons is handled exactly. As we shall discuss in Appendix A, the forward regeneration and overall attenuation can be incorporated into a simple matrix form:

$$\begin{pmatrix} a_S \\ a_L \end{pmatrix} \rightarrow e^{-x/2} \begin{pmatrix} T_{SS} & T_{SL} \\ T_{LS} & T_{LL} \end{pmatrix} \begin{pmatrix} a_S \\ a_L \end{pmatrix}, \tag{7.9}$$

where x is the total number of interaction lengths through which the kaon passes. The elements of the transformation matrix T depend on the forward scattering amplitudes $f(0)$ and $\bar{f}(0)$ of the K^0 and $\bar{K}^0$ for the material in the kaon beam. The form for T's elements can be found in the appendix.

The sample of kaons which reach our decay volume does not consist solely of the kaons which have propagated coherently from the target. There is some contamination of kaons which have scattered elastically in the common absorber and, in the regenerator beam, in the movable absorber. These scattered kaons essentially modify the spectrum $dN/dp\,dp_t^2$ of kaons which enter our decay volume, as the probability of a kaon scattered with a given p_t^2 has a greater chance to remain in the beam if the scattered kaon had a high momentum rather than a low momentum. The scattering also tends to blur out the edges of the beam.

As kaons passing through each of the absorber materials — the lead portion and beryllium portion in the common absorber and the beryllium shadow absorber — we have allow for a single elastic scatter in the Monte Carlo simulation. The scatters were distributed with a p_t^2 spectrum of $\exp(-\alpha p_t^2)$, and slope α and scattering probability were taken from the K^+ and K^- elastic scattering cross sections and slopes measured by Schiz *et al* [90]. The values used are listed in Table 14.

The scattering and coherent regeneration were included before the final spectrum tuning mentioned above was made.

7.2.3 Beam Collimation and Targetting

The finishing details for the simulation of the beam were the fine tuning of the beam collimator positions and the inclusion of the jitter of the proton beam spot on the target face. In general, the effect of a particular collimator face could be identified in a unique region of the beam profile, allowing both the average collimator position and the angle of the collimator slab relative to the z axis to be extracted. The position of the beam spot was measured several times during each 20 second beam spill. A typical distribution of the average beam position over a data subset is shown in Figure 74. This jitter tends to blur the edges of the beam profile, just as the elastic scattering did. The intensity profile of the beam itself was roughly a two-dimensional Gaussian with a width of 0.8 mm in x and y. This profile was also included in the simulation.

In the charged mode, the beam shapes were studied using the projected kaon position at the regenerator. For the neutral mode, the beams shapes for a given $2\pi^0$ subset were initially estimated from the collimator positions measured in the bracketing $\pi^+\pi^-$ subsets. The final tuning was then done based on the center of energy distributions measured in the lead glass calorimeter for the $2\pi^0$ and $3\pi^0$ decays. The final beam shapes are shown for the charged mode in Figure 75 and for the neutral beam in Figure 76.

7.3 Decays and Interactions

7.3.1 Particle Decays

For all of the decay modes we have studied, we have simulated the dynamics of the decays at as detailed a level as we could. For example, in the Ke3 decays, the time dependent charge asymmetry for the given K_S and K_L amplitudes is used to decide whether the final state will be $\pi^+e^-\bar{\nu}_e$ or $\pi^-e^+\nu_e$:

$$\delta\tau = \frac{R(\pi^- e^+ \nu) - R(\pi^+ e^- \bar{\nu})}{R(\pi^- e^+ \nu) + R(\pi^+ e^- \bar{\nu})}, \tag{7.10}$$

with the decay probabilities R given in terms of the K_S and K_L amplitudes $a_S(\tau)$ and $a_L(\tau)$ by

$$\begin{aligned} R(\pi^- e^+ \nu) &= \frac{|1+\varepsilon|^2}{2(1+|\varepsilon|^2)} |a_S(\tau) + a_L(\tau)|^2 \\ R(\pi^+ e^- \bar{\nu}) &= \frac{|1-\varepsilon|^2}{2(1+|\varepsilon|^2)} |a_S(\tau) - a_L(\tau)|^2. \end{aligned} \tag{7.11}$$

The form factor governing this decay is also included. Similarly, the decay probabilities for the $\pi\pi$ and $\pi\pi\pi$ decays also included the CP–violating amplitudes,

$$\begin{aligned} R(\pi\pi) &= |a_S(\tau) + \eta a_L(\tau)|^2 \\ R(\pi\pi\pi) &= |\eta a_S(\tau) - a_L(\tau)|^2. \end{aligned} \tag{7.12}$$

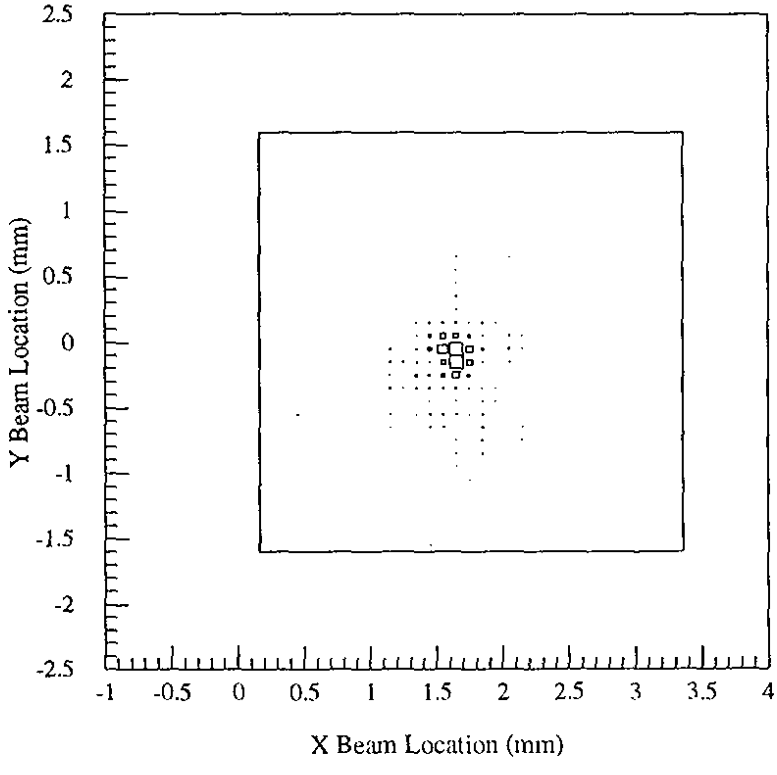

Figure 74. The measured motion of the mean beam position on the target over the course of data taking for the C3 $\pi^+\pi^-$ subset. The size of each box is proportional to the fraction of data collected with the beam at this position. For reference, the target outline is shown as the superimposed square.

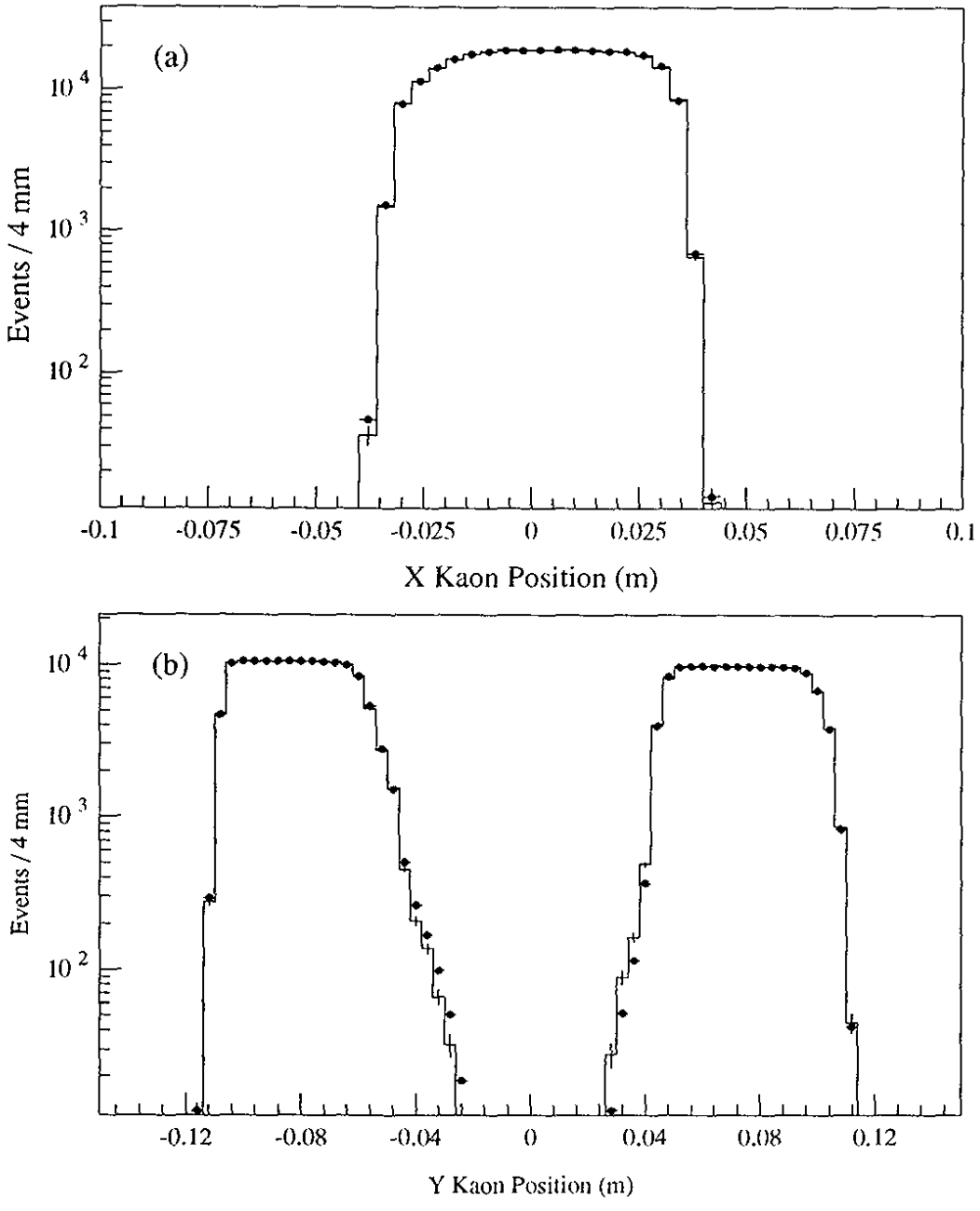

Figure 75. The projection of the kaon trajectory to the regenerator position for all $\pi^+\pi^-$ decays collected from the vacuum beam. The x projection is shown in (a), and the y position in (b). The Monte Carlo simulation (solid circles) has been overlaid on top of the data distribution (histogram).

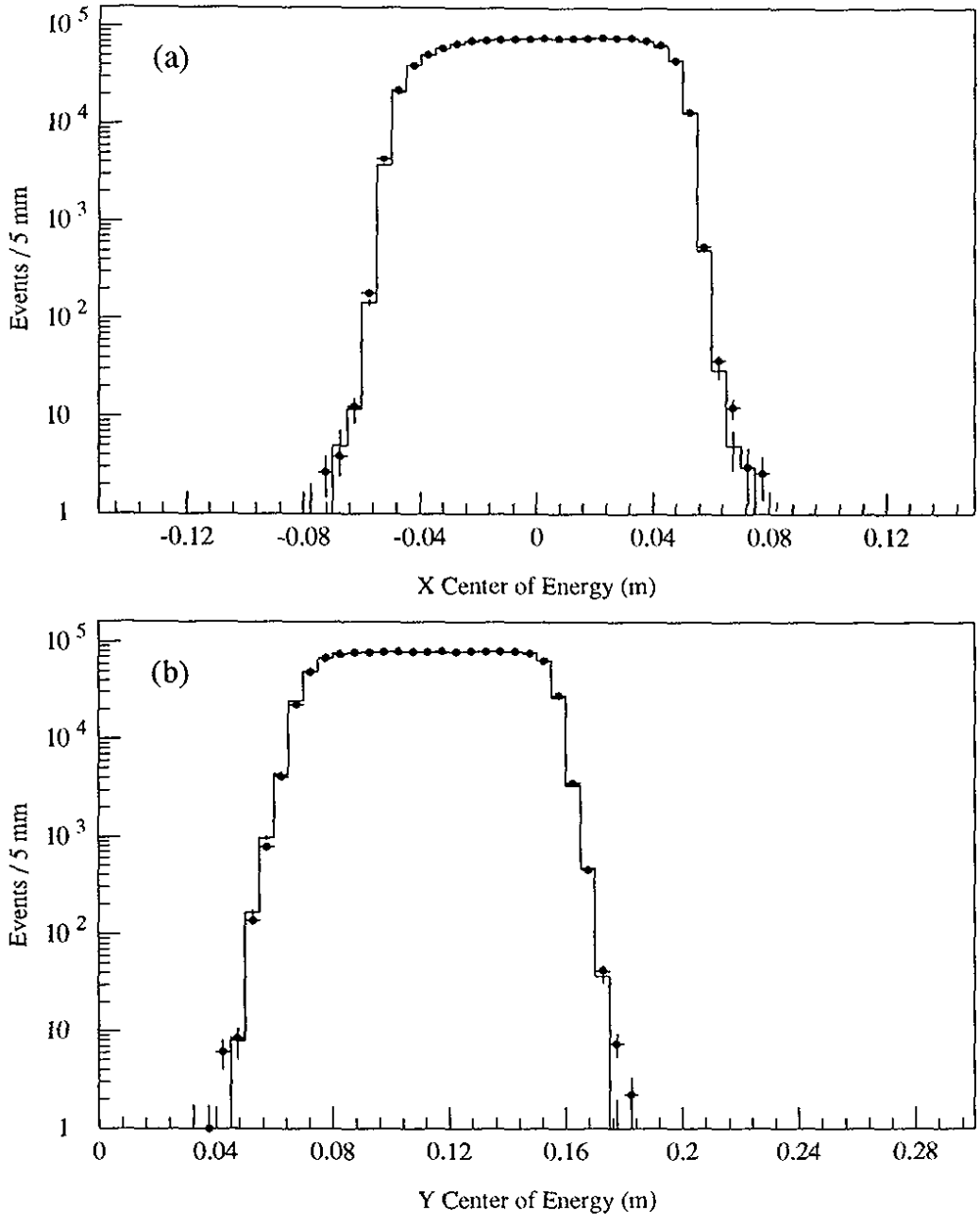

Figure 76. The center of energy distribution measured in the lead glass calorimeter for all $3\pi^0$ decays collected from the vacuum beam. The x projection is shown in (a), and the y position in (b). The Monte Carlo simulation (solid circles) has been overlaid on top of the data distribution (histogram).

Table 15. Scattering and photon conversion sites and the thickness of each site in radiation lengths.

Detector Element	Location (m from Target)	Thickness (Radiation Lengths)
V hodoscope	137.792	3.23×10^{-3}
Pb sheet[a]	137.804	9.36×10^{-2}
T hodoscope	137.815	3.43×10^{-3}
Vacuum Window	158.965	2.50×10^{-3}
Drift Chamber 1	159.292	3.42×10^{-3}
Drift Chamber 2	165.867	3.86×10^{-3}
Drift Chamber 3	171.857	3.63×10^{-3}
Drift Chamber 4	178.004	2.10×10^{-3}
Chamber Field Wires[b]	—	5.70×10^{-3}
Chamber Sense Wires[c]	—	6.43×10^{-3}
C Hodoscope	179.502	4.0×10^{-2}
B Hodoscope	179.520	4.0×10^{-2}

[a]Used only in some $2\pi^0$ subsets. Average radiation length is listed.

[b]This contribution is identical in all four chambers. Only the 9.9% of the tracks which hit these wires (per chamber) see this contribution.

[c]This contribution is identical in all four chambers. Only the 0.7% of the tracks which hit these wires (per chamber) see this contribution.

for at least one of the four photons to convert at the HDRA, f_v (f_r) is the fraction of $2\pi^0$ decays upstream of the HDRA in the vacuum (regenerator) beam, and there is a bias of Δ in the conversion probability in the Monte Carlo ($c_{MC} = c[1+\Delta]$), then the bias introduced into the vacuum to regenerator beam ratio R_{00} will be

$$R_{00} \rightarrow R_{00}\left\{1 + (f_r - f_v)\frac{c}{1-c}\Delta\right\}. \tag{7.13}$$

Had we accepted only decays from upstream of the HDRA, we would have had $f_r = f_v = 1$ and the photon conversions would not have affected R_{00} whether the photon conversion probability were correct or not.

To estimate our sensitivity to the material at the HDRA plane, consider f_r and f_v for

the decay volume we use, which are 92% and 66%, respectively. The lead sheet causes by far the most conversions; 23.7% of the $K \rightarrow \pi^0\pi^0$ decays upstream of the Pb sheet will have at least one conversion. Only 2% of the decays suffer a conversion due to the rest of the material. Since the lead sheet was present for only 65% of the data taking, the average probability for one or more conversion is 17.1%. A mismeasurement Δ in the conversion probability would therefore bias R_{00} by 0.054Δ. To keep the bias in $Re(\varepsilon'/\varepsilon)$ under 10^{-4}, we therefore have to keep $\Delta < 1.1\%$. As we will discuss in Section 10.4, we have achieved this using a combination of direct measurement of the sheet over its entire surface, and by measuring the step in the $3\pi^0$ z distribution at the HDRA induced by photon conversion in the lead sheet. The Monte Carlo simulation included both the measured variation in the lead sheet thickness and the complete energy dependence of the photon cross section in lead calculated by Hubbell, Gimm, and Øverbø[91].

A more subtle way of biasing the average value of c for the HDRA would be to have the incorrect ratio of simulated $2\pi^0$ decays with and without the lead sheet present. To prevent such a bias from creeping into the analysis, the $2\pi^0$ subsets with and without the sheet are always treated as two independent data sets when predicting the expected number of events in the fits for $Re(\varepsilon'/\varepsilon)$ and the other parameters.

For charged particles, such as the pions from $\pi^+\pi^-$ decays or the electrons from Ke3 decays and photon conversions, the multiple scattering process was fully implemented with a parametrization that included the nongaussian tail due to hard scattering. In addition, the charged particles could emit a bremsstrahlung photon at the various scattering sites.

7.3.3 Limiting Apertures

In general, the trajectories of the decay products from both $\pi^+\pi^-$ and $2\pi^0$ decays which satisfy the trigger are well contained within the detector. Only a small fraction of the daughter particles approach the edges of the few defining apertures, which keeps the sensitivity of $Re(\varepsilon'/\varepsilon)$ to the exact aperture locations low. Furthermore, the fractional loss of events near the edge of an aperture is generally compensated twice in the measurement of $Re(\varepsilon'/\varepsilon)$, once in the vacuum to regenerator beam ratio and again when comparing the

$\pi^+\pi^-$ mode to the $2\pi^0$ mode. To ensure that the biases would be minimal, however, we endeavored to measure the effective aperture edges as precisely as possible. To determine the physical edge, we have used the large sample of electrons from Ke3 decays. While direct physical measurement (*ie.*, with a precise rule) might give a more accurate, detailed map of edge, this is not necessarily what we need. The combination of the finite thickness of the apertures in z with the trajectories of the particles being close to, but not precisely parallel with z can lead to a shift of the effective edge. Particles can nick the edges without necessarily being stopped. As we will see, we were particularly insensitive to small motions of th apertures in time, and it was sufficient to determine the average location of each aperture for each data subset.

The components of the detector serving to limit the acceptance were the active mask, the HDRA, the vacuum window aperture, and the collar anti. The limiting apertures were first tuned in size and location (x and y only) by comparing illuminations[1] of electrons from Ke3 decays in a portion of the NC subset to those from simulated decays for that subset. After this initial tuning, the sizes of the apertures were fixed in the Monte Carlo. The location of the apertures were then tracked by directly comparing the Ke3 data from different subsets to the reference portion of the NC subset. The z positions of the apertures were measured directly in a survey at the completion of the run.

The event by event resolution of the track projection depended on how far the aperture being illuminated was located from the chamber system. For the aperture farthest upstream, the mask anticounter, the resolution for the x or y projection was of order 1.2 mm for a typical track, with 600 microns from chamber resolution and about 1 mm coming from multiple scattering. For the collar anti, which was quite close to the downstream most chamber, the resolution was closer to 220 microns, with approximately equal contributions from chamber resolution and scattering in the B and C hodoscopes. These two apertures, at the two extremes of the resolution, were the apertures to which $Re(\varepsilon'/\varepsilon)$ was most sensitive, though this sensitivity was small (see Section 10.3.1). The Ke3 electron illumination at one

[1]The illumination of an aperture upstream of the analysis magnet is made by projecting the upstream track segments measured in the drift chamber for a particle (or particles) of a decay which occurred upstream of the aperture. For an aperture downstream of the magnet, the downstream segment is projected.

edge of each of these two apertures after a reasonable adjustment, but before the final adjustment, is shown in Figure 77.

From the illuminations plotted, it is clear that a final adjustment is needed in both cases. The needed adjustment might be estimated reliably for the Collar Anti directly from the illumination plots, since the track projection resolution is quite good. It is clear, though, that estimating the edge adjustment for the mask to better than several hundred microns

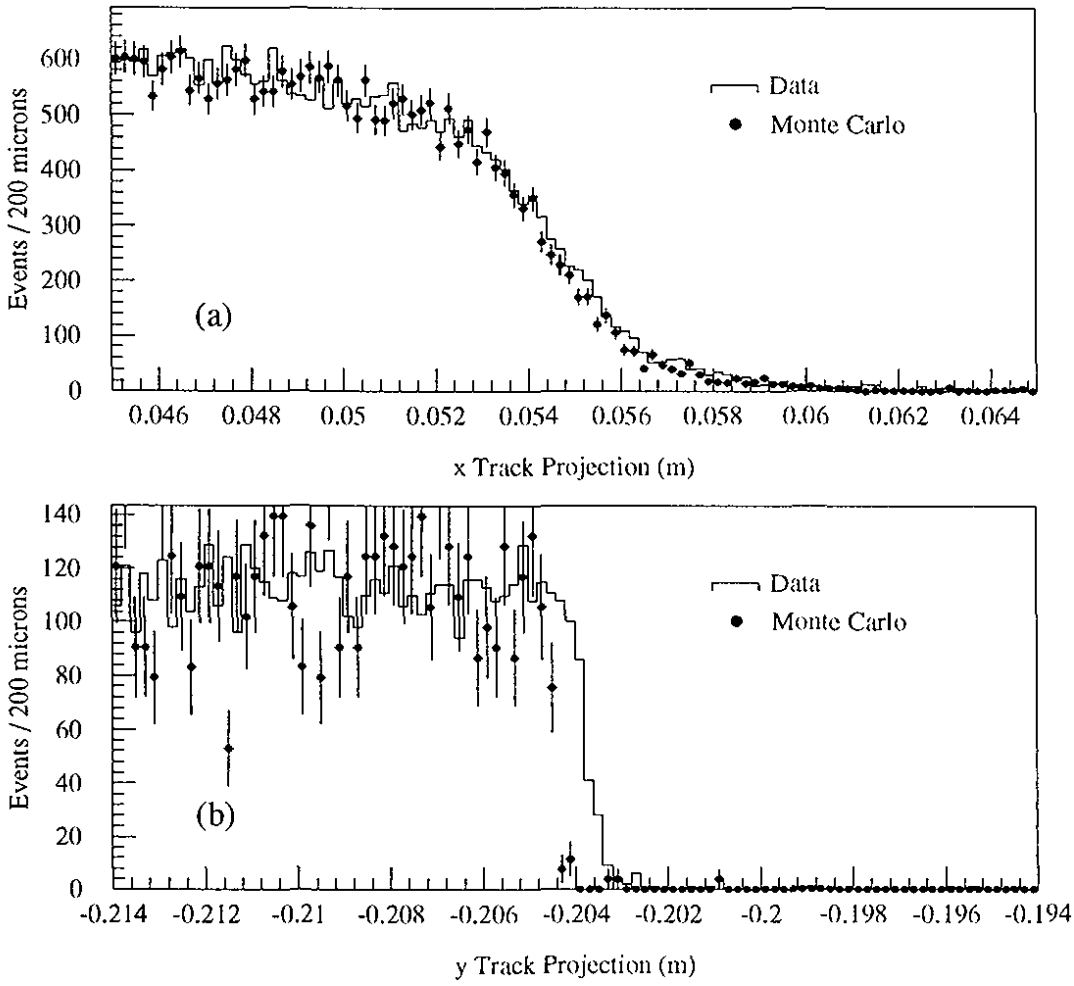

Figure 77. Illumination of two of the aperture edges by electrons from Ke3 decays in the NC subset. The histogram shows the data illumination, while the dots show the MC prediction before the final tuning of the aperture positions. (a) Horizontal edge of the active mask. (b) East half of the bottom edge of the Collar Anti surrounding the lower beam. These edges showed the largest misalignment of their respective apertures before the final position adjustment. The mask edge is shifted about 230 microns, and the Collar Anti edge by about 700 microns.

would be difficult. To determine the relative positions of an edge in data and Monte Carlo for a given aperture, we instead make use of the χ^2 distribution for the agreement between the data and Monte Carlo illuminations near that edge. The Monte Carlo illumination of an edge is shifted in 100 micron steps relative to that in the data, and a χ^2 for the data and Monte Carlo illuminations to come from the same parent distribution is calculated.

When the illumination is plotted with a binning that is small relative the single event resolution, and when a shift between the illuminated edge in data and in the Monte Carlo simulation is also small on that scale, the χ^2 depends quadratically on the shift. For the Mask edge illumination pictured in Figure 77, this quadratic behavior is clear in the plot of χ^2 versus shift in Figure 78. The reduced χ^2 (χ^2 per degree of freedom) has been plotted since the number of degrees of freedom can change as bins in the data (Monte Carlo) histogram move beyond the window of illumination in the Monte Carlo (data). When the shift is much larger than the resolution, the χ^2 behavior enters a linear regime.

The shifts of the Monte Carlo relative the reference data subset, and of different data

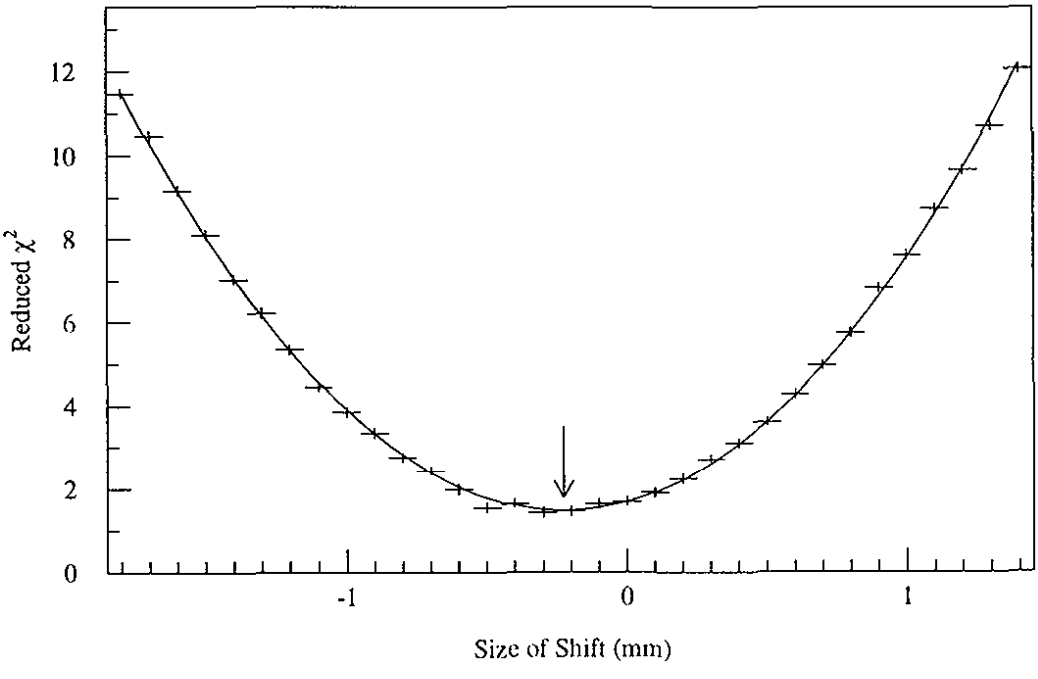

Figure 78. Distribution of the reduced χ^2 for the data and Monte Carlo $+x$ Mask edge illuminations to come from the same parent distribution versus the Monte Carlo shift. The curve is the best fit quadratic, and the arrow indicates the minimum at -226 ± 7 microns.

sets relative the reference subset, have been determined for each edge by fitting to the χ^2 distribution in the quadratic regime. The shift is located at the point of minimum χ^2. The statistical errors on the shifts located in this fashion were under 10 microns for the Mask and the Collar Anti. The errors were consistent with a precision of $\sigma/\sqrt{N}$, with σ the track projection resolution, and N the number of events in the window of illumination around the edge of the aperture. The better track resolution at the Collar Anti compensated for the lower density of events near that aperture's edge. This procedure relies on the shape of the illumination in the Monte Carlo agreeing with the data shape. Because of the work on the beam shapes and because all of the apertures were generally within 200 microns of their final tuning, this assumption was quite good. To evaluate the systematic uncertainty, however, this procedure was repeated with windows of different sizes around each edge, with different ranges of fits in the quadratic regime, and by fitting to the expected linear behavior farther from the edge rather than to the quadratic behavior near the edge. From these studies, we have limited the uncertainty on each measured edge to under 50 microns.

This systematic error does not include the position uncertainty from the chamber alignment. This uncertainty cancels in determining the *size* of the aperture, since the bias is identical for all edges of the aperture and will cancel when looking at the difference between the left and right or top and bottom edges of an aperture. It enters only when tracking the edges as a function of time. As we will discuss in Section 10.3.1, there is an additional uncertainty of 60 microns from chamber alignment for each measurement of the Mask shift, but only 15 microns for the Collar Anti.

The time dependent shifts measured for the Mask and the Collar Anti are plotted in Figure 79. The collar anti position was stable relative our global coordinate system, as we would expect since it is rigidly attached to the lead glass, which defines one end of the coordinate system. The mask, however, appears to have drifted on the order of 800 microns in y and 600 microns in x over the course of the run. It turns out that this is an artifact of tying our global coordinate system to the target. The entire target pile was sinking over the course of the run, dropping several millimeters at the target location. If an aperture is located at z_a, the target at $z_t = 0$, and the lead glass at $z = z_{PbG}$, then an aperture will appear to be shifted by $s_a = (1 - z_a/z_{PbG})s_t$, where s_t is the target motion. The apparent

shift of the mask, the other apertures, and the collimators are all consistent with the target pile motion.

After all the tunings based on the Ke3, it is interesting to compare the illuminations of some of the apertures in $\pi^+\pi^-$ and $2\pi^0$ decays. For $\pi^+\pi^-$ decays, the appropriate track segments are projected to the aperture just as the electron tracks were projected in Ke3 decays. Projecting the photons in $2\pi^0$ decays is somewhat more complicated, because we do not directly measure the photon trajectories or the transverse coordinates of the decay vertex. We can infer the x and y coordinates of the decays by projecting the position of the center of energy measured in the lead glass calorimeter back to the z of the vertex along the line of sight between the target and the center of energy. The photon can then be projected to the z of an aperture along the line connecting the measured cluster position and the deduced vertex position. More precisely, the x projection x_p of a photon to an aperture located at z_a is given by

$$x_p = x_v + \frac{z_a - z_v}{z_{PbG} - z_v}(x_{PbG} - x_v), \tag{7.14}$$

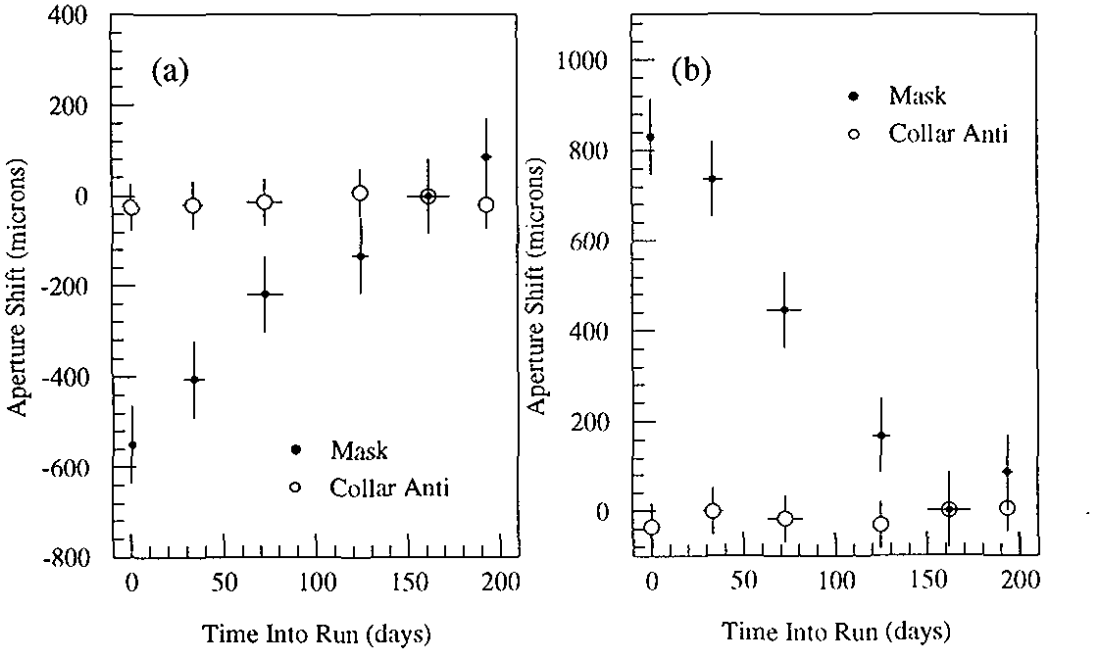

Figure 79. Apparent motion of the Collar Anti and Mask apertures with time. (a) Horizontal motion. (b) Vertical motion. The shifts are measured relative to th NCa subset (fifth data point).

where z_{PbG} and x_{PbG} are the cluster coordinates, and z_v is the z of the decay vertex. The x position of the vertex is

$$x_v = x_t + \frac{z_v}{z_{PbG}}(x_{CE} - x_t), \tag{7.15}$$

with x_{CE} the x coordinate of the center of energy and x_t that of the target. This procedure is fine for $2\pi^0$ decays of coherent kaons, but the backgrounds can somewhat distort the illuminations. We have therefore included the expected background contributions to the "Monte Carlo" predictions in the overlays presented.

The mask illuminations for the two decay modes are shown in Figure 80 (the x view) and Figure 81 (the y view). Only the vacuum beam illuminates the mask. Overall, the agreement is excellent in both modes except for the small excess in the simulation over the data at the $-x$ edge in the neutral mode. This mismatch is consistent with a small mismatch in the $2\pi^0$ beam shape at that edge. What if we were to attribute this mismatch to a badly measured edge of the mask? Since the $+x$ edge agreement is excellent, the size of the mask would have to be wrong, in this case by about 650 microns. Since the same size mask is used in all of the data sets, and the agreement in the $\pi^+\pi^-$ mode is excellent, this is unlikely. The mismatch also starts to farther away from the edge than we would expect for a shift of this size. However, we can march along and assume that the edge is off to get a feeling for the sensitivity of $Re(\varepsilon'/\varepsilon)$ to this aperture. From Monte Carlo studies, we know that a mismatch of 650 microns at one edge would shift the vacuum to regenerator beam ratio after acceptance corrections by -0.030%, and hence bias $Re(\varepsilon'/\varepsilon)$ by -0.50×10^{-4}.

The vacuum and regenerator beam illuminations at the HDRA are shown in Figures 82 and 83 for the x and y views, respectively. Finally, the illuminations at the lead glass are pictured in Figures 84 and 85 for the x and y views. For the latter plot, the measured photon cluster positions are plotted directly — the somewhat jagged structure is due to a small bias towards the center of a lead glass block in the cluster position reconstruction algorithm.

With the apertures under control, the "outer" acceptance has been defined. It is now time to examine our modelling of the response of the detector elements, which determines the "inner" acceptance of the detector.

7.4 Detector Response

In simulating the response of the detector, we had to satisfy two somewhat incompatible needs. The response has to be simulated well enough that the smearing of events past momentum and z bin boundaries is mimicked well. The most optimal simulation would involve use of one of the detailed packages for propagating each decay particle through the detector. On the other hand, we required large event samples, both to keep the "statistical" uncertainty from the acceptance correction minimal and to have sufficient sensitivity to small biases when shaking down the simulation package. To obtain these large Monte Carlo samples in a reasonable period[2], we had to simulate events rapidly. The following sections will describe the resulting compromise between these two requirements.

[2]The $3\pi^0$ background simulation still took 3 months with 25 dedicated IBM RS6000 processors to generate the 6×10^9 $K \to 3\pi^0$ decays!

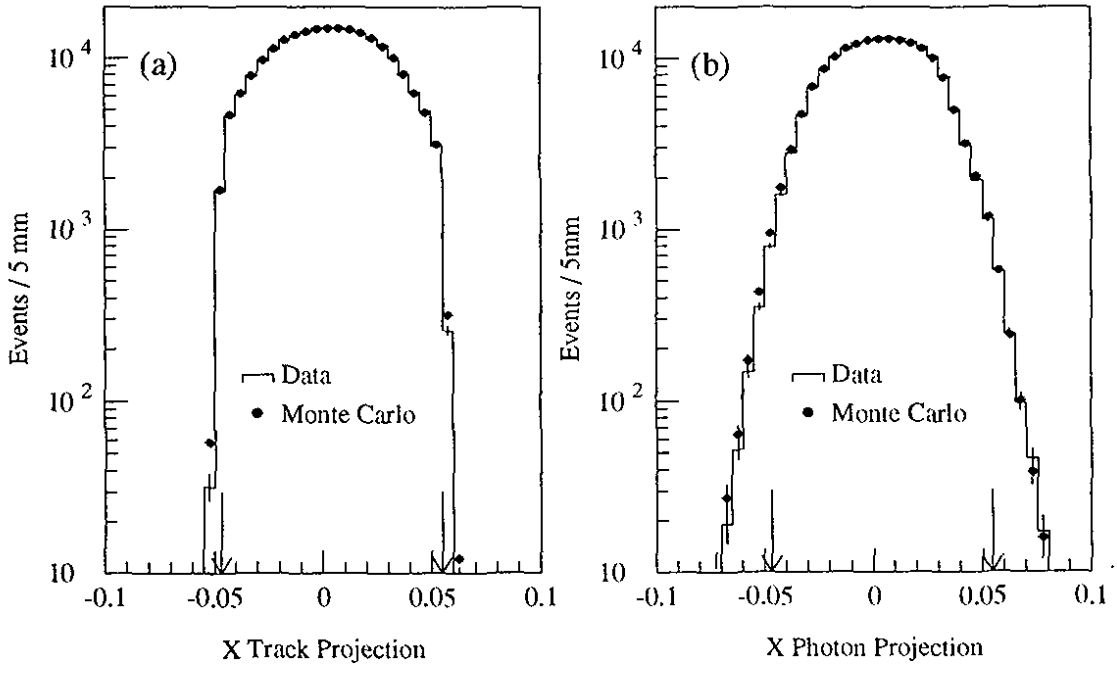

Figure 80. Vacuum beam $\pi^+\pi^-$ track illumination and $2\pi^0$ photon illumination in the x view at the plane of the active mask for data and Monte Carlo simulation. (a) $\pi^+\pi^-$ track projection. (b) $2\pi^0$ photon projection. The arrows indicate the locations of the mask edges.

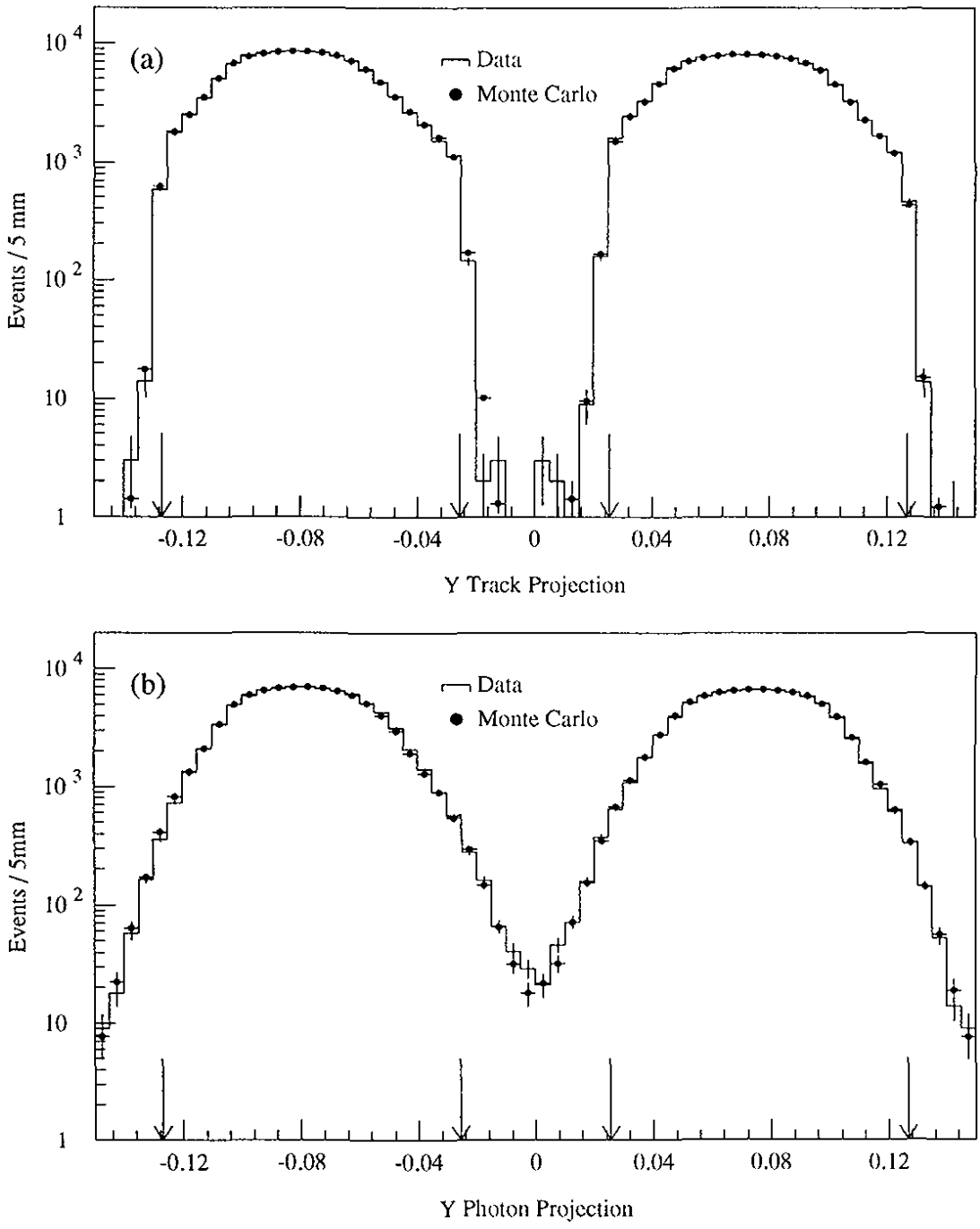

Figure 81. Vacuum beam $\pi^+\pi^-$ track illumination and $2\pi^0$ photon illumination in the y view at the plane of the active mask for data and Monte Carlo simulation. (a) $\pi^+\pi^-$ track projection. (b) $2\pi^0$ photon projection. The arrows indicate the locations of the mask edges. Only the vacuum beam illuminations are shown.

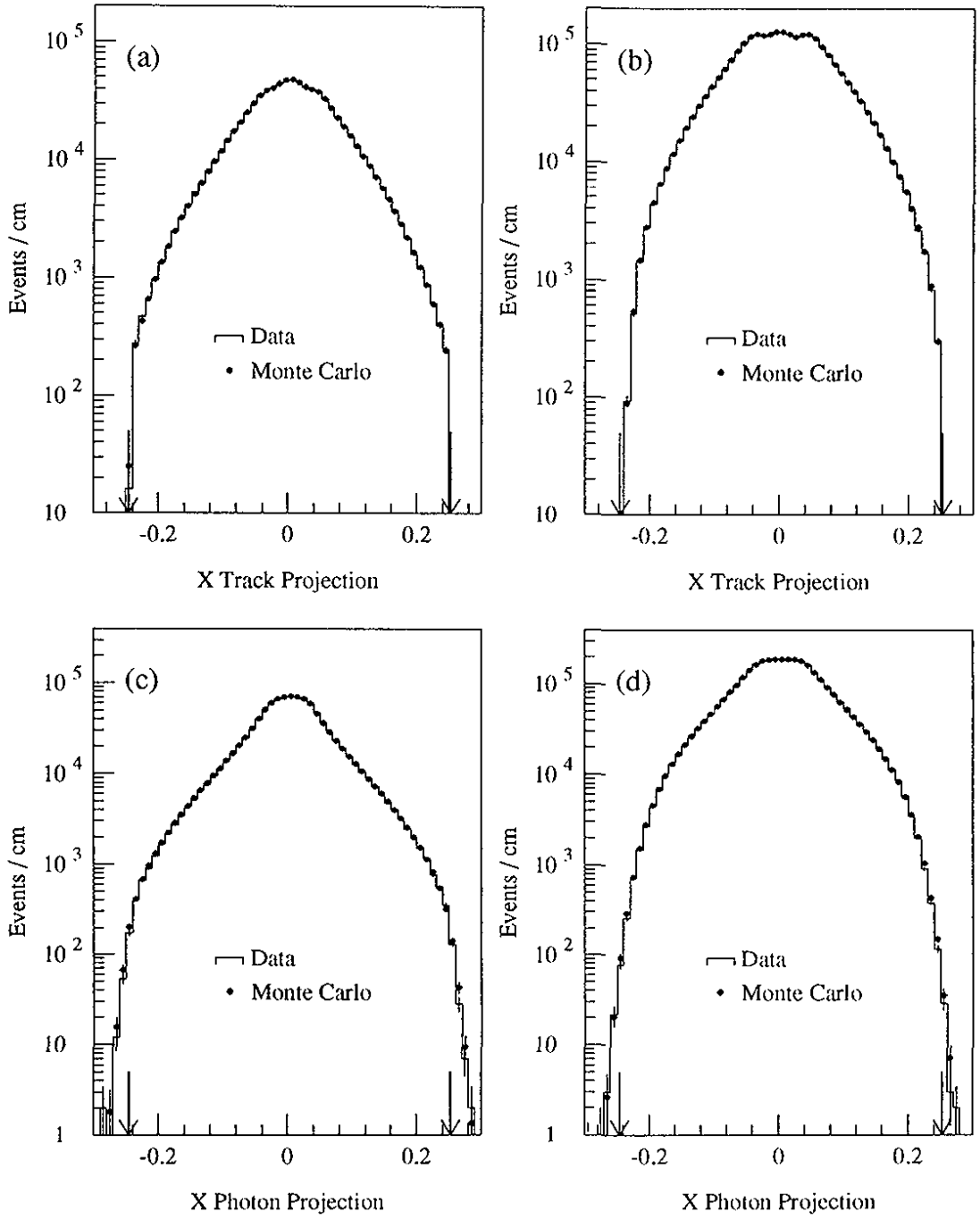

Figure 82. $\pi^+\pi^-$ track illumination and $2\pi^0$ photon illumination in the x view at the plane of the HDRA for data and Monte Carlo simulation. (a) Vacuum beam $\pi^+\pi^-$ track projection. (b) Regenerator beam $\pi^+\pi^-$ track projection. (c) Vacuum beam $2\pi^0$ photon projection. (d) Regenerator beam $2\pi^0$ photon projection. The arrows indicate the locations of the HDRA edges.

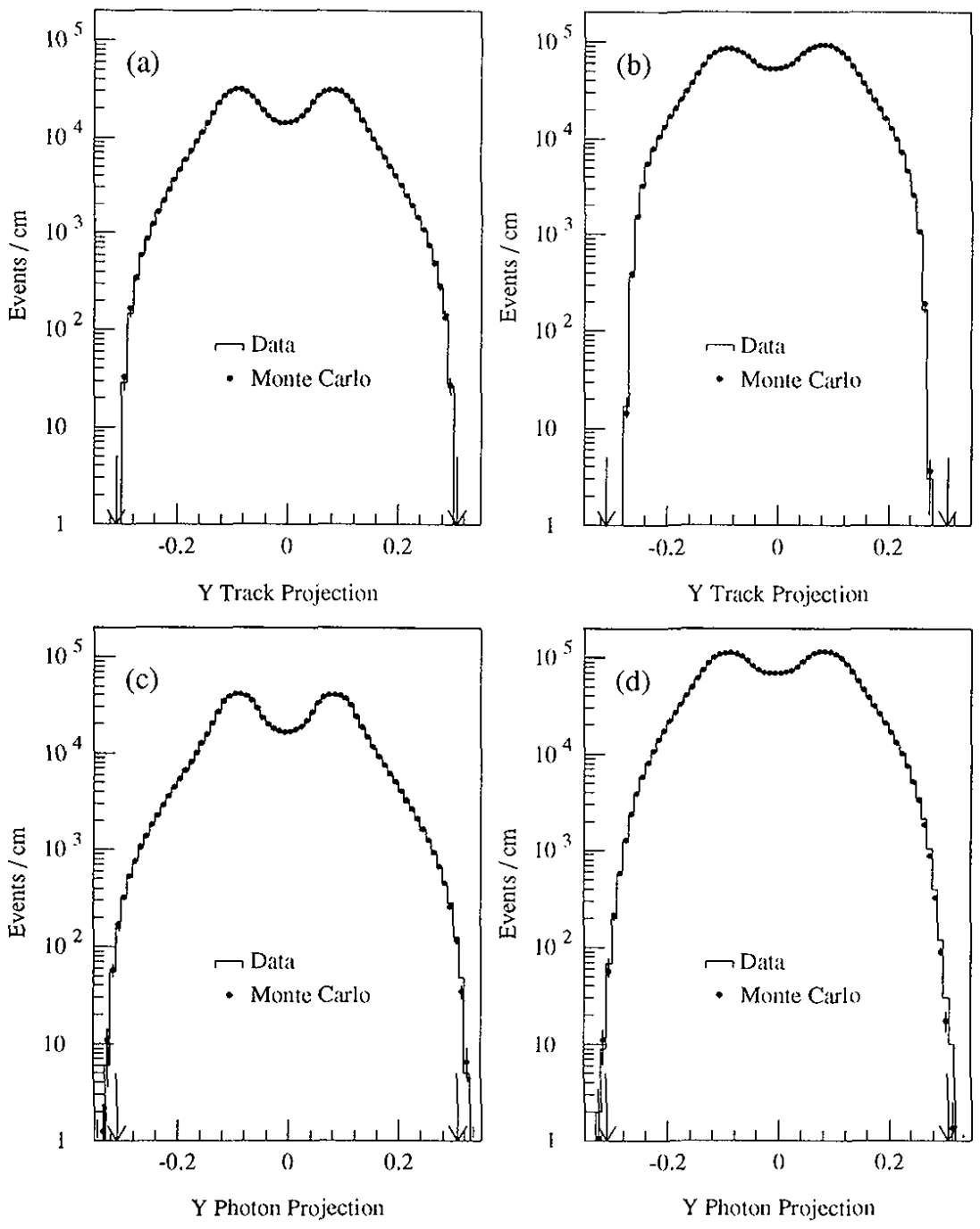

Figure 83. $\pi^+\pi^-$ track illumination and $2\pi^0$ photon illumination in the y view at the plane of the HDRA for data and Monte Carlo simulation. (a) Vacuum beam $\pi^+\pi^-$ track projection. (b) Regenerator beam $\pi^+\pi^-$ track projection. (c) Vacuum beam $2\pi^0$ photon projection. (d) Regenerator beam $2\pi^0$ photon projection. The arrows indicate the locations of the HDRA edges.

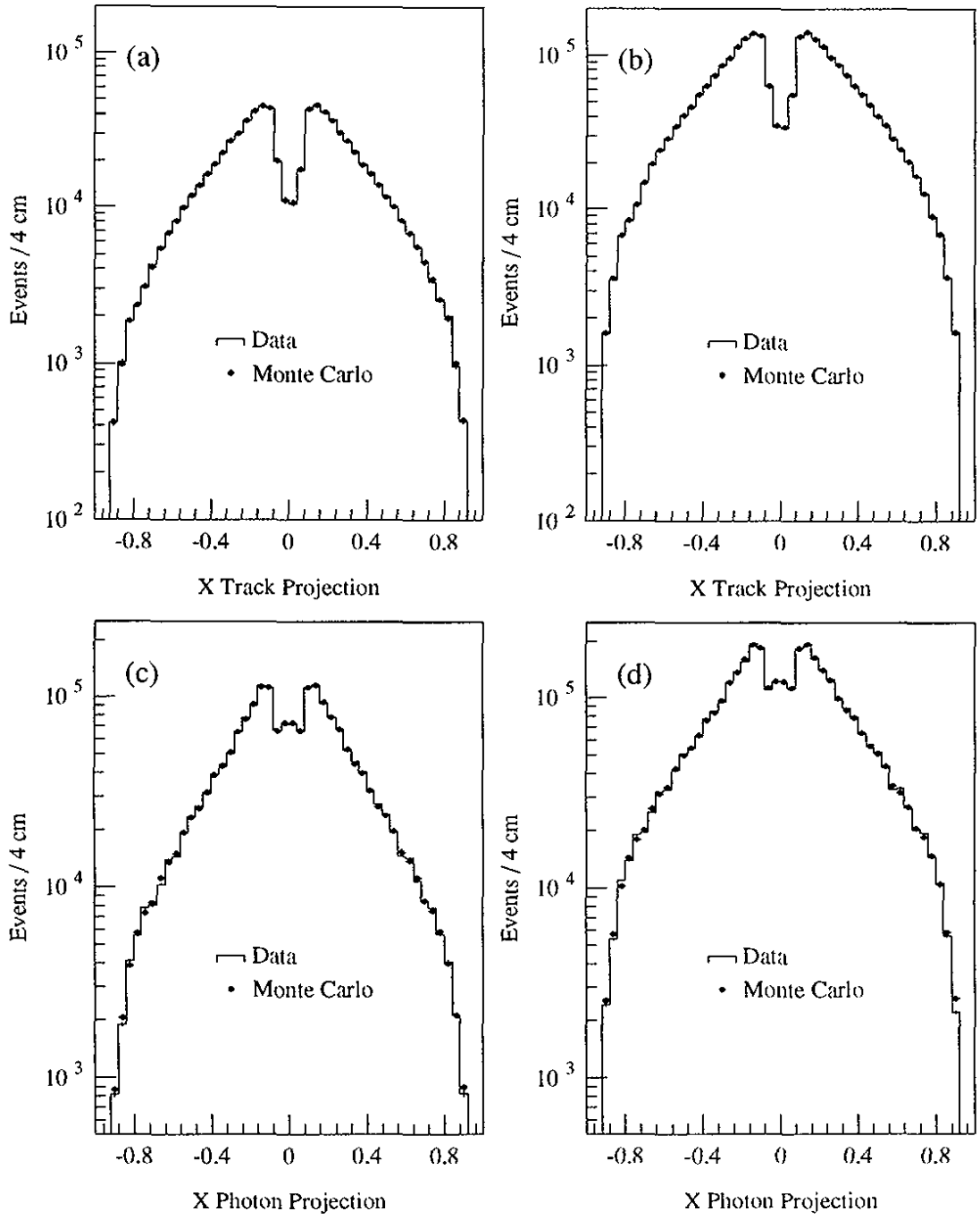

Figure 84. $\pi^+\pi^-$ track illumination and $2\pi^0$ photon illumination in the x view at the plane of the lead glass for data and Monte Carlo simulation. (a) Vacuum beam $\pi^+\pi^-$ track projection. (b) Regenerator beam $\pi^+\pi^-$ track projection. (c) Vacuum beam $2\pi^0$ photon position. (d) Regenerator beam $2\pi^0$ photon position.

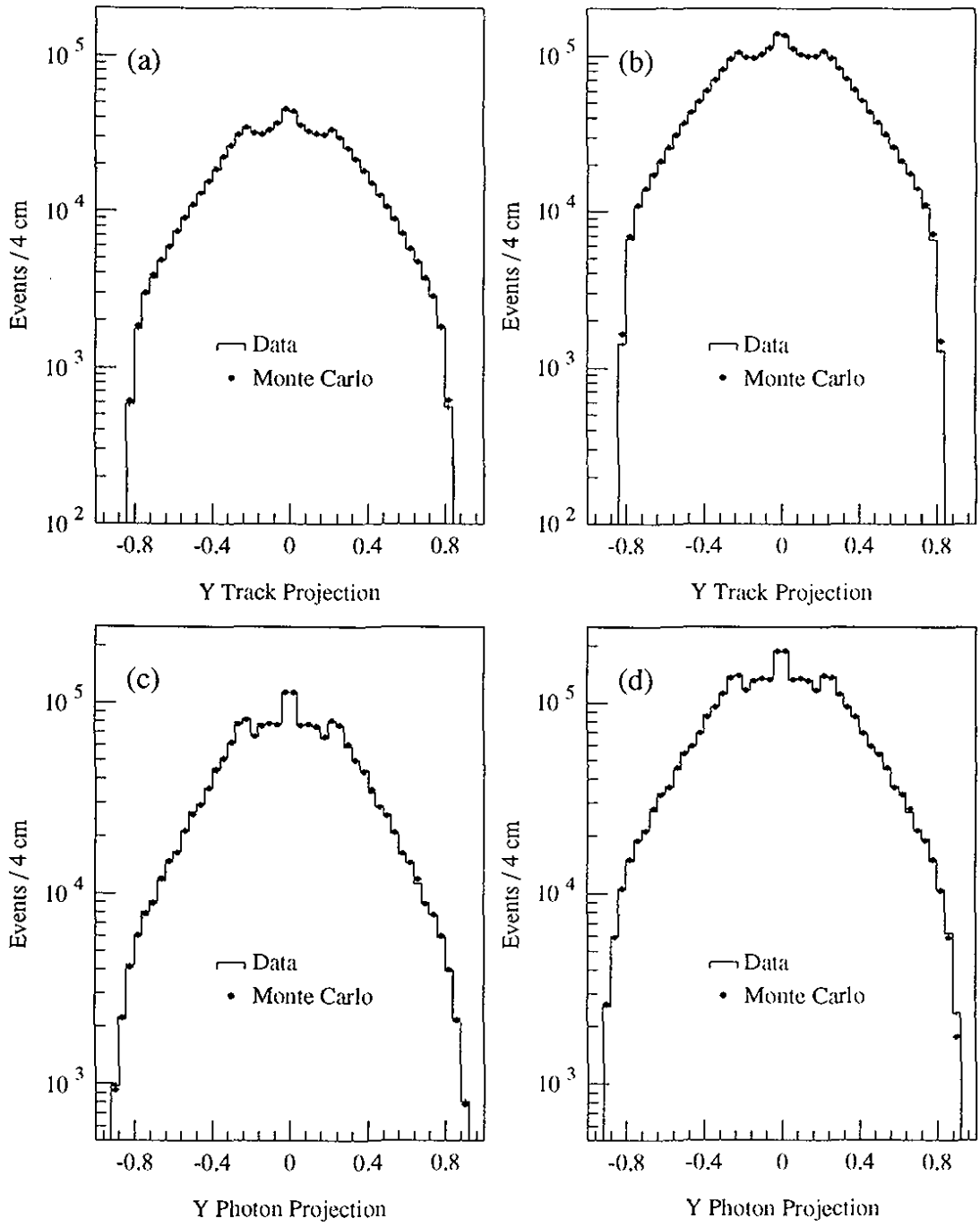

Figure 85. $\pi^+\pi^-$ track illumination and $2\pi^0$ photon illumination in the y view at the plane of the lead glass for data and Monte Carlo simulation. (a) Vacuum beam $\pi^+\pi^-$ track projection. (b) Regenerator beam $\pi^+\pi^-$ track projection. (c) Vacuum beam $2\pi^0$ photon position. (d) Regenerator beam $2\pi^0$ photon position.

7.4.1 Simulation of the Lead Glass Response

For each electron or photon which strikes the lead glass calorimeter, we do not simulate a complete electromagnetic shower as this would be far too time consuming. The response of the lead glass was instead parametrized as a function of electron energy, Çerenkov light absorption coefficient α (see Section 4.2), and, when applicable, the photon conversion depth based on a standalone study of lead glass using the EGS4 [84] shower simulation package. The model for the attenuation length has been described in some detail in Section 4.2.1, and in great detail in the Ph.D. thesis of Ritchie Patterson [74]. The details of the EGS cluster generation can also be found in reference [74]. Only a brief recap will be presented here.

7.4.1.1 Parametrization of the lead glass response to electrons

The response of the lead glass to electrons was modelled by assuming that the absorption of Çerenkov light is uniform through the length of the block. We have calibrated with this assumption, and from each electron calibration we have extracted an average absorption coefficient α (typically 3% to 4% per radiation length) for each block. Using the EGS4 package, a large sample of electron showers was generated with incident electron energies E_i ranging from 0.25 GeV to 90.51 GeV. We expect the variations in response of the lead glass to be dominated by the depth t_{max} of the maximal energy deposition. In turn, t_{max} depends logarithmically on E_i [92, 83], and we therefore generated showers with energies spaced uniformly in lnE_i over this energy range. For each shower, the track length of each charged particle was weighted by the number of Çerenkov photons that the particle would radiate, $N_c = 1 - 1/n^2\beta^2$, where n is the index of refraction of the lead glass. The sum of the total weighted track length was then recorded in cells measuring $0.36 \times 0.36 \times 0.5$ radiation lengths[3]. The cells covered a volume 30 radiation lengths deep and 7×7 block widths transversely.

For each generated electron shower, the Çerenkov light within each cell was attenuated using a given absorption coefficient to the back of a block of a given length. The response

[3]For reference, our crystals measure $1.8 \times 1.8 \times 18.7$ radiation lengths

of the block to that shower was defined by the ratio of the total Çerenkov light reaching the back of the block to the total Çerenkov light produced. For each shower we calculated the response using a set of attenuation coefficients which spanned the range of coefficients measured in the various electron calibrations. For the modelling of photons, it was also useful to calculate the response for blocks of different lengths. As discussed in Section 4.2.1, we treat a photon by having it first convert at a depth t_0 within the block, and then treat the photon showers as 2 independent electron showers in a block of length $18.7 - t_0$ radiation lengths.

The response of a block to each electron shower of a certain energy E_i was then accumulated for each pair of absorption coefficient and block length parameters. Based on the observed distribution of responses to the EGS showers, we parametrized the block response with a simple functional form in terms of the absorption coefficient, the incident electron energy, and conversion depth (if the electron was from photon which converted inside the glass block). In our Monte Carlo simulation, we then randomly generated a response to an incident electron distributed according to our parametrization.

For our initial result [74, 50] based on the NC subset, the responses were parametrized by a simple Gaussian using the means and RMS widths of the shower distributions. Unfortunately, there are sizable tails in many of the response distributions: tails on the high side from showers which fluctuate deeper into the block and hence have less attenuation of the Çerenkov radiation, and in the shorter blocks, tails on the low side from showers which lose too many of the charged particles out of the back of the block. From studies with electrons from Ke3 decays, we found that this parametrization resulted in somewhat poorer average resolution in the Monte Carlo than we observed in the data because the tails had inflated the RMS width.

For the current simulation, we have incorporated the tails explicitly into the parametrization. For each distribution of shower responses, we first fit using a Gaussian parametrization. If over 1.25% of the distribution fell higher (lower) than 2.5 times the width of this Gaussian, then a high (low) side tail was added to the parametrization. If one or both tails were needed, the distribution was refit simultaneously to the sum of the Gaussian+tail(s). The parametrization for the high side tail we used was

$$\frac{dN}{df} = \begin{cases} \gamma(f - f_0)e^{-\beta(f-f_0)}, & f > f_0 \\ 0, & f < f_0 \end{cases} . \tag{7.16}$$

Here, f is the response, and f_0, β, and γ were parameters for each of the distributions. We used an analogous parametrization for the low side tail. This parametrization was very successful over the range of absorption coefficients, block lengths and energies of interest. A handful of response distributions for different energies, attenuation coefficients, and block lengths are plotted in Figure 86. The absorption coefficients plotted span the range into which the majority of the coefficients measured in our blocks fall. The parametrization works quite well in all cases, accurately mocking up the tails where present.

The fits generally resulted in a smooth variation of the parameters as a function of the absorption coefficient and block length. The variation of the Gaussian mean and width, the two parameters which still characterize the bulk of the response, is shown for two different energies in Figure 87, after some smoothing of the fluctuations in the fit parameters were made. Most of the parameters could be easily fit to a simple function of the absorption coefficient and block length. For those with a more complicated behavior, we interpolated linearly between the fit parameters. For electron energies E between the EGS shower energies, the parameters were interpolated linearly in $\ln E$.

To simulate the response to an incident electron, or to an electron from a photon conversion, the Monte Carlo first obtains the parametrization of the three response regions — central Gaussian, high side tail, or low side tail — based on the electron energy, the struck block's absorption coefficient, and the photon conversion depth. The simulation then decides randomly in which of the three regions to generate the response based on the relative areas in the three regions for this set of parameters. Once the region is chosen, the electron response can be generated randomly using the distribution given by that region's parametrization. For all practical purposes, this recipe gives the total number of Çerenkov photons reaching the phototube for this electron.

The above recipe parametrizes the smearing of the calorimeter response due to electromagnetic shower fluctuations. Additional smearing occurs due to random fluctuations in the number of photoelectrons liberated from the photocathode. For the phototube on each block, we have extracted the number of photoelectrons per ADC count for each of the 804

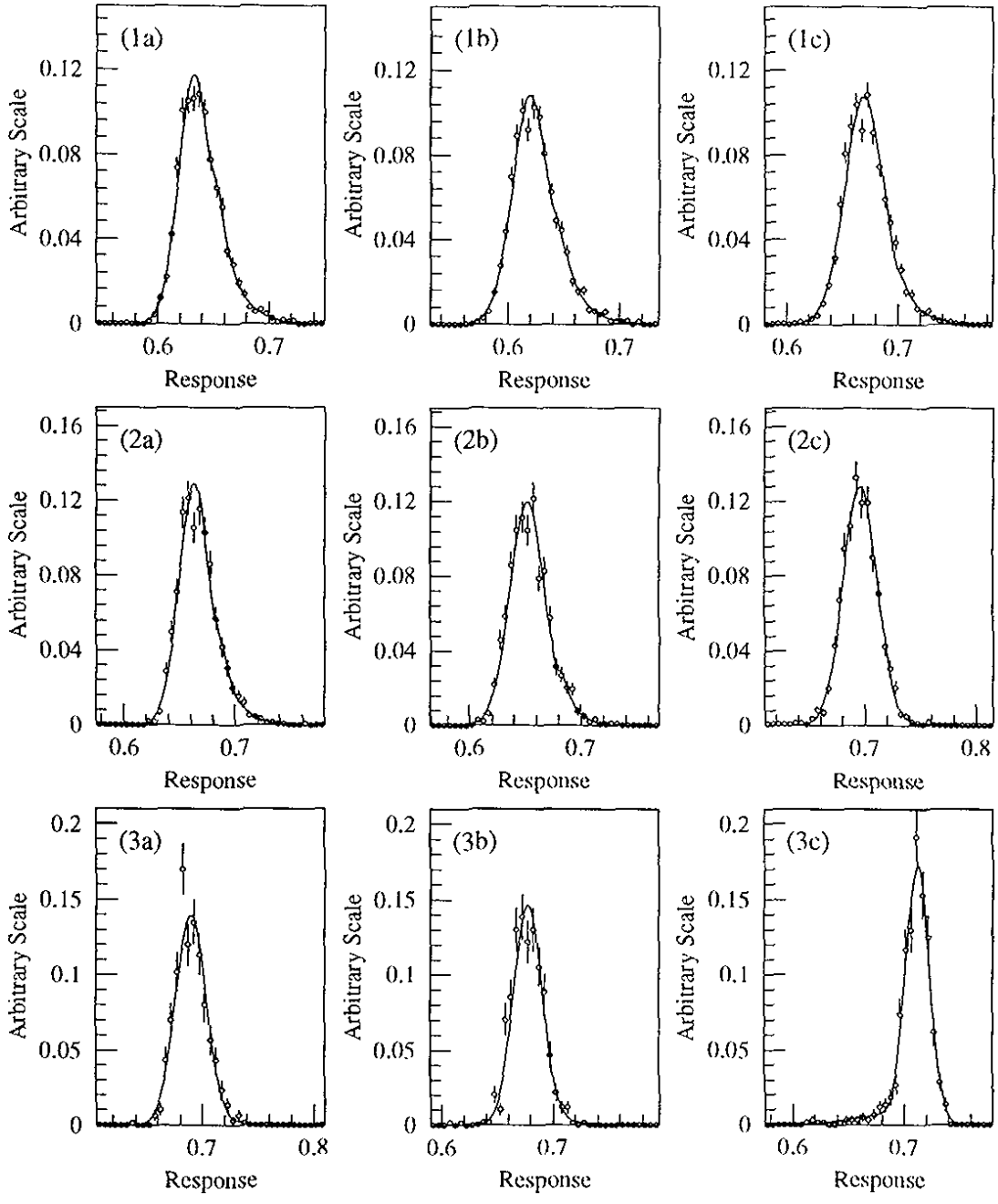

Figure 86. The distribution of the fractional response for EGS electron showers. Rows 1 to 3 correspond to energies of 2 GeV, 8 GeV, and 32 GeV, respectively. The absorption coefficient α and block length L in radiation lengths for each column are (a) $\alpha = 0.034, L = 18.7$, (b) $\alpha = 0.040, L = 17.2$, and (c) $\alpha = 0.038, L = 15.7$. In each plot, the curve is the best fit parametrization.

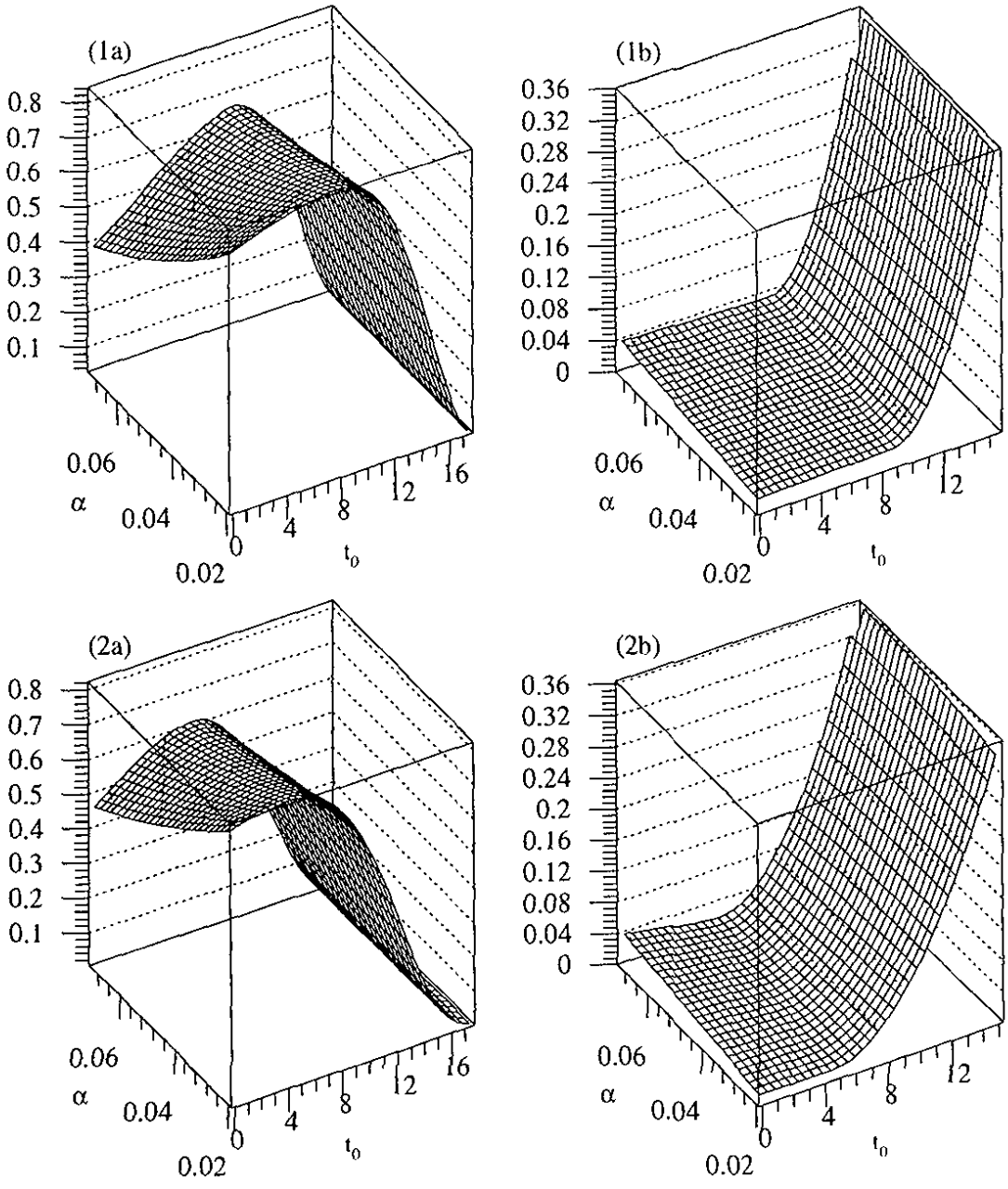

Figure 87. The variation of response parameters with absorption coefficient and block length. Rows 1 and 2 correspond to energies of 2 GeV and 22.63 GeV, respectively. Column (a) and (b) correspond to the central Gaussian mean and the central Gaussian width, respectively.

phototubes from the observed width of that block's response to the flash lamp (see Section 3.2.2). From the measured phototube gains, this gives us the number of photoelectrons per Çerenkov photon. Using this factor and the number of Çerenkov photons obtained for the electron shower at hand, the simulated response finally receives a photostatistical Gaussian smearing. The average number of photoelectrons obtained in each of the 804 blocks for a 1 GeV electron is plotted in Figure 88.

7.4.1.2 Generating a cluster from shower response

The lead glass response to electrons discussed above assumes the calorimeter was one glass block extending infinitely all directions transverse to the incident electron. Since much of a shower is contained within the physical block struck by an electron hitting our calorimeter, this is a reasonable starting point. We must, however, simulate the sharing of energy among the blocks surrounding the block struck. Since we make cuts based on cluster

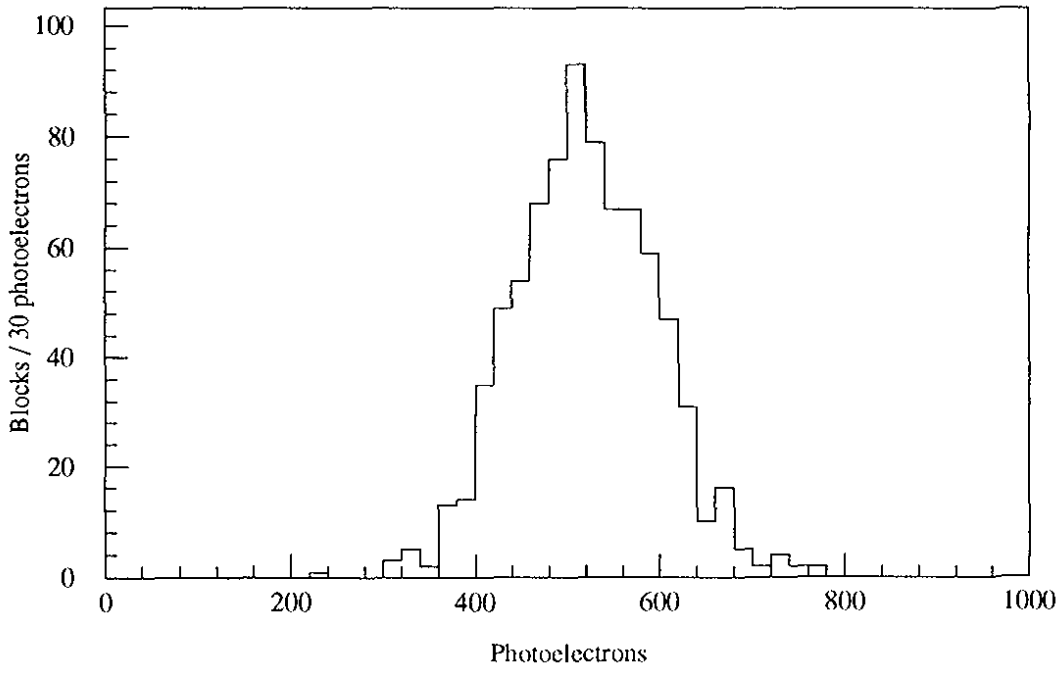

Figure 88. The average number of photoelectrons obtained from the shower of a 1 GeV electron for each of the 804 blocks.

shapes to help reduce the $3\pi^0$ background in the $2\pi^0$ sample, simulating this lateral energy distribution is important.

Rather than modelling the lateral distribution from first principles, we have accumulated a large cluster library using a very clean sample of electrons from the e^+e^- calibration samples where no minimum readout threshold was used. For each cluster in the library, we have stored the pattern of the energy distribution within a 5×5 array of blocks centered on the block struck by an electron. The clusters are grouped according to the incident electron energy and the position in the block where the electron landed, both of which can be measured in the charged spectrometer. More detail on this library is in reference [75].

In the Monte Carlo simulation, a cluster shape is chosen from the library based on the true electron energy and transverse electron position in the glass block. The signal in each block from the cluster library cluster is scaled by the ratio of the simulated block response to the energy of the cluster library electron as measured by the charged spectrometer. With this scaling, the fluctuations in the transverse energy loss outside the 5×5 array is automatically simulated by the real fluctuations in the cluster library itself.

For photons, the signal in each block from the shower simulated for each conversion electron is summed. Similarly, the signals in any overlapping blocks for two nearby showers are summed. To complete the simulation, the final signal in each block of the array is converted to ADC counts using the block gain measured in electron calibration, and the ADC readout threshold is applied.

The final stage of the simulation of the lead glass array involved simulating the hardware cluster finder (HCF). Since the "seeds" used in the offline cluster finding algorithm were obtained from the HCF, it was necessary to simulate the HCF properly. Indeed, much effort (see reference [75]) went into determining the correct signal threshold for each block above which the HCF would register a "hit" for that block. Once the pattern of hit blocks was obtained, the software simulation of the cluster finding algorithm itself was straightforward.

7.4.1.3 Electrons, Ke3 Data and Monte Carlo simulation

When electrons in Ke3 decays are simulated with the above procedure, the resolution matched better between data and Monte Carlo than with the straight Gaussian parametrization of the response. The resolution was still slightly better in the data than in the Monte Carlo, though, and we believe the cause of this to be a nonuniform absorption profile through the length of the lead glass blocks. The glass blocks sustain greater damage from hadronic showers deeper into the block, and that the ultraviolet curing tends to cure the front of the block more than the back. As a result, the absorption increases into the block. This actually tends to compensate for showers which fluctuate more deeply into the block — more of the Çerenkov radiation is absorbed than one would expect from uniform absorption. This leads to a smaller high side tail and better resolution than our model would predict.

To compensate for the difference between data and Monte Carlo, we made a small adjustment to the parametrization slightly for absorptions coefficients $\alpha > 0.032$. The width and the exponential slope of the high side tail were changed linearly as a function of $\alpha - 0.032$, such that for a block with $\alpha = 0.04$, which was fairly common near the center of the array, the Gaussian width was reduced by 4% of itself and the area under the high side tail was halved. The two parameters that accomplished this were the only tunable parameters introduced into the electron response simulation. With only this small amount of tuning, the agreement between the data and Monte Carlo electron resolution as a function of energy and absorption was very reasonable. In Figure 89, the energy resolution in the Monte Carlo is compared to the energy resolution in the Ke3 data versus the incident electron energy for blocks in three different ranges of α. For the Ke3 data, the energy resolution was calculated by measuring the resolution of E/p and subtracting off the resolution contribution on the track momentum p using Equation 3.2. For the Monte Carlo electrons, the resolution was determined by directly comparing the reconstructed and generated energies. The agreement between the data and Monte Carlo electron resolution, both as a function of energy and α, is very reasonable. The turn up in resolution at low energies because of the photostatistics contribution is clear. We can also see that the effect of the damaged blocks was to increase the resolution at high momentum from about 2% to 2.6%.

7.4.1.4 Photons, $\pi^+\pi^-\pi^0$ Data and Monte Carlo simulation

To check the photon response, we studied the reconstructed π^0 mass in $\pi^+\pi^-\pi^0$ decays. We found that the simulated photon resolution was again somewhat wider than the resolution for photons in the data, which is what we expected if our model explaining the electron resolution was correct. That is, the difference can again be understood with a model where the absorption increases towards the back of the block. The deeper a photon converts in a block, the less the Çerenkov light from its shower will be attenuated. If the absorption is increasing from front to back however, the spread of absorptions will be smaller than for a block with uniform absorption. Hence for photons as well as electrons, we expect the radiation damage to compensate fluctuations into the block. Since we can not directly measure the absorption profile, we allowed one tunable parameter in the photon simulation.

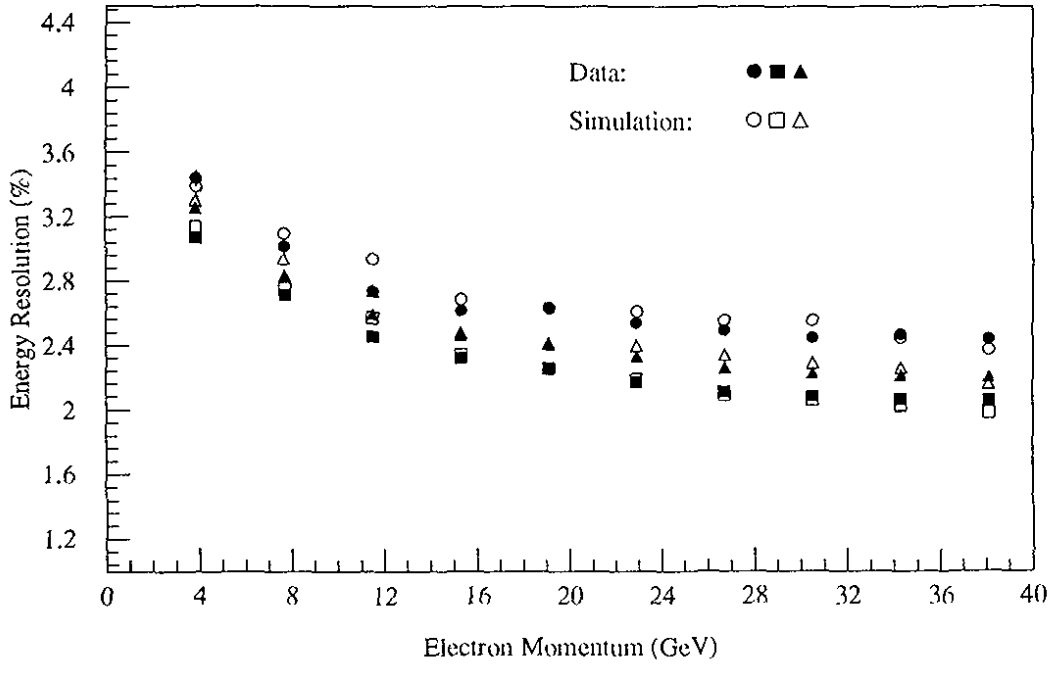

Figure 89. Ke3 electron energy resolution versus incident electron energy for 3 different ranges of the lead glass absorption coefficient, α. The resolution is measured using the events in all blocks within a quoted range of α to obtain adequate statistics. The data electrons are the solid points, the Monte Carlo electrons are the hollow points. The three absorption coefficient ranges (in percent per radiation length) are *squares:* 3.4–3.6, *triangles:* 3.8–4.0, and *circles:* 4.2–4.4.

Assuming that the absorption is increasing into the block, the average absorption α_t seen by the e^+e^- pair from the photon conversion will vary with the photon conversion depth, t_0. We parametrize this change as

$$\alpha_t = \alpha(1 + 0.03t_0), \tag{7.17}$$

where α is the absorption coefficient of the block measured in calibration. The 3% per radiation length constant was determined from the study of the reconstructed $\gamma\gamma$ mass width in $\pi^+\pi^-\pi^0$ decays.

The $\gamma\gamma$ mass in $\pi^+\pi^-\pi^0$ decays was quite useful for studying photons in the lead glass. Since the z location of the kaon, and therefore the π^0, decay can be measured directly from the charged pions in the drift chamber system, the $\gamma\gamma$ mass obtained from Equation 6.1 is directly related to two measured photon energies. This is much simpler than the situation for $3\pi^0$ and $2\pi^0$ decays, where the z must first be inferred from photon pairing, and then the mass calculated from the average z of the paired photons. For tuning the photon response in the Monte Carlo, we compared the $\gamma\gamma$ mass distributions for $\pi^+\pi^-\pi^0$ decays in data and Monte Carlo as a function of the average of the absorption coefficients of the two photon clusters. The $\gamma\gamma$ mass distribution for four different ranges of the average absorption coefficient is plotted in Figure 90. The tuning was done using only the NC set, yet the Monte Carlo described the data quite well in earlier subsets as well. For example, the $\gamma\gamma$ mass resolution as a function of the average absorption is plotted for the NC subset and the C2 subset in Figure 91. The data and Monte Carlo agree well in both subsets in the region $\alpha > 0.032$, where we tuned. In the earlier subsets, the Monte Carlo resolution seems somewhat better at very low values of α than we observe in the data. These low absorptions occur at the outside of the array where the photon intensity is quite low, and have little effect on the average resolution. The effects of an average resolution will be discussed further in Chapter 10.

7.4.1.5 What about $2\pi^0$decays?

In general, the Monte Carlo simulation of the $2\pi^0$ decays worked admirably. The energy and overall photon illumination agree very well between data and Monte Carlo, as we have

seen earlier in this chapter. In an arena closer to the shower simulation, we have already seen in Section 6.1 that the line shape of the $2\pi^0$ mass distributions in the data and the Monte Carlo simulation are very close, aside from an overall shift due to the residual nonlinearity in the data. In Chapter 10, we will see that a small difference in the $2\pi^0$ mass shape for decays from the vacuum beam and the regenerator beam, due to the differences in the energy spectra of the two beams, is also faithfully reproduced by the simulation.

Another, even more fundamental, quantity to compare between data and the Monte Carlo simulation is the pairing χ^2 for combining the 4 photons into 2 π^0s. This distribution

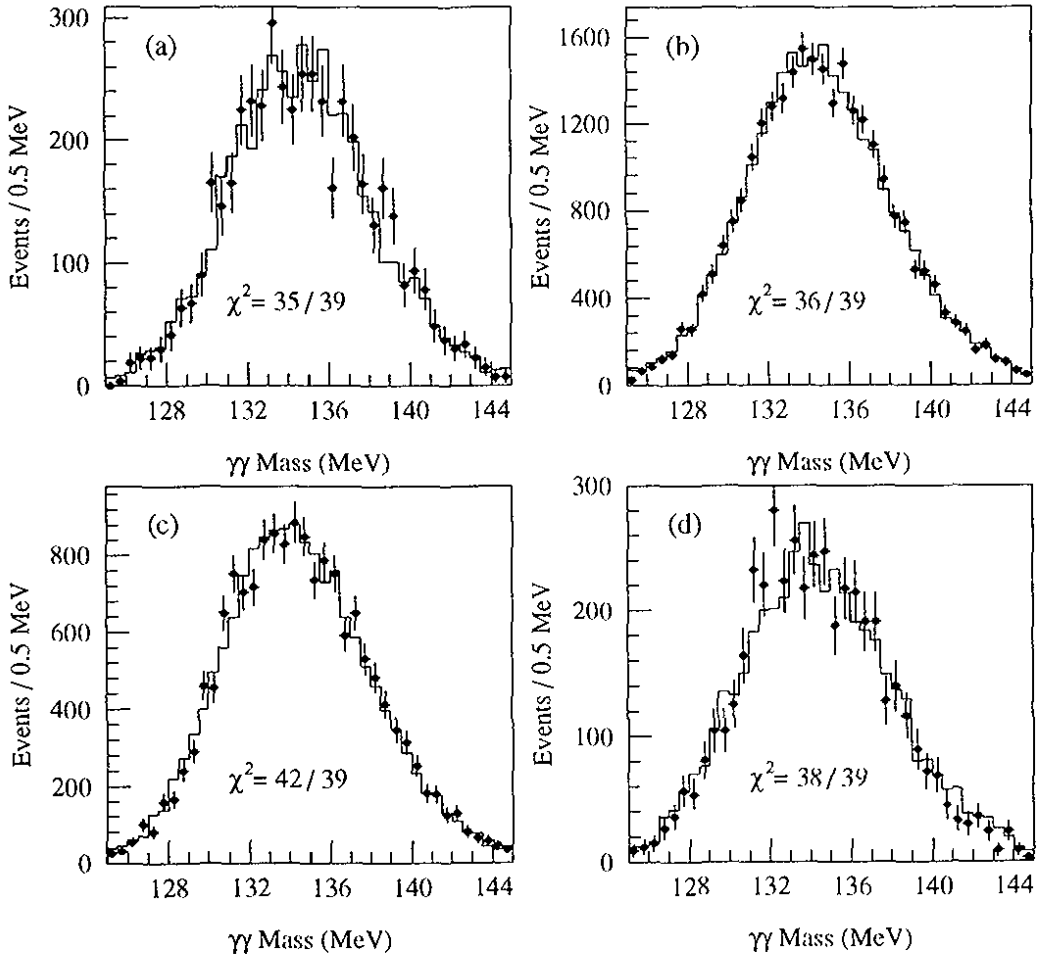

Figure 90. $\gamma\gamma$ mass for $\pi^+\pi^-\pi^0$ decays from the NC subset. The events have been divided into different ranges of the average absorption coefficient $\bar{\alpha} = (\alpha_1 + \alpha_2)/2$ of the two photon clusters. (a) $0.032 \leq \bar{\alpha} < 0.033$. (b) $0.035 \leq \bar{\alpha} < 0.036$. (c) $0.038 \leq \bar{\alpha} < 0.039$. (d) $0.040 \leq \bar{\alpha} < 0.041$.

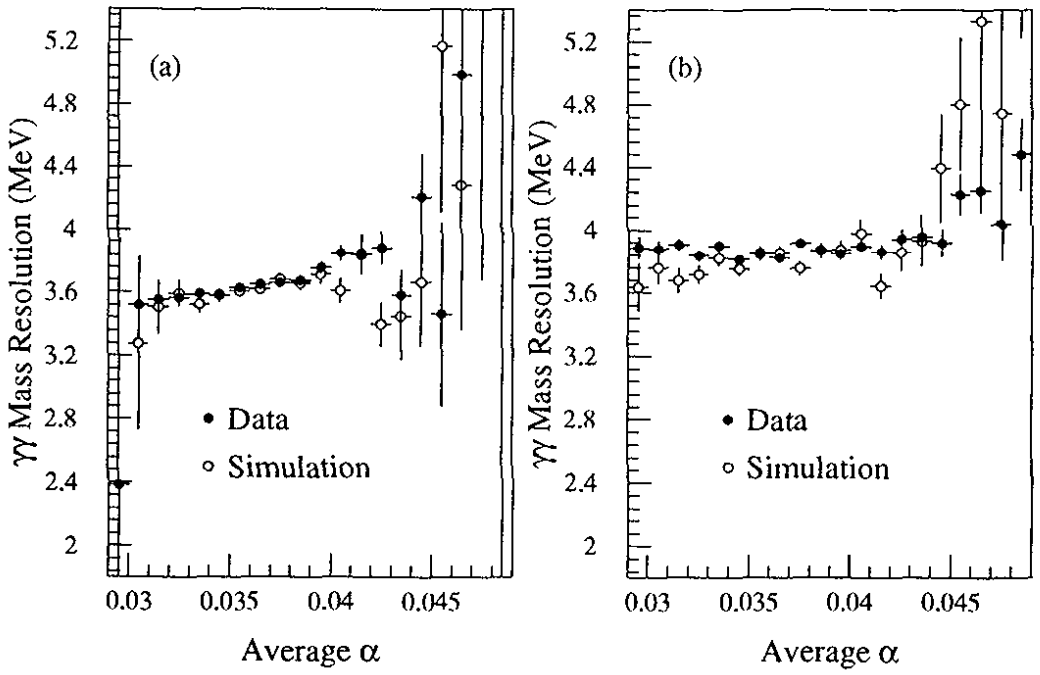

Figure 91. Resolution on the $\gamma\gamma$ mass in $\pi^+\pi^-\pi^0$ data and Monte Carlo simulation. The resolution is plotted as a function of the average absorption coefficient $\bar{\alpha} = (\alpha_1 + \alpha_2)/2$ of the two photon clusters. (a) NC subset. (b) C2 subset.

is plotted for $2\pi^0$ data and simulation in Figure 92. The overall shape agrees quite well over the bulk of the distribution, with the data finally beginning to show some excess over the Monte Carlo for badly reconstructed events. Some excess of the $2\pi^0$ data relative the simulation at large χ^2 is expected because of accidental activity in the detector.

Also directly related to the cluster simulation is the distribution of cluster separation in the $2\pi^0$ data and Monte Carlo simulation. The shape of this distribution is affected by the cluster shape cuts used to reduce the $3\pi^0$ background, and by the remaining $3\pi^0$ background in the $2\pi^0$ sample. The distribution for the cluster separation is shown for data and Monte Carlo in Figure 93. The predicted background contributions (see Section 6.5) have been added to the coherent Monte Carlo simulation in this figure. The agreement between the two distributions extends over four order of magnitude in both the vacuum and the regenerator beams, including in the region where the clusters overlap!

The individual cluster energies are also interesting to examine. Curiously enough, the one distribution where the simulation failed to precisely describe the data was in the maxi-

mum cluster distribution. This distribution is shown in Figure 94 for the entire $2\pi^0$ sample in both the vacuum and regenerator beams. Also shown are the regenerator beam distributions for the subsets with and without the lead sheet. The change in the vacuum beam distributions for these two sets is identical to the change in the regenerator beam. While the Monte Carlo describes the data quite well in all cases below energies of about 60 GeV, the data shows a higher acceptance on average than the Monte Carlo at high energy. This discrepancy is time dependent, showing clearly in the early subsets and at a much reduced level or not at all in later subsets.

The bulk of the discrepancy comes from the blocks surrounding the beam pipe, with the remainder from the ring of blocks just outside of these pipe blocks. The discrepancy seems to be related to the actual acceptance of high energy photons and not an effect due to smearing alone, since the smearing required to mimic this problem would make the $2\pi^0$ mass distribution extremely broad. The excess smearing also distorts the low end of the

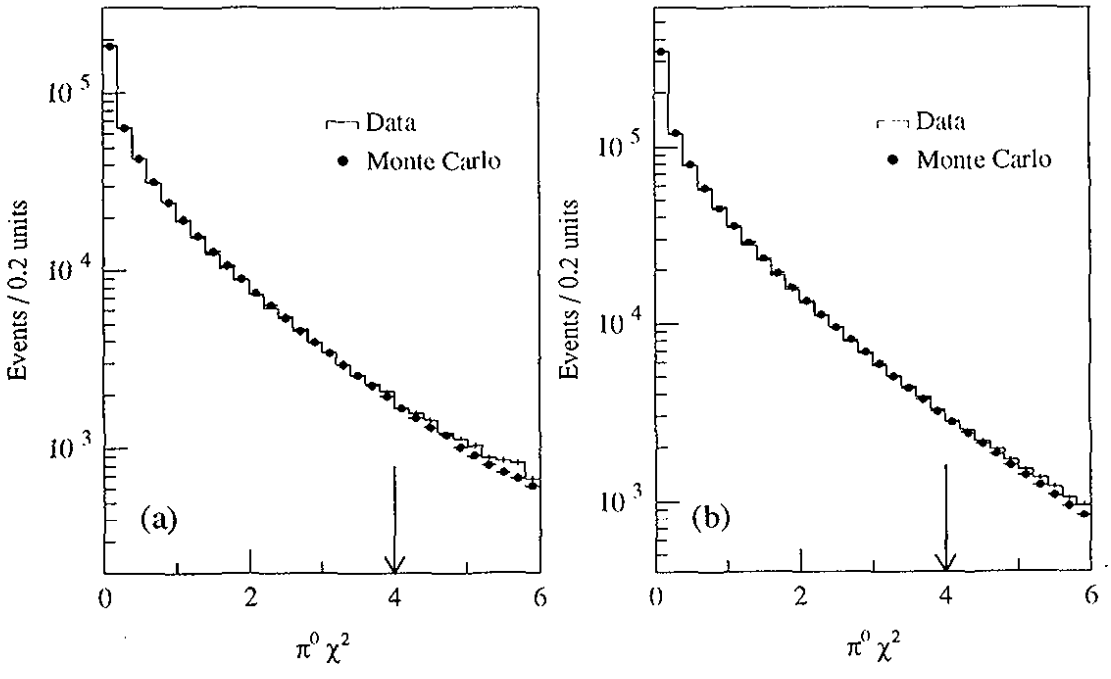

Figure 92. Pairing χ^2 for $2\pi^0$ decays in the data and Monte Carlo simulation. (a) Vacuum beam. (b) Regenerator beam. The expected background contribution has been added to the Monte Carlo prediction. The arrow in each plot marks the position of the analysis cut

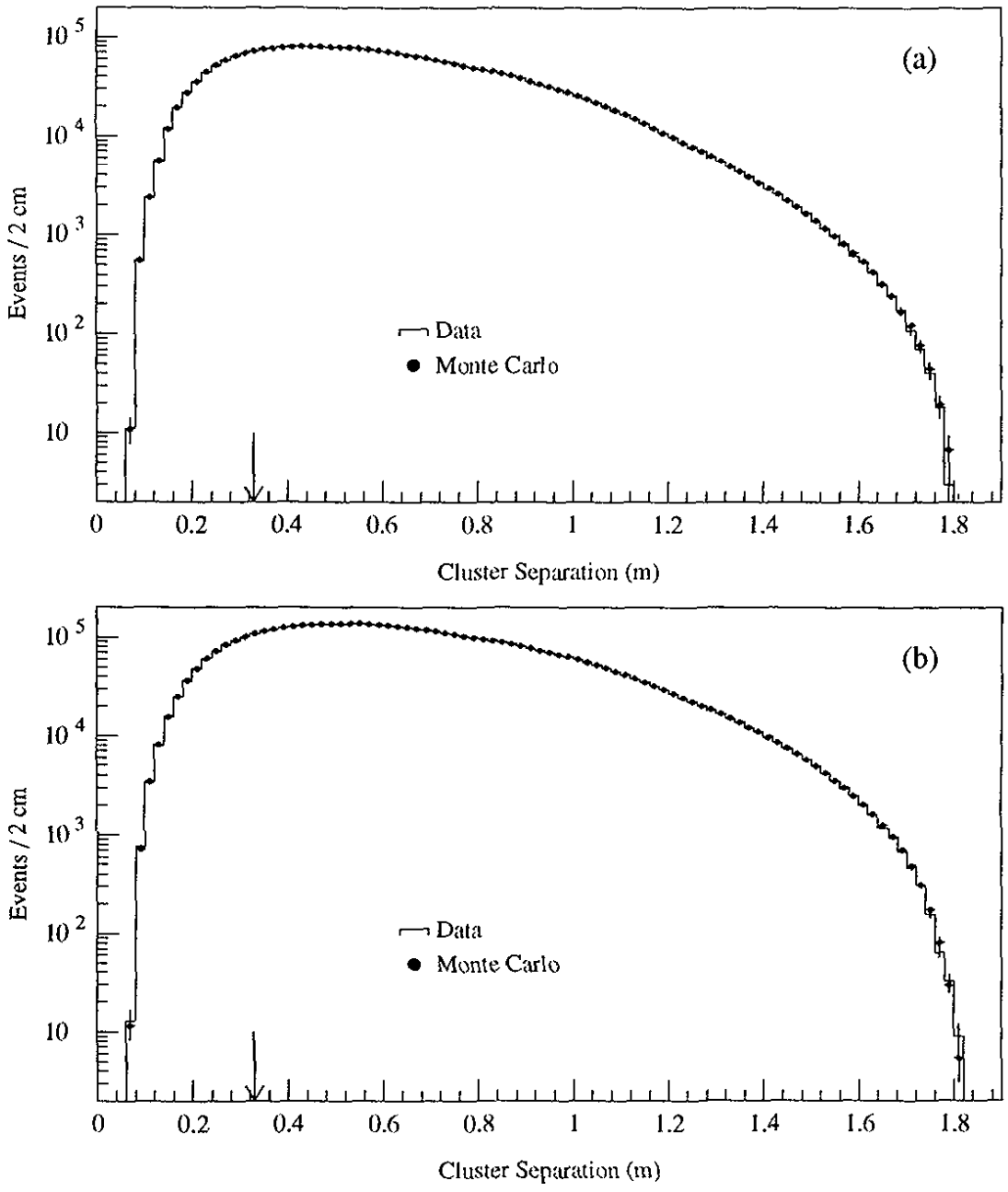

Figure 93. Cluster separation for $2\pi^0$ decays in the data and in the Monte Carlo simulation. The arrow indicates the minimal separation for each of the standard 3×3 block clusters to be distinct (complete separated). Not cut is made on this variable. (a) Vacuum beam. (b) Regenerator beam. The predicted background level has been add to the $2\pi^0$ Monte Carlo simulation.

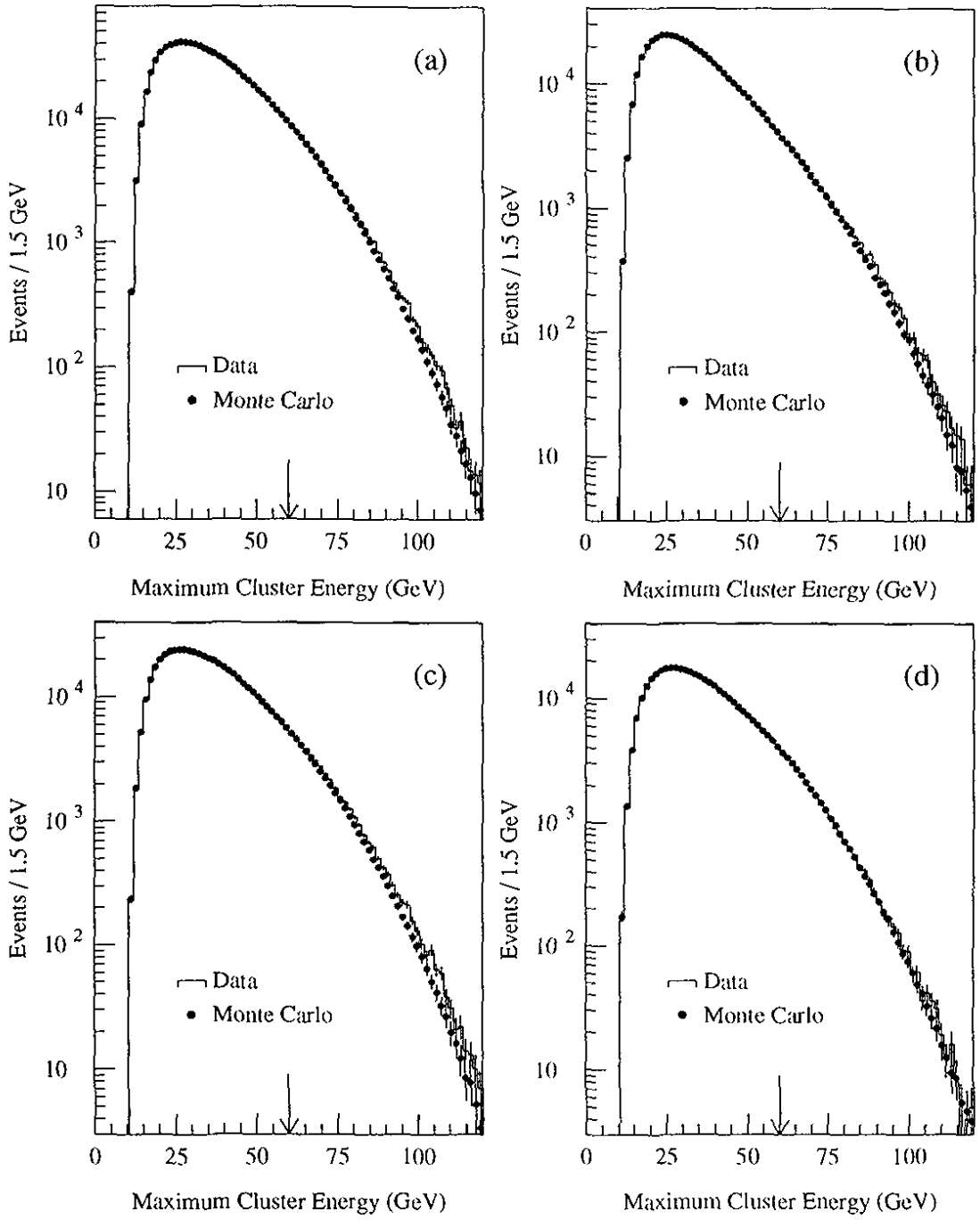

Figure 94. Distribution of the maximum cluster energy for $2\pi^0$ decays in the data and the Monte Carlo simulation. The arrow indicates the position of the analysis cut. (a) Vacuum beam distributions for the entire data set. (b) Regenerator beam distributions for the entire data set. The regenerator beam distributions are plotted separately for (c) the $2\pi^0$ subset with the lead sheet, and (d) the subset without the lead sheet. The background contributions have been included in all of the Monte Carlo overlays.

maximum cluster energy distribution, which agrees with the data without such a smearing. The problem seems to be a photon simulation problem, not a problem with the collar anti, since the collar anti position is very stable in the Ke3 data, and also since the problem appears for clusters located outside of the pipe blocks, which are not affected by the collar anti position. The cluster simulation hypothesis is supported by the problem occurring when the radiation damage in these blocks was the worst. This might seem contrary, since the problematic subsets occurred "early" in the run. However, the lead glass had seen substantial beam time without any curing when we began collecting useful $2\pi^0$ data, while the lead glass had received substantial curing before the later $2\pi^0$ sets were collected. Some of the absorption coefficients measured for the pipe blocks in the early subsets were over 50% larger in the early subsets than in the later.

It was not too surprising to us that the simulation had problems in this area, since we lacked the means to obtain the longitudinal absorption profile in the blocks as a function of time. The showers for high energy photons fluctuate more deeply into the block, where it is most difficult to simulate the fluctuations in the response. In light of this, we decided to restrict ourselves to the subsample of $2\pi^0$ decays where the maximum cluster energy was under 60 GeV/c. This has the further advantage of limiting the $2\pi^0$ cluster energy to the kinematic regime which is occupied by our $3\pi^0$ sample. Since we use the $3\pi^0$ decays to limit the systematic acceptance error for the neutral acceptance, this seemed like the most conservative course. We will return to this issue as part of our systematic discussion in Section 10.1.2.

7.4.2 Drift Chamber Simulation

Relative to the lead glass, the drift chamber simulation was simple, and we kept this simulation very basic. We did not include a detailed simulation of the electron drift and δ-ray production for the passage of a charged particle passed through each drift cell. The observed TDC time distribution was simulated by inverting the measured time to distance function (see Section 4.1.1) for the time period being simulated. The chamber resolution was included by hand by first smearing the true position of the particle in the drift chamber

sense plane by using a Gaussian distribution whose width was the resolution measured in the data for that sense plane [4]. This smeared distance was then converted to a TDC time using the inverted time to distance function.

In addition to the resolution smearing, we have included the measured drift chamber efficiencies. As we can see from Figure 95, the individual wire efficiencies were very uniform across a plane. This was true even in the most inefficient plane. In general, this uniformity allowed us to characterize the efficiency for each drift chamber plane with a single number averaged over all of the wires. In a system of over 2000 sense wires, however, one does expect a few wires to be more problematic than others. Hence wires that were broken, or were disconnected because they were drawing large dark currents, or were just plain misbehaving, and hence had efficiencies lower than the average efficiency, were handled individually. The criteria used to separate these wires depended on their position in the chamber. If they were at the edge of the chamber, where the illumination was low, wires with efficiencies more than 5% away from the mean were handled separately. In the central region of the chambers, where the illumination was much higher and the efficiencies more crucial, the cutoff was much tighter, and any wire whose efficiency deviated by more that 0.5% of the mean was handled individually. The efficiency measured individually for each of these wires was used in the simulation, and this wire was excluded from measurement of the average efficiency of the sense plane to which it belonged. There were only a handful of these special cases, typically about 25 wires, of which most were only marginally different from the average plane efficiency.

These particularly inefficient wires had very little effect on the acceptance. In part, this was due to most of these wires being located near the edges of the chamber, where the pions travelled only rarely. Only two to three of the inefficient wires were in a "hot" region of the chamber system. Furthermore, the tracking algorithm was forgiving of missing hits, particularly in the y view, and very few tracks were seriously misreconstructed or missed entirely because of these individual wires. The x track illumination in chamber 2 before and after a sense wire in a fairly hot region of the chamber broke is shown in Figure 96. There is not a great change in the illumination near this wire, but the deficit in the NC set

[4] The Ke3 and $\pi^+\pi^-$ data gave consistent results for the 16 plane resolutions.

is visible. The rest of the structure in this overlay results from the change in beam shape over time. The Monte Carlo simulation for the NC set, also shown in the figure, mocks up the small change quite well.

While tracks in the drift chambers are generally well separated in one view, particularly in the x view where the tracks are bent by the analysis magnet, the two pions do occasionally pass through bordering or identical drift cells. This will be most strongly a function of the kaon momentum, but will also be more probable for pions from decays which occurred downstream rather than upstream. The track separation is shown in one of the planes in Figure 97. With our simple modelling, the Monte Carlo simulation does a fine job of describing acceptance decrease as the pion track separation decreases to the size of a drift cell.

The only shortcoming with our drift chamber simulation was the lack of δ-rays. This exclusion means that the broad tails in the track quality variables were not simulated, but, as we have seen in Chapter 5, the δ-rays affect the vacuum beam and regenerator beam decays identically, as we had expected. There is an overall loss of events because of the

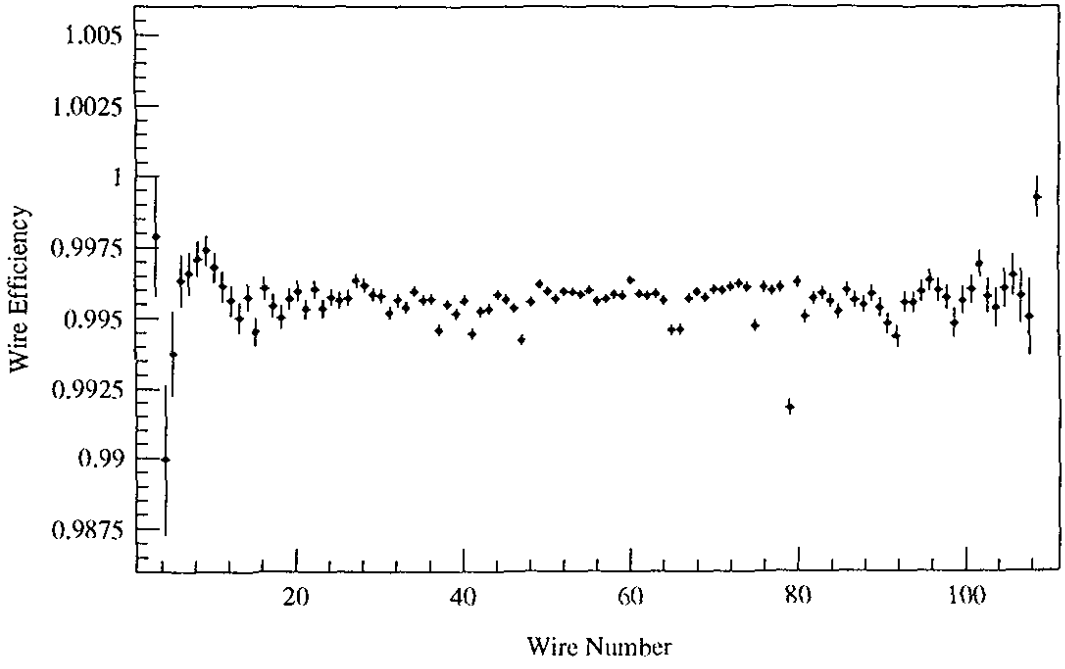

Figure 95. Individual wire efficiency for the downstream y plane in Chamber 2 measured with the Ke3 sample in the NC data subset.

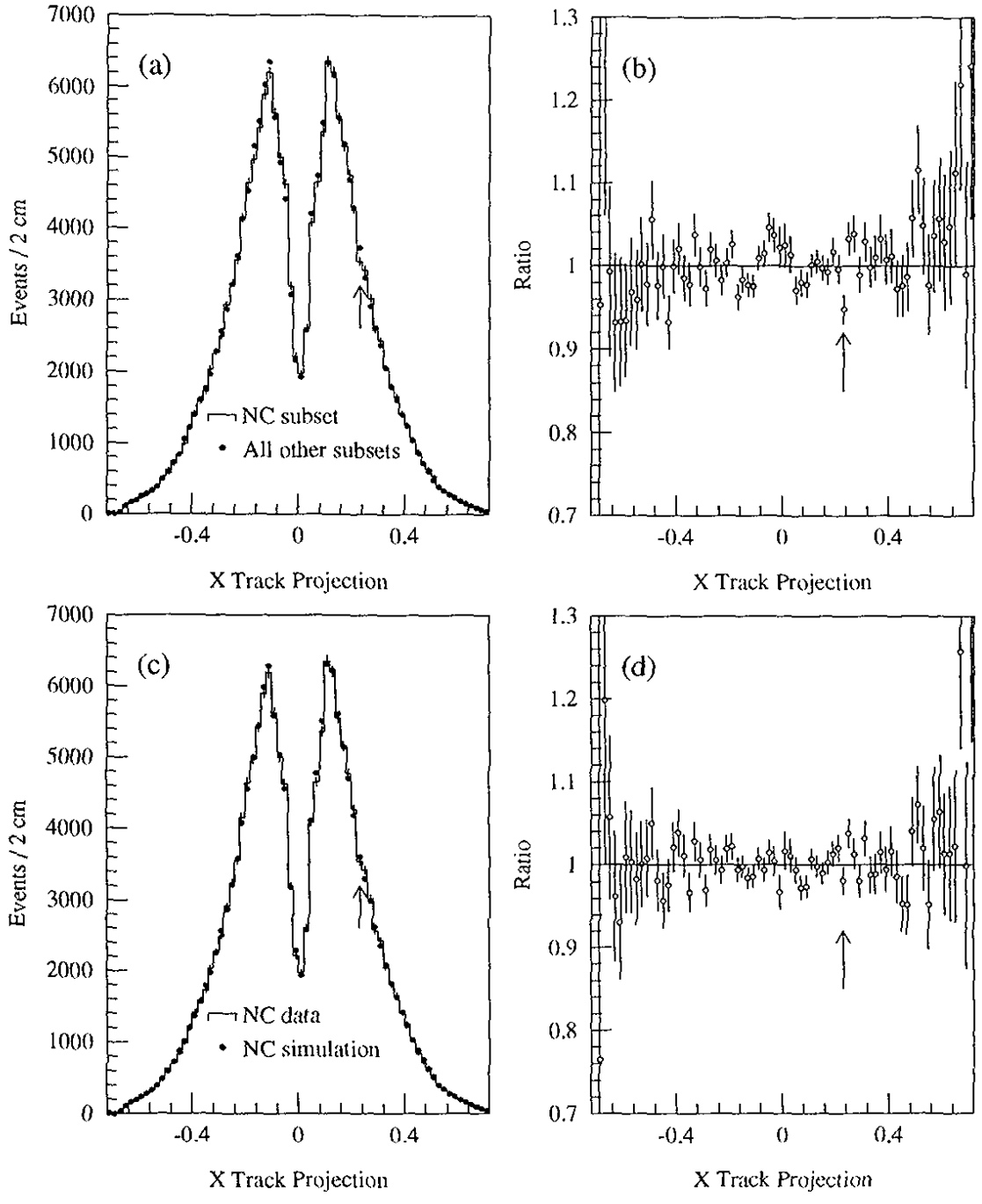

Figure 96. Chamber 2 x illumination by pions from $\pi^+\pi^-$ decays in data before and after one x view sense wire broke. (a) The data collected before the wire broke (circles) overlaid on the NC subset data collected after the wire broke (histogram). (b) The ratio of these distributions. (c) Monte Carlo simulation for the NC $\pi^+\pi^-$ data subset (circles) overlaid on the data for that set (histogram), and (d) the ratio of these distributions. The arrows indicate the position of the wire in question.

effect of the δ-rays on the track quality requirements, particularly from the track χ^2 cut, but this loss cancels in the vacuum to regenerator beam ratio. We will further investigate our sensitivity to this effect in Chapter 10.

7.4.3 Hodoscope and Photon Veto Response

Like the drift chamber simulation, the simulations of the hodoscope banks and photon veto counters were elementary. The average trigger and latch efficiencies, the former over 99.9% efficient and the latter over 99% efficient, were measured using muon tracks. In addition, the cracks between the different counters in the trigger counters were mapped minutely using the chamber alignment muon samples and the small gaps included in the Monte Carlo. In Chapter 10, we will examine the insensitivity of $Re(\varepsilon'/\varepsilon)$ to the efficiency of the individual counters.

The photon veto responses were most important for the simulation of the four cluster

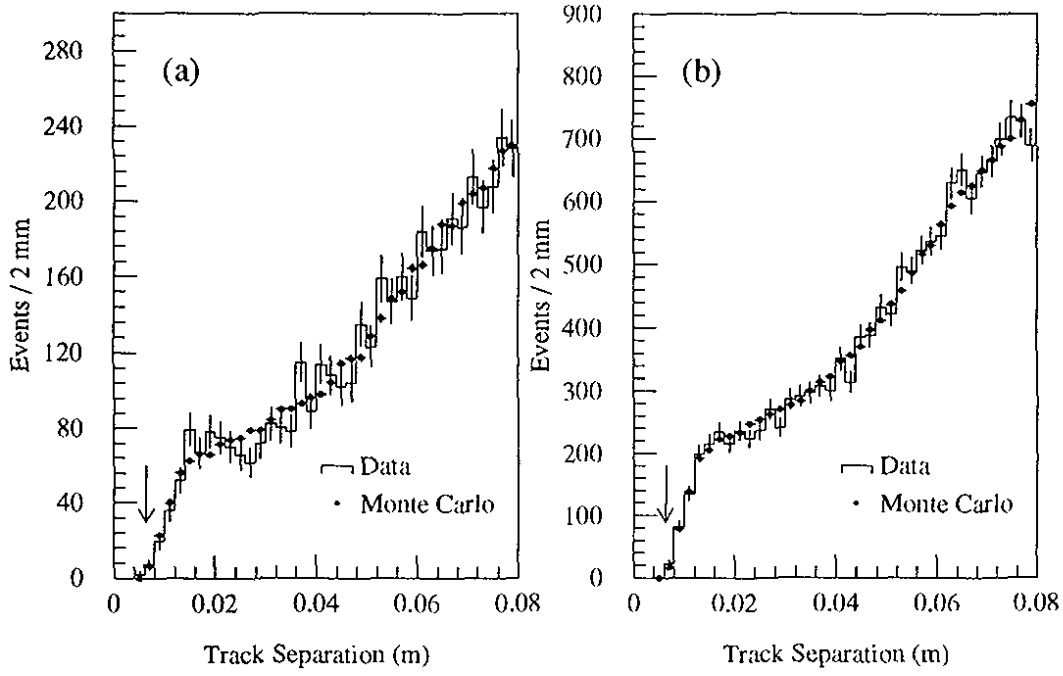

Figure 97. Separation of the two pion tracks in the x view at Chamber 4 for the $\pi^+\pi^-$ data and Monte Carlo simulation. (a) Vacuum beam. (b) Regenerator beam. The arrows indicate a separation the size of one drift cell. No cut is made on this variable.

$3\pi^0$ background. An elegant technique [76] which utilized $\pi^+\pi^-\pi^0$ decays with only one photon detected in the calorimeter was employed to map the response of these counters. The direction and energy of the missing photon could be inferred from the kinematics of the charged pions and reconstructed photon. Often this missing photon passed through one of the photon veto counters. By comparing the observed signals in the veto counters to the predicted energy of the "undetected" photon, the gains and resolution of the counters were extracted. A mismeasurement of the photon veto response would have manifested itself clearly in the background distribution of the $3\pi^0$ background. As we have seen already in Chapter 6, the predicted and observed z shapes of the $3\pi^0$ background agree well.

7.5 Z Comparisons

So far, we have examined the Monte Carlo simulation of the individual detector components, and compared the reconstructed quantities in the data and the Monte Carlo simulation relevant to that component. On the whole, the simulated distributions agree quite well with the distributions observed in the data. We now wish to step back and examine the distribution most crucial to the $Re(\varepsilon'/\varepsilon)$ analysis, the z-distribution of the kaon decays. When we fit for $Re(\varepsilon'/\varepsilon)$, we will integrate the contents of each 10 GeV/c momentum bin over the entire z range. A bias in the acceptance versus z, coupled with the difference in the vacuum and regenerator beam z distributions, would lead to a bias in the ratio of events in the vacuum and regenerator beams.

From the plots already shown, it is clear that our simulation of the apparatus mocks up the data quite well. We therefore expect that any bias in the acceptance is small, and expect the z distributions to match quite well. For most problems that would affect the acceptance in this experiment, such as a misplaced aperture edge or a bias resolving closely spaced tracks or closely spaced clusters, we would expect bias introduced into the acceptance to either increase or decrease fairly uniformly in z. For example, if an aperture is too wide, $2\pi^0$ decays close to the aperture will not be affected, while $2\pi^0$ decays farther upstream, whose photons have had a chance to spread and approach the aperture's edges, will be accepted more often in the simulation than they should. We therefore generally look

for a linear bias as a function of z. In all of the studies we have done, the χ^2 for a linear fit to the ratio of data to Monte Carlo have all been excellent, indicating that higher order terms are not necessary.

Since we always bin the data in 10 GeV/c momentum bins for our fits, the comparison between the z distributions in data and Monte Carlo simulation are of fundamental interest. Plotted are the distributions in the vacuum beam for two different momentum bins: the 60 GeV/c to 70 GeV/c bin, which is near the mean kaon energy in both decay modes for this experiment, and the 110 GeV/c to 120 GeV/c bin, which was picked randomly. The vacuum beam z distributions in the lower energy bin for the $\pi^+\pi^-$ decays and the $2\pi^0$ decays for the subsets with the lead sheet are plotted in Figures 98 and 99, respectively. The vacuum beam z distributions in the higher energy bin for the $\pi^+\pi^-$ decays and the $2\pi^0$ subsets without the lead sheet are shown in Figures 100 and 101. For the bins shown (and the bins not shown) the χ^2 for the z distributions in the data and simulation having the same shape are all very good.

When fitting for a linear bias in the ratio of data to Monte Carlo, the observed slopes were consistent with what one might expect from statistical fluctuations. For example, for the 48 momentum bins in the two neutral subsets, the slopes in 24 bins had significances under 1 standard deviations (s.d.), 15 under 2 s.d., and 9 over 2 s.d.. Many of the slopes over 2 s.d. occurred in high momentum bins with low statistics, where the Gaussian error estimates on the number of events in a 1/2 m bin were inappropriate, and the resulting significances overestimated. The relative numbers of positive and negative slopes observed were also consistent with expected statistical fluctuations.

To probe any residual biases at a much more sensitive level, it is convenient to combine all of the momentum bins, not only in the $2\pi^0$ and $\pi^+\pi^-$ data, but also in the Ke3 and $3\pi^0$ data, where we have very large event samples. Because of all the efforts made in properly simulating the energy spectrum and beam shapes observed in the data, the z distribution in the Monte Carlo simulation, integrated over all momenta, should match the observed z distribution in the data very well. Any bias observed in the z comparisons we can therefore attribute to an acceptance problem as opposed to a mismatch in the kaon energy spectrum. This is particularly true in the modes with charged final states. In the neutral mode,

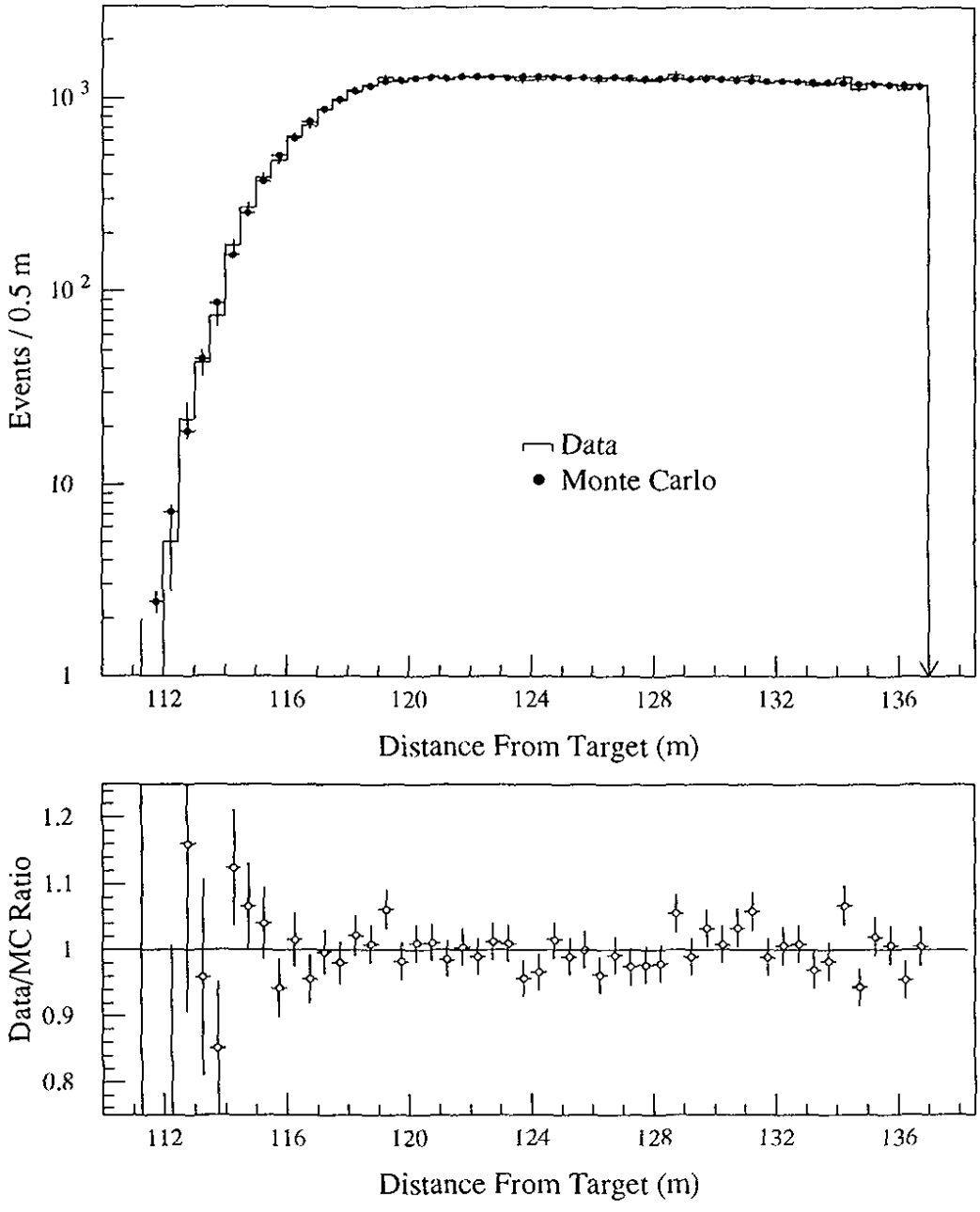

Figure 98. Vacuum beam z distribution for the $\pi^+\pi^-$ data and Monte Carlo simulation in the 60 GeV/c to 70 GeV/c bin momentum bin. All final cuts have been made. *Top:* The z distribution for the two event samples, with the simulation statistics normalized to the data statistics. *Bottom:* The ratio of data events to simulated events in each 1/2 m bin.

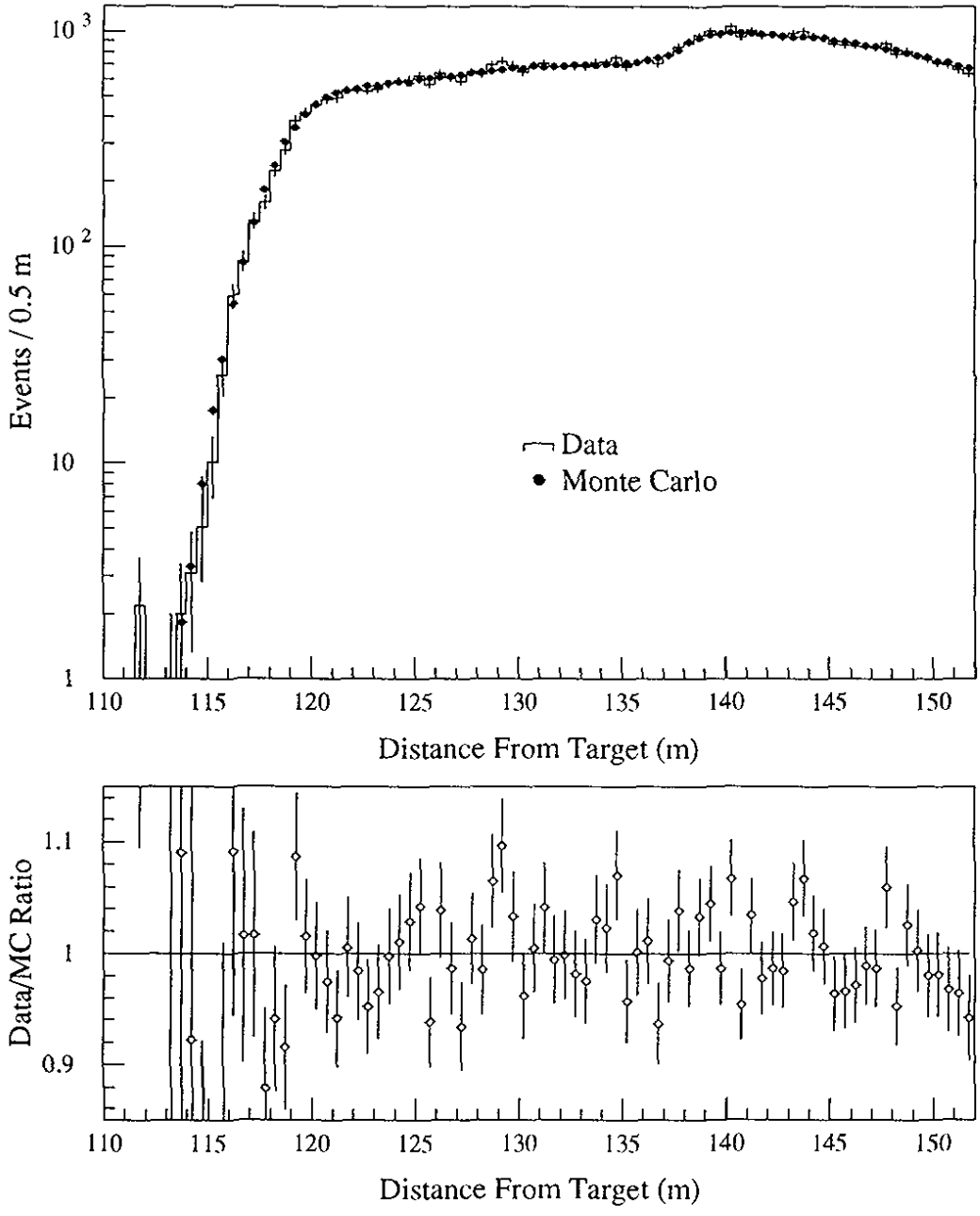

Figure 99. Vacuum beam z distribution for the lead sheet subset of the $2\pi^0$ data and Monte Carlo simulation in the 60 GeV/c to 70 GeV/c bin momentum bin. All final cuts have been made. *Top:* The z distribution for the two event samples, with the simulation statistics normalized to the data statistics. *Bottom:* The ratio of data events to simulated events in each 1/2 m bin.

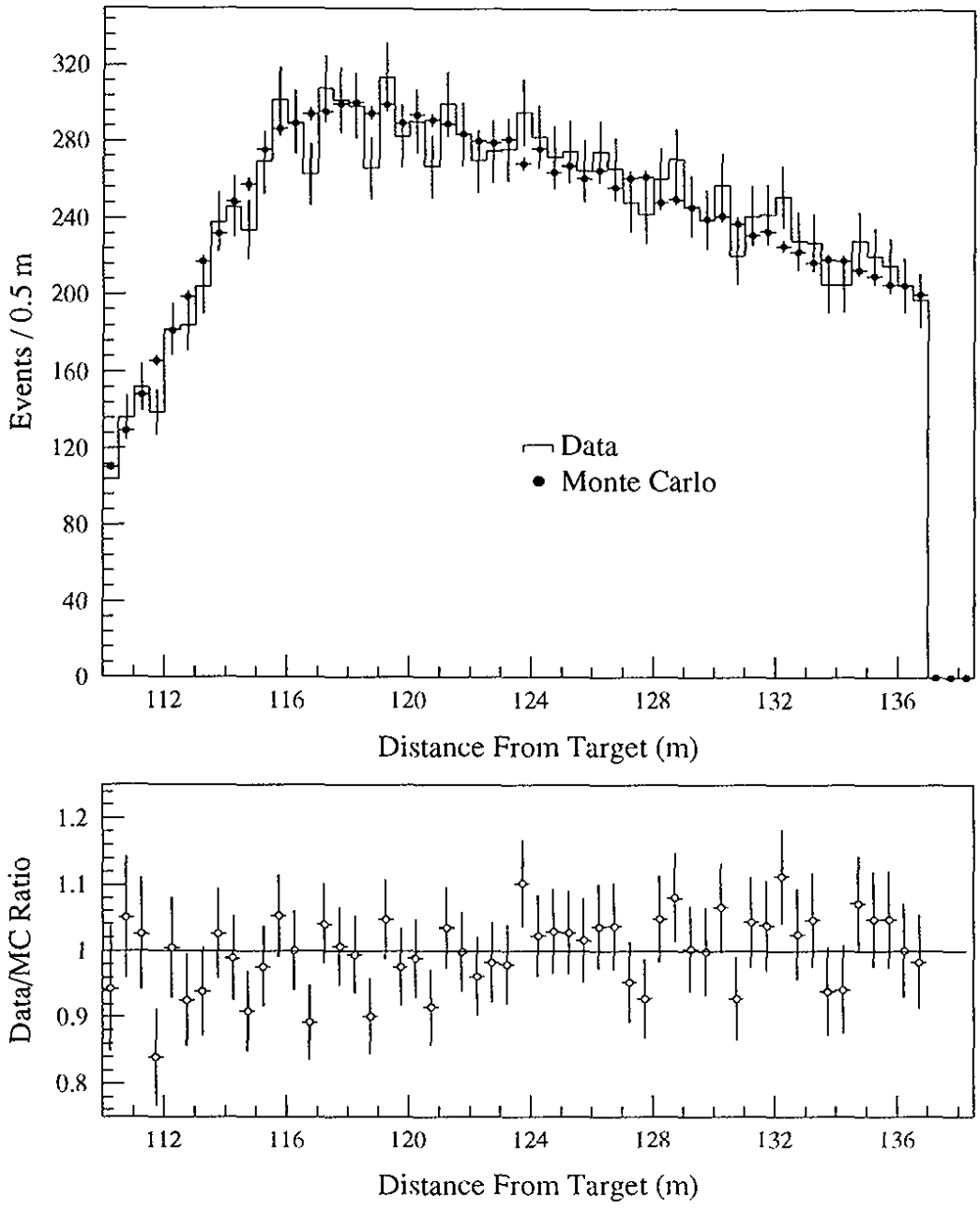

Figure 100. Vacuum beam z distribution for the $\pi^+\pi^-$ data and Monte Carlo simulation in the 110 GeV/c to 120 GeV/c bin momentum bin. All final cuts have been made. *Top:* The z distribution for the two event samples, with the simulation statistics normalized to the data statistics. *Bottom:* The ratio of data events to simulated events in each 1/2 m bin.

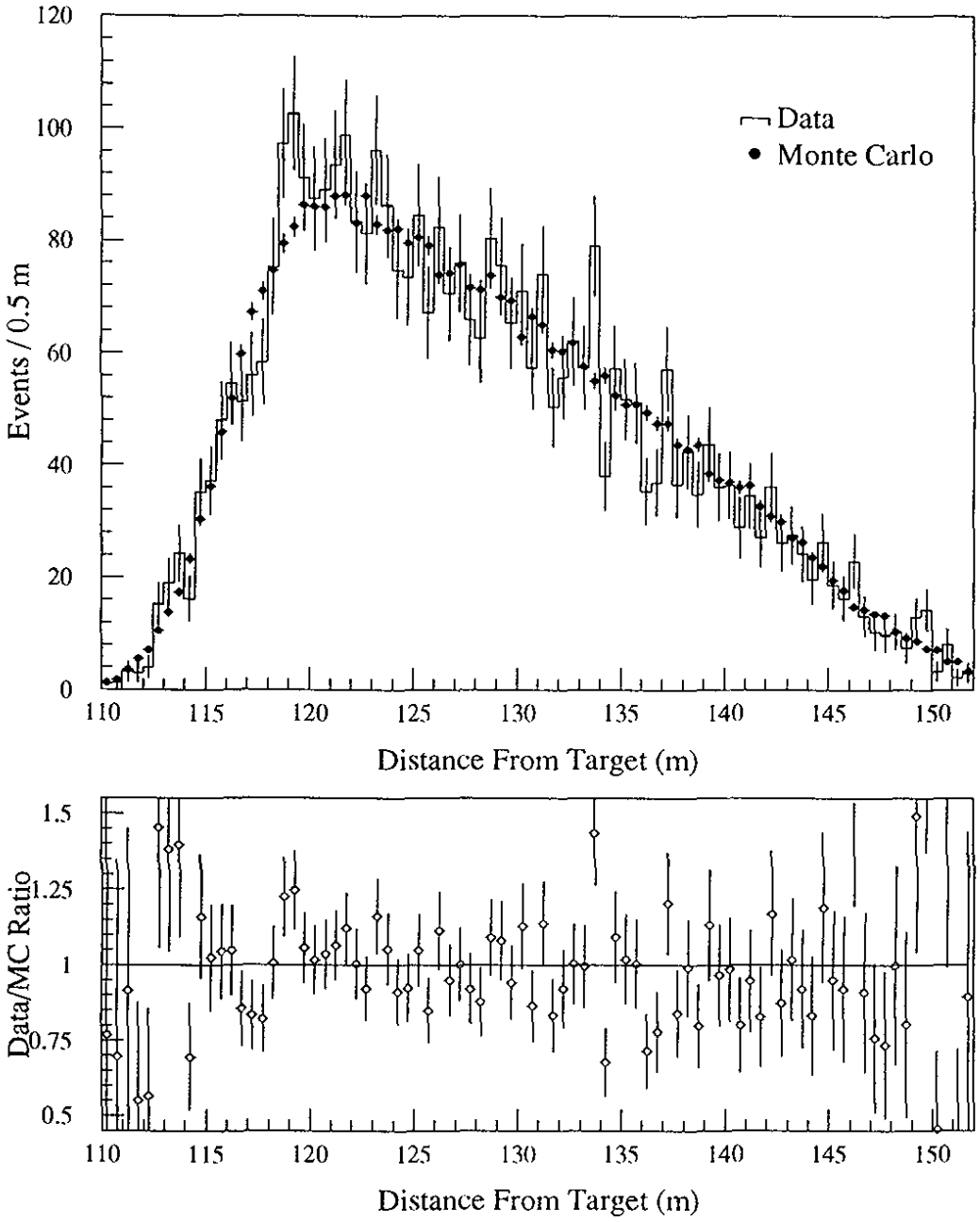

Figure 101. Vacuum beam z distribution for the subset of the $2\pi^0$ data and Monte Carlo simulation without the lead sheet in the 110 GeV/c to 120 GeV/c bin momentum bin. All final cuts have been made. *Top:* The z distribution for the two event samples, with the simulation statistics normalized to the data statistics. *Bottom:* The ratio of data events to simulated events in each 1/2 m bin.

we must be more careful because of the coupling between the measured z position of the kaon decay and the measured photon energies. If there is a bias in the photon energy measurement, the decays pushed by the location of a sharp change in the acceptance shape, such as at the lead sheet or near the active mask, will mimic an acceptance problem.

The Ke3 and $3\pi^0$ decay modes have some very nice features for use as samples to limit the acceptance biases in the $2\pi^0$ mode, as we initially remarked at the beginning of the chapter. First and foremost, we have very large samples of these decays in the vacuum beam. Having the high statistics will obviously help the sensitivity, but perhaps just as important is having this large sample from the vacuum beam. Limiting the acceptance bias using decays from the regenerator beam would be complicated by the scattering of the kaons within the regenerator, and by the interference of the regenerated K_S component with the K_L component, coupled with the imperfect knowledge of the precise values of parameters like Δm which affect the interference. Another benefit arises from these decays being 3 body decays, and as a result having decay products which are less forward than the $\pi\pi$ decays. A larger fraction have decay products which approach the detector edges, making these decays more sensitive to aperture positions than the $\pi\pi$ decays. In the case of the $3\pi^0$ decays, the photons in the glass have a higher probability to overlap than photons from $2\pi^0$ decays. Hence the $3\pi^0$ decays will also be more sensitive problems with the cluster simulation than the $2\pi^0$ decays. With the increased sensitivity of the high statistics modes to potential biases, limits on the acceptance for $\pi\pi$ decays obtained using the high statistics modes are fairly conservative estimates.

The Ke3 z distribution for one of the data subsets is shown in Figure 102. The z distributions in the data and in the simulation agree very well over the entire decay volume, even upstream of the 110 m $\pi^+\pi^-$ analysis cut, where the simulation tracks the order of magnitude drop in acceptance over 5 m very reliably. While the full Ke3 sample was used to track the aperture motion, and initial data and Monte Carlo studies were done with samples containing several 10^6 events each, the subsamples used to limit the acceptance biases contained about 10^6 decays (1% bites of the total sample). Samples of this size were sufficient to limit the acceptance in the charged mode at the level we needed. We have conservatively estimated the acceptance bias in the charged mode at the level of 0.03% per

meter, while the Ke3 samples had slopes which were consistent with flat at the 0.02% per meter level.

In order to bound the acceptance bias for the $2\pi^0$ mode, the $3\pi^0$ sample we used was limited to a region away from the active mask, where the rapid change in the acceptance shape coupled with residual uncertainties in the photon energy reconstruction can cause problems. For the subset with no lead sheet, the z distribution in data and Monte Carlo is shown in Figure 103. In this region, the agreement between data and Monte Carlo is excellent, and we can place a strong limit on a linear bias in the acceptance. Upstream of this region, the acceptance changes shape rapidly, and there is a dip in the ratio of data to Monte Carlo, which is about 1% at 120 m. The data to Monte Carlo ratio is again consistent with one when the accepted decay distribution is again relatively flat a few more meters upstream. This is the behavior we expect from a small energy scale mismatch — in this case an overall energy scale shift of under 0.02% would cause this effect. This sample places a 0.074% percent per meter limit on the acceptance bias for the $2\pi^0$ sample. It is interesting to note that at our mean kaon energy, we would have introduced a slope of order 0.04% per meter into the overlay had we ignored the K_L lifetime in the simulation.

Finally, we have the $\pi^+\pi^-$ and $2\pi^0$ distributions themselves. In terms of examining the acceptance, the vacuum beam plots are the most interesting. We have plotted the distribution of the $\pi^+\pi^-$ decays from the vacuum beam in Figure 104. The simulated and observed z distribution agree very well over the entire decay volume. The two bins at the end of the plot are right next to the HDRA, and the data points contain some background from beam interactions with the HDRA. Our downstream z cut is far enough from this detector element to be free of this background. The vacuum beam z distributions for the $2\pi^0$ decays without and with the lead sheet are shown in Figure 105 and Figure 106, respectively. Again, the z distributions agree favorably between data and Monte Carlo. The z region from 137 m to 139 m has been excluded from the analyses because of the sensitivity of that area to biases in the photon energy scale. There does appear to be an excess of data over Monte Carlo in part of that region, though the excess is consistent with an energy scale shift of under 0.03%.

The shape of the regenerator beam distribution depends on the physics parameters, such

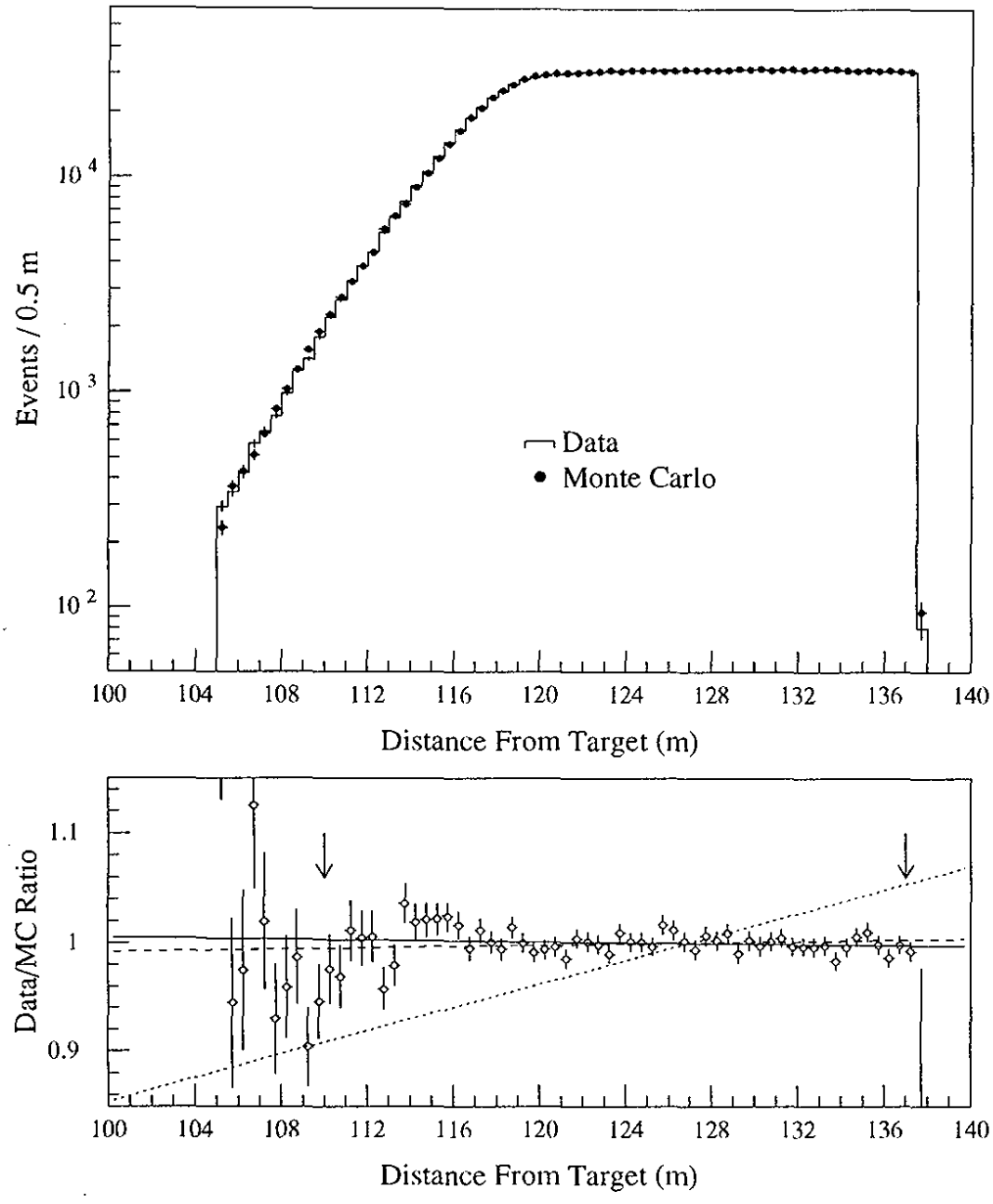

Figure 102. Vacuum beam z distribution for Ke3 decays in the data and Monte Carlo simulation after all other cuts. The sample shown is a portion of the NC subset. *Top:* The z distribution for the two event samples, with the simulation statistics normalized to the data statistics. *Bottom:* The ratio of data events to simulated events in each 1/2 m bin. The solid line is the best fit slope of $-0.021\% \pm 0.018\%$ per meter. The dashed line is the slope used for the systematic estimate, 0.03% per meter. The dotted line is the slope required to shift the final result for $Re(\varepsilon'/\varepsilon)$ by 10^{-3}. The arrows in the ratio plot indicate the z fiducial region used in the $\pi^+\pi^-$ analysis.

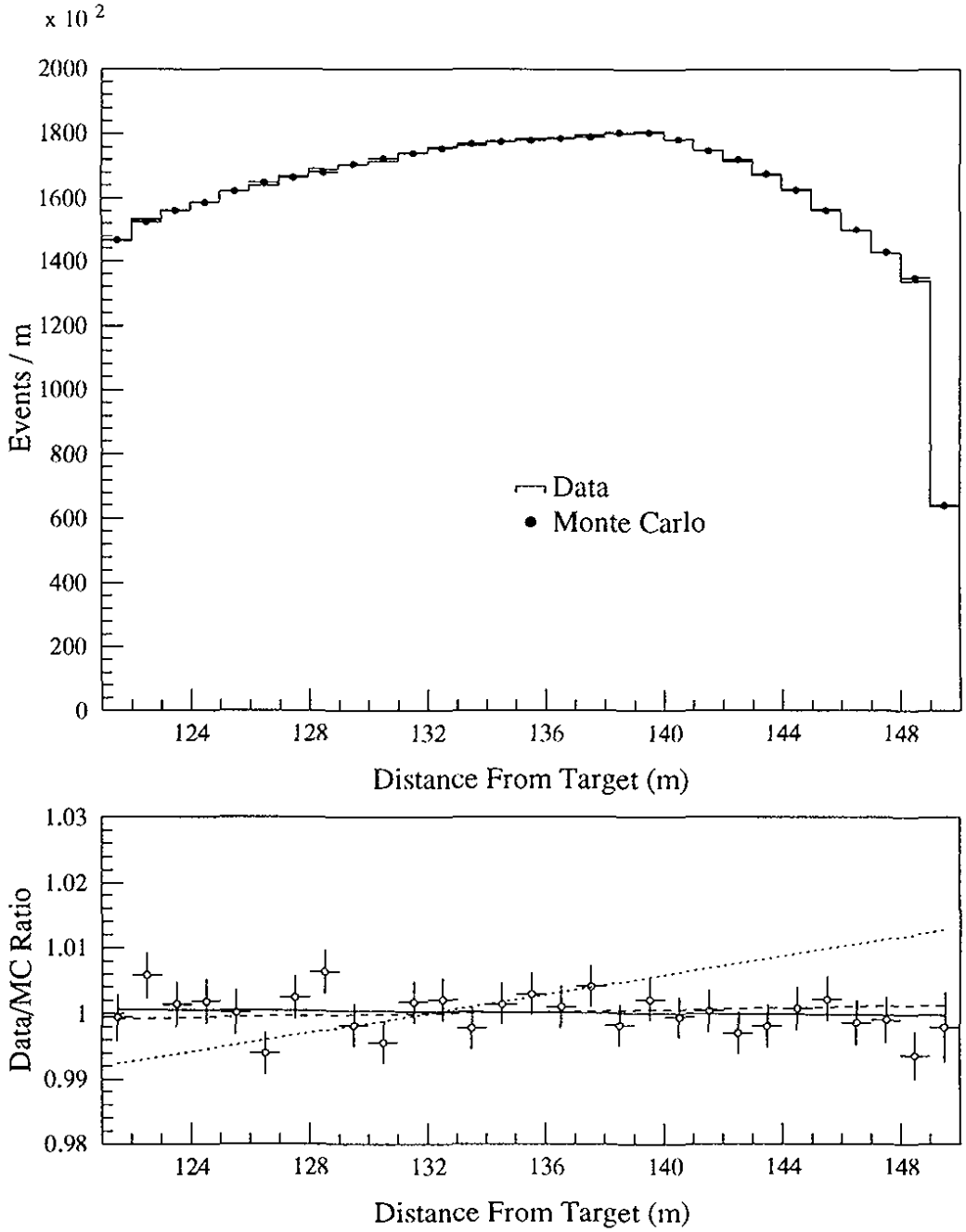

Figure 103. z distribution for $3\pi^0$ decays in the data and Monte Carlo simulation after all other cuts. The sample shown had no lead sheet installed. *Top:* The z distribution for the two event samples, with the simulation statistics normalized to the data statistics. *Bottom:* The ratio of data events to simulated events in each 1 m bin. The solid line is the best fit slope of $-0.0036\% \pm 0.0074\%$ per meter. The dashed line is the slope used for the systematic estimate, 0.074% per meter. The dotted line is the slope required to shift the final result for $Re(\varepsilon'/\varepsilon)$ by 10^{-3}.

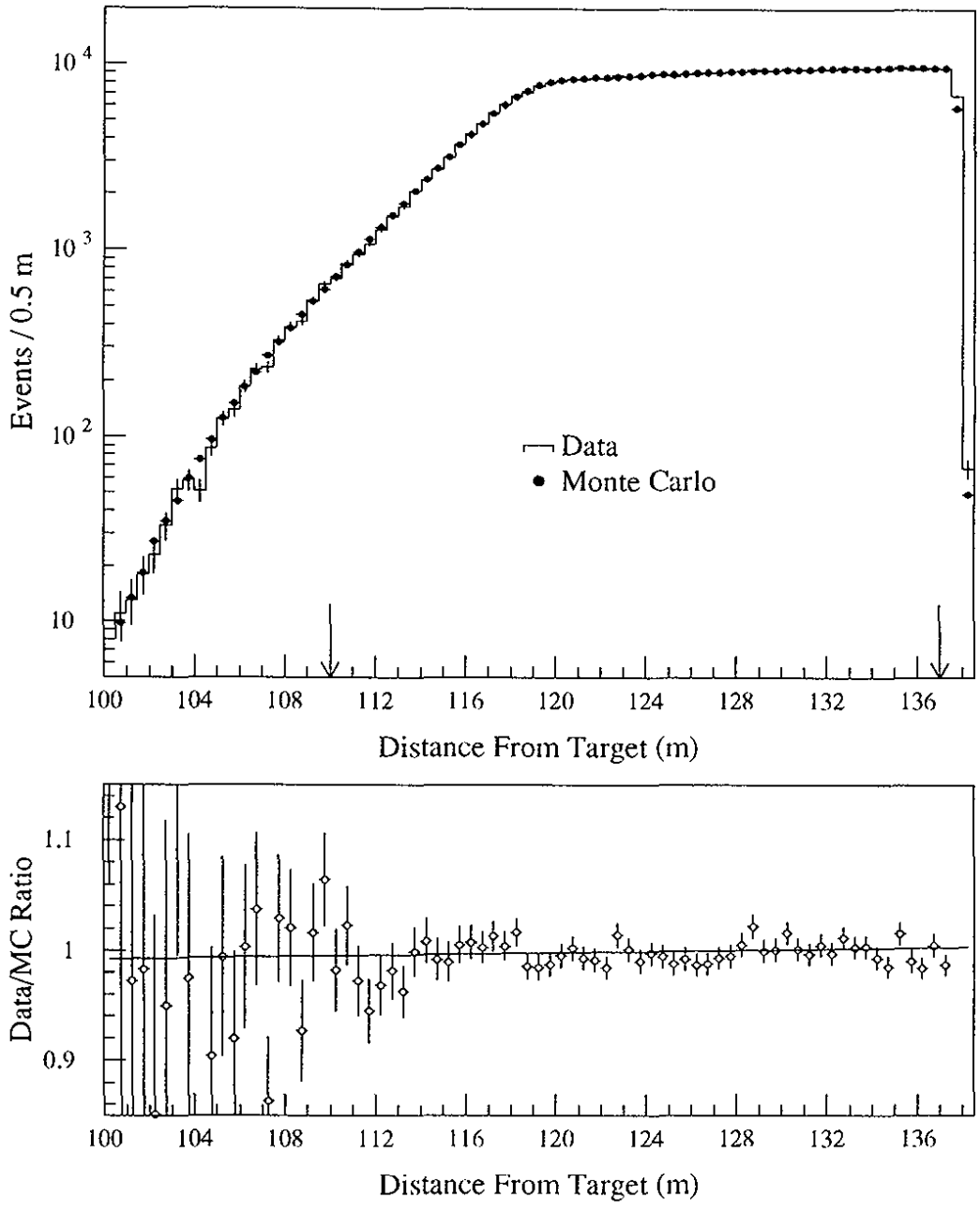

Figure 104. The z distribution for vacuum beam $\pi^+\pi^-$ decays in the data and Monte Carlo simulation after all other cuts. The sample shown is a portion of the NC subset. *Top:* The z distribution for the two event samples, with the simulation statistics normalized to the data statistics. The arrows indicate the fiducial z region used in the analysis. *Bottom:* The ratio of data events to simulated events in each 1/2 m bin. The solid line is the best fit slope of $0.025\% \pm 0.022\%$ per meter.

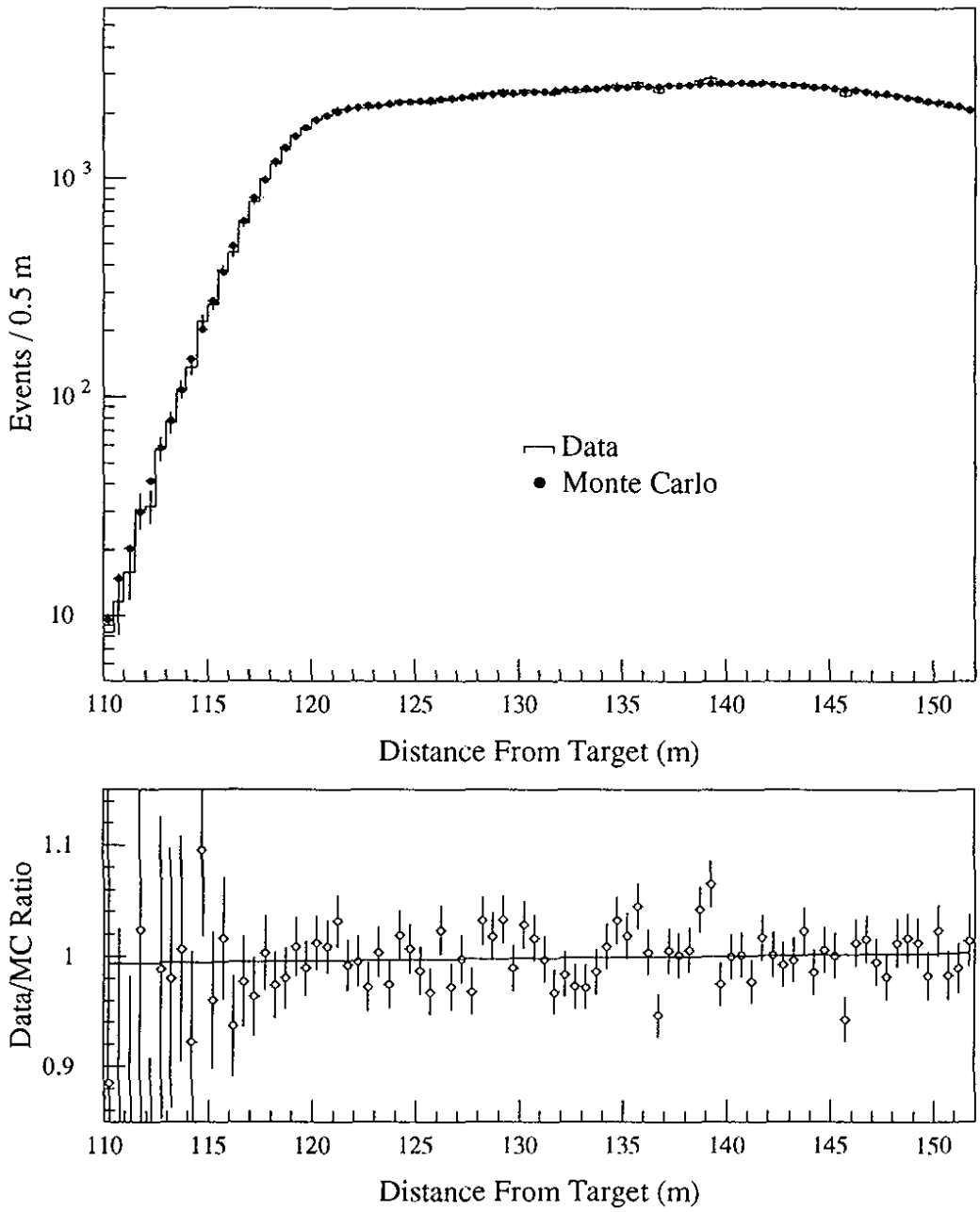

Figure 105. z distribution for vacuum beam $2\pi^0$ decays after all other cuts from the data and simulation subsets with no lead sheet. *Top:* The z distribution for the two event samples, with the simulation statistics normalized to the data statistics. *Bottom:* The ratio of data events to simulated events in each 0.5 m bin. The solid line is the best fit slope of $0.024\% \pm 0.028\%$ per meter.

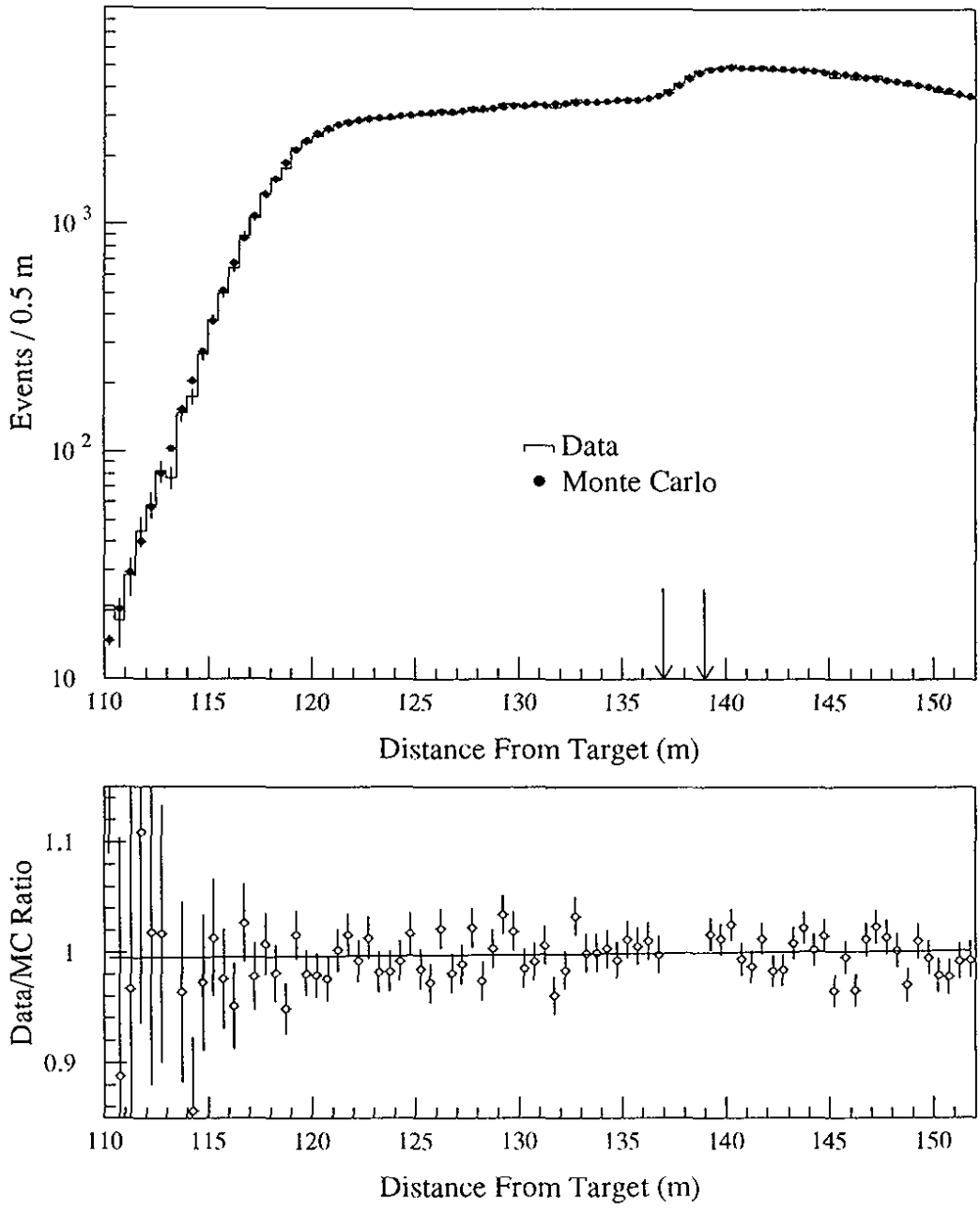

Figure 106. z distribution for vacuum beam $2\pi^0$ decays after all other cuts from the data and simulation subsets with the lead sheet. *Top:* The z distribution for the two event samples, with the simulation statistics normalized to the data statistics. The arrows mark the region around the HDRA excluded from the fits. *Bottom:* The ratio of data events to simulated events in each 0.5 m bin. The solid line is the best fit slope of $0.018\% \pm 0.021\%$ per meter.

as ρ and Δm that are used in the Monte Carlo simulation, and our imperfect knowledge of these parameters make studies of the acceptance over a large range of p and z more problematic. The uncertainties in these parameters, however, do translate into significant uncertainties in the acceptance corrections at our level of precision. For completeness, however, we have included them here. The $\pi^+\pi^-$ z distribution for this beam is shown in Figure 107, and the $2\pi^0$ distribution in Figure 108. These simulated regenerator beam distributions in general agree fairly well with the data distributions. In particular, the agreement in the z shape at the sharp turn on of decays at the regenerator is very good. This shape is completely determined by the details of the resolution, yet even in the $2\pi^0$ mode the Monte Carlo predicts the number of data events at the 10% level three orders of magnitude down from the peak.

7.6 Summary

The most apt summary of the Monte Carlo simulation is the plot of the vacuum beam z overlays for the five different data sets considered in this experiment (Figure 109. We have seen many of these distributions before, but are presented here in a view to help give more information. In the $\pi\pi$ and Ke3 modes, we have seen that the Monte Carlo simulation tracks the data z distribution over several orders of magnitude in the previous log plots. We can now see the details of the agreement over the bulk of the decay region. For the $3\pi^0$ plots, we have now opened up the window over the entire z region to show the agreement upstream of the mask.

We also show the χ^2 for the shapes of the distributions in the data and the Monte Carlo simulation to be the same. In all but the $3\pi^0$ case, these χ^2 values are close to or within a one standard deviation fluctuation. In the neutral mode plots, both $2\pi^0$ and $3\pi^0$ the excess in the χ^2 tends to come from the upstream region right at the rolloff in acceptance, where the z distribution is the most sensitive to residual problems with the photon energy scale. This is particularly true for the $3\pi^0$ case, where 52 units of χ^2 come from the 4 bins in the range 116 m to 120 m, where the data is most sensitive to residual nonlinearities in the photon energy reconstruction.

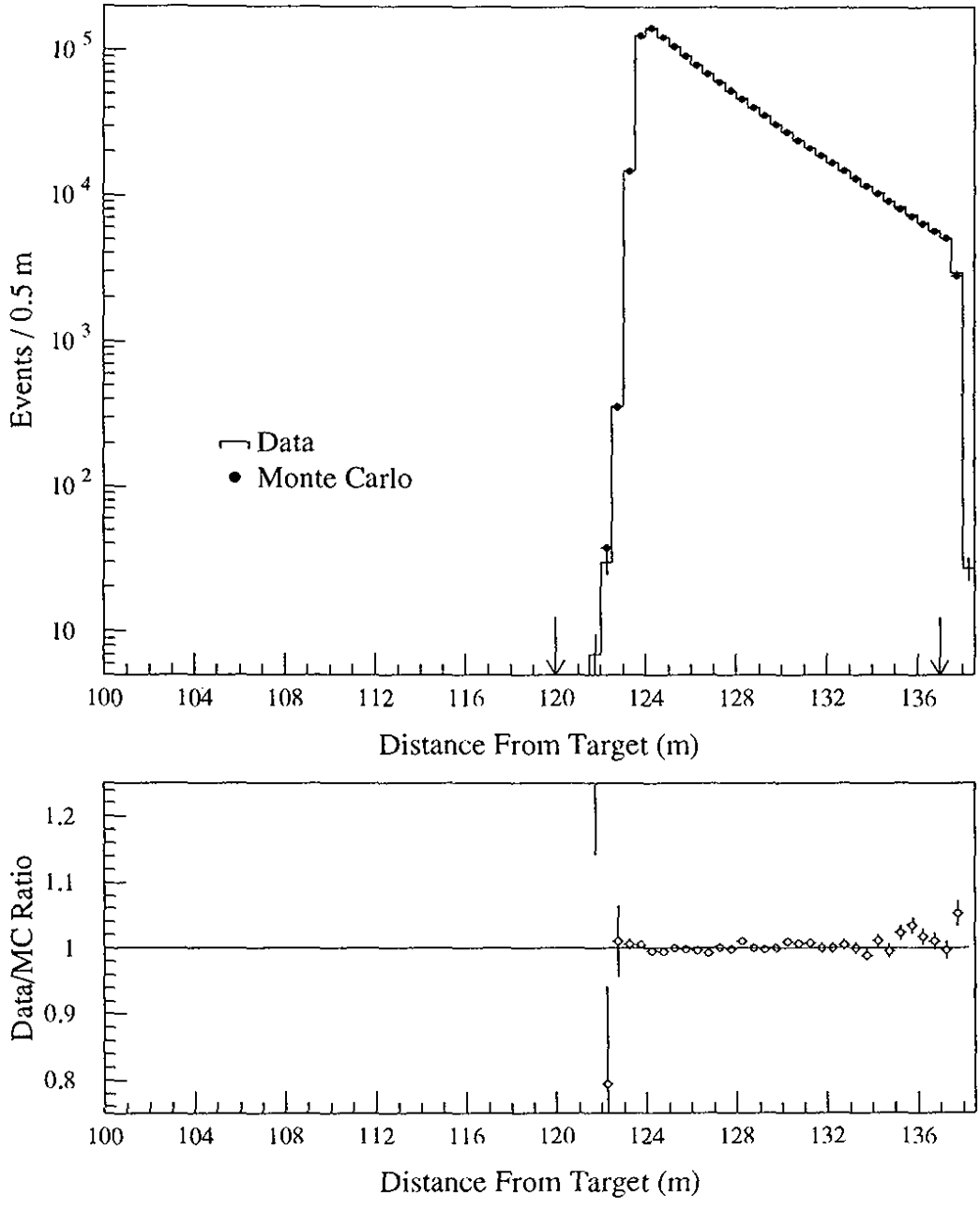

Figure 107. The z distribution for regenerator beam $\pi^+\pi^-$ decays after all other cuts for the data and Monte Carlo simulation. *Top:* The z distribution for the two event samples, with the simulation statistics normalized to the data statistics. *Bottom:* The ratio of data events to simulated events in each 0.5 m bin. The solid line at one is for reference only.

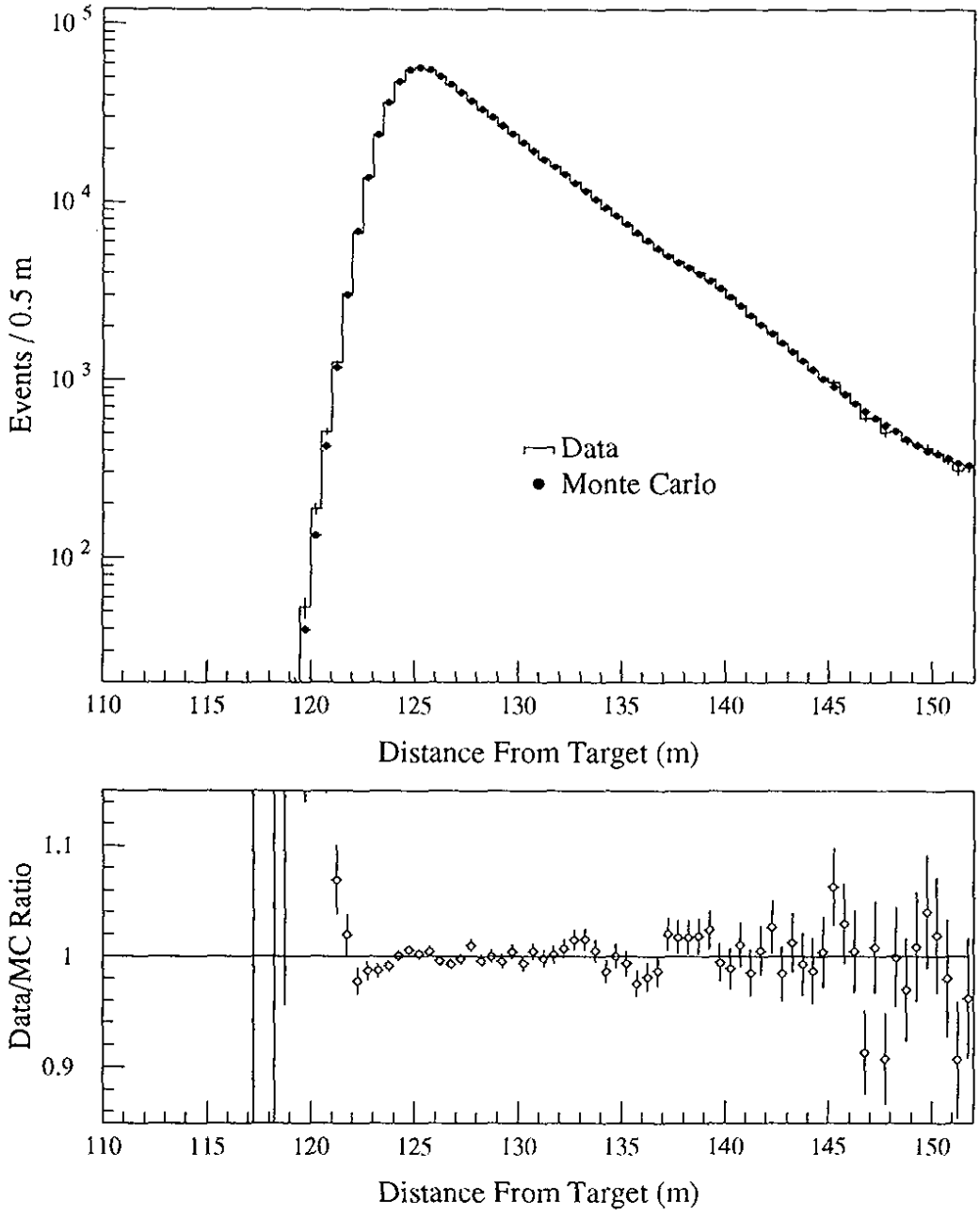

Figure 108. The z distribution for regenerator beam $2\pi^0$ decays after all other cuts for the data and simulation with the lead sheet and no lead sheet subsets combined. *Top:* The z distribution for the two event samples, with the simulation statistics normalized to the data statistics. *Bottom:* The ratio of data events to simulated events in each 0.5 m bin. The solid line at one is for reference only.

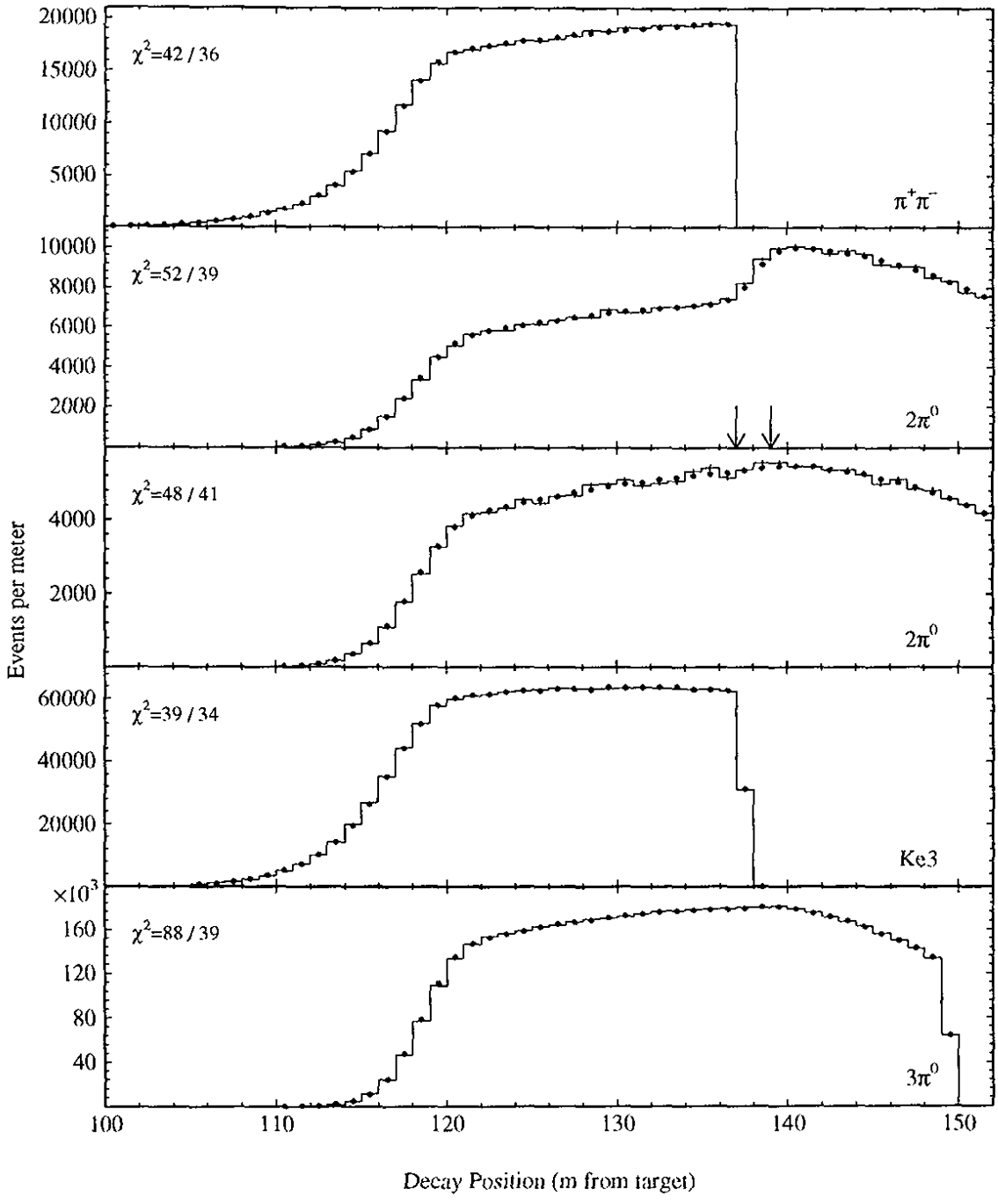

Figure 109. The vacuum beam z distributions in data and Monte Carlo simulation for the $\pi^+\pi^-$ $2\pi^0$ Ke3 and $3\pi^0$ kaon decay modes. The two $2\pi^0$ subsets with and without the lead sheet are shown separately. The χ^2 for the z for the overlay is listed for each distribution. All other cuts have been applied. For the $3\pi^0$ overlay, 52 units of χ^2 come from the 4 z bins at 116 to 120 m, where the data is most sensitive to an energy scale mismatch. The arrows shown for the lead sheet $2\pi^0$ lead sheet subset indicate the z region excluded from the analysis.

When considering these χ^2, one should also remember the statistics involved: the $\pi\pi$ data samples shown range in size from 150,000 to 350,000 events, and the Monte Carlo samples from about 4 million to 8 million events. The Ke3 sample shown has about a million events in both the data and Monte Carlo samples. The $3\pi^0$ sample has about 5,000,000 data events and 6,000,000 Monte Carlo events.

When digesting these plots, it is important to remember that the kinematics of the different decay modes is very different. For example, the undetected neutrino in the Ke3 decays causes very different correlations between the two observed tracks than in the much more symmetric $\pi^+\pi^-$ decays. The illuminations of the apertures by the Ke3 decays tend to be much broader, and hence are more sensitive to the aperture locations. Even the correlations between the B and C hodoscope counters which satisfy the charged trigger are different, helping to prevent any trigger biases from escaping notice.

The situation is much the same in the $3\pi^0$ sample relative the $2\pi^0$ sample. The fully reconstructed $3\pi^0$ subset is much more prone to affects from biases in cluster shape simulation, cluster separation, aperture positions, trigger thresholds, etc., because of the larger number of photons, the broader illumination of the photons, and greater probability for photons to overlap in the lead glass.

In spite of the different characteristics of the decay modes, the Monte Carlo manages to faithfully reproduce the data distributions, not only for the z distributions shown here, but also for many of the other distributions, of which we've still seen only a handful in this chapter. With this detailed simulation in hand, we can now take the accepted and generated $\pi\pi$ distributions from the Monte Carlo and use these to help extract values for $Re(\varepsilon'/\varepsilon)$ and other parameters of the neutral kaon system. We will now turn to the description of the techniques used to determine these parameters.

CHAPTER 8

THE FITTING PROCEDURES

In previous chapters we have discussed the data collection, the background subtraction, and the Monte Carlo simulation for this experiment. The purpose of this chapter is to describe the fitting techniques with which we extract the parameters of interest in the kaon system from the distributions of coherent kaon decays. The discussion will begin with a description of the general procedure used to extract the results, and of the functional form used to describe the data in the fits. The fits for the different parameters and the results obtained will then be described in the next chapter.

For the purposed of many readers, this chapter presents a more detailed breakdown of our fitting procedure than is needed to understand the gist of the results presented in the following chapter. The introduction describes the basic methods we have used to extract the physical parameters of interest, and many readers may simply wish to jump to the next chapter after the introduction.

8.1 Introduction

There were two distinct fitting techniques we used in the analysis of our $\pi\pi$ data sets. The first technique, which we will refer to as "constrained" fitting, was used to determine the values of parameters which affect the shape of the regenerator beam z distribution: Δm, τ_S, ϕ_{+-}, and $\Delta\phi$. The vacuum beam data in each 10 GeV/c bin was corrected for acceptance in a single, large z bin, and compared to the vacuum beam decay rate for that bin in the

Monte Carlo simulation. The vacuum beam decay rate in the Monte Carlo relative to the data was constrained to have a particular form[1], and the vacuum beam constraint served to predict the number of kaons incident on the regenerator in each momentum bin. With the incident number of kaons known for a given momentum bin, the number of decays in each z bin in the regenerator beam can be predicted as a function of Δm, τ_S, etc. for that momentum bin.

For the measurement of $Re(\varepsilon'/\varepsilon)$, we were not as concerned with the shape of the z distribution in the regenerator beam as with the total number of decays in each beam. In the fits for $Re(\varepsilon'/\varepsilon)$, we predicted the ratio of the number of accepted decays in the vacuum and regenerator beam for each momentum bin. There was no constraint on the shape of the vacuum beam decay rate in the data relative to the Monte Carlo; loosely speaking, the incident kaon flux cancels when the ratio of the two beams is taken in each 10 GeV/c momentum bin.

The remainder of this chapter will describe in detail how the prediction for either the number of events in a pz bin in the regenerator beam, or for the vacuum to regenerator beam ratio in a p bin is calculated.

8.2 The Functional and General Fit Procedure

At its heart, the fitting procedure is going to compare the observed number of events in bins of the reconstructed kaon momentum p and decay position z in the vacuum and regenerator beams to the number expected, given a set of decay parameters. Suppose that for a pz bin with the momentum range p_i to $p_i + \Delta p$ and z range z_j to $z_j + \Delta z$, we observe d_{ij} events in one of the beams. The number of events d_{ij} is given by

$$d_{ij} = \int_{p_i}^{p_i+\Delta p} dp \int_{z_i}^{z_i+\Delta z} dz \int dp' \, F(p') \int dz' \, s(p,z;p',z') \, a(p',z') \, r(p',z'). \qquad (8.1)$$

In this expression, the primed quantities p' and z' represent the true momentum and the true decay position.

$F(p')$ is the flux of K_L entering the decay volume with momentum p'.

[1] The form consisted of an overall normalization plus small correction terms.

The detector acceptance and response functions are embodied in the functions $a(p', z')$ and $s(p, z; p', z')$. The former is the probability that a kaon of momentum p' that has decayed at z' will reconstruct in the final sample — independent of what p and z are finally measured for the decay. The function s incorporates all of the resolution and misreconstruction effects, giving the probability that an kaon with momentum in the range p' to $p' + \delta p'$ and decaying in the range from z' to $z' + \delta z'$ will reconstruct in the ranges from p to $p + \delta p$ and z to $z + \delta z$.

All of the physics of the decay process, and hence the various parameters we wish to measure, are incorporated in Equation 8.1 via the decay rate $r(p', z')$. In the regenerator beam, for example, r_r will depend on the regeneration amplitude $\rho(p')$, the K_S lifetime, Δm, etc.

Each of these contributions to the decay rate will be discussed in some detail. For some of the discussions, however, an understanding of the general procedure involved will help to clarify many of the issues.

8.2.1 General Fitting Procedures

8.2.1.1 Binning

The first step in our fitting procedure was to bin the data in reconstructed momentum and decay position, combining the data from the two regenerator positions in the process. In all of the fits performed, the momentum bins were 10 GeV/c wide, while the width of the z bins varied from fit to fit. When we were only interested in the total decay rate in a beam, we used a single z bin measuring the length of the entire fiducial volume. For fits which depended upon the shape of the decay distribution within a beam, we subdivided the beam into several z regions.

To take advantage of the double beam technique, we wished either to use the observed data rate in one beam to predict the incident kaon flux in the other, or alternatively to predict the ratio of the rates in the two beams in each pz bin. In an ideal double beam experiment, the incident kaon flux in the two beams would be identical, and the observed

decay rates in the vacuum and regenerator beams would be independent of the regenerator position. The kaon flux then cancels when comparing the two beams.

What happens if the two beam intensities are different? Let us consider what happens when the kaon flux in the top beam is greater than that in the bottom beam, $I_t > I_b$. The trigger rate is dominated by (non $\pi\pi$) kaon decays in the vacuum beam, hence there will a higher trigger rate when the regenerator is in the lower beam and the top beam, with the higher intensity, is not attenuated by the shadow absorber and the regenerator. With a higher trigger rate for one regenerator position, the chance of the data acquisition system being preoccupied with writing an earlier event to tape when a new event arrives is higher. This leads to slight differences in the livetimes L_u and L_d for up and down regenerator position, respectively. Furthermore, the different intensities can lead to different accidental rates in the detector, because, for example, of the rate of interactions of neutrons in the beam changes with the regenerator position. The different accidental activity can cause a difference in the efficiency of reconstructing $\pi\pi$ decays for the two different regenerator positions. For this discussion, suppose that the loss of events due to accidental activity is $(1-\varepsilon_u)$ when the regenerator is up, and $(1-\varepsilon_d)$ when the regenerator is down.

One final issue can affect the relative number of decays collected with the regenerator in a given position, and that is simply the fraction of time f_d that the regenerator spends in the lower beam. In our experiment, the incident kaon flux in the top beam was about 8% higher than that in the bottom beam, and f_d was not exactly 50%. The deviations of f_d from 50% were of order 1% and varied from subset to subset.

Now suppose that n_v (n_r) is the probability for a kaon entering the decay region to decay and be reconstructed in a given pz bin in the vacuum (regenerator) beam. Then the number of events we would collect for the regenerator sample in the top (bottom) beam would be $N_r^t = f_u L_u \varepsilon_u I_t n_r$ ($N_r^b = f_d L_d \varepsilon_d I_b n_r$), while for the vacuum beam we would have $N_v^t = f_d L_d \varepsilon_d I_t n_v$ ($N_v^b = f_u L_u \varepsilon_u I_b n_v$). If we naively took the arithmetic mean of the data samples from the top and bottom beams, the single ratio would become

$$\frac{N_v^t + N_v^b}{N_r^t + N_r^b} = \frac{(f_d L_d \varepsilon_d I_t + f_u L_u \varepsilon_u I_b) n_v}{(f_u L_u \varepsilon_u I_t + f_d L_d \varepsilon_d I_b) n_r}. \tag{8.2}$$

In general, this will be biased away from the "true" ratio n_v/n_r which we wish to obtain.

This bias can be avoided by using the geometric rather than the arithmetic mean when calculating the vacuum to regenerator ratio:

$$\frac{(N_v^t N_v^b)^{\frac{1}{2}}}{(N_r^t N_r^b)^{\frac{1}{2}}} = \frac{(f_d L_d \varepsilon_d I_t)^{\frac{1}{2}} (f_u L_u \varepsilon_u I_b)^{\frac{1}{2}} n_v}{(f_u L_u \varepsilon_u I_t)^{\frac{1}{2}} (f_d L_d \varepsilon_d I_b)^{\frac{1}{2}} n_r} = \frac{n_v}{n_r}. \tag{8.3}$$

By forming the ratio this way, all of the factors which depend on the different intensities of the two incoming beams cancel, and we are left with the desired ratio n_v/n_r. Using the geometric mean to combine the data from the two different regenerator positions restores the advantageous cancellations of the double beam.

With the data binned, we wished to fit the decay distributions to extract the physics parameters. In all the fits, we use the MINUIT program to perform a χ^2 minimization. The types of fits, however, fall into two distinct classes, which we shall refer to as "unconstrained" and "constrained".

8.2.1.2 Unconstrained Fitting

The first class of fits we will discuss are the unconstrained fits which were used to extract $Re(\varepsilon'/\varepsilon)$. For these fits, the data were binned in momentum only, that is, the entire fiducial volume was taken as one large z bin. The functional was then used to predict the ratio of the number of accepted events in the vacuum beam (N_v) to the number of accepted events in the regenerator beam (N_r) beam, or, more precisely, the ratio $p = N_v/(N_r + N_v)$, in each momentum bin. The χ^2 in this fit is then given by

$$\chi^2 = \sum_{i=1}^{n_p} \frac{(p_i - p_i')^2}{\sigma_i^2}, \tag{8.4}$$

where n_p is the number of momentum bins, p_i is the observed ratio, and p_i' is the predicted ratio. As we will see later, the predicted ratio p_i' contained all of the acceptance corrections to the predicted decay rates in the two beams.

The error σ_i in Equation 8.4 has two contributions, of which the binomial error associated with the ratio p_i dominates. To calculate this contribution, we used the predicted ratio p_i' rather than the measured ratio p_i to reduce the small bias inherent in a χ^2 minimization. There is a second, smaller contribution to σ_i from the finite statistics of the Monte Carlo

sample used to determine the acceptance correction, though the Monte Carlo sample was sufficiently large that the final statistical error on $Re(\varepsilon'/\varepsilon)$ was affected at less than the 10^{-5} level.

If P_{v_i} (P_{r_i}) is the predicted number of vacuum (regenerator) beam decays and $\bar{\varepsilon}_{v_i}$ ($\bar{\varepsilon}_{r_i}$) is the average acceptance for that beam, then the predicted ratio p_i' is

$$p_i' = \frac{P_{v_i}\bar{\varepsilon}_{v_i}}{P_{v_i}\bar{\varepsilon}_{v_i} + P_{r_i}\bar{\varepsilon}_{r_i}}. \tag{8.5}$$

Since

$$\frac{dp_i'}{d\bar{\varepsilon}_{v_i}} = \frac{P_{v_i}P_{r_i}\bar{\varepsilon}_{r_i}}{(P_{v_i}\bar{\varepsilon}_{v_i} + P_{r_i}\bar{\varepsilon}_{r_i})^2} = \frac{p_i'(1-p_i')}{\bar{\varepsilon}_{v_i}}, \tag{8.6}$$

and

$$\frac{dp_i'}{d\bar{\varepsilon}_{r_i}} = \frac{P_{v_i}P_{r_i}\bar{\varepsilon}_{v_i}}{(P_{v_i}\bar{\varepsilon}_{v_i} + P_{r_i}\bar{\varepsilon}_{r_i})^2} = \frac{p_i'(1-p_i')}{\bar{\varepsilon}_{r_i}}, \tag{8.7}$$

the acceptance contribution to the error is simply

$$\sigma^2_{p_i'} = p_i'^2(1-p_i')^2\left(\left(\frac{\sigma_{\bar{\varepsilon}_{r_i}}}{\bar{\varepsilon}_{r_i}}\right)^2 + \left(\frac{\sigma_{\bar{\varepsilon}_{v_i}}}{\bar{\varepsilon}_{v_i}}\right)^2\right). \tag{8.8}$$

The acceptance errors $\sigma_{\bar{\varepsilon}_{r_i}}$ and $\sigma_{\bar{\varepsilon}_{v_i}}$ are also binomial, $\sigma^2_{\bar{\varepsilon}} = \sigma_{\bar{\varepsilon}}(1-\sigma_{\bar{\varepsilon}})/N_g$, where N_g is the number of Monte Carlo decays in the p bin and beam under consideration.

The total error in σ_i appearing in Equation 8.4 is thus

$$\sigma_i^2 = \frac{p_i'(1-p_i')}{N_{r_i} + N_{v_i}} + \sigma^2_{p_i'}, \tag{8.9}$$

where the first term is the binomial error on the predicted ratio and the second term is the contribution from the acceptance correction given above.

The unconstrained fitting technique had the advantage of being quite insensitive to the detailed shape of the incident kaon flux. Across a given 10 GeV/C momentum bin within the momentum range of the fits which used this technique, the acceptance, decay rate and kaon flux were all fairly slowly varying functions. This feature, combined with the fact that we collected vacuum and regenerator beam events simultaneously, caused the incident flux largely to cancel in the regenerator to vacuum beam ratio. This cancellation in turn led to the insensitivity. We will return to this issue when we discuss the systematic evaluation of $Re(\varepsilon'/\varepsilon)$.

8.2.1.3 Constrained Fitting

The second class of fitting derived its name from the fact that the shape of the kaon momentum spectrum was constrained in the fit. In essence, the entire vacuum beam sample was used to predict the flux of kaons incident on the regenerator in a given momentum bin by constraining the shape of the vacuum beam momentum spectrum. By contrast, in the method described above the regenerator beam was normalized to the vacuum beam in each individual momentum bin, which essentially allowed the kaon flux to float independently from momentum bin to momentum bin. The constrained technique had the advantage of enhancing the sensitivity to the kaon parameters we wish to extract from this fit: τ_S, Δm, ϕ_{+-} and $\Delta\phi$. On the other hand, we had to know the kaon energy spectrum quite well.

To implement the vacuum beam constraint, we normalized the total number of kaon decays in the vacuum beam of the Monte Carlo simulation to the total number of decays observed in the vacuum beam in the data (after correcting for the average acceptance). If the spectrum in the Monte Carlo described the data perfectly, then the normalization would have been simple – we would simply have fit for a scale factor α to make the number of vacuum beam decays in the data and Monte Carlo match. As we have seen in the previous chapter, though, there are small discrepancies between the kaon spectra in the data and Monte Carlo (Figure 72) vacuum samples. We therefore included two additional parameters β_1, β_2 for a correction $c(p;\beta_1,\beta_2)$ to the Monte Carlo spectrum. If $F_{MC}(p)$ is the kaon spectrum in the Monte Carlo, then the normalization factor n_i for the ith momentum bin is given by

$$n_i = \alpha \frac{\int_{p_i}^{p_i+\Delta p} dp\, F_{MC}(p) \int_{z_u}^{z_d} dz\, r_v(p,z)\, c(p;\beta_1,\beta_2)}{\int_{p_i}^{p_i+\Delta p} dp\, F_{MC}(p) \int_{z_u}^{z_d} dz\, r_v(p,z)}, \tag{8.10}$$

where $r_v(p,z)$ is the vacuum beam decay rate and z_u and z_d are the upstream and downstream limits of the vacuum beam decay volume used for the normalization. We tried both quadratic and piecewise linear correction functions.

In the fits for $Re(\varepsilon'/\varepsilon)$ we were interested in the total *number* of decays in each beam, but for the other parameters, we were most interested in the proper time distribution of the decays, and hence in the *shape* of the decay distribution as a function of z. To this end, the regenerator data was binned in several z bins for each momentum bin.

There are two separate contributions to the total χ^2 in this class of fit. The first is the implementation of the vacuum beam constraint as a "soft" constraint, which means that the constraint enters as the χ^2 term

$$\chi^2_{constraint} = \sum_{i=1}^{n_p} \frac{(N_{v_i} - n_i D^{MC}_{v_i} \bar{\varepsilon}_{v_i})^2}{(1+n_i)N_{v_i}}. \tag{8.11}$$

N_{v_i} is the total number of vacuum beam data events in the ith momentum bin, while $D^{MC}_{v_i}$ is the total number of kaon decays, accepted or not, in the Monte Carlo sample. $\bar{\varepsilon}_{v_i}$ is the average vacuum beam acceptance for that momentum bin. The n_i term in the denominator arises from the combination of statistical errors from $D^{MC}_{v_i}$ and $\bar{\varepsilon}_{v_i}$.

The functional for this class of fits calculated the expected number of accepted kaon decays, $N'_{r_{ij}}$ in a pz bin of the regenerator beam. For the ith momentum bin and jth z bin, we have

$$N'_{r_{ij}} = \frac{n_i D^{MC}_{v_i}}{d_{v_i}} p_{r_{ij}}. \tag{8.12}$$

$p_{r_{ij}}$ is the probability for this pz bin of accepting a kaon decay in the regenerator beam, and d_{v_i} is the probability of a kaon decaying in the vacuum beam in this momentum bin. The fraction on the right hand side is simply the number of kaons incident on the regenerator beam. Adding the contribution from the regenerator beam prediction to the χ^2 brings the total χ^2 for a constrained fit to

$$\chi^2 = \chi^2_{constraint} + \sum_{i=1}^{n_p}\sum_{j=1}^{n_z} \frac{(N_{r_{ij}} - N'_{r_{ij}})^2}{N'_{r_{ij}} + (N'_{r_{ij}} \sigma_{\bar{\varepsilon}_{r_{ij}}} / \bar{\varepsilon}_{r_{ij}})^2} \tag{8.13}$$

This ends the general discussion of the fitting techniques used in this experiment. We now turn back to a more detailed discussion of the kaon flux, the acceptance definition, and the decay rates in the two beams. These were the building blocks of the functional we used to approximate Equation 8.1.

8.2.2 The Kaon Flux $F(p)$

In both the unconstrained and constrained fits, the final results were very insensitive to the exact shape of the overall kaon flux used in the functional approximating Equation 8.1. This resulted because over most of the momentum range that we use, the acceptances and

decay rates vary slowly across the 10 GeV bins we use, and the incident flux shape cancels to a large extent when we compare the regenerator beam to the vacuum beam.

What was more important was the difference in the K_L flux between the vacuum and regenerator beams. In an ideal double beam experiment, the K_L flux shape would be identical in the two beams. In reality, there are small deviations of the regenerator beam flux shape away from the vacuum shape because of kaon interactions with the additional material in the regenerator beam. The flux shape modifications due to kaon interactions in the common absorber were implicitly accommodated by the direct measurement of the vacuum beam $\pi^+\pi^-$ spectrum. The additional modifications to the regenerator beam spectrum arose from three distinct effects, primary $K_S \rightarrow K_L$ regeneration, elastic scattering in the movable absorber, and the energy dependence of the kaon total cross section with the additional material in the regenerator beam.

The spectrum of kaons predicted by our final Monte Carlo simulation to enter the decay volume in the vacuum beam is shown in Figure 110. The corrections to the spectrum were small perturbations on this shape.

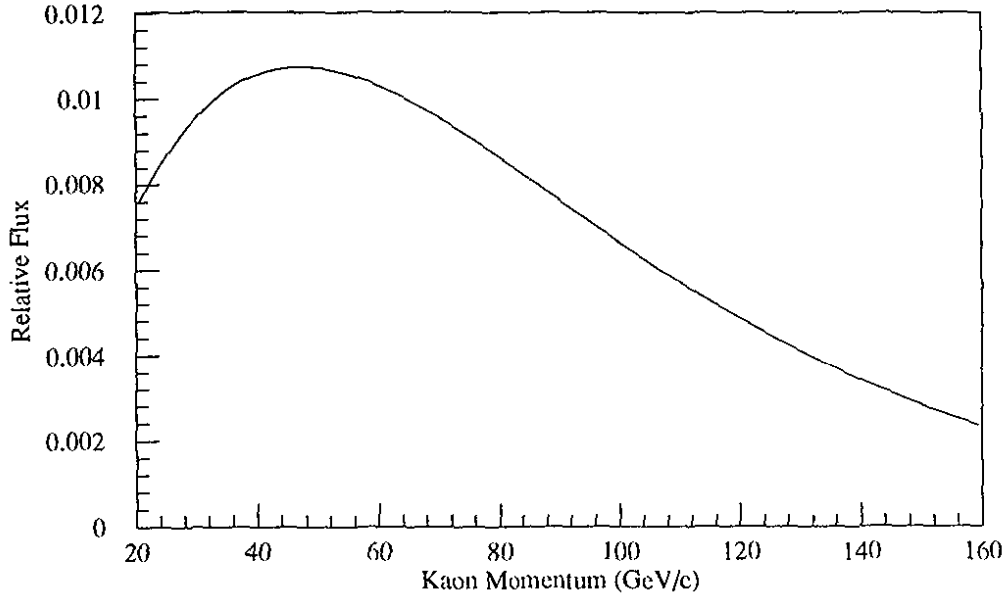

Figure 110. The Monte Carlo prediction for the momentum spectrum of kaons incident at $z = z_{reg}$ in the vacuum beam.

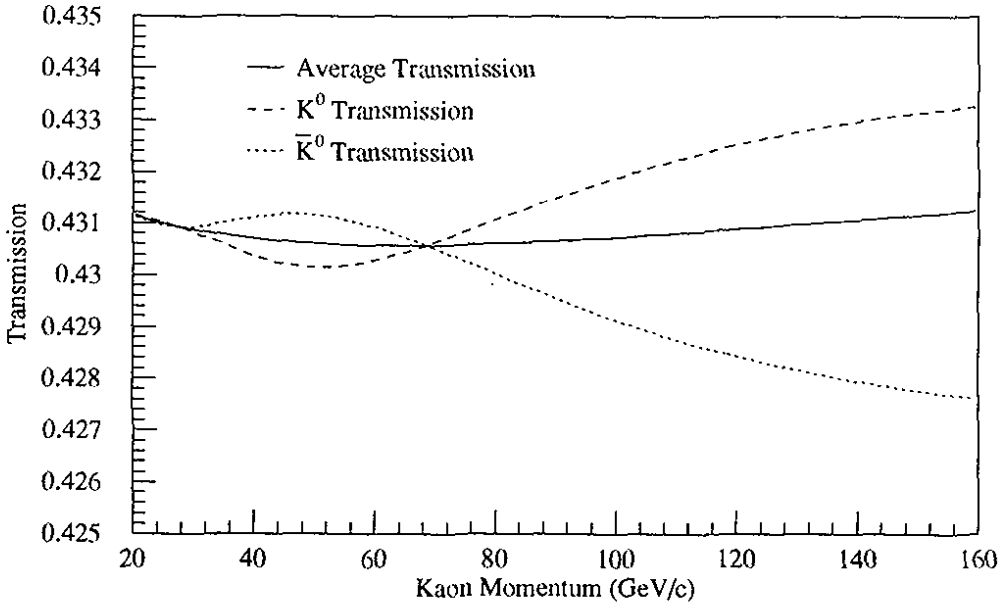

Figure 111. Ratio of K_L flux in the regenerator beam relative to the vacuum beam after the shadow absorber. The shapes result from regeneration of the primary K_S component to K_L in the shadow absorber. The effect is opposite for K^0 and $\bar{K}^0$ because of the opposite relative K_S and K_L phases. The average curve has been calculated by weighting the K^0 and $\bar{K}^0$ with their relative production probabilities.

8.2.2.1 Primary $K_S \rightarrow K_L$ regeneration

Much of the difference between the vacuum beam and regenerator beam momentum spectra came from the presence of the shadow absorber (see Section 3.1) near the upstream end of the regenerator beam. Because the absorber was located quite close to the primary production target, there was still a substantial primary K_S amplitude left in the initially K^0 or $\bar{K}^0$ state. Regeneration works both ways, and the primary $K_S \rightarrow K_L$ regeneration slightly modified the shape of the final K_L spectrum incident on the regenerator. This effect can be easily calculated, and the relative shape change due to this effect, normalized at a kaon momentum of 70 GeV, is shown in Figure 111.

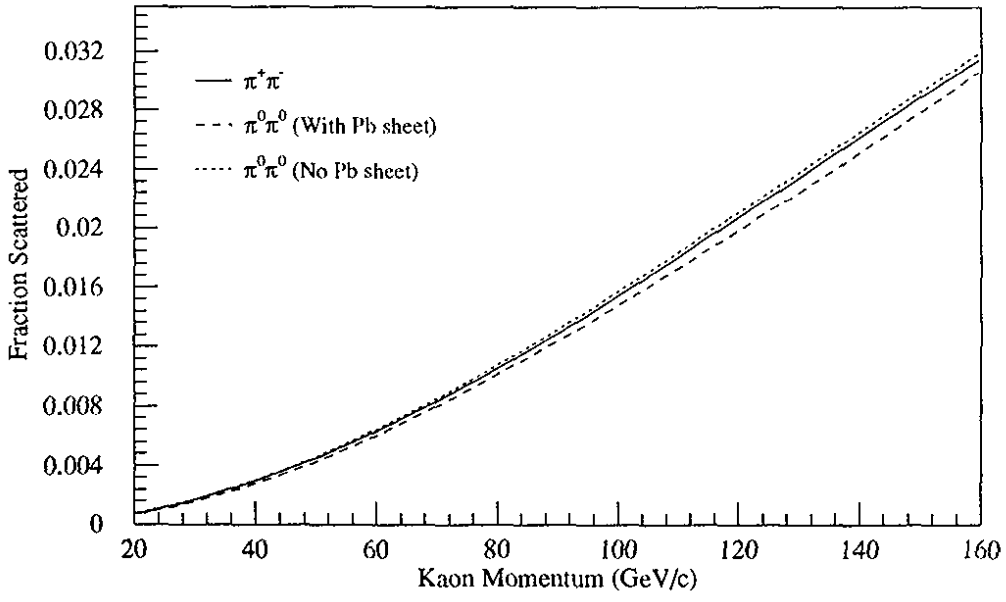

Figure 112. Fraction of kaons incident on the regenerator which have scattered in the shadow absorber. The fraction depends weakly on the relative beam and collimator positions, leading to the small differences in the different sets.

8.2.2.2 Kaon Scattering in the Absorbers

The shadow absorber also modified the regenerator beam K_L spectrum because of the extra elastic scattering some of the kaons suffered. Because the p_t^2 spectrum for the scattering is independent of the kaon momentum, low energy kaons scattered through larger angles more often than high energy kaons. Kaons scattered through large angles were, in turn, more likely than kaons scattered through small angles to be lost in the collimation of the beam farther downstream. We obtained quite accurate collimator orientations by studying the details of the observed kaon beam shape. We have fine tuned the collimators in the Monte Carlo to match the observed beam shape (Figure 75), and then used the Monte Carlo to predict the kaon enhancement in the regenerator beam because of this scattering. The predicted enhancement for the charged data sample and for the neutral samples with and without the lead sheet are shown in Figure 112.

As we will discuss more fully in the systematic evaluation, this process had little effect upon the measurement of $Re(\varepsilon'/\varepsilon)$ because the bulk effect is common to both the charged

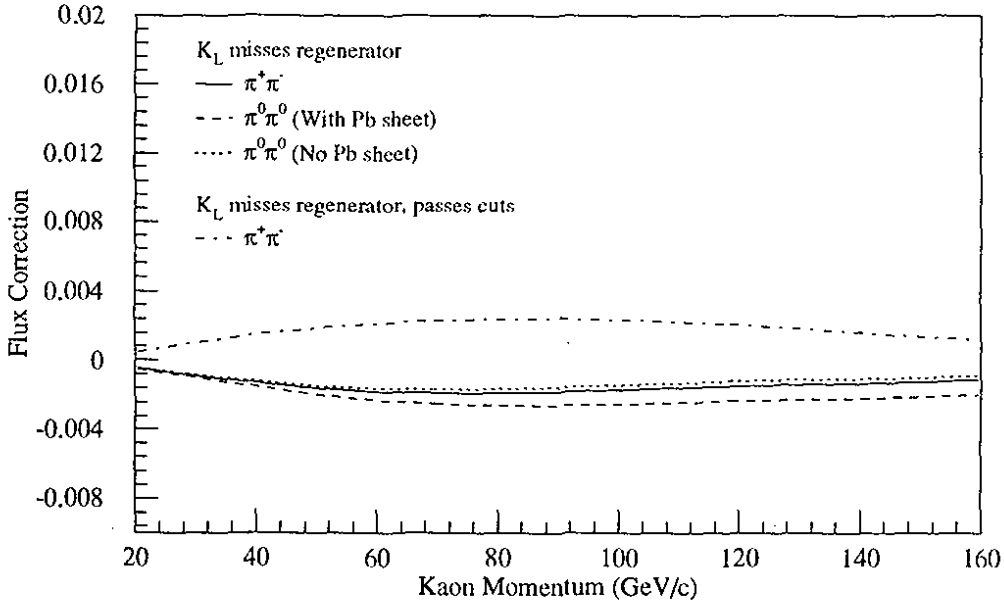

Figure 113. Fractional correction to the flux of kaons which pass through the regenerator as a result of elastic kaon scattering in the absorbers. The fraction depends on the average beam and collimator positions. In the charged mode, some of the kaons which miss the regenerator and decay as pure K_L pass all analysis cuts. The probability of this (relative to the total kaon flux) is shown as the dot-dash curve.

and neutral data samples. The largest effect came from the small differences between the samples. The scattering is somewhat more important for the other fits because its neglect would distort the observed slope of the regeneration momentum dependence and hence also the regeneration phase predicted with analyticity from that slope (see Sections 2.4 and 8.2.3).

Due to a small misalignment of the collimators, it was possible for a kaon to scatter through certain angles, particularly in the lead of the common absorber, and survive collimation yet miss the regenerator. The fraction of incident kaons which missed the regenerator is shown for the three data sets in Figure 113. Many of these kaons ("sneakbys") were eliminated in the neutral analysis by the cuts which reduced the noncoherent regeneration background. All of the sneakbys, for example, landed near the edge or in the tails of the beam and were eliminated in neutral mode by the ring number cut.

The charged mode p_t^2 cuts are not as effective because we calculate the p_t^2 assuming

the kaon scattered in the regenerator. If z_{reg} and z_{abs} are the regenerator and absorber z locations, then the p_t^2 reconstructed in the $\pi^+\pi^-$ analysis (call it $p_{t_c}^2$) is diluted by

$$p_{t_c}^2 = \left(\frac{z_{abs}}{z_{reg}}\right)^2 p_t^2 \tag{8.14}$$

relative to the true p_t^2 kick at the absorber. For our absorber and regenerator locations, the dilution factor implies the p_t^2 we measure is only 2% of the true p_t^2, and hence a large fraction of the kaons that scatter and miss the regenerator remain in the charged sample. For this mode, the relative flux of kaons which miss the regenerator and survive the transverse momentum cut is shown as the dot-dash line in Figure 113.

Fortunately, these kaons were K_Ls, so they contributed very little to the decay rate in the regenerator beam (0.015% at 70 GeV/c). Nevertheless, this component of the regenerator beam decay distribution is included in the functional.

8.2.2.3 Energy dependence of the kaon-nucleus total cross section

The final modification to the shape of the regenerator spectrum is due to the small energy dependence of the kaon-nucleus total cross section, and hence of the kaon absorption in the shadow absorber and regenerator. The average transmission has been accurately measured by comparing the vacuum and regenerator beam samples in the $3\pi^0$ and $\pi^+\pi^-\pi^0$ modes. The measurements were made using kaons in the momentum range from 40 GeV/c to 150 GeV/c, and yielded 6.33(3)% for the $3\pi^0$ mode and 6.43(6)% for the $\pi^+\pi^-\pi^0$ mode. Combining these, we get average kaon transmission of 6.35(3)%. We now need to incorporate the energy dependence.

The kaon-nucleon total cross sections are fairly well understood [93] and predictions are in good agreement with the measured energy dependence of the cross sections. The largest uncertainty in the calculation of the cross section is in the size of the correction due to inelastic screening of the nucleons within the nucleus. The cross section predictions for Carbon with and without the screening correction pictured in Figure 114a. The uncertainty in the correction is estimated at 30% of itself.

Because of the small piece of lead at the end of the regenerator, we also need to know

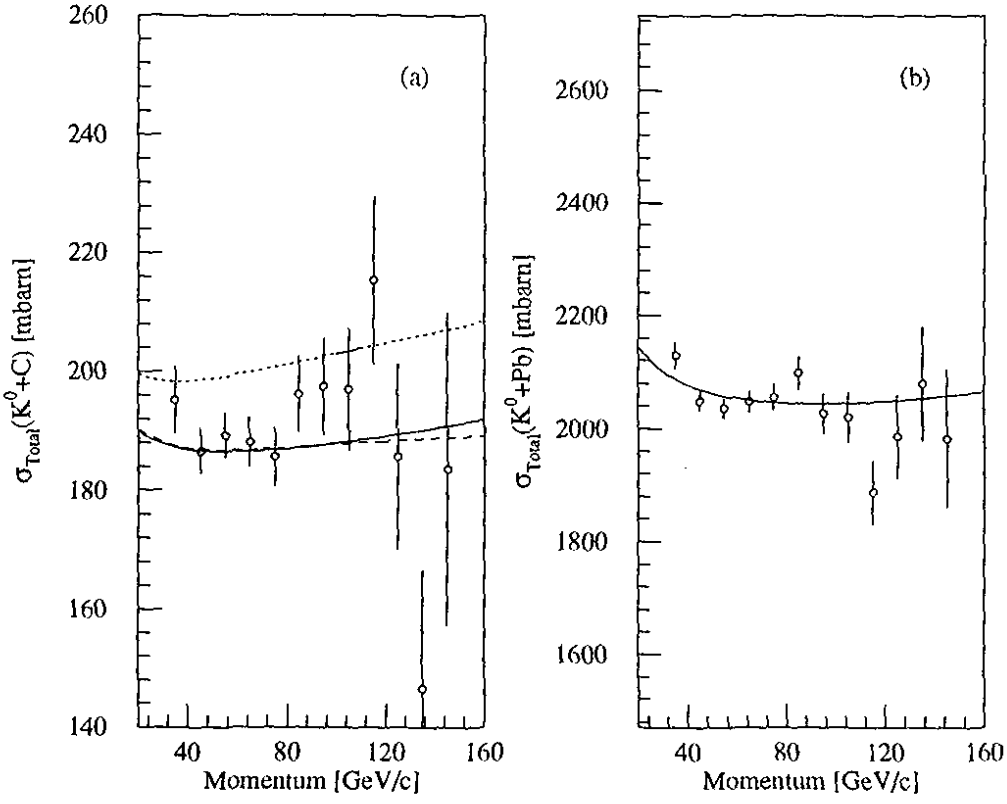

Figure 114. Energy dependence of the Kaon-Carbon and Kaon-Lead total cross section. (a) The solid line is the prediction of the Glauber-Franco model [94] with inelastic screening corrections. The dotted line is the prediction without the screening. The cross section with the correction preferred by our data is shown as the dashed line, and is well within the 30% uncertainty on the inelastic correction. (b) The model prediction for Kaon-Lead scattering, with the inelastic correction. The data in both (a) and (b) are from reference [93].

the total cross section for kaon-lead scattering. This cross section is well measured and predictions are again in good agreement with the measurements [93] (see Figure 114b).

To implement the energy dependence of the absorption, the shape of the total cross section for Carbon was scaled to Boron and Beryllium using the measured average cross sections. Because of the uncertainty in the inelastic correction, we introduce a correction parameter μ for each of the fits. The rise in the cross section at high energy is very close to quadratic, and the correction is parametrized as a quadratic with the same minimum (near 56 GeV/c). That is, the correction has the form $\mu(p-56)^2$. The lead cross section is used without modification. The average kaon transmission in the 40 GeV/c to 160 GeV/c range

is constrained to agree with the transmission measured with the $\pi^+\pi^-\pi^0$ and $3\pi^0$ samples. This constraint was implemented by adding a small constant to the cross section. The fits yield a correction to the kaon-Carbon cross section of -2.8 ± 1.1 mbarn at 156 GeV/c. The change in the predicted shape is shown for Carbon as the dashed line Figure 114a.

In summary, the kaon flux in the regenerator beam relative to the vacuum beam is given by

$$F_r(p) = \bar{t} F_v(p) c(p), \tag{8.15}$$

with the bulk of the difference incorporated in the average kaon transmission $\bar{t} = 6.35\%$ and $c(p)$ a small correction factor for the momentum-dependent effects which is of order 0.4% at our average kaon energies.

8.2.3 Decay Rates

All of the kaon physics in which we are interested is embodied in the 2π decay rates $r_v(p,z)$ and $r_r(p,z)$ for the vacuum beam and regenerator beam, respectively. For a pure K_L beam, the 2π decay rate is given by

$$r_v(p,z) = \frac{dN_v}{dp\,dz} = |\eta_{+-(00)}|^2 e^{-(z-z_{reg})/\gamma\beta c\tau_L}, \tag{8.16}$$

where $\gamma\beta$ is the kaon boost, $\gamma\beta = p/m_K c^2$. The subscript on η differentiates the charged $(+-)$ and neutral (00) decay rates. The K_L amplitude has been normalized to 1 at $z = z_{reg}$, the downstream end of the regenerator.

The 2π decay rate in the regenerator beam is more complicated, and depends on the regeneration amplitude $\rho(p)$, which is the ratio of the K_S amplitude to K_L amplitude after a kaon has passed through the regenerator. Given a pure incoming K_L beam, and normalizing the K_L amplitude as above, the regenerator beam decay rate is

$$\begin{aligned} r_r(p,z) &= \frac{dN_r}{dp\,dz} \\ &= |\rho(p)|^2 e^{-(z-z_{reg})/\gamma\beta c\tau_S} + |\eta_{+-(00)}|^2 e^{-(z-z_{reg})/\gamma\beta c\tau_L} \\ &+ 2|\rho(p)||\eta_{+-(00)}| \cos(\Delta m(z-z_{reg})/\gamma\beta c + \phi_\rho - \phi_{+-(00)}) e^{-(z-z_{reg})/\gamma\beta c\tau_{av}}. \end{aligned} \tag{8.17}$$

The quantity τ_{av} is defined by

$$\frac{1}{\tau_{av}} = \frac{1}{2}\left(\frac{1}{\tau_S} + \frac{1}{\tau_L}\right), \tag{8.18}$$

and ϕ_ρ is the phase of the regeneration amplitude $\phi_\rho = \arg(\rho)$. Because the K_S and K_L amplitudes are equally attenuated when passing through the regenerator, we can group the effect of kaon attenuation through the regenerator into the overall kaon flux for the regenerator beam, $F_r(p)$. This property was implicit in the discussion of absorption in the previous section . Recall that $|\rho/\eta|$ is roughly 15 for the mean kaon momentum in our sample, so the K_S decay term dominates the total rate.

Implicit in the normalization of the K_L amplitude to unity at $z = z_{reg}$ in Equation 8.18 is the thick regeneration approximation. In this approximation, we ignore higher order regeneration effects, such as the secondary regeneration of K_S back to K_L, and the only normalization effect of the K_L amplitude in the regenerator beam relative the vacuum beam is the kaon attenuation. This approximation gives the ratio of the K_S and K_L amplitudes at the end of the regenerator as

$$\rho(p) = \imath\pi\gamma\beta c\frac{f(0) - \bar{f}(0)}{k}\left(\frac{p}{70}\right)^{\alpha} g(L). \tag{8.19}$$

with

$$n = \frac{N_A d}{A}. \tag{8.20}$$

The parameters in the above expressions are defined as follows:

n	density of scattering sites
N_A	Avogadro's Number
d	Density of the regenerator material
A	Atomic Number of the regenerator material
$f(0)$, $\bar{f}(0)$	K^0, $\bar{K}^0$ forward scattering amplitude at 70 GeV/c
k	kaon wave number
α	slope of momentum power-law dependence

The function $g(L)$ is a complex geometric factor originating in the kaon propagation through the regenerator. It is given by

$$g(L) = \frac{1 - \exp[-L(\frac{1}{2\tau_S} - \imath\Delta m)/\gamma\beta c]}{(\frac{1}{2\tau_S} - \imath\Delta m)}. \tag{8.21}$$

In both the fitting program and the Monte Carlo, we actually use the exact propagation of the kaon amplitude through the regenerator (see Appendix A or the excellent discussion in [95]). (We have also used the thick regenerator approximation in fitting, and for $Re(\varepsilon'/\varepsilon)$ it gives identical results within 2×10^{-5}). For this discussion, the physics issues are somewhat more transparent using the thick regenerator formulation.

In Equation 8.19, we have explicitly incorporated the expected power-law momentum dependence of the difference of the K^0 and $\bar{K}^0$ forward scattering amplitudes:

$$\left|\frac{f(0)-\bar{f}(0)}{k}(p)\right| = \left|\frac{f(0)-\bar{f}(0)}{k}(70)\right| \left(\frac{p[\mathrm{GeV}/c]}{70}\right)^{\alpha}. \tag{8.22}$$

This dependence results from the difference in scattering being dominated by a single Regge trajectory, that for the exchange of the ω-meson in KN scattering (see, for example, [96], [97] for general discussions of Regge theory, and [77] for application to the $K^0 - \bar{K}^0$ system).

To measure Δm and ϕ_{+-}, it is clear from Equation 8.18 that we need to know the regeneration phase ϕ_ρ. There are two contributions to this phase. The geometric phase $\phi_g \equiv \arg[g(L)]$ can be trivially calculated, which leaves the phase contribution from the forward scattering amplitude, $\phi_{f-} \equiv \arg[(f(0) - \bar{f}(0))/k]$. Fortunately, the dispersion relations which result from requiring analytic behavior of the forward scattering amplitudes determine this phase. For a power law dependence as in Equation 8.22, the phase is related to the power law slope α via

$$\phi_{f-} = -\frac{\pi}{2}(2+\alpha). \tag{8.23}$$

To calculate the regeneration amplitude for our regenerator, we need to take into account its compound structure. The regenerator consists of 4 separate blocks of boron carbide of length $L_{B_4C} = 19.00$ cm separated by vacuum gaps of length $L_v = 3.75$ cm. At the end of the regenerator is a piece of lead which is $L_{Pb} = 1.25$ cm thick. If ρ_{B_4C} is the regeneration amplitude for one of the boron carbide blocks, and ρ_{Pb} is that for the lead piece, then the total regeneration at the end of the regenerator is

$$\begin{aligned} \rho_{total} &= \rho_{B_4C}\left(e^{-3(L_{B_4C}+L_v)\Lambda_S} + e^{-2(L_{B_4C}+L_v)\Lambda_S} + e^{-(L_{B_4C}+L_v)\Lambda_S} + 1\right) e^{-L_{Pb}\Lambda_S} \\ &+ \rho_{Pb}, \end{aligned} \tag{8.24}$$

with

Table 16. Regeneration parameters for the Boron Carbide and lead in the regenerator used in the fits. For the Boron Carbide, values of regeneration parameters which float in the fitting are presented.

Material	Atomic Weight	density (gm/cm^3)	$(f-\bar{f})/k$ (mbarn)	power-law slope	phase (degrees)
B_4C	55.26	2.52	5.791 [a]	-0.604 [a]	-125.6 [b]
Pb	207.19	11.35	9.71 ± 0.14 [c]	-0.654 ± 0.018 [d]	122.2 ± 1.8 [d]

[a] Always extracted as a parameter in the fits. This is a typical value.

[b] Always obtained via analyticity from the current value of α_{B_4C} in the fits. This is a typical value.

[c] Value obtained using the data in [86], with a correction for the change in η_{+-}. The error includes the error quoted in [86] added in quadrature with the contribution from the current uncertainty η_{+-}.

[d] From [86].

$$\Lambda_S \equiv \frac{1}{\gamma\beta c}\left(\frac{1}{2\tau_S} - i\Delta m\right). \tag{8.25}$$

The exponentials in Equation 8.24 result from the propagation of the regeneration amplitude from each block to the end of the regenerator.

In each of our standard fits, the power-law dependence α_{B_4C} and scattering amplitude difference at 70 GeV/c, $(f(0) - \bar{f}(0)/k)|_{70}$, for boron carbide are parameters of the fit. The scattering phase for the boron carbide is obtained from the analyticity relation (Equation 8.23). For the lead parameters we use the values obtained in a previous experiment [86]. The values of the regeneration parameters used in the fits are summarized in Table 16. For typical values of the boron carbide parameters, the lead piece accounts for 3.3% of the regeneration amplitude at 70 GeV/c.

These are the basic concepts that we implement in calculating the decay rates in our fit. There are two issues that complicate the fitting procedure beyond what we have discussed so far. The first complication involves the assumption made above that the beams arriving at the decay volume are pure K_L beams. The second involves the modification of the decay rate to accommodate the material in the HDRA. The former affects all fits, while the latter affects only neutral mode data downstream of the HDRA.

8.2.3.1 Primary K_S corrections

There are two methods for accommodating the primary K_S correction. The most exact way would be to start kaon propagation at the primary production target, calculating the effects of all the absorbers, weighting the K^0 and $\bar{K}^0$ contributions according to their production spectrum, etc., etc. In practice, this is computationally very time consuming, and it turned out to be sufficient to correct the observed data distribution to make it *appear* that the incident beams were pure K_L beams.

The absolute primary K_S correction was small, as the fractional correction was largest where we had the fewest data: the far upstream z region for high kaon momentum. The fraction of the total number events in the momentum range from 40 GeV/c to 160 GeV/c and z range from 110 m to 137 m in the charged sample is shown as a function of momentum and z in Figure 115. The total correction in the charged sample in this range is -0.62% ($+0.0013\%$) for the vacuum (regenerator) beam sample. Almost half of the vacuum correction comes from the 160 GeV momentum bin alone. For the same z and p range in the neutral sample, the correction is -0.14% ($+0.0035\%$). The size of the correction is under 0.002% for both beams in the neutral sample downstream of 137m.

In principle, when fitting for Δm and τ_S, the K_S correction will change depending on the current value for these parameters. Since the corrections are small, particularly in the momentum and z ranges with the most sensitivity to Δm and τ_S, and since the parameters themselves are quite well known, this dependence turns out not to matter at our level of sensitivity. From extensive testing on different high statistics Monte Carlo samples, we have found that fits using this correction technique yield the correct values of Δm and τ_S to within 10% of the statistical precisions we can obtain in this experiment. $Re(\varepsilon'/\varepsilon)$ is even less sensitive to this correction, with the level of discrepancy well below 10^{-5}, even when the values for Δm, τ_S and the $k\bar{k}$ dilution factor are varied over ranges commensurate with their uncertainties.

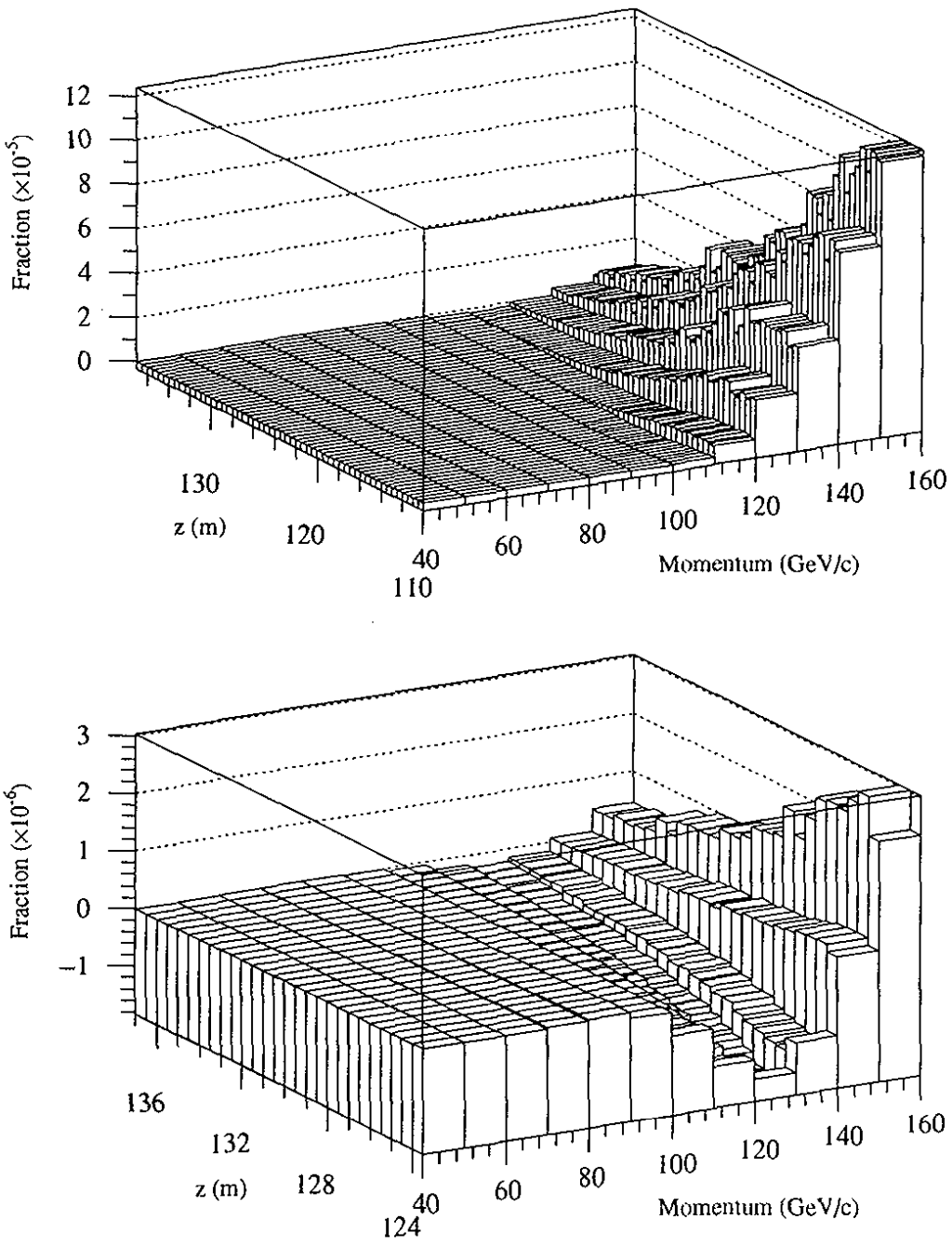

Figure 115. Fraction of the total sample of $K \to \pi^+\pi^-$ decays which are subtracted to correct for primary K_S in the kaon beam. The top (bottom) plot is the vacuum (regenerator) beam correction. The "subtracted" number of events is sometimes negative because the primary K_S amplitude can suppress the decay rate, depending on its phase.

8.2.3.2 Regeneration in the HDRA

In all of our fits involving the neutral mode, the data came from a z region extending beyond the HDRA. For any portion of a z bin upstream of the HDRA, the decay rate given in the previous discussion is still correct. For the z region downstream of the HDRA, however, the K_S and K_L amplitudes have to be modified to include regeneration and attenuation in the HDRA.

The components of the HDRA (see Table 3) are very thin, particularly considering that for the minimum kaon momentum in the neutral mode, the K_S decay length is 2 meters. For this reason, we can treat all of the regeneration from the HDRA as coming from a single plane in z. The regeneration amplitude for each material is calculated using the thin regenerator approximation. When the regeneration length L satisfies $L \ll \gamma\beta c\tau_S$, then the geometric term $g(L)$ (Equation 8.21) reduces to

$$g(L)_{thin} \approx \frac{L}{\gamma\beta c} \tag{8.26}$$

and the thin regenerator approximation is thus given by

$$\rho(p)_{thin} = \imath\pi N L \frac{f(0) - \bar{f}(0)}{k} \left(\frac{p}{70}\right)^{\alpha}. \tag{8.27}$$

If ρ^H is the sum of the regeneration amplitudes from the materials listed in Table 3, T^H is the fraction of the kaon beam transmitted through the HDRA, and a_L^r (a_S^r) is the K_L (K_S) amplitude at $z = z_{reg}$, then the K_L and K_S amplitudes after passage through the HDRA are

$$\begin{aligned} a_L^H &= \sqrt{T^H} a_L^r e^{-\Delta z/2\gamma\beta c\tau_L} \\ a_S^H &= \sqrt{T^H}(a_S^r e^{-\Delta z(\frac{1}{2\tau_S} - \imath\Delta m)/\gamma\beta c} + \rho^H a_L^r e^{-\Delta z/2\gamma\beta c\tau_L}). \end{aligned} \tag{8.28}$$

Δz in this expression is the distance from the downstream regenerator edge, where a_L^r and a_S^r are defined, to the HDRA, $\Delta z = z_H - z_{reg}$. For the vacuum beam $(a_S^r, a_L^r) = (0, 1)$, while for the regenerator beam it is $(\rho(p)_r, 1)$. The decay rate downstream of the HDRA is a trivial modification of Equation 8.18,

$$\begin{aligned}\frac{dN^d}{dz\,dp} &= |a_S^H|^2 e^{-(z-z_H)/\gamma\beta c\tau_S} + |a_L^H \eta_{00}|^2 e^{-(z-z_H)/\gamma\beta c\tau_L} \\ &+ 2|a_S^H||a_L^H \eta_{00}| \cos(\Delta m(z-z_H)/\gamma\beta c + \phi_{a_S^H} - \phi_{a_L^H}) e^{-(z-z_H)/\gamma\beta c\tau_{av}}.\end{aligned}$$

To give an idea of the effect of the HDRA material on the measured parameters, if one neglected the regeneration, $Re(\varepsilon'/\varepsilon)$ would shift by -4×10^{-4}. Thus the *total* effect is of the order of the statistical and systematic error we are trying to achieve. Most of this effect comes from the additional decay rate in the vacuum beam. Since the physical properties of the material in the HDRA are known at the percent level, the uncertainty in $Re(\varepsilon'/\varepsilon)$ from the HDRA material is negligible.

The other measurements most affected in principle are the mass difference and phase-related measurements, which will depend on the shape of the downstream decay distribution. For the typical kaon momentum of 70 GeV/c, the K_S amplitude contributed from regeneration in the HDRA is under 2% of the K_S amplitude from the regenerator propagated to the HDRA. In any of the fits, the regeneration parameters and thicknesses of the materials in the HDRA are known well enough that the uncertainty from the HDRA regeneration is negligible.

8.2.4 Acceptance Corrections

With the kaon fluxes and $\pi\pi$ decay rates in hand, the last ingredient needed for our prediction functional is the acceptance. As we saw in the previous chapter, our Monte Carlo simulates the detector resolution effects very reliably. The physical parameters (Δm, τ_S, $(f-\bar{f})/k$ for B_4C, etc.), used in the Monte Carlo were also very close to the parameters derived in the final fit. This allows us to define an average acceptance over a certain range in momentum and z as the ratio of events *reconstructed* in this range to the number of actual decays in this range. In the terms of Equation 8.1, the acceptance $\bar{\varepsilon}_{v(r)_{ij}}$ in the vacuum (regenerator) beam for the pz bin starting at momentum p_i and decay position z_j is

$$\bar{\varepsilon}_{v(r)_{ij}} = \frac{\int_{p_i}^{p_i+\Delta p} dp \int_{z_i}^{z_i+\Delta z} dz \int dp'\, F_{v(r)}(p') \int dz'\, s(p,z;p',z')\, a(p',z')\, r_{v(r)}(p',z')}{\int_{p_i}^{p_i+\Delta p} dp'\, F_{v(r)}(p') \int_{z_i}^{z_i+\Delta z} dz'\, r_{v(r)}(p',z')}. \quad (8.29)$$

As before, if the integration variables are unprimed, they refer to reconstructed quantities, and if primed, to true quantities.

The acceptances defined in this fashion are shown for the two charged mode beams in Figure 116 and the two neutral mode beams in Figures 117 and 118. The bin sizes are 1 GeV/c in momentum and 1m (3m) in z in the charged (neutral) figure. Note that on a p and z scale of 1 GeV/c by 1/2 m, the vacuum beam and regenerator beam acceptances are nearly identical. The detector, of course, has no idea whether a decay at a given p and z came from the regenerator or charged beam, so the acceptance at the infinitesimal scale is independent of the beam. Even at 20 GeV/c, where the both the acceptance and decay distributions change most rapidly as a function of p and z, the decay distribution is locally flat enough that the effect of smearing in and out of the bin is very similar in both beams.

The similarity of the vacuum and regenerator beam acceptances is demonstrated in Figure 119, where the average acceptances as a function of z in four different 10 GeV/c momentum bins are shown. The regenerator and vacuum beam acceptances appear noticeably different in the 20 GeV/c momentum bin, slightly different at 40 GeV/c , and virtually identical above 60 GeV/c. These differences do not appear because the acceptance at a given p and z is different in the two beams, the change in the decay rate from one end of a 10 GeV/c momentum bin to the other is simply much larger in the regenerator beam than in the vacuum beam at the lowest momenta. Since the acceptance also varies quite rapidly across the lowest two momentum bins, the acceptance *weighted* by the decay rate looks quite different in the two beams. In the 20 GeV/c and 40 GeV/c bins, the regenerator beam acceptances from the Monte Carlo have been overlaid with the acceptances predicted by weighting the vacuum beam acceptance calculated in 1 GeV/c bins with the shape regenerator beam decay rate across the momentum bin. The agreement is excellent.

The Monte Carlo used in calculating the acceptance has the same primary K_S remnant that the data possesses. In the standard fits which use the primary K_S correction, the generated and accepted Monte Carlo samples are also corrected before the acceptance is calculated.

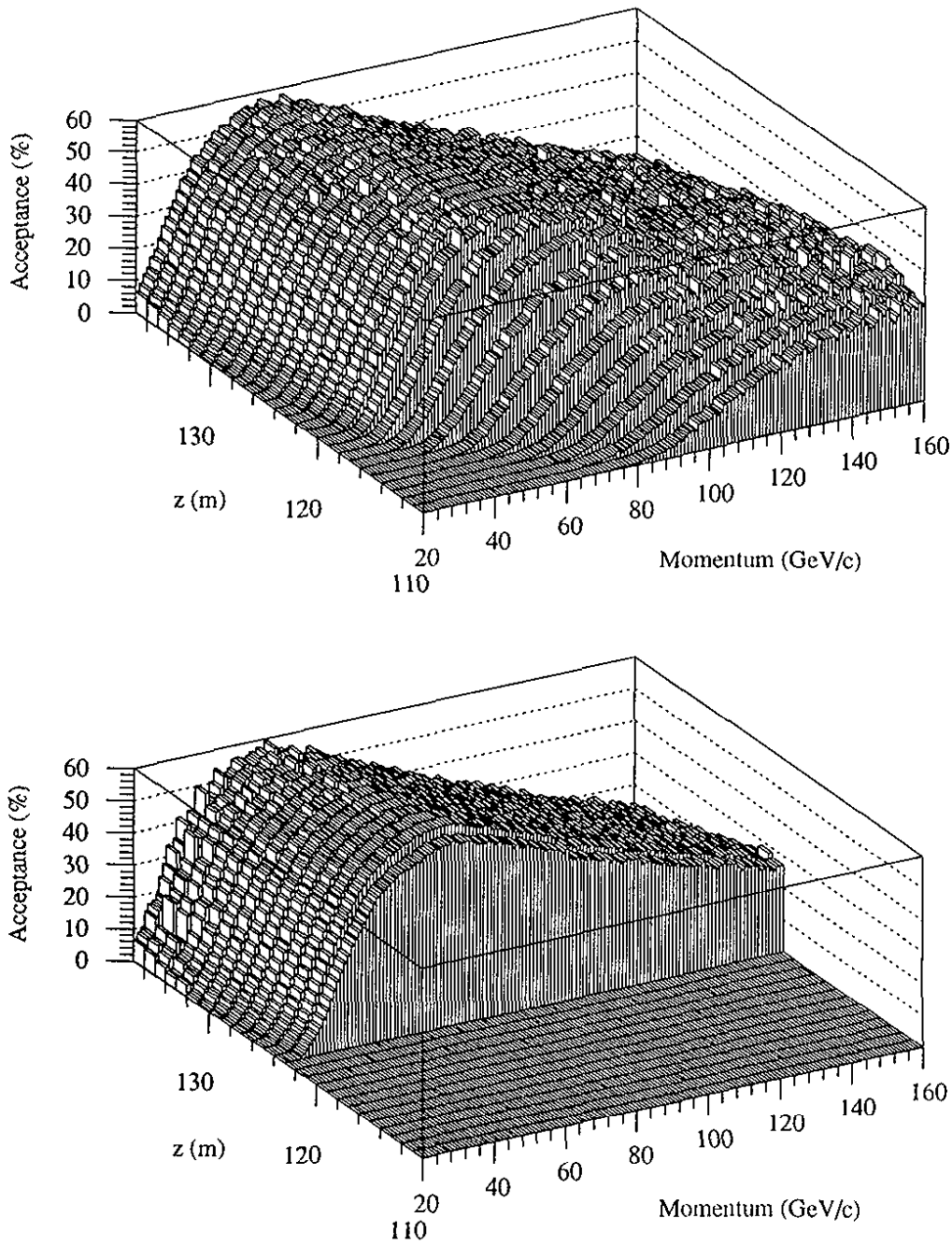

Figure 116. Acceptance as a function of momentum and z for $K \to \pi^+\pi^-$ decays. The acceptance for the vacuum (regenerator) beam is the top (bottom) plot. The upstream acceptance in the vacuum beam is limited by the mask anti. The regenerator is located at 123.5 m.

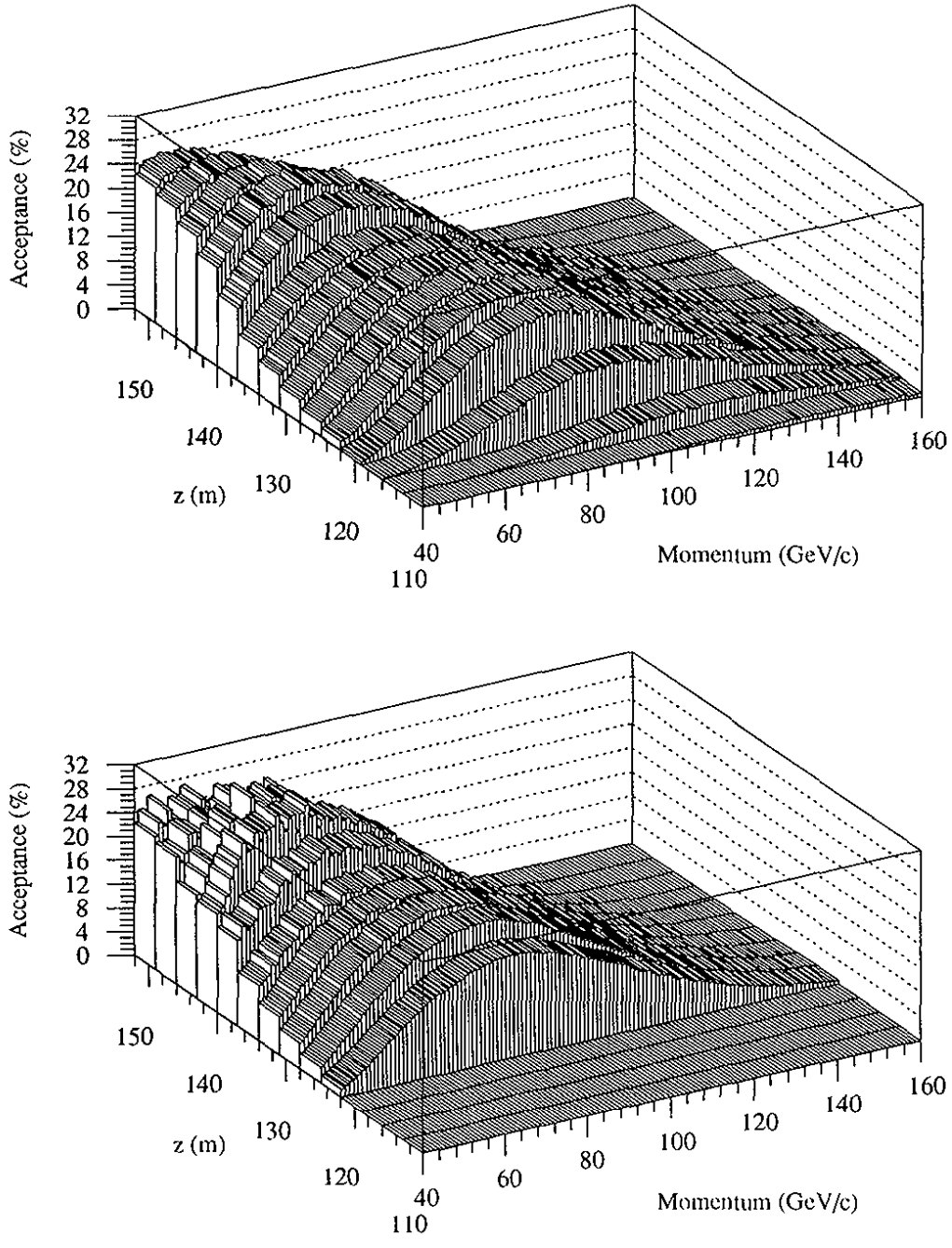

Figure 117. Acceptance as a function of momentum and z for $K \to \pi^0\pi^0$ decays with the lead sheet in place. The acceptance for the vacuum (regenerator) beam is the top (bottom) plot. The upstream acceptance in the vacuum beam is limited by the mask anti. The regenerator is located at 123.5 m.

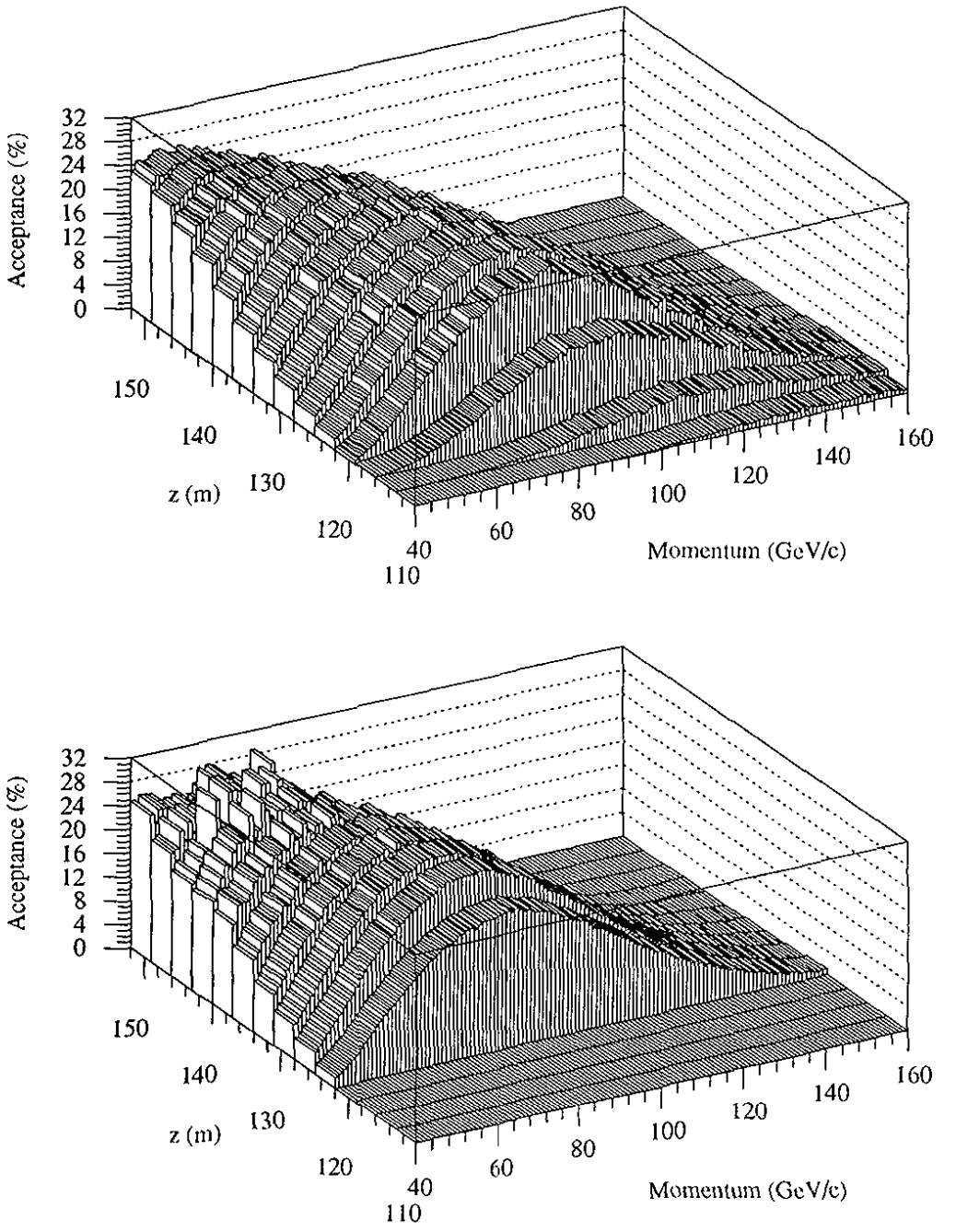

Figure 118. Acceptance as a function of momentum and z for $K \to \pi^0\pi^0$ decays with the lead sheet removed. The acceptance for the vacuum (regenerator) beam is the top (bottom) plot. The upstream acceptance in the vacuum beam is limited by the mask anti. The regenerator is located at 123.5 m.

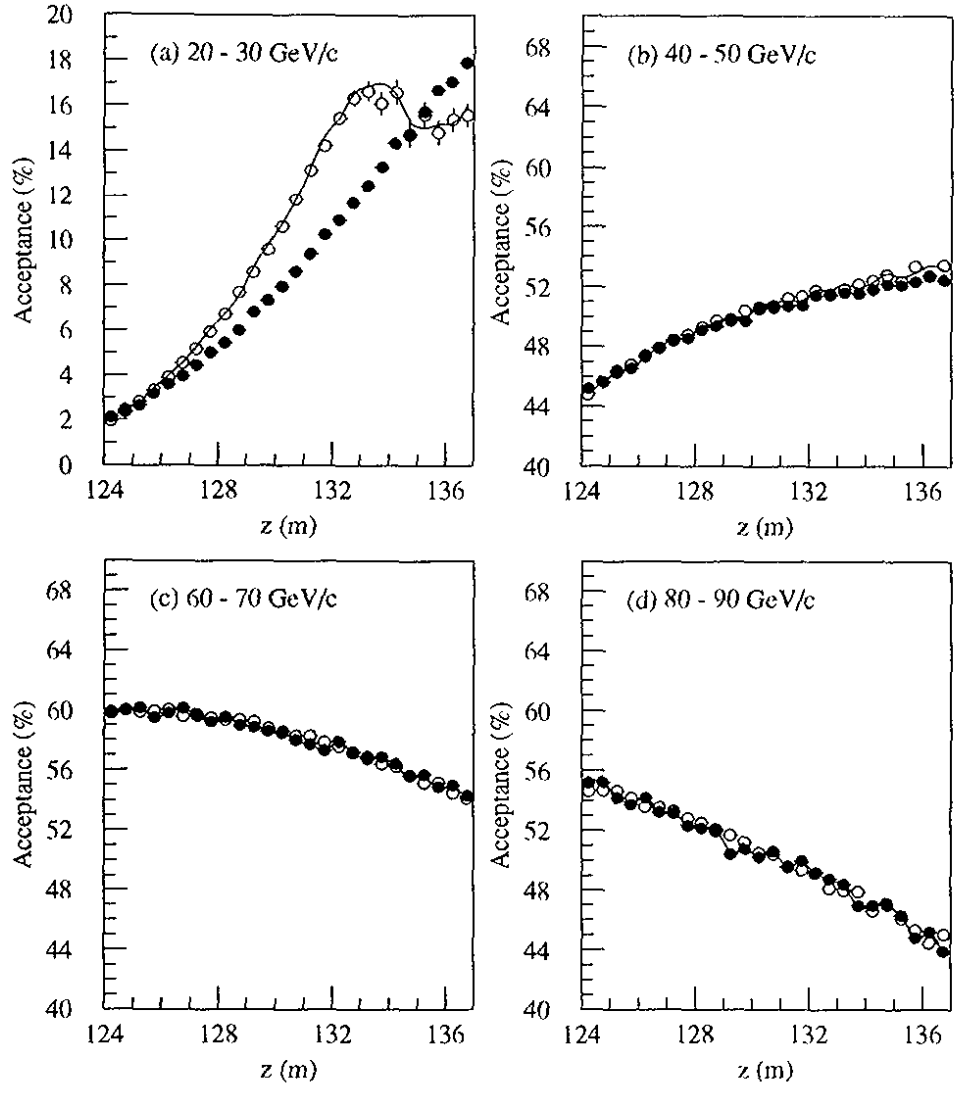

Figure 119. The $\pi^+\pi^-$ acceptance as a function of z in 4 of the 10 GeV/c momentum bins. The vacuum (regenerator) acceptance is shown as solid (hollow) circles. The lines are the regenerator beam acceptances predicted by weighting the vacuum beam acceptances in 1 GeV/c momentum bins with the regenerator beam decay rates.

8.2.5 The Prediction Functional

We have now discussed all of the ingredients entering the prediction functional we use in our fits. In our representation of Equation 8.1, the integral over momentum actually becomes a sum over in n_b regions of width δp. In the unconstrained fits, the prediction for

the observed collection rate in the pz bin starting at $p = p_i$ and $z = z_i$ becomes

$$\begin{aligned} R_{v_{ij}}^{pred} &= \delta p \sum_{k=1}^{n_b} F_v(p_{i_k}) \bar{\epsilon}_{v_{i_k j}} \int_{z_j}^{z_j+\Delta z} r_v(p_{i_k}, z) dz \\ R_{r_{ij}}^{pred} &= \bar{t} \delta p \sum_{k=1}^{n_b} F_v(p_{i_k}) c((p_{i_k}) \bar{\epsilon}_{r_{i_k j}} \int_{z_j}^{z_j+\Delta z} r_r(p_{i_k}, z) dz, \end{aligned} \tag{8.30}$$

and the functional returns the predicted ratio (see Equation 8.4)

$$p_{ij}^{pred} = \frac{R_{v_{ij}}^{pred}}{R_{v_{ij}}^{pred} + R_{r_{ij}}^{pred}}. \tag{8.31}$$

In the regenerator beam expression, we have used Equation 8.15 for the regenerator beam kaon flux. In calculating the flux and the decay rate integrals, the momentum p_{i_k} is the midpoint of the "microbin":

$$p_{i_k} = p_i + (k - \frac{1}{2})\delta p. \tag{8.32}$$

For z bins which begin upstream of z_{reg}, the z integral for the regenerator beam in the charged mode begins at $z = z_{reg}$. In the neutral mode, there is a small probability for all four of the photons to pass through the lead piece at the end of the regenerator without converting. The Monte Carlo begins all decays at the downstream edge of the regenerator, so this effect is not automatically compensated by the acceptance correction, and we must correct for it in the fit. Fortunately, the convolution of this survival probability with K_S regeneration is easily calculated. The resulting rate corresponds to an increase in the decay volume of 1.8 mm, that is, the integral for a z bin containing the regenerator begins at $z = z_{reg} - 0.0018$ for the neutral mode. The only fit using a z region upstream of the regenerator is the fit for $Re(\varepsilon'/\varepsilon)$ and the correction in this case shifts the final result by $\Delta Re(\varepsilon'/\varepsilon) = -0.8 \times 10^{-4}$.

In the constrained fits, the calculation for the regenerator beam rate is identical, but for the vacuum beam, the decay rate (as opposed to accepted rate) for the entire decay volume is calculated:

$$d_{v_i} = \delta p \sum_{k=1}^{n_b} F_v(p_{i_k}) \int_{z_{start}}^{z_{end}} r_v(p_{i_k}, z) dz \tag{8.33}$$

As discussed in Section 8.2.1, the functional predicts the number of regenerator beam decays observed, with the vacuum beam rate providing the normalization:

$$N_{r_{ij}}^{pred} = \frac{n_i D_{v_i}^{MC}}{d_{v_i}} R_{r_{ij}}^{pred}. \tag{8.34}$$

A sharp reader may have noticed that the vacuum beam flux has entered the equations for the constrained fits in two separate ways. The most important place is in the vacuum beam constraint, which one can essentially view as determining the ratio of total kaon flux two different 10 GeV/c momentum bins. This spectrum also enters as the flux $F_v(p)$ in the prediction functional, and there is used to weight the relative contribution of each 1 GeV/c momentum "bite" to the total decay rate in a 10 GeV/c bin. The vacuum beam constraint is the more important contribution, since one has to know the relative flux between the different momentum bins in order not to bias the power-law behavior of the regeneration amplitude. $F_v(p)$ is essentially a refinement to the prediction, however, and much of its effect cancels in the vacuum to regenerator beam ratio, particularly in momentum bins above 40 GeV/c. As we shall see in the next chapter, the fits are relatively insensitive to the shape of $F_v(p)$ used in the fits.

In the fits from which we quote final results, the acceptances are calculated in 1 GeV/c bins in momentum. In z, the average acceptance is calculated in the bin size used in the fit. The momentum bin size was chosen largely because the decay rate and acceptance vary fairly rapidly across the momentum range from 20 to 30 GeV/c in the regenerator beam, and are sensitive to the values of Δm and τ_S. To avoid biases in charged fits using this bin, we acceptance-correct the predicted decay rates on a scale insensitive to the fit parameters. No difference was found between fits using 1 GeV/c and 0.5 GeV/c bins for the acceptance correction.

The final detail in any of the methods used for fitting regards the handling of the neutral data subsets with and without the lead sheet. Because of the step introduced by photon conversions in this sheet in the middle of the decay volume, it was dangerous to simply combine these two subsets into one grand neutral subset. In doing so, one would need the ratio of Monte Carlo simulations with and without the lead sheet to be almost perfect in order not to introduce a bias in the upstream acceptance corrections relative to the downstream corrections. To avoid such a bias, these two subsets were treated independently: for each pz bin we obtained a prediction in each of the two subsets independently, and each subset added an independent contribution to the total χ^2.

This ends the discussion of all of the details used in our fits to the 2π data samples. We now move on to discuss the results of the fits themselves.

CHAPTER 9

THE RESULTS OF THE FITS

This chapter will present the final results for our determinations of the various parameters of the neutral kaon system. First and foremost will be the discussion of $Re(\varepsilon'/\varepsilon)$, the measurement for which this experiment was designed. Following this, the fits for Δm and τ_S, the fits for $\Delta\phi$, and the fits for ϕ_{+-} will be reviewed.

9.1 Fitting for $Re(\varepsilon'/\varepsilon)$

In the fits for $Re(\varepsilon'/\varepsilon)$, the same momentum range of 40 GeV/c to 160 GeV/c was used for both the charged and neutral data samples. Within this momentum range, deviations from a power-law behavior for the regeneration amplitude are expected to be very small. If there are deviations, $Re(\varepsilon'/\varepsilon)$ remains insensitive to them because the charged and neutral mode will be affected almost identically.

As the first step in extracting $Re(\varepsilon'/\varepsilon)$ from our 2π samples, we wanted to check the data quality and power-law behavior in the individual subsets. To this end, we performed four unconstrained fits with $Re(\varepsilon'/\varepsilon)$ fixed at zero. The three parameters for which we fit in all cases are (1) $(f(0)-\bar{f}(0))/k$ at 70 GeV/c (which we will call $\Delta f|_{70}$), (2) the regeneration slope α and (3) the cross section correction μ. One of the four fits was to the entire charge sample. The other three fits were all neutral fits, first to the subsets with and without the lead sheet individually, and then to the two subsets simultaneously. For the charged mode

fits, the z range used was 110m to 137m, and for the neutral fits, the range was 110 m to 152 m.

What do we expect to see with these fits? Since the K_s term dominates the regenerator beam decay rate, the ratio that we predict is approximately

$$p^{pred} \approx \frac{|\eta|^2}{|\eta|^2 + |\rho|^2} = \frac{1}{1 + |\rho/\eta|^2}. \tag{9.1}$$

Since $Re(\varepsilon'/\varepsilon)$ is fixed at zero in the fit, a nonzero value for $Re(\varepsilon'/\varepsilon)$ in the data will force ρ away from its true value, and bias the value of $\Delta f|_{70}$ that we measure. Since ε' shifts η_{+-} and η_{00} in opposite directions, we should see a shift between the values for $\Delta f|_{70}$ measured in the charged and neutral fits. On the other hand, the shift in η_{+-} or η_{00} should be fairly independent of momentum, so the measured power should not be greatly biased. The same regenerator was used throughout the experiment, so the same power should be measured (within statistical limits) in all of the subsets.

The results of the fits are summarized in Table 17, and plots of the charged and combined neutral fits are presented in Figure 120. The χ^2 for each fit is excellent, as is the agreement in the measured powers. From the figure, it is clear that if $Re(\varepsilon'/\varepsilon)$ is nonzero, it is small! Parts (b) and (c) of the figure show the fractional deviation of the measured regeneration amplitude in each momentum bin from a common power obtained in a simultaneous fit to the $\pi^+\pi^-$ and $2\pi^0$ data. This shows the scatter of the points about the best fit power more clearly. No bias as a function of momentum is present. The lines shown are the average deviations from the power-law, and a small apparent splitting between the charged and neutral modes now begins to be visible.

To extract $Re(\varepsilon'/\varepsilon)$, we fit the charged and neutral data simultaneously. The regeneration and absorption parameters are now common to the charged and neutral samples and $Re(\varepsilon'/\varepsilon)$ becomes a parameter of the fit. The result is $Re(\varepsilon'/\varepsilon) = (7.4 \pm 5.2) \times 10^{-4}$, with a χ^2 of 26 for 32 degrees of freedom. This error is statistical only. The remaining parameters are listed in Table 17 together with the results from the previous fits. The χ^2 contours for $Re(\varepsilon'/\varepsilon)$ versus each of the 3 other parameters are plotted in Figure 121. From these plots, we can see that there are no other nearby minima.

The values of kaon parameters kept fixed in the fit, the precision of the values, and the variation of $Re(\varepsilon'/\varepsilon)$ as these parameters vary are listed in Table 18. The final column

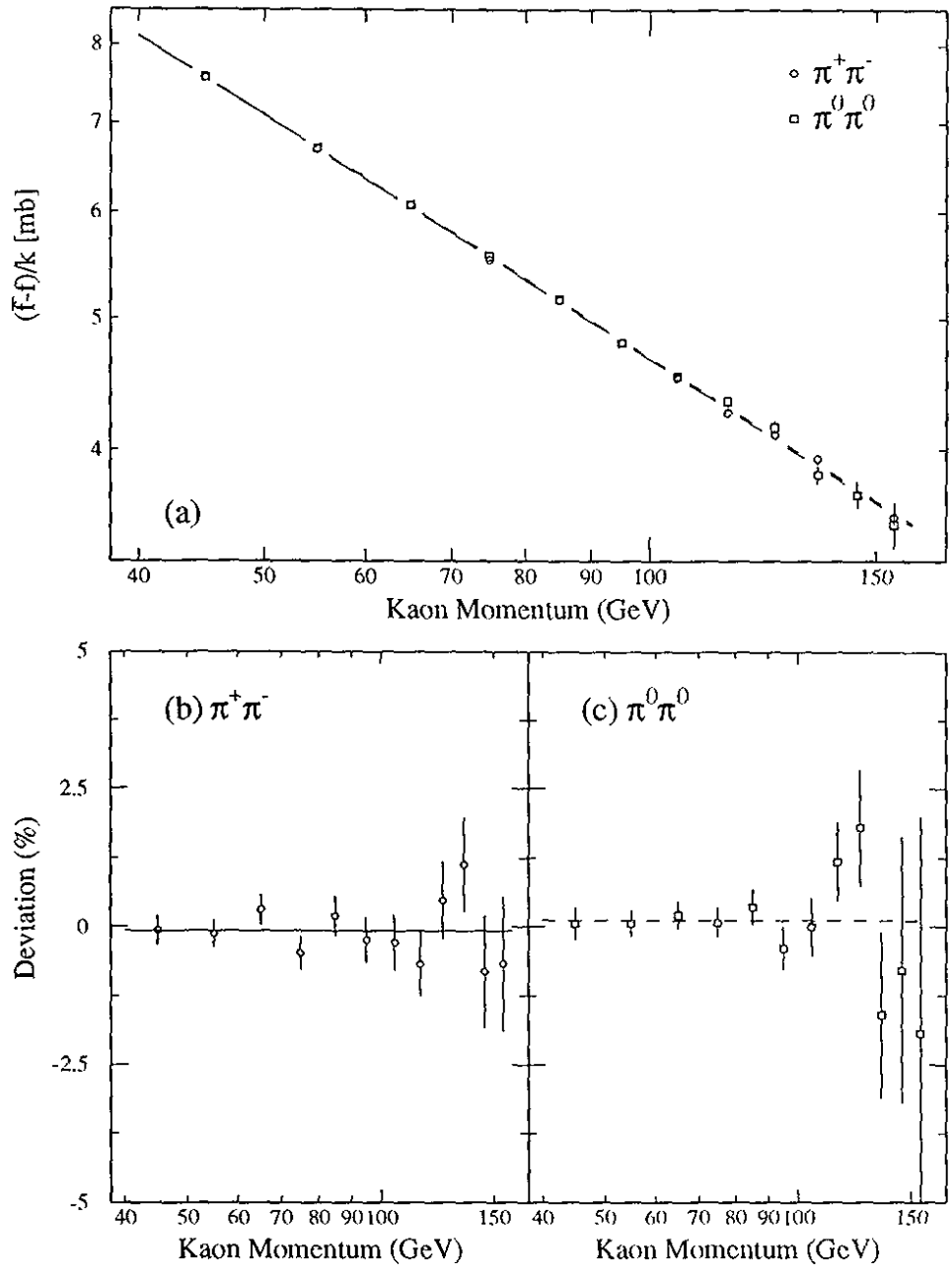

Figure 120. Regeneration amplitude versus kaon momentum. (a) The average amplitude in each momentum bin for the $\pi^+\pi^-$ (open circles) and $2\pi^0$ (open squares) data. The solid line is the best fit power to the $\pi^+\pi^-$ data. The best fit power for the $2\pi^0$ data is just visible as a dashed line above the $\pi^+\pi^-$ power. (b),(c) The fractional deviation of the average amplitude in each momentum bin from the simultaneous fit to the $\pi^+\pi^-$ and $2\pi^0$ data. The line is the average deviation.

Table 17. Results of the unconstrained fits used to determine $Re(\varepsilon'/\varepsilon)$. $Re(\varepsilon'/\varepsilon)$is fixed at 0 in the first four fits to the charged and neutral subsets so that the regeneration parameters from these sets may be compared. The cross section correction is quoted in terms of the correction to the carbon cross section at 156 GeV/c.

Fit	$Re(\varepsilon'/\varepsilon)$ ($\times 10^{-4}$)	$\Delta f\|_{70}$ (mbarns)	α	$\Delta\sigma_T$ (mbarns)	χ^2/degrees of freedom
$\pi^+\pi^-$	0[a]	5.786 ± 0.008	-0.605 ± 0.007	-3.1 ± 1.4	8.9/9
$2\pi^0$ (Lead Sheet)	0[a]	5.799 ± 0.009	-0.598 ± 0.010	-2.4 ± 2.8	8.2/9
$2\pi^0$ (No Pb Sheet)	0[a]	5.801 ± 0.011	-0.609 ± 0.011	-1.8 ± 3.2	6.2/9
$2\pi^0$ (Combined)	0[a]	5.800 ± 0.007	-0.603 ± 0.007	-2.1 ± 2.1	16.8/21
Simultaneous $\pi^+\pi^-$ and $2\pi^0$	7.4 ± 5.2	5.791 ± 0.005	-0.604 ± 0.005	-2.8 ± 1.1	25.8/32

[a]Fixed at this value for this fit.

gives the change in $Re(\varepsilon'/\varepsilon)$ for a one standard deviation change in the given parameter. From these values, it is clear that $Re(\varepsilon'/\varepsilon)$ is quite insensitive to the parameters used. For self-consistency, we have use values of Δm and τ_S obtained from our own data (see Section 9.2), which are comparable in precision to current world averages. For $|\varepsilon|$, we have used the Particle Data Group average of $|\eta_{+-}|$ [32]. CPT symmetry is implicit in our use of the natural phase [26, 18] for the phase of ε, $\phi_\varepsilon = \tan^{-1}[2\Delta m/(\Gamma_S - \Gamma_L)]$. The phase of ε' comes from the $\pi\pi$ phase shift analysis of Ochs [48].

As a final check, we relax the power-law assumption for the momentum dependence of $(f(0) - \bar{f}(0))/k$, and fit for $Re(\varepsilon'/\varepsilon)$ and the average regeneration amplitude in each momentum bin. There does not seem to be any bias in the measured value of $Re(\varepsilon'/\varepsilon)$ as a function of momentum, as the plot of the results in Figure 122 shows. The average of the momentum bin fits is in excellent agreement with the power-law fit, yielding a value only $+0.15 \times 10^{-4}$ away.

Measuring $Re(\varepsilon'/\varepsilon)$ by taking the momentum bin average has the distinct advantage that it is very insensitive to the energy dependence of the absorption cross section. If

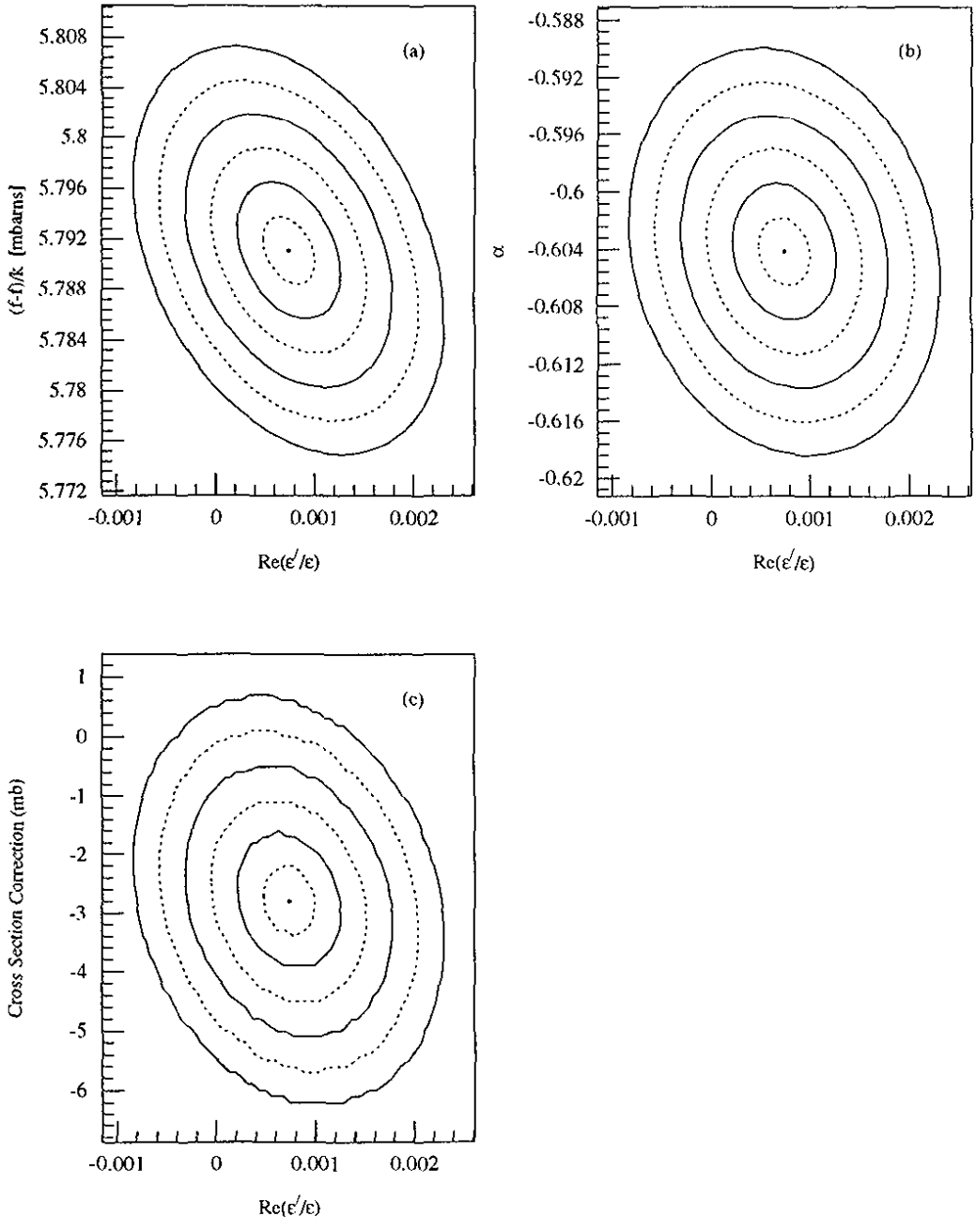

Figure 121. Contours of equal χ^2 in the fit for $Re(\varepsilon'/\varepsilon)$. The contours are plotted in steps of 1/2 standard deviations. (a) $[f(0) - \bar{f}(0)]/k|_{70GeV/c}$ versus $Re(\varepsilon'/\varepsilon)$. (b) α versus $Re(\varepsilon'/\varepsilon)$. (c) Kaon-Carbon total cross section correction parameter (at 156 GeV/c) versus $Re(\varepsilon'/\varepsilon)$.

Table 18. Variation of the extracted value for $Re(\varepsilon'/\varepsilon)$ with the values of physical constants in the fit. The units assumed for each of the constants is given in square brackets in the first column. $\Delta Re(\varepsilon'/\varepsilon)$ is the change in $Re(\varepsilon'/\varepsilon)$ for an increase in the constant by one standard deviation. The correction to $Re(\varepsilon'/\varepsilon)$ as a function of the physical constants is presented in the last column.

Parameter	Value	Error	$10^4 \times \Delta Re(\varepsilon'/\varepsilon)$ ($+1\sigma$ variation)	$10^4 \times Re(\varepsilon'/\varepsilon)$ dependence
Δm $[10^{10}\hbar s^{-1}]$	0.5286	0.0028	+0.41	$77.2(\frac{\Delta m - 0.5286}{0.5286})$
τ_S $[10^{-10}s]$	0.8929	0.0016	−0.26	$-147(\frac{\tau_S - 0.8929}{0.8929})$
τ_L $[10^{-8}s]$	5.17	0.004	+0.05	$5.8(\frac{\tau_L - 5.17}{5.17})$
$\lvert\varepsilon\rvert$ $[10^{-3}]$	2.279	0.022	−0.11	$-11.4(\frac{\lvert\varepsilon\rvert - 2.279}{2.279})$
ϕ_ε	43.4°	0.2°	−0.15	$-0.75(\phi_\varepsilon - 43.4°)$
$\phi_{\varepsilon'}$	43°	6°	−0.11	$-0.018(\phi_\varepsilon - 43°)$

we completely ignored this energy dependence, the predicted rate from momentum bin to momentum bin would be slightly biased, and this in turn would bias the measured power. It turns out that because the momentum distributions in charged and neutral are slightly different, this would lead to a bias in the measurement of $Re(\varepsilon'/\varepsilon)$ of order 10^{-4}. When the power-law constraint is relaxed however, and we fit for $Re(\varepsilon'/\varepsilon)$ in individual momentum bins, the effect of the absorption cancels between the charged and neutral modes. In tests of the fitting procedure, the observed sensitivity to the cross section energy dependence was an order of magnitude smaller for the bin average than for the power-law fit.

In previous measurements of $Re(\varepsilon'/\varepsilon)$ that used this technique but had limited statistics, the added constraint of the power-law boosted the sensitivity to $Re(\varepsilon'/\varepsilon)$. For this result, the power-law constraint no longer helps the sensitivity issue, but we report the value using the power-law for consistency with the remaining fits that rely more heavily on the power-law to obtain the regeneration phase.

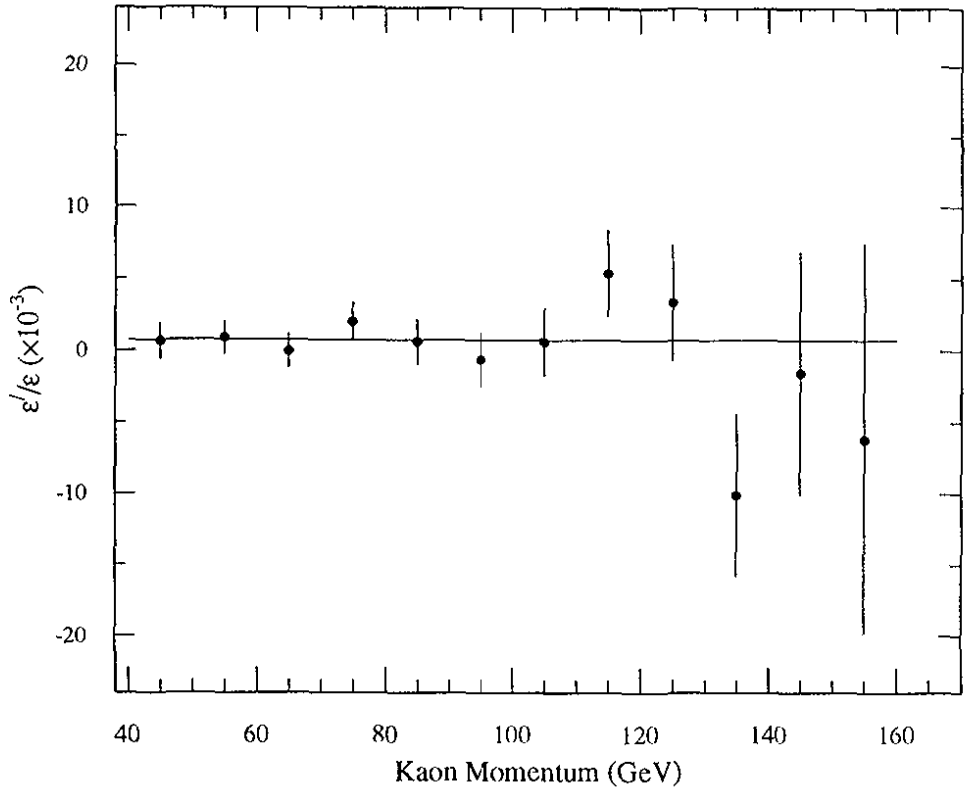

Figure 122. Momentum dependence of $Re(\varepsilon'/\varepsilon)$. The values of $Re(\varepsilon'/\varepsilon)$ in each momentum bin (dots) have been determined independently, with no regeneration power-law constraint. The line is the weighted average of the individual momentum bin fits.

The stability of $Re(\varepsilon'/\varepsilon)$ with respect to momentum is also a sign that the primary K_S corrections are not biasing the extraction of $Re(\varepsilon'/\varepsilon)$. As is clear in Figure 115, these corrections are extremely small below 100 GeV, though they begin to climb rapidly for higher momentum. If the adjustments were incorrect, a momentum dependence would be observable.

Some of the issues concerning the relation between the "raw" double ratio and the value of $Re(\varepsilon'/\varepsilon)$, and the also concerning the acceptance calculation in large z bins, are covered in Appendix C.

9.1.1 $Re(\varepsilon'/\varepsilon)$ and Accidental Biases

While the double beam technique leads to a cancellation of accidental biases to first order, there are second order effects that could potentially bias the final result. For example, the vacuum beam has a higher particle flux than the regenerator beam, and one possibility is that extra soft clusters in the lead glass could be hidden more easily in $2\pi^0$ decays in the vacuum beam than in the regenerator beam. The method, which used a sample of random triggers that were overlaid on top of Monte Carlo $\pi\pi$ decays, is detailed in [74] and in the next chapter. Here we present only the results of the studies.

In the charged mode sample, the highest intensity subset was the NC subset. The accidental study of this set yielded a correction of $-0.04\% \pm 0.07\%$ for the change in the vacuum to regenerator beam ratio, which is consistent with zero. We therefore made no correction in the charged sample.

In the highest intensity neutral samples, however, we have found that the accidentals do introduce a small bias in the relative vacuum beam and regenerator beam acceptances. The correction needed for the vacuum to regenerator beam ratio is $-0.17\%(-0.15\%)\pm 0.06\%$ for the high intensity subsets with (without) the lead sheet. We can compare this result to the neutral mode accidental study in the lower intensity NC subset presented in reference [74] by scaling the high intensity result down by the ratio of intensities. This scaling implies we should see a correction in the lower intensity NC subset of only 0.06%. This is consistent with the low intensity study of the NC set in [74], where a correction to the single ratio of $-0.04\% \pm 0.07\%$ was found[1]. When the high and low intensity accidental corrections are applied, the final result for $Re(\varepsilon'/\varepsilon)$ shifts by $\Delta Re(\varepsilon'/\varepsilon) = +2.5 \times 10^{-4}$. This correction has already been made in the fits presented in the previous section.

9.1.2 Summary of $Re(\varepsilon'/\varepsilon)$ fit Results

The value extracted for $Re(\varepsilon'/\varepsilon)$ from our entire data sample is $Re(\varepsilon'/\varepsilon) = (7.4 \pm 5.2) \times 10^{-4}$. This is the result from the power-law fit, and it includes the very small corrections for both accidental biases and for photons which do not convert within the regenerator.

[1] This is only coincidentally the same result as that obtained in the charged mode accidental study.

We have also refit the data subset used to obtain our previously published value [50] of $Re(\varepsilon'/\varepsilon) = (-4 \pm 14 \pm 6) \times 10^{-4}$. There have been many improvements in the analysis, Monte Carlo simulation, and fitting technique since that publication. The systematic error for that result was dominated by uncertainty in the energy scale, and as Figures 32 and 39 demonstrate, our understanding of the energy scale has substantially improved. The new central value for this subset after complete reanalysis and simulation is -2.4×10^{-4}. The shift is well within the systematic uncertainty of that time, and an indication of the robustness of the double beam technique.

This ends the discussion of the fit for $Re(\varepsilon'/\varepsilon)$. Before any final conclusion can be drawn, the systematic evaluation must be completed. This will be deferred until the next chapter, and the results of the constrained fits for the other kaon parameters will be presented next.

9.2 The Δm and τ_S Fits

In fitting for Δm and τ_S, we will extract values for the charged mode data and neutral mode data separately. The two different modes have different systematic contributions, and we prefer to combine the results with the proper statistical and systematic errors.

The fits for these values assumed no direct CP violation, that is, we set $Re(\varepsilon'/\varepsilon) = 0$ while fitting. We have also implicitly assumed CPT symmetry by using the natural phase $\tan^{-1}[2\Delta m/(\Gamma_S - \Gamma_L)]$ for the phase of ε. For $|\varepsilon|$, we use the same value as in the $Re(\varepsilon'/\varepsilon)$ fits (see Table 18). For given data subset, Δm, τ_S, $\Delta f|_{70}$, and α are all parameters to be fit. In addition, there are the the three vacuum beam constraint parameters and the cross section correction parameter (Section 8.2.1). The charged sample and neutral samples with and without the lead sheet have separate sets of constraint parameters to allow for variations in the flux from data set to data set.

Since the measurement of Δm and τ_S depend on the observed shape of the decay distribution as a function of z, these measurements can be sensitive to the smearing of events from bin to bin. From Monte Carlo studies, we have found that systematic biases in the measurement of Δm and τ_S are exacerbated when trying to use the z region including the regenerator edge in fits. For this reason we use only the z region in the regenerator beam

downstream of 124.5m (125m) in the charged (neutral) mode fits. With this z range for the regenerator beam, the sensitivity to smearing was $\approx 0.05\%$ for both quantities.

The z bin sizes used for these fits were chosen to be commensurate with the z resolution of the individual mode. For $\pi^+\pi^-$ decays, the z resolution varied from 10 cm (downstream) to 25 cm (upstream), so the z bin sizes used in the fits were at least 1 m. For the neutral mode, the resolution was closer to 1 m, so the z bins used in the fit were at least 2 m.

The fits that depend on the shape of the z distribution become more sensitive the farther out one can probe in proper time. In the fits to the charged mode sample, we can accomplish this by relaxing the lower momentum limit to 20 GeV/c. This has some systematic ramifications because the momentum dependence of $(f - \tilde{f})/k$ can begin to deviate from a power-law — increasing the uncertainty in the associated regeneration phase — and the decay rate, acceptance and incident kaon flux all vary quite rapidly in the 20 GeV/c to 30 GeV/c range. This latter problem is most severe at the downstream end of the $\pi^+\pi^-$ decay volume, and for this reason, the z range was restricted to 135 m in the charged mode fits. In spite of these limitations, the overall sensitivity was enhanced by using the lower momentum events.

The lower limit of the momentum range used in the neutral mode is limited by the E_T trigger threshold, so the fits used the same momentum range as the $Re(\varepsilon'/\varepsilon)$ fits, 40 GeV/c to 160 GeV/c. In spite of this, the extended z range available in the $2\pi^0$ mode resulted in the $2\pi^0$ sample yielding the best statistical precision.

A summary of the fit results for the two modes and different z binnings is shown in Table 19. The Δm value for the charged mode fits using 1 m and 2 m z binnings differ by about 1/2 of a standard deviation. We chose to average the two values for the final result. The averaged result for Δm is $\Delta m = (0.5311 \pm 0.0044) \times 10^{10}\hbar s^{-1}$, and for τ_S we find $\tau_S = (0.8952 \pm 0.0015) \times 10^{-10} s$. The results from neutral fits with 2 m and 3 m binnings were very close, and we take the 3 m bin results, this binning being better matched to the 1 m resolution. The two neutral subsets give very consistent results. Before the charged and neutral results can be compared directly and averaged, however, the systematic contributions for the two modes must be determined, so we will defer this until Chapter 11.

The absorption correction parameters obtained in these fits were consistent with those

Table 19. Summary of fits for Δm and τ_S for both the $\pi^+\pi^-$ and $2\pi^0$ modes.

Set	z bin size	Δm $(10^{10}\hbar s^{-1})$	τ_S $(10^{-10}s)$	$\Delta f\|_{70}$ (mbarn)	α	χ^2/degrees of freedom
$\pi^+\pi^-$	1 m	0.5302(44)	0.8952(15)	5.774(9)	−0.590(3)	157/160
$\pi^+\pi^-$	2 m	0.5319(45)	0.8953(15)	5.773(9)	−0.590(3)	92/90
$2\pi^0{}_{all}$	2 m	0.5277(30)	0.8911(16)	5.804(11)	−0.590(3)	335/302
$2\pi^0{}_{all}$	3 m	0.5274(30)	0.8912(17)	5.802(11)	−0.603(7)	221/203
$2\pi^0{}_{Pb}$	3 m	0.5289(39)	0.8904(22)	5.803(15)	−0.604(10)	118/99
$2\pi^0{}_{NoPb}$	3 m	0.5251(47)	0.8920(25)	5.803(17)	−0.601(11)	100/99

in the $Re(\varepsilon'/\varepsilon)$ fits. As for the shape corrections to the Monte Carlo vacuum beam kaon flux, the corrections in the neutral mode were consistent with the Monte Carlo having the correct flux shape, while the corrections in the charged mode indicated a small bowing in the spectrum, with the data preferring the flux at the extremes of the momentum range to be several percent lower than in the center. This is consistent with the overlays of the data and Monte Carlo momentum spectra in the previous chapter.

The χ^2 contours showing the correlations between the most important parameters of the fit are plotted in Figure 123 for charged mode and 124 for neutral mode. As in the $Re(\varepsilon'/\varepsilon)$ fits, no other local χ^2 minima appear. For the charged mode, the contours presented are from the fit with the 2 m binning.

The τ_S and Δm values obtained in the fits are insensitive to most of the physical parameters which we have set at fixed values in the fit. The one exception to this is the variation with the phase of ϕ_{+-}, for which there is a mild dependence. For τ_S this variation is -0.09%/degree, and for Δm it is $+0.59\%$/degree.

To give a more physical picture of the interference and K_S decay terms in the data, one can fix the fix the regeneration, absorption, and flux parameters at the values from one of the above fits. If one fixes τ_S, then there is enough information to extract *the average* value of the cosine term in Equation 8.18 in a pz bin. Conversely, by fixing Δm one can extract the average value of the K_S decay exponential. We have done this in both the neutral and

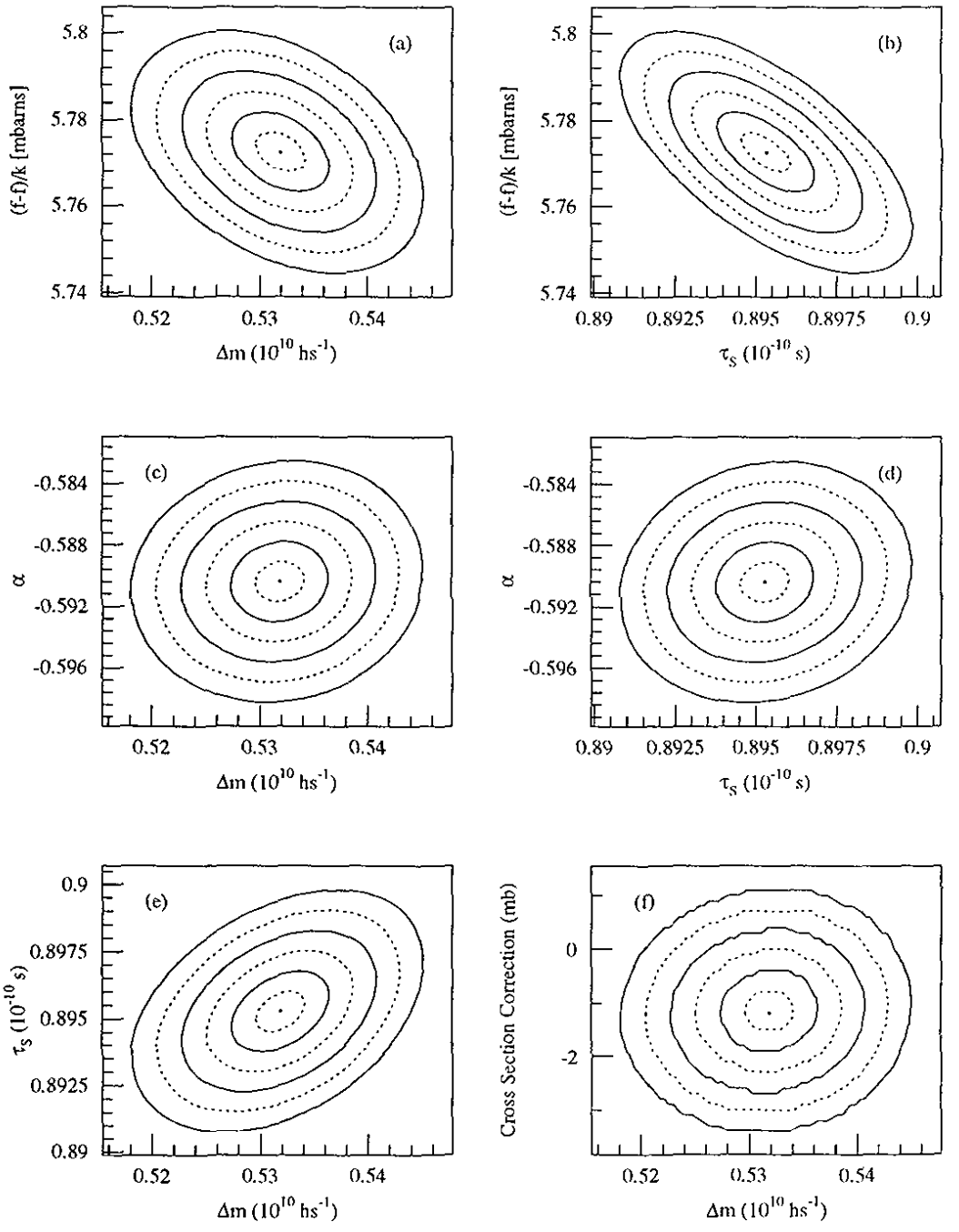

Figure 123. Contours of equal χ^2 in 1/2 standard deviation intervals in the fit for Δm and τ_S to the $\pi^+\pi^-$ data. (a) $\Delta f|_{70}$ versus Δm. (b) $\Delta f|_{70}$ versus τ_S. (c) Power-law slope α versus Δm. (d) Power-law slope α versus τ_S. (e) τ_S versus Δm. (f) Carbon cross section correction (at 156 GeV/c) versus Δm.

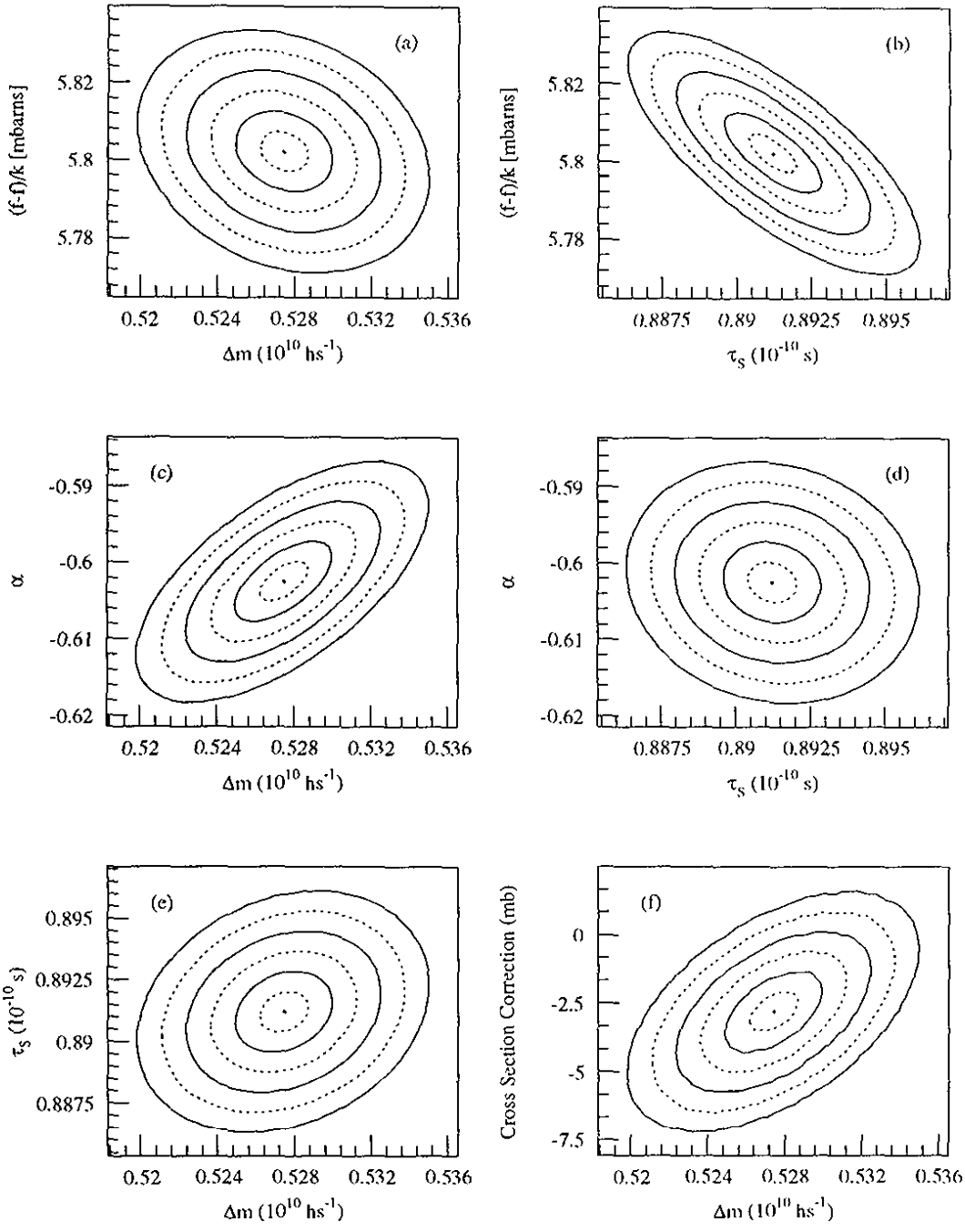

Figure 124. Contours of equal χ^2 in 1/2 standard deviation intervals in the fit for Δm and τ_S to the $2\pi^0$ data. (a) $\Delta f|_{70}$ versus Δm. (b) $\Delta f|_{70}$ versus τ_S. (c) Power-law slope α versus Δm. (d) Power-law slope α versus τ_S. (e) τ_S versus Δm. (f) Carbon cross section correction (at 156 GeV/c) versus Δm.

charge data using 1 m by 10 GeV bins. The results for kaons with momentum under 90 GeV/c are plotted against the average proper time for that bin in Figures 125 (charged mode) and 126 (neutral mode). For higher momenta kaons, the results are presented in Figures 127 and 128. The proper time $\tau = 0$ corresponds to the downstream face of the regenerator.

9.3 Extracting the Phases

The fitting methods used to extract $\Delta\phi$ and ϕ_{+-} are in essence identical to those used to extract Δm and τ_S. Rather than trying to extract the frequency of the interference curve in Figures 125 through 128, we are now trying to measure the intercept of the interference curve at the proper time $\tau = 0$. The value of the intercept for $\pi^+\pi^-$ ($2\pi^0$) decays is $\cos(\phi_\rho - \phi_{+-(00)})$, and the regeneration phase ϕ_ρ will cancel when comparing the two modes. To isolate ϕ_{+-}, however, we must use analyticity to obtain a value for the regeneration phase.

In extracting the phases, we make no assumptions regarding either CPT symmetry or CP violation — $Re(\varepsilon'/\varepsilon)$, $\Delta\phi$ and ϕ_{+-} are all parameters of the fits presented here. The z and momentum ranges are the same as those used in the Δm and τ_S fits. In the fit for $\Delta\phi$, Δm and τ_S are fixed to the average values obtained in the previous fit. Since we assumed that ϕ_{+-} had its natural value of $\tan^{-1}(2\Delta m/[\Gamma_S - \Gamma_L])$ in obtaining Δm and τ_S, we cannot report a value for ϕ_{+-} from that fit. To determine ϕ_{+-}, we set τ_S to the world average of $0.8922 \times 10^{-10} s$ [32] and allow Δm to float as a parameter of the fit.

Since we have already observed a small dependence of Δm on the z bin size in the $\pi^+\pi^-$ mode, we tried extracting $\Delta\phi$ with several different bin sizes. The results of the fits are summarized in Table 20. The fits using the 1 m and 2 m bins again show a small relative shift, and we again average the results for these two fits, obtaining $\Delta\phi = -1.6° \pm 1.0°$. There is a small dependence on the values of Δm and τ_S assumed in the fit, given by

$$\delta\Delta\phi = 190° \frac{\tau_S \times 10^{10} s - 0.8929}{0.8929} + 32° \frac{\Delta m \times 10^{-10} \hbar^{-1} s - 0.5286}{0.5286}. \qquad (9.2)$$

The results of the fit for ϕ_{+-} with Δm as an additional parameter are also summarized in

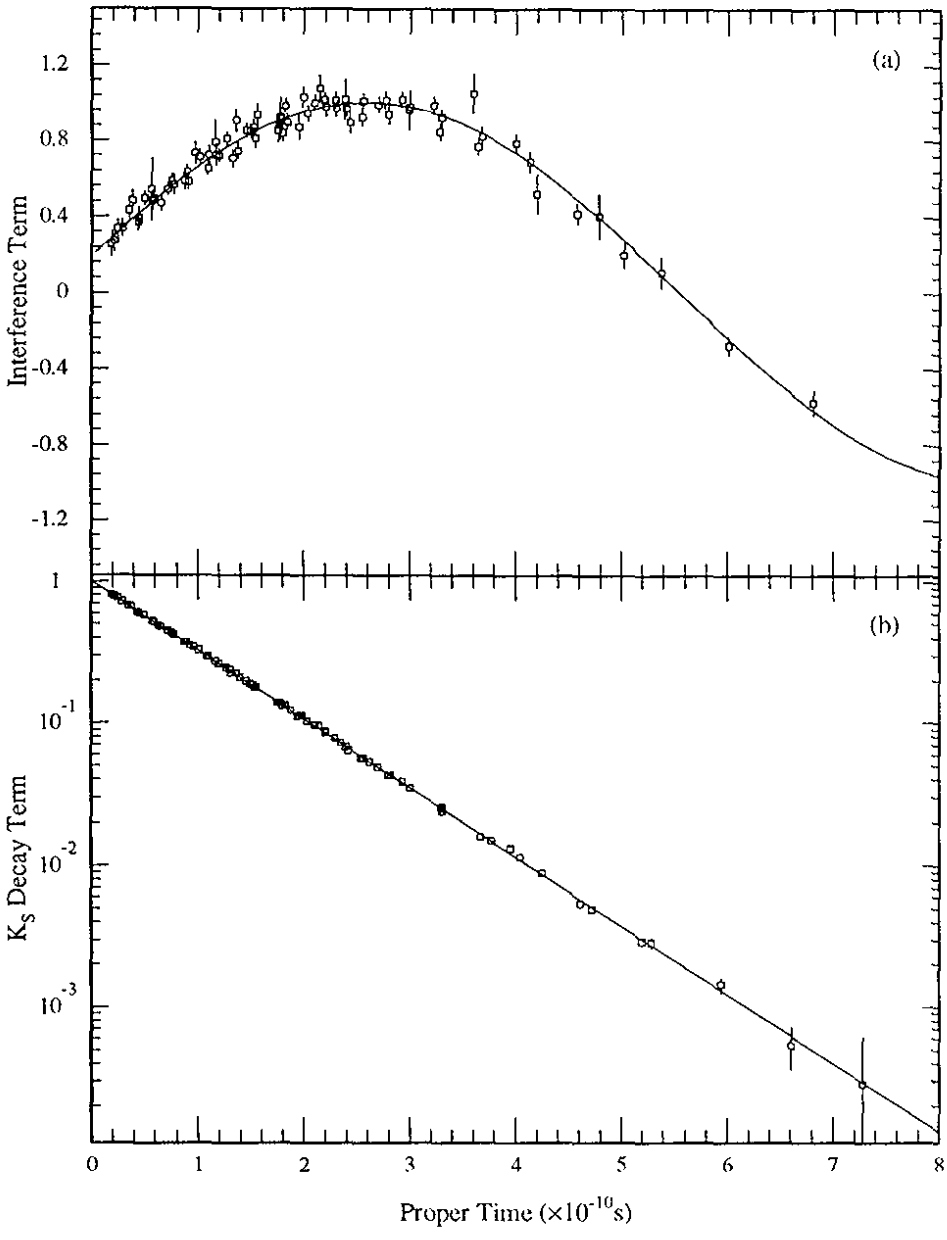

Figure 125. The interference and K_S decay curves measured for $\pi^+\pi^-$ decays with momentum under 90 GeV/c. (a) The average interference versus the average proper time in 1 m by 10 GeV bins. (b) The K_S decay term versus proper time, both measured at the center of the 1 m by 10 GeV bin. The Δm and τ_S results from the grand fit to the $\pi^+\pi^-$ data are shown as the curves.

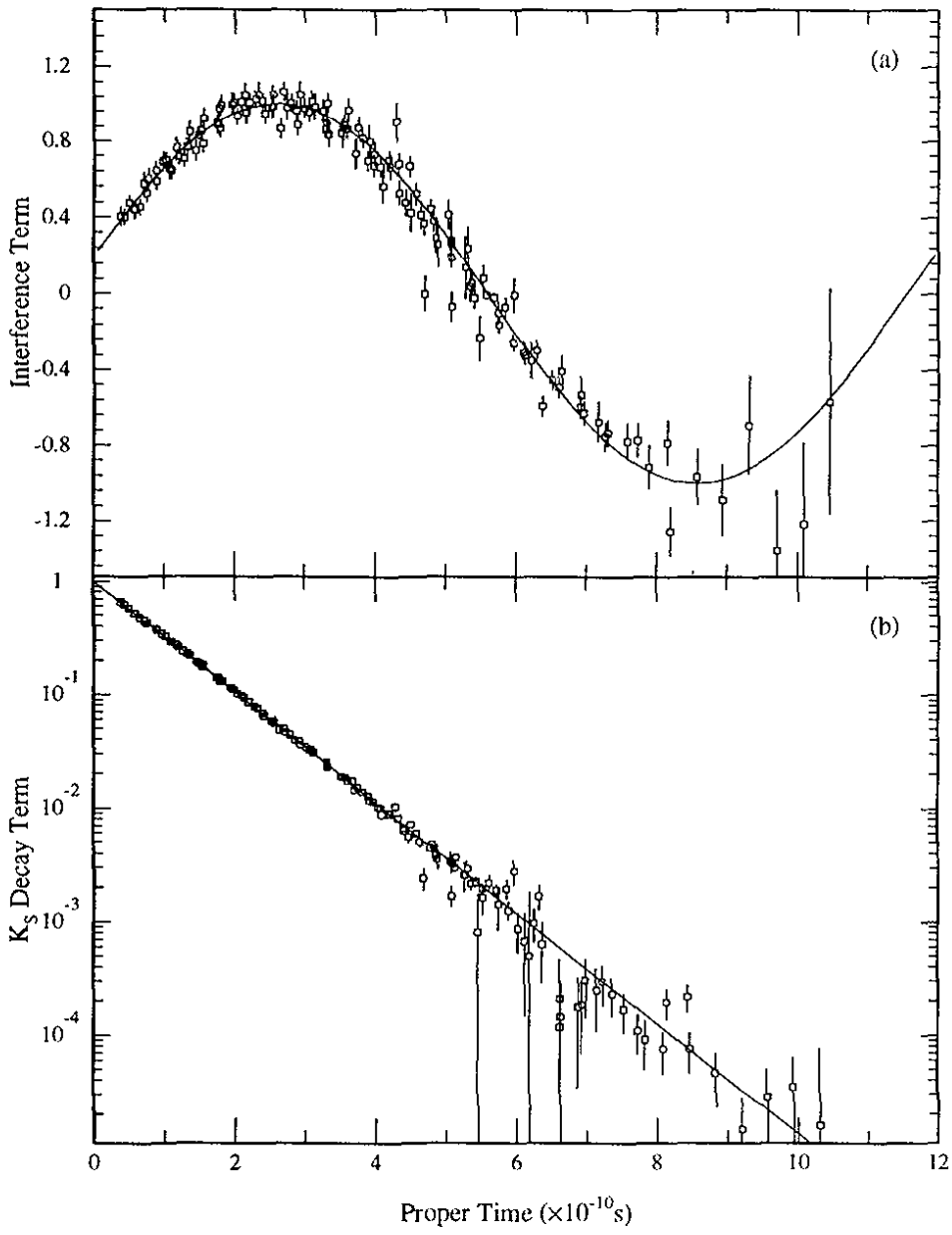

Figure 126. The interference and K_S decay curves measured for $2\pi^0$ decays with momentum under 90 GeV/c. (a) The average interference versus the average proper time in 1 m by 10 GeV bins. (b) The K_S decay term versus proper time, both measured at the center of the 1 m by 10 GeV bin. The Δm and τ_S results from the grand fit to the $\pi^+\pi^-$ data are shown as the curves.

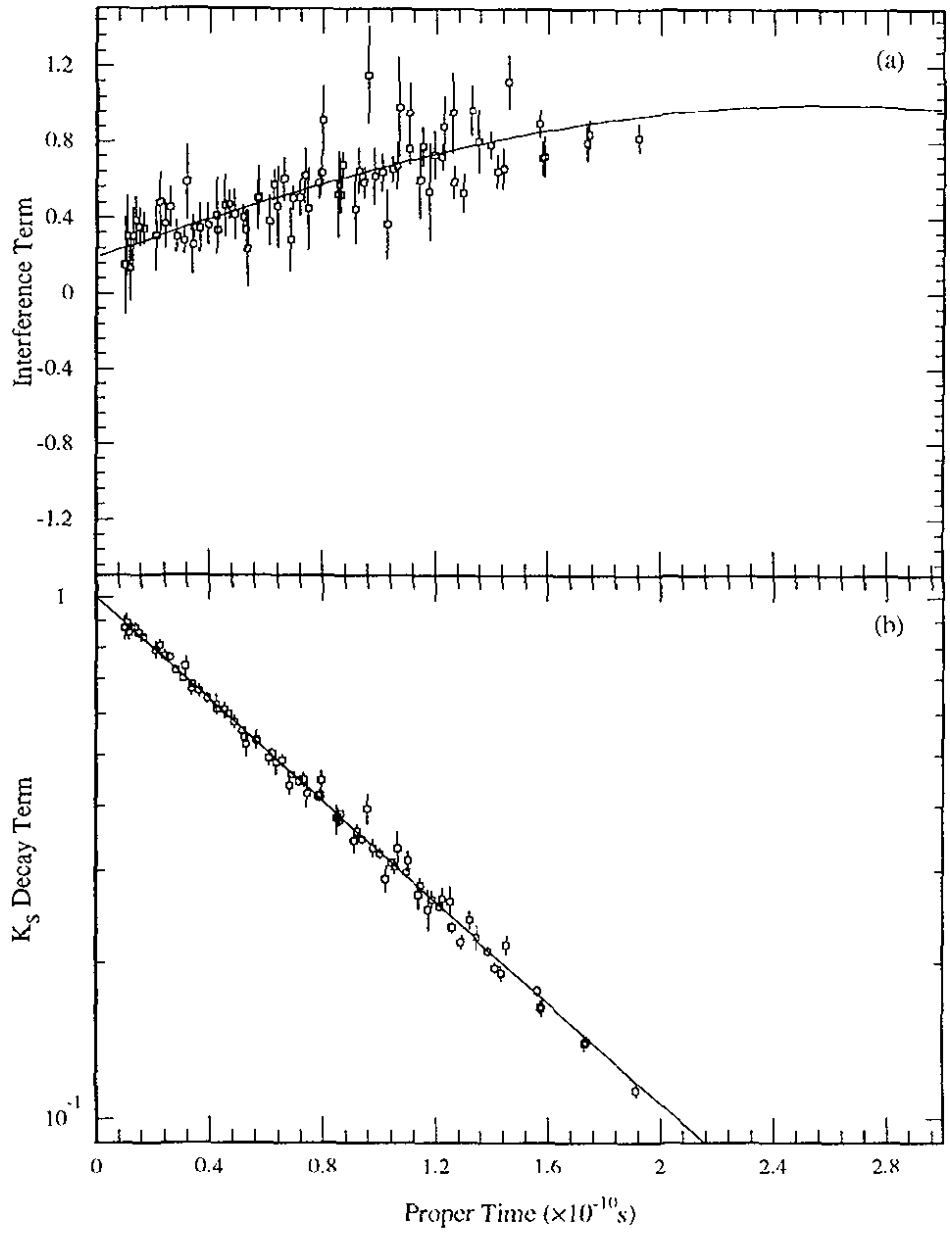

Figure 127. The interference and K_S decay curves measured for $\pi^+\pi^-$ decays with momentum above 90 GeV/c. (a) The average interference versus the average proper time in 1 m by 10 GeV bins. (b) The K_S decay term versus proper time, both measured at the center of the 1 m by 10 GeV bin. The Δm and τ_S results from the grand fit to the $2\pi^0$ data are shown as the curves.

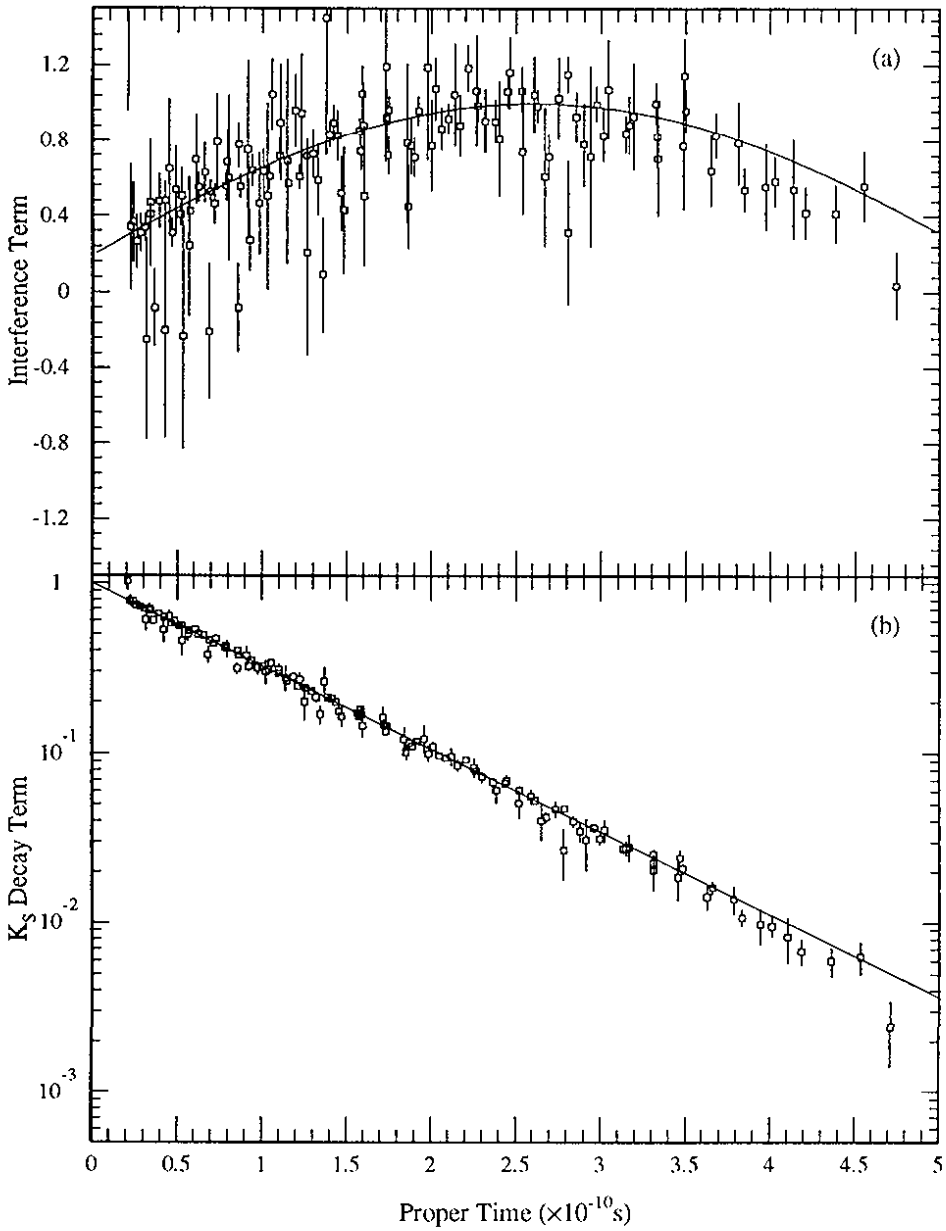

Figure 128. The interference and K_S decay curves measured for $2\pi^0$ decays with momentum above 90 GeV/c. (a) The average interference versus the average proper time in 1 m by 10 GeV bins. (b) The K_S decay term versus proper time, both measured at the center of the 1 m by 10 GeV bin. The Δm and τ_S results from the grand fit to the $2\pi^0$ data are shown as the curves.

Table 20. Results of the fits for $\Delta\phi$ and ϕ_{+-}.

fit	$\Delta\phi$	ϕ_{+-}	$Re(\varepsilon'/\varepsilon)$ (10^{-4})	$\Delta f\|_{70}$ (mbarns)	Power α	Δm $(10^{10}\hbar s)$
$\Delta\phi$ (1m bins)	$-1.7° \pm 1.0°$	$44.1° \pm 0.9°$[a]	3.2 ± 6.7	5.787(7)	$-0.592(3)$	0.5286[b]
$\Delta\phi$ (2m bins)	$-1.2° \pm 1.0°$	$43.8° \pm 0.9°$[a]	4.7 ± 6.7	5.785(7)	$-0.592(3)$	0.5286[b]
ϕ_{+-}	$-1.7° \pm 1.0°$	$42.2° \pm 1.3°$	8.8 ± 6.7	5.781(9)	$-0.592(3)$	0.5257(49)

[a]Correlated with assumed values of Δm and τ_S (see text).
[b]Held constant in this fit.

Table 20. The value of Δm obtained in this fit is consistent with the results of the previous fit.

In both of these fits, the value of $Re(\varepsilon'/\varepsilon)$ is consistent with the result of the unconstrained fit presented above. These two values share a large data sample in common, but are not completely correlated — the charged mode momentum range has been lowered from 40 GeV/c to 20 GeV/c, and the z range in the regenerator beam now starts downstream of the regenerator. The latter difference is quite significant. The measurement of $Re(\varepsilon'/\varepsilon)$ is at a fundamental level a counting experiment. By choosing a z range which will contain all events that misreconstruct upstream of the regenerator, we make the result very insensitive to the details of the mismeasurement. With the z range used in these fits, the smearing must be accurately modelled to avoid a bias in $Re(\varepsilon'/\varepsilon)$ from the loss of events.

The χ^2 contours of $\Delta\phi$ and ϕ_{+-} versus several of the other parameters are graphed in Figures 129 and 130, respectively.

9.3.1 Analyticity Check

Since the phase and Δm measurements use the assumption of analyticity to subtract the regeneration phase contributions, we would like to check the analyticity relationship. This

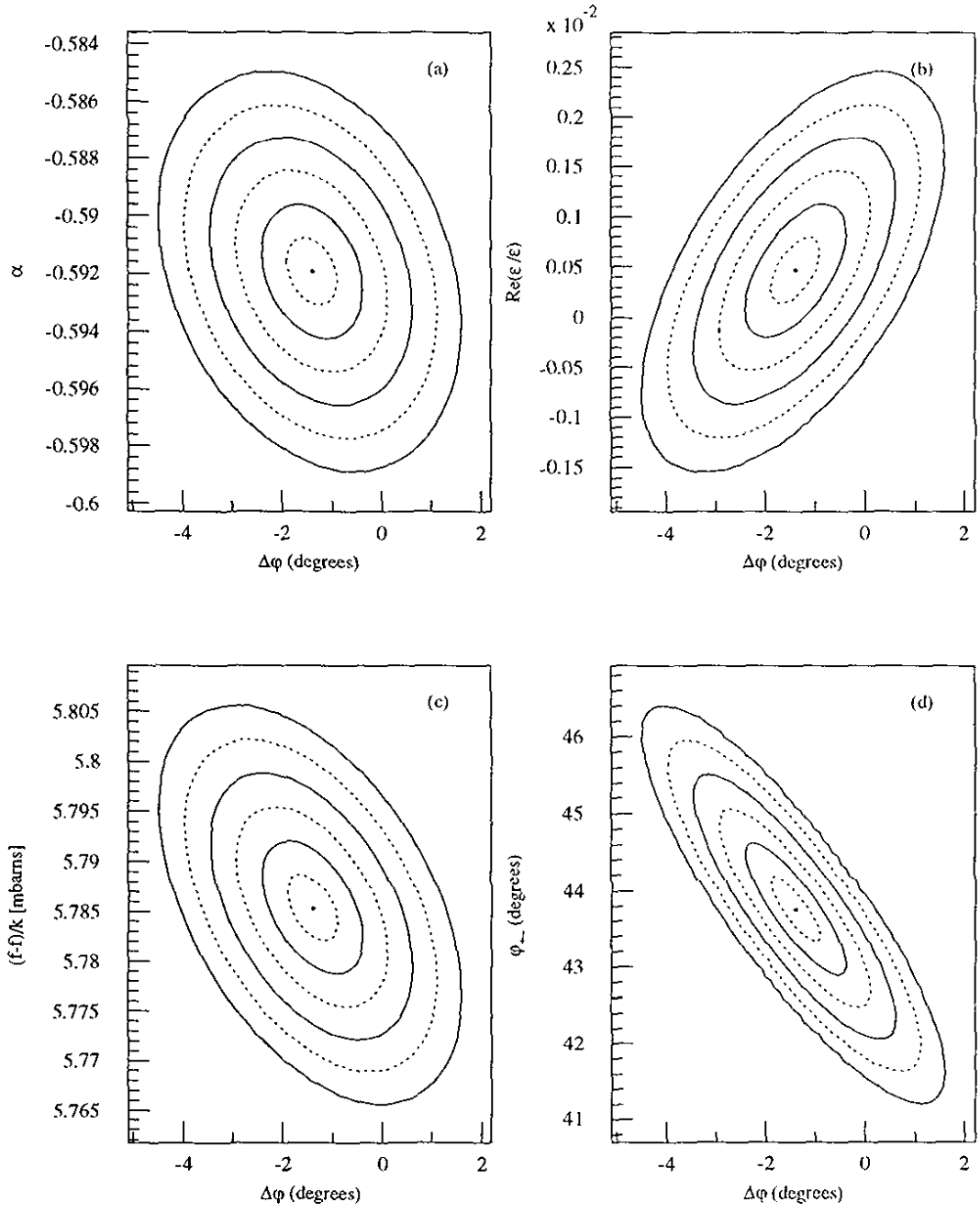

Figure 129. Contours of equal χ^2 in the fit for $\Delta\phi$ in 1/2 standard deviation intervals. (a) Power-law slope α versus $\Delta\phi$. (b) $Re(\epsilon'/\epsilon)$ versus $\Delta\phi$. (c) $\Delta f|_{70}$ versus $\Delta\phi$. (d) ϕ_{+-} versus $\Delta\phi$. The contours are from the fits using a 2 m z binning for the $\pi^+\pi^-$ decays.

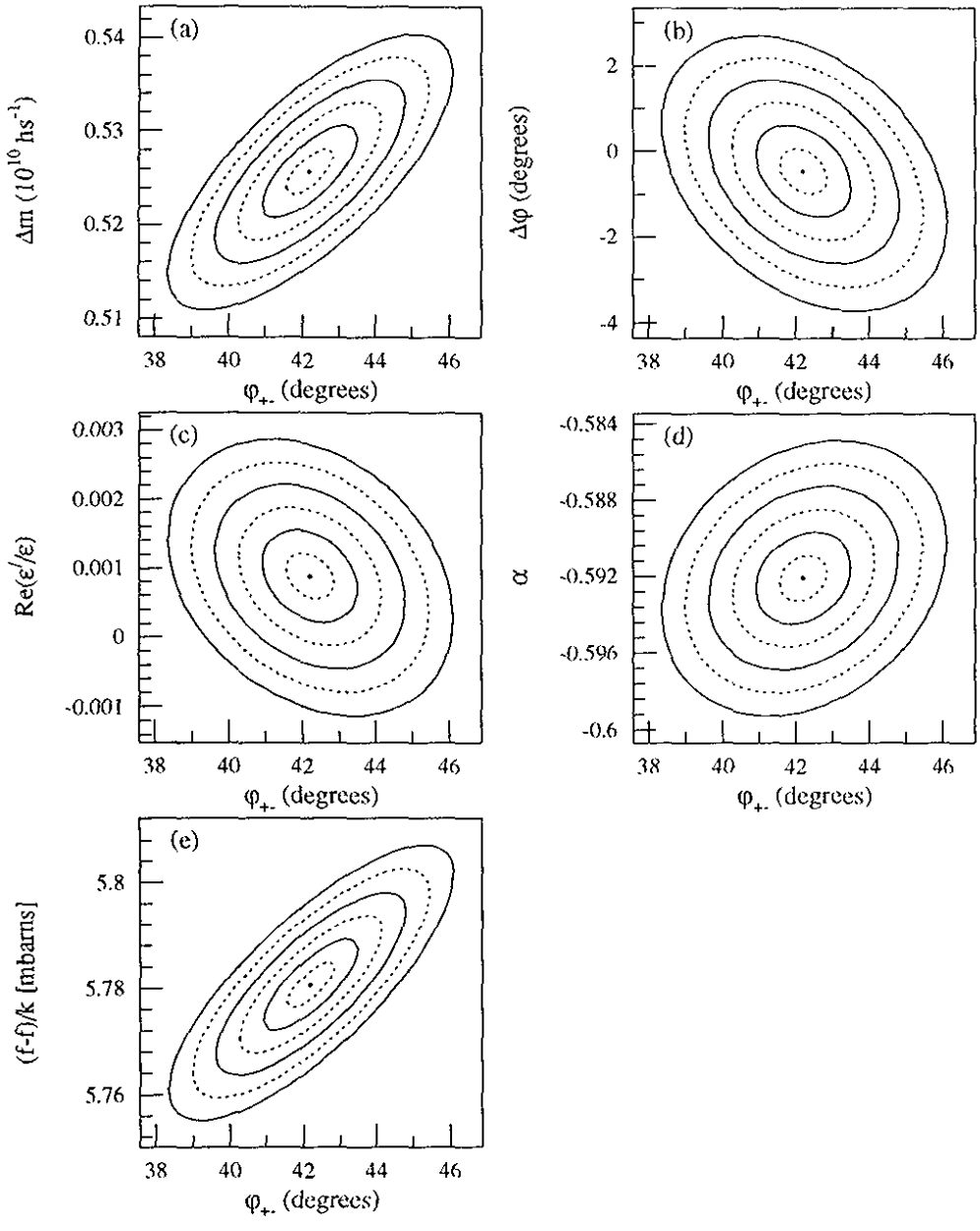

Figure 130. Contours of equal χ^2 in the fit for ϕ_{+-} in 1/2 standard deviation intervals. (a) Δm versus ϕ_{+-}. (b) $\Delta\phi$ versus ϕ_{+-}. (c) $Re(\varepsilon'/\varepsilon)$ versus ϕ_{+-}. (d) Power-law slope α versus ϕ_{+-}. (e) $\Delta f|_{70}$ versus ϕ_{+-}.

Table 21. The measured regeneration phase and corresponding analyticity predictions. in simultaneous fits to the $\pi^+\pi^-$ and $2\pi^0$ data.

Δm $(10^{10}\hbar s^{-1})$	α	ϕ_{pred} (analyticity)	$\phi_{f-\bar{f}}$ (measured)	$\phi_{f-\bar{f}} - \phi_{pred}$
0.5286[a]	−0.5922(25)	$-126.70° \pm 0.23°$	$-125.92° \pm 0.45°$	$0.78° \pm 0.51°$
0.5351[a]	−0.5912(24)	$-126.79° \pm 0.23°$	$-127.56° \pm 0.45°$	$-0.77° \pm 0.51°$
0.5275(47)	−0.5925(26)	$-126.68° \pm 0.23°$	$-125.6° \pm 1.3°$	$1.1° \pm 1.3°$

[a]Fixed.

has been done before for using regenerators of different materials [98, 79]. The measured regeneration phases agreed with the analyticity prediction within errors of order 1° to 2°.

We can also try to extract the regeneration phase $\phi_{f-\bar{f}}$ directly from the data, using a fitting technique similar to that used in extracting Δm and τ_S. The only differences are that the regeneration phase becomes an independent parameter of the fit, with Δm and τ_S now fixed, and we fit both the $\pi^+\pi^-$ and $2\pi^0$ data simultaneously. The fit results using our own value for Δm and the world average Δm are summarized in Table 21. The measured value of $\phi_{f-\bar{f}}$ depends on the value of Δm used in the fit. When we use our own measurement of Δm, the uncertainty in Δm corresponds to an additional uncertainty in $\phi_{f-\bar{f}}$ of 0.71°. When we use the world average, the uncertainty in Δm corresponds to an uncertainty in $\phi_{f-\bar{f}}$ of 0.61°. Adding these uncertainties in quadrature with the statistical uncertainties from the measurement of α and $\phi_{f-\bar{f}}$, we see that the predicted and measured phases agree to within an uncertainty of 0.9°. With Δm allowed to float, the phases agree within 1.3°.

The regenerator used in reference [98] was made of carbon, and we expect that carbon and boron carbide will have similar power-laws. The regeneration phase measured for the carbon regenerator in that experiment was $-124.7° \pm 1.7°$, in good agreement with the values shown in Table 21.

9.4 Summary

This chapter has presented a detailed description of the fitting techniques used to extract the physics parameters of interest, and then a description of the fits themselves. The results of the physics measurements of interest, with statistical errors only, are given below:

$$
\begin{aligned}
Re(\varepsilon'/\varepsilon) &= (7.4 \pm 5.2) \times 10^{-4} \\
\Delta m_{+-} &= (0.5311 \pm 0.0044) \times 10^{10} \hbar s^{-1} \\
\tau_{s_{+-}} &= (0.8952 \pm 0.0015) \times 10^{-10} s \\
\Delta m_{00} &= (0.5274 \pm 0.0030) \times 10^{10} \hbar s^{-1} \\
\tau_{s_{00}} &= (0.8912 \pm 0.0017) \times 10^{-10} s \\
\Delta\phi &= -1.6^{\circ} \pm 1.0^{\circ} \\
\phi_{+-} &= 42.2^{\circ} \pm 1.3^{\circ}
\end{aligned}
$$

Before we can draw any conclusions from this set of numbers, the systematic uncertainties must be evaluated. The next chapter will describe the systematic evaluation, with a focus on the systematic issues of $Re(\varepsilon'/\varepsilon)$. The implications of these results will then be discussed in the concluding chapter.

CHAPTER 10

SYSTEMATICS

This chapter presents the treatment of the systematic uncertainties in the measurements presented in the previous chapter. The discussion will focus on the uncertainty in the measurement of $Re(\varepsilon'/\varepsilon)$, but will also cover the major systematic contributions to the other measurements.

There are five major issues which affect this measurement of $Re(\varepsilon'/\varepsilon)$: the neutral mode energy reconstruction, detector acceptance, HDRA material, accidental biases and assumptions in the fitting procedure. Of these, the uncertainty in the energy reconstruction dominates, particularly because of residual nonlinearities. The discussion will begin with some general consistency checks, and then each of the five classes will be treated in turn.

10.1 Consistency Checks

Perhaps one of the most important aspects of the evaluation of this experiment was to monitor the consistency of results obtained for $Re(\varepsilon'/\varepsilon)$ as kinematic and fiducial cuts were changed, and as the fitting technique was modified. Since the statistical fluctuations involved in some of these checks are as large as or larger than many of the systematic effects we wish to examine, it is difficult to use these studies directly to evaluate the systematic uncertainty. The variation of $Re(\varepsilon'/\varepsilon)$ should, however, at least be consistent with the expected statistical fluctuation, and significant departures of $Re(\varepsilon'/\varepsilon)$ could point to unresolved problems in the background subtraction, photon energy reconstruction, etc.

Over a thousand fits on this data set have been performed, checking for any inconsistencies in the fitting routine, between data subsets, between different fiducial regions, between different analysis cuts, and with various defects embedded into the Monte Carlo. The most important checks are presented in this section.

10.1.1 Fitting and Analysis Cut Variations

The results of some of the more important studies performed are summarized in Table 22, where they are grouped into two categories. The first category comprises studies which involve a change primarily in the fit for $Re(\varepsilon'/\varepsilon)$, including changes in the momentum and z ranges used in the fit. The second category consists of studies involving changes in the basic kinematic or event quality cuts. The latter studies are computationally very intensive, as they require a reanalysis of the final data, signal Monte Carlo and background Monte Carlo event samples, which total over 3.6×10^7 events in the neutral sample alone.

10.1.1.1 Varying the fitting technique and fiducial cuts

In the first fit, the heart of the fitting procedure has been modified. The data binning remains as that used in the $Re(\varepsilon'/\varepsilon)$ fit presented in the previous chapter, where a single z bin spans the entire fiducial decay volume. In calculating the predicted vacuum to regenerator beam ratio ratio, however, the predicted number of decays is acceptance corrected in much smaller z bins — here, of size 1 m. As discussed in Section C.2, this avoids possible biases from the uncertainty in the regeneration parameters and kaon decay parameters used in the Monte Carlo to determine the acceptance. We knew the parameters accurately enough that we expected no difference in the result for $Re(\varepsilon'/\varepsilon)$ obtained with this modification, and indeed, none was observed beyond the level of 10^{-5}.

We have also changed the binning used in the fit for the $2\pi^0$ data, in this case using bins that were 3 m in z rather than 42 m. Because the vacuum to regenerator beam ratio is predicted in each pz bin, the events upstream of the regenerator position can no longer be used. This loss of statistics, combined with the different statistical weighting of the events, can lead to a sizable shift in the result. To estimate the expected shift, we divided the $2\pi^0$

Table 22. Shifts in $Re(\varepsilon'/\varepsilon)$ for changes in the fitting technique and for changes in the fiducial cuts. For the studies involving the change of a cut, the "allowed" shifts are the one standard deviation shifts expected from the change in statistics. For a change in methodology, the shift was predicted using Monte Carlo studies. The shift observed with the mass cut is discussed in the text.

Analysis Change or Fit Modification	$\Delta Re(\varepsilon'/\varepsilon)$ $(\times 10^{-4})$	"Allowed" Shift
Acceptance correct prediction in 1 m bins rather than 27 m ($\pi^+\pi^-$) or 42 m ($2\pi^0$) bins.	< 0.1	—
Bin $2\pi^0$ data in 3 m $\times$ 10 GeV/c pz bins	-2.48	2.21
Momentum range changed to 40 GeV/c to 150 GeV/c	$+0.21$	0.27
Neutral z range changed to 110 m to 137 m	$+0.42$	2.65
Relax analyticity assumption	-0.22	—
Loosen Ring Cut from 112 to 128	$+0.46$	0.47
Tighten Mass cut from ± 24 MeV/c^2 to ± 18 MeV/c^2	$+1.28$	0.32
Loosen Mass cut from ± 24 MeV/c^2 to ± 28 MeV/c^2	-0.30	0.19
Loosen charged mode cuts	-0.25	1.01

Monte Carlo into 11 different samples, where the first sample was 15 times the data size and was used to calculate the acceptance corrections. Each of the 10 remaining samples was the same size as our data, and were used as independent "data" samples. When we compared the result for the fit using a single 42 m z bin to that using 3 m bins in each of these 10 samples, we found the distribution of the shift in $Re(\varepsilon'/\varepsilon)$had a width of $(2.21 \pm 0.49) \times 10^{-4}$. The shift of -2.48×10^{-4} observed in the data is within this distribution of shifts.

In addition to modifying the fitting procedure, the z and momentum range used in the fit have been varied since the sensitivity to potential biases changes as the fiducial cuts are changed. For example, if we limit the momentum range of the kaon sample used in the fit to 150 GeV/c, we reduce the size of the total primaryK_S correction (Section 8.2.3) from

-0.62% (-0.07%) in the charged (neutral) vacuum beam to -0.33% (-0.04%). In spite of the change of almost 50% in the total primary K short correction, the shift in the result is completely consistent with the fluctuation allowed because of the small loss of statistics. In conjunction with the Monte Carlo tests mentioned in Section 8.2.3, these results verify that the primary K_S component of the K_L beams does not bias our final result.

We have, of course, also restricted the neutral z range to match that of the charged mode, which has several small systematic advantages. For example, the small dependence of $Re(\varepsilon'/\varepsilon)$ on the K_L lifetime (see Table 18) virtually disappears, and there is more cancellation of the primary K_S corrections between the two decay modes. There are also small systematic advantages in terms of the $2\pi^0$ sample itself. The momentum distributions in the two beams match even more closely than with our standard $2\pi^0$ z cut, and this makes the mass distributions match almost exactly in this mode. In turn, $Re(\varepsilon'/\varepsilon)$ becomes much more insensitive to the mass cut when there are residual nonlinearities in the photon energy reconstruction which shift the mass between data and Monte Carlo. Finally, this z range is completely upstream of the HDRA, and we do not have to understand the photon conversion probability as strictly because the conversion probability now cancels in the ratio of of vacuum beam to regenerator beam decays.

We use the larger decay volume, however, because these small systematic advantages are heavily outweighed by the doubling of the vacuum beam statistics. Furthermore, the "crossover" background from inelastic kaon scattering in the regenerator beam becomes much less important, as fractionally it is reduced by a factor of two. This is one of the hardest backgrounds to understand systematically, so increasing the decay volume into a region where this background contributes little was also a major boon systematically.

When we restrict the size of the neutral decay volume, we see a shift in $Re(\varepsilon'/\varepsilon)$ of $+0.42 \times 10^{-4}$, which is well within the one standard deviation shift of 2.65×10^{-4} expected because of the change in statistics. This result is 1.8×10^{-4} higher than our preliminary result for $Re(\varepsilon'/\varepsilon)$ presented in 1991 [99]. The shift is dominated by the change to a new, larger Monte Carlo sample for the acceptance correction. The statistical uncertainty in the older, smaller Monte Carlo sample corresponded to a one standard deviation shift of 1.9×10^{-4} in $Re(\varepsilon'/\varepsilon)$. There were also small systematic contributions to the shift from

improvements in the Monte Carlo simulation, the fitting technique, and the energy scale correction.

The final check involving a change in the fitting procedure that we will report here, involved relaxing the assumption of analyticity to obtain the regeneration phase. Instead, the regeneration phase was set to the phase previously measured for carbon (see Section 9.3.1). The shift of -0.22×10^{-4} was exactly the shift expected given the dependence of $Re(\varepsilon'/\varepsilon)$ on the phase (see ϕ_{+-} dependence in Table 18) and the difference between the previously measured regeneration phase and the regeneration phase implied by our measured power.

10.1.1.2 Trial Analysis cuts

With the variations of the analysis cuts which will now be presented, the stability of $Re(\varepsilon'/\varepsilon)$ under changes in the background subtraction will be most strongly probed. Some of the differences between data and the Monte Carlo simulation are also important, however, and we will discuss these when relevant.

For the first study, we have relaxed the ring number cut used in the analysis from 112 to 128. The largest effect of this cut is to increase the noncoherent kaon background (see Figure 59). This background increases by 12.6% (13.3%) in the vacuum (regenerator) beam, while the total signal increases by only 1.2% (1.3%). Hence the change of this cut will test the background subtraction most strongly.

While the change in background level is the most dramatic effect, there are still other issues affected by changing this cut. As the plots of the background subtracted ring number distributions for top and bottom beams (Figure 131) show, the regenerator and vacuum beams have very similar shapes, but the regenerator beam is overall marginally wider because of the kaons that scatter in the shadow absorber. As mentioned in the several of the previous chapters, the scattering of kaons in the shadow absorber is included in the Monte Carlo simulation, and the relative regenerator and vacuum beam shapes are reproduced well by the coherent Monte Carlo distributions (also shown in the figure). In the bottom beam (right hand plots), the broadening of the vacuum beyond the regenerator beam at high ring number is due to kaons which scatter in the common absorber. This is the tail of

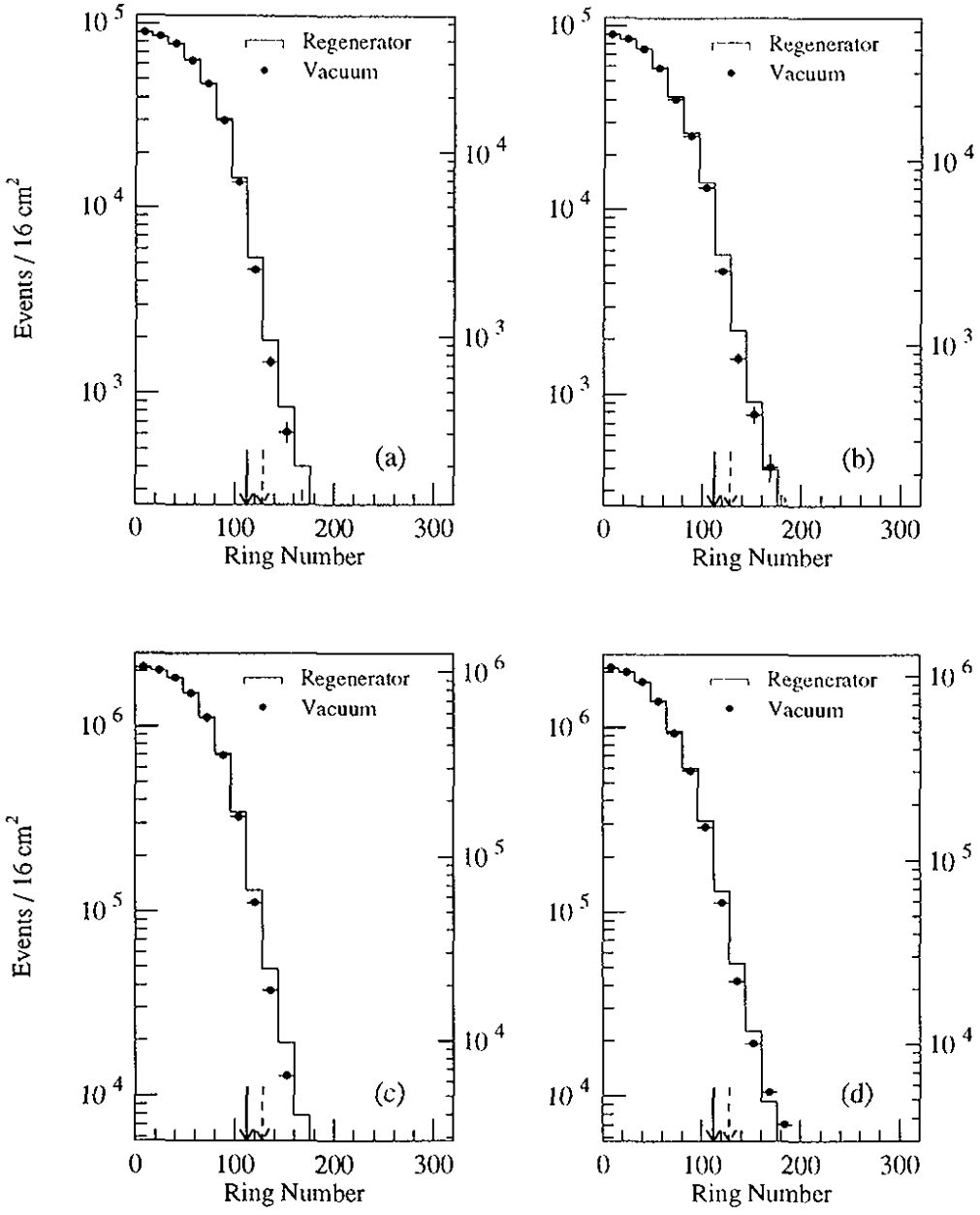

Figure 131. Regenerator beam and vacuum beam ring number distributions in the top and bottom beams for the background-subtracted $2\pi^0$ data sample and the coherent Monte Carlo sample. In all plots, the histogram shows the distribution for the regenerator beam (left scale) and the dots show the distribution for the vacuum beam. The solid arrow indicates the cut for the standard analysis, while the dashed arrow indicates the looser cut used in the systematic study. (a) Data, top beam. (b) Data, bottom beam. (c) Monte Carlo, top beam. (d) Monte Carlo, bottom beam.

kaons that can miss the regenerator when it is in the lower beam — the "sneakby" kaons discussed in the Chapter 8. Since the regenerator beam $\pi\pi$ samples are dominated by the regenerated K_S decays, this beam tail is suppressed by a factor of $|\rho/\eta|^2$ (ie, by 100 to 200) and does not appear in the regenerator beam. There is no such suppression of this tail in the vacuum beam. The Monte Carlo mimics this small effect remarkably well.

With the looser ring number cut, we begin to probe the region of the beam where the regenerator and vacuum beam shapes begin to deviate. Since the Monte Carlo reproduces this deviation, we do not expect to observe any significant bias. Indeed, with the looser cut, we observe a change in $Re(\varepsilon'/\varepsilon)$ of 0.46×10^{-4}. This is again consistent with the change allowed by statistics. The allowed change is dominated by the change in the number of coherent kaons (0.42×10^{-4}), but also has a sizable contribution from fluctuations in the background (0.20×10^{-4}), yielding a one standard deviation shift of 0.47×10^{-4}.

If we turn now to studies with different the $2\pi^0$ mass cuts, we do not expect as clean a situation as with the ring numbers study because of the residual nonlinearities in the photon energy reconstruction which shift the $2\pi^0$ mass distributions in the data relative to those in the Monte Carlo. Since we collect the K_S and K_L decays simultaneously, the resolution for the two samples is very similar, as the background subtracted $2\pi^0$ distributions in Figure 132 show. What is also clear, however, is that the vacuum beam $2\pi^0$ mass distribution is somewhat wider than the regenerator beam mass distribution. As we discussed above, this width difference results from the contribution of the lower energy kaons in the vacuum beam downstream of the HDRA.

With our standard mass cut of (498 ± 24) MeV/c^2, the number of signal events is small enough at the cut that we expect very little bias ($< 10^{-5}$) on $Re(\varepsilon'/\varepsilon)$. If we tighten the cut to (498 ± 18) MeV/c^2, however, the signal size is now almost an order of magnitude higher at the cut boundary. Earlier we tabulated the observed shift of the $2\pi^0$ mass in the data relative to that in the Monte Carlo (see Table 8) because of the residual nonlinearity in the photon energy scale. These shifts were combined with the shape of the vacuum and regenerator beam mass distributions in Figure 132 and used to estimate the expected bias in $Re(\varepsilon'/\varepsilon)$ for the tighter mass cut. We found we should expect a bias of the order of $+0.8 \times 10^{-4}$. When we reanalyze the $2\pi^0$ data and Monte Carlo with this tighter mass cut,

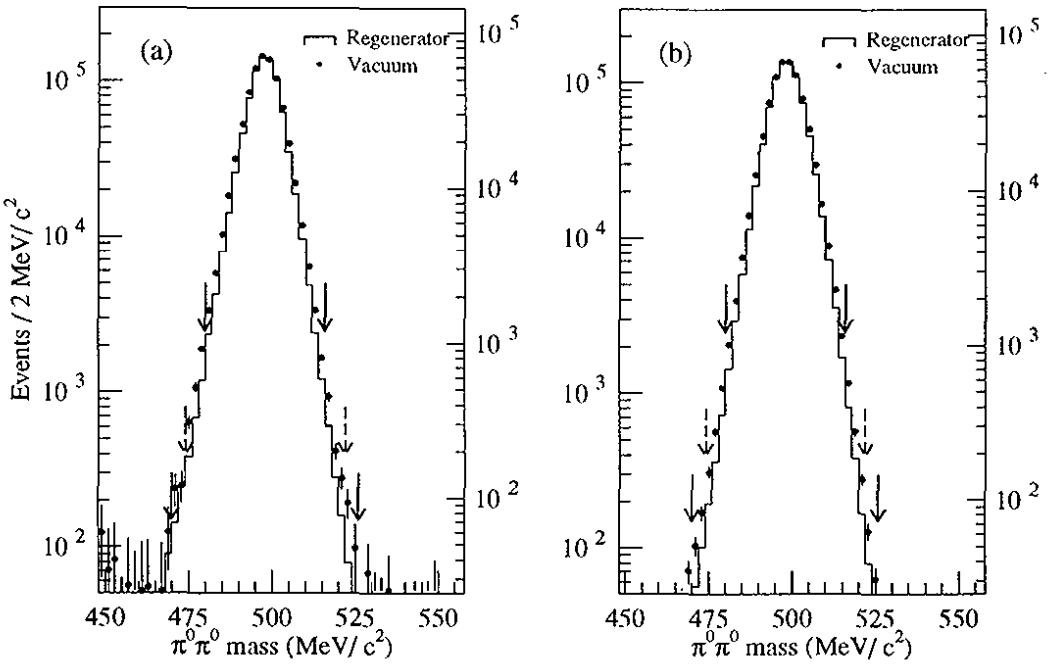

Figure 132. Overlay of the vacuum and regenerator beam mass distributions for the total $2\pi^0$ data sample. (a) Background subtracted data. (b) Coherent Monte Carlo. The full Monte Carlo sample is plotted, but it has been scaled to the same total area is the data. For both data and Monte Carlo, the histogram is the regenerator beam distribution (left-hand scale), and the dots show the vacuum beam distribution (right-hand). The innermost and outermost pair of arrows indicate the mass cuts used in two of the systematic studies. The dashed pair of arrows show the standard mass cut.

we observe a shift of $+1.28 \times 10^{-4}$. Given that the change in the data and background statistics would allow a one standard deviation fluctuation of 0.32×10^{-4} on $Re(\varepsilon'/\varepsilon)$, the observed shift is consistent with the systematic effect we expect.

When we adjust the mass cut in the other direction, we are no longer strongly probing the effects of the mass shift, since the number of signal events beyond our standard mass cut is quite small. A looser mass cut does, however, allow a large number of background events to enter the data sample, particularly in the vacuum beam (see Figures 66 and 67). For example, with a mass cut of (498 ± 28) MeV/c^2 (the outmost pair of arrows in Figure 132), the $2\pi^0$ signal in the vacuum beam increases by only 200 events, while the $3\pi^0$ and beam interaction backgrounds increase by 1800 events! The allowed statistical fluctuations are dominated by the new background events, though there is a small contribution from the signal statistics. A one standard deviation fluctuation of $Re(\varepsilon'/\varepsilon)$ is 0.19×10^{-4}, and with

this looser mass cut applied to the data we observed a shift of -0.30×10^{-4}. This shift is consistent with a statistical fluctuation, though it is also in the direction that the bias just discussed would be expected to shift $Re(\varepsilon'/\varepsilon)$. Whether the source of the shift is systematic or statistical, the errors assigned for either the background subtraction or the residual nonlinearity are more than adequate to accommodate this shift.

As a final check of the sensitivity of $Re(\varepsilon'/\varepsilon)$ to the analysis cuts, we made the track quality cuts and E/p cut in charged mode much looser. In particular, the cut on the track χ^2, whose tail (Figure 40) is not reproduced in the Monte Carlo because we have not included δ-rays in the chamber simulation, has been relaxed from 30 to 100. The probability to obtain a δ-ray in a drift chamber is to a very good approximation flat as a function of momentum over the momentum range of the pions from the $K \to \pi^+\pi^-$ decays in this experiment. The distribution of material across the chamber (perpendicular to the beam) is also very uniform, so the δ-ray production probability will be independent of the track position. Hence we expect the vacuum and regenerator beam decays to be affected identically by the track χ^2 cut, and the loss to cancel in the ratio of the two beams.

The other track quality cuts relaxed were cuts on the segment matching at the magnet (Figure 41) and the distance of closest approach of the two measured tracks (Figure 42), which were loosened by a factor of two. In addition, the E/p cut was relaxed from 0.80 to 0.84, which increased the semileptonic background in the K_L beam by 25% of itself. The new backgrounds levels were determined using the procedure described in Section 5.2.

The overall change in statistics with these relaxed cuts was quite large — an 8% increase in each beam. This increase is completely dominated by the relaxation of the χ^2 cut. The statistical one standard deviation fluctuation in $Re(\varepsilon'/\varepsilon)$ is 1.01×10^{-4}. We observe a change of 0.25×10^{-4}, well within the statistical uncertainty, and there is not any large bias introduced by either the χ^2 cut or the change in the background level.

10.1.2 Some Benefits of the Double Beam Technique

The stability of $Re(\varepsilon'/\varepsilon)$ in many of the studies we have performed, including some of the studies mentioned above, arises from the use of the double beam. Collecting K_S and

Table 23. Shifts in $Re(\varepsilon'/\varepsilon)$ for studies demonstrating the stability of $Re(\varepsilon'/\varepsilon)$ due to the simultaneous collection of K_S and K_L decays.

Study	$\Delta Re(\varepsilon'/\varepsilon)$ ($\times 10^{-4}$)	Allowed Shift
Introduce 10% inefficiency into 2 B bank trigger counters, and 100% inefficiency into 4 drift chamber wires, in the $\pi^+\pi^-$ Monte Carlo simulation	-1.50	—
Loosen maximum photon energy cut in $2\pi^0$ analysis from 60 GeV to 90 GeV	$+2.00$	1.16
Loosen maximum photon energy cut in $2\pi^0$ analysis from 90 GeV to 120 GeV	$+0.10$	0.27

K_L decays simultaneously from (nearly) identical beams results in cancellation of many of the effects of the detector. This section will examine two studies where the benefits of simultaneously collecting K_S and K_L decays to a particular final state are very apparent. The results of the fits used in these studies are summarized in Table 23.

In the first of these studies, we introduced a 10% inefficiency into the Monte Carlo response of two of the B-hodoscope counters which form a vertical stripe near the center of the beam. In addition to this, four wires in the drift chambers were assigned an efficiency of zero. Because of the different z distributions, the illuminations of the doctored counter and wires by decays from the vacuum and regenerator beams are not expected to be completely identical. However, the inefficiencies should largely cancel. Indeed, when we use the doctored Monte Carlo for the acceptance corrections in the fit, $Re(\varepsilon'/\varepsilon)$ is shifted by only -1.5×10^{-4}.

This situation, is, of course, rather artificial. The counter efficiencies were determined with muons and the wire efficiencies with the Ke3 sample at the sub percent level. Such efficiency mismatches are also completely obvious in the data–Monte Carlo comparisons, as the data / Monte Carlo ratio of track illumination at the lead glass in Figure 133 shows.

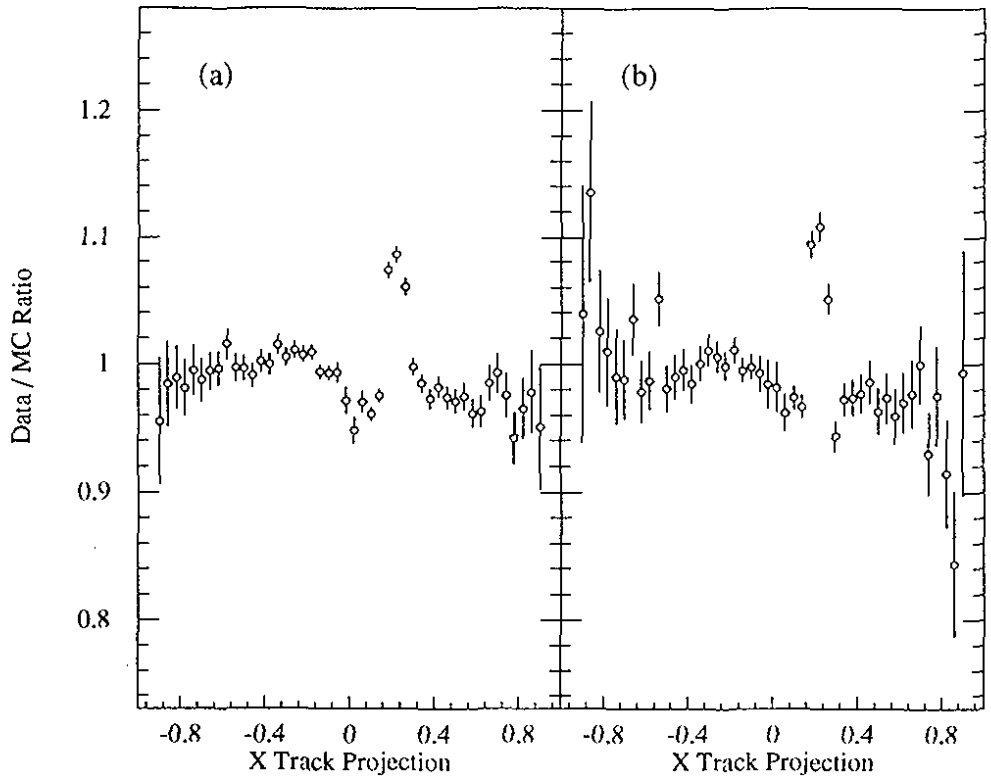

Figure 133. Ratio of the data and Monte Carlo track illumination at the lead glass when a 10% inefficiency is introduced into the response of two of the B hodoscope counters in the Monte Carlo. The two counters form a vertical stripe in the hodoscope bank. The data and Monte Carlo simulation are from the $\pi^+\pi^-$ subset C4. (a) Regenerator beam ratio. (b) Vacuum beam ratio.

Only the C4 charged data (about 20% of the total sample) is shown, but the location of the inefficient counters shows up clearly as the 10% spike in the ratio for both the vacuum and regenerator beam ratios. The step at the center of the plot, and the curvature of the ratio on the negative side, are the result of the interaction of the right-left $\pi^+\pi^-$ trigger requirement with the counter inefficiency.

The next study is based upon the one issue not resolved in this experiment — the loss of high energy clusters in the Monte Carlo simulation that is not observed in the data. This problem has been discussed previously in Section 7.4.1. We know that the disagreement is limited mainly to the 24 blocks surrounding the beam pipes in the center of the calorimeter, though there is also a hint of the problem in the next ring of blocks surrounding the pipe blocks. The pipe blocks are the blocks most seriously affected by radiation damage, and the

combination of radiation damage and curing causes the mismatch between data and Monte Carlo to change over time.

The time dependence is apparent, for example, in the difference between the data and Monte Carlo ratios of the maximum cluster energy distributions for the $2\pi^0$ subsets with and without the lead sheet (Figure 134a). The "early" lead sheet subset was collected after a startup period where the inner blocks were exposed to a fair amount of beam. The first curing periods for the glass occurred well into the data taking for this subset. Conversely, most of the data collection for the subset without the lead sheet occurred after a long shutdown during which the calorimeter was given a healthy long cure. We thus expect the radiation damage in the inner blocks to be most severe for the early subsets, and this is verified by the larger nonlinearities measured for the inner blocks in the early relative to the later calibrations. We also expect our modelling of the lead glass to have the most problems with blocks with large radiation damage, since the damage is likely to be nonuniform as a function of depth into the block. The maximum cluster energy disagreement tracks the nonlinearity of the innermost blocks.

Since we collect the decays from the vacuum and regenerator beams simultaneously, however, each beam is affected identically. The ratio of data to Monte Carlo maximum cluster energy distributions for the entire data set are clearly similar for the two beams (Figure 134b), and the bias as a function of energy disappears in the ratio of ratios (Figure 134c). The latter ratio is what affects our experiment, and would not have been flat had we not collected the K_S and K_L decays simultaneously.

Since we accept only events before the disagreement between data and Monte Carlo, we will not be significantly affected by the problem. To gauge the effect, however, we have relaxed the cut on the maximum cluster energy from 60 GeV to 90 GeV and 120 GeV, where the mismatch is much more severe. There is again a sizable change in the sample sizes, which allow fluctuations in $Re(\varepsilon'/\varepsilon)$ at the level of 1.2×10^{-4} The observed shift is in that statistical netherworld of $+1.7$ standard deviations. It might be a statistical fluctuation, but the direction is what we might expect from a small bias arising from an average energy spectrum that is slightly stiffer in the regenerator beam than in the vacuum beam. This

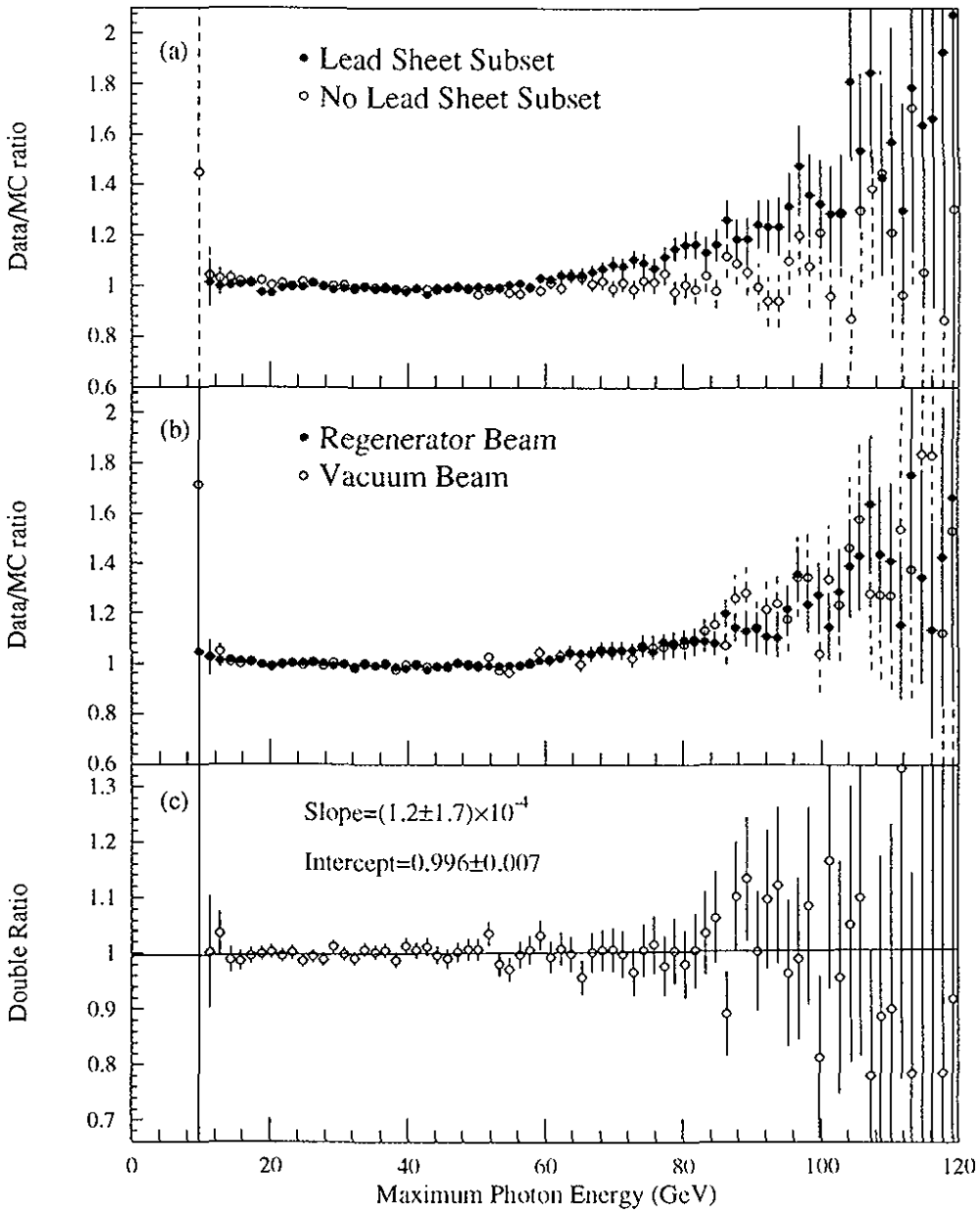

Figure 134. Ratio of the data and Monte Carlo maximum cluster energy distribution in $2\pi^0$ decays. The predicted background contribution has been included in the Monte Carlo distribution. (a) The ratio for decays in the regenerator beam for the early $2\pi^0$ subsets with the lead sheet (solid circles) and the later sets without the sheet (open circles). (b) The ratios for the total $2\pi^0$ data set in the regenerator beam (solid circles) and vacuum beam (open circles). (c) The ratio of the two ratios in (b). The best fit line to the double ratio has been superimposed.

leads to a slightly larger faction of events having a pipe block in the regenerator beam, and to an artificially enhanced regenerator beam sample after the acceptance correction.

We have restricted ourselves to a cluster energy regime where there is little, if any, mismatch between the data and the Monte Carlo simulation. Furthermore, this maximum photon energy cut restricts the $2\pi^0$ sample to a regime where the softer photon energies in the $3\pi^0$ decays are plentiful. If there is a residual bias at lower energies, the $3\pi^0$ sample will be also be affected. Since we use the $3\pi^0$ sample to limit possible biases in the acceptance, any residual problem introduced by the maximum cluster energy disagreement be safely limited as well.

10.1.3 Individual Subsets

For the final topic of this section on systematic studies, we turn to a useful property of our experimental technique which allows us to check both time and intensity dependences. Since the same regenerator is used throughout the experiment, we should measure a consistent regeneration amplitude in each data subset of each decay mode[1].

The various subsets span a range of configurations. Intensities vary by a factor of three between the various sets (see Table 4), the lead sheet is present or not present in different $2\pi^0$ subsets, and the degree of radiation damage in the inner part of the array varies substantially[2]. In spite of these very different conditions, the regeneration amplitude measured in each subset agree very well (Figure 135) within each decay mode. The small corrections for accidental biases (see Sections 9.1.1 and 10.7) have already been made in the different subsets.

10.1.4 Summary

In general, the systematic studies we have performed have given us much confidence in the stability of our result. In most tests, the observed fluctuations in $Re(\varepsilon'/\varepsilon)$ are

[1]Remember, we cannot directly compare the regeneration amplitudes between fits to the $2\pi^0$ or $\pi^+\pi^-$ samples since a nonzero value of $Re(\varepsilon'/\varepsilon)$ will shift the amplitudes measured in each mode relative to each other.

[2]The average nonlinearities measured in the pipe blocks in different subsets can vary by as much as 40%.

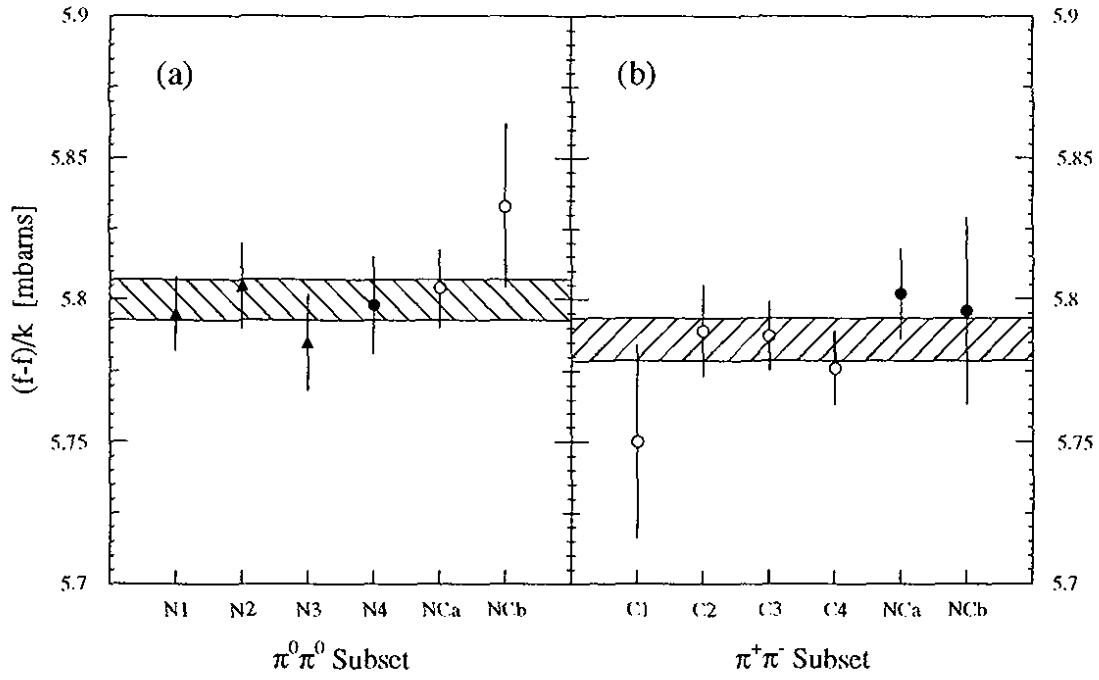

Figure 135. The regeneration amplitude measured in individual data subsets. The $2\pi^0$ measurements are plotted in part (a) and the $\pi^+\pi^-$ measurements in part (b). The one standard deviation bands from the fits to the entire $2\pi^0$ or $\pi^+\pi^-$ sample described in Section 9.1 have been plotted as well. The highest (lowest) intensity data for each mode is plotted with solid (hollow) points. In part (a), the subsets with (without) the lead sheet are indicated by triangles (circles).

consistent with the expected statistical fluctuations. In the cases where there appear to be shifts beyond those allowed by statistics, the analysis cuts to enter a purposely enter a regime affected by known problems for the study, and the shifts are compatible with the expected behavior. The following sections will now describe the methods used to limit the systematic uncertainty on $Re(\varepsilon'/\varepsilon)$ and the other measurements.

10.2 Neutral Energy Reconstruction

The first systematic contribution we will evaluate is that from the photon energy reconstruction in the $2\pi^0$ decay, where there are several potential biases. For example, the energy resolution yields a z resolution of the order of 1 m, and a mismatch of the resolution in data and Monte Carlo could result in a bias in the acceptance correction. What will turn

out to be a much more severe uncertainty, however, are systematic biases in the measured energy. We will investigate the effects from biases, both linear and nonlinear, as a function of the cluster energy.

10.2.1 Resolution

We are most sensitive to any residual mismatches between data and Monte Carlo when one of the boundaries of a fiducial region in z is located very near to a sharp step in the decay distribution. We would be sensitive to the resolution, for example, if we were to begin our own z fiducial region upstream of, and very close to the location of the regenerator. In this region, events which smear upstream are not compensated by events smearing downstream. For both our previous result [50] and for this result our z cut completely contained the regenerator edge, which made the result quite insensitive to this issue. At the downstream end of the fiducial z region, the acceptance does not changing very rapidly in either beam, and the smearing of events upstream and downstream of the location of our downstream z tends to cancel.

The use of a single large z bin for the data also helps to minimize any ill effects of a residual resolution mismatch between data and Monte Carlo because the effects of smearing are restricted to the upstream and downstream ends of the decay volume. This makes the total number of events which smear in and out of a z bin for the fit a very small fraction of the total events in that bin.

To investigate the sensitivity of the measurements to the resolution, we have introduced additional smearing in the reconstructed photon energy. The $2\pi^0$ z distribution with 2% additional photon energy smearing (Figure 136) now shows a glaring mismatch between the data and the standard Monte Carlo distributions. In spite of this mismatch, however, refitting for $Re(\varepsilon'/\varepsilon)$ using the smeared data and standard acceptance corrections yields a shift in $Re(\varepsilon'/\varepsilon)$ of only 1.5×10^{-4}. By comparing the the shape of the z edge in data and Monte Carlo near the regenerator we can limit the resolution mismatch to 0.5%. Smearing with 0.5% yields a shift of 0.36×10^{-4}, consistent with scaling down the shift with the 2% smearing. Much of this sensitivity comes from introducing the ± 1 m cut around the

HDRA in the $2\pi^0$ subset with the lead sheet. This was offset, however, by a decrease in our sensitivity to the energy scale, which we will discuss next.

For the measurements using the constrained fits, the contribution from smearing to the total systematic uncertainty of those measurements is very small. As we discussed previously, the insensitivity results from the choice to begin the fiducial range in z downstream of the regenerator (Section 9.2). Using the 0.5% extra resolution study to limit the uncertainty, we have a contribution of $0.0004 \times 10^{10}\ \hbar s^{-1}$ to the uncertainty of the measurement of Δm in the $2\pi^0$ data, $0.0003 \times 10^{-10}\ s$ to that of τ_S in the $2\pi^0$ data, and less than $0.01°$ (that is, none!) to the measurement of $\Delta\phi$.

10.2.2 Energy Scale and Nonlinearity

The largest effort of this experiment has certainly gone into the refinement of the calibration and simulation of the lead glass calorimeter. A bias in the reconstructed photon energy scale will move events past both of the energy and the z fiducial boundaries, so the effort to limit biases in the photon reconstruction was crucial. While we have seen that the

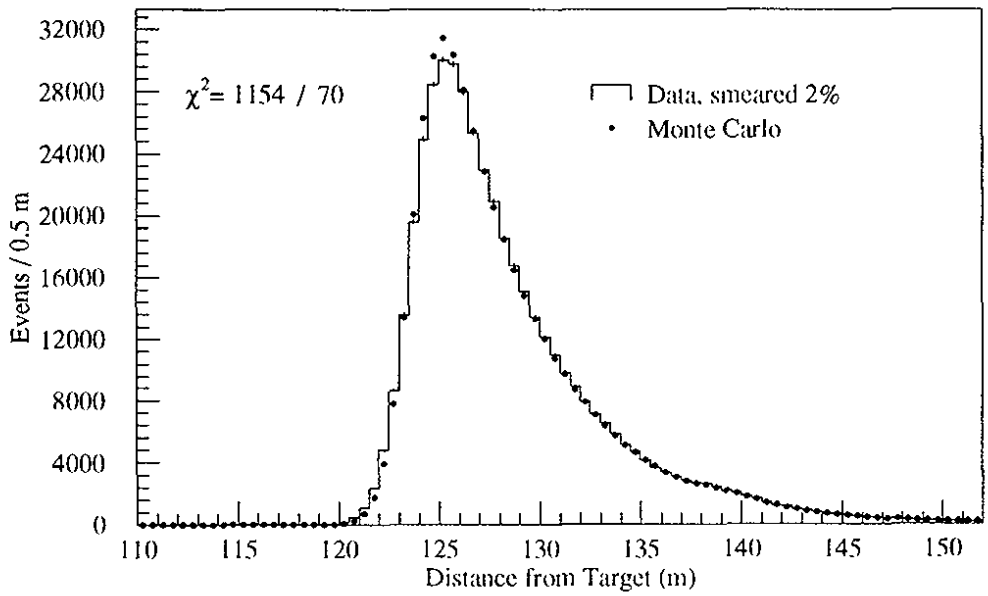

Figure 136. The z location of $2\pi^0$ decays in the regenerator beam for the data and the Monte Carlo simulation after the photon energies in the data were smeared by an additional 2%. Only the subset with the lead sheet is shown here.

Table 24. Shift in $Re(\varepsilon'/\varepsilon)$ induced by some of the systematic biases introduced into the photon energy reconstruction procedure. The resolution bias was discussed in the previous section.

Reconstruction bias	$\lvert\Delta Re(\varepsilon'/\varepsilon)\rvert$ $(\times 10^{-4})$
0.5% energy smear	0.36
0.03% average energy scale change $(\Delta E = 3 \times 10^{-4} E)$	0.93
Quadratic energy scale change $(\Delta E = qE^2)$	1.57
20 MeV per cluster "pedestal" shift	0.46

electron response in Ke3 decays and the photon response in $\pi^+\pi^-\pi^0$ decays are mimicked quite well by the Monte Carlo (see Section 7.4.1), we also know that shifts between the reconstructed $2\pi^0$ mass in the data and the Monte Carl (see Table 8) indicate the presence of small residual nonlinearities in our photon energy reconstruction. This section will evaluate our sensitivity to the energy scale.

The results from some of the systematic studies related to the photon energy scale which we have performed are summarized in Table 24. Most of these studies followed the same general procedure. First a specific bias was introduced into the reconstruction of photons in the data sample, while the reconstruction of photons in the Monte Carlo simulation was unmodified. After the bias was introduced, the regenerator edge in the biased data was rematched to the regenerator edge in the data (see Section 6.4) as a function of the reconstructed kaon energy to obtain a new energy scale correction. The data was then analyzed a second time with both the bias and the new compensating scale correction. We finally fit to the reanalyzed data to determine what effect the residual bias had on our determination of $Re(\varepsilon'/\varepsilon)$.

The only study where this procedure was not applied was when an average energy scale bias of 0.03% was introduced into the photon energy reconstruction. Since small biases in E and z are linearly coupled, the procedure of matching the z edge almost fully compensated

for this bias. To set the scale of how sensitive $Re(\varepsilon'/\varepsilon)$ is to an average bias, we have refit the data without the z edge compensation, and the 0.03% scale change resulted in a shift of 0.93×10^{-4}. Since the regenerator z edge provides a measure of the average energy scale bias which is more sensitive than this (which is clear from Figure 62), however, the most troublesome effects come from nonlinear biases in the reconstruction.

When we introduced different nonlinear biases into the photon reconstruction, we indeed found that the z edge matching could not completely compensate for the bias. An example of such a bias would be a residual pedestal shift in the data. To gauge our sensitivity to pedestal shifts, we uniformly shifted the energy of every cluster by 20 MeV, which resulted in a shift in $Re(\varepsilon'/\varepsilon)$ of 0.46×10^{-4}. We have measured the pedestal shifts using both data where every the signal in every lead glass block was read out (*i.e.*,there was no minimum readout threshold), and in $3\pi^0$ data. The pedestals measured with these two samples agreed very well, giving us much confidence in the pedestals measured using the $3\pi^0$ decays in sets with a readout threshold. Typical pedestal shifts were of the order of 40 to 50 MeV per cluster, and we could determine these at the level of 10 MeV or better. Corrections for the shifts are, of course, already applied in the standard analysis.

To estimate the effect of the remaining nonlinearities, we introduced a quadratic correction to the cluster energy, $E \rightarrow (1 + qE)E$. Since a nonlinearity introduced into the reconstruction shifted the mean reconstructed $2\pi^0$ mass, the value of q was chosen to shift the mean $2\pi^0$ mass in the data to match that in the Monte Carlo simulation. The reconstructed Monte Carlo mass was used as the reference mass because we expect our mass reconstruction technique to result in a small positive mass shift when coupled with finite energy resolution. This shift, of the order of several tenths of an MeV/c^2, was indeed observed in the Monte Carlo. Had we used the nominal kaon mass, we would have underestimated q.

The mass shift as a function of the curvature q of the correction is shown in Figure 137. Separate curves were determined for the pipe blocks (surrounding the beam pipes). The uncertainty in the nonlinearity arises from our lack of knowledge of the change in the Çerenkov light absorption as a function of depth into a lead glass block. We expect the nonuniformity to be greatest in the pipe blocks, which received the most radiation damage,

and hence the residual nonlinearities in these blocks to be greatest. The average of the pipe and non-pipe block curvatures needed in the different $2\pi^0$ subsets are indicated by the arrows in the figure.

After reanalyzing the data as described above with the quadratic biases applied, the measured value of $Re(\varepsilon'/\varepsilon)$ shifted by -1.57×10^{-4}. While the quadratic bias shifts the mass as desired, it does tend to distort the shape of the mass distribution. The most obvious changes are large asymmetries that appear in the mass distribution. These asymmetries actually broaden the mass distribution beyond that induced when we smeared all of the photon energies by an extra 1/2%! Hence we believe that a distortion as severe as the quadratic bias applied is not favored by the data. To be conservative, we take the full shift as an estimate of the residual bias in the energy reconstruction.

Combining the nonlinear bias with the bias from smearing, we have a total systematic contribution from photon energy reconstruction of 1.61×10^{-4}. This is the largest systematic contribution to our uncertainty in $Re(\varepsilon'/\varepsilon)$.

The cluster energy reconstruction uncertainties also dominate the systematic uncer-

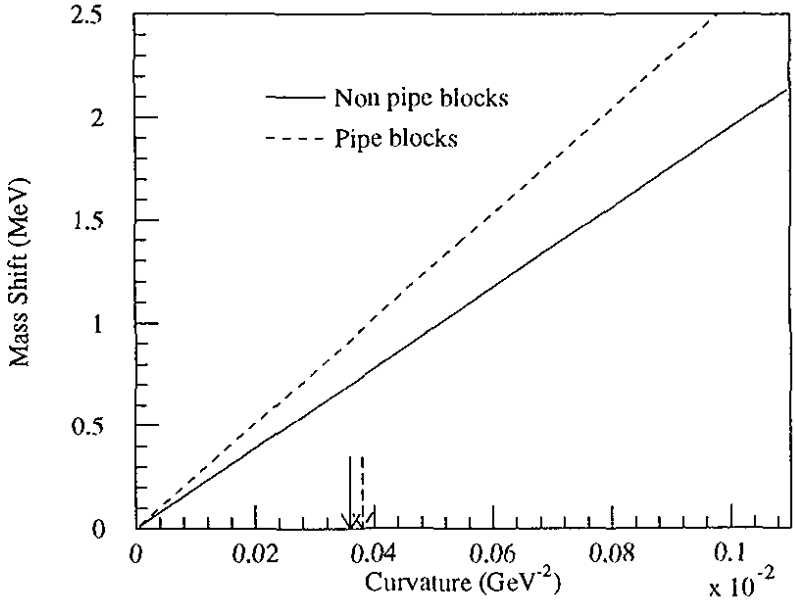

Figure 137. Mass shift as a function of the curvature of the quadratic cluster energy bias. The observed shift is shown for events with (dotted line) and without (solid line) clusters in the pipe blocks. The arrows indicate the average of the curvatures used in the systematic studies.

tainty in the other measurements which use the $2\pi^0$ sample. From studies similar to those described above, we have contributions of 0.0012×10^{-10} s on the systematic uncertainty of the neutral τ_S measurement, and 0.0014×10^{10} $\hbar s^{-1}$ and 0.52° on those of the neutral Δm and the $\Delta\phi$ measurements, respectively. The $2\pi^0$ data sample is used in the ϕ_{+-} measurement to obtain a more precise determination of the regeneration power α and therefore, via analyticity, of the regeneration phase ϕ_ρ. When the energy scale nonlinearities were introduced into the $2\pi^0$ analysis, the bias introduced into ϕ_{+-} was negligible.

10.3 Acceptance

10.3.1 Acceptance Biases and $Re(\varepsilon'/\varepsilon)$

As we discussed in Chapter 7, the acceptance of the experiment is largely governed by several limiting apertures. The two apertures to which we were most sensitive were those defined by the active mask and the collar anticounter, since the illumination of the boundaries of these counters by decay products was still relatively high. Both of these were active counters, which helped to make them clean and clearly resolvable within the data. The lead glass and the HDRA trigger counters (T and V) also provide some definition to the accepted decay region, but the decay particle illumination at these outer edges are low enough to make the measurement of $Re(\varepsilon'/\varepsilon)$ quite insensitive to their precise size and location.

The most important property of these apertures is the actually the average effective size of the aperture, as apposed to the exact placement of the aperture. To keep the systematic uncertainty in $Re(\varepsilon'/\varepsilon)$] from the acceptance correction within acceptable limits (at the 10^-4 level), we need to know the average effective size of the apertures at the level of 200 microns or better. As section 7.3.3 discussed, we measured the effective size of the aperture with electrons from Ke3 decays since this will automatically compensate for the thickness in z of the counters, for small dead regions (or skin depth) at the edges, and errors in the uncertainty of the z location[3]. Since any bias from the uncertainty in chamber alignment is

[3]All of the critical apertures and detector elements were surveyed independently by a team of experimenters and a FNAL survey crew. The measurements of the veto counter and aperture positions agreed at

common to the edges on both sides of an aperture, this bias cancels when we compare the two edges to determine the aperture size. Our systematic estimate on the position of each edge, independent of the chamber calibration, was 50 microns, so the average aperture size is measured at the 70 micron level, well under the limit we wished to achieve. In principle, we could have surveyed the sizes and locations more accurately and then modelled the response to obtain more accurate values than this. We shall see that this accuracy is more than sufficient. For the temperature range in our beam line, conservative estimates of the size changes due to thermal expansion are generally well under this systematic estimate.

$Re(\varepsilon'/\varepsilon)$ is less sensitive to the small systematic shifts of an aperture in the Monte Carlo because the loss of events on one side of the aperture is largely compensated for by the event gain on the other side of the aperture. If the size of the aperture is incorrect, however, no such compensation occurs: if the aperture is too large in the Monte Carlo, we overestimate the acceptance, if too small, we underestimate the acceptance.

Our ability to locate an aperture's position with the Ke3 electrons depends, of course, on the accuracy of the chamber alignment. There will be an uncertainty in projecting the tracks measured in the chamber system back to the aperture location which depends on the relative alignment of the chambers. In addition, there is an uncertainty in the chamber positions relative to the coordinate system fixed by the production target and calorimeter. This latter corresponds to an uncertainty at the 10 to 20 micron level (see Chapter 4). Since we can track the relative locations of two chambers at the 10 micron level, the systematic uncertainty in the track projection corresponds to a 60 micron uncertainty at the mask, 35 microns at the HDRA, and 15 microns at the collar anti. These uncertainties, as well as those from the expansion and contraction of the stands holding the vacuum pipe, are all contained by an uncertainty of approximately 70 microns.

We have estimated the effects of the aperture sizes and positions by studying the event gain/loss when the aperture edges in the Monte Carlo are adjusted. Table 25 outlines the effect on $Re(\varepsilon'/\varepsilon)$ for the most important of these studies. When adjusting the aperture sizes, a worst case scenario has been adopted where all edges of the aperture are simultaneously moved to cut farther into the event flux. The effects of the aperture size adjustments

the 2 mm level, and the relative positions of the regenerator, chambers and calorimeter were known at the 1 mm level.

Table 25. Change in the single ratios and in $Re(\varepsilon'/\varepsilon)$ when the size of a limiting aperture is changed in the Monte Carlo. ΔR_{00} and ΔR_{+-} are the changes in the vacuum to regenerator beam ratios in the charged and neutral mode samples. In each case, the size of the apertures in the x and y were simultaneously changed by 70 microns in order to maximize the effect.

Aperture adjustment	ΔR_{00} (percent)	ΔR_{+-} (percent)	$\lvert\Delta Re(\varepsilon'/\varepsilon)\rvert$ ($\times 10^{-4}$)
Change Mask Size 70 μm	-0.013	-0.014	0.02
Change HDRA size 70 μm	-0.002	negligible	0.03
Change CA size 70 μm	-0.021	negligible	0.35

are correlated between the charged and neutral mode samples, and tend to cancel in the double ratio. This makes $Re(\varepsilon'/\varepsilon)$ very insensitive, for example, to the size of the mask aperture, which affects only the vacuum beam acceptance, but has very similar effects on the $\pi^+\pi^-$ and $2\pi^0$ vacuum beam acceptances. In the end, the result was most sensitive to the size of the collar anti, where a simultaneous decrease (or increase) of both the x and y sizes by 70 microns induced a shift of order 0.3×10^{-4} in $Re(\varepsilon'/\varepsilon)$. As we will see, this is quite a bit smaller than our limit on the acceptance bias we obtain from the $3\pi^0$ sample and use for our final systematic.

Except for the NC set, where all four decay modes were collected simultaneously, biases in the aperture position measurements do not cancel between the charged and neutral data sets, though the compensation of the event loss at one edge by the event gain at the opposite edge keeps our experiment insensitive to a shift in a measured aperture position. In our Monte Carlo studies of the change in sample size for different aperture shifts, the biggest change was found when the mask was shifted in neutral mode. For a 1 mm shift however, the bias introduced in $Re(\varepsilon'/\varepsilon)$ was only 0.1×10^{-4}. A shift of this size would have been clearly observable in our data (see Figure 78).

The lead glass (in particular, the position of the outer edge of the lead glass) and the vacuum window have not been listed in this table because the illumination at these edges is so low. For example, if one decreases the radius of the vacuum window by a full millimeter,

the single ratios change by less than 0.001%! The same is true if the lead glass edge were pulled in by 1 mm.

Of course, the apertures do not solely determine the overall acceptance. Energy thresholds, the minimal separation of two tracks or two clusters before they can be resolved, detector resolution and other aspects of the detector can all have some impact upon the final acceptance. Using the the limits from the apertures alone would therefore underestimate the acceptance systematic.

To try to limit the systematic error from the acceptance calculation, we turn to the high statistics samples of $K_L \to 3\pi^0$ and $K_L \to \pi e\nu$ from the vacuum beam. As with the $\pi\pi$ decay modes (Chapter 7), we have checked the track and cluster aperture illuminations, track and cluster separations, etc. in the Monte Carlo relative to the data, with no surprises. For the final systematic error, we use these modes to limit an acceptance bias as a function of z, to which the $Re(\varepsilon'/\varepsilon)$ measurement is ultimately most sensitive.

A z bias in the charged mode has a smaller effect on $Re(\varepsilon'/\varepsilon)$ than a bias in the neutral mode because of the shorter decay region used in that mode. We have spot checked the z acceptance with Ke3 subsets, with results similar to that shown in Figure 102. As we discussed in Chapter 7, we have limited the bias in acceptance for the $\pi^+\pi^-$ mode by limiting a linear bias in the relative shapes of the z distribution in the data and the Monte Carlo simulation. For simplicity, we will simply refer to the linear bias as the "acceptance bias" for the remainder of this discussion. In the charged mode, we have used only a small fraction of the total available statistics in the Ke3 sample, but it was sufficient to place a limit on the acceptance bias of 0.03% per meter. We also observed no bias in the vacuum beam $\pi^+\pi^-$ data–Monte Carlo z comparison beyond this level. This limit, as well as the acceptance bias needed to shift $Re(\varepsilon'/\varepsilon)$ by 10×10^{-4}, have been superimposed on the ratio of the data and Monte Carlo Ke3 z distributions in Figure 102.

If we introduce this acceptance bias into our fits, then the measured value of $Re(\varepsilon'/\varepsilon)$ shifts by 0.65×10^{-4}.

The longer decay region in the neutral mode, and the upstream localization of the K_S decays versus the more uniform distribution of the K_L decays makes the neutral mode much more sensitive to a z bias than the charged mode. To limit the acceptance bias we have

used the full sample of $3\pi^0$ decays. Because the average photon energy for the $3\pi^0$ decays is much softer than for the $2\pi^0$ decays, a greater fraction of the $3\pi^0$ decays have photons which probe the edges of the detector than the $2\pi^0$ decays. Similarly, with six photons in the lead glass rather than four, the $3\pi^0$ sample will be more sensitive than the $2\pi^0$ sample to the ability to resolve individual photons in the calorimeter. Thus a limit to the acceptance bias obtained using the $3\pi^0$ sample is a reasonably conservative limit to use for the $2\pi^0$ sample.

From the $3\pi^0$ sample, we can limit the bias in the z acceptance to less than 0.007% per meter (Figure 103). The uncertainty introduced by the lead sheet will be evaluated later (Section 10.4). If a bias of this level is introduced, the value obtained for $Re(\varepsilon'/\varepsilon)$ now shifts by 1.00×10^{-4}. Even though this acceptance limit is much stronger than that used in the charged mode, the uncertainty from the longer decay region makes the neutral acceptance one of the largest contributors to the systematic uncertainty. This z bias, and the bias needed to introduce a 10×10^{-4} shift in $Re(\varepsilon'/\varepsilon)$ are superimposed on the data to Monte Carlo ratio for the $3\pi^0$ z distribution.

Combining the charged and neutral mode limits, we have a total uncertainty on $Re(\varepsilon'/\varepsilon)$ of 1.19×10^{-4}.

10.3.2 Acceptance Biases and the Constrained Fit Results

Because the limit on the acceptance bias is limited so strictly by the $3\pi^0$ sample, the uncertainty in the constrained fit results which use the $2\pi^0$ sample is quite small. For the neutral Δm measurement, there is only a $0.0001 \times 10^{10}\ \hbar s^{-1}$ contribution to the systematic uncertainty from the neutral acceptance, and for the neutral τ_S measurement, the contribution is only $0.0002 \times 10^{-10}\ s$. These estimates include uncertainties from accidental affects (see Section 10.7). The effect on $\Delta\phi$ is negligible.

Because the acceptance was not as crucial for $Re(\varepsilon'/\varepsilon)$ in the charged mode as it was in the neutral mode, we did not push as hard on limiting the acceptance bias as was possible with the Ke3 sample. One unfortunate side effect of this, however, is a fairly large contribution to the systematic uncertainty in the results from the constrained fits using the

$\pi^+\pi^-$ sample. For the Δm and τ_S measurements in the $\pi^+\pi^-$ sample, we have systematic contributions of $0.0009 \times 10^{10}\ \hbar s^{-1}$ and $0.0020 \times 10^{-10}\ s$, respectively. These errors include contributions both from varying the acceptance within the range constrained by the Ke3 sample, and from the shifting of the results as the z bin size was varied. Similar studies for $\Delta\phi$ and ϕ_{+-} show a contribution of $0.35°$ to the systematic error on both of these results.

10.3.3 Regenerator Anticounters

One acceptance detail which affects only the measurement of $Re(\varepsilon'/\varepsilon)$ is the location of the last regenerator anticounter relative to the regenerator. The other measurements use a z region that begins far enough downstream of this counter to be unaffected by its position.

The detail of the downstream end of the regenerator and the anticounter is shown in Figure 138. The anticounter introduces a small asymmetry between the $\pi^+\pi^-$ and $2\pi^0$ decay modes because all of the $\pi^+\pi^-$ decays upstream of (and inside) the anticounter are vetoed. Some of the photons from $2\pi^0$ decays upstream of the anticounter will also convert in the anticounter and veto the event, but this only partially compensates the veto of all of the $\pi^+\pi^-$ decays. The uncertainty in the number of decays vetoed by this anticounter depends on the relative position of the regenerator and anticounter in two ways. The most obvious parameter is the separation Δz of the counters from the downstream face of the regenerator. From direct measurement, we know this distance to about 1.2 mm. The uncertainty in this distance introduces to an uncertainty of 0.58×10^{-4} in $Re(\varepsilon'/\varepsilon)$.

The finger structure of the anticounters also makes the relative vertical positions of the regenerator and the anticounters important. The regenerator blocks are 88.9 mm high, while the anticounters span a height of 92.4 mm. Because the highest and lowest anticounter "fingers" are at different z positions, the number of decays vetoed will depend on whether the regenerator is centered closer to the top counter or the bottom counter. We know that counters extended beyond the regenerator at both the top and bottom, but do not know the exact value on each side. We have reported the final result assuming that the anticounter was centered on the regenerator. $Re(\varepsilon'/\varepsilon)$ varies by 0.08×10^{-4} per millimeter as the anticounter is moved off center. A motion of ± 1.5 mm in either direction is a

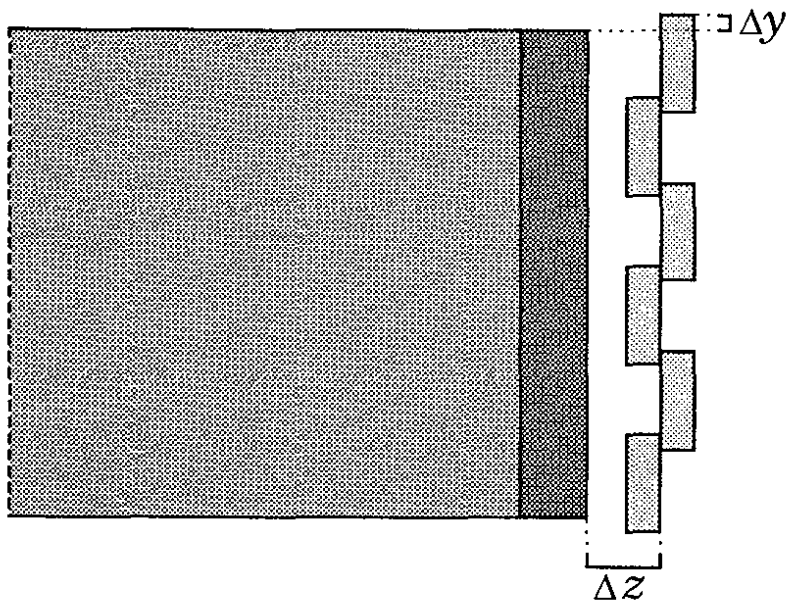

Figure 138. Detail of the downstream end of the regenerator and the RA4 anticounter. The drawing is not to scale.

reasonable estimate of how far off center the anticounter might be, corresponding to an error of 0.12×10^{-4} on $Re(\varepsilon'/\varepsilon)$.

Combining these effects, the regenerator anticounters contribute a total uncertainty of 0.59×10^{-4}.

10.4 The HDRA and Regenerator Lead Piece

The affects of the material in the HDRA overlap with many of the topics discussed in other sections of this chapter. The background level, the acceptance, and the fit functional are all affected by this detector element. However, the systematic biases in these different areas all stem from the same two issues: the thickness of the materials in the HDRA and the regeneration amplitudes of those materials. To account properly for systematic correlations in the extraction of $Re(\varepsilon'/\varepsilon)$ arising from these two issues, the background level, acceptance, etc. are modified simultaneously for a given change in material thickness or regeneration amplitude.

10.4.1 Contribution of the HDRA to the Systematic Uncertainty on $Re(\varepsilon'/\varepsilon)$

As we have discussed earlier in Section 6.5.2, the two elements which dominate the systematic uncertainties at the HDRA are lead, which is in the lead sheet, and carbon, which is in the scintillator and is also a major component of most of the other material. The regeneration amplitudes for kaons in our momentum range have been measured at the 1.4% level ([80, 78, 86]). These measurements had to assume a value for η_{+-} in order to isolate the regeneration amplitude, and the uncertainty given here includes the combination of the experimental errors on the regeneration measurements with the uncertainty in the world average of η_{+-}. The regeneration amplitudes for oxygen and nitrogen were scaled from that of carbon using the measured A-dependence [80] of the regeneration amplitude. When the regeneration amplitude for lead (carbon) was varied within the uncertainty given above, the shift in $Re(\varepsilon'/\varepsilon)$ observed was 0.31×10^{-4} (0.15×10^{-4}). These uncertainties are dominated by the change in the diffractive background level.

The chemical analysis of the lead used in making the HDRA's lead sheet shows the sheet to have been 99.9793% pure, with bismuth as the largest impurity at 0.017% [100]. Hence the uncertainty from assuming the sheet was pure lead is negligible.

The only other elements present in any significant quantities were hydrogen and aluminum. The regeneration amplitudes for these elements have also been measured for these ([87, 80]), but they were present in too small a quantity for $Re(\varepsilon'/\varepsilon)$ to be significantly affected when their amplitudes were varied.

When we varied the regeneration parameters of lead, the regeneration amplitude calculated for a kaon passing through the HDRA and the regeneration amplitude for a kaon passing through the regenerator[4] were both affected. We allowed both to change simultaneously so that any correlations would be properly considered. If we isolate the effect of the lead piece at the end of the regenerator on $Re(\varepsilon'/\varepsilon)$, it is found to be well under 0.1×10^{-4}. The variation in $Re(\varepsilon'/\varepsilon)$ when the lead regeneration phase is changed within its known errors (1.8°) was also under this level.

The bulk of the systematic uncertainty from the HDRA comes from uncertainty in the

[4]Recall that there was a 1.25 cm piece of lead at the end of the regenerator.

thickness of the material in the HDRA. The uncertainty for the four photons from a $2\pi^0$ decay upstream of the HDRA to pass through the HDRA without converting is in turn the dominant effect of an uncertainty in thickness. When the lead sheet is in place, the conversion probability for four photons can be deduced very accurately from the *six* photon conversion probability measured in the much larger sample of $3\pi^0$ decays.

The sheet had an average thickness of 518 microns, and was initially measured at 5 cm intervals both vertically and horizontally to an accuracy of 10 microns. The sheet was flat within 10 microns in the horizontal direction, but had a taper of order 50 microns over its 62 cm vertical length. This structure was put into the Monte Carlo, and then refined by comparing the size of the acceptance step in z (see, for example, the lead sheet $2\pi^0$ plot in Figure 106) observed in data and in the Monte Carlo in both the top vacuum and bottom vacuum beams. This gives a direct measurement of the 6 photon transmission probability, and we found on average that we were underestimating the transmission of events in the bottom beam by $1.1\% \pm 0.2\%$ (corresponding to roughly 13 microns). The Monte Carlo simulation was then adjusted to match the $3\pi^0$ data sample.

The accuracy of the 6 photon conversion probability corresponds to an accuracy on the 4 photon conversion probability of 0.16%. This is the accuracy for each beam individually. While the average conversion probability in the $3\pi^0$ sample is known more accurately than this, we take a limit of 0.16% as the uncertainty for the $2\pi^0$ sample to allow for residual uncertainties in the change in thickness over the height of the sheet. If we vary the sheet thickness corresponding to this uncertainty in the transmission probability, then $Re(\varepsilon'/\varepsilon)$ varies by 0.96×10^{-4}. Again, the variations in backgrounds and coherent regeneration are included in this study, but the photon transmission dominates completely.

The bulk of the remaining material was the 1 mm scintillator used in the T and V counters, whose thicknesses were known at the 25 micron level. We estimated the equivalent of 50 microns of scintillator uncertainty to cover the T and V counters and the remaining membranes (see Table 3). With this uncertainty introduced, $Re(\varepsilon'/\varepsilon)$ changed by 0.46×10^{-4}, again dominated by the uncertainty in the photon transmission.

Finally, there are the systematic uncertainties associated with the statistical uncertainty on the diffractive background and the total uncertainty on the inelastic background. The

background errors quoted in Section 6.5.2 correspond to an uncertainty in $Re(\varepsilon'/\varepsilon)$ of 0.23×10^{-4} from the diffractive statistical uncertainty and 0.42×10^{-4} from the inelastic background.

Combining all of the errors associated with the HDRA, we have a total uncertainty in $Re(\varepsilon'/\varepsilon)$ of 1.22×10^{-4}, making the HDRA one of the most sizable sources of systematic uncertainty in this measurement.

10.4.2 Effect of the HDRA on the Constrained Fit Results

The HDRA plays a much more minor role in the contribution to the systematic uncertainty of the results which use the constrained fits compared to its role in the uncertainty on $Re(\varepsilon'/\varepsilon)$. In the constrained fits, the vacuum beam was used to predict the number of kaons incident on the regenerator, and this prediction depends both on our knowledge of the acceptance and background level for the vacuum beam, and the level of absorption of kaons in the shadow absorber and the regenerator. While the uncertainty in the prediction does depend on the uncertainty in the photon conversion probability, the level of coherent regeneration in the HDRA, and the background level from the HDRA, these uncertainties are small relative to the uncertainty in the total transmission probability through the shadow absorber and the regenerator. As we will see in Section 10.6.1, even the uncertainty in the absorption has only a small effect on the constrained fits, and the uncertainties in the vacuum beam from the HDRA have negligible effect.

In the regenerator beam, the dominant uncertainty comes from the background level from the HDRA inelastic background. This background is only a small fraction of the total regenerator beam $2\pi^0$ sample, and even with the large systematic uncertainty of 40% (see Section 6.5.2), this background plays only a minor role in the systematic uncertainty in $Re(\varepsilon'/\varepsilon)$. The constrained fits, however, depend on the shape of the decay distribution in the regenerator beam, and hence on the relative numbers of events upstream and downstream of the HDRA. The HDRA inelastic background is more important to consider when its size relative to the number of downstream events only is concerned. This background is about 0.2% of the downstream events in the $2\pi^0$ sample without the lead sheet, and reaches 0.9%

Table 26. Contribution to the systematic uncertainty in $Re(\varepsilon'/\varepsilon)$ from backgrounds.

Background Source	Uncertainty	
	$\pi^+\pi^-$	$2\pi^0$
Noncoherent Regeneration (in regenerator)	0.18×10^{-4}	0.84×10^{-4}
Semileptonic Decays	0.23×10^{-4}	—
$3\pi^0$ Decays and Beam Interactions	—	0.60×10^{-4}
Total	0.29×10^{-4}	1.03×10^{-4}

in the sample with the sheet. With the large systematic systematic uncertainty in its level, this background contributes 0.0001×10^{-10} s and 0.0008×10^{10} $\hbar s^{-1}$ to the neutral τ_S and Δm measurements, respectively, and 0.2° to the uncertainty in $\Delta\phi$. The photon conversion probability and regeneration amplitudes are known well enough that the contribution from these sources to the uncertainty of the measurements is negligible.

10.5 Backgrounds

Sections 5.2 and 6.5 have already discussed the systematic and statistical uncertainties on the background levels for the $\pi^+\pi^-$ and $2\pi^0$ data samples. The contribution of the backgrounds to the uncertainty are here summarized in Table 26. The uncertainty from the HDRA backgrounds in the $2\pi^0$ have been included in the overall HDRA systematic contribution. The uncertainty in the subtraction of the remaining backgrounds in the $2\pi^0$ sample add an uncertainty of 1.03×10^{-4} to $Re(\varepsilon'/\varepsilon)$, while the backgrounds in the $\pi^+\pi^-$ sample contribute 0.29×10^{-4}.

In the above estimates of the uncertainty in $Re(\varepsilon'/\varepsilon)$, we have treated the regenerator background in the vacuum and regenerator beams as completely independent. In fact, this is quite conservative because the backgrounds are correlated and they would largely in the single ratio even without background subtraction (though not enough to be completely ignored).

The situation with the uncertainty in the constrained fit measurements from these re-

maining background sources is the same as the situation for the uncertainty from the material in the HDRA. The constraints required by the measurement of $Re(\varepsilon'/\varepsilon)$ were far more stringent than for the other measurements, and hence the systematic contributions to these measurements from uncertainty in the background levels are mostly negligible, particularly those in the vacuum beam. The largest uncertainty comes from the level of noncoherent background from the regenerator in the regenerator beam, yet this contributes only $0.00007 \times 10^{10}\ \hbar s^{-1}$ and $0.00005 \times 10^{-10}\ s$ to the neutral Δm and τ_S measurements, and under 0.02° to the $\Delta\phi$ measurement.

10.6 Fitting Related Uncertainties

In the previous two chapters, some of the systematic uncertainties involved in the fitting technique used to extract $Re(\varepsilon'/\varepsilon)$ have already been discussed. For example, the bias in $Re(\varepsilon'/\varepsilon)$ from the acceptance correction is under 10^{-5} when the regeneration or kaon decay parameters are within several percent of their true values. The only other inputs to the fitting routine, aside from the decay rate integration, are the vacuum beam kaon momentum spectrum ($F_v(r)$), and corrections to this spectrum for the regenerator beam (the average transmission t, and the energy dependence $c(p)$ in Equation 8.15). We will now discuss the sensitivity of the various measurements to these input spectra, and also to the assumption of analyticity used to obtain the regeneration phase. Much of the following discussion will focus on issues that were introduced in Chapter 8.

10.6.1 Incident Kaon Flux $F_v(p)$

The measurement of $Re(\varepsilon'/\varepsilon)$ tends to be quite insensitive to the detailed shape of the kaon momentum spectrum used in the fitting routine. The most important feature of the spectrum as far as the measurement of the regeneration power and average amplitude is concerned is the change of the average kaon flux between the 10 GeV/c momentum bins. The decay rate and acceptance change slowly across a 10 GeV/c bin, causing the kaon flux to largely integrate out of the prediction functional. There are then two different cancellations

which occur. The incident kaon flux $F_v(r)$ cancels in the regenerator to vacuum beam ratio within a single $\pi\pi$ decay mode, while the spectrum corrections to the regenerator beam flux cancel when comparing the charged mode regenerator rate to the neutral rate.

In Table 27, the variation of $Re(\varepsilon'/\varepsilon)$ with different modifications to the flux shapes is summarized. For the incident flux shape $F_v(r)$, the variations introduced were quite extreme. Even as drastic a change as changing the incident kaon spectrum[5] (see Figure 110) to a flat spectrum introduced a bias of only 1.21×10^{-4} in the measurement of $Re(\varepsilon'/\varepsilon)$. Introducing a 10% bowing into the spectrum resulted in only a 0.12×10^{-4} shift when applied to both the $\pi^+\pi^-$ and $2\pi^0$ data sets, and 0.04×10^{-4} shift when applied to the $\pi^+\pi^-$ set only. From the data–Monte Carlo comparisons (see Figures 72 and 73) we know that the spectrum has at most a few percent bowing, implying that the systematic bias from this quantity is negligible.

The measurements done using the constrained fitting technique are also quite insensitive to the shape of the vacuum flux used to calculate the relative contribution of a 1 GeV/c momentum "bite" to the predicted rate in a 10 GeV/c momentum bin. With a change as extreme as using a flat incident spectrum, the shifts in the measured quantities are on the order of one statistical standard deviation (Table 28). Most of the contribution to a shift induced by one of these changes arise from the use of kaons with momentum under 40 GeV/c in the $\pi^+\pi^-$ sample. In these low momentum bins, the acceptance changes more rapidly across the bin than at higher momentum. Since much of the Δm information in the $\pi^+\pi^-$ fits comes from these low bins, the result is more sensitive to a change in the momentum distribution across the bin. In contrast, the Δm and τ_S measurements using the $2\pi^0$ decay mode (and kaons in the 40 GeV/c to 160 GeV/c momentum range) shift at most 10% of the average shift shown in the table when a flat vacuum flux is used for the fit functional.

More realistically, when the "gentler" 10% bowing was introduced, the shifts in Δm and τ_S were completely negligible, and the shifts in $\Delta\phi$ and ϕ_{+-} were quite small. Extrapolating the shifts introduced by this large bowing to a level more reasonable given our knowledge

[5]This change affects only the calculation of the rate in a p and z bin in the fitting routine for a given set of test parameters. It does not change the *acceptance* calculation.

Table 27. Change in $Re(\varepsilon'/\varepsilon)$ for different modifications to the kaon flux shapes assumed in the fitting program. Note that these changes *are not* made in determining the acceptance, they only affect the relative contribution of the *predicted rate* of a 1 GeV/c momentum bite to the total predicted rate in a 10 GeV/c bin.

Modification to vacuum or regenerator beam spectrum	$\delta Re(\varepsilon'/\varepsilon)$ (10^{-4})
Flat Incident spectrum ($F_v(p)$ = constant)	−1.21
Quadratic distortion — both $2\pi^0$ and $\pi^+\pi^-$ samples ($F'_v(p) = F_v(p)\{1 + 0.1[(p-60)/100]^2\}$)	+0.12
Quadratic distortion, $\pi^+\pi^-$ sample only	+0.04
Increase average regenerator beam transmission by 1 standard deviation ($t \rightarrow 1.005t$)	−0.13
No shadow absorber scattering correction to regenerator beam flux	−0.36
Use shadow absorber scattering correction determined for the $\pi^+\pi^-$ sample[a] for all data sets.	−0.27
Use shadow absorber scattering correction determined for the $2\pi^0$ lead sheet subset for all data sets	−0.27
Change dilution factor used to calculate change in the relative flux shape between the regenerator and vacuum beam from regeneration in the movable absorber[b]	+0.04
Ignore "sneakby" rate[c].	−0.76
Correct for "sneakby" kaons, but ignore the rate of K_L decay from these kaons	−0.26
Use the "sneakby" rate determined for the $\pi^+\pi^-$ set for all of the subsets.	−0.47
Use the "sneakby" rate determined for the lead sheet $2\pi^0$ set for all of the subsets.	−0.46

[a] See Section 8.2.2.

[b] See Figure 111.

[c] That is, assume the entire flux of kaons observed in the vacuum beam passes through the regenerator. See Figure 113.

Table 28. Change in Δm, τ_S, $\Delta\phi$ and ϕ_{+-} for different distortions of the vacuum and regenerator beam kaon momentum spectra.

Modification to vacuum or regenerator beam spectrum	$\lvert\delta\Delta m\rvert$ $(10^{10}\hbar s^{-1})$	$\lvert\delta\tau_S\rvert$ $(10^{-10}s)$	$\lvert\delta\Delta\phi\rvert$	$\lvert\delta\phi_{+-}\rvert$
Flat Incident spectrum ($F_\nu(p)$ = constant)	0.0038	0.0007	1.3°	1.2°
Quadratic distortion:	0.0001	0.0001	0.3°	0.5°
$(F'_\nu(p) = F_\nu(p)\{1 + 0.1[(p-60)/100]^2\})$				
Change average regenerator beam transmission by 1 standard deviation:	0.0004	0.0002	$< 0.1°$	0.3°
$(t \rightarrow 1.005t)$				
No shadow absorber scattering correction to regenerator beam flux	0.0007	0.0002	0.1°	0.3°
Use the shadow absorber scattering correction determined for the $\pi^+\pi^-$ sample for all data sets	< 0.0001	< 0.0001	$< 0.1°$	$< 0.1°$
Ignore "sneakby" rate	0.0003	0.0002	0.5°	0.3°
Use the "sneakby" rate determined for the $\pi^+\pi^-$ set for all of the subsets	< 0.0001	< 0.0001	$< 0.1°$	$< 0.1°$

of the shape of the spectrum, a systematic uncertainty of 0.2° is assigned to the ϕ_{+-} and $\Delta\phi$ measurements.

10.6.2 Regenerator Beam Flux Corrections

The corrections to the regenerator beam flux — the average transmission, the shadow absorber corrections, and the correction for kaons ("sneakbys") which miss the regenerator — also introduce systematic uncertainties into the fits. Some of the studies involving variations to these corrections are also listed in Tables 27 and 28.

As we mentioned in the previous chapter, we have measured the average kaon transmission through the shadow absorber with a precision of 0.5% of itself. At this level, all of the

parameters we have measured are reasonably insensitive to changes in the absorption. In the two measurements where the charged and neutral modes are compared, that is, for $Re(\varepsilon'/\varepsilon)$ and $\Delta\phi$, the change in absorption tends to cancel between the regenerator beam samples of the two different modes. $Re(\varepsilon'/\varepsilon)$ is affected at the 0.1×10^{-5} level only, and the shift in $\Delta\phi$ is under 0.1°. The quantity most affected by this is the absolute phase ϕ_{+-}, which shifts by 0.3°. The measurements of Δm and τ_S receive contributions of $0.0004 \times 10^{10}\ \hbar s^{-1}$ and $0.0002 \times 10^{-10}\ s$, respectively, to the uncertainty in their measurements. These latter two uncertainties are completely correlated between the charged and neutral measurements, and will be added after the results from the two modes are combined.

For the remaining corrections, the most striking feature for $Re(\varepsilon'/\varepsilon)$ was the sensitivity of the result mainly to the *difference* between the charged and neutral corrections, but not to the overall shape. When the regenerator beam flux correction for either the absorber scattering correction or for kaons sneaking by the regenerator was removed, roughly 70% of the shift in $Re(\varepsilon'/\varepsilon)$ resulted from the fact that the change in the flux shape was different on average for the $\pi^+\pi^-$ mode and the $2\pi^0$ mode. In Figures 112 and 113, we can see that the difference in the correction for the various sets is small relative to the total correction, but it is that difference, not the total correction, to which the result is most sensitive. The fact that it is the difference to which $Re(\varepsilon'/\varepsilon)$ is most sensitive was reiterated when the correction determined for one data set is applied to all three data sets ($\pi^+\pi^-$, and $2\pi^0$ with and without the lead sheet). As we can see in Table 27, no matter which set we chose for the correction[6] the bias we observed in $Re(\varepsilon'/\varepsilon)$ was the same. The absolute level of the correction applied was different in the two different studies, but the change of the kaon flux in the $\pi^+\pi^-$ relative to that in the $2\pi^0$ set was the same.

The uncertainty in the absolute levels of the absorber scattering and the sneakby corrections were dominated by the uncertainties in the kaon-nucleon elastic cross sections. We have used the cross sections reported in [90], yielding an uncertainty in the scattering of 20%, depending mostly on how the values reported are in [90] interpreted.

The change in the correction from set to set, on the other hand, is dominated by the change in beam collimation from set to set. The beam collimation itself changed mostly

[6] In the table, the change for globally applying the $\pi^+\pi^-$ corrections and the $2\pi^0$ lead sheet corrections are listed.

because of the motion (sinking) of the target pile, which changed the position of the target relative to the collimator edges. These changes could be tracked quite well, but as a conservative estimate we have assigned the uncertainty on the corrections to be 50% of the difference between the most disparate pair of corrections. This corresponds to a contribution to the systematic uncertainty in $Re(\varepsilon'/\varepsilon)$ of 0.14×10^{-4} for the scattering correction and 0.23×10^{-4} for the sneakby correction. The remaining uncertainty from the absolute level of the corrections in negligible.

Because the scattering and sneakby corrections vary quite slowly across an individual 10 GeV/c momentum bin, they do not contribute significantly to the systematic uncertainty in the other measurements, as the studies listed in Table 28 indicate. If we make the most drastic change of completely ignoring the correction, some small biases in the results appear. Since we know the absolute level of the corrections to about 20% of themselves, however, the contribution to the systematic uncertainties of constrained fit measurements is negligible.

10.6.3 Analyticity Assumption

Moving away from the issues associated with the kaon flux, the final aspect of the fitting methodology which contributes to the systematic uncertainties is the use of the analyticity assumption to obtain the regeneration phase. If the regeneration amplitude deviated from a pure powerlaw behavior, then a bias in the phase extracted from the analyticity relationship could be introduced. Such a deviation would result from the rescattering of the kaon, where, for example, there is the additional Regge exchange of a Pomeron contributing to the kaon-nucleon scattering along with the ω or ρ exchange. The Pomeron affects the regeneration amplitude, contributing logarithmic terms that disrupt the pure powerlaw behavior. It is, however, essentially purely imaginary and does not affect the regeneration phase. Since there is no longer a pure powerlaw behavior, the use of analyticity to determine the regeneration phase from the "best fit" power could lead to a small bias in this phase. The size of the Pomeron contribution can be estimated from the magnitude of the rise in the total cross section [98] (Section 8.2.2), and we can limit the effect on the regeneration phase to $< 0.4°$ [31] in fits which use the full momentum range down to 20 GeV/c.

The deviation of the regeneration amplitude is expected to be a problem only at the lowest momenta, and in the fits presented here, only the fits using the charged data below 40 GeV/c are affected. In these fits, the accuracy of the measured powerlaw slope α corresponds to an uncertainty of 0.3° in the regeneration phase. Because of the analyticity constraint in the fits, the errors in the measured parameters already reflect this uncertainty. In addition to this, we include an additional uncertainty of 0.6° for nonpure powerlaw biases. This is commensurate with both the limit on the Pomeron contribution and with the observed fluctuations in the slope α when the fits are limited to momenta above 40 GeV/c. The contribution to the uncertainty on the charged τ_S fit is relatively small, only 0.0003×10^{-10} s. The Δm measurement is much more sensitive to the regeneration phase, however, and the uncertainty in the regeneration phase contributes a systematic uncertainty of 0.0019×10^{10} $\hbar s^{-1}$ to the Δm measurement.

The ϕ_{+-} measurement is completely correlated with the measured regeneration phase ϕ_ρ, since what we measure is the difference of phases $\phi_\rho - \phi_{+-}$ (see Equation 8.18). Hence, the ϕ_{+-} measurement has the full 0.6° uncertainty, which is the dominant systematic contribution in this measurement. Since we fit the $2\pi^0$ and $\pi^+\pi^-$ samples simultaneously to obtain $\Delta\phi$, the same regeneration phase is used to extract the charged and neutral phases. The regeneration phase thus cancels exactly and the uncertainty in that phase does not contribute to the uncertainty in $\Delta\phi$.

In the fit for $Re(\varepsilon'/\varepsilon)$ and the neutral mode fits for Δm and τ_S, the kaon momentum range was restricted to the range above 40 GeV/c in both the $\pi^+\pi^-$ and $2\pi^0$ modes. The deviation of the regeneration amplitude from a pure powerlaw behavior is expected to be much smaller. For the neutral Δm and τ_S measurements, the uncertainty in the regeneration phase due to the statistical uncertainty on α already corresponds to 0.7°. The correlation between the Δm and τ_S values extracted and the regeneration phase is implicit in the fits through the analyticity constraint, and the errors on these two quantities already reflect this uncertainty in the regeneration phase. The additional uncertainty from nonpure powerlaw behavior is negligible. The latter is also true in the $Re(\varepsilon'/\varepsilon)$ measurement, where both the $\pi^+\pi^-$ and $2\pi^0$ samples are restricted to the momentum range above 40 GeV/c.

10.6.4 Summary

The measurements we make are not greatly dependent on the shape of the kaon flux assumed in the vacuum and regenerator beams. For $Re(\varepsilon'/\varepsilon)$, the combination of errors due to absorption, scattering in the movable absorber, and sneakbys amounts to a total contribution to the systematic uncertainty of 0.30×10^{-4}. For the $\Delta\phi$ measurement there is an uncertainty of 0.2° from the momentum spectrum shape of the incident kaon beam, and to the ϕ_{+-} measurement there is an uncertainty of 0.4° from the incident spectrum and the average transmission level in the regenerator beam. The effects of the kaon flux shape on the Δm and τ_S measurements are negligible.

The uncertainty from the assumption of analyticity to obtain the regeneration phase contribute only to the fits which use the charged mode data below 40 GeV/c. The uncertainty on the regeneration phase in these fits results in the largest contribution to the systematic uncertainty on ϕ_{+-} of 0.5°. The charged Δm measurement is also fairly sensitive to this phase, and its systematic receives a contribution of $0.0019 \times 10^{10}\ \hbar s^{-1}$. The charged τ_S measurement is less sensitive, receiving only a 0.0003×10^{-10} s contribution to its systematic uncertainty.

10.7 Accidental Activity

The final contribution to the systematic uncertainty results from the uncertainty in the effect of accidental activity on the vacuum to regenerator beam ratios measured in the two decay modes. The corrections applied because of this activity have been mentioned before (Section 9.1.1), and here we will describe both the method used to obtain the corrections and the uncertainty on the corrections.

The most important studies of the accidental effects are for the highest intensity data samples in each of the two decay modes. For the $\pi^+\pi^-$ data, the relevant data set for this study is the NC subset used to obtain our initial result on 20% of the data [50]. The study of the accidental effects in this data set has already been detailed in [50] and I will not repeat this discussion. That study found that for an average proton intensity of 0.8×10^{12}, the

vacuum to regenerator beam ratio changes by $-0.04\% \pm 0.07\%$. Since the change in the ratio is consistent with the statistical precision of that study, we have made no correction to the vacuum to regenerator beam ratio in the $\pi^+\pi^-$ sample. For the NC subset, we include the full statistical error of 0.07% on the single ratio. For the remainder of the data, however, the intensity was a factor of 2.7 lower, and the uncertainty on the change in the single ratio can be scaled accordingly. The combination yields a total uncertainty on $Re(\varepsilon'/\varepsilon)$ of 0.67×10^{-4}.

Since the $2\pi^0$ NC subset was the lowest intensity subset in the Monte Carlo, we cannot extrapolate the result ($-0.04\% \pm 0.07\%$ for this mode as well) of this study into the higher intensity region without a large sacrifice to the systematic uncertainty. We have instead repeated the study for the high intensity $2\pi^0$ data subsets.

All of the accidental studies used a set of random triggers that were collected simultaneously with the $\pi\pi$ triggers. The triggers were provided by a pair of scintillator counters which formed a telescope that pointed at the beam dump and target. A trigger was formed when a charged particle produced in the interaction of the proton beam with the target or dump passed through the telescope. The timing for the pair of scintillator signals was provided by the Fermilab RF signal, just as for the $\pi\pi$ triggers. The telescope was located about 50 m upstream of the regenerator, which meant that a particle which passed through the telescope could not also pass through the detector. Hence the activity seen in the detector is not correlated with the particle triggering the readout. Since these triggers were collected simultaneously with the $\pi\pi$ data, they sampled exactly the same ambient environment in which the kaon decays were detected, and, in particular, had exactly the same intensity distribution.

To examine the effect of the ambient activity on the accepted event samples, the detector activity in the accidental events was overlaid on coherent $\pi\pi$ events generated with the Monte Carlo simulation. The regenerator position in each Monte Carlo event was determined by the regenerator position in the accidental trigger that was to be overlaid. All of the detector activity in the accidental trigger was then added to the Monte Carlo event as it was generated. Dead time effects in such devices as the drift chamber TDCs were fully

simulated. Each Monte Carlo event was fully analyzed both with and without the overlaid accidental trigger to measure changes in the accepted event samples.

The analysis of the Monte Carlo sample with the overlays completely paralleled that of the data. For example, in the $2\pi^0$ data, energy scale corrections based on the position of the regenerator edge in the overlaid Monte Carlo sample were applied in the final analysis of the overlaid events.

Of course, what is most important is the change in the vacuum to regenerator beam ratio brought about by the accidental activity in the detector. The change in this ratio after each $2\pi^0$ analysis cut which resulted in any event loss (after the accidental is overlaid) are listed in Table 29. The changes in the table are sequential, that is, the change in the single ratio after a given cut is applied is relative to the single ratio after the previous cut. A positive change in the table implies a smaller fraction of events are lost in the vacuum beam than in the regenerator beam.

As we had expected, there was a small tendency for clusters to hide more easily in $2\pi^0$ decays from the vacuum beam than in the regenerator beam. The accidental activity in the calorimeter tends to center around the more intense vacuum beam, resulting in a small asymmetry between the decays from the vacuum and regenerator beams in the probability for an extra cluster to hide in an event by merging with a photon cluster from the $2\pi^0$ decay. The asymmetry is apparent in the vacuum to regenerator beam changes in Table 29. For cuts that eliminate events where extra photons are apparent — the 4 cluster and cluster fusion cuts — there is a greater loss of regenerator beam events. For cuts that rid events where a hidden extra cluster has caused misreconstruction — χ^2, mass, etc. — there is a greater loss of vacuum beam events. The losses from these two classes of events, however, almost compensate each other, and the total induced asymmetry is quite small.

The losses, however, are not the total story. To estimate the total bias due to accidental activity, we cannot start from events which have passed all of the analysis cuts because the accidental activity will cause some events which were just outside of the analysis cuts to satisfy those cuts after the overlay. The most important effect is the z shift introduced by the accidental overlays. The distribution of difference in the measured z position before and after the event overlay is presented in Figure 139. While the shift is strongly peaked at

Table 29. Sequential change in observed $2\pi^0$ vacuum beam to regenerator beam ratio due to accidental event loss as each analysis cut is applied. Events which would not have passed cuts except for the presence of the accidental activity are *not* included in these numbers.

Analysis Cut	Change in Ratio (percent)
4 clusters	$+0.065\pm0.021$
Best pairing $\chi^2 < 4$	-0.137 ± 0.013
Cluster fusion	$+0.234\pm0.048$
2nd best χ^2 cuts	-0.017 ± 0.005
Chamber, BC hodoscope hits	$+0.099\pm0.028$
Collar Anti	-0.055 ± 0.012
Cluster energy cuts	-0.002 ± 0.001
Ring number	-0.001 ± 0.003
$2\pi^0$ mass	-0.032 ± 0.004
Total energy	-0.018 ± 0.002
z fiducial cut	-0.051 ± 0.002
Total	$+0.085\pm0.062$

zero, there is an asymmetry in the tails between the upstream shifts (negative side) and the downstream shifts. This is expected because extra energy tends to push the reconstructed z away from the calorimeter. Since the fraction of decays near the downstream fiducial z cut is larger in the vacuum beam than in the regenerator beam, the bias in the z shift can change the observed vacuum beam to regenerator beam ratio. When both event gains and losses were considered, the total change we found in the vacuum beam to regenerator beam ratio was $0.169\% \pm 0.060\%$.

This particular study had the lead sheet installed. The results without the lead sheet were similar, though the difference between the change in the vacuum and regenerator beam sample sizes was marginally smaller.

The absolute fraction of $2\pi^0$ events lost in each of the vacuum and regenerator beam samples because of accidental activity depended on the exact value of the cuts used in the

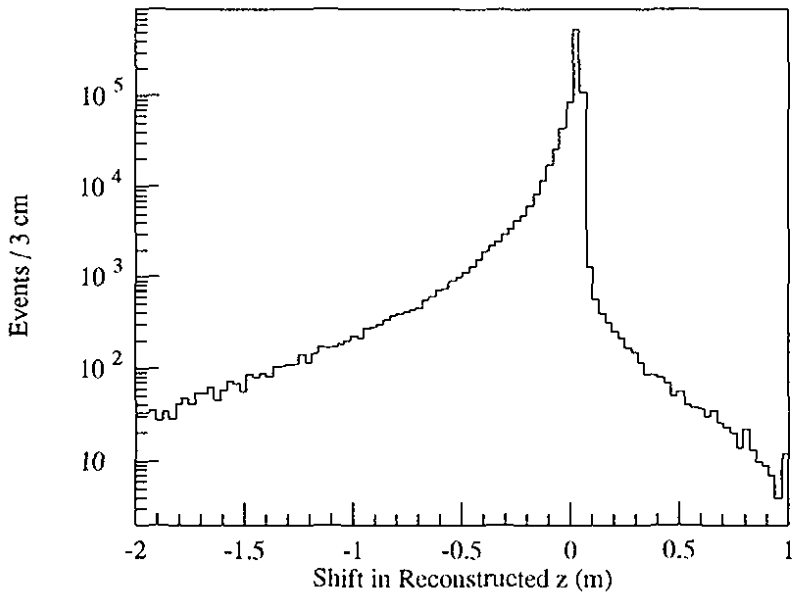

Figure 139. Shift in the reconstructed z position in $2\pi^0$ decays as a result of accidental activity in the detector. A negative shift corresponds to an upstream shift.

analysis. For example, the event selection criteria used in our $2\pi^0$ analysis which were designed to minimize the $3\pi^0$ background also tended to remove events in which accidental activity in the lead glass was nearby (or on) a photon cluster from a $2\pi^0$ decay. However, since we collected the vacuum and regenerator beam $2\pi^0$ samples simultaneously, the $2\pi^0$ single ratio remained almost unchanged by the loss due to accidental activity, as we have seen above. Systematically, it was worthwhile to tighten the cuts to reduce the $3\pi^0$ background, which was much larger in the vacuum beam than in the regenerator beam, and live with the increased loss of events from the accidental activity, which was almost identical in the two beams. It was also simpler to determine the change in the single ratio due to accidental activity than to simulate the $3\pi^0$ background. With our final set of cuts, the absolute change in the event sample size due to accidental activity in the detector was about 17% in this high intensity study. The dominant loss came from the combination of the 4 cluster requirement, the fused cluster removal, and the pairing χ^2 requirement, ie., from accidental activity in the lead glass which "mimicked" the presence of a $3\pi^0$ background event.

The total change in the observed vacuum to regenerator beam ratio found in this study is $0.169\% \pm 0.060\%$ for the high intensity data with the lead sheet present[7]. Without the

[7]This means the required *correction* is -0.169%.

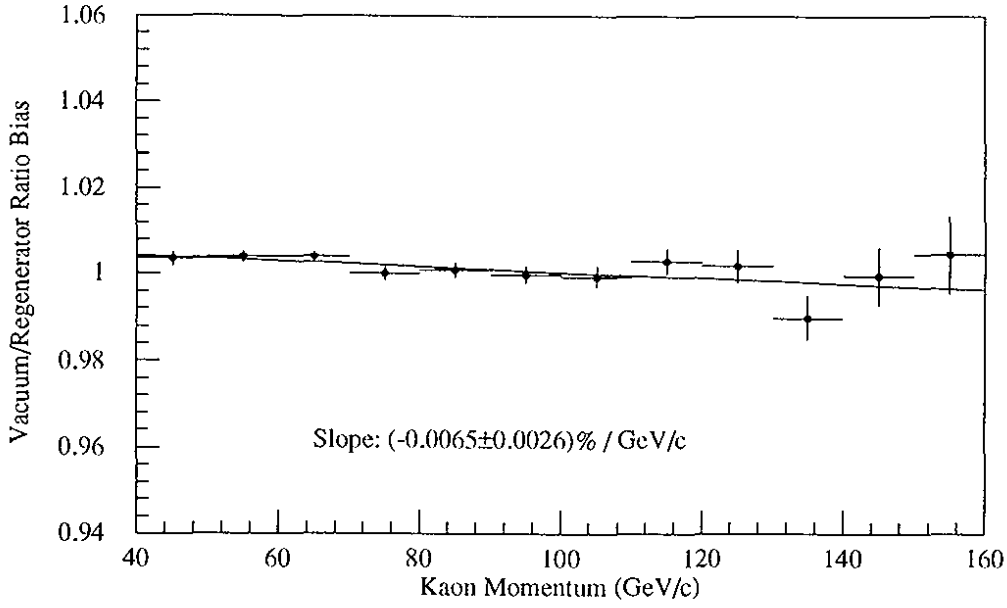

Figure 140. Bias as a function of energy of the observed vacuum to regenerator beam ratio in the high intensity $2\pi^0$ data due to accidental activity. The line drawn is the best linear fit, which has the listed slope.

step in the z distribution induced by the lead sheet, the correction is slightly smaller at 0.154%. Scaling the latter value down to the intensity of the NC set (a factor of 2.7 lower) yields a low-intensity correction factor consistent with the previous study. After weighting the accidental uncertainty according to the fractions of data at high intensity (about 80%) and low intensity, the total correction to $Re(\varepsilon'/\varepsilon)$ was $+2.51 \times 10^{-4}$, while the contribution to the uncertainty in $Re(\varepsilon'/\varepsilon)$ was 0.84×10^{-4}.

The measurements obtained using the constrained fits are not particularly sensitive to the absolute level of the accidental correction. The uncertainty in the vacuum to regenerator beam ratio is almost an order of magnitude lower than the uncertainty in the kaon absorption in the regenerator beam, and hence is negligible. Of more importance are the biases in the vacuum to regenerator beam ratio as a function of energy (since this can bias the observed powerlaw) and in the regenerator beam z distribution. The former is plotted in Figure 140 and the latter in Figure 141.

There is a small bias as a function of energy visible in the accidental loss. If we introduce such a bias into the acceptance for the high intensity data, the observed powerlaw shifts slightly. This results in a small bias in $\Delta\phi$ of size 0.1° and in a bias of the neutral Δm

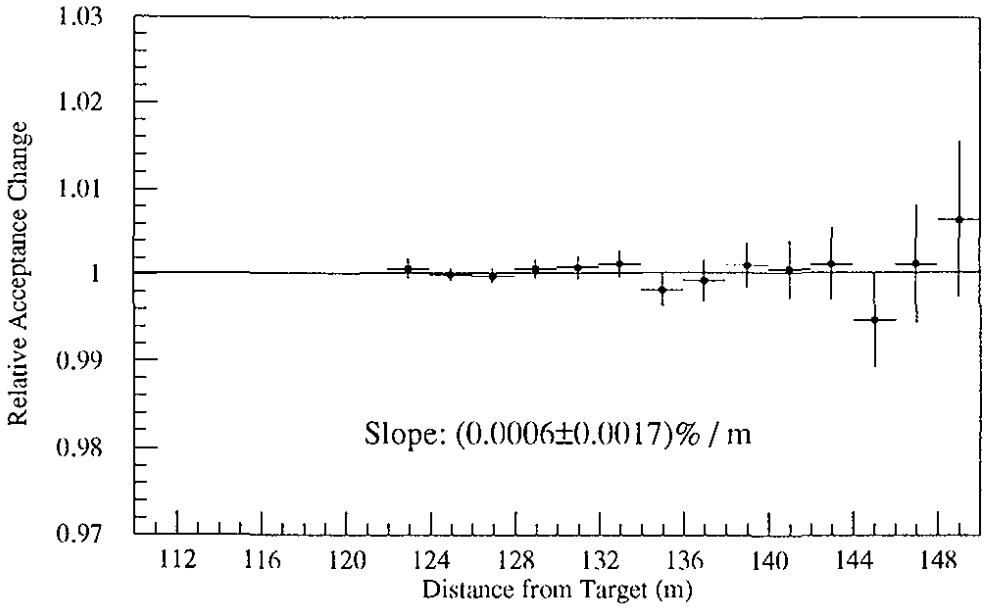

Figure 141. Bias as a function of z of the regenerator beam acceptance in the high intensity $2\pi^0$ data due to accidental activity. The line drawn is the best linear fit, which has the listed slope.

measurement of size $0.0004 \times 10^{10}\ \hbar s^{-1}$. The other measurements, including $Re(\varepsilon'/\varepsilon)$, are affected only negligibly.

The observed bias in the regenerator z acceptance is consistent with zero. The uncertainty in the bias is very small, and has little affect on the systematic uncertainty of the results. The uncertainty is included in the acceptance uncertainties given previously.

10.8 Conclusion

In general, the measurement of the $Re(\varepsilon'/\varepsilon)$ with the double beam technique is very robust. The combination of two possible cancellations — between the vacuum beam and regenerator beam within a decay mode for some effects, and between the regenerator beam samples of the two modes for others — tends to prevent various effects, such as the beam absorption, accidental activity, possible aperture measurements, etc., from introducing serious biases into the measurement. The contributions to the systematic uncertainty on $Re(\varepsilon'/\varepsilon)$ are summarized in Table 30, and the total systematic uncertainty is 2.87×10^{-4}.

The systematic uncertainties in the measurements of Δm and τ_S in both the charged

Table 30. Summary of systematic uncertainties on $Re(\varepsilon'/\varepsilon)$, Δm and τ_S measured in the $\pi^+\pi^-$ and $2\pi^0$ decay modes, $\Delta\phi$, and ϕ_{+-}.

Systematic	$Re(\varepsilon'/\varepsilon)$	τ_S $(10^{-10}\ s)$		Δm $(10^{10}\ \hbar s^{-1})$		$\Delta\phi$	ϕ_{+-}
Source	(10^{-4})	$2\pi^0$	$\pi^+\pi^-$	$2\pi^0$	$\pi^+\pi^-$		
γ energy	1.61	0.0012	—	0.0014	—	0.5°	—
$\pi^+\pi^-$ acceptance	0.65	—	0.0020	—	0.0009	0.4°	0.35°
$2\pi^0$ acceptance	1.00	0.0002	—	0.0001	—	—	—
RA4 position	0.59	—	—	—	—	—	—
HDRA material	1.22	0.0001	—	0.0008	—	0.2°	—
$2\pi^0$ backgrounds	1.03	—	—	—	—	—	—
$\pi^+\pi^-$ backgrounds	0.29	—	—	—	—	—	—
Kaon flux	0.30	0.0002[a]	0.0002[a]	0.0004[a]	0.0004[a]	0.2°	0.4°
Analyticity	—	—	0.0003	—	0.0019	—	0.5°
Accidentals	1.07	—	—	0.0004	—	0.1°	—
Totals	2.87	0.0012	0.0020	0.0017	0.0021	0.7°	0.7°

[a]This error is completely correlated between the $\pi^+\pi^-$ and $2\pi^0$ samples, and is not included in the total error listed here.

and neutral modes, and in the measurements of $\Delta\phi$ and ϕ_{+-} have also been summarized in Table 30. For the Δm and τ_S measurements, the error from the total kaon absorption in the regenerator beam (under kaon flux in Table 30) has not been included in the total errors listed. This error is completely correlated between the charged and neutral modes, and will be added after the results are averaged in the next chapter.

Congratulations! With the systematic uncertainties in hand, we have ended our journey through this complex of detailed measurements. To end, we will now examine some of the ramifications of these measurements.

CHAPTER 11

CONCLUSION

With the systematic errors now in hand, we can now make final comparisons of our results to previous measurements, and to current predictions. We will first examine our final result for $Re(\varepsilon'/\varepsilon)$ and the conclusions we can draw about direct CP violation based on this result, and then discuss the remaining results, largely in the context of their bearing on tests of CPT invariance.

11.1 $Re(\varepsilon'/\varepsilon)$

Combining the results of our fits for $Re(\varepsilon'/\varepsilon)$ from Section 9.1 with the systematic estimate from the previous chapter, we have

$$Re(\varepsilon'/\varepsilon) = (7.4 \pm 5.2 \pm 2.9) \times 10^{-4}, \tag{11.1}$$

where the first error is the statistical uncertainty and the second error is the systematic uncertainty. Comparing this result to our previous publication [50], this is an improvement in the statistical precision by a factor of 2.7, and in the systematic uncertainty by a factor of 2.1. While the earlier analysis was based on approximately 20% of the accumulated data, we have improved our statistical uncertainty beyond the expected factor of $\sqrt{5}$ by extending the fiducial z regions of both modes[1]. The statistically limiting decay mode in this analysis was the $K_L \to \pi^+\pi^-$ decay, where we had a total of 328980 decays after

[1] Though the largest gain came from extending the $2\pi^0$ z region 15 m downstream, which was not possible in the $\pi^+\pi^-$ mode.

background subtraction. The dominant systematic contribution came from the uncertainty in the energy scale of the lead glass calorimeter. This is the most precise determination of $Re(\varepsilon'/\varepsilon)$ to date, and the measurement with our technique is currently statistically limited.

Combining the statistical and systematic uncertainties in quadrature, we have

$$Re(\varepsilon'/\varepsilon) = (7.4 \pm 5.9) \times 10^{-4}, \tag{11.2}$$

which is not significantly different from zero. Our result is consistent with no direct CP violation in $K_L \to \pi\pi$ decays, and the superweak hypothesis can not yet be excluded based on this measurement. At the 95% confidence level, we can place an upper limit on the value of $Re(\varepsilon'/\varepsilon)$ of

$$Re(\varepsilon'/\varepsilon) < 17 \times 10^{-4}, \tag{11.3}$$

which does not support the evidence for the large level of CP violation reported [49] by the NA31 collaboration. Our new result is compared to previously published measurements of $Re(\varepsilon'/\varepsilon)$ in Figure 142. NA31 has presented several preliminary results based on new data sets they obtained in 1988 and 1989. Their most recent recent announcement, where their previous result has been combined with the two more recent measurements, was [101] $Re(\varepsilon'/\varepsilon) = (23 \pm 3.4 \pm 6.5) \times 10^{-4}$, where again the first error is the statistical uncertainty and the second error is the systematic uncertainty. This preliminary result is still a 3 standard deviation effect. Though the central value of the NA31 result has decreased, there is still a discrepancy at the 1.7 standard deviation level between their preliminary result and our new result.

The great experimental effort on both sides of the Atlantic to improve the precision in the measurement of $Re(\varepsilon'/\varepsilon)$ has not been unmatched by attempts to improve the precision in the calculation of $Re(\varepsilon'/\varepsilon)$. The calculation of $Re(\varepsilon'/\varepsilon)$ is quite difficult, particularly since the matrix elements $\langle(\pi\pi)_I|\, Q_i(\mu)\,|K\rangle$ for the decay of the neutral kaon into the $I = 0, 2$ $\pi\pi$ final states receive contributions from long-distance effects in QCD where perturbative approaches are not applicable. The calculation uncertainties are exacerbated by uncertainties in many of the physical parameters needed for the final evaluation of the calculations, such as the top quark and strange quark masses m_t and m_s, the size of CKM matrix elements $|V_{cb}|$ and $|V_{ub}|$, and the QCD scale $\Lambda_{\overline{MS}}$. While the strong penguin digram

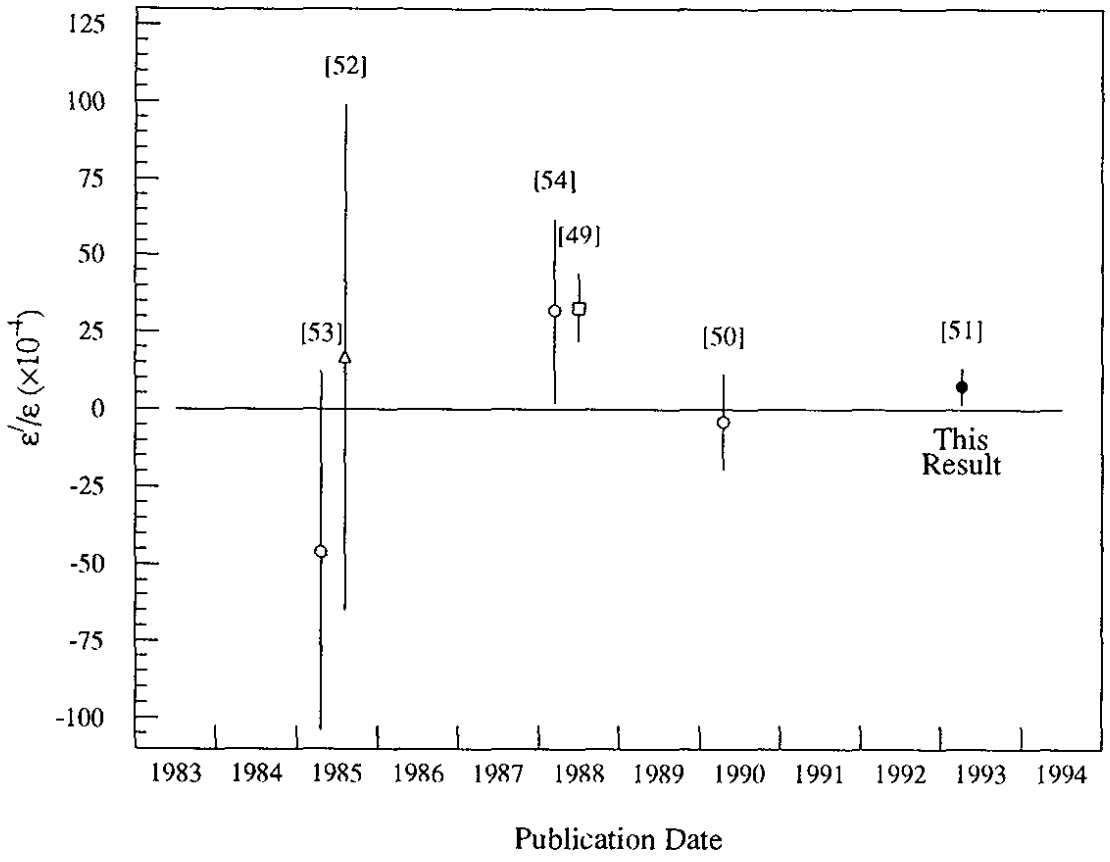

Figure 142. The publication history of $Re(\varepsilon'/\varepsilon)$.

(see Figure 5) dominates the contribution to CP violation for low top mass, Flynn and Randall [73] noticed that for higher top quark masses, the electromagnetic penguin diagram could contribute to a significant cancellation of the effect of the strong penguin. Since a new limit on the top quark mass of $m_t > 118$ GeV/c^2 is expected soon from CDF [102], this cancellation could be quite significant. For top masses above 200 GeV/c^2, the cancellation could be nearly complete, which would render $Re(\varepsilon'/\varepsilon)$ very difficult to experimentally distinguish between CP violation arising from the Standard Model and from superweak models.

In spite of these difficulties, two different groups have recently finished calculations at the next–to–leading order in QCD; a Rome group which has used lattice methods [103], and a Munich group using renormalization techniques [104]. It is very heartening that the two groups obtain fairly compatible results using the different techniques. A recent

summary of both of these new calculations was recently presented by Peccei [66], who makes a "representative prediction" of

$$\frac{\varepsilon'}{\varepsilon} = \begin{cases} (11\pm4)\times 10^{-4}A^2\eta & (m_t = 140\ \mathrm{GeV}/c^2), \\ (3\pm4)\times 10^{-4}A^2\eta & (m_t = 200\ \mathrm{GeV}/c^2), \end{cases} \tag{11.4}$$

where A and η are parameters of the CKM matrix introduced in Chapter 1. From the information on η and A which we have from $|\varepsilon|$, $B^0 - \bar{B}^0$ mixing, and recent $|V_{ub}|/|V_{cb}|$ measurements, it would appear that these calculations favor values for $Re(\varepsilon'/\varepsilon)$ of order several 10^{-4}.

The Rome group has calculated the allowed range of $Re(\varepsilon'/\varepsilon)$ versus $\cos\delta$, where δ is the CP violating phase in the CKM matrix (see Section 1.3.2). The striped regions shown in Figure 143 result when all parameters are allowed to vary within their experimental or estimated uncertainties. The Rome figure was generated with an older, larger value experimental value for $|V_{ub}|$, though a reevaluation of $Re(\varepsilon'/\varepsilon)$ using updated parameters is under way. The central values and range for $Re(\varepsilon'/\varepsilon)$ do not change greatly as $|V_{ub}|$ decreases, but the allowed regions in $\cos\delta$ (or ρ) tend to coalesce and favor the first quadrant. The top quark mass assumed in this particular calculation was 140 GeV/c^2. The Munich results showing the variation with $Re(\varepsilon'/\varepsilon)$ on $\Lambda_{\overline{MS}}$ are plotted in Figure 144 for a top mass of $m_t = 130$ GeV/c^2. These results are very compatible with our new measurement, and somewhat lower than might be expected from the NA31 results. As the top quark mass varies in either direction, both predictions are consistent with our result. The NA31 result, on the other hand, prefers a lower value for m_t. Unfortunately, it is clear from the figures our current measurement does not have the sensitivity needed to limit the range of values allowed for parameters like $\Lambda_{\overline{MS}}$ and m_t. If the theoretical uncertainty continues to diminish, the next experimental efforts may well be able to provide a test of the CKM paradigm[2].

[2]The importance of *establishing* an unambiguous signal for direct CP violation should not be diminished even if the theoretical uncertainties remain at their current level.

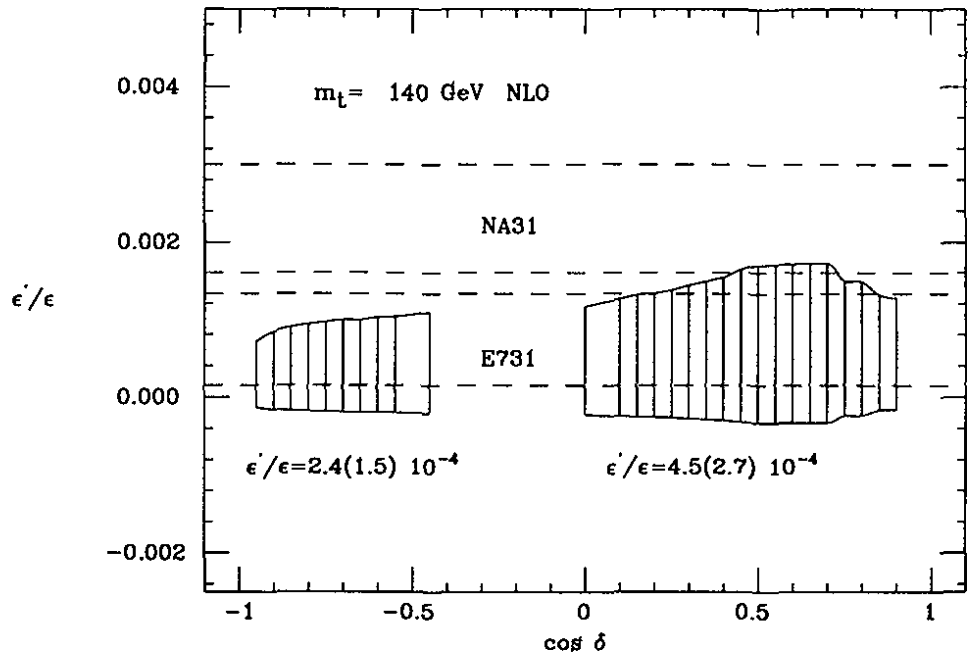

Figure 143. Variation of $Re(\varepsilon'/\varepsilon)$ vs $\cos\delta$ in the calculation of the Rome group [103]. The experimental 1 standard deviation bands for this result and the preliminary NA31 result indicated by the dashed lines. The top mass used in the calculation was 140 GeV/c^2. *Plot courtesy L. Reina.*

11.1.1 The Future for $Re(\varepsilon'/\varepsilon)$

The technique we have employed to measure $Re(\varepsilon'/\varepsilon)$ still holds much promise for future refinements in precision. Our current result is statistically limited, and many of the dominant contributions to the systematic uncertainty are addressable in the design of a new detector in straightforward fashion. Our group has recently been approved to run a new experiment (FNAL E832) at Fermilab which will also uses the double beam technique. The heart of the new detector will be a new Cesium Iodide (CsI) electromagnetic calorimeter that will replace the current lead glass calorimeter. Compared to our current lead glass calorimeter, the new calorimeter is expected to have much better electron and photon resolutions (of order 1%), much smaller nonlinearities, better light yields, faster timing, and (since the crystals are 9 radiation lengths longer) have little difference in response to electrons and photons. With this new calorimeter, it should be straightforward to dramatically

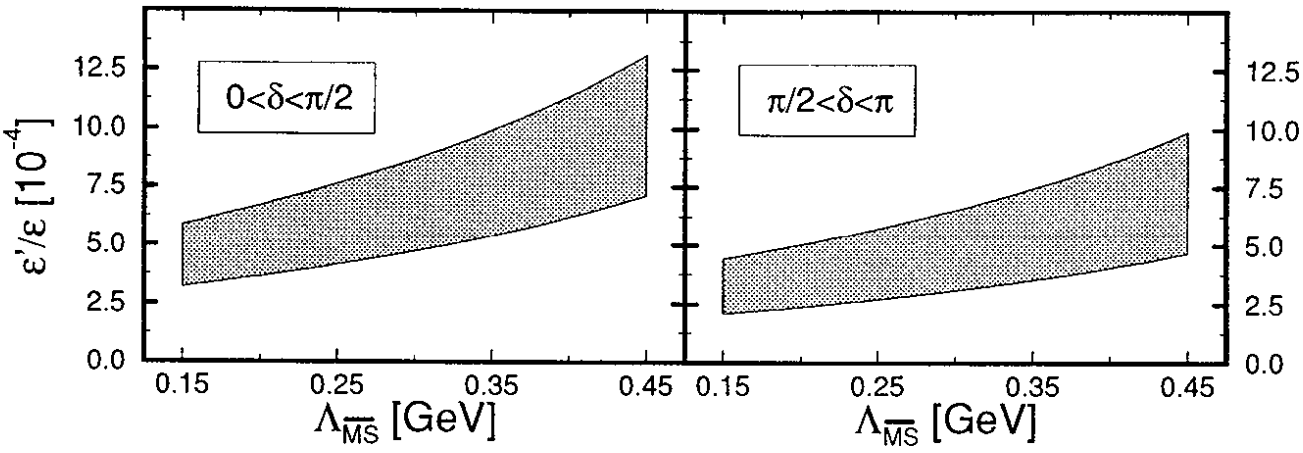

Figure 144. Variation of $Re(\varepsilon'/\varepsilon)$ as a function of $\Lambda_{\overline{MS}}$ in the calculation of the Munich group [104]. The bands are shown for the allowed region in the first and second quadrants of the $\rho - \eta$ plane. *Plot courtesy M. Jamin.*

reduce contribution to the systematic uncertainty on $Re(\varepsilon'/\varepsilon)$ from the $2\pi^0$ energy scale, which is the largest systematic contribution in our current measurement.

Many other areas of the experiment are also being improved. The regenerator will be fully active and hence will be able to suppress the inelastic (and possibly even the diffractive) backgrounds further than this experiment. Such a regenerator has already been used very successfully by this group in an experiment (FNAL E773) dedicated to measuring $\Delta\phi$. In addition, the $3\pi^0$ background will be highly suppressed by an improved photon veto system and the finer granularity of the CsI calorimeter. All four $\pi\pi$ decay modes will be detected simultaneously in this experiment, as they were in the 20% subsample used for our first result [50]. While collecting all four modes simultaneously allows some convenient cross checks, it is not crucial for the success of the double beam technique.

The new experiment, slated to run in 1995, hopes to collect a staggering 10×10^6 $K_L \to \pi^0\pi^0$ decays and 20×10^6 $K_L \to \pi^+\pi^-$ decays, and reach an ultimate precision of order 10^{-4} on $Re(\varepsilon'/\varepsilon)$.

The CERN NA31 experiment also has a new proposal (CERN NA48), though they are abandoning their current technique[3] in favor of a double beam method. Rather than use a regenerator to produce the K_S decays, however, the CERN group will be employing two

[3]For a description of the NA31 experiment, see reference [105].

separate targets. They are also switching from a calorimetry-based charged mode detection system to a magnetic spectrometer. They also hope to achieve a sensitivity approaching 10^{-4} on $Re(\varepsilon'/\varepsilon)$.

11.2 Other Kaon Parameters

11.2.1 Δm, τ_S, and the Superweak Phase

With the systematic contributions to the Δm and τ_S now estimated, we can begin comparing the results from the $\pi^+\pi^-$ and $2\pi^0$ modes, and to combine the results from the two modes to compare to the current world averages. The results for τ_S are

$$\tau_S = \begin{cases} (0.8952 \pm 0.0015 \pm 0.0020) \times 10^{-10}\ s & (\pi^+\pi^-) \\ (0.8912 \pm 0.0017 \pm 0.0012) \times 10^{-10}\ s & (\pi^0\pi^0) \end{cases} \tag{11.5}$$

Combining the systematic and statistical errors in quadrature gives

$$\tau_S = \begin{cases} (0.8952 \pm 0.0025) \times 10^{-10}\ s & (\pi^+\pi^-) \\ (0.8912 \pm 0.0021) \times 10^{-10}\ s & (\pi^0\pi^0) \end{cases} \tag{11.6}$$

These numbers are in quite good agreement, with the difference at the level of 1.2 standard deviations. It is therefore fine to combine these two results, and our new measurement of τ_S becomes [37]

$$\tau_S = (0.8929 \pm 0.0016) \times 10^{-10}\ s, \tag{11.7}$$

which is in good agreement with previous measurements of τ_S and the world current world average value of $(0.8922 \pm 0.0020) \times 10^{10}\ \hbar s^{-1}$ [32]. This is a 25% improvement in precision over the current world average. Our result is compared with previous measurements in Figure 145.

For Δm, the results from the two modes are

$$\Delta m = \begin{cases} (0.5311 \pm 0.0044 \pm 0.0020) \times 10^{10}\ \hbar s^{-1} & (\pi^+\pi^-) \\ (0.5274 \pm 0.0030 \pm 0.0017) \times 10^{10}\ \hbar s^{-1} & (\pi^0\pi^0) \end{cases}, \tag{11.8}$$

and combining the errors in quadrature gives

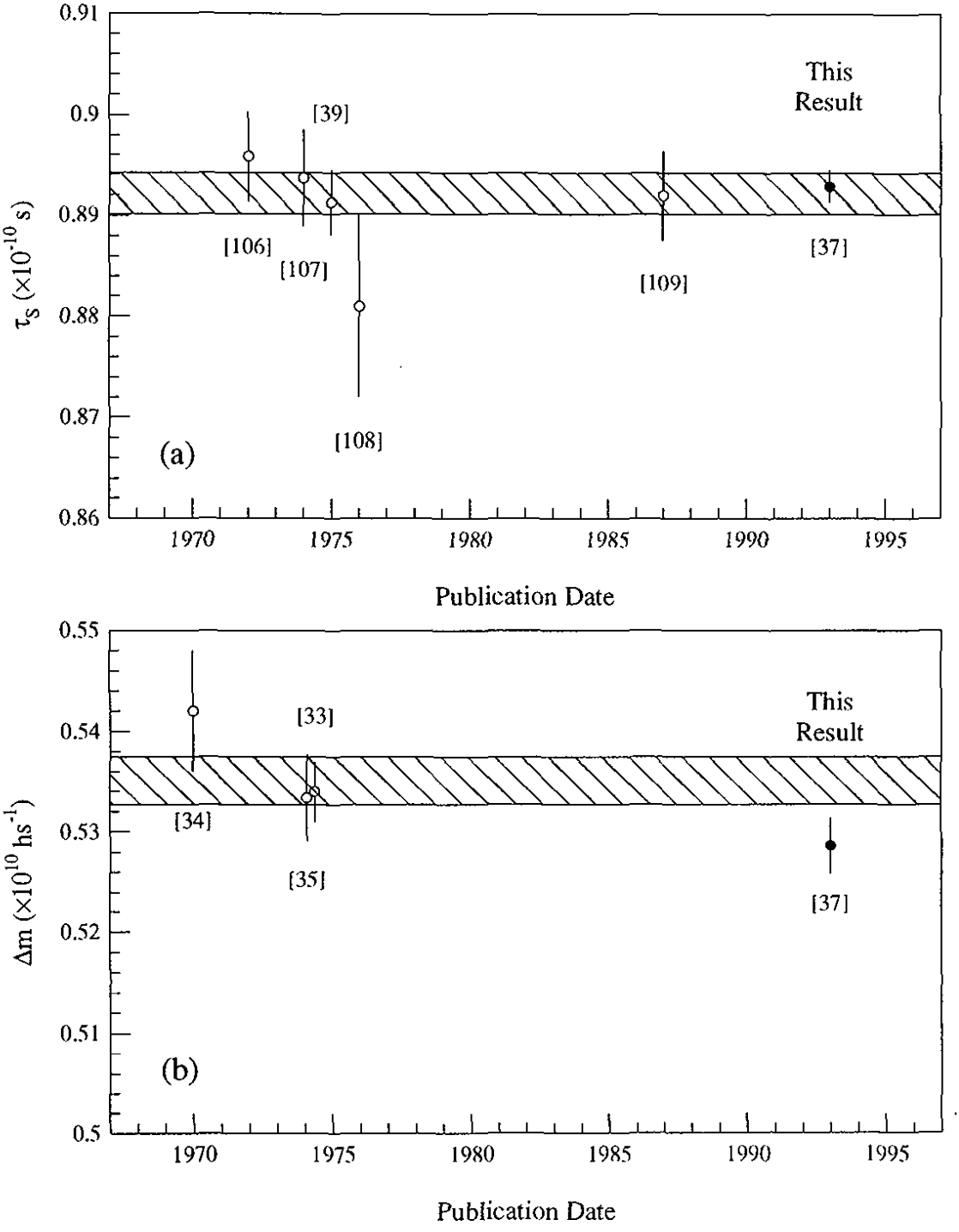

Figure 145. The publication history of τ_S and Δm. (a) τ_S, (b) Δm. The band drawn in each plot is the one standard deviation range of the world average before our measurement.

$$\Delta m = \begin{cases} (0.5311 \pm 0.0048) \times 10^{10}\ \hbar s^{-1} & (\pi^+\pi^-) \\ (0.5274 \pm 0.0034) \times 10^{10}\ \hbar s^{-1} & (\pi^0\pi^0) \end{cases} . \tag{11.9}$$

These two results are also in excellent agreement. The consistency both of the Δm and of the τ_S measurements, which depend on the shape of the decay distributions and hence are sensitive to biases in the acceptance, in the two different decay modes makes a powerful crosscheck for our $Re(\varepsilon'/\varepsilon)$ measurement. When we combine the Δm results from the two decay modes, our final result for Δm is

$$\Delta m = (0.5286 \pm 0.0028) \times 10^{10}\ \hbar s^{-1}. \tag{11.10}$$

This new value of Δm is also compared with previous measurements in Figure 145. Note that ours is the first new measure of this quantity in almost 20 years. While our result is in reasonable agreement with the previous two measurements, it is inconsistent with earliest measurement used in calculating the world average. As a result, our new result is two standard deviations lower than the current world average of $(0.5351 \pm 0.0024) \times 10^{10}\ \hbar s^{-1}$. Our precision is comparable to that of the current world average.

The systematic errors common to both the charged and the neutral mode (Section 10.8) have been included in the total errors for both Δm and τ_S.

Even though our Δm result is shifted lower than the world average, the value for the superweak phase we obtain using our new Δm and τ_S results does not change significantly. We find $\tan^{-1}(2\Delta m/[\Gamma_S - \Gamma_L]) = 43.4^\circ \pm 0.1^\circ$.

11.3 The $\Delta\phi$ and ϕ_{+-} Measurements

11.3.1 Testing CPT Symmetry

The first test of CPT symmetry rests on the direct comparison of the phases ϕ_{+-} and ϕ_{00} of the CP violating parameters η_{+-} and η_{00}. We have found

$$\Delta\phi = -1.6^\circ \pm 1.0^\circ \pm 0.7^\circ, \tag{11.11}$$

and when the statistical and systematic errors are combined in quadrature the result becomes

$$\Delta\phi = -1.6^\circ \pm 1.2^\circ. \tag{11.12}$$

The accuracy of our final result is a substantial improvement over that of the current world average[4]. The 95% confidence level limit obtained from our result is $|\Delta\phi| < 3.7^\circ$.

To get more intuition about the how this phase difference relates to CPT, let us first consider the case where we have CPT violation directly in $K \to \pi\pi$ decays. Following Barmin *et al.* [19], this can be accomplished by explicitly incorporating manifestly CPT–violating terms B_I into the $I = 0$ and $I = 2$ decay amplitudes,

$$\langle I|\,\mathbf{H}_{eff}\left|K^0\right\rangle = (A_I + B_I)e^{i\delta_I}, \tag{11.13}$$

$$\langle I|\,\mathbf{H}_{eff}\left|\bar{K}^0\right\rangle = (A_I^* - B_I^*)e^{i\delta_I}. \tag{11.14}$$

After making the same isospin decomposition as in Chapter 1, the definition of ε' in Equation 1.43 is slightly modified,

$$\varepsilon' \to \frac{i}{\sqrt{2}}e^{i(\delta_2-\delta_0)}\frac{ImA_2 - iReB_2}{A_0}. \tag{11.15}$$

In this expression, we have assumed that $|ImB_0| \ll A_0$, since A_0 determines the rate for the dominant $K_S \to \pi\pi$ $(I = 0)$ decay rate, and it is very unlikely that a CPT–violating rate is this large. The CPT violating component adds a term that is 90° degrees out of phase with our previous CP–violating but CPT–conserving definition. Since the final state $\pi\pi$ phase shifts place ε' so close to parallel with ε and since $\Delta\phi$ is so small, we can use the above expression in conjunction with the Equations 1.46 and 1.48 to give

$$\frac{ReB_2}{ReA_2} = \frac{1}{|\omega|}\frac{ReB_2}{A_0} \approx \frac{1}{3}\frac{|\varepsilon|}{|\omega|}(\phi_{+-} - \phi_{00}), \tag{11.16}$$

where $\omega = 1/22$ is, as before, the measured violation of the $\Delta I = 1/2$ rule. Using the PDG value for $|\eta_{+-}|$ as the value of $|\varepsilon|$ and our new result for $\Delta\phi$ we get

$$\frac{ReB_2}{ReA_2} = (4.6 \pm 3.5) \times 10^{-4}. \tag{11.17}$$

According to Barmin *et al.* [19], with some reasonable assumptions about isospin, one can relate the K^+ and K^- lifetime difference to the above ratio,

[4]The current world average for $\Delta\phi$ includes our previous result based on 20% of the data sample included in this analysis.

$$\frac{\tau^+ - \tau^-}{\tau^+} \approx -0.84 \frac{ReB_2}{ReA_2}. \tag{11.18}$$

This allows us to compare the strength of the CPT test based on this result relative to the direct comparison of the lifetimes, and perhaps place the $\Delta\phi$ CPT test in a more intuitive framework:

$$\frac{\tau^+ - \tau^-}{\tau^+} = \begin{cases} (-4 \pm 3) \times 10^{-4} & (\Delta\phi) \\ (11 \pm 9) \times 10^{-4} & ([32]) \end{cases}$$

The first result was obtained from our $\Delta\phi$ measurement, and the second from the experimental measurements of the charged kaon lifetimes. In this framework, we can see that the current $\Delta\phi$ measurement is beginning to place stronger bounds on possible CPT violation than is placed by the direct lifetime measurements.

11.3.2 The ϕ_{+-} Measurement

The final measurement we have made is the measurement of ϕ_{+-} itself, and we have found

$$\phi_{+-} = 42.2^\circ \pm 1.3^\circ \pm 0.7^\circ, \tag{11.19}$$

where, as usual, the first error is statistical and the second error is systematic. Combining the errors in quadrature, we have

$$\phi_{+-} = 42.2^\circ \pm 1.5^\circ. \tag{11.20}$$

This is in excellent agreement with the superweak phase $\phi_\epsilon = 43.4^\circ$ (43.7°) found using our (PDG) values for Δm and τ_S. On the other hand, this result seems at first glance to disagree with the current world average for ϕ_{+-} of $46.5^\circ \pm 1.2^\circ$ at slightly over the 2 standard deviation level. The value for ϕ_{+-} extracted from each of the previous experiments, however, depends on the value of Δm assumed. The world average value of Δm has been assumed when calculating the current world average.

Since our Δm result is lower than the current world average, it is interesting to compare results of different phase experiments after correcting the experiments with our value of Δm, which is of comparable precision to the current world average. The results of the individual corrections to ϕ_{+-} are listed in Table 31, and the previous measurements agree

Table 31. Our result for and previous best measurements of ϕ_{+-}. We have corrected the previously reported value of ϕ_{+-} for the change in the assumed Δm to our current result for Δm using the reported experimental dependences.

Experiment	ϕ_{+-} (degrees)	Internal Error (degrees)	Assumed Δm ($\times 10^{10}\ \hbar s^{-1}$)	$\Delta\phi_{+-}$ *for* $+1\%\ \delta\Delta m$ (degrees)	ϕ_{+-} (our Δm) (degrees)
C. Geweniger *et al.* [38]	49.4	1.0	0.5400	3.05	43.0
W.C.Carithers *et al.* [39]	45.5	2.8	0.5348	1.20	44.1
R.Carosi *et al.* [40]	46.9	1.6	0.5351	3.10	43.4
This result [37]	42.2	1.4	floated[a]	—	42.2

[a]See Section 9.3

very well with our own. When we now average the previous results with our own, we obtain a new world average of

$$\phi_{+-} = 42.8^\circ \pm 1.1^\circ, \tag{11.21}$$

which agrees very well with the superweak phase.

Note that no conclusions of this argument are significantly altered when we use the value of Δm which we obtained when extracting ϕ_{+-}[5].

We can again try and relate this measurement to other physical parameters of the kaon. Of particular interest is the difference between the masses of the K^0 and $\bar{K}^0$, which should be equal if CPT is a good symmetry of nature. Let us reconsider for a moment the quantity $\bar{\varepsilon}$ originally defined in Equation 1.11, which we now rewrite as

$$\begin{aligned} \bar{\varepsilon} &= \frac{\imath(M_{11} - M_{22}) + \frac{1}{2}(\Gamma_{11} - \Gamma_{22})}{2(\imath\Delta m - \frac{1}{2}(\Gamma_S - \Gamma_L))} \\ &= \imath e^{\imath\phi_\varepsilon} \frac{\imath(M_{11} - M_{22}) + \frac{1}{2}(\Gamma_{11} - \Gamma_{22})}{2\kappa\sqrt{2}\Delta m}, \end{aligned} \tag{11.22}$$

where $\kappa \equiv (1 + 1/2\Delta m\tau_S)^{\frac{1}{2}}/\sqrt{2} = 1.024$. Since we assumed $\mathbf{M}$ and $\mathbf{\Gamma}$ were hermitian, M_{11} and M_{22} are real, and if their difference is non-zero (that is, if the K^0 and $\bar{K}^0$ masses are not equal) then $\bar{\varepsilon}$ adds a term common to *both* η_{+-} and η_{00} that is 90° out of phase with the contribution from ε. If we suppose that the $I = 0$ $\pi\pi$ decays saturate $\mathbf{\Gamma}$ [66, 110], then

[5]In fact, that result was even slightly lower than our reported result (see Sections 9.2 and 9.3).

applying our current results for $|\eta_{00}/\eta_{+-}| \approx (1 - 3Re(\varepsilon'/\varepsilon))$ and for $\Delta\phi$ to the argument in Barmin *et al.* [19] implies one would not expect the second term to change the component of η parallel to ε beyond a limit of roughly 5%. For our purposes here, will therefore simply ignore this possible CPT-violating contribution.

Since the CPT-violating term from $\bar{\varepsilon}$ that arises from the mixing matrix is perpendicular to the CP-violating term, they form a right triangle with η along the hypotenuse, and we therefore have

$$\tan(\phi_{+-} - \phi_\epsilon) = \frac{1}{\varepsilon}\frac{m_{K^0} - m_{\bar{K}^0}}{2\sqrt{2}\kappa\Delta m}. \tag{11.23}$$

With our adjusted world average for ϕ_{+-} and our new value of the superweak phase, $\tan(\phi_{+-} - \phi_\epsilon) = -0.010 \pm 0.019$. Combining this result with the world average of $|\eta_{+-}|$ for $|\varepsilon|$, the world average value of the neutral kaon mass, and our new value for Δm of $(3.479 \pm 0.018) \times 10^{-12}$ MeV/c^2, we can limit

$$\left|\frac{m_{K^0} - m_{\bar{K}^0}}{m_{K^0}}\right| < 2.5 \times 10^{-18} \tag{11.24}$$

at the 95% confidence level. This limit is about a factor of 2 better than the current limit based on the current world average value of ϕ_{+-} [32], with the improvement coming mainly *from the shift in ϕ_{+-} towards the superweak phase.*

In all, the combination of our new Δm, $\Delta\phi$ and ϕ_{+-} measurements further improve the limits on CPT violation. We can soon expect further improvements when FNAL experiment E773 finishes its data analysis. This new experiment, using a similar configuration as E731, but now with two regenerators placed to enhance the sensitivity to interference, should obtain precision measurements of both $\Delta\phi$ and ϕ_{+-} at the 0.5° level.

11.4 Summary

The experimental work covered in this thesis has provided competitive new measurements of several fundamental parameters of the neutral kaon system. Regarding the primary purpose of E731, we have made the most precise measurement of $Re(\varepsilon'/\varepsilon)$ to date, with $Re(\varepsilon'/\varepsilon) = (7.4 \pm 5.9) \times 10^{-4}$. The precision achieved was almost a factor of two better than the original design goal of 10^{-3}! This result is statistically limited, and the prospects

for FNAL E832 (KTEV) to achieve a precision of 10^{-4} using the same basic technique are very good. This result is consistent with no direct CP violation in $K \rightarrow \pi\pi$ decay.

The loose, unbiased triggering and the understanding of the detector needed to attain this level of precision in $Re(\varepsilon'/\varepsilon)$ led to our ability to obtain very competitive measurements of other parameters in the kaon system. In particular, we have made new measurements of the K_S lifetime and the $K_L - K_S$ mass difference at the level of precision of the current world averages. Our new Δm measurements helps to resolve the long standing problem of the discrepancy between ϕ_{+-} and the expected superweak phase, and both our new $\Delta\phi$ and ϕ_{+-} measurements agree well with the expectations of CPT symmetry.

In short, this experiment has produced strong new bounds on both direct CP violation and CPT violation.

APPENDIX A

REGENERATION AND KAON PROPAGATION

As a neutral kaon passes through a material, the K^0 and $\bar{K}^0$ components interact strongly with the nuclei in the material. Since the strong interaction conserves strangeness, different reaction channels are going to be open for the K^0 and the $\bar{K}^0$, and hence lead to different total cross sections for the K^0 and the $\bar{K}^0$ on nucleons. This implies that the scattering amplitudes $f(\theta)$ and $\bar{f}(\theta)$ for the K^0 and $\bar{K}^0$ are different, and that the relative mixture of the K^0 and $\bar{K}^0$ states will change as a kaon passes through material.

If an initially pure K_L state enters a material, the outgoing state will become (*c.f.* Equation 1.9)

$$\begin{aligned} |\text{out}\rangle &= \frac{1}{\sqrt{2(1+|\varepsilon|^2)}}\left[(1+\varepsilon)f(\theta)\left|K^0\right\rangle - (1-\varepsilon)\bar{f}(\theta)\left|\bar{K}^0\right\rangle\right] \\ &= \frac{f(\theta)-\bar{f}(\theta)}{2}|K_S\rangle + \frac{f(\theta)+\bar{f}(\theta)}{2}|K_L\rangle\,. \end{aligned} \tag{A.1}$$

The difference in $f(\theta)$ and $\bar{f}(\theta)$ results in the "regeneration" of a K_S component in the initially pure K_L state. This phenomena was first predicted by Pais ad Piccioni [111], and detailed discussions of regeneration can be found in the literature [112, 95, 113]. Here we will briefly describe the different classes of regeneration, and then discuss the coherent propagation of kaons through matter.

A.1 Classes of Regeneration

Regeneration can generally be divided into three different categories: coherent regeneration, where the amplitudes for scattering at sites separated over macroscopic distances add coherently, diffractive regeneration, where the kaon is scattered elastically through a small angle, and inelastic regeneration, where the kaon imparts a significant portion of its energy to the scattering site.

Because the masses (and hence the Compton wavelengths) of the K_S and K_L are extremely close ($\Delta m/m_{K^0} < 10^{-14}$), the phase difference between an incident K_L and a forward scattered K_S will remain almost fixed over very large distances. For a given incident kaon, the phase shift introduced by scattering at different sites depend only on the scattering angle, so the amplitudes for forward scattering at different nuclear sites will add coherently. By examining the phases of an incident K_L and scattered K_S, it is simple to show [113] that the coherence length L_c is roughly

$$L_c \approx \frac{1}{\Delta m}\frac{p}{m_K}, \tag{A.2}$$

where p is the kaon momentum. For the kaon energies of this experiment, L_c is of order several meters. One can also show that coherence over macroscopic distances is rapidly lost as the scattering angle moves away from the forward direction. The limiting angle θ_c for coherence is roughly

$$\theta_c < \frac{\sqrt{2m_K\Delta m}}{p} \approx \frac{10^{-7}}{p[\mathrm{GeV}]}. \tag{A.3}$$

Beyond this limit, the phase shift introduced by the scattering becomes appreciable over the distance between nuclei, and coherence is lost.

Kaons scattering through angles larger than the coherent limit enter a diffractive regime. While coherence between the incident and scattered component is lost between different nuclei, the nucleus is small enough that the individual nucleons act coherently. Also, some coherence in the scatter from a *single* nucleus is maintained between the incoming K_L and the scattered K_S over measurable scattering angles. This leads to a discernable diffraction pattern (see, for example, reference [86]) for kaons passing through a thin regenerator, with the first minimum generally occurring for momentum transfers on the order of 100 MeV. For extended regenerators, multiple scattering tends to destroy the diffraction pattern.

In this experiment, diffractive regeneration was the principle source of background in the regenerator beam. The amplitude for diffractive regeneration grows with the atomic weight A of the regenerator material, which was one of our primary reasons for choosing a low Z material to form the bulk of the regenerator. The diffractive turn up in the p_t^2 distribution at low p_t^2 (Figure 48) and in the ring number distribution under the beam (Figure 68) was due primarily to the 1.25 cm lead piece at the end of the regenerator.

The final class of regeneration is inelastic regeneration, where the nucleus enters an excited state or breaks apart as a result of the scattering process. Since the kaon transfers a large portion of its energy in these processes, coherence between the incoming and scattered state is lost. The scattering angles can also be very large in an inelastic scatter, and the p_t^2 spectrum for this process is much shallower than for diffractive scattering. Often in an inelastic scatter, other particles are produced. By detecting these particles in the scintillator counters between the four boron carbide blocks comprising the regenerator, we were able to veto a large fraction of the inelastic scatters.

A.2 Coherent Kaon Propagation

Turning back to coherent regeneration, it is useful to examine how an arbitrary kaon state incident on a regenerator is modified by passage through the regenerator. In particular, we wish to know the form for the coherently propagated forward amplitude. Both the Monte Carlo simulation (Chapter 7 and the fitting procedures (Chapter 8) made use of this amplitude. This treatment roughly follows that of references [95] and [114].

As in optics, the basic parameter governing the behavior of a kaon passing through a material is given by the effective index of refraction (for the kaon) of that material. To a very good approximation, the indices of refraction for the K^0 and the $\bar{K}^0$ are in turn related to the forward elastic scattering amplitude by [95]

$$\begin{aligned} n &= 1 + (2\pi N/k^2) f(0) \\ \bar{n} &= 1 + (2\pi N/k^2) \bar{f}(0), \end{aligned} \tag{A.4}$$

where N is the density of scattering centers in the medium and k is the wave number of

the kaon in vacuum, $k = p/\hbar$. Simply restated, the wavenumbers for the K^0 and the $\bar{K}^0$ in the medium, respectively k_m and $\bar{k}_m$, become

$$\begin{aligned} k_m &\approx k + 2\pi N \frac{f(0)}{k} \\ \bar{k}_m &\approx k + 2\pi N \frac{\bar{f}(0)}{k}. \end{aligned} \tag{A.5}$$

From the definition of the wave number, it therefore follows that the modification to the kaon wave function Ψ because of interactions with the medium is given by

$$-i\frac{d}{dz}\Psi_{med} = \begin{pmatrix} 2\pi N f(0)/k & 0 \\ 0 & 2\pi N \bar{f}(0)/k \end{pmatrix} \Psi_{med}. \tag{A.6}$$

Since the distance z travelled by the kaon is related to the proper time by $z = \gamma\beta c\tau$, where βc is the kaon velocity and $\gamma = (1-\beta^2)^{-1/2}$, the above term changes our effective Hamiltonian (*c.f.* Equation 1.4) to

$$\mathbf{H}_{tot} = \mathbf{M} - i\mathbf{\Gamma} - \frac{2\pi\gamma\beta cN}{k} \begin{pmatrix} f(0) & 0 \\ 0 & \bar{f}(0) \end{pmatrix}. \tag{A.7}$$

As in Chapter 1, we wish to solve for the eigenvalues $\lambda_\pm$ and eigenstates $|K_\pm\rangle$ of the new Hamiltonian. A straightforward calculation yields the eigenvalues

$$\lambda_\pm = M - i\Gamma/2 - x/2 \pm \frac{1}{2}(-\Delta m - i\Delta\Gamma/2)\sqrt{1+r^2}, \tag{A.8}$$

where $\Delta\Gamma \equiv \Gamma_S - \Gamma_L$, and, as usual $\Delta m = m_L - m_S$. The parameters x and r are given in terms of the forward scattering amplitudes as

$$x = 2\pi\gamma\beta cN \frac{f(0) + \bar{f}(0)}{k}, \tag{A.9}$$

and

$$r = 2\pi\gamma\beta cN \frac{\left[f(0) - \bar{f}(0)\right]/k}{-\Delta m - i\Delta\Gamma/2}. \tag{A.10}$$

We will see that the quantity x governs the attenuation of the kaon passing through the material, while r governs regeneration.

So far, this discussion has made no assumption about CP-violation. It can be shown [115, 116] that CP-violating terms cancel to first order in the transmission matrix. Rather

than explicitly derive this result here, we will now assume CP conservation to simplify the remainder of the discussion. Under this assumption, we can then associate $M = (m_S + m_L)/2$, $\Gamma = (\Gamma_S + \Gamma_L)/2$, $M_{12} = -\Delta m/2$, and $\Gamma_{12} = \Delta\Gamma/2$.

The two eigenstates $|K_\pm\rangle$ which will be convenient to work with are the unnormalized states given by

$$|K_\pm\rangle = \left|K^0\right\rangle + (r \pm \sqrt{1+r^2})\left|\bar{K}^0\right\rangle. \tag{A.11}$$

By construction, the evolution of these states as a function of the kaon proper time τ is given by

$$K_\pm(\tau) = K_\pm(\tau = 0)e^{-\lambda_\pm \tau}. \tag{A.12}$$

The K^0 and $\bar{K}^0$ states can be written in terms of the propagation eigenstates $K_\pm$ as

$$\begin{aligned} \left|K^0\right\rangle &= \frac{1}{2\sqrt{1+r^2}}\left[(r+\sqrt{1+r^2})\,|K_-\rangle - (r-\sqrt{1+r^2})\,|K_+\rangle\right] \\ \left|\bar{K}^0\right\rangle &= \frac{1}{2\sqrt{1+r^2}}\left[|K_+\rangle - |K_-\rangle\right]. \end{aligned} \tag{A.13}$$

With these relationships in hand, we can now construct the transfer matrix $\mathbf{T}$ for the evolution of an arbitrary kaon state through a material of length $z = \gamma\beta c\tau$. After another straightforward calculation, one can show that an initial state (a_S, a_L), where a_S and a_L are the K_S and K_L amplitudes, evolves after a time τ to the state (a'_S, a'_L) given by

$$\begin{pmatrix} a'_S \\ a'_L \end{pmatrix} = e^{-\imath(m_S+m_L-Re x)\tau/2} e^{-(\Gamma_S+\Gamma_L+Imx)\tau/2} \begin{pmatrix} T_{SS} & T_{SL} \\ T_{LS} & T_{LL} \end{pmatrix} \begin{pmatrix} a_S \\ a_L \end{pmatrix}. \tag{A.14}$$

If we let

$$c(\tau) = \cosh[-\imath\tau(\Delta m + \imath(\Gamma_S - \Gamma_L)/2)\sqrt{1+r^2}/2] \tag{A.15}$$

and

$$s(\tau) = \sinh[-\imath\tau(\Delta m + \imath(\Gamma_S - \Gamma_L)/2)\sqrt{1+r^2}/2], \tag{A.16}$$

then the diagonal matrix elements are given by

$$T_{SS} = c(\tau) - \frac{s(\tau)}{\sqrt{1+r^2}}, \tag{A.17}$$

and

$$T_{LL} = c(\tau) + \frac{s(\tau)}{\sqrt{1+r^2}}. \tag{A.18}$$

These elements depend on the regeneration parameter r only at second order, which one would expect since any process taking, for example, K_L back to itself will be of the form

$K_L \xrightarrow{r} K_S \xrightarrow{r} K_L$, and this type of process is second order. The off-diagonal elements are equal and of the form

$$T_{SL} = T_{LS} = \frac{rs(\tau)}{\sqrt{1+r^2}}, \tag{A.19}$$

which is linearly in r and thus in $(f(0) - \bar{f}(0))/k$.

The prefactor in Equation A.14, shows that Imx results in attenuation of the kaon state beyond the vacuum decay rate. From the definition of x given above and the optical theorem,

$$\sigma_{tot} = \frac{4\pi}{k} Imf(0), \tag{A.20}$$

we have

$$\begin{aligned} \tau Imx &= (\gamma\beta c\tau) N 4\pi \left[Imf(0) + Im\bar{f}(0)\right]/2 \\ &= zN(\sigma_{tot} + \bar{\sigma}_{tot})/2, \end{aligned} \tag{A.21}$$

where σ_{tot} ($\bar{\sigma}_{tot}$) is the total K^0–nucleus ($\bar{K}^0$–nucleus) cross section for the material under consideration. The average interaction length for a kaon is simply

$$L_{av} = [N(\sigma_{tot} + \bar{\sigma}_{tot})/2)]^{-1}, \tag{A.22}$$

and therefore

$$\tau Imx = z/L_{av}, \tag{A.23}$$

which is the number of interaction lengths in the regenerator.

The standard discussions of regeneration in the literature generally consider a pure incoming K_L state. The regeneration amplitude ρ is then defined as the ratio of the regenerated outgoing K_S amplitude to the *outgoing* K_L amplitude. With $\Delta H \equiv -(\Delta m + i\Delta\Gamma/2)$, our result for the transfer matrix given above implies

$$\rho = r \frac{\sinh(\Delta H\sqrt{1+r^2}\tau/2)}{\sqrt{1+r^2}\cosh(\Delta H\sqrt{1+r^2}\tau/2) + \sinh(\Delta H\sqrt{1+r^2}\tau/2)}. \tag{A.24}$$

Keeping terms to first order in r, substituting the definition of r with $z = \gamma\beta c\tau$, and taking $\Delta\Gamma = \Gamma_S - \Gamma_L \approx \Gamma_S$, ρ becomes

$$\rho = -iz\pi N \frac{f(0) - \bar{f}(0)}{k} \frac{1 - e^{i\Delta m\tau} e^{-\Gamma_S\tau/2}}{i\Delta m - \Gamma_S/2}, \tag{A.25}$$

which is the standard thick regenerator approximation. With the regenerator and kaon energies in this experiment, the r^2 corrections to this approximation are roughly of order

1%. In calculating the regeneration amplitudes both in fitting and in the Monte Carlo simulation, the more exact transfer matrix calculation was used.

APPENDIX B

KINEMATICS WITH A MISSING PARTICLE

Several of the analyses in this experiment made use of modes where one particle in the final state of a decay was either missing or ignored. The Ke3 analyses had two examples of this: the Ke3 mode itself has a neutrino in the final state which cannot be detected, and the $K_L \to \pi^+\pi^-\pi^0$ with the π^0 missing is one of the largest backgrounds in the Ke3 sample. The purpose of this appendix is to present a concise review of the kinematics of this situation and to define the kinematic quantities used to isolate signal from background.

In the general situation, we have a particle of mass M and momentum $P = (E, \vec{P})$ which will decay into a set of particles which can be reconstructed and one particle which cannot. Let m_u and $p_u = (E_u, \vec{p}_u)$ be the mass and momentum of the unobserved particle. All of the reconstructed particles will be treated as a single system with an observed mass m_o and an observed momentum $p_o = (E_o, \vec{p}_o)$. All of the quantities with a superscript star $(*)$ will refer to quantities in the center of mass of the decay particle.

The first basic requirement is, of course, that

$$m_o < M - m_u. \tag{B.1}$$

Also of interest are the center of mass energy and the magnitude of the center of mass momentum of the unobserved particle, as they will lead to another useful kinematic variable. By combining

$$P \cdot P = M^2 = m_o^2 + m_u^2 + 2(E_o E_u - \vec{p}_o \cdot \vec{p}_u) \tag{B.2}$$

and

$$P \cdot p_u = M E_u^* = m_u^2 + E_o E_u - \vec{p}_o \cdot \vec{p}_u \tag{B.3}$$

we trivially obtain

$$\begin{aligned} E_u^* &= \frac{M^2 + m_o^2 - m_u^2}{2M} \\ p_u^{*2} &= \frac{\frac{1}{4}(M^2 - m_o^2 - m_u^2)^2 - m_o^2 m_u^2}{M^2}. \end{aligned} \tag{B.4}$$

In a fixed target experiment, generally one can get a very good measurement of the direction vector $\hat{D}$ of the decaying particle by setting it along the line of sight from the production target to the measured decay vertex. The momentum of the observed system this direction vector determine the transverse momentum $\vec{p}_t$ of the missing particle. The kinematic test variable of interest is the center of mass momentum of the missing particle along the direction of the decay particle, or rather its square, $p_{u_l}^{*2}$, given by

$$\begin{aligned} p_{u_\parallel}^{*2} &= p_u^{*2} - p_t^2 \\ &= \frac{\frac{1}{4}(M^2 - m_o^2 - m_u^2)^2 - m_o^2 m_u^2}{M^2} - p_t^2 \\ &= p_{o_\parallel}^{*2} \end{aligned} \tag{B.5}$$

Neglecting resolution effects from smearing, this quantity should be positive if we have correctly identified the decay.

Although we have found the magnitude of the longitudinal component of the momentum in the decay rest frame, we do not know whether the longitudinal momentum for the unobserved particle was aligned parallel or antiparallel to the decay particles flight path. This leads to a two-fold ambiguity in reconstructing the total momentum of the decay particle in the lab frame. To examine this, consider the product $P \cdot p_o$

$$\begin{aligned} P \cdot p_o = m E_o^* &= E E_o - \vec{P} \cdot \vec{p}_o \\ &\equiv E E_o - P p_{o_\parallel}. \end{aligned} \tag{B.6}$$

Regrouping and squaring, we have

$$(E_o^2 - p_{o_\parallel}^2) P^2 - 2M E_o^* p_{o_\parallel} P + M^2 (E_o^2 - E_o^{*2}) = 0. \tag{B.7}$$

Using the more manifestly invariant form $m_o^2 + p_t^2$ for $E_o^2 - p_{o_\parallel}^2$ and solving for P, we obtain the simple expression for the boost

$$\gamma\beta = \frac{P}{M} = \frac{E_o^* p_{o_\parallel} \pm E_o p_{o_\parallel}^*}{m_o^2 + p_t^2}. \tag{B.8}$$

We see that an invariant scaling of our kinematic variable in Equation B.6 occurs naturally in B.8. This rescaled quantity k_{+-0}

$$k_{+-0} = \frac{p_{o_\parallel}^{*2}}{m_o^2 + p_t^2} \tag{B.9}$$

has often been used rather than the longitudinal momentum, particularly in this and other experiments when trying to remove background arising from $K_L \to \pi^+\pi^-\pi^0$ decays. In the literature [117], a variable "pp0kin" has been quoted which is simply $4M_K^2 k_{+-0}$.

APPENDIX C

THE ACCEPTANCE AND ε'/ε

In this appendix, we will discuss some of the acceptance issues related to our measurement of $Re(\varepsilon'/\varepsilon)$. The most important issue is the relationship of the measured value to the "raw" ratio of the number of events collected in each of the modes, the detector acceptance, and the length of the fiducial decay volume in each of the modes. We will also discuss some of the issues involved in using the average acceptance for a long z bin to correct the data in our fits.

C.1 Acceptance and the Raw Double Ratio

If one naively compares the raw double ratio of events in the charged and neutral modes (after background subtraction and primary K_S corrections), one has

$$R_{raw} = \frac{N_{v+-}/N_{r+-}}{N_{v00}/N_{r00}} = \frac{327,006/1,060,687}{410043/800037} = 0.6015. \qquad \text{(C.1)}$$

The double ratio of decay rates which corresponds to the central value value of $Re(\varepsilon'/\varepsilon)$ which we measure, on the other hand, is 1.0044. On the surface, this appears to be a large correction, though calling this difference an "acceptance correction" is incorrect. If we simply calculate the ratio of the of K_L decays[1] for 70 GeV/c kaons in the vacuum beam in the charged mode (a 27 m fiducial volume) and in the neutral mode (a 42 m fiducial volume), we get $\int_0^{27}\exp[-z/\gamma\beta c\tau_L]/\int_0^{42}\exp[-z/\gamma\beta c\tau_L] \approx 64.5\%$. Already we can see that

[1] Ignoring the branching fractions, which cancel in the double ratio.

the bulk of the difference between the raw double ratio of events and the desired double ratio of decay rates arises from the difference in the different length of the fiducial volume for the two decay modes, and not from the detector acceptance. It is true that we need to *understand* our acceptance in order to use different z regions, but from the Figure 109, it is clear that we do.

In order to quantify the effect of our detector acceptance, of the difference in the length of the decay volumes, and of the presence of the lead sheet in part of data sample more accurately, we can examine the true number and observed number of kaon "decays" in our Monte Carlo simulation samples. If our detector had perfect acceptance and no lead sheet, the convolution of our kaon momentum spectrum with the kaon decay rate in the two beams would have resulted in a double ratio of decays collected in the two modes (using the 27 m $\pi^+\pi^-$ decay volume and the 52 m $2\pi^0$ decay volume) of

$$R_a = 0.6887. \tag{C.2}$$

As expected, this is the dominant effect in our observed ratio R_{raw}. Any bias in this correction will come simply from the value of τ_L used in the fitting procedures, and as we have seen in Table 18, any such bias is very small.

If we now turn on the acceptance, and predict the raw double ratio assuming we had performed the experiment without the lead sheet, we would have

$$R_b = 0.6267 = 0.91 R_a. \tag{C.3}$$

Hence the correction due to the geometrical acceptance is only 9%. Comparing R_b to R_{raw} in C.1, we see that the presence of the lead sheet in part of the data changes the observed ratio by only 4% of itself. The correction for lead sheet depends mainly upon the photon conversion probability, which we measured adequately with the $3\pi^0$ sample.

C.2 Acceptance and Extended Z Bins

The second acceptance issue that has often been raised is the possibility of a bias in the average acceptance calculation for large (27 m and 42 m) z bins. The fear is, for example, that a finite ε' would lead to a nonnegligible bias in the weighting that an upstream decay

receives relative to a downstream decay. The bias would affect charged and neutral modes differently, leading to a bias in the measured value of $Re(\varepsilon'/\varepsilon)$.

We can address this issue in several ways. First of all, we can modify the prediction function to treat the z calculation analogously to the momentum calculation. That is, we subdivide the large z bin into n_z smaller bins of width $\delta z = \Delta z/n_z$, and calculate the contribution to the total observed rate from each of these bins. For example, the regenerator beam z integration in Equation 8.31,

$$I_z = \bar{\varepsilon}_{r_{i_k}j} \int_{z_j}^{z_j+\Delta z} r_r(p_{i_k}, z)dz \tag{C.4}$$

becomes the sum of integrals

$$I_z = \sum_{m=1}^{n_z} \bar{\varepsilon}_{r_{i_k}jm} \int_{z_j+(m-1)\delta z}^{z_j+m\delta z} r_r(p_{i_k}, z)dz. \tag{C.5}$$

The only effects not incorporated in this method come from the small change in event smearing. Almost all events which smear into a given pz bin, however, come from the neighbouring pz bins, and hence a small change in the physics parameters has negligible effect on the fraction of events smearing into a bin. In this formulation the acceptance of each small pz is effectively reweighted for each new set of the test physics parameters in the decay rate $r(p, z)$ calculated by the prediction functional.

To compare the results of this fitting method with our standard (much faster) procedure, we need to compare results using all of the statistics, including events which have smeared upstream of the regenerator. In the regenerator beam, therefore, the z region upstream of 125m was treated as a single z region, independent of the width δz used downstream of 125 m. Recall that the downstream regenerator edge is located at $z_{reg} = 123.55$ m. We have compared this method using values of δz ranging from tens of meters down to 0.5 m. The variations in the results obtained for $Re(\varepsilon'/\varepsilon)$ were less than 10^{-5}.

The entire reconstruction and fitting program have also been run through extensive Monte Carlo tests, including fits to samples of Monte Carlo that have been generated using different values of $Re(\varepsilon'/\varepsilon)$. The fits reproduced the expected values for $Re(\varepsilon'/\varepsilon)$ and regeneration parameters very accurately.

This insensitivity results because both the numerator (accepted Monte Carlo decays) and denominator (generated Monte Carlo decays) in Equation 8.29 are equally affected

by a bias as a function of z introduced by a *kaon decay* or *regeneration* parameter in the Monte Carlo[2]. This property, and the fact that the acceptance does not change very rapidly as a function of z leads to a large cancellation of a "bias" of this sort in the acceptance calculation. This is not the case if there is a bias because of a *detector* acceptance issue, which will only affect the numerator in Equation 8.29.

[2]We are in particular talking about small deviations in the decay rates since the uncertainty in most of the parameters is of the order of 1% or better.

REFERENCES

[1] A.A. Michelson and E.W. Morley, *The American Journal of Science* **XXXIV**, 333 (1887).

[2] W. Pauli, *Niels Bohr and the Development of Physics*, Pergamon Press, Elmsford, N.Y., 1955.

[3] J. Schwinger, *Phys. Rev.* **91**, 713 (1953).

[4] J. Schwinger, *Phys. Rev.* **94**, 1362 (1954).

[5] G. Lüders, *Kgl. Danske Videnskab Selskab. Mat. Fys. Medd.* **28**, 1 (1954).

[6] T.D. Lee and C.S. Wu, *Ann. Rev. Nuc. Sci.* **15**, 381 (1965).

[7] T.D. Lee and C.N. Yang, *Phys. Rev.* **104**, 254 (1956).

[8] C.S. Wu et al., *Phys. Rev.* **105**, 1413 (1957).

[9] R.L. Garwin, L.M. Lederman, and M. Weinrich, *Phys. Rev.* **105**, 1415 (1957).

[10] J.I. Friedman and V.L. Telegdi, *Phys. Rev.* **105**, 1681 (1957).

[11] S.S. Gerstein and Y.B. Zeldovich, *JETP* **2**, 576 (1956).

[12] R.P. Feynman and M. Gell-Mann, *Phys. Rev.* **109**, 193 (1958).

[13] E.C.G. Sudarshan and R. Marshak, *Phys. Rev.* **109**, 1860 (1958).

[14] J.J. Sakurai, *Nuovo Cim.* **7**, 649 (1958).

[15] L. Landau, *JETP* **5**, 336 (1957).

[16] J.H. Christenson, J.W. Cronin, V.L. Fitch, and R. Turlay, *Phys. Rev. Lett.* **13**, 138 (1964).

[17] T.D. Lee and C.S. Wu, *Ann. Rev. Nuc. Sci.* **16**, 511 (1966).

[18] L. Wolfenstein, *Nuovo Cim.* **63 A**, 269 (1969).

[19] V.V. Barmin et al., *Nucl. Phys.* **B247**, 293 (1984).

[20] J.W. Cronin, *Acta Phys. Pol. B* **15**, 419 (1984).

[21] R.G. Sachs, *The Physics of Time Reversal*, The University of Chicago Press, Chicago, 1987.

[22] K. Kleinknecht, in *CP Violation*, edited by C. Jarlskog, (World Scientific, Singapore, 1989), page 41.

[23] B. Winstein and L. Wolfenstein, Preprint EFI 92-55, The Enrico Fermi Institute, 1992, (to be published in Rev. Mod. Phys., Oct., 1993).

[24] M. Gell-Mann and A. Pais, *Phys. Rev.* **97**, 1387 (1955).

[25] T.D. Lee, R. Oehme, and C.N. Yang, *Phys. Rev.* **106**, 340 (1957).

[26] T.T. Wu and C.N. Yang, *Phys. Rev. Lett.* **13**, 380 (1964).

[27] R.G. Sachs, *Ann. Phys.* **22**, 239 (1963).

[28] J.S. Bell and J. Steinberger, in *Proceedings of the Oxford International Conference on Elementary Particles, 1965*, edited by A.E. Taylor T.R. Walsh and B. Southworth, (Rutherford Laboratory, Chilton, England, 1966), page 195.

[29] K. Lande et al., *Phys. Rev.* **103**, 1901 (1956).

[30] V.L. Fitch, R.F. Roth, J.S. Russ, and W. Vernon, *Phys. Rev. Lett.* **15**, 73 (1965).

[31] B. Winstein, private communication.

[32] Particle Data Group, K. Hikasa, et al., *Phys. Rev. D* **45**, 1 (1992).

[33] C. Geweniger et al., *Phys. Lett.* **52B**, 108 (1974).

[34] M. Cullen et al., *Phys. Lett.* **32B**, 523 (1970).

[35] S. Gjesdal et al., *Phys. Lett.* **52B**, 113 (1974).

[36] R.G. Sachs and S.B. Treiman, *Phys. Rev. Lett.* **8**, 137 (1962).

[37] L.K. Gibbons et al., *Phys. Rev. Lett.* **70**, 1199 (1993).

[38] C. Geweniger et al., *Phys. Lett.* **52B**, 119 (1974).

[39] W.C. Carithers et al., *Phys. Rev. Lett.* **34**, 1244 (1975).

[40] R. Carosi et al., *Phys. Lett.* **B237**, 303 (1990).

[41] M. Karlsson et al., *Phys. Rev. Lett.* **64**, 2976 (1990).

[42] C.O. Dib and B. Guberina, *Phys. Lett.* **4B255**, 113 (1991).

[43] L.K. Gibbons et al., *Phys. Rev. Lett.* **61**, 2661 (1988).

[44] V. Papadimitriou et al., *Phys. Rev. Lett.* **63**, 28 (1989).

[45] A.R. Barker et al., *Phys. Rev. D* **41**, 3546 (1990).

[46] V. Papadimitriou et al., *Phys. Rev. D* **44**, R573 (1991).

[47] G.E. Graham et al., *Phys. Lett.* **B295**, 169 (1992).

[48] W. Ochs, Munich Preprint MPI-Ph/Ph91-35, (to be published in πN Newsletter), 1991.

[49] H. Burkhardt et al., *Phys. Lett.* **B206**, 169 (1988).

[50] J.R. Patterson et al., *Phys. Rev. Lett.* **64**, 1491 (1990).

[51] L.K. Gibbons et al., *Phys. Rev. Lett.* **70**, 1203 (1993).

[52] J.K. Black et al., *Phys. Rev. Lett.* **54**, 1628 (1985).

[53] R.H. Bernstein et al., *Phys. Rev. Lett.* **54**, 1631 (1985).

[54] M. Woods et al., *Phys. Rev. Lett.* **60**, 1695 (1988).

[55] M. Kobayashi and A.I. Sanda, *Phys. Rev. Lett.* **69**, 3139 (1992).

[56] V.A. Kostelecký and Robertus Potting, Preprint IUHET 236, Indiana University, 1992.

[57] S.B. Treiman and R.G. Sachs, *Phys Rev.* **103**, 1545 (1956).

[58] L. Wolfenstein, *Phys. Rev. Lett.* **13**, 562 (1964).

[59] J.L. Rosner, in *B Decays*, edited by S.L. Stone, (World Scientific, Singapore, 1990), page 312.

[60] M. B. Wise, in *Proceedings of the Banff Summer Institute* (Banff, Alberta,1988), edited by A.N. Kamal and F.C. Khanna, (World Scientific, Singapore, 1989), page 124.

[61] G. Buchalla, A.J. Buras, and M.K. Harlander, *Nucl. Phys.* **B337**, 313 (1990).

[62] Jarlskog, in *CP Violation*, edited by C. Jarlskog, (World Scientific, Singapore, 1989), page 3.

[63] N. Cabibbo, *Phys. Rev. Lett.* **10**, 531 (1963).

[64] M. Kobayashi and Maskawa T., *Prog. Theor. Phys.* **49**, 652 (1973).

[65] L. Wolfenstein, *Phys. Rev. Lett.* **51**, 1945 (1983).

[66] R.D. Peccei, Preprint UCLA/93/TEP/19, University of California, Los Angeles, 1993.

[67] G. Buchalla, A.J. Buras, and M.K. Harlander, *Nucl. Phys. B (Proc. Suppl.)* **26**, 31 (1992).

[68] T. Inami and C.S. Lim, *Prog. Theor. Phys.* **65**, 297 (1981).

[69] F.J. Gilman and M.B. Wise, *Phys. Rev.* **D27**, 1128 (1983).

[70] J. Bartelt et al., Preprint CLNS-93-1207, The CLEO Collaboration, 1993, (submitted to Phys. Rev. Lett.).

[71] H. Albrecht, *Z. Phys.* **C55**, 357 (1992).

[72] J. Bartelt et al., paper submitted to the EPS conference, Marseille, July 1993.

[73] J.M. Flynn and L. Randall, *Phys. Lett.* **224B**, 221 (1989).

[74] J.R. Patterson, PhD thesis (The University of Chicago, December, 1990).

[75] V. Papadimitriou, PhD thesis (The University of Chicago, December, 1990).

[76] M. Karlsson, PhD thesis (Princeton University, August, 1990).

[77] Frederick J. Gilman, *Phys. Rev.* **171**, 1453 (1968).

[78] J. Roehrig et al., *Phys. Rev. Lett.* **38**, 1116 (1977).

[79] W.R. Mozlon et al., *Phys. Rev. Lett.* **41**, 1213 (1978).

[80] A. Gsponer et al., *Phys. Rev. Lett.* **42**, 13 (1979).

[81] M.B.Woods, PhD thesis (The University of Chicago, June, 1988).

[82] M. Asner, *Nucl. Instr. and Meth.* **A291**, 577 (1990).

[83] E. Longo and I. Sestili, *Nucl. Instr. and Meth.* **128**, 283 (1987).

[84] W.R. Nelson, H. Hirayama, and W.O. Rogers, The egs4 code system, Preprint SLAC-Report-265, Stanford Linear Accelerator Center, 1985.

[85] E.J. Ramberg et al., *Phys. Rev. Lett.* **70**, 2525 (1993).

[86] W.R. Molzon, PhD thesis (The University of Chicago, March, 1979).

[87] G.J. Bock et al., *Phys. Rev. Lett.* **42**, 350 (1979).

[88] A.J. Malensek, Preprint FN-341, Fermi National Accelerator Laboratory, October 1981.

[89] R.A. Briere, private communication.

[90] A. Schiz et al., *Phys. Rev. D* **21**, 3010 (1980).

[91] J.H. Hubbell, H.A. Gimm, and I. Øverbø, *J. Phys. Chem. Ref. Data* **9**, 1023 (1980).

[92] B. Rossi, *High Energy Particles*, Prentice-Hall, Inc., Englewood Cliffs, NJ, 1952.

[93] A. Gsponer et al., *Phys. Rev. Lett.* **42**, 9 (1979).

[94] R.J. Glauber and V. Franco, *Phys. Rev. Lett.* **156**, 1685 (1967).

[95] T.D. Lee and C.S. Wu, *Ann. Rev. Nuc. Sci.* **16**, 511 (1966).

[96] V.D. Barger and D.B. Cline, *Phenomenological Theories of High Energy Scattering*, W.A. Benjamin, Inc., New York, 1969.

[97] R.J.N. Phillips, in *Proceedings 1966 International School of Physics "Ettore Majorana" at Erice*, edited by A. Zichichi, (Academic Press, New York, 1966), page 268.

[98] J. Roehrig, PhD thesis (The University of Chicago, December, 1977).

[99] E.C. Swallow, in *The Vancouver Meeting, Particles and Fields '91*, edited by D. Axen, D. Bryman, and M. Comyn, (World Scientific, Singapore, 1992), page 581.

[100] D'Huart Industrie S.A., Certificat d'analyse chimique, Coulee No. 873, 1976.

[101] A.C. Schaffer, Talk presented at 1991 Division of Particles and Fields meeting, Vancouver, 1991.

[102] D. Saltzberg, private communication.

[103] M. Ciuchini, E. Franco, G. Martinelli, and L. Reina, *Phys. Lett.* **301B**, 263 (1993).

[104] A.J. Buras, M. Jamin, and M.E. Lautenbacher, Preprint TUM-T31-35/93, Technische Universität München, 1993.

[105] H. Burkhardt, *Nucl. Instr. and Meth.* **A268**, 116 (1988).

[106] J. Skjeggestad et al., *Nucl. Phys.* **B48**, 343 (1972).

[107] C. Geweniger et al., *Phys. Lett.* **48B**, 487 (1974).

[108] S.H. Aronson et al., *Nuovo Cim.* **32A**, 236 (1976).

[109] N. Grossman et al., *Phys. Rev. Lett.* **59**, 18 (1987).

[110] J.W. Cronin, *Rev. Mod. Phys.* **53**, 373 (1981).

[111] A. Pais and O. Piccioni, *Phys. Rev.* **100**, 1487 (1955).

[112] M.L. Good, *Phys. Rev.* **106**, 591 (1957).

[113] K. Kleinknecht, *Fort. Phys.* **21**, 57 (1973).

[114] H. Yamamoto, Internal Memo, 1987.

[115] R.G. Sachs, *Phys. Rev.* **129**, 2280 (1963).

[116] R.A. Briere and L.H. Orr, *Phys. Rev. D* **40**, 2269 (1989).

[117] A. Carroll et al., *Phys. Rev. Lett.* **44**, 529 (1980).